The HKIE Geotechnical Division 41st Annual Seminar 2021

Adapt to Challenges, Create to Thrive

THE HONG KONG INSTITUTION OF ENGINEERS
香港工程師學會
Geotechnical Division
岩土分部

Co-organiser

HKGES 香港岩土工程學會 Since 2003

IEM The Institution of Engineers, Malaysia

中國工程師學會 Chinese Institute of Engineers

Supporting Organisations

HKIE THE HONG KONG INSTITUTION OF ENGINEERS 香港工程師學會 Civil Division 土木分部

HKIE THE HONG KONG INSTITUTION OF ENGINEERS 香港工程師學會 Structural Division 結構分部

atkinsglobal.com
snclavalin.com

ATKINS
Member of the SNC-Lavalin Group

INNOVATION TO BRING CLARITY TO COMPLEXITY

At Atkins, we pride ourselves to be at the forefront of innovative solutions to bring clarity to complex projects. Our strong integrated domain expertise, international and local experiences, further strengthened by the use of data and digital technology, allow us to successfully navigate complexity to create greater outcomes for our clients and society.

Hong Kong International Airport Three-Runway System

Hong Kong Link Road

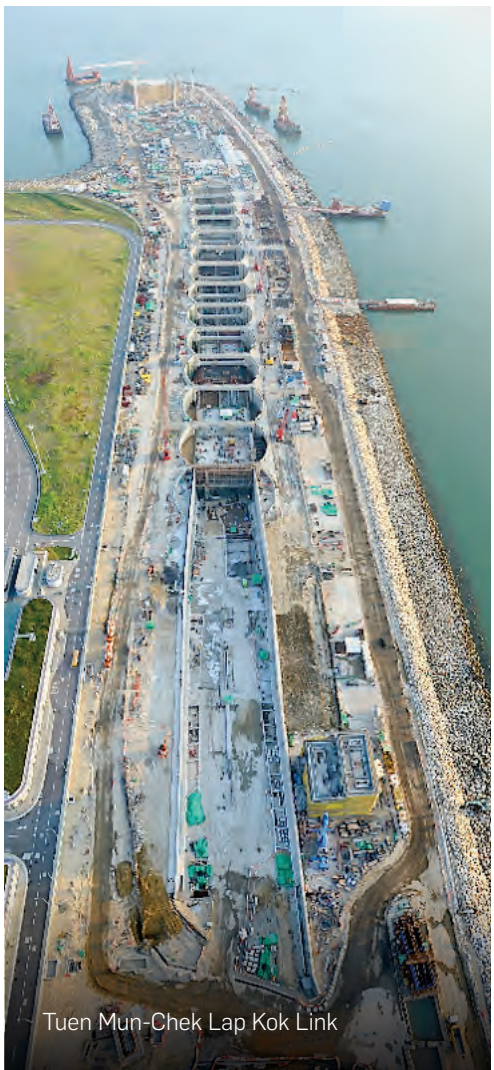

Tuen Mun-Chek Lap Kok Link

Central Reclamation Phase III

HY/2009/15 Central Wan Chai Bypass

AECOM

TOGETHER, WE THRIVE.

At AECOM, we partner with clients to solve the world's most complex challenges and build legacies for generations to come.

Relocation of Sha Tin Sewage Treatment Works to Caverns

aecom.com

ARUP

Delivering offshore infrastructure innovation

From optimising business models to designing innovative foundations, Arup combines its wide range of engineering expertise with digital and analytical insight to help our clients deliver successful offshore wind projects that power a sustainable future.

www.arup.com

aurecon

Bringing ideas to life

REIMAGINE ENGINEERING FOR A BETTER FUTURE

As a leading engineering, design and advisory company that knows Asia well, we bring vital geotechnical experience, technical capability and design expertise to create clever, innovative solutions to solve for Hong Kong's most complex challenges.

At Aurecon, we imagine a better tomorrow, bring ideas to life and design solutions engineered for life.

aurecongroup.com

C M WONG & ASSOCIATES LTD
黃志明建築工程師有限公司

11/F Universal Trade Centre
3-5A Arbuthnot Road, Hong Kong
Tel: (852)2522-1068
Fax: (852)2526-3111
www.cmwal.com
cmwal@cmwal.com

C M Wong & Associates Ltd is a Hong Kong based consulting engineer in providing a full range of professional services including feasibility studies, planning, design and supervision in relation to building and infrastructure projects. Our clients include various Hong Kong Government departments, institutions and major developers.

We adopt a flexible approach to suit clients' needs. We are also renowned for providing innovative engineering solutions for challenging projects especially for those with difficult ground conditions.

ISO 9001 : 2015
Certificate No.: CC 801

ISO 14001 : 2015
Certificate No.: CC 5408

ISO 45001 : 2018
Certificate No.: CC 7033

中国地质工程集团有限公司
CHINA GEO-ENGINEERING CORPORATION



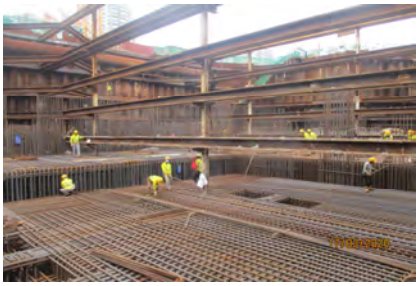


我們的主要業務包括：
Our Business includes:

- 基礎工程
  Foundation Works
- 斜坡及擋土牆長遠防治山泥傾瀉工程
  Construction of Landslip Preventive and Mitigation Works to Slopes and Retaining Walls
- 道路及渠務工程
  Roads and Drainage
- 水務工程
  Waterworks
- 地盤平整工程
  Site Formation








香 港 灣 仔 港 灣 道 30 號 新 鴻 基 中 心 24 樓 2421 - 25 室
Rm. 2421-25, 24/F., Sun Hung Kai Centre, 30 Harbour Road, Wanchai, Hong Kong
TEL : (852) 2511 9001 FAX : (852) 2580 0697

ESA 工程顧問有限公司
CONSULTING ENGINEERS LTD

ESA Consulting Engineers Ltd. (ESA) is a multi-disciplinary consulting firm with proven expertise in civil, geotechnical and structural engineering.

Our vision is to provide economical engineering services and innovative, practical solutions of the highest quality.

Delivering Excellence.
Building Your Visions.
Creating Reality.

http://www.esa.com.hk/
mail@esa.com.hk

FUGRO

UNLOCKING **INSIGHTS** FROM **GEO-DATA** FOR A **SAFE** AND **LIVEABLE** WORLD

For more information visit
fugro.com

Gammon

At Gammon, we are committed to pushing the boundaries further in our business by way of innovation and technological applications to reach the ultimate goal of integrated digital project delivery, consolidating processes from design to post-construction using advanced information communications technology and other smart technologies.

安全 SAFETY

卓越 EXCELLENCE

誠信 INTEGRITY

www.gammonconstruction.com


MTR
caring for life's journeys
Connecting People To New Possibilities Around The World
All across the world, cities are expanding. People need better connections to access new places. MTR makes it happen in Hong Kong, the United Kingdom, Sweden, Australia, as well as in the Mainland of China and Macao.
With our sophisticated approach of integrating railways and urban development, we continue to grow and connect vibrant communities for a better future.
For more details

ARCADIS

Maximizing Impact

Today, in an ever-changing world, that purpose has never been more important. Developing scalable solutions that are sustainable and digitally-enabled is the best way we can continue addressing our biggest societal challenges. Through our projects, in our communities and in our work for clients, we enhance human experiences and foster personal, societal, and business growth.

Our design and engineering consultancy services are characterized by our sense of responsibility and acute focus on quality. We strive to use our understanding and expertise to achieve optimum social and economic outcomes that are in line with our clients' and stakeholders' priorities.

Connect with us : +852 2911 2000 : ArcadisDE-HK@arcadis.com : www.arcadis.com/asia Arcadis. Improving quality of life.

World Record

A 10000 kJ Rockfall Barrier

FONG ON GEOTECHNICS LTD

GEOBRUGG®
BRUGG
Safety is our nature

RXE - 10000:
This rockfall barrier in the RXE series sets new standards with its maximum capacity of 10000kJ. First and only in this energy class, this certified system provides an economical alternative to the massive protective check dam.

Marketing Manager:
Thomas Mok
Tel: 2893 0444
Mobile: 9887 0410
Email: fog@fong-on.com.hk

CE European Technical Approval
www.eota.eu

LAMBETH

Distinctly Different


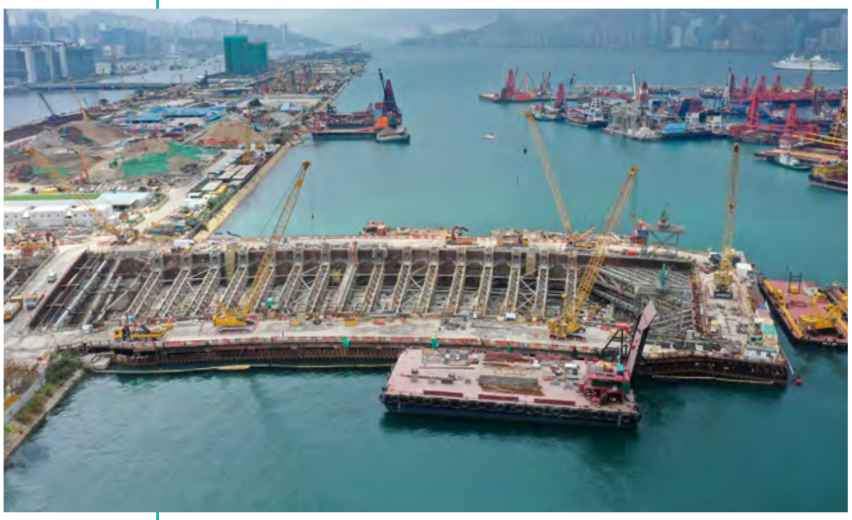
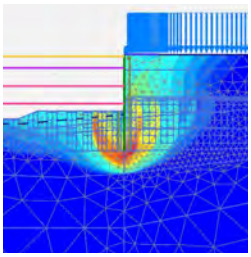

Lambeth brings together the diverse experience of operations, planning,commercial and design professionals – ensures it remains at the forefront of new techniques and new thinking in Geotechnical Engineering Excellence. We set the standard in innovation and technological for Quality Assurance in different disciplines – foundation, geotechnical, environmental, civil, buildings and safety.

A member of the Gammon Group

22/F, Tower 1, The Quayside, 77 Hoi Bun Road, Kwun Tong, Kowloon, Hong Kong Tel: 2516 8790 Fax: 2516 6352


Inspiration with Excellence

MANNINGS Consultants

Mannings (Asia) Consultants Limited
Wholly owned subsidiary of Boltek Holdings Limited (HKEX Stock Code 8601)
5/F, Winning Commercial Bldg., 46-48 Hillwood Rd., Tsim Sha Tsui, Kln., Hong Kong
Tel : (+852) 3168 2028 Fax: (+852) 3168 2022

http://www.manningsasia.com

your FIRSTCHOICE
Innovative • High-quality • Value-added Solutions

MEINHARDT
Consulting Engineers . Planners . Managers

Over 50 Offices Worldwide
www.meinhardtgroup.com
www.meinhardt-china.com
mcehk@meinhardt.com.hk

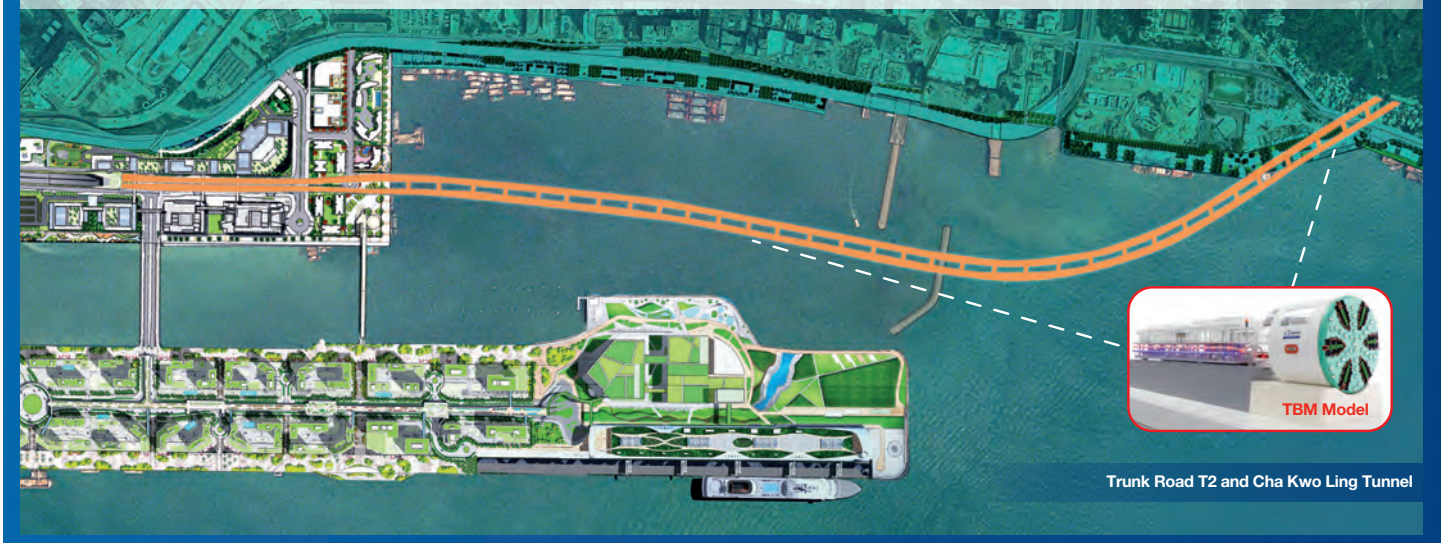

Trunk Road T2 and Cha Kwo Ling Tunnel


Three Runway System Project


Tung Chung New Town Reclamation


Cross Bay Link

Proceedings of the 41st Annual Seminar
Geotechnical Division, The Hong Kong Institution of Engineers

Adapt to Challenges, Create to Thrive

18 May 2021
Hong Kong

Jointly organised by:
Geotechnical Division, The Hong Kong Institution of Engineers
The Hong Kong Geotechnical Society

Supported by:
The Institution of Engineers, Malaysia
Chinese Institute of Engineers
Civil & Structural Divisions, The Hong Kong Institution of Engineers

Soft copy available on the HKIE Geotechnical Division's website
http://mobile.hkieged.org/download/as/AS2021.pdf

ORGANISING COMMITTEE

Chairman
Ir Dr Gavin Toh

Members
Ir Derek Kwok
Ir Y C Lam
Ir Dr S W Lee
Ir Alex Leung
Ir Becky Lui
Ir Grace Tam
Ir Terence Yau
Ir Jack Yiu

Any opinions, findings, conclusions, or recommendations expressed in this material do not reflect the views of the Hong Kong Institution of Engineers or the Hong Kong Geotechnical Society

Published by:
Geotechnical Division
The Hong Kong Institution of Engineers
9/F., Island Beverley, 1 Great George Street, Causeway Bay, Hong Kong
Tel: 2895 4446 Fax: 2577 7791

Prepared in Hong Kong

FOREWORD

I would like to welcome all distinguished guests, speakers, academics, and geotechnical professionals to the 41st HKIE Geotechnical Division Annual Seminar. This year's seminar is held together with the Tripartite Seminar, jointly with CIE and IEM, and the HKGES Bright Spark Lecture 2021.

The 2021 Annual Seminar is titled "Adapt to Challenges, Create to Thrive". In the last four decades we have seen geotechnical engineers play an important part in the growth and development of Hong Kong. There has been notable advancement and innovative engineering in different areas: safety control and management of HK's sloping terrain; deep excavation in urban areas; larger and deeper tunnels and caverns for transportation, storage and treatment works; deep foundations with complex geology and on steep terrain for housing; and reclamations for high-rise buildings and infrastructure development. We have also seen progress in soil modelling and computation with the support of sound site investigation, refined laboratory testing and real-time instrumental monitoring. In recent years, a further advancement is a big shift to the harnessing of digital technology that helps to transform our approach in geotechnical design, control, and construction.

With the aim of generating useful insights for the profession, this year's seminar provides a platform for practitioners to share innovations, ideas, and techniques in geotechnical engineering to pursue higher goals and to meet new demands in Hong Kong and overseas.

On behalf of the HKIE GD, I would like to express my gratitude to the invited speakers and authors contributing to this seminar. My special thanks go to all members of the Organising Committee, led by Ir Dr Gavin Toh, who have worked hard in making this event happen. I would also like to thank the Hong Kong Geotechnical Society (HKGES) for jointly organising this seminar, as well as the HKIE Civil Division and Structural Division for their support.

Ir Maureen Ng
Chairlady, Geotechnical Division
Hong Kong Institution of Engineers (2020/21 Session)

ACKNOWLEDGEMENTS

The Organising Committee would like to acknowledge the support of the following sponsors for their generous support of the Seminar:-

Atkins China Ltd.

AECOM Asia Co., Ltd.

ARUP

Aurecon (Hong Kong) Ltd.

C M Wong & Associates Ltd.

China Geo-Engineering Corporation

ESA Consulting Engineers Ltd.

Fugro Geotechnical Services Ltd.

Gammon Construction Limited

MTR Corporation Limited

ARCADIS Design & Engineering Ltd.

Fong On Geotechnics Ltd.

Geotech Engineering Ltd.

Lambeth Associates Ltd.

Mannings (Asia) Consultants Ltd.

Meinhardt Infrastructure and Environment Ltd.

TABLE OF CONTENTS

Engineering Geological Ground Models: Industry Applications for Geotechnical Investigation Planning, Data Acquisition & Appraisal

A.N. Al-Nuaimi, J. Cunningham, H.L.K. Fu, G. Li & K.A. Styles
Fugro (Hong Kong) Limited

C. Garcia
Fugro, Philippines

C.K. Loh & C.M. Warnest
CSan Miguel Aerocity, Inc.

ABSTRACT

Adoption of an engineering geological ground model (EGGM) prior to ground investigation, as a conceptual site characterisation approach, empowers users with the capacity to predict subsurface data trends, test assumptions, refine geotechnical inputs and better manage ongoing ground investigations. This approach informs the planning of ground investigation (GI) locations, in-situ testing, and non-intrusive surveys to ensure high-quality, efficient, and cost-effective data yield. This theme is explored using a case study at Manila Bay, in the Philippines, where a ground model was developed for planning and execution of site investigations and to add-value to site characterisation and geotechnical appraisal for nearshore site formation.

1 INTRODUCTION

1.1 Ground Modelling using a Ground Risk Management Framework

As part of industry practice, ground models (Parry, 2014) are essential tools for design of scope, scheduling and evaluation of ground investigations for site characterisation and geotechnical appraisal.

The ground modelling approach to site characterisation initiates during the conceptualisation stage of geotechnical projects. This develops further through the construction and operational stages of the project life cycle. Adopting a Ground Risk Management Framework approach (GRMF, Wood & Eddies 2021) provides strategic direction for managing ground-related risk including ground modelling implementation targeting more economic construction (Figure 1). Each stage targets data streams that maximise time, cost, and quality efficiencies using Geo-data to inform on-going geotechnical works. The predictive elements of ground models evolve over time and are best iterated and modelled implicitly to generate value. This approach builds confidence that data used for geotechnical design, construction and management of assets is robust, well informed, and applicable.

This paper explores the construction of a bespoke ground model to plan a CPT site investigation programme, conduct site characterisation and geotechnical appraisal of site formation works for the proposed Manila International Airport (MIA), in the Philippines. The commercial software Leapfrog Works Version 4.0 (Seequent, 2020) was used for digital transformation, analysis, and visualisation.

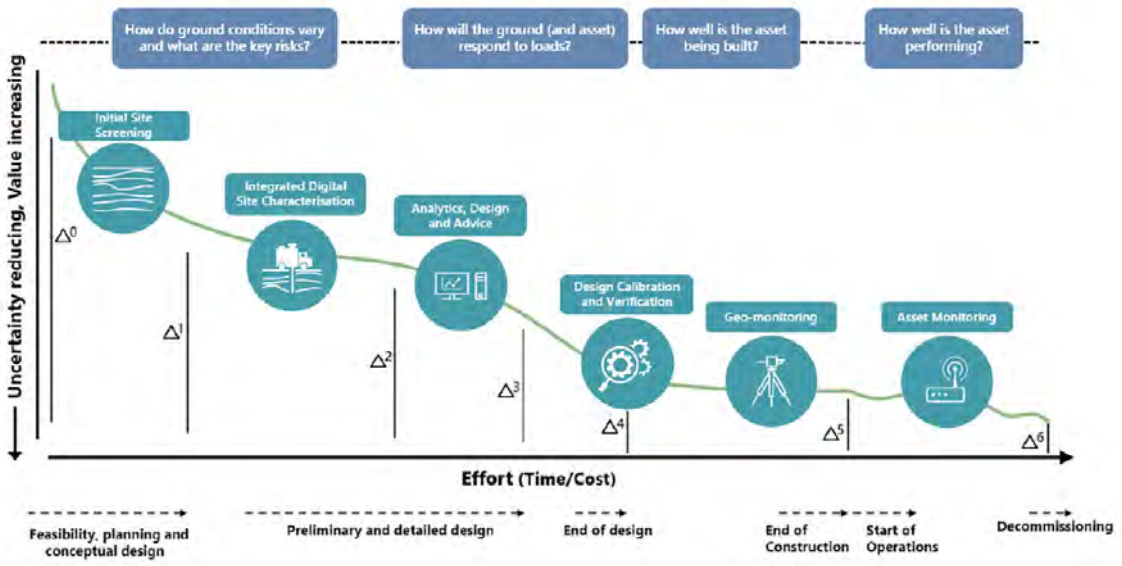

Figure 1: Ground Risk Management Framework (Wood & Eddies (2021). Along the timeline, Δ0 represents an initial state, Δ1 to Δ6 represent delivery points and data interfaces between cycle phases.

Stages Δ1 to Δ2 and elements toward Δ3 of the Ground Risk Management Framework (GRMF) were implemented (Figure 1) as follows:

- Stage Δ1 – existing Geo-data and desktop study information was digitally transformed into a Conceptual Ground Model (CGM) database. This provided geospatial context to the geological and geomorphological setting. Predictive digital surface trends were derived for site screening and informing proposal of CPT locations to fill gaps in the existing information.
- Stage Δ2 – CPT records from on-going site investigation were added to the CGM. From a project perspective, the resulting database transitioned into an observational dataset.

  During this stage, the intertidal, deltaic site area was often remote and difficult to access, including human and environmental challenges that restricted data collection. The ground model enhanced the timely relocation of proposed CPT by identifying alternative positions that could test data trends and ensure suitable data yield and quality was suitable to bridge data gaps.
- Transition from Stage Δ2 toward Stage Δ3 – unique soil sub-units were identified from CPT records. The 3D ground modelling environment helped isolate and visually verify patterns of occurrence. Site teams were informed about the predicted presence of these sub-units to acquire information on their performance and behaviour. The discussions concluded that sub-units were persistent across the site and could be targeted for in-situ testing to better understand their geotechnical properties.
- End of Stage Δ2 & early elements of Δ3, the Observational Ground Model (OGM) integrated all qualitative and quantitative data categories. Quantitative values such as cone resistance (q_c), SPT and laboratory test data were compared to qualitative categories such as engineering geological descriptions and CPT soil unit summaries. The additional sub-units identified provided further understanding of the engineering constraints and associated geological influences and constraints. Digital surface trends were used to define geotechnical zones, where patterns of homogeneity in soil geotechnical properties informed geotechnical analyses.

2 DEVELOPING THE SITE-SCALE GROUND MODEL TO PLAN SITE INVESTIGATIONS

2.1 Geological & Geomorphological Setting

The proposed MIA is located north of Manila in Bulakan, in Bulacan Province. An initial review of published lithostratigraphy highlighted a consistency with recent experience in existing borehole data within the project regional area. The geomorphological setting comprised Quaternary Plio-Pleistocene-aged Guadalupe Formation, Holocene, and more recent deposits. The Guadalupe Formation makes up the dominant basement unit and consists of upper and lower members, the Diliman Tuff and Alat Conglomerate respectively (AMH Philippines Inc. 2017). The geomorphological setting of the site is characteristic of a broad tidal deltaic river complex, with the Guadalupe Formation being unconformably overlain by sequences of basal shallow-marine clay, mangrove-peat, beach sand, fluvial sand and terrigenous floodplain clay deposits as shown in the schematic cross section (Dell et al. 2001, Figure 2). The site has significant anthropogenic disturbance including the formation of fisheries-related and associated dikes, river training/realignments and intermittent periods of flooding and dewatering. Some initial questions arose during early review:

1) Do the factual records of recent deposits and underlying soil units follow the expected patterns of cyclic and a pro-grading deltaic environment? Can these patterns be tracked and tested during the site investigation to better inform the geotechnical appraisal?
2) Could unique soil sub-units be identified within the overall stratigraphy and can their patterns of occurrence be identified and mapped?
3) Could these sub-units be tested in the field and would their properties be assessed as adverse (introduce design risk), beneficial (reduce design constraints) or benign (no influence) to geotechnical appraisal?

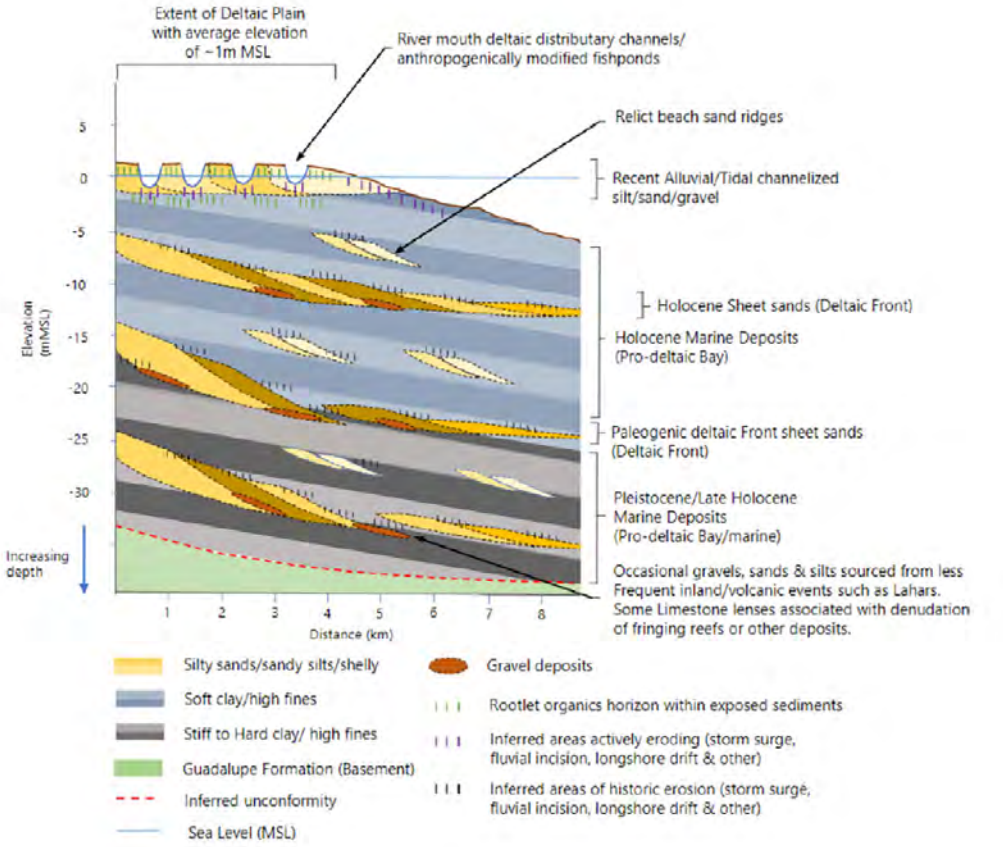

Figure 2: Schematic of general site stratigraphy (Dell et al. 2001)

2.2 The Ground Model Approach Digital Transformation

The Ground Model approach began with digital transformation of soil properties into qualitative (categorical) and quantitative (continuous) data paired with geo-referenced positions (easting, northing and elevation). The schematic of site stratigraphy (Figure 2) guided the interpretative process for the proposed MIA. The depth of interpreted soil interfaces provided base elevation levels for each overlying soil unit. Using a geographical information system (GIS), these data provide point cloud neighbourhoods for mathematical interpolation.

The method of interpolation in Leapfrog Works 4.0 (Seequent, 2020) is the Fast Radial Basis Functions (FastRBF). RBFs are commonly used to approximate a method of kriging called Dual Kriging (Horowitz et al 1996). RBF is the creation of volume function as a sum of basis functions that use a linear weighting method in the same manner as dual kriging (Cowen et al, 2003). However, because it is a global interpolant it requires the entire dataset to be used when computing the weighting function. This can limit its application to smaller data volumes. The FastRBF operates in the same way as RBF, without the RBF requirement of infinite precision for the weighted calculation. Instead, input coefficients are only computed using a pre-determined accuracy, enabling rapid computation.

Areas of interest (no known factual values) are estimated by interpolating and referencing nearby data points with known factual measurements using FastRBF. Each reference point has a weight-of-influence (factual measurement) that helps prioritize the estimation process. The function considers distance between the point of interest (point to be estimated) and weight of nearby reference points (factual values) and assumes reference points with higher weights of influence, that are nearer to the point of interest are more influential than points with less weight of influence or increased distance from the point of interest.

The rapid implicit ground modelling process (i.e., data driven) enabled timely updating and testing of the CGM, keeping the models dynamic and in synch with data acquisition and geological interpretation. As new data became available, continued updating and data review enhanced site characterization and geotechnical planning.

2.3 Visualisation of Stratigraphic & Geotechnical Data

During desktop study, three main soil units were classified:

1) Unit 1 – Recent undifferentiated alluvial and coastal deposits;
2) Unit 2 – Holocene-aged marine clay sediments; and
3) Unit 3 – Pleistocene to Holocene marine clays/coastal sands and alluvial gravels.

Point clouds were generated for the base depth of each soil unit and geotechnical properties including particle size distribution (PSD), moisture content and others (Figure 3). Digital surface trends were interpolated for each point cloud. For example, trends in SPT-N values were visualised in the manner shown in Figure 3 to define transitions from soft to stiff clays and loose to dense sands. When used

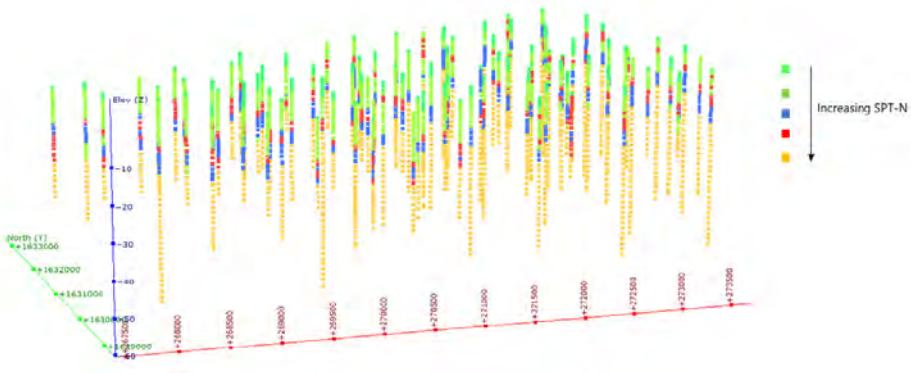

Figure 3: Point cloud for geological stratigraphy & geotechnical properties (SPT-N values, view northward)

collectively, these data helped to visualise relationships between soil type and geotechnical properties, allowing the interval points of the main soil units to be well informed and reviewed at an early stage. Trends and variations in the data, including anomalous or erroneous records were easy to isolate and interrogate in the 3D ground modelling environment for investigative follow-up.

2.4 Using the Ground Model to Inform Site Investigation

Block volumes for each soil unit were calculated using the interpolated digital surface trends. The thickness of finer sediments (Unit 2) increased with distance from the shoreline, and marine deposits with coarser sand and gravel sediments (Unit 3) were more abundant shoreward. The coastal and alluvial sediments often occurred as localized sheets and lenses of sand. The thickness of Unit 1 varied across the site and was generally dependent on the extent of anthropogenic disturbance. Based on the macro-scale evidence, the CGM was consistent with the pro-grading geomorphological setting, that had experienced cyclic sea level oscillations and changes in depositional environments.

The CGM evaluated predicted soil conditions for each proposed CPT location and reflects the findings from desk study and review of the general site stratigraphy. At each position, soil unit descriptive categories were extracted from the block volumes for the length of each CPT (Figure 4). A predictive log, including soil type, thickness, and expected geotechnical properties were derived for each location. This evaluation process ensured data acquisition was suitably scheduled and informed. When site constraints were encountered alternative CPT locations could be evaluated quickly, and intelligently screened to inform suitable CPT relocation, promptly and efficiently.

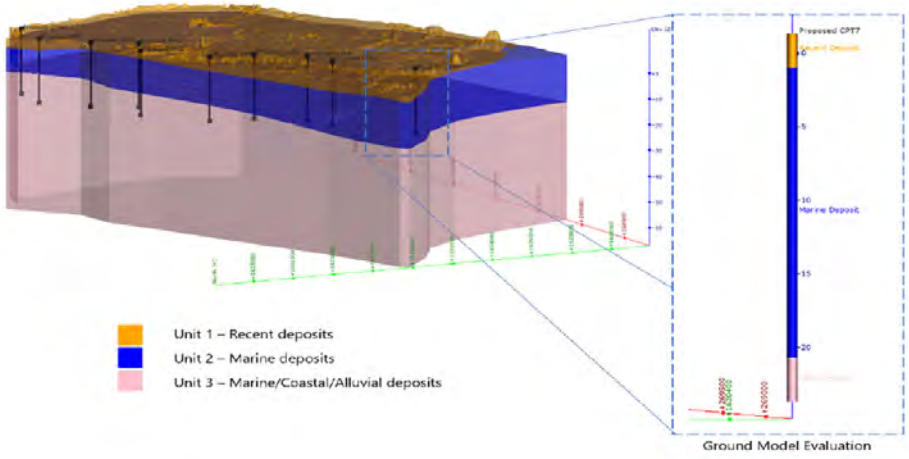

Figure 4: Using the conceptual Ground Model to evaluate stratigraphy at the location of Proposed CPT7 (view eastward)

3 TRANSITION INTO AN OBSERVATIONAL GROUND MODEL & IMPROVING DATA ACQUISITION

3.1 Using Implicit Modelling to Evaluate & Visualise Unique Soil Units

A key component of GRMF Stage Δ2 is digital transformation and integration of newly acquired CPT data with the existing CGM. The digitized cone resistance (q_c MPa), sleeve friction ratio (R_f %) and pore pressure (u kPa) numerical measurements were visualised and compared to soil behaviour type index (I_c, Robertson, 2010) qualitative measurements. CPT data measurements were cross-examined within the CGM block volumes. As shown in Figure 5, unique soil sequences, including lenses of shelly/silty sand mixtures were evident in the CPT Ic and qc measurements.

Two methods of interpolation were used to evaluate continuity and vertical and lateral variability of these unique soil sequences, namely Leapfrog Works Intrusion and Vein FastRBF.

The Intrusion FastRBF implicitly modelled ellipsoid 3D volumes of the shelly/silty sand mixtures. The depositional context (orientation of channels and delta plains, geological process), thickness of unique

soil sequences and GI spacing were considered when assigning anisotropic input values for global trend and ellipsoid maximum, intermediate and minimum semiaxes. Ellipsoid output volumes were compared and checked visually with I_c and q_c stick logs (Figure 5) to explicitly refine these input values. The input parameters shown in Table 1 were deemed sufficient for the OGM derivatives. The final ellipsoid volumes highlighted continuity between the unique soil sequences across the site. However, gaps in the predictive data were evident (Figure 6a) and were likely associated with data density and measured thickness of these unique soil sequences.

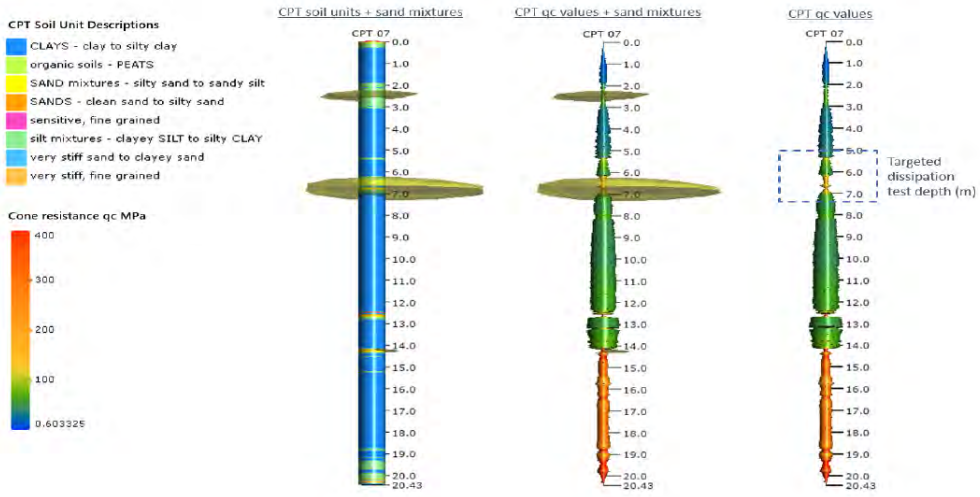

Figure 5: Comparison of sand mixtures ellipsoid volumes with I_c & q_c values of proposed CPT7

Table 1: Compositing & trend parameters used to define model sand/shelly soil unit ellipsoid volumes.

Surface editing options	Ellipsoid Parameters	Input Values
Compositing	Filter interior	<0.2
	Filter exterior	<0.2
Trend	Dip°	0.2
	Azimuth	260
	Pitch	150
	Maximum ratio	500
	Intermediate ratio	250
	Minimum ratio	1
Model	Surface resolution	10.0

The Vein FastRBF models 3D volumes between two interpolant surfaces, that are computed from the upper and base depth values of each soil unit. The interpolant surfaces are extrapolated between each GI location with a measurement (i.e., the calculated surfaces must pass through each data point). A total 61 no. CPT locations, some 93.5% had recorded measurements of unique soil sequences. The Vein FastRBF produced output volumes with a continuous trend, inclusive of variable thickness for the unique soil sequences across the site (Figure 6b). The dip, azimuth, pitch, and surface resolution inputs of the global trend shown in Table 1 were used to inform the Vein FastRBF computations.

The Intrusion and Vein FastRBF 3D volume outputs both highlighted some degree of continuity for the unique soil sequences across the site. However, the ellipsoid 3D volumes were not always continuous. As mentioned, gaps in the ellipsoid data were likely influenced by data density and/or measured total thickness of unique soil sequence measurements. Additional geospatial analysis was conducted to test these assumptions.

A kernel density spatial analysis was applied to calculate a magnitude-per-unit-area (in this case m^2) using all 61 no. of CPT locations. This generated heat maps that visualise the spatial density of these geographic data (blue in Figure 7). The darker the colour, the higher the data density per m^2.

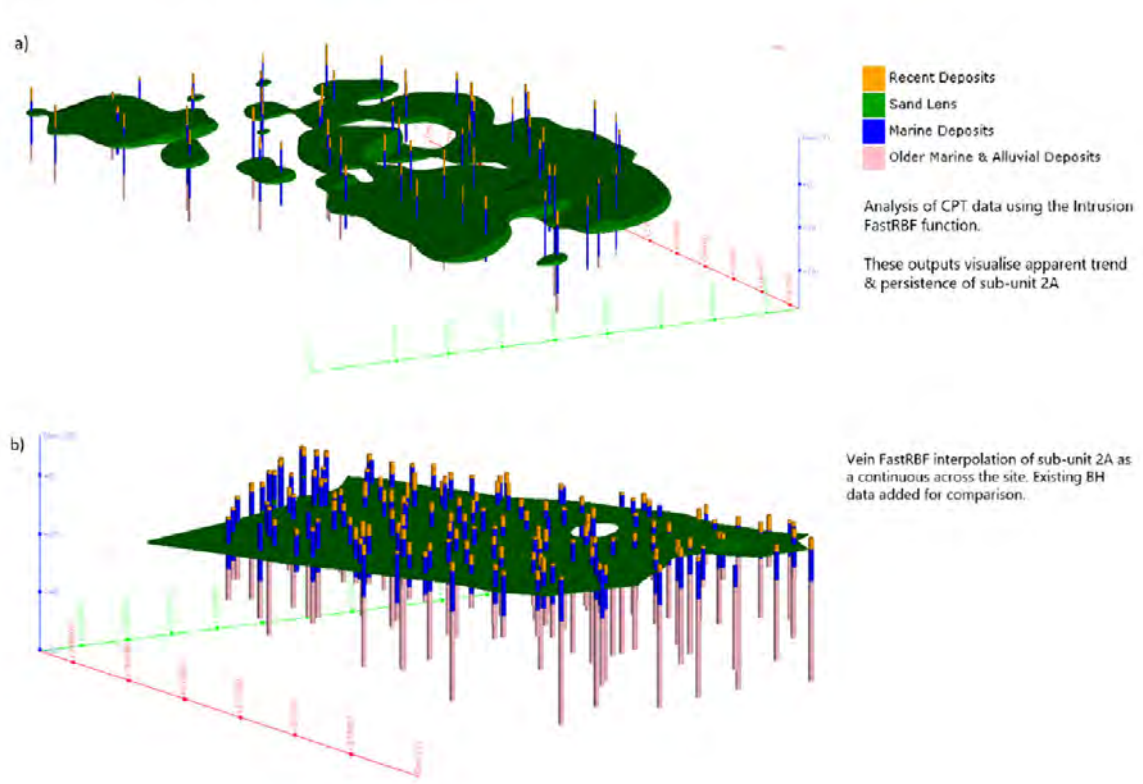

Figure 6a & 6b: Intrusion (a) & Vein (b) FastRBF output volumes

A Natural Neighbour interpolation was conducted and used the measured thickness of unique soil sequences recorded in each CPT location. Contour plot trends were derived from the output rasters (Figure 7). The plan extent of the ellipsoid volumes was mapped against both the kernel density heat maps and the thickness of unique soil sequences contours. A correlation between CPT density and/or thickness of unique soil sequences to ellipsoid mapped extent was evident. In summary, the following patterns are apparent:

1) Areas with low density & low measured thickness have limited ellipsoid extents;
2) Areas with high density but low measured thickness have some, often localised ellipsoid extents;
3) Areas with low density but high measured thickness have some, often localised ellipsoid extents; and
4) Areas with high density and high measured thickness have greater, higher continuity ellipsoid extents.

The assessments supported the interpretation of a continuous unique soil sequence within the Holocene marine clays (Unit 2). It was classified as Sub-unit 2A and represented shelly/silty sand mixtures. After review of the geostatistical analyses and comparison of the Intrusion and Vein FastRBF output 3D volumes, the Vein FastRBF was considered most suitable to represent this Sub-unit within the OGM.

Updated predictive logs were evaluated from the OGM and used to further refine/inform the ground investigation expectations. When compared with preliminary factual logs these data added value by providing methods for review and conducting quality assurance and control of incoming data (Figure 8).

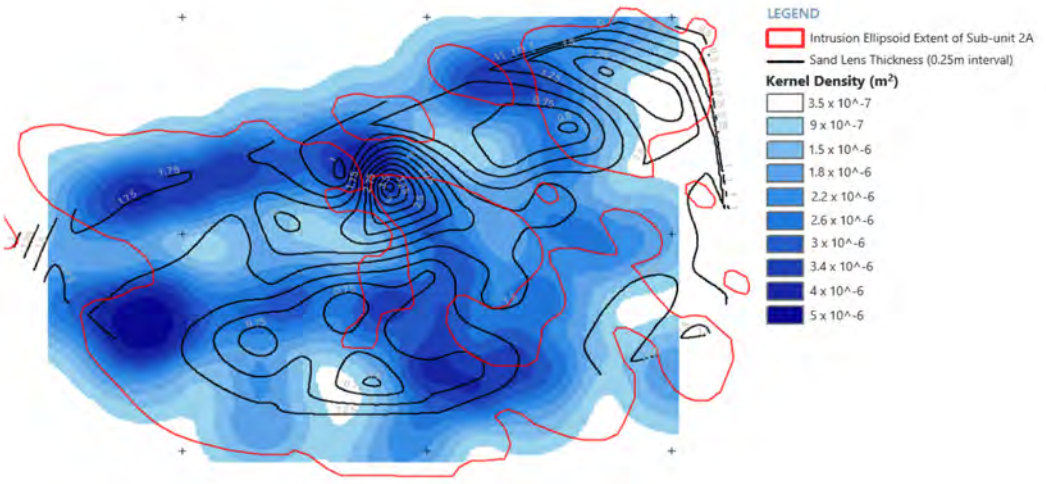

Figure 7: Comparison between ellipsoid extent, data density & unique soil thickness contours

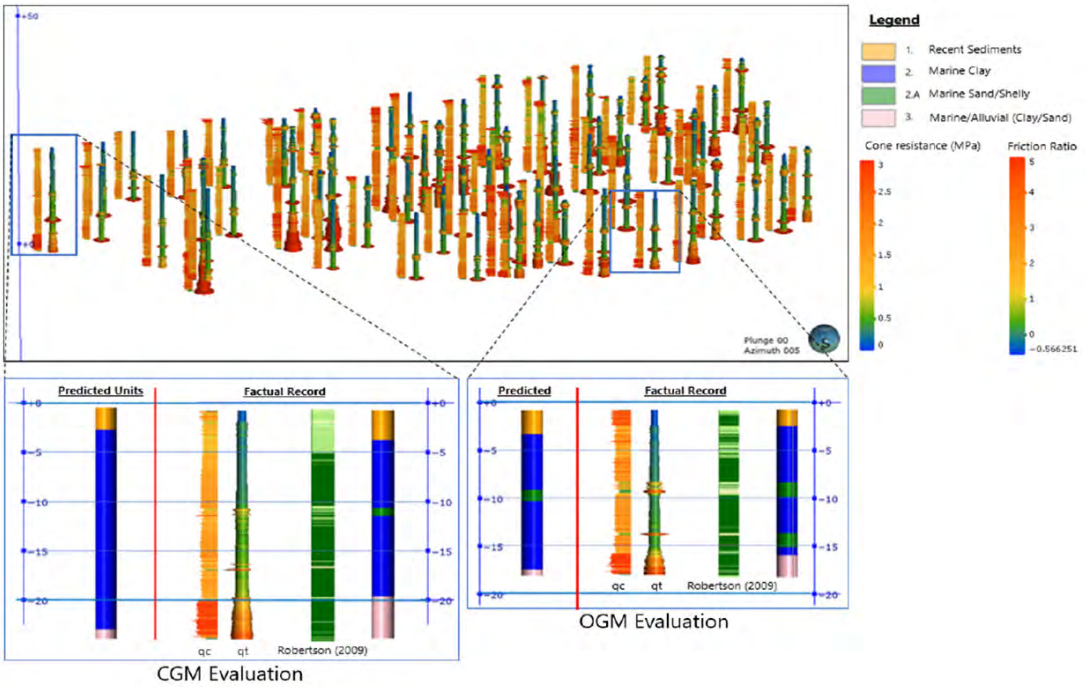

Figure 8: Visualisation of CPT data & comparison of predicted/factual records (left from CGM & right from OGM)

3.2 Improved Data Acquisition & Targeting Dissipation of Tests

The field team were informed about the expected soil properties discussed in Section 3.1 which assisted in their on-site review of the field test results and in making decisions for additional testing. The program allocation for the dissipation tests were aligned with the identified geotechnical units, with emphasis on establishing the hydraulic conductivity properties of the identified sand lens in the block model.

The geotechnical model assisted in the forecast of termination depths of the CPTs. As the execution of the program depended on the rise and fall of the tides, this led to better scheduling and allocation of resources during the geotechnical investigation. Early termination of CPTs to mitigate the risk of the CPT platform being stranded caused by the impending low tides was avoided in the program execution.

4 GEOTECHNICAL ZONATION & ANALYSIS

4.1 Using the Integrated Observational Model for Geotechnical Review

As described above, the integrated geotechnical model facilitates the visualization of the geospatial distribution of various sub-strata information, including soil properties and parameters derived from in-situ and lab testing. Data of interest can be visually graded or banded to establish the trends of material changes and their interrelation with the evolving ground model stratification, all contextualized within the geological and geomorphological site development history.

With the use of the 3D model, the relationship of proposed development layouts with underlying changes in the soil strata and the variation of soil properties affecting ground performance, such as strength and compressibility characteristics, can be fully appreciated by all stakeholders in the development of the project. Geotechnical project constraints and risks can more easily expressed and mitigation measures to manage such risks be taken into consideration early-on in the project life-cycle.

Within the MIA project, the desktop study identified some areas of high moisture contents (Figure 9). With the model evolution, these high moisture content soils were observed to have a high lateral continuity beneath the base of the newly mapped Sub-unit 2A and were therefore distinguished from the upper soft clay Unit 2 as a further sub-unit, Sub-unit 2B. The soil properties and parameters, including the geomechanical properties affecting soil behaviour, were separately evaluated for Unit 2, Sub-unit 2A and Sub unit 2B for subsequent analysis. The presence of the high moisture content layer tying in with the Sub unit 2A layer of sandy/shelly/silty sand mixtures was contextualized within the site evolution as a cyclical change in the pro grading depositional environment.

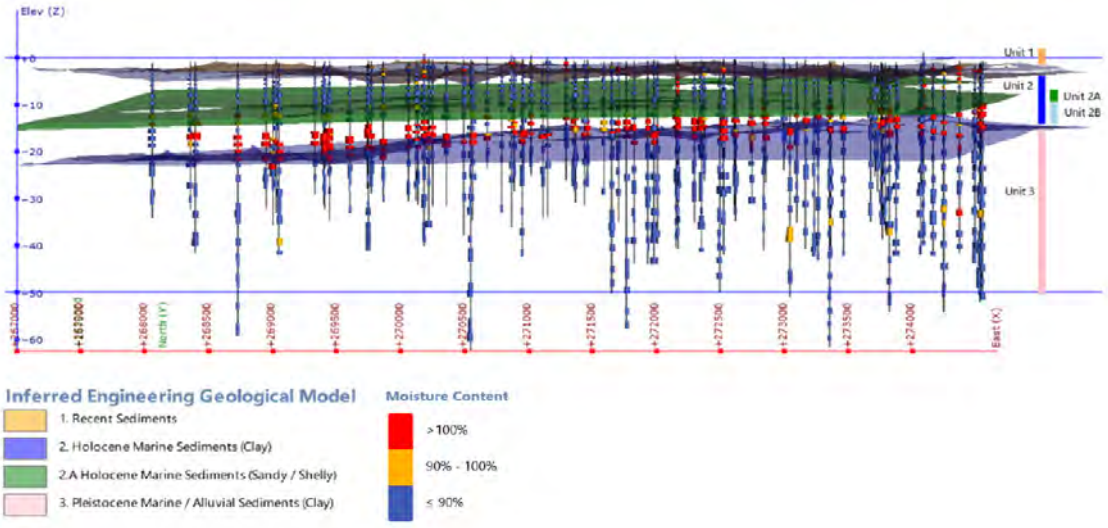

Figure 9: Comparing digital trends in soil moisture contents (view northward)

4.2 Zonation of the Site for Geotechnical Analysis

Within the context of any development project, geotechnical assessments can be provisionally undertaken on a generic basis, but more meaningful assessments generally need to consider the relationship between various elements of the development (such as different types of structures, loadings, foundations, and serviceability sensitivities) with variations in ground conditions upon which they are to be constructed. The facility zonation is generally derived from the development plot layouts in consultation with designers and project owners. Depending on the nature of the development and facilities, various factors of the ground performance will be of interest to designers and developers which will steer the geological/geotechnical zonation of the site in conjunction with the ground model. The scope of the required engineering assessments is subsequently based on the interrelation of facility and geological zonations.

In the case of the MIA project, the focus of the assessment was in relation to the site performance characteristics required for the new airport. Key issues under consideration were the compressibility of the soils, settlement magnitudes, consolidation durations as well as risk of liquefaction. Based on the modelled ground conditions, the site was split into 5 no. geological zones largely based on banded variations in thickness of highly compressible clay layers, the governing factor in settlement magnitude (Figure 10). Each of the 5 no. geological zones were examined in a 3D context to determine typical and worst-case profiles for settlement assessment with consideration to the filling zonation for the runways, aprons, and surrounding areas. An evaluation of the anticipated range of settlements over the site for consideration in the subsequent site formation and ground improvement design was carried out.

In reviewing consolidation settlements, both the magnitude and duration for settlements were of interest with the latter influenced by the drainage conditions at the site. In this context, the targeted data acquisition and dissipation testing during the CPT investigation campaign was able to aid the evaluation of the newly identified sandy/shelly layer Sub-unit 2A to act as a drainage layer. Further, in a localized corner of the site, the absence of Sub-unit 2A was also identified as a separate geological sub-zone where the duration for consolidation of the thick compressible soils without an intermediate drainage layer was most critical.

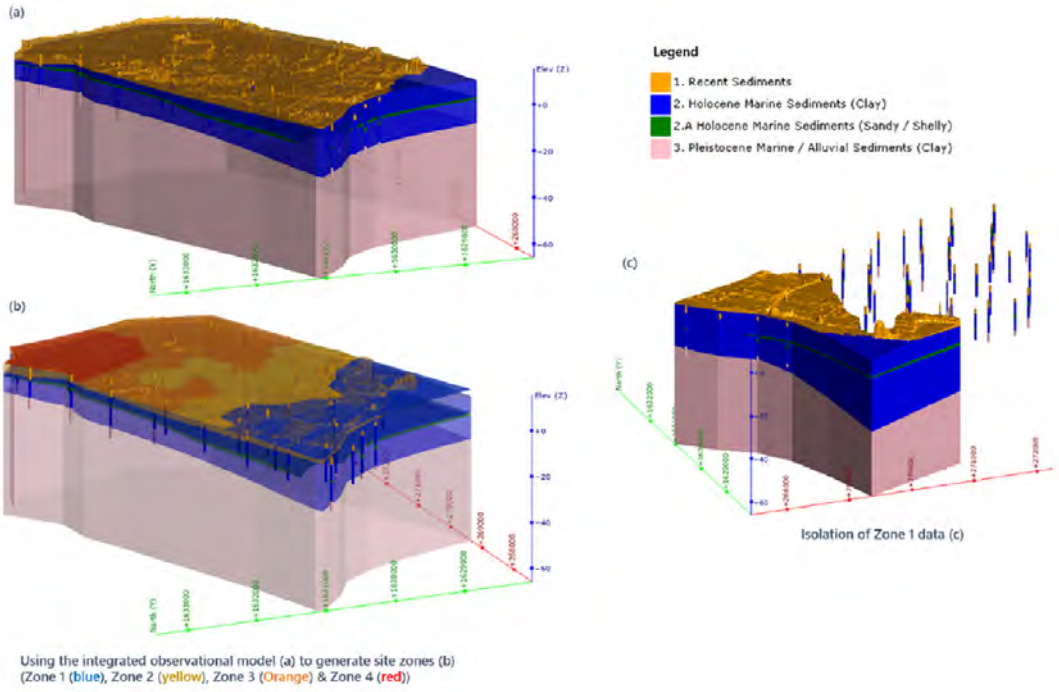

Figure 10: Using the Ground Model to generate geotechnical site zones (view eastward (a/b)

The findings of the settlement analysis showed that the settlement magnitude was not only affected by the overall thickness of the compressible layer but also the proportional thicknesses of the sub-units within the highly compressible layers that were identified through the geospatial modelling of soil property data. Where there was a greater proportion of the high moisture content layer Sub-unit 2B, greater magnitudes of settlements were anticipated resulting from the higher compression ratio of that sub-unit. Ultimately, the evaluation of settlement magnitudes across the development site allows for a preliminary estimate on the order of magnitude of top up fill to attain the site formation profiling for consideration in the reclamation design. The distinction of the 2 no. soft clay layers above and below the sandy/shelly layer and the attribution of different parameter data would enable a more refined assessment of those magnitudes.

Furthermore, the refinement of the ground modelling that identified a laterally continuous sandy/shelly layer allowed for the consideration of a potential drainage layer within the thick, highly compressible clay layer. The effect of the refined drainage conditions reduced the time for 90% consolidation (t90) between some 23 to 57 years. Whilst the reduction in t90 was significant and demonstrates the

potential benefit of using an integrated observational model, the time for consolidation will ultimately be governed by the method of ground improvement adopted by future contractors.

5 ADDED-VALUE FROM THE GROUND MODELLING APPROACH & CONCLUSIONS

5.1 Improved Planning of Site Investigations & Geotechnical Appraisal

For successful implementation of the ground modelling approach and to maximize project returns it must be adopted at the beginning of a project and used to set the precedence for future works. In this study, the ground model approach commenced during Stage Δ1 of the Ground Risk Management Framework and was utilized through Stages Δ1 and Δ2. The purpose was to establish efficient project management, contract flexibility and clear communication of the understanding of ground conditions and ground investigation expectations.

Some key takeaways of the approach are that ground models combine implicit and explicit elements to allow geological knowledge to be tested, acquired, and validated more quickly, robustly and cost effectively. When used to interrogate data and inform ground investigation expectations digital models enhance focus and the targeting of high-quality data acquisition and geotechnical assessment. The ground model approach facilitates equitable and transparent sharing of ground knowledge and associated risks in geotechnical appraisal between all stakeholders. This leads to less conflict and easier project implementation.

For the proposed Manila International Airport (MIA), the ground model approach provided the following answers to the questions in Section 2.1:

1) The conceptual ground model constructed from existing information and desktop study data highlighted consistency with the known regional lithostratigraphy and soil sequences associated with a fluctuating deltaic geomorphological setting. The digital transformation and digital surface trend analysis of existing data was effective in predicting and enhancing ground investigation planning and expectations;

2) Using the implicit modelling elements of Leapfrog Works 4.0 (Seequent, 2020), newly acquired data were digitized and integrated seamlessly within the CGM framework. The 3D modelling environment enhanced the methods of data interrogation; observations of unique soil unit sequences could be quickly tested, reviewed and patterns established. Through Stage Δ 2, the continued testing, comparison, and screening of new CPT data culminated in the identification of a soil Sub-Unit 2A. This encouraged further review of existing data, resulting in further refinement with the identification of an additional unique soil unit (high moisture content clays Unit 2B). The ground model approach allowed patterns and regional relationships to be carefully mapped, and correlations developed as more supporting data were acquired and eventually used to enhance the ground investigation and inform geotechnical assessment and zonation.

3) The use of the integrated observational model has allowed for refinement in the visualization and modelling of the ground conditions through targeted data acquisition during the CPT investigation campaign. In situ testing allowed for some understanding of the hydraulic and consolidation properties and more accurately classified the sub-soil units and their properties for subsequent geological zonation and engineering assessments. These refinements facilitate a more representative assessment on the potential settlement implications of the fill materials for consideration in detailed design. Based on the specific parameters of the sub-units, the compression ratio of the high moisture soft clay layer was approximately 20% higher than mean compression ratio over the whole of the highly compressible stratum. Without being modelled, this would have led to an underestimation in the expected magnitudes of consolidation settlement particularly in those areas where the proportion of the high moisture content sub-unit is greater. It was also observed that in general the proportion of prior sampling and geomechanical testing of the high moisture content sub-unit was relatively limited and targeting this layer for some additional data validation in the subsequent design and build stage has been advised.

Spatial variability in the ground model data can be reduced by continued management and integration of new data throughout the project lifespan This initial MIA ground model was a first-step benchmark to visualize the site conditions for GRMF Stage Δ1 and Δ2. As GRMF Stage Δ3 commences, and beyond, new geotechnical data, instrumentation monitoring, and construction feedback should be used to refine the assumptions of the evolving ground model to improve its quality and representativeness. This will enhance its capacity to support analytics, design, and open opportunities for integration with Building Information Modelling (BIM) as a supplementary toolkit providing advice and recommendations to project stakeholders.

ACKNOWLEDGEMENTS

The innovative approach used during this work would not have been possible without the technical support and contributions from San Miguel Aerocity, Inc. and their associated teams. The authors would like to extend thanks to the Fugro teams for their involvement, support, feedback, and enthusiasm that ensured strong delivery of the proposed Manila International Airport geotechnical appraisal.

REFERENCES

AMH Philippines,Inc. (2017). Interim/Progress Report for the Horizon Manila Reclamation Project Coastal Engineering. Downloaded from http://eia.emb.gov.ph/wp-content/uploads/2016/06/EIS.pdf.

Cowen, E.J., Beatson, R.K., Ross, H.J., Fright, W.R., McLennan, T.J., Evans, T.R., Carr, J.C., Lane, R.G., Bright, D.V., Gillman, A.J., Oshust, P.A., Titley, M. (2003) Practical Implict Modelling. 5th International Mining Geology Conference, Bendigo, Victoria. pp 89 – 99.

Dell, T., McClun, J., & Morales, E. (2001). Characterisation of the reclaimed soils in the foreshore area of Manila Bay, Philippines. Presented on the 15th Vancouver Geotechnical Symposium Program.

Horowitz F.G., Hornby P., Bone D & Craig M (1996). Fast Multidimensional Interpolations, Proceedings of the Application of Computers and Operations Research in the Mineral Industry (APCOM 26), Ramani R V (ed), (Society Mining Metallurgy and Exploration (SME): Littleton, Colorado), 583 p.

Parry, S., Baynes, F.J., et al. (2014). Engineering geological models – an introduction: IAEG Commission 25. Bulletin of Engineering Geology and the Environment, 73, 689–706, https://doi.org/10.1007/s10064-014-0576-x.

Robertson, P.K. (2010), Soil behavior type from the CPT: an update, 2nd International Symposium on Cone Penetration Testing.", Canadian Geotechnical Journal, Vol. 33, No. 3, pp 488-498.

Seequent (2020). Leapfrog Works (4.0). © Seequent Limited.

Wood, R.W. & Eddies, R. D. (2021). Ground Risk Management Framework. All in the Frame article, New Civil Engineer, April 2021.

A Study of Heaving Material Resulted from Deep Cement Mixing Construction

Jian Chen
China Harbour Engineering Corporation, Hong Kong

L. Tony Chen
Arcadis Design & Engineering Limited, Hong Kong

Yuen Ping Chan
China Harbour Engineering Corporation, Hong Kong

ABSTRACT

The deep cement mixing (DCM) method has been used to form foundations for some of the marine structures in Hong Kong. Injection of cementitious slurry into the seabed will inevitably cause the seabed to rise, resulting in a raised soil-and-cement mixture above the top of DCM clusters, which is referred to as heaving material in this paper. The amount and characteristics of heaving material are influenced by several factors such as soil type, improvement depth and area ratio, cement-water ratio, cement injection pressure and workmanship. Due to its weaker strength, heaving material is conventionally dredged to avoid forming a weak layer in the DCM foundation. This paper aims to investigate how to retain heaving material in the DCM foundation system to avoid both causing pollution and incurring additional costs due to dredging. It has four objectives, namely: firstly, to study its formation mechanism; secondly, to investigate its shear strength characteristics, through the results of various lab and in-situ tests; thirdly, to discuss design and construction considerations concerning heaving material; and finally, to discuss the results of a full scale test involving heaving material. It is shown that heaving material may be retained provided it can meet design requirements.

1 INTRODUCTION

The DCM method involves in-situ treatment of soft soils by mixing in cementitious and/or other materials to form a column of solid element, hereafter referred to as the "DCM Cluster". The ground may be fully or partially treated with DCM, depending on the design area ratio, and is referred to as the DCM treated ground. This technique has been widely used to improve soft marine deposits for the construction of marine structures such as seawalls and breakwaters.

Injection of cementitious slurry into the seabed will inevitably cause the seabed to rise, due to ground volume increase, resulting in a raised soil-and-cement mixture above the top of DCM clusters, which is referred to as "heaving material" in this paper. The generated volume and the characteristics of heaving material are influenced by several factors such as soil type, improvement depth and area ratio, cement-water ratio, cement injection pressure and workmanship. Due to its uncertain engineering properties and its weaker shear strength than that of a DCM cluster, heaving material is conventionally dredged to avoid forming a weak layer in the DCM foundation. However, dredging is not only time consuming

and costly, but also prone to causing marine pollution due to diffusion of its fine particles during the dredging and dumping process.

For example, if a marine DCM project involves installing 10,000 DCM clusters (each cluster having a depth of 30m and an area of 4.62m^2), the volume of heaving material will be approximately 970,000m^3, based on the assumption that it is about 70% of the injected cement volume. Significant resources will be required to undertake dredging work and environmental measures which will involve installing silt curtains, amongst others, to minimize suffusion of fine particles. This will no doubt negate the DCM application and prolong its construction duration, resulting in delays of subsequential construction activities.

This paper aims to investigate how to retain heaving material in the DCM foundation system to avoid both causing pollution and incurring additional project costs due to dredging. It has four objectives, namely: firstly, to study its formation mechanism; secondly, to investigate its shear strength characteristics, through the results of various lab and in-situ tests; thirdly, to discuss design and construction considerations concerning heaving material; and finally, to discuss the results of a full scale test involving heaving material.

2 FORMATION MECHANISM AND KEY CHARACTERISTICS

To prevent fine particle diffusion, a 2m thick sand blanket is conventionally placed on the seabed prior to DCM construction. During the cement injection process, the marine deposit will be gradually extruded upwards and mixed with cement slurry, consequently pushing upwards the original seabed and hence the sand blanket. The material located directly above the top of DCM clusters and between the design DCM top level and the top of sand blanket after DCM is referred to as heaving material in the present study, as depicted in Figure 1.

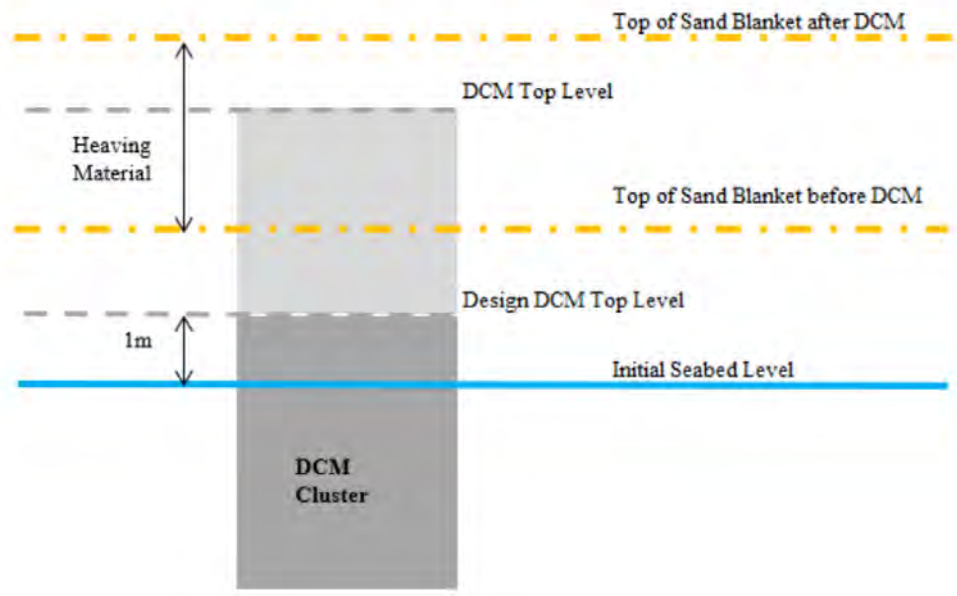

Figure 1: Definition of DCM heaving material

According to past experiences, the volume and properties of heaving material are influenced by a number of key factors including the in-situ soil properties, improvement depth and area ratio, cement dosage, workmanship and construction sequence.

The volume has close correlation with the particle size distribution of in situ soil. A clayey soil tends to induce a larger volume due to its higher incompressibility as compared with a sandy soil. The improvement depth also plays an important role; the deeper the improvement depth, the larger the volume because more soils are replaced by cement slurry. Similarly, the larger the improvement area ratio, the larger heave volume.

The Japanese solidification treatment research committee has proposed an empirical equation to

calculate heaving thickness based on DCM cluster depth. Building office of Kansai airports has suggested that heaving thickness can be estimated as 5 to 10% of improvement depth for grid type or wall type DCM based on their experiences. Some researchers believe that the dominant factor affecting heaving volume is the injected cement volume based on detailed investigations into past projects. Some researchers, for example EuroSoilStab (2014), have reported that heaving volume accounts for 70 to 80% of the injected cement volume. In the revetment project of Port of Yokohama, the measured heaving volume was about 108% of cement injection and maximum heaving thickness was about 3m (DCM dosage: 160kg/m^3; water cement ratio:0.6; improvement depth: 24 to 32m). In the revetment project of Kansai airports Phase II, heaving volume varied from 58 to 73% of cement injection and maximum heaving thickness was about 3.4m (DCM dosage: 180kg/m^3; improvement depth: 33m). Heaving thickness is also affected by DCM construction sequence in that heaving material from earlier DCM installation can spread sideways to areas where DCM clusters are to be installed later.

Confining pressure of treated soil plays an important role for DCM mixing quality. A low confining pressure cannot effectively prevent leakage of cement slurry and maintain an ideal curing condition for DCM mixture. As compared with DCM clusters, more cracks can be observed from cored samples taken from heaving material, which can affect its intactness and strength. As heaving material lies above the original seabed, its confining pressure is low or even zero, resulting in poor mixing quality.

3 SHEAR STRENGTH CHARACTERISTICS

A series of site trials, involving installing DCM clusters and the associated post-DCM Unconfined Compressive Strength (UCS) tests and CPT tests, have been carried out under the current study to investigate the shear strength characteristics of heaving material. For the trials, the design of DCM clusters aims to achieve a UCS value of not less than 1.2MPa.

UCS values are plotted versus depth in Figure 2. While the majority of UCS values are much greater than 1.2MPa for DCM clusters, thus meeting the design requirement, they fall below 1.2MPa for heaving material, although being generally above 0.45MPa, except for the top 1m which consists of predominately sand. The likely reasons are, where heaving material is formed: (1) the confining pressure is low; (2) sand content is high due to the existence of the sand blanket; and (3) due to leakage of cement slurry and bad curing condition, cementing stress is not enough to bond cement slurry, soft clay and sand together as a unit.

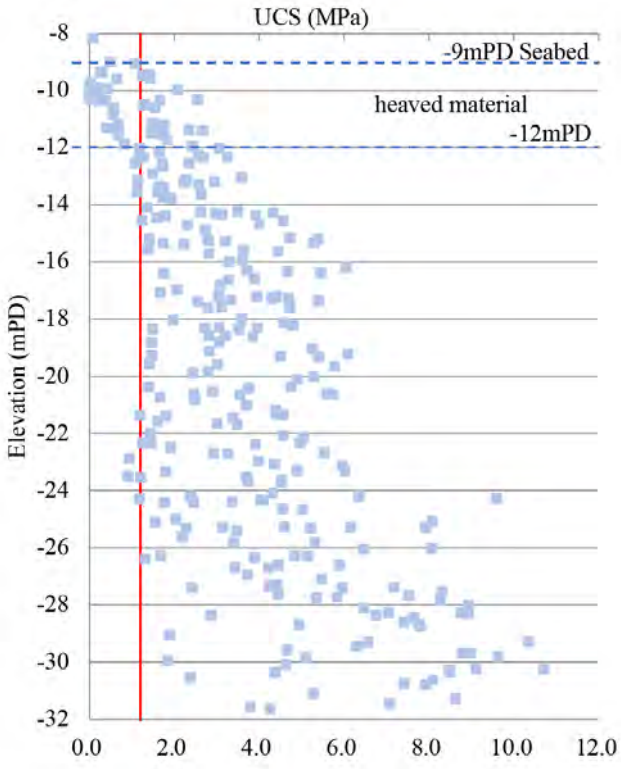

Figure: 2 Plot of UCS values along DCM depth

Shallow in-situ CPT tests have been undertaken through the heave zone down to the top of DCM clusters. Figure 3 shows a typical plot of the measured CPT net cone resistance along depth. It can be seen that the cone resistance tends to increase with depth in the heave zone and is generally greater than 5MPa, except for the top 1m which consists of predominately sand.

When the CPT results are interpreted using the well established empirical methods, it can be observed that the behavior of heaving material is similar to that of a granular material. Figure 4 plots the inferred friction angles using the correlations proposed by Robertson & Campanella (1983) and Kulhawy & Mayne (1990). It can be seen that the friction angles at the DCM heave zone generally range between 45° and 52°, with some limited data showing about 40°, except for the top 1m. For the top 1m, the frication angles are generally greater than 30°.

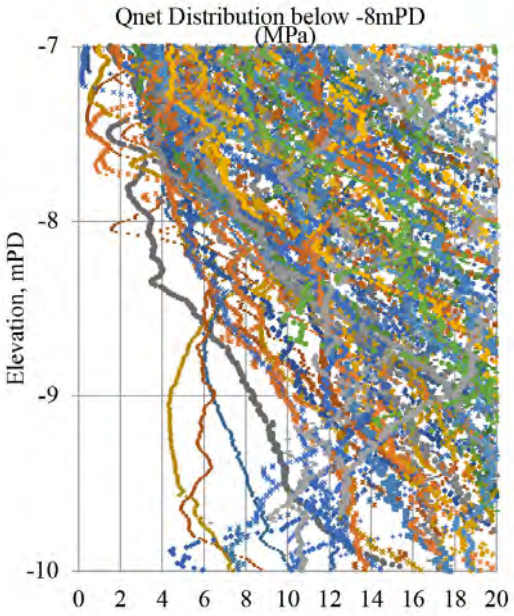

Figure 3: Plot of CPT net cone resistance along depth

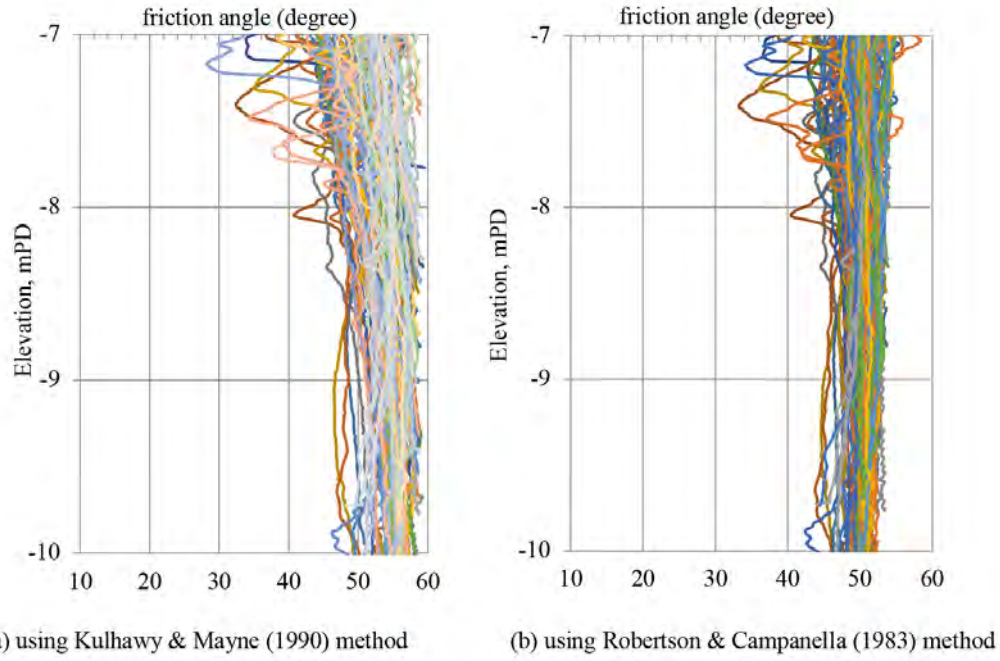

Figure 4: Plot of friction angle inferred from CPT results

To further understand the heaving material behavior, direct shear tests have also been carried out on the heaving material samples following the method modified from ASTM D5607-02. Some tests are carried out on samples with a pre-sheared plane to introduce a defined failure mode, which is considered to be representative of residual shear strength because the DCM cement bonding is completely destroyed. Other tests are on intact samples to provide the peak shear strength.

The test results are shown in Figure 5, while the deduced shear strength values are presented in Table 1.

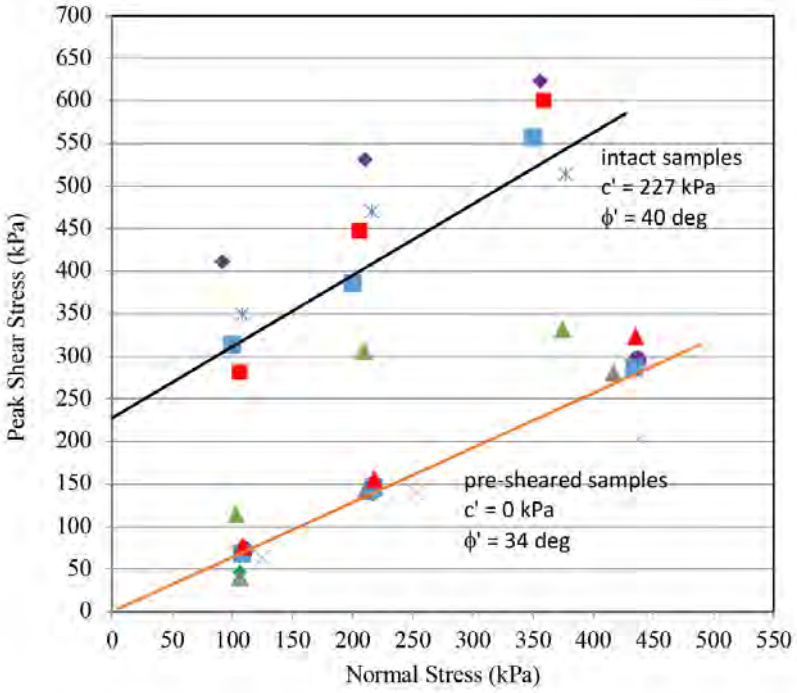

Figure 5: Plot of direct shear tests

Table 1: Shear strength parameters deduced from direct shear tests

Shear strength	Cohesion c (kPa)	Effective frictional angle f (°)
Peak shear strength	227	40
Residual shear strength	0	34

4 DESIGN AND CONSTRUCTION CONSIDERATIONS

This section will discuss, from design and construction perspectives, how to assess whether heaving material can be retained in a DCM foundation system and how to improve its engineering properties if it is to be retained.

4.1 Design considerations

Whether heaving material can be retained in a DCM foundation system depends on whether it has the required shear strength and stiffness parameters which can meet the design requirements of a foundation. For a seawall or breakwater structure, the design requirements will include achieving satisfactory safety factors against sliding, overturning and bearing failure of the foundation, while limiting settlement and lateral movement of the structure.

If heaving material has the required engineering properties to meet design requirements, then it can be retained in the DCM foundation system. Otherwise, it will need to be either dredged or further treated.

Based on the test results discussed above in Section 3, it is proposed to adopt the values presented in Table 2 as the design geotechnical parameters for the heaving material under the present study. These shear strength parameters can be used to check sliding, overturning and bearing. The corresponding Young modulus values have been estimated using relevant correlations or past experience.

These parameters will be used for the full scale test discussed later in Section 5.

Table 2: Adopted geotechnical design parameters for heaving material

Heave zone	Undrained		drained		
	Young's modulus Eu (MPa)	UCS (kPa)	Young's modulus E' (MPa)	cohesion c' (kPa)	Friction angle ϕ' (°)
top 1m[(1)]	–	-	10	0	30
below top 1m	162[(2)]	450	20[(3)]	50[(4)]	34

Notes:
(1) The adopted parameters for the top 1m heaving material are the same as those for sand blanket;
(2) The adopted undrained Young's modulus is assumed to be 300 times UCS following the recommendation given in FHADM for DCM clusters;
(3) The adopted drained Young's modulus is the same as that for a rubble mound consisting of rock fill;
(4) The adopted drained cohesion of 50kPa is considered to be conservative based on the test results presented in Table 1.

4.2 Construction considerations

If a heaving material is to be retained, then efforts should be exercised to improve its engineering properties.

The challenge of cement mixing for heaving material is to inject cement slurry within heaving material and achieve good mixing quality under low confining pressure. To fulfil this objective, construction parameters of high cement dosage, low water cement ratio, low injection pressure, low water injection and low BRN are recommended to minimize leakage of cement and maximize the cementation. Due to the variations of DCM rigs and cement supply systems, the specific construction parameters are not discussed here.

During the mixing process, stringent quality control and monitoring should be undertaken to ensure that the required strength can be achieved in the soil. Field trials should be carried out to obtain or verify design parameters, mixing designs (such as optimal site-specific soil to cement ratio, water cement ratio, etc) and construction methods (such as blade rotation number, etc).

5 FULL SCALE TEST

As part of the present study, a full scale test involving loading a 31m by 32m DCM improvement area has been carried out. The heaving material following DCM construction was measured to be about 2.1m thick and was decided to be retained in the DCM foundation based on stability and settlement analysis results.

The design UCS value for DCM clusters is 1.2MPa and the design geotechnical parameters for heaving material are the same as those presented in Table 2 which have shown to meet the stability, settlement and lateral movement requirements of the loading platform.

5.1 Test setup

Prior to DCM installation, a 2m thick sand blanket was placed on the existing seabed. With a 50% improvement area ratio, a total of 123 numbers of DCM clusters, about 20m deep, were then installed, followed by the placement of a 1.6m thick rubble mound which was used as a loading platform. Loading was applied to the loading platform on a 15m by 15m area, at the centre of the DCM treated ground, through a gradual placement of precast concrete blocks amounting to a total height of 10.8m. This is equivalent to a uniform loading of about 340kPa corresponding to a mean lower low sea level of +0.4mPD. The DCM layout and a typical section of the test setup are illustrated in Figure 6. A site photo showing the loading concrete blocks is presented in Plate 1.

6 numbers of Shape Array Vertical (SAAV) Inclinometers and 3 numbers of yield point Multiple Rod Extensometer have been installed to monitor the settlement and lateral movement of both the loading platform and the DCM body. All the instruments were connected to a data logger fixed on a prefabricated steel platform which is located about 5.8m away from the test area, as indicated in Figure 6a.

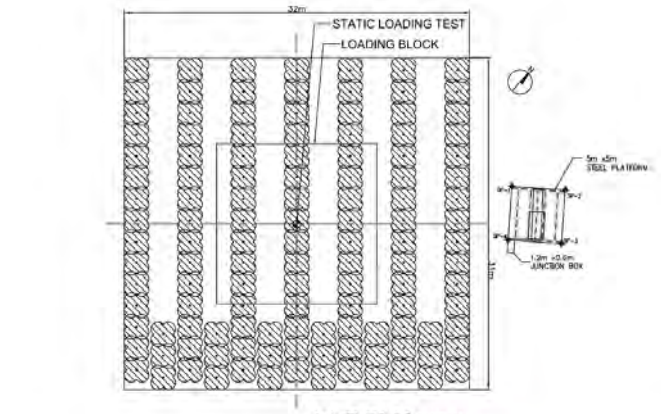

(a) DCM layout

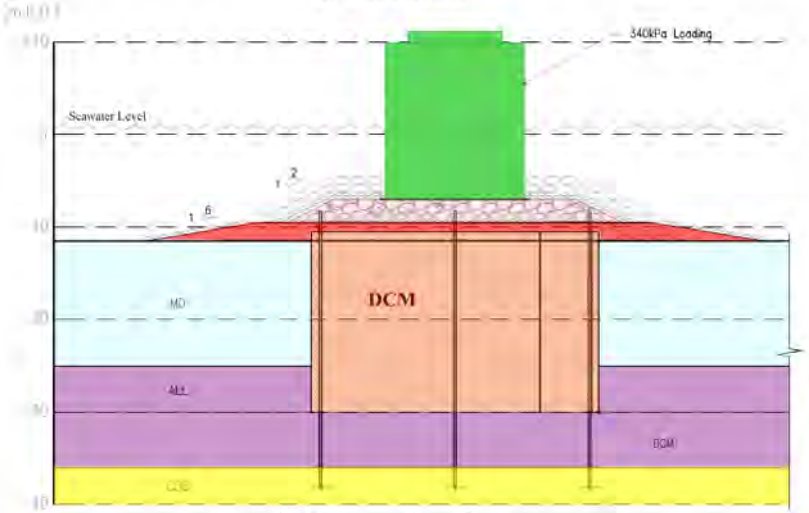

(b) typical cross section of test setup

Figure 6: DCM layout and test setup

Plate 1: Site Photo of loading concrete blocks

5.2 Test results

Throughout the test the loading platform was observed to have remained stable. The settlement and lateral movement were measured at different depths, from the loading platform downward, and then compared with their theoretical predictions. In the present paper, only compression of both the DCM body and heaving material is discussed below.

Plaxis 3D has been employed to model the loading process and predict compression of the DCM and heaving material. Heaving material was assumed to be under an undrained condition due to the relatively short test period. The measured and predicted results are presented in Table 3.

Table 3: Comparison of measured and predicted compression

Material	Compression (mm)	
	measured	predicted
DCM treated ground	1.4	38
DCM heaving material	1.5	22

As can be seen, the predicted compression value is much smaller than the measured, for both the DCM treated ground and heaving material, indicating that the theoretical assumptions are on the conservative side. Based on these results, it can be concluded that the heaving material can satisfy design requirements and hence can be retained in the DCM foundation system.

6 CONCLUSION

A series of lab and in-situ tests including a full scale static loading test have been carried out under the present study to investigate whether heaving material, resulted from DCM construction, can be retained in the DCM foundation system.

Lab tests include UCS and direct shear tests on samples taken from heaving material, while shallow CPT tests are conducted through the heave zone down to the top of the DCM clusters. The test results have shown that the shear strength parameters of heaving material are much less than those of the DCM clusters but may still be able to meet design requirements.

The results of the full scale static loading test which involves loading a 30m by 30m DCM treated area, with an improvement area ratio of 50%, have indicated that the heaving material can meet design requirements and hence can be retained in the DCM foundation system for the loading test.

REFERENCES

EuroSoilStab. 2014. Design Guide Soft Soil Stabilization, CT97-0351, Project No.: BE 96-3177.

FHADM 2013 - Federal Highway Administration Design Manual: Deep Mixing for Embankment and Foundation Support.

Kawasaki, T., A. Niina, S. Saitoh, Y. Suzuki, and Y. Honjo. 1981. Deep mixing method using cement hardening agent. In: Proceedings of 10th International Conference on Soil Mechanics and Foundation Engineering, Stockholm, 15–19 June 1981. Edited by Publications Committee of X. ICSMGE, 721–724. Balkema, Rotterdam.

Kulhawy, F.H. and Mayne, P.W. 1990. Manual on estimating soil properties for foundation design, Technical Report No. EPRI-EL-6800, Electric Power Research Inst., Palo Alto, CA (USA); Cornell Univ., Ithaca, NY (USA). Geotechnical Engineering Group.

Larsson, S., and Kosche, M. 2005. A laboratory study on the transition zone around lime-cement columns. Proc., Int. Conf. on Deep Mixing, Best Practice and Recent Advances, Vol. 1, Swedish Geotechnical Institute, Linkoping, 111–118.

Robertson, P.K. and Campanella, R.C. 1983. Interpretation of cone penetration tests, Canadian Geotechnics Journal, Vol. 20.

Shen, S. L., Han, J., Huang, X. C., and Du, S. J. 2003a. Laboratory studies on property changes in surrounding clays due to installation of deep mixing columns. Marine Georesources & Geotechnology, 21_3, 15–35.

Insights on Debris Flow Growth: Collisions and Contractile Skins

C.E. Choi

Department of Civil Engineering, The University of Hong Kong, HKSAR, China (cechoi@hku.hk)

ABSTRACT

Soil bed erosion is perhaps the most important momentum exchange process that governs the growth and destructive potential of landslides, such as debris flow. Existing erosion models only consider shear stresses induced by the basal friction of the flow as the driving mechanism and adopt saturated soil mechanics to describe the failure of the soil bed. However, field observations have hinted at the importance of collisional stresses as a major driving mechanism of erosion and soil beds in nature are rarely saturated when landslides occur. In this plenary paper, unsaturated soil mechanics is used to characterize soil bed erosion by flows dominated by collisional stresses. Experiments were conducted to model the erosion of unsaturated sandy beds with a wide range of initial matric suction, which is a measure of the capillary stresses, by gravel flows. Key findings and their implications to the delineation of debris flow hazards are discussed.

1 INTRODUCTION

Landslides, such as debris flow, travel at high speeds and may cause fatalities and damage to infrastructure in mountainous regions (Froude & Petley 2018; Jakob et al. 2012). The destructive potential of a debris flow hinges on its ability to erode soil bed material along its flow path (Hungr et al. 2005). Therefore, reliable predictions of erosion are crucial when delineating debris flow hazards. Despite a strong foundation of research work on erosion (Cao et al. 2004; Fraccarollo & Capart 2002; McDougall & Hungr 2005; Medina et al. 2008; Pirulli & Pastor 2012; Sovilla et al. 2006; Sutherland 1967; Takahashi 1978), it remains one of the most difficult momentum exchange process to model and predict (Hungr et al. 2005; Iverson 2012). Reliable predictions of erosion have direct implications on the design capacity of the mitigation measures used to arrest debris flows.

The bulk of existing erosion theories in the literature rely on shear stress induced by the friction at the base of the flow as the driving mechanism (Iverson 2012; Takahashi 1978). However, unique field measurements of natural debris flows taken from Illgraben, Switzerland, show that large boulders at the flow front generate high collisional stresses (McArdell et al. 2007), which may have an even more prominent effect on erosion compared to friction-induced basal shear stress. In fact, field observations show that collisional stresses at the base of a flow may drive erosion by generating point loads as high as 10 MPa (Okuda et al. 1980), which is more than sufficient to cause even bedrock to fail (Stock & Dietrich 2006). Despite the important role played by collisional stresses, the bulk of existing erosion theories for soil beds still focus on friction-induced basal shear stress as the driving mechanism and overlook the effects of basal collisional stresses.

Another common idealization made in existing theoretical models of soil bed erosion is that the strength of soil can be estimated using saturated soil mechanics (Iverson 2012). However, channel beds are seldom saturated in nature when landslides occur (McCoy et al. 2012). In fact, for unsaturated soils, capillary stresses due to the presence of air-water interfaces significantly contribute to the

shear strength (Fredlund et al. 1996; Vanapalli et al. 1996). The peak shear strength of unsaturated soil has been reported to be up to three times larger than that at its saturated state (Fredlund et al. 1996; Vanapalli et al. 1996). Furthermore, in saturated soils, any external undrained loading is directly transferred to the pore water. However, for unsaturated soils, the compressibility of the pore air also plays an important role in the transfer of undrained loading to the soil bed (Skempton 1954). Evidently, considering the capillary stresses in the soil bed is an important step towards the realistic modelling of debris flow erosion and growth in the event that the soil bed is unsaturated.

In this plenary paper, details of a new theory on soil bed erosion based on unsaturated soil mechanics and the assumption that soil bed erosion is driven by collisional stresses are presented. A series of experiments were carried out to evaluate the proposed erosion theory.

2 MODIFIED STRENGTH NORMALISED COLLISIONAL STRESS FOR EROSION OF UNSATURATED SOIL BEDS

The point loads imposed on a soil bed by a debris flows scale with the collisional stresses σ_i, which is defined by Bagnold (1954) as follows:

$$\sigma_i = \nu_s \rho_s D_e^2 \dot{\gamma}^2 \tag{1}$$

where ν_s is the solid fraction of the debris flow, ρ_s is the density of the solid particles, D_e is the characteristic grain diameter of the solid particles and $\dot{\gamma}$ is the shear rate near the base of a debris flow. The erosion rate $\dot{e}$ of a soil bed by collisional stresses is proportional to the strength normalized collisional stress NSNCS, which is defined as the ratio of the basal collisional stresses to the shear strength of the soil bed τ_f:

$$\dot{e} = K \cdot N_{SNCS} \tag{2a}$$

$$N_{SNCS} = \frac{\nu_s \rho_s D_e^2 \dot{\gamma}^2}{\tau_f} \tag{2b}$$

where K is a coefficient related to the properties of the flow material and may be interpreted as the ratio of the stresses from point loads imposed on the soil beds to the collisional stresses (Equation 1). Equation 2 was originally proposed to estimate the erosion of bedrock by collisional flows (Stock & Dietrich 2006), where the erosion rate was reported to exhibit a linear relationship with N_{SNCS}. However, the failure mechanisms for soil and rock are different. For soil beds, failure occurs when the induced shear stress exceeds the shear strength (Terzaghi 1936). After which, soil particles will slide along a failure plane. In contrast, rock beds fail by tensile failure, which is initiated at discontinuities (Jaeger et al. 2009). Thus, the denominator of N_{SNCS} is modified to cater for unsaturated soils.

For unsaturated soils, the voids and soil skeleton enable capillary action, whereby air-water interfaces called contractile skins act as elastic membranes to hold soil particles together via surface tension (Fredlund et al. 1978). The shear strength of unsaturated soils τ can be expressed as follows (Fredlund et al. 1978; Lu 2008):

$$\tau = (\sigma_n - u_a) \tan\phi' + (u_a - u_w)\tan\phi^b \tag{3}$$

where σ_n, u_a and u_w are the normal stress, pore air pressure and pore water pressure, respectively, ϕ' is the internal friction angle of the soil and $\tan\phi^b$ quantifies the effect of matric suction $(u_a - u_w)$ on the shear strength. Equation 3 shows that the shear strength of unsaturated soils is governed by two stress state parameters, specifically the net normal stress $(\sigma_n - u_a)$ and the matric suction. Although the shear strength of soil subjected to rapid loading may be rate-dependent, these effects are not considered here for simplicity.

Debris flows impose rapid loading on soil beds (Hungr et al. 2014; Takahashi 1978). If the rate of loading is higher than that at which the pore fluid drains from the soil matrix, the loading is considered

undrained and pore pressure will increase. The response of the pore air pressure Δu_a and pore water pressure Δu_w to external undrained loading $\Delta\sigma$ can be calculated as follows (Skempton 1954):

$$\Delta u_a = B_a \cdot \Delta\sigma \tag{4a}$$

$$\Delta u_w = B_w \cdot \Delta\sigma \tag{4b}$$

where B_a is the pore air pressure parameter and B_w is the pore water pressure parameter.

In saturated soils, the pore water pressure parameter is assumed to be unity because the compressibility of the pore water is relatively low compared to that of the soil skeleton (Bishop 1954; Hasan & Fredlund 1980; Skempton 1954). However, in unsaturated soils, the high compressibility of the pore air renders increases in both the pore water pressure and pore air pressure smaller than the external loading. For unsaturated soils subjected to undrained loading, the pore pressure parameters can be expressed as follows (Hilf 1948):

$$B_a = B_w = 1/\left[1 + \frac{(1 - S_0)\, n_0}{m_v (u_{a0} + \Delta u_a)}\right] \tag{5}$$

where S_0 is the initial degree of saturation of soil bed, n_0 is the initial void ratio of the soil, m_v is the compressibility of the soil and u_{a0} is the initial pore air pressure. If the pore air pressure is assumed to be atmospheric, then the pore pressure during undrained loading can be calculated as follows:

$$u_a = B_a \cdot \Delta\sigma \tag{6a}$$

$$u_w = -(u_a - u_w)_0 + B_w \cdot \Delta\sigma \tag{6b}$$

where $(u_a - u_w)_0$ is the initial matric suction. Equation 6b can then be used to explain why positive pore water pressure is more readily generated for soil beds with a higher bed water content, as observed by Iverson et al. (2011). The change in the pore pressure during undrained loading results in a change in the shear strength of the unsaturated soil. By substituting Equation 6 into Equation 3, the shear strength of an unsaturated soil bed undergoing undrained loading can be expressed as follows:

$$\tau_f = \sigma_n \tan\phi' + (u_a - u_w)_0 \tan\phi^b - B_a \sigma_n \tan\phi' \tag{7}$$

Equation 7 can then be substituted into Equation 2 to estimate the erosion rate of an unsaturated soil bed subjected to collisional stresses:

$$\dot{e} = K \cdot N_{SNCS} \tag{8a}$$

$$N_{SNCS} = \frac{\nu_s \rho_s D_e^2 \dot{\gamma}^2}{\sigma_n \tan\phi' + (u_a - u_w)_0 \tan\phi^b - B_a \sigma_n \tan\phi'} \tag{8b}$$

The modified dimensionless number N_{SNCS} will be evaluated using the physical experimental data, which will be discussed later in this plenary paper.

4 PHYSICAL MODELLING OF SOIL BED EROSION BY COLLISIONAL FLOWS

The goal of the erosion experiments was to model a debris flow front, which generally consists of a permeable assembly of coarse grains (Iverson 1997). The viscous stress caused by the interstitial fluid can be neglected compared to the collisional inter-particle stresses generated by the coarse grains at the front of a debris flow (McArdell et al. 2007). The Savage number N_{Sav}, which characterizes the relative importance between interparticle collisional and frictional stresses, is the most relevant dimensionless number for scaling the modelling flows:

$$N_{Sav} = \frac{\nu_s \rho_s D_e^2 \dot{\gamma}^2}{pgh \tan\phi'} \quad (9)$$

The inter-particle collisional stresses dominate the interaction of solid grains when the Savage number N_{Sav} is greater than 0.1 (Savage & Hutter 1989). The configuration of the experimental setup was selected based on the aforementioned scaling considerations to ensure the generated flows are dominated by collisional stresses.

The flume model (Fig. 1) used in this study is 2 m in length and 0.2 m in width. The channel bed has a 1.3-m long rigid section, followed by a 0.7-m long erodible section. During each test, a gravel assembly with an initial depth h_0 of 0.48 m and a width r_0 of 0.5 m was prepared in the container. The friction angle for the gravel is 43.5°. The grain size of the gravels used in this study range from 10 mm to 15 mm, with an effective diameter De of 12 mm. The gate lifts vertically and is controlled pneumatically to simulate dam-break initiation of the dry gravel material retained behind the gate (Stansby et al. 1998). Upon dam-break initiation, the mass of gravel was allowed to accelerate down the rigid bed before flowing on top of the erodible one. The erodible bed consists of sandy soil with negligible clay content to represent the channel bed deposits observed in the field (Chen & Lee 2004). The volumetric water content of the erodible bed was varied from 0 to 0.3, corresponding to initial matric suctions from 97.8 kPa to 0.1 kPa. The dry density of the bed material was controlled and only varied by less than 3% for each test. Table 1 shows a summary of the test program. Details of the experimental setup are discussed in Song & Choi (2021).

A pore pressure transducer installed at a depth of 0.12 m in the erodible soil bed along the centerline of the channel and at an inclined distance of 0.4 m downstream from the interface between the non-erodible and erodible beds. A high-speed camera was installed at the side of the flume to capture the flow kinematics. The images captured by a high-speed camera installed at the side of flume. Images from the camera are analyzed with the Particle Image Velocimetry (PIV) technique (Thielicke & Stamhuis 2014) to deduce the velocity field of the flow. An ultrasonic sensor was mounted above the channel bed just before the erodible bed to measure the flow depth. The initial matric suction of the soil bed was measured using a tensiometer. To reveal the erosion depth, 12 erosion columns were installed along the centerline of the erodible section at distances of 0.04 m, 0.08 m, 0.12 m, 0.16 m, 0.20 m, 0.26 m, 0.32 m, 0.38 m, 0.44 m, 0.50 m, 0.56 m and 0.62 m from the interface between the non-erodible and erodible beds (Fig. 2). The washers have inner and outer diameters of 3.1 mm and 7 mm, respectively The washer columns were prepared before the soil bed was prepared to the same height as the initial height of the columns. Then, the rods were removed without disturbing the soil and washers. The erosion depth is the difference between the height of the columns before and after each test.

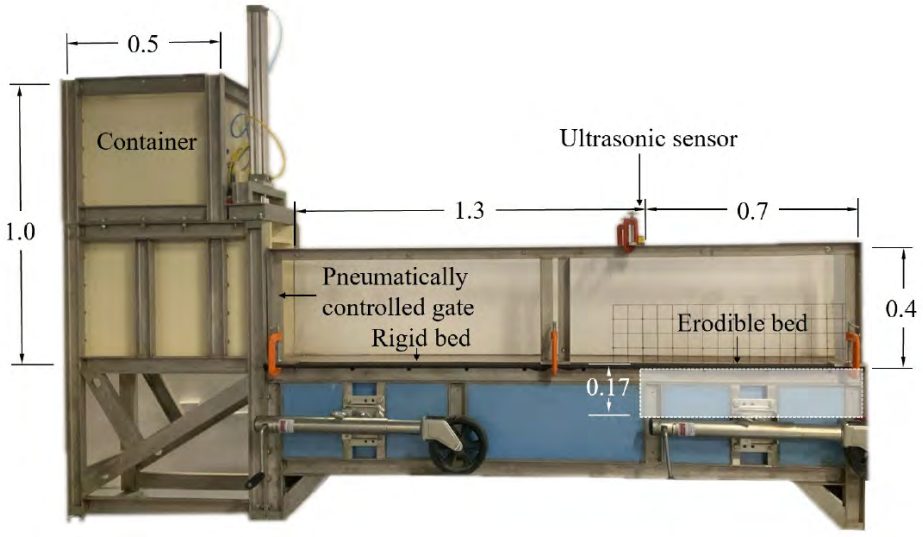

Figure 1: Experimental setup

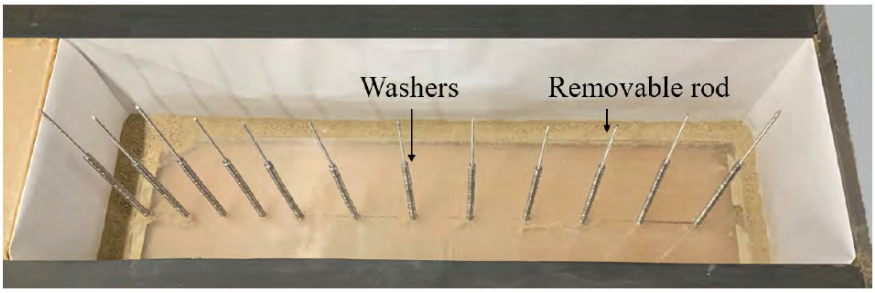

Figure 2: Erosion columns

Table 1: Summary of test program (Song & Choi 2021)

Test ID	Dry density, ρ_d (kg/m^3)	Void ratio, n	Volumetric water content, θ	Initial matric suction, $(u_a - u_w)_0$ (kPa)	Pore pressure parameter, B	Shear strength at failure, τ_f (kPa)
θ_0	1305	1.01	0.00	-	0.48	0.62
θ_006	1307	1.00	0.06	97.8	0.51	1.10
θ_011	1315	0.99	0.11	79.5	0.54	5.60
θ_013	1329	0.97	0.13	68.0	0.55	7.38
θ_016	1319	0.99	0.16	26.0	0.58	6.74
θ_018a	1319	0.99	0.18	14.0	0.59	4.12
θ_018b	1310	1.00	0.18	10.8	0.59	3.24
θ_020	1339	0.96	0.20	5.0	0.60	1.93
θ_021	1327	0.97	0.21	1.7	0.61	0.95
θ_022	1329	0.97	0.22	1.3	0.63	0.85
θ_024	1323	0.98	0.24	0.9	0.64	0.71
θ_028	1329	0.97	0.28	0.4	0.68	0.53
θ_030	1340	0.96	0.30	0.1	0.71	0.37

5 INTERPRETATION OF RESULTS

5.1 Erosion kinematics

Typical kinematics captured by the high-speed camera mounted at the side of the 2-m flume and the corresponding PIV analysis for each snapshot are shown in Fig. 3. The size of the vectors denotes the magnitude of the velocity. Fig. 3a shows the arrival of the dispersed flow front of gravel flow in the field of view. The dispersed flow front was collisional and without sustained contact. The gravel particles at the flow front were observed to collide with the erodible bed and some of the bed material is observed to be picked up into the flow. This indicates that on top of friction induced stresses, collisional stresses in the flow front also play a role in erosion. Erosion occurs without persisting contacts between gravel particles. This implies that collisional stresses are the dominant grain stress causing erosion at the flow front. Fig. 3b shows the deceleration of the flow, which is accompanied by the gradual increase of the flow height. The motion of the gravel particles exhibits a transition from a gas-like flow to a dense one. The velocity of the gravel particles at the base of the flow gradually decreases. Fig. 3c shows the deposition process, where the velocity of the gravel at the bottom layer of the flow decreases to zero and deposits (Fig. 3d).

5.2 Effects of matric suction on soil bed erosion

Fig. 4 shows the relationship between the average erosion rate, the shear strength of the soil bed at failure, and the initial matric suction of the soil bed. The average erosion rate is calculated by dividing

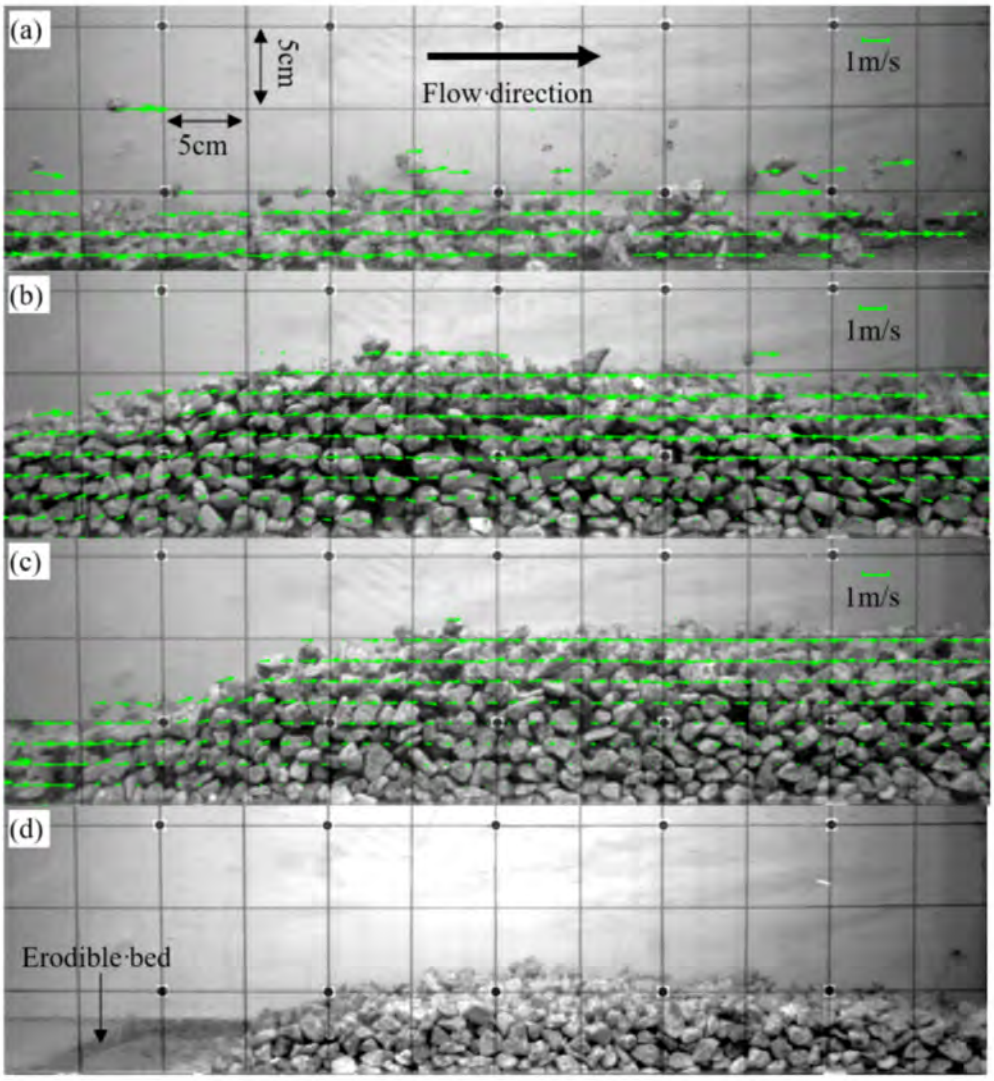

Figure 3: Observed flow kinematics captured using the high-speed camera with PIV analysis with a bed volumetric water content θ = 0.22. (a) t = 0.22 s, flow front passes the erodible bed; (b) t = 1.19 s, deceleration of the flow; (c) t = 2.16 s, deposition of the flow; (d) t = 3.14 s, final deposited profile

the average erosion depth by the erosion duration estimated from the videos captured by the high-speed camera. The variation in the average erosion rate with initial matric suction exhibits a parabola-like relationship. The average erosion rate decreases with increasing matric suction until a minimum is reached. Afterwards, the average erosion rate increases with the matric suction. However, the variation in the shear strength with the matric suction exhibits an inverted parabola-like relationship. This observation agrees with Equation 2 in that the erosion rate should be inversely related to the shear strength. Iverson et al. (2011) shows that the average erosion depth increases linearly with the bed water content from the large-scale flume experiments. However, a linear trend only tells part of the story. The erosion depth tends to increase with the bed water content when it is higher than a specific value, as shown by the parabola-like relationship proposed in this study (Fig. 5a). The measured data exhibits parabola-like relationship between the average erosion depth and the bed water content. A more comprehensive set of field data reported by McCoy et al. (2012) can be used to validate the proposed parabola-like relationship between the erosion rate and the bed water content (Fig. 5b). The field data was obtained from an observation station at Chalk Cliffs, Colorado, U.S., from September 2009 to June 2011. The field data further corroborates the parabola-like relationship between the average erosion rate and the bed water content. Thus, to improve the fundamental understanding and predictions of soil bed erosion, it is necessary to consider hydro-mechanical coupling.

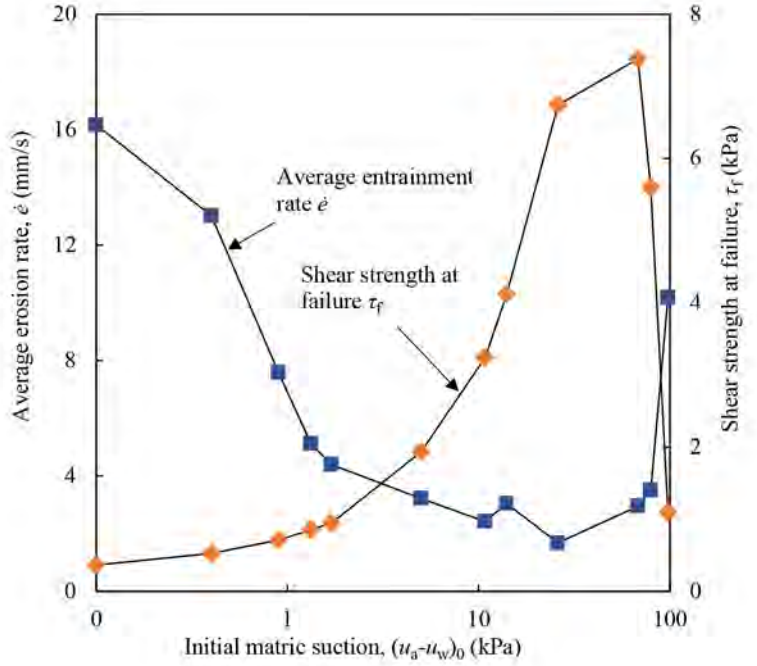

Figure 4: Measured erosion rate ė and the calculated shear strength of bed material at failure τ_f against the measured initial matric suction of the erodible bed $(u_a - u_w)_0$. The shear strength at failure τ_f is calculated using Equation 7

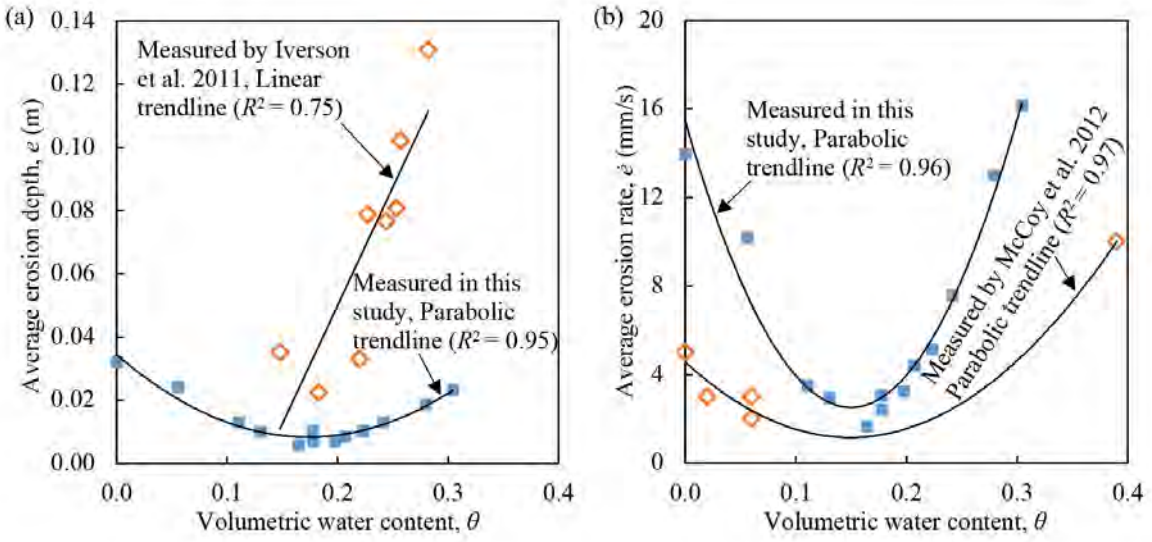

Figure 5: Effects of volumetric water content of the erodible bed θ on erosion: (a) variation of the measured average erosion depth e; (b) variation of measured average erosion rate ė

5.3 Evaluation of the NSNCS

The strength normalized collisional stress N_{SNCS} can be calculated using Equation 8b with the necessary parameters obtained from the experiments. The experimental erosion data exhibits a positive linear correlation between the average erosion rate and NSNCS (Fig. 6). This trend shows that the erosion of a soil bed is strongly influenced by the collisional stresses at the base of the flow. In the flume experiments carried out in this study, the maximum basal friction induced shear stress is estimated to be 1.4 kPa based on a flow depth of 0.1 m, which is the maximum flow depth obtained from all the experiments. Even though the shear strengths of the soil beds, with water contents from 0.11 to 0.20, are larger than the estimated maximum shear stress induced by the flow, erosion still occurs. Therefore, traditional

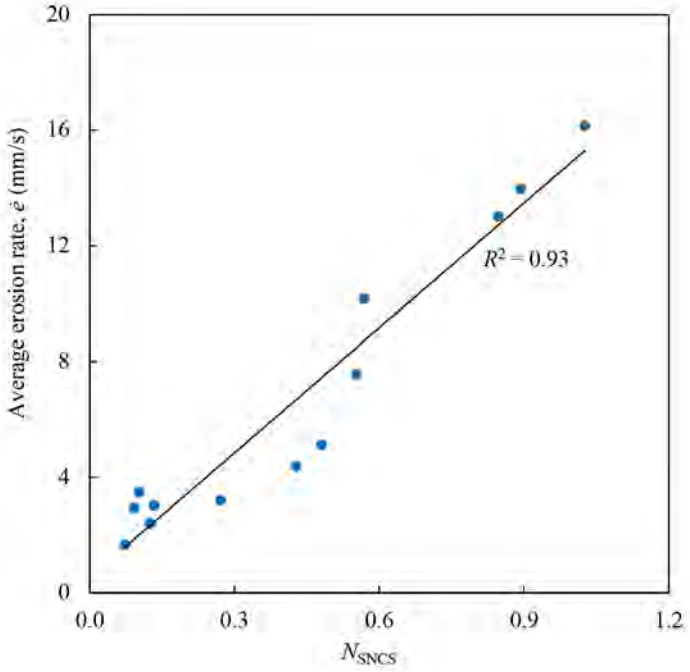

Figure 6: Erosion rate ė against the strength normalized collisional stress N_{SNCS}

erosion theories may need to be supplemented by the proposed collision-induced erosion theory to enhance erosion predictions. Another interesting observation supporting the notion that collisional stresses play a dominant role during erosion is that the dispersed fronts observed from the high-speed imagery do not have enduring contacts among grains, so the shear stress imposed on the soil bed can be assumed to be negligible. Yet, the soil bed is still eroded.

Similar evidence supporting the notion of collision-induced erosion can also be found in the field measurements reported by Berger et al. (2011) at Illgraben, Switzerland. For the debris flow that occurred on the 1st of July 2008, the basal normal stress, pore water pressure and basal shear stress were measured by the force plate and reported to be 35 kPa, 2 kPa and 14 kPa, respectively, when erosion was detected by the erosion sensor. If the internal friction angle of the bed material is assumed to be 34°, then the shear strength can be calculated as the product of the normal effective stress (i.e., measured normal stress 35 kPa minus the measured pore water pressure 2 kPa) and the tangent value of the assumed friction angle (i.e., 34°). The shear strength calculated is approximately 22 kPa, which is still larger than the measured basal shear stress. This simple back-of-the-envelope calculation shows that aside from basal friction-induced shear stress, there undoubtedly should be other stresses (i.e. collisional stresses) contributing to the erosion of the soil bed. Another observation that supports the importance of collisional stresses on soil bed erosion is that the basal shear stress measured by the force plate remains relatively stable during the entire flow process (Berger et al. 2011). However, erosion predominantly occurs during the passage of the flow front, where the most collisional stresses were reported (McArdell et al. 2007).

6 DISCUSSION AND CONCLUSIONS

The findings from this study demonstrate the importance of hydro-mechanical coupling for delineating debris flow hazards. This is evident from the measured parabola-like relationship between water content and erosion, which is a stark contrast from the notion that erosion increases linearly with the bed water content as demonstrated by Iverson et al. (2011). There are of course many questions that remained unanswered from this conclusion alone. For instance, it appears that modelling of debris flow erosion is even more complicated of a problem than initially thought. Erosion not only depends on both the dynamic properties of the flow and the water content of the soil bed in a highly non-linear manner. Further compounding the challenges of modelling this problem are the effects of three-dimensional channel geometries and the non-uniform spatial distribution of bed water content that may occur in

the field (i.e., higher water content along the centerline than further up the banks). A clear and indirect outcome from this study is that there is a pressing need to couple the hydrological and mechanical effects of soil behavior to advance the current state of debris flow modelling and hazard assessment. More importantly, soil-atmospheric interaction is very much relevant to debris flow hazard mitigation. Given the importance of capillary effects, the question that remained unanswered are how the competing effects between rainfall and humidity, driven by climate change, govern the strength of soil beds and their susceptibility to erosion? Answering these questions will help to advance the current state of landslide growth modelling and prediction.

Based on the unique field observation data (Berger et al. 2011) and the findings from this study, the theory of collision-induced erosion can help to explain the deficiencies of theories relying on purely basal friction-induced erosion. The theory of collision-induced erosion can explain why most erosion occurs mainly during the passage of the flow front (Berger et al. 2011; McCoy et al. 2012), which typically consists of highly-collisional boulders. In contrast, insignificant erosion occurs during the passage of the flow body and tail (Berger et al. 2011; McCoy et al. 2012), which have low concentrations of large boulders, and thus, weak collisional stresses. Therefore, highly erosive debris flows may develop in channels that are enriched with boulders. It is acknowledged that collisional stresses may not be the sole mechanism that drives erosion, but collisional stresses are important and often overlooked. Perhaps, models that can capture the spatial variation of collisional stresses would yield even more realistic erosion volumes and rates compared to the existing models. These considerations are required to advance debris flow predictions and delineations.

ACKNOWLEDGEMENTS

The author would also like to thank Mr. Song Pengjia for his role in advancing the research about erosion and his help to prepare this plenary paper, and Dr, Du Jianting for vetting the manuscript. The author would like to thank the Geotechnical Division Committee of the Hong Kong Institution of Engineers and the International Society for Soil Mechanics and Geotechnical Engineer for the Bright Spark Lecture Award. The author would like to express his gratitude to his colleagues in the Department of Civil Engineering at the University of Hong Kong, and his former colleagues and mentor Prof. Charles W.W. Ng from the Hong Kong University of Science and Technology for their support. Finally, the author would like to acknowledge the support provided by the Department of Civil Engineering and Faculty of Engineering at the University of Hong Kong for their support provided by the startup fund, and the support from the Research Grants Council of Hong Kong, particularly the funding from the General Research Fund (16212618; 16210219), the Early Career Scheme (27205320), and the Areas of Excellence (AoE/E-603/18).

REFERENCES

Bagnold, R.A. 1954. Experiments on a gravity-free dispersion of large solid spheres in a Newtonian fluid under shear. *Proceedings of the Royal Society of London. Series A. Mathematical and Physical Sciences,* 225(1160): 49-63.

Berger, C., McArdell, B.W. & Schlunegger, F. 2011. Direct measurement of channel erosion by debris flows, Illgraben, Switzerland. *Journal of Geophysical Research: Earth Surface,* 116: F01002.

Bishop, A.W. 1954. The use of pore-pressure coefficients in practice. *Geotechnique,* 4(4): 148-152.

Cao, Z., Pender, G., Wallis, S. & Carling, P. 2004. Computational dam-break hydraulics over erodible sediment bed. J*ournal of Hydraulic Engineering,* 130(7): 689-703.

Chen, H. & Lee, C.J. 2004. Geohazards of slope mass movement and its prevention in Hong Kong. *Engineering Geology,* 76(1-2): 3-25.

Faug, T. 2015. Macroscopic force experienced by extended objects in granular flows over a very broad Froude-number range. *The European Physical Journal E,* 38(5): 1-10.

Fraccarollo, L. & Capart, H. 2002. Riemann wave description of erosional dam-break flows. *Journal of Fluid Mechanics*, 461: 183-228.

Fredlund, D.G., Morgenstern, N.R. & Widger, R.A. 1978. The Shear-Strength of Unsaturated Soils. *Canadian Geotechnical Journal,* 15(3): 313-321.

Fredlund, D.G., Xing, A.Q., Fredlund, M.D. & Barbour, S.L. 1996. The relationship of the unsaturated soil shear strength to the soil-water characteristic curve. *Canadian Geotechnical Journal,* 33(3): 440-448.

Froude, M.J. & Petley, D.N. 2018. Global fatal landslide occurrence from 2004 to 2016. *Natural Hazards and Earth System Sciences,* 18(8): 2161-2181.

Hasan, J.U. & Fredlund, D.G. 1980. Pore pressure parameters for unsaturated soils. *Canadian Geotechnical Journal,* 17(3): 395-404.

Hilf, J. 1948. Estimating construction pore pressures in rolled earth dams. *2nd International Conference on Soil Mechanics and Foundation Engineering,* Rotterdam, Netherlands.

Hungr, O., Leroueil, S. & Picarelli, L. 2014. The Varnes classification of landslide types, an update. *Landslide,* 11(2): 167-194.

Hungr, O., McDougall, S. & Bovis, M. 2005. *Debris-flow hazards and related phenomena.* Heidelberg, Berlin: Springer.

Iverson, R.M. 1997. The physics of debris flows. *Reviews of Geophysics,* 35(3): 245-296.

Iverson, R.M. 2012. Elementary theory of bed-sediment entrainment by debris flows and avalanches. *Journal of Geophysical Research: Earth Surface,* 117: F03006.

Iverson, R.M. 2015. Scaling and design of landslide and debris-flow experiments. *Geomorphology,* 244: 9-20.

Iverson, R.M., Reid, M.E., Logan, M., LaHusen, R.G., Godt, J.W. & Griswold, J.P. 2011. Positive feedback and momentum growth during debris-flow entrainment of wet bed sediment. *Nature Geoscience,* 4: 116–121.

Jaeger, J.C., Cook, N.G. & Zimmerman, R. 2009. *Fundamentals of rock mechanics.* New York: John Wiley & Sons.

Jakob, M., Stein, D. & Ulmi, M. 2012. Vulnerability of buildings to debris flow impact. *Natural Hazards,* 60(2): 241-261.

Lu, N. 2008. Is matric suction a stress variable? *Journal of Geotechnical and Geoenvironmental Engineering,* 134(7): 899-905.

McArdell, B.W., Bartelt, P. & Kowalski, J. 2007. Field observations of basal forces and fluid pore pressure in a debris flow. *Geophysical Research Letters,* 34(7): L07406.

McCoy, S.W., Kean, J.W., Coe, J.A., Tucker, G.E., Staley, D.M. & Wasklewicz, T.A. 2012. Sediment entrainment by debris flows: In situ measurements from the headwaters of a steep catchment. *Journal of Geophysical Research: Earth Surface,* 117: F03016.

McDougall, S. & Hungr, O. 2005. Dynamic modelling of entrainment in rapid landslides. *Canadian Geotechnical Journal,* 42(5): 1437-1448.

Medina, V., Hürlimann, M. & Bateman, A. 2008. Application of FLAT Model, a 2D finite volume code, to debris flows in the northeastern part of the Iberian Peninsula. *Landslides,* 5(1): 127-142.

NILIM (National Institute for Land and Infrastructure Management) 2007. Manual of technical standards for designing sabo facilities against debris flow and Driftwood, *Technical Note of NILIM No. 365. Tsukuba, Japan: Natural Institute for Land and Infrastructure Management, Ministry of Land, Infrastructure and Transport* (in Japanese).

Okuda, S., Okunishi, K. & Suwa, H. 1980. Observation of debris flow at Kamikamihori Valley of Mt. Yakedade. *3rd Meeting of IGU Commission on Field Experiment in Geomorphology,* Kyoto, Japan.

Pirulli, M. & Pastor, M. 2012. Numerical study on the erosion of bed material into rapid landslides. *Geotechnique,* 62(11): 959-972.

Savage, S.B. & Hutter, K. 1989. The motion of a finite mass of granular material down a rough incline. *Journal of Fluid Mechanics,* 199: 177-215.

Skempton, A.W. 1954. The pore-pressure coefficients A and B. *Geotechnique,* 4(4): 143-147.

Song, P. & Choi, C.E. 2021. Revealing the importance of capillary and collisional stresses on soil bed erosion induced by debris flows. *Journal of Geophysical Research: Earth Surface*. (accepted).

Sovilla, B., Burlando, P. & Bartelt, P. 2006. Field experiments and numerical modeling of mass entrainment in snow avalanches. *Journal of Geophysical Research: Earth Surface,* 111: F03007.

Stansby, P.K., Chegini, A. & Barnes, T.C.D. 1998. The initial stages of dam-break flow. *Journal of Fluid Mechanics,* 374: 407-424.

Stock, J.D. & Dietrich, W.E. 2006. Erosion of steepland valleys by debris flows. *Geological Society of America Bulletin,* 118(9-10): 1125-1148.

Sutherland, A.J. 1967. Proposed mechanism for sediment entrainment by turbulent flows. *Journal of Geophysical Research,* 72(24): 6183-6194.

Takahashi, T. 1978. Mechanical characteristics of debris flow. *Journal of the Hydraulics Division,* 104(8): 1153-1169.

Terzaghi, K.V. 1936. The shearing resistance of saturated soils and the angle between the planes of shear. *1st International Conference on Soil Mechanics,* Harvard University, US.

Thielicke, W. & Stamhuis, E.J. 2014. PIVlab – Towards User-friendly, Affordable and Accurate Digital Particle Image Velocimetry in MATLAB. *Journal of Open Research Software,* 2(1): e30.

Vanapalli, S.K., Fredlund, D.G., Pufahl, D.E. & Clifton, A.W. 1996. Model for the prediction of shear strength with respect to soil suction. *Canadian Geotechnical Journal,* 33(3): 379-392.

An Innovative Design of Retaining Wall in Lung Shan Tunnel Construction

Kelvin Y.M. Choi
Dragages Hong Kong Ltd, Hong Kong

Victor Li
Victor Li & Associates Ltd, Hong Kong

Alan Y.S. Tam
Keystone Design Consultants Ltd, Hong Kong

ABSTRACT

The Heung Yuen Wai Highway opened on 26 May 2019. The 4.8km Lung Shan Tunnel, as one of the main sections of the Heung Yuen Wai Highway, is the longest land-based road tunnel in Hong Kong. It was a success after 5 years of efforts by the project team. Most of tunnel excavation commenced at its Northern Portal near Princess Hill where a mega-sized tunnel boring machine was launched.

The original design of the Northern Portal required 3m diameter bored pile walls for supporting a slope cutting to reach the invert level of the tunnel. Early completion of the portion formation works would be essential to accelerating the overall construction programme for the project. An innovative design involving composite retaining walls and gravity wall with sloping wall backs was proposed to replace the bored pile walls to enhance the programme and improve works quality. The composite wall involved installation of a soldier pile wall temporarily supported by tie-backs. Upon reaching the final excavation level, the soldier pile wall was integrated with a reversed L-shaped R.C. wall to form a permanent composite wall with a maximum retaining height of 29.33m under the temporary stage and 20.975m under the permanent stage for supporting the cut slope behind the wall.

In this paper, design concepts of the proposed composite wall and retaining wall with sloping wall backs are discussed and the benefits of the revised scheme over the conforming design are highlighted. To assure quality works, a comprehensive monitoring system, including the monitoring of the stress developed in the tie-backs, was implemented for performance review. The benefits of the innovative approach and construction difficulties are discussed.

1 INTRODUCTION

1.1 The project

The Heung Yuen Wai Highway (HYWH) under the Liantang / Heung Yuen Wai Boundary Control Point project is an approximately 11-km dual two-lane carriageway connecting the Fanling Highway and the Heung Yuen Wai Boundary Control Point. The section of 4.8km long Lung Shan Tunnel (LST) of the HYWH was constructed by Dragages Hong Kong Limited (DHK) (a member of the Bouygues Construction Group)

using mechanical and drill and blast excavation techniques, together with the largest earth pressure balance (EPB) tunnel boring machine (TBM) with a diameter of 14.1m used in Hong Kong (Storry et al, 2017). The TBM was launched from the Northern Portal to form the northern section of the road tunnel to deal with the challenges of excavating through multiple faults and mixed ground conditions.

At the Northern Portal, major site formation works involving a relatively large volume of materials to be excavated (650,000m3) were necessary under the temporary conditions to create the space necessary for the logistic of tunnel construction and under the permanent conditions for formation of the trunk road. The original ground level of the site varied from approximately +50mPD to +30mPD. Cut slopes or soil-nailed cut slopes were to be formed to lower the existing ground level. In addition, cantilever bored pile walls comprising mostly bored piles of 3m in diameter were proposed in the original design with retaining height up to 17.5m to support the existing or new cut slopes to be formed above the retaining wall. Conventional rectangular-shaped mass concrete wall had also been proposed as permanent retaining walls with a smaller retaining height. The permanent formation level in front of the Northern Portal would be about +9.45mPD.

Plate 1 shows the site formation works needed to create the formation profiles at the Northern Portal.

Plate 1: Aerial view of Northern Portal taken in the end of 2016

1.2 Site Description and Ground Conditions

The Northern Portal is located at the foothill area of Princess Hill. The hillside is covered by Colluvium approximately 2m to 5m thick. The Colluvium layer is typically described in the drillhole records as 'firm, sandy silt with occasional subangular fine gravel sized Tuff fragments' and "firm, slightly sandy clayey silt". The thickness of Colluvium decreases downslope. Alluvium of approximately 4m to 8m thickness occupies most of the lowland area. The superficial deposits are underlain by completely decomposed Tuff (CDT) of approximately 30m thick, followed by slightly to moderately decomposed coarse-ash crystal Tuff bedrock. The CDT is typically described in the drillhole records as 'extremely weak, firm to stiff, slightly sandy silt'. Soil/rock materials comprising partial rock (PR) 10/30 (IV/V) and PR 50/75 (IV) (up to 5m thick) are anticipated above the bedrock in the area. The Princess Hill is bounded by the NE-SW striking Sha Tau Kok Fault and the NW-SE striking photogeological lineaments. Fault related features, e.g. fault breccia, fault zone, quartz breccia, fault gouge and brecciated tuff were logged in drillholes. Bedrock is encountered at the level varying between +15mPD to –20mPD approximately.

2 PROGRAMME CONSTRAINT AND SOLUTION

2.1 Portal formation for tunnel excavation and TBM launching

The tunnel project was scheduled to utilize a single TBM to complete two TBM drives for twin tubes of the Northern section of LST. To achieve this goal, it would require launching of the TBM for southbound tunnel at the Northern Portal to be commenced early. An initial programme assessment indicated that the site formation works based on the original design would require approximately 20 months before the tunneling works could be commenced. This was because temporary platforms would be required for construction of the bored piles on sloping ground and that lowering of the ground profile could only be commenced after completion of the bored pile walls. This would render the goal of using a single TBM for both tunnel drives impossible to meet the tight construction programme.

To secure earlier launching of TBM for the southbound tunnel at the Northern Portal, two alternative designs of retaining walls to replace the bored pile walls were adopted:

(1) Gravity walls with sloping wall backs (also known as the goose-shaped wall).

(2) Composite retaining walls formed by integrating a permanent soldier pile wall temporarily supported by tie-backs with a permanent reversed L-shaped reinforced concrete wall.

The concepts of the above two alternative designs had been used with great success in past projects for widening of Tuen Mun Highways and Tolo Highways (Li, 2012 & Li & Chung, 2013). The scheme of composite retaining wall has also been proposed recently for the site formation works of a project at Yau Tong commissioned by the Civil Engineering and Development Department.

The goose-shaped walls were used to replace the bored pile walls with design maximum height of up to 16.1m above the site formation level. For larger retaining heights, composite retaining walls with a maximum retaining height of 29.33m temporarily supported by 444 nos. of tie-backs were used as an alternative. The advantages of a composite retaining wall in performing both as a temporary embedded wall and a permanent retaining wall had been fully harnessed in this project to allow early commencement of the tunneling works for the southbound tunnel.

By adopting these alternative design schemes, tunnel excavation could be commenced for the southbound tunnel 10 months after the commencement of the contract, saving 10 months of time than would otherwise be required if the original bored pile wall scheme was to be used. This had made the option of using only one TBM for both tunnel drives possible for meeting the target construction programme.

Plate 2 shows the construction of the southbound tunnel while the construction of soldier pile wall for the composite retaining wall was in progress well before completion permanent retaining walls.

Plate 2: Southbound tunnel at the Northern Portal in phase with construction of the soldier pile wall

3 DESIGN OF GOOSE-SHAPED WALL

The design concept of a goose-shaped wall is simple and well discussed by Li (2012) and Li & Chung (2013). It is based on the key factor that the active earth pressure acting on a retaining wall will be reduced if it has a sloping wall back slanting against a cut slope. Figure 1 shows some geometries of a goose-shaped wall proposed by Li (2012) used for road widening projects in Hong Kong. They are designed to keep the total volume of concrete low. This will necessitate an extended reinforced concrete wall toe to be provided to enhance the stability of the wall against bearing and overturning failure. The term of a goose-shaped wall was coined by Li (2012) and Li & Chung (2013) for retaining wall geometries shown in Figure 1, particularly that of Figure 2(b), because they resemble a swimming goose. Perhaps, a swan-shaped wall would have been nicer name.

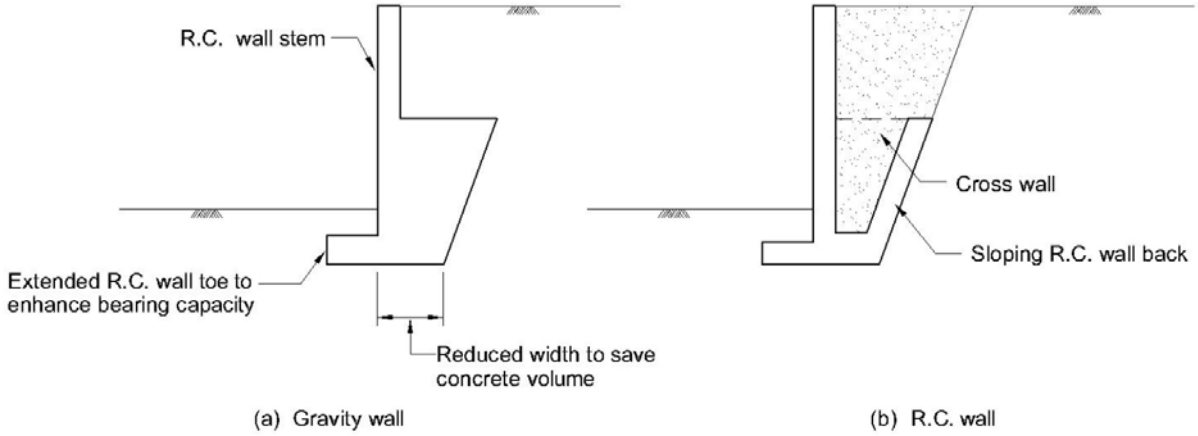

Figure 1: Some geometries of goose-shaped wall (after Li, 2012)

The goose-shaped wall can be formed by initially forming a temporary soil cut slope stabilized by soil nails and then the permanent retaining wall in front of the soil-nailed cut slope. Although the temporary soil nails are ignored in the design of the permanent goose-shaped wall, they will in fact contribute significantly to further reducing the earth pressure and enhancing the stability of the retaining wall.

For this tunnel project, goose-shaped walls were used as alternative for replacing some of the bored pile walls as well as the conventional L-shaped rectangular walls at the Northern Portal and Southern

Plate 3: Construction of goose-shaped wall in progress

Portal. The gradient of the soil-nailed cut slope was 70o for forming the goose-shaped gravity wall. Plate 3 shows the construction of a goose-shaped wall in progress. Figure 2(a) compares the geometries of tallest goose-shaped gravity walls for some of the past projects in Hong Kong described by Li & Chung (2013) with those of this tunnel project at the Northern Portal (Figure 2(b)) and the Southern Portal (Figure 2(c)).

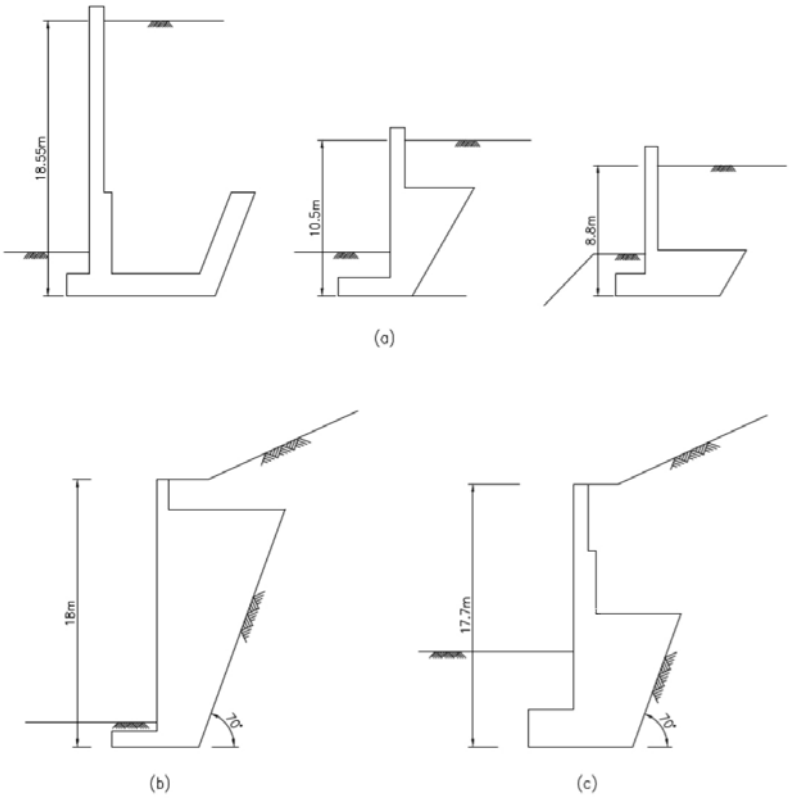

Figure 2: Geometries of completed goose-shaped wall

4 DESIGN OF COMPOSITE WALL

The scheme of composite retaining wall used in the LST construction was first developed by Li (2012) and Li & Chung (2013) by modifying the concept of a retaining wall with a stabilizing based described by Carder et al (1999) and Powrie et al (1999). The scheme as depicted in Figure 3 was first used with success for the project of widening of Tolo Highways as an alternative scheme to bored pile walls.

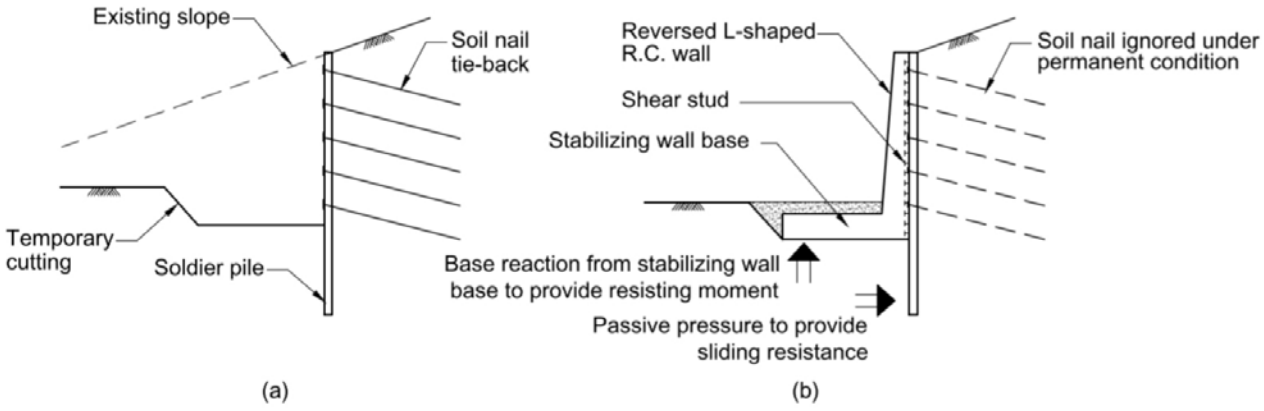

Figure 3: Design scheme of a composite retaining wall (after Li, 2012; Li & Chung, 2013)

For the tunnel project described in this paper, the flexibility offered by the scheme of a composite retaining wall, which can act as both a temporary and a permanent wall, was fully utilized to enable ground profiles to be lowered sufficiently quickly to allow early commencement of the tunnel works. The construction procedures of the composite wall are described in Figure 4.

The upper part of the permanent soil-nailed cut slopes above the composite retaining wall, which formed an integral part of the site formation works, was commenced early to create a working platform on sloping ground sufficient for construction of the soldier pile wall and to serve as a haul road (see Figure 4(a)). The extent of the working space required would have been much larger if the original scheme of bored pile walls were to be used. Once the soldier pile wall was completed, it could serve as an embedded wall for supporting the bulk excavation to enable the ground surface to be quickly lowered to create a working area sufficient for launching of the TBM for the southbound tunnel.

After launching of the southbound tunnel, further bulk excavation was carried out in front of the soldier pile wall to reach the bottom level of the R.C. wall as indicated in Figure 4(b). By then, there would be sufficient space for construction of the northbound tunnel, allowing the construction works for the tunnel and the composite retaining wall to be decoupled.

The R.C. wall in front of the soldier pile wall could then constructed to integrate with the permanent soldier pile wall to form the complete composite wall as shown in Figure 4(c). The beauty of the composite retaining wall scheme is that the R.C. wall could be constructed while upper part of the soldier pile wall could still be used a temporary embedded wall for supporting the temporary working platform behind the wall. Finally, the remaining part of the permanent soil-nailed cut slope was formed and the temporary part of the soldier pile wall would be removed to complete the permanent composite wall as shown in Figure 4(d).

Although anchor heads of the tie-backs were progressively disconnected in phase with construction of the R.C. wall, the presence of the left-in-place tie-backs would help to reduce the earth pressures acting on the composite retaining wall.

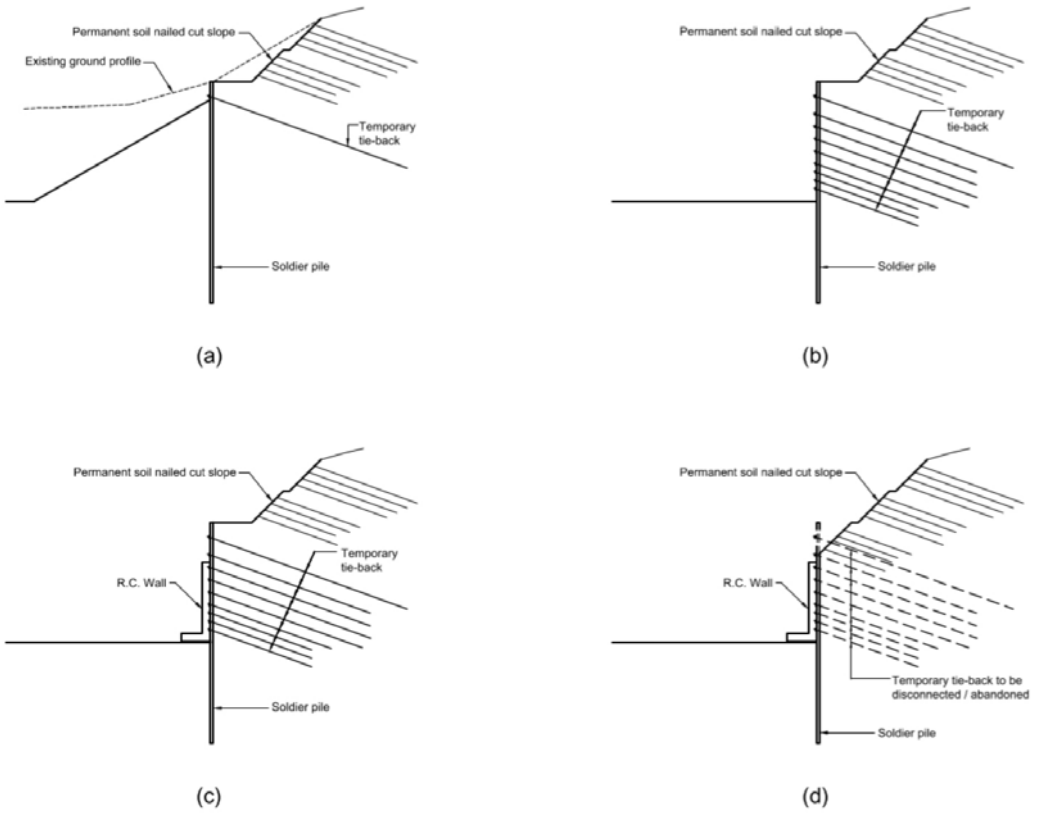

Figure 4: Construction sequence of composite retaining wall

Figure 4 clearly demonstrates the advantages of the composite retaining wall in offering a high flexibility in planning the construction works. As the soldier pile wall acts both as a temporary and permanent retaining wall, it can be utilized as an embedded wall for supporting a deep excavation both before and even after integrating it with the R.C. wall. For the LST construction work, details of the composite retaining wall are as follows:

Max. retaining height of soldier pile wall under temporary condition: 29.33m
Max. retaining height of composite wall under permanent condition: 20.975m
Number of tie-backs: 444 nos. plus 9 nos. for pull-out test
Maximum length of tie-backs: 48m
Types and strength of tie-back: Dywidag bars (yield strength 555 / 670 / 835 / 930MPa)

Figure 5 compares the geometry of composite retaining wall for used in the road widening works for the Tolo Highway (Figure 5(a)) with those of the LST construction (Figure 5(b) & 5(c)). The composite retaining wall geometry in Figure 5(b) was located adjacent to the proposed ventilation building, thus limiting the maximum base width of the R.C. wall. To achieve stability of the wall, the base slab was designed to be propped against the pile caps, transferring some of the soil loading to the foundation of the building. Away from the building, a wider base of the R.C. wall could be used as shown in Figure 5(c) to provide stability of the composite retaining wall.

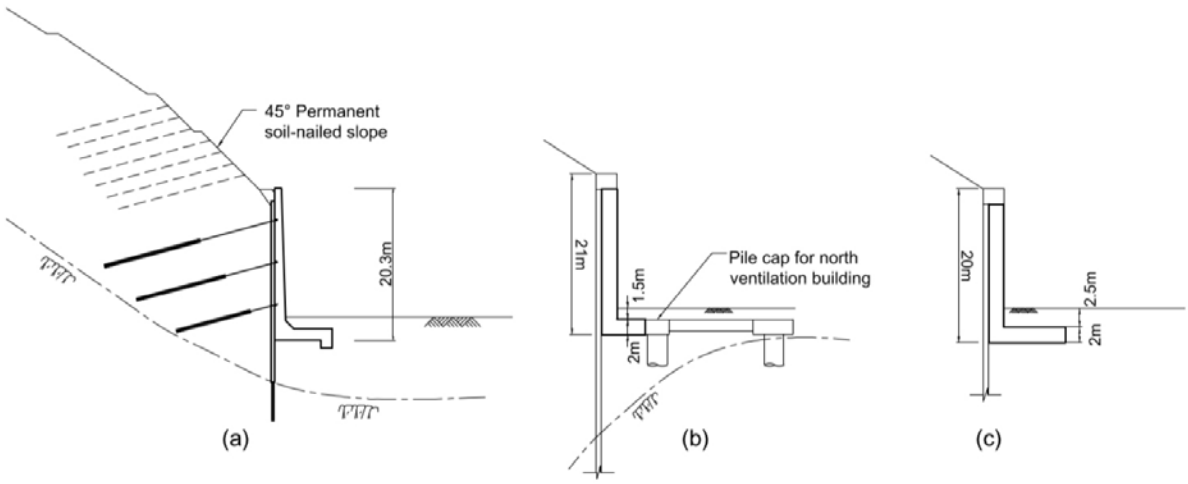

Figure 5: Geometries of completed composite retaining wall (a) Tolo Highway; (b) & (c) The LST construction

Plate 4 shows some photographs of the composite retaining wall at the Northern Portal under construction. Plate 4(a) shows the installation of tie-backs; Plate 4(b) shows the bulk excavation in front of the soldier pile wall to close the final formation level; Plate 4(c) shows construction of northbound tunnel once bulk excavation had reached the invert level of the tunnel and Plate 4(d) shows the R.C. wall under construction.

5 CONSTRUCTION AND INSTRUTMENTATION

The proposed tie-backs for the composite retaining walls of the LST construction work were designed to be embedded in soils based on the guidelines described in Geoguide 7 (GEO, 2008). The tie-backs for this project, with lengths of up to 48m maximum, were perhaps the longest tie-backs of this kind in Hong Kong. The long design length and the many layers of tie-backs used for the composite retaining wall of this project were a direct result of a maximum limit of 300 kPa recommended in Geoguide 7 for the bond resistance between cement grout and soils. This is in stark contrast to only three rows of relatively short tie-backs used for another project shown in Figure 5(a) for which a much higher design bond resistance of closed to 1MPa was used in the design based on the recommendation of British Standard BS8081:1989.

Plate 4: Construction of composite retaining wall at Northern Portal

Given the long length of tie-backs, a specialist subcontractor was commissioned for forming the boreholes for the tie-backs. No hole collapse issue was observed without the use of casing. Drilling rig, Soilmec SM-14, was utilized for the drilling and also for installation of bars after adding a clamp to the rotary head. The drilling was carefully executed with a special drag bit and with air as flushing system. Although water ingress was observed for boreholes at lower levels, there was no major difficulties encountered during the works.

The design of soldier pile wall under the temporary conditions and the composite retaining wall under the permanent condition were based on certain profile of groundwater table. As a measure of risk control under the temporary condition, an active dewatering system together with a passive drainage system of raking drains were proposed to prevent the phreatic surface of the groundwater water exceeding the design profiles.

Standpipes were installed behind the soldier pile wall for the composite retaining wall and temporary soil-nailed cut slope for the goose-shaped wall to monitor the groundwater level. The groundwater monitoring records indicated that the groundwater levels were, as expected, dropped progressively during excavation works, generally in line with the design assumptions.

Strain gauges were installed on the tie-backs at one particular section of the soldier pile wall to monitor the loading distributions along the tie-backs and compare the maximum measured loads with their design pullout capacities. 8 rows of tie-backs were instrumented in 9 locations along their length, giving a total of 72 strain gauges installed. Although the strain gauges recorded uneven distribution of load between different rows of tie-backs, they consistently indicated the stress in the tie-back reached at peak near the boundary of the active zone and then diminished beyond the location of peak stress. Plate 5 shows a photograph of the strain gauge installed on a tie-back.

Plate 5: Strain gauge installed on a tie-back

6 CONCLUSIONS

The use of innovative retaining wall designs, optimized construction sequence and a comprehensive geotechnical instrumentation monitoring system have contributed to a success in delivering of this major scale project on time. The Heung Yuen Wai Highway – Lung Shan Tunnel Section was honoured as the "Tunneling Project of the Year (over USD$500M)" by New Civil Engineer (NCE) Tunnelling Awards 2019.

ACKNOWLEDGEMENTS

Thanks are gratefully given to Mr. Roger Storry of DHK who provided valuable comments on the monitoring and design of the retaining walls.

REFERENCES

Carder, D.R., Watson, G. V.R., Chandler, R.J. and Powrie, W. 1999. Long-term performance of an embedded wall with a stabilizing wall base. *Geotechnical Engineering*. ICE, 137, April, 63-74.

Geotechnical Engineering Office (GEO). 2008. *Geoguide 7 – Guide to Soil Nail Design and Construction*.

Li, V. 2012. Some useful retaining wall options for road widening works. *Bridging Research & Practice – the VLA Experience*. Vol.2. Centre for Research & Professional Development, 163-174.

Li, V. and Chung, E. 2013. Some useful schemes for retaining wall design for forming building platforms. Proc. of the HKIE Geotechnical Division Annual Seminar 2013, 123-138.9

Powrie, W., Chandler, R.J., Carder, D.R. and Watson, G.V.R. 1999. Back-analysis of an embedded retaining wall with a stabilizing base slab. *Geotechnical Engineering,* ICE, 137, April, 75-86.

Storry, R.B., Monin, X. and Poon, N. 2017, Large span mined tunnels in soft ground: support design, instrumentation and observational approach. *Proceedings of The World Tunnelling Congress 2017.*

Modeling mechanical reinforcement of vegetation to wall stability: A case study of a short retaining wall in Hong Kong

Ricky Y.S. Choi & Arthur K.O. So
Meinhardt Infrastructure and Environment Limited

ABSTRACT

A numerical investigation is conducted to examine the effect of mechanical reinforcement of vegetation (trees and shrubs) on the enhanced factor of safety of gravity wall using the Rankine-Bell equation with common geotechnical checking on sliding and overturning. A case study in Hong Kong with a masonry wall and tree groups at the crest is selected for analysis. Results show that the root reinforcement could more than offset the surcharge from the weight of the vegetation and stabilize the wall in normal condition, but the detrimental effects outweigh the benefits under extreme gusts. Parametric studies have also been conducted to assess the sensitivity of wall stability to the variation of vegetation effect (root cohesion c_r and root zone h_r). A noticeable increase in factor of safety is observed and wall stability is more sensitive to the depth of root zone h_r than root cohesion c_r. Results of the current study encourage practitioners to consider the mechanical reinforcement of vegetation in geotechnical assessments of the stability of wall and it could be useful in solving conventional design problems of wall less than 3m and with less structural measures.

Keywords: Shallow Failure, Wall Vegetation, Root Reinforcement, Stability Analysis

1 INTRODUCTION

Old stone retaining walls with vegetation are unique features in Hong Kong. Though they are of high preservation value, many of them are substandard as they were built in the old days and often situated in areas with many site constraints (Jim, 2012). Technical guidelines on slope mitigation often go with structural works for reinforcement as conventional practice, in which their properties are more controllable, and the slope is more robust in return. However, the urge for more environmentally friendly solutions is raising. There have been extensive research and engineering in providing a multitude of examples and protocols for representing and calculating the stabilizing effects of tree roots in slope stability models. Vegetative crib walls have been put into practice as a bio-engineering measure to improve the stability of a soil slope (Tardío & Mickovski, 2016). The presence of plants, living components, changes the soil conditions and even serve as structural members when they are well established. Better recognition and limitation of root-soil interactions shall enable engineers to choose the best additions for stability.

In Hong Kong, studies on stabilization and restoration with vegetation have been launched on natural terrain landslide sites in 2006 (GEO, 2008) while the use of bioengineering is mainly related to landscaping in man-made slopes (GEO, 2011a). Effect of wall trees on stability of masonry walls was examined in GEO Report No. 257 (GEO, 2011b) but the contribution of root reinforcement is neglected in the analysis due to the difficulty in quantifying the effect of roots. There is currently little information

or specific case studies that can provide guidance on how to numerically assess the stabilizing effect of the roots behind the wall permeating the backfill.

In this paper, a case study of a 3m high masonry wall in Hong Kong with mechanical reinforcement of vegetation is investigated following the modified Wu model (So & Choi, 2021) on wall stability. Field data are collected for root reinforcement modeling and cross-reference with literatures. Conventional geotechnical assessments on sliding and overturning of retaining wall are performed. Parametric studies are carried out to evaluate the sensitivity of wall stability to the variation of vegetation effect (root cohesion c_r and root zone h_r).

2 CASE STUDY

A masonry retaining wall located near the crest of the soil slope has a maximum retaining height ranging from 1.5m to 3.2m. A grassy sloping ground with mature trees (trunk diameter varies from 300mm to 750mm) with a spacing of 2m to 3m are located all along the back of the masonry wall (Plate 1). An existing box culvert and existing covered surface channel (Plate 2) were located just behind the masonry wall.

Plate 1: A tree group at the crest of the masonry wall

Plate 2: Crest facility at the study feature

Ground investigation revealed that the masonry wall is founded on loose-fill and retaining a fill slope at the crest. Stability analyses showed that the calculated minimum factors of safety are lower than the required minimum factor of safety from conventional checking of gravity walls. As the slope does not possess adequate factors of safety to meet the required safety standard, slope upgrading works are necessary.

Pit by pit excavation and backfilling with lightweight concrete and soil nailing with tie column were selected for different portions of the wall following their retaining height to cater for site constraints.

During construction, intermingled roots of different individual trees were observed. The extent of soil replacement was much less in the presence of trees. Because of this, the feasibility of providing alternative means to effectively stabilize the wall while retaining the tree had been examined in detail but not forthcoming. In the absence of any other feasible mitigation measures, the removal of three trees/shrubs is necessary to upgrade the masonry wall to the current standard and to ensure public safety.

A post-construction review was carried out to determine the mechanical reinforcement of tree roots on the stability of the masonry wall. (Gray & Sotir, 1996) mentioned the mechanical effects as shown in Table 1. A single tree with the largest DBH at the crest area is selected for modeling and parameters required including the root cohesion, tree weight, and wind forces are presented.

Table 1: Influence of vegetation on slope stability (modified after Gray & Sotir, 1996)

Mechanical mechanism	Result	Influence
Reinforcement and anchorage by root	Increasing shear strength	+
Weight of trees surcharges the slope	Increasing normal and downhill force components	+/-
Vegetation exposed to wind	Transmits dynamic forces into the slope	-
Roots bind soil particles at the ground surface	Reducing susceptibility to erosion	+

3 ESTIMATION OF ROOT COHESION

Methods in modeling the root reinforcement began with (Wu, 1976), (Waldron et al., 1977), and (Wu et al., 1979) in the late 70s, also known as "Wu and Waldron's model" (WWM). The increased shear strength due to root reinforcement τ is commonly modeled via an additional term called "root cohesion", c_r, into Mohr-Coulomb failure envelope equation.

$$\tau = c_r + c_s + \sigma \tan\phi \quad (1)$$

where c_r is the additional "root cohesion", c_s is the soil cohesion, σ is the normal stress on the shear plane and tanϕ is the slope of the failure envelope while ϕ is the soil friction angle.

When there is a soil movement like a translational shallow failure, soil shear stress is developed and roots crossing the failure plane are mobilized in tension. Figure 1 shows the mechanism of soil-root reinforcement and the fiber breakage model. The resulting additional shear strength can be predicted by:

$$c_r = (\sin\xi + \cos\xi \tan\emptyset') \cdot T_r \cdot RAR \quad (2)$$

where ξ is the shear distortion angle of a root within the shear zone, T_r is the mean tensile strength of roots and RAR is the root area ratio, i.e., the sum of the total cross-sectional area of root (A_r) over soil (A_s). (Wu, 1976) proposed an average value of 1.2 for (sin ξ + cos ξ tanØ'), considering the roots are not oriented perpendicular to the slip surface.

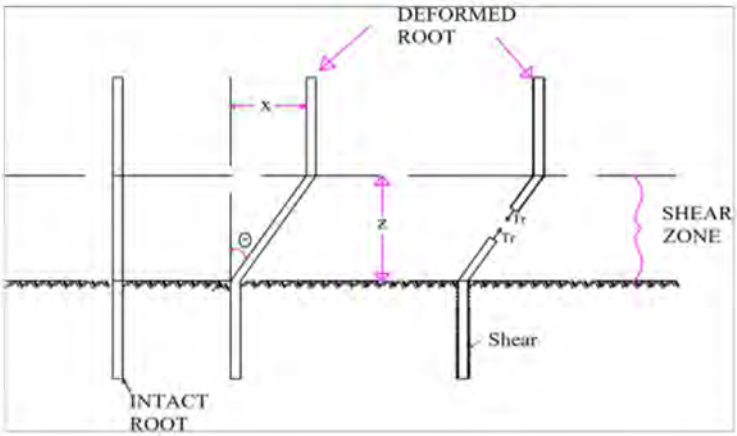

Figure 1: Fiber breakage model (adapted from Tsige et al., 2019)

(Leung et al., 2015) further narrowed the typical values to 1.15-1.17 with consideration of Hong Kong geological information. (So & Choi, 2021) proposed a presumed value of 1.15 for conservative use and this value is adopted in this study. Combining the above all and the root cohesion can be estimated as:

$$c_r = 1.15 \cdot T_r \cdot RAR \quad (3)$$

4 RAR DETERMINATION

There are generally two methods in obtaining the RAR values, namely the "core break" sampling (Schmid & Kazda, 2002) and the "profile wall" method (Böhm, 1979). As the site works included pit by pit excavation and backfilling with lightweight concrete right behind the wall, the latter method was selected for sampling. Root counting is performed with image processing on the trench profile wall photographs followed by counting pixels that contain roots in the image histograms in Photoshop (Eab et al., 2015). A profile of rooted soil down to 3m depth was exposed and several images were taken. However, it turned out the root distribution can hardly be recognized and rightly mapped with image

processing in the presence of coarse roots and similar colors of roots and soil, though they provide anchorage effects. Manual data labeling was done instead for data correction.

One tree sample photo with depth up to 1.25m is shown in Figure 2. For fitting in the modified Wu model, only the roots with diameters between 1mm to 10mm are counted and it is assumed to be 1/3 of total roots (Leung, 2014). RAR for a eucalyptus tree after discounting are 4.84%, 8.22%, 4.82%, 4.26%, 1.95% with an increment of 0.25m up to 1.25m along with the depth.

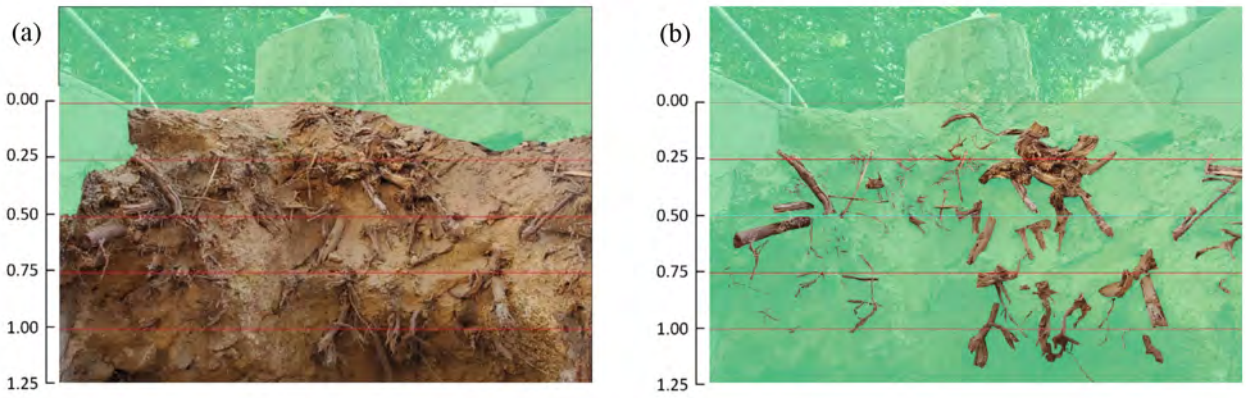

Figure 2 (a) rooted soil photograph taken from a 30m high species with a DBH of 750mm up to 1.25m depth (b) processed image with manually filtered roots and a root area ratio from 1.95% to 8.22%

5 TENSILE STRENGTH DETERMINATION

In the view that no pull-out test / tensile strength test is conducted for the tree species on-site, a presumed value of 8MPa is adopted for our case (So & Choi, 2021).

6 ROOT DEPTH AND ROOT ZONE

Though a rough rule of thumb the mechanical reinforcement of roots is suggested to be limited to a zone about 1.5m from the surface (Gray & Sotir, 1996). On-site pit excavation revealed the eucalyptus tree could extend deep into the ground (observable up to 2.3m) (Plate 3). A maximum root depth of 2.25m is selected for modeling. The field result is comparable to the dataset of three 25-year old excavated

Plate 3: Exposed root system of a 30 m high eucalyptus tree and root depth = 2.3 m

Monterey pine trees with an average height of 30m and a mean stump diameter of 60cm (0.2m above ground), and their vertical roots penetrated 2.93m on average (Watson & O'Loughlin, 1990). Therefore, the rooted zone is assumed to be 1.7m (W) * 3m (L) * 2.25m (D) due to high stiffness structures at the back of the wall, limiting the spread of tree roots.

It is not certain that the semi-empirical formula of calculating c_r can be used with RAR beyond 0.7%, though the field results were up to 8%. A uniform root architecture RAR value = 1.0% is considered for conservative use. Following Eq. (3), an average value of root cohesion with depth corresponded to c_r = 92.0 kPa. However, this value still appears to be larger than the typical c_r values recommended in Table 8 of Geoguide 1 (GEO, 2020) for in-situ completely decomposed granites. Therefore, the value is capped at a maximum of c_r = 15 kPa and used to simulate the effect of uniform roots on wall stability. Superposition effects from tree groups are suggested by (Docker, 2003) but they are ignored in this study for simplicity.

7 TREE WEIGHT

The weight of vegetation is considered as a surcharge load and it would have a major influence on slope stability when the vegetation cover is heavy. It increases the slice weight and in turns increases the slice base normal and shear resistance. (Greenwood et al., 2004) suggests that DBH > 0.3m of a tree is a threshold value of considering a major implication of tree weight to slope stability. Some of the key indicators in determining the surcharge loads due to the weight of trees include the size, density, and species of vegetation. (Emadi-Tafti & Ataie-Ashtiani, 2019) summarised the surcharge loads reported by numerous researchers. GEO Report No. 257 (GEO, 2011a) recommends equations using biomass regression method with DBH as main parameters developed by (Jenkins et al., 2003) to determine the dry mass of trees and the species group of "hard ample/ oak/ hickory/ beech" was selected. There is also a 50% increase in tree truck density with moisture content. In this study, we adopted the equations suggested from GEO Report No. 257 (GEO, 2011a) for calculation.

$$b_m = \mathrm{Exp}(\alpha_0 + \alpha_1 \ln DBH) \quad (4)$$

$$\text{ratio} = \mathrm{Exp}(\beta_0 + \beta_1 / DBH) \quad (5)$$

where b_m is the total aboveground biomass (kg) for trees 2.4cm DBH and larger, DBH is the diameter at breast height (cm) which measured at 1.3 m above the trunk base, α_0 = -2.0127, α_1 = 2.4342, ratio = component to total aboveground biomass, β_0 = -0.3065, β_1 = -5.4240 for stem wood.

8 WIND LOADING

Much of the masonry wall failure is associated with tree uprooting during hurricanes in Hong Kong GEO Report No. 257 (GEO, 2011a). Urban trees are often grown with many big branches, shallow roots, and shallow root plates (Ken James, 2020). When they are exposed to wind, an overturning moment is acted on the root plate. If the root anchorage is not strong enough, tree uprooting will happen. These additional dynamic forces will also be transmitted into the masonry walls, having an adverse effect on their stability. GEO Report No. 257 (GEO, 2011a) outlines the procedures in estimating the static and dynamic force of the wind acting on trees and in turn evaluate the stability of the wall tree. Herein the static drag force is only considered and estimated by the following equation with a conservative assumption that the wind flow is acting downslope.

$$F = \frac{1}{2} \rho C_D A V^2 \quad (6)$$

F = the wind force (newtons, N), ρ = the density of air (kg/m^3), C_D = the drag coefficient (dimensionless), A = the frontal area (m^2), V = the wind velocity (m/s)
Wind velocity = 26m/s, a critical wind speed of tree failure as reported in GEO Report No. 257 (GEO, 2011b)
Frontal area of the truck = tree height * DBH =22.5m^2

Frontal area of the crown = 12m (spread of crown) * 15m (upper half of tree height) * 0.25 (an assumed reduction factor) = 45m^2
Drag coefficient of truck = 0.5, Crown = 1.2
Uniform distributed load = Loading / Load spread area (extent of lateral roots = 1.7m (W) * 3m (L))

Table 2: Summary of the tree weight and the wind load for the eucalyptus tree

DBH (cm)	Height (m)	Tree root spread area (m^2)	Tree Weight (kN)	Distributed load (kNm/m)	Wind load (kN)	Distributed load (kN/m/m)	Moment (kN/m/m)
75	30	5.1	64.5	12.64	27.03	9.01	218

9 EXTERNAL STABILITY

Same as typical retaining structure, bio-engineering structure is also checked along with existing geotechnical engineering standards (sliding and overturning) and expressed with factor of safety for their stability according to Geoguide 1 (GEO, 2020). Forces, i.e., self-weight, earth pressure from the backfill, hydrostatic pressure, loads from structures, which are acting on the wall are considered, and the wall is assumed as a monolithic structure. In this study, global factor is adopted for conventional checking, except in examining wind load with a partial factor in overturning moment checking. The resistance to sliding and overturning will be affected by the apparent cohesion from roots. The internal stability of masonry wall is ignored for conventional checking. Yet, it is worth mentioning that plant roots tend to avoid zones of stress and thus not disrupting or compromising the structural integrity of the wall (Gray & Sotir, 1996).

The apparent cohesion value calculated by Eq. (3) will be further incorporated into the calculation of active soil pressure on retaining wall following Bell's equation (for a cohesive backfill with a horizontal ground surface) and Rankine theory in the root zone, with a tension crack developing to a depth z_c. Negative earth pressures within this zone and cases of tension cracks filled with water are ignored in this study. Development of tension crack is confined to the root zone only if the critical depth is larger than the depth of root zone. Figure 3 and Figure 4 illustrate a modified wall geometry and the normal stress acting on the wall with the tree.

$$k_a = \frac{1 - \sin\phi}{1 + \sin\phi} \tag{7}$$

$$P_a = \sigma_z \cdot k_a - 2c\sqrt{k_a} \tag{8}$$

$$z_c = \frac{1}{\gamma \cdot} \left(\frac{2c}{\sqrt{k_a}} - q\right) \tag{9}$$

10 MODELLING

A 3m high and 0.9m width masonry wall with the following assumptions is modeled as a typical example.

- 2D plane strain model
- The wall is with a vertical back and the ground surface is horizontal.
- Isotropic, homogenous soil layer
- The interface slope is horizontal.
- 1/3 water at retaining height to cater for the groundwater rise during a 1 in 10 years return period rainstorm.
- Wall friction is assumed to be 2/3ϕ and base friction = 0.9ϕ

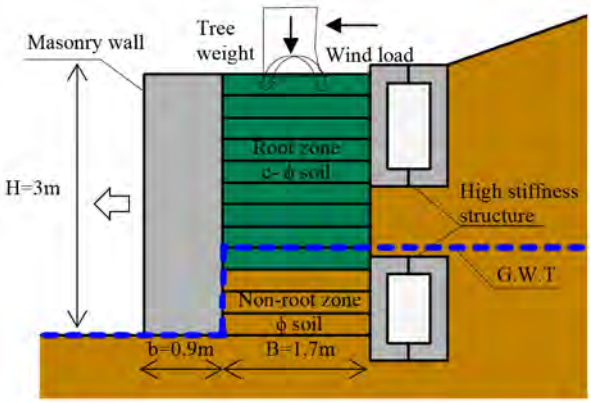

Figure 3: Typical example of a masonry wall with tree

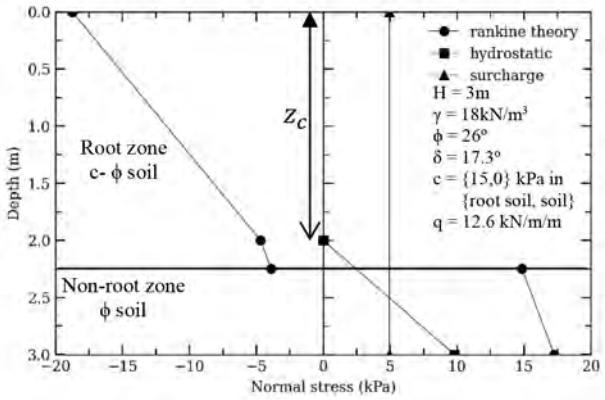

Figure 4: Illustration of the normal stress acting on wall

Table 3: External stability check. Sliding and overturning safety factor formula adapted from Geoguide 1 (GEO, 2020)

Mode of Failure	No vegetation	With vegetation (Tree weight)	With vegetation (Tree weight and wind load)
FoS sliding	0.85	1.28	0.88
FoS overturning	1.06	3.09	0.08<1.0 (Partial Factor for wind load)

11 RESULTS

The external stability analysis without vegetation gave results of FoS = 0.85 and 1.06 for sliding and overturning respectively, which is as expected for a slender wall with limited self-weight. When mechanical reinforcement and surcharge from tree weight are considered, it yields FoS = 1.28 for sliding and 3.09 for overturning which are a significant increase. The wall that was initially unsafe/marginal safe (FoS <1 and ~1) is now safer. However, when wind effect is considered, the FoS against sliding falls back to 0.88 and overturning even diminishes to 0.08. Wall failure by overturning is expected. In fact, many walls would fail, based on the stability analysis using field data, but remain intact for a long time. The root reinforcement should more than offset the surcharge from the weight of the vegetation (Gray & Sotir, 1996). The mechanical effect of vegetation is the major factor in stabilizing the wall.

12 PARAMETRIC STUDIES

It is of practical interest to demonstrate the effect of root reinforcement by FoS increment with respect to bare slope. Parametric studies were performed for depth of root zone h_r and apparent root cohesion c_r and applied in the typical example. Young trees and shrubs are considered which are with negligible weight and windthrow problems. Figure 5 and Figure 6 show how the value of FoS increment is influenced by h_r and c_r.

Both FoS increment against sliding and overturning follows similar trends. The FoS increments increase with increasing c_r at a gentle rate when c_r lies between 5 kPa and 10 kPa and remain constant when c_r goes beyond 10 kPa. Increments of 0.27 against sliding and 1.25 against overturning are observed at h_r = 1.0m and c_r = 15kPa. When c_r increases from 5 kPa to 15 kPa, the increment is increased by 78% for h_r = 2m and by 0% for h_r = 1m against sliding, while overturing yields a FoS increment of 114% for h_r = 2m and 3% for h_r = 1m. Particular attention is drawn to the cases in which the increased FoS are almost constant. It is because the development of tension crack is limited by the depth of root zone and a further increase in root cohesion would have limited beneficial effects on wall stability.

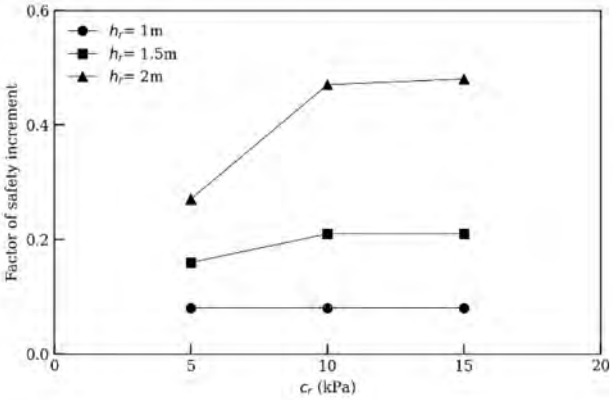

Figure 5: Factor of safety increments for the root zone with respect to bare slope against sliding

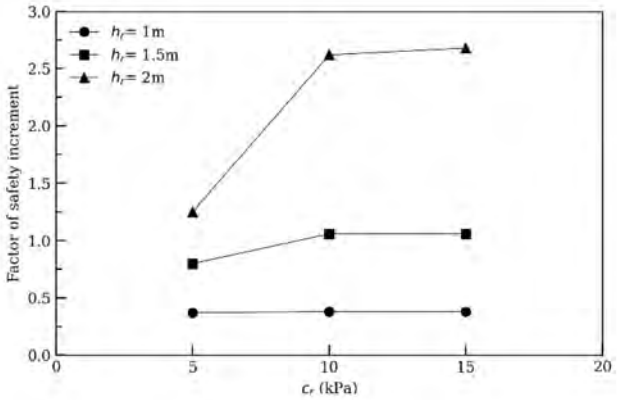

Figure 6: Factor of safety increments for the root zone with respect to bare slope against overturning

13 DISCUSSION

13.1 Stone wall failure versus tree failure

Though the FoS against overturning under windthrown condition indicates there is an overturning failure, the tree is much likely uprooted rather than wall failure. A review of wall failure history in Hong Kong was conducted by (Jim, 2012). Reported cases of two recent stonewall tree failures indicated there were tree failures without damage to wall structure. The lack of joints or avenues for roots to penetrate the wall is considered as the fundamental cause of insecure root anchorage, and thus leading to tree overturning under extreme gusts. On the other hand, wall failures were mainly attributed to poor design, workmanship, maintenance, and sometimes associated with leaking pipes situated behind the wall.

13.2 Tree anchorage and lateral root

For fitting in Wu model, the contribution from coarse roots (diameter >10mm) is not counted in this study and they shall act as bending beams to counteract the shear force. For woody root species such as trees and shrubs, the majority of the total root mass are structural and coarse roots. 62% of the total roots are coarse roots (>5mm) in one study of a spruce tree reported by (Parr & Cameron, 2004). Structural analysis, i.e. using p-y models, can be used to estimate the root-soil interaction when the roots are subject to lateral loading (Meijer et al., 2019). The selection of prediction models on root reinforcement is discussed in (So & Choi, 2021). When considering engineering use of vegetation to stabilize the walls, roots must cut through the failure surface to provide a stabilizing effect. For a $(45° + \phi/2)$ active failure plane, woody plants with propensity of deep rooting and lateral spreading is advisable for maximizing the mechanical reinforcement of vegetation (Liang et al., 2020).

14 FUTURE WORK AND LIMITATION

While the beneficial effects of roots are notable in wall stability, the following areas shall be considered in future works

- Probabilistic study of root distribution on wall stability shall be examined given that the randomness of root depth and distribution. A dataset of maximum root depth for woody plant with fitted distribution indicates it is a lognormal distribution (Zhu et al., 2017). Deterministic analysis on uniform root length could not accurately capture the effect of mechanical reinforcement.
- In considering the mechanical effect of a single species, the increase in shear strength of soil is often exponentially reduced with depth. Root cohesion with a non-linear distribution would

give a better estimation of root effect. Yet, much of the root reinforcement studies reveal the vegetation exhibit a central zone with the most contribution to soil strength in the first two meters. For woody plants with intervals, it would be more practical to model the root cohesion with a stepped function in shallow depth when examining the slope stability.

- Evapotranspiration is ignored in this study. Consideration of matric suction shall further increase the safety factor and prevent shallow landslides.

15 CONCLUSION

The effect of root reinforcement is conventionally neglected due to difficulties in quantifying the roots as suggested in GEO Report No. 257 (GEO, 2011a). However, consideration of the mechanical effect of roots could be effective, particularly in a congested site in reducing the use of structural measures in stabilizing retaining wall with physical constraints and construction difficulties at shallow depth. For example, tree roots could replace the top row of soil nails or otherwise, the tree roots would act as obstructions to the installation of soil nails if the root strengthening effect is ignored. A real case history showing the retaining wall with tree groups at the crest that was below the safety margin and substantial upgrading works were conducted to meet the statutory requirements. Application of mechanical reinforcement of tree roots to slope stabilization have been reviewed in a companion paper (So & Choi, 2021) and a post-construction review is conducted on tree roots effects on wall stability. The apparent root cohesion c_r has been incorporated in the wall stability analysis using Rankine-Bell equation. Deep-rooted trees are beneficial to wall stability when wind speeds are low. In one example the 2.25m deep-rooted trees provide 51% and 192% in FoS against sliding and overturning respectively. However, when windthrow failure is considered, the wall stability will drastically decrease. There is not much increase in FoS against sliding and FoS against overturning even drops to a very unsafe point. Parametric studies reveal that the wall stability is more sensitive to the depth of root zone h_r than root cohesion c_r. The development of tension crack is limited by the depth of root zone and further increase in root cohesion would have limited beneficial effects on wall stability. For engineering application in wall stabilization, shrubs with propensity of deep rooting and lateral spread are recommended to be used to minimize surcharge and windthrow problems while maximizing the mechanical reinforcement. The result of this post-construction review is encouraging and further investigation on the application of root reinforcement is recommended.

REFERENCES

Böhm, W. (1979). Methods of Studying Root Systems. In *Ecological Series* (Vol. 33). Springer-Verlag.

Docker, B. B. (2003). *Biotechnical engineering on alluvial riverbanks of southeastern Australia: A quantified model of the earth-reinforcing properties of some native riparian trees*. The University of Sydney.

Eab, K. H., Likitlersuang, S., & Takahashi, A. (2015). Laboratory and modelling investigation of root-reinforced system for slope stabilisation. *Soils and Foundations,* 55(5), 1270–1281.

Emadi-Tafti, M., & Ataie-Ashtiani, B. (2019). A modeling platform for landslide stability: A hydrological approach. *Water (Switzerland),* 11(10).

Gray, D.H., Sotir, R.B., 1996. Biotechnical and Soil Bioengineering Slope Stabilization: A Practical Guide to Erosion Control. John Wiley and Sons, New York.

Geotechnical Engineering Office. (2008). Guidelines for soil bioengineering applications on natural terrain landslide scars. *GEO Report No. 227*, Geotechnical Engineering Office, Civil Engineering and Development Department, HKSAR Government, 162.

Geotechnical Engineering Office. (2011a). Study on masonry walls with trees. *GEO Report No. 257,* Geotechnical Engineering Office, Civil Engineering and Development Department, HKSAR Government, 157p.

Geotechnical Engineering Office. (2011b). Technical Guidelines on Landscape Treatment for Slopes. *GEO Publication No. 1/2011,* Geotechnical Engineering Office, CEDD, The Government of HKSAR, 220p.

Geotechnical Engineering Office. (2020). Guide to Retaining Wall Design (Geoguide 1) (Continuously updated e-version released on 1 June 2020). Geotechnical Engineering Office, Civil Engineering and Development Department, HKSAR Government, 245 p.

Greenwood, J. R., Norris, J. E., & Wint, J. (2004). Assessing the contribution of vegetation to slope stability. *Proceedings of the Institution of Civil Engineers – Geotechnical Engineering,* 157(4), 199–207.

Jenkins, J. C., Chojnacky, D. C., Heath, L. S., & Birdsey, R. A. (2003). National-scale biomass estimators for United States tree species. *Forest Science,* 49(1), 12–35.

Jim, C. Y. (2012). *Study on Stonewall Trees: Maintenance Approach for the Six Stonewall Trees on Slope no. 11SW-A/R577, Bonham Road Highways Department Government of the HKSAR 2012.*

Leung, Flora T.Y., Yan, W. M., Hau, B. C. H., & Tham, L. G. (2015). Root systems of native shrubs and trees in Hong Kong and their effects on enhancing slope stability. *Catena,* 125, 102–110.

Leung, Flora Tsz Yan. (2014). *Native Shrubs and Trees as an Integrated Element in Local Slope Upgrading* (Issue September). HKU.

Liang, T., Knappett, J. A., Leung, A., Carnaghan, A., Bengough, A. G., & Zhao, R. (2020). A critical evaluation of predictive models for rooted soil strength with application to predicting the seismic deformation of rooted slopes. *Landslides,* 17(1), 93–109.

Meijer, G., Bengough, G., Knappett, J., Loades, K., & Nicoll, B. (2019). *Measuring the Strength of Root-Reinforced Soil on Steep Natural Slopes Using the Corkscrew Extraction Method.* 1–19.

Parr, A., & Cameron, A. D. (2004). Effects of tree selection on strength properties and distribution of structural roots of clonal Sitka spruce. *Forest Ecology and Management, 195*(1–2), 97–106.

Schmid, I., & Kazda, M. (2002). Root distribution of Norway spruce in monospecific and mixed stands on different soils. *Forest Ecology and Management, 159*(1–2), 37–47.

So, A. K. O., & Choi, R. Y. S. (2021). *On the Application of Mechanical Reinforcement of Tree Roots to Slope Stabilization.* 1–12.

Tardío, G., & Mickovski, S. B. (2016). Implementation of eco-engineering design into existing slope stability design practices. *Ecological Engineering,* 92, 138–147.

Tsige, D., Senadheera, S., & Talema, A. (2019). Stability Analysis of Plant-Root-Reinforced Shallow Slopes along Mountainous Road Corridors Based on Numerical Modeling. *Geosciences,* 10(1), 19.

Waldron, L.J. 1977. The shear resistance of root-permeated homogeneous and stratified soil. *Soil Science Society America Journal,* 41(5): 843-849.

Watson, A., & O'Loughlin, C. (1990). Structural root morphology and biomass of three age-classes of Pinus radiata. *New Zealand Journal of Forestry Science,* 20(1), 97–110.

Wu, T.H. 1976. Investigation of landslides on Prince of Wales Island, Alaska. *Geotechical Engineering Report 5,* Civil Engineering Department, Ohio State University, Columbus, Ohio, USA.

Wu, T.H., Mckinnel, W.P. & Swanton, D.N. 1979. Strength of tree roots and landslides on Prince of Wales Island, Alaska. Canadian Geotechnical Journal, 16(1): 19-33.

Zhu, H., Zhang, L. M., Xiao, T., & Li, X. Y. (2017). Enhancement of slope stability by vegetation considering uncertainties in root distribution. *Computers and Geotechnics*.

Using radar satellite data for ground deformation monitoring: ATLAS InSAR

Devanthery, N., Garcia-Boadas, E. & Giralt, A.
Sixense Iberia, Satellite & Data Solutions Department, Barcelona

Le-Goff, D. & Lam, B.
Sixense Hong Kong, Hong Kong

ABSTRACT

Radar satellite interferometry (InSAR) is a non-invasive surveying technique based on the exploitation of SAR images, able to measure millimetric motion of terrain structures over wide areas in both urban and non-urban environments. Sixense processing chain, ATLAS, has been successfully used to detect and monitor ground motion in many different projects, cities and sectors to follow subsidence, heave, building stability and landslides amongst others. ATLAS reaches high density of measurement points, and covers large areas with high-resolution imagery, and weekly revisits.

This presents a huge opportunity for the monitoring and management of infrastructures. However, the unprecedent spatial and temporal volume of InSAR measurements- which are only going to increase with new sensors to come- presents a challenge. Thus, ATLAS is in continuous development to efficiently extract characterized information of maximum benefit to end users by implementing different algorithms and AI methodologies over InSAR Big Data results to provide ready-to-use, actionable information.

1 INTRODUCTION

When executing any type of construction work, one of the major challenges is to guarantee that the different infrastructures adjacent to the construction activity are not affected by it, and if they are that it remains within acceptable tolerance. This is exacerbated in heavily urbanised areas, like large cities, due to the high density of population and infrastructures that can be affected by movements related to construction.

The use of traditional monitoring, which entails in-situ instrumentation, requires a good deal of third parties management, installation and preparation, often not allowing much time between the installation of the instrumentation and the start of construction work, which might not provide enough background and historical data to properly understand the behaviour of the terrain. Furthermore, traditional monitoring will be typically focused on an expected "area of influence", few tens of meter around the axis of a tunnel for example, which may limit the understanding of ground movement in case of unexpected movement or overlook potential impact of others construction projects near the "area of influence".

These limitations can be overcome by using remote sensing techniques such as InSAR, which has been broadly implemented for civil engineering purposes due to its advantages. These advantages include the potential availability of historical data, the removal of any on site access issue, and the large coverage of satellite images that allows detecting measurements over very large areas. Its use also provides a huge cost saving due to no (or very limited) installation costs while maintaining a similar accuracy to more traditional manual monitoring systems.

InSAR, or radar satellite interferometry, is a fully remote sensing technique based on the exploitation of synthetic aperture radar images (SAR), able to measure millimetric motion of terrain and/or structures over wide areas in both urban and non-urban environments.

Atlas, Sixense's InSAR processing chain, has been developed with the aim of monitoring geotechnical and structural deformations linked to urban construction activities and has proven to be a useful and complementary source of information to the traditional monitoring instrumentation.

This paper shows how the Atlas InSAR processing chain has been successfully applied in two different case studies. In the first case study, InSAR has been used for infrastructure monitoring and soil reclamation control in the city of Hong Kong. The city has been monitored with ATLAS using a set of high-resolution TerraSAR-X images acquired over Hong Kong from July 2017 to February 2021. Atlas provided the deformation maps and the displacement time series for a dense network of points over the area during the study period.

The second case study is focused in the use of InSAR in the ground settlement monitoring of a major tunnelling project in the city of London (United Kingdom). This project comprises the construction of a new railway line, which crosses Greater London from east to west and has five tunnelled sections totalling up to 42 km in length. In this case, the area of interest has been monitored with ATLAS using a set of high-resolution TerraSAR-X images acquired over London from August 2013. ATLAS provided accumulated deformation maps and the displacement time series for a dense network of points over the area of interest, during the extended study period.

2 DEFORMATION MONITORING FROM SPACE: ATLAS SAR INTERFEROMETRY

2.1 SAR interferometry

Synthetic Aperture Radar Interferometry (InSAR) is a non-invasive remote sensing technique capable to monitor wide areas of terrain with millimetric precision, making it ideal for the monitoring of infrastructures. InSAR is based on the exploitation of Satellite aperture radar (SAR) images, which are complex radar images containing phase and amplitude information over a very large area, usually few hundreds square km. The InSAR technique consists in analysing the same two SAR images at different date and computing the ground displacement information based on the differences of the phase components (Figure 1).

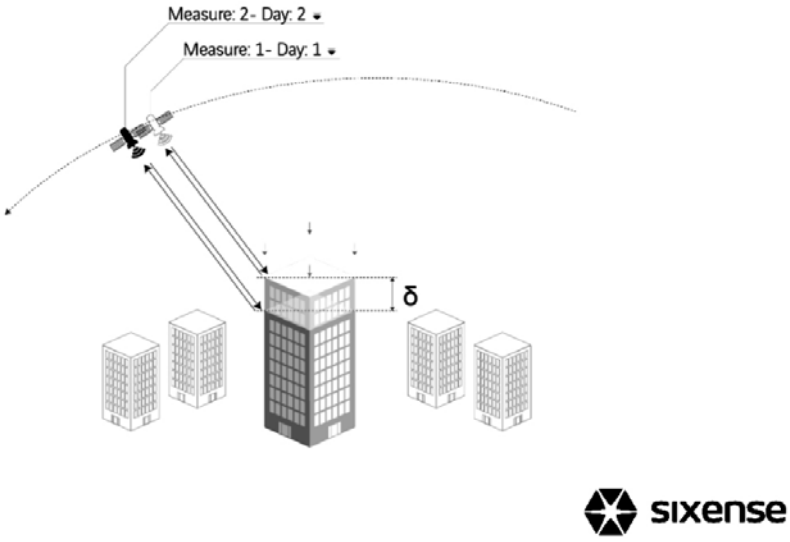

Figure 1: SAR interferometry working principle

To retrieve millimetric measurements, InSAR advanced technique are required. Those techniques produce better precision in the results by correcting atmospheric, orbital, and topographic components of the interferometric phase. Those techniques require at least fifteen SAR images and a robust selection of measurement points reflecting persistently the radar signal back to the sensor. These locations, called persistent scatterers (PS), are permanent highly reflective targets, whose reflections remain constant over the whole image stack during the duration of study. They are generally manmade structures or rocks but can also be arid terrains and other ground features whose orientation and surface characteristics allow a perfect reflection of radar waves.

2.2 Atlas Processing Chain

Sixense has developed its own treatment processing chain, ATLAS, around the core software GAMMA. ATLAS allows for measuring vertical ground and structure movements, with special attention to urban works and critical non-linear movements, on permanent scatterers with millimetric accuracy.

For each measurement point, the ATLAS solution provides maps of accumulated displacement along the study period, time series of deformation for each point monitored mean deformation velocity of deformation, and quality indexes of the measurements.

ATLAS PSI uses more than 15/20 SAR images with atmospheric compensation to derive highly accurate elevation and average displacement rate values for each stable point. The high-level of error compensation allows the generation of time series charts, visualizing the evolution of the displacement of each stable point. Urban, semi-urban or rural areas can be studied in detail (both in terms of high spatial resolution and the historical variation of the displacement) over long time periods.

The processing steps are summarized as follows:

Image extraction: SAR data is read from the original media and all the auxiliary parameters are retrieved from the product annotations into ASCII auxiliary files.

Image selection: Analyse the set of available images, quality control is done at this stage to detect images with acquisition defects (images altered by satellite manoeuvres, erroneous annotation file parameters and severe weather conditions during the acquisition, etc.).

Image co-registration: A stack of images must be co-registered to a geometry. One image is selected as master and then all the other data is aligned to have a common geometry. Every pixel in all the images must contain the radar response coming from the same ground resolution cell.

Generation of differential interferograms: Selection and generation of interferometric pairs based on the acquisition time, the perpendicular base and the difference in the Doppler centre of each image. The complex interferogram is generated by multiplying the first SAR complex image, named master, with the complex conjugate of the second one, named slave. The DEM in radar geometry is removed from the interferograms to remove the topography component. Note that a component related to height of buildings and DEM errors, called topographic residual error, is still contained in the interferometric phase. The interferograms are also corrected for the so-called flat earth removal and orbital errors.

Selection of measurements points: Selection of the initial measuring points, that is, pixels with low noise level that allow to derive reliable phase measurements, i.e. the so-called Persistent Scatterers (PS). They are points of constant phase quality during the entire study period, whose signal refers to the predominant reflection of the signal in the same object (point-target). They are points that are little affected by the effects of spatial and temporal decorrelation. They are usually found in urban areas, in buildings and infrastructures, and allow to fully exploit the high spatial resolution of high-resolution sensors. The pixels with low temporal variability of the backscattering coefficient during the period of interest are selected.

Ground motion estimation: Obtention of the speed, vertical height and associated quality index for study points referenced to a previously selected reference point. The goal is to estimate and remove the

different components of the interferometric phase to reach mm precision on the measurement of the displacement. This is achieved by applying an iterative procedure consisting in a set of spatio-temporal filters to estimate and remove phase component related to atmospheric effects and precise estimation of the residual topographic error (difference between DEM and real height of the measured objects). This is fundamental for a further precise geocoding of the measurements points, as well as to isolate the phase component related to deformation and achieve precise results. The velocity of deformation is derived considering a linear model on the deformation. A quality index of best fit to the model is also derived in this step. Note that thermal effects, i.e. thermal dilation typically over metallic structures, bridges or skyscrapers, can also be modelled and removed.

Precise estimation of deformation time series (linear and no linear) by means of an advanced combination of the so-called spatial phase unwrapping method and a robust least square procedure which makes uses of redundancy to retrieve deformation time series.

Quality control on measurement points. Although each processing step has its own quality indexes, in this step the final quality thresholds are selected depending on the case at hand and the final table of measurement points in LOS is generated. The quality thresholds generally used are the indicator of degree of fit to the phase models used for the estimation of the terrain deformation, and the standard deviation of the motion measure (time series), which is an indicator of the level of noise.

Precise geocoding. This is the last step of ATLAS processing chain. Measurement points needs to be geocoded to obtain map coordinates with an accuracy below 1-2 m. To meet this requirement, both DEM and residual topographic error needs to be used.

3 ATLAS INSAR CASE STUDIES IN CIVIL ENGINEERING

ATLAS InSAR has proven to be useful for a variety of application in civil engineering, such as linear infrastructure assets, (highways, railways, bridges, pipelines, power-lines and tunnelling), huge surfaces (soil reclamation, offshore oil plants, dams and landfills) and small assets (singe buildings).

In this paper we will present how ATLAS InSAR has been used in two different major cities: Hong Kong & London (United Kingdom). First, we will focus on how InSAR has been used for infrastructure monitoring and soil reclamation control in the city of Hong Kong. After that, an example of the use of InSAR in a major construction tunnelling project in the city of London will be presented.

3.1 ATLAS InSAR infrastructure monitoring in Hong Kong

ATLAS was successfully applied to Hong Kong using a set of high-resolution TerraSAR-X images (radar interferometry satellite constellation), acquired from July 2017 to February 2021. 394 km^2 have been monitored with an approximate density of more than 15000 points/km^2 over urban areas and more than 2000000 measurements points. ATLAS InSAR monitoring has allowed the monitoring of extended areas and at the same time to control several infrastructures, such as roads and buildings with high density of points.

The quality assessment on the deformation time series show that 68% of the measurement points presents high quality, 31% medium quality and 1% low quality, being this classification based on the standard deviation of the time series (σ) as follows: High quality $\sigma < 1$ mm, Medium quality $1 \leq \sigma < 1.7$, and Low Quality $1.7 \leq \sigma < 2.5$. Points with higher standard deviation have been discarded.

Two examples of road monitoring are shown in this section. The first one is the New Territories Circular Road (9). Figure 3 shows the velocity of displacement map over the road and its surroundings. It shows a general stability (in green) and settlement deformation around points A and B of about 3mm/year and 15mm of accumulated deformation during all the period around.

The high density of measurement points obtained and the average sampling rate of 11 days in this project allows to continuously monitor roads and other infrastructures. Figure 4 shows an example of mainly stable road located in the South-West part of Hong Kong during the monitoring period.

Figure 2: Velocity of deformation map over Hong Kong

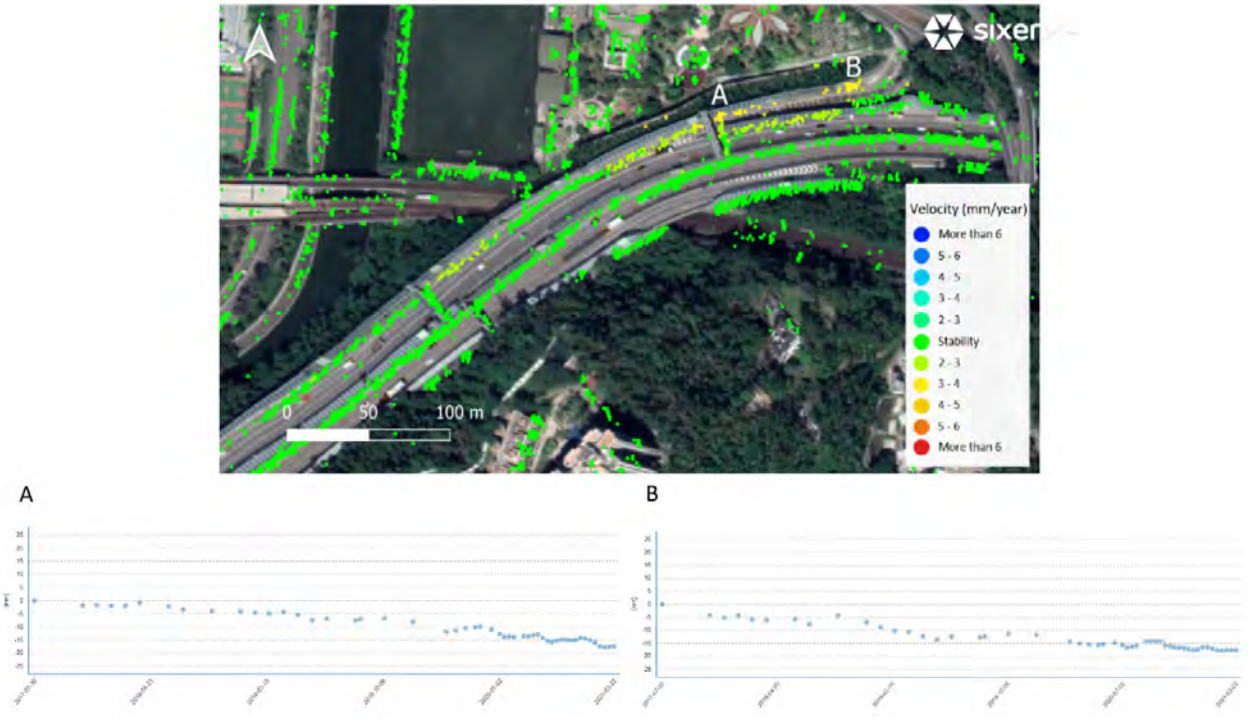

Figure 3: Velocity of deformation map and corresponding time series of a road showing deformation in the north east of Hong Kong

Figure 4: Velocity of deformation map showing stability in a road located at South-West Hong Kong

3.2 ATLAS InSAR Soil reclamation monitoring in Hong Kong

Hong Kong is one of the leading cities in the world and one of the most densely populated places. Hong Kong has a small surface and limited options for expansion, so a way to solve the absence of land and flat territory is soil reclamation. In Hong Kong, between 1877 and 2020, over 70 km^2 of land has been constructed over the sea. This kind of construction needs to be monitored carefully. To this purpose, ATLAS InSAR can monitor the long-term movements, right after the end of the construction activity, and also after many years, in continuous or discontinuous monitoring, if required.

3.2.1 ATLAS InSAR HKBCF island monitoring

An example of use InSAR over areas constructed over the sea is the Hong Kong Boundary Crossing Facilities (HKBCF) island, which is part of the Hong Kong-Zhuhai-Macau bridge and serves as a strategic transportation hub on the west of Hong Kong. HKBCF, located east of the Hong Kong International Airport, consists of about 130 hectares of newly reclaimed land. The construction started on January 2016 and ends up on October 2018 with the public opening of the Hong Kong-Zhuhai-Macao Bridge Hong Kong Port.

ATLAS InSAR was successfully applied to Hong Kong Boundary Crossing Facilities (HKBCF) using a set of high-resolution TerraSAR-X images (radar interferometry satellite constellation), acquired over Hong Kong from January 2019 to February 2021. ATLAs results allowed to monitor the long-term movements over the island, after the end of the construction activity. Figure 5 shows the velocity of displacement map over the South-West seawall in HKBCF island. The velocity of displacement map shows differential movements along the coastline (see points A to C in Figure 5).

3.2.2 ATLAS InSAR Power Station Lamma monitoring

ATLAS InSAR is also useful for continuous monitoring of land reclamation areas. Next example shows the deformation monitoring on the south of Lamma Power Station plant, situated at the Southern edge of Lamma Island (South Hong Kong). The extension was developed on reclaimed land to the south of the

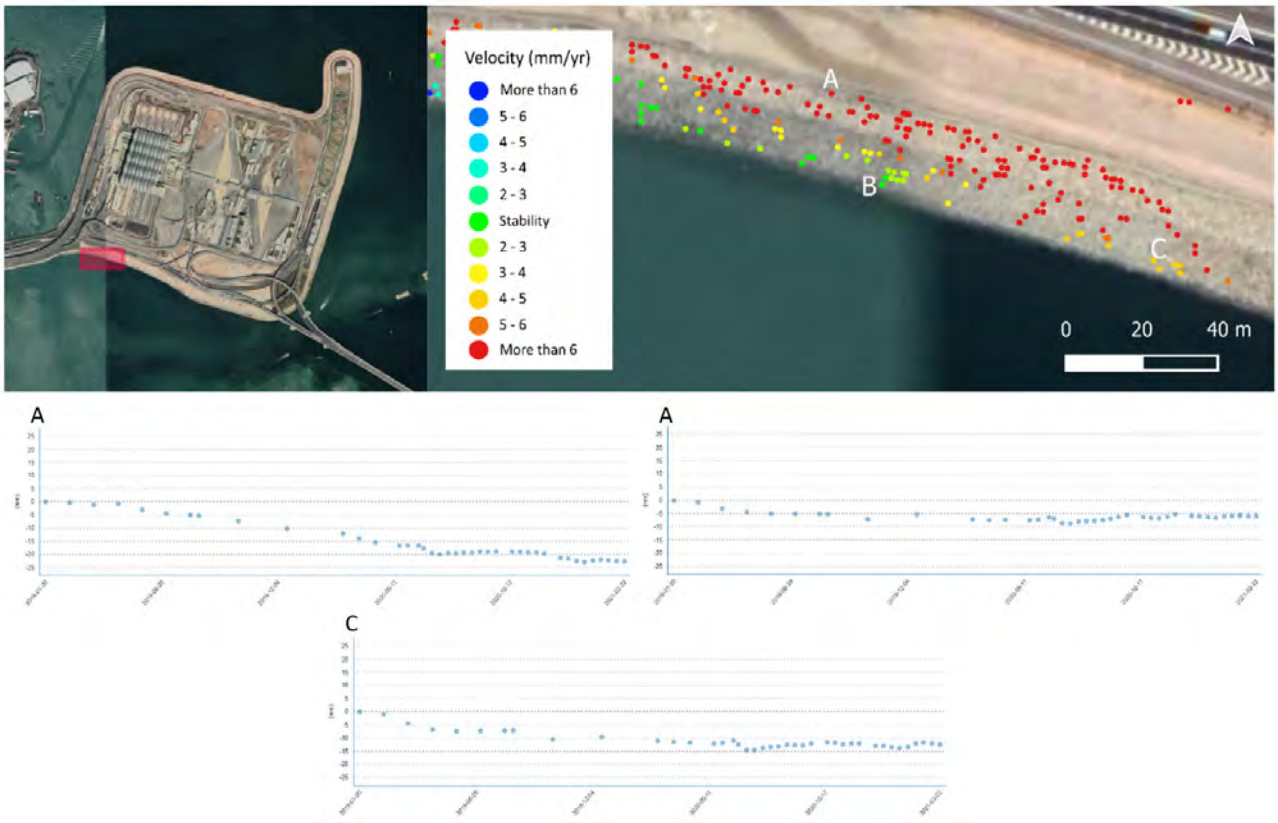

Figure 5: Velocity of deformation map (upper-right) and deformation time series (middle and bottom) over the seawall HKBCF island highlighted in upper-left figure

Figure 6: Velocity of deformation map in the South of Lamma Island (Hong Kong)

power station. The current extension of the reclamation covers about 22 hectares, the first part of which was finished in July 2006.

ATLAS was applied to Lamma island using high-resolution TerraSAR-X imagery (radar interferometry satellite constellation), covering the period from July 2017 to February 2021. Figure 6 shows the velocity of displacement map, which shows a circular settlement deformation in the centre of the island. The maximum subsidence velocity measured is around 12 mm/year with an accumulated deformation reaching 53 mm in settlement during the period of study.

3.3 ATLAS in Tunnelling project: Crossrail (London) case study

Crossrail is one of the major tunnelling projects done in a heavily urbanised area. It consisted in the construction of a new railway line which crosses Greater London from east to west, with five tunnelled sections totalling up to 42 km in length.

InSAR and the ATLAS processing chain were successfully applied to the project using high-resolution TerraSAR-X imagery, acquired over London from August 2013. The main uses of ATLAS InSAR in Crossrail have been: (a) a source of information for the ground/structure behaviour before the start of the construction activity; (b) a complementary source of settlement data during construction; (c) a check for the long term movements, right after the end of the construction activity, or after many years if claims are raised in a later stage.

ATLAS InSAR measurements allowed to study the effects of dewatering activities, which usually result in settlement of the ground. Satellite measurements cover a very large area, which allowed to study a larger extent than the one initially planned, including zones in which there were no ground instruments results. This advantage of the InSAR technology was crucial to determine the total extension of the settlement due to dewatering activities, which reached a much wider extension than the area estimated at the design phase. This example is shown in Figure 7, which displays the accumulated displacement over the Limmo peninsula and its surroundings from August 2013 to August 2015.

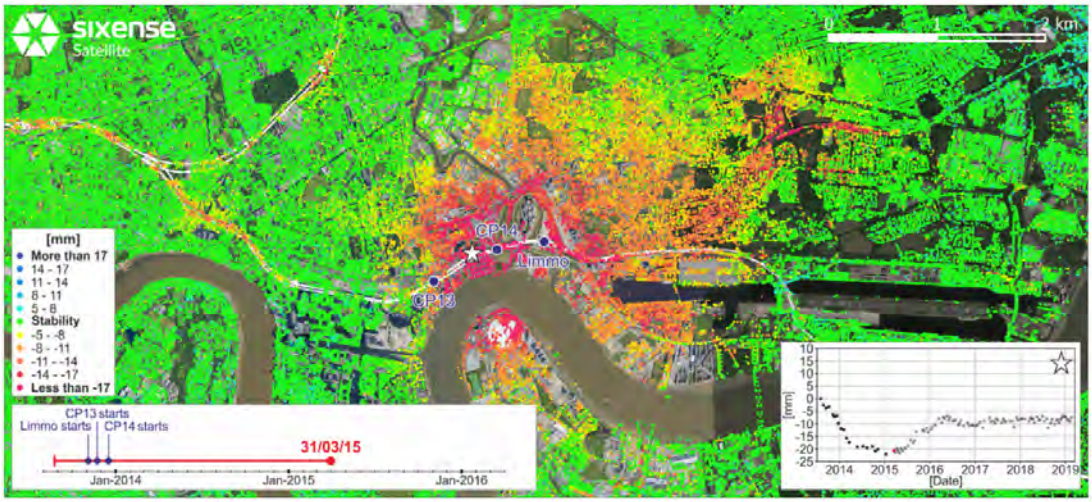

Figure 7: Accumulated deformation map showing the deformation by dewatering in Limmo area (London) derived during the period August 2013 to August 2015. An example of deformation time series of a point located on the area affected by the dewatering is also shown.

Additionally, InSAR results were used to check any widening of the settlement on the planned zone of interest, since tunnelling usually results in settlement movements associated to the loss of volume during the perforation phase. Figure 8 shows the deformation related to the tunnelling activities of the Crossrail project. The image shows deformations of more than 15 mm of subsidence during the period from August 2013 to May 2018.

4 CONCLUSIONS

ATLAS Synthetic Aperture Radar Interferometry (InSAR) is a remote sensing technique, which uses radar satellite-acquired images, which has proven to be a suitable monitoring technique in the field of civil engineering. In this paper, ATLAS processing chain has been presented and three different case applications in two major cities, Hong Kong and London, have been shown.

In Hong Kong city, it has been monitored 394 km2 with high-resolution TerraSAR-X imagery from July 2017 to February 2021 using ATLAS InSAR. Velocity of deformation maps and deformation time series

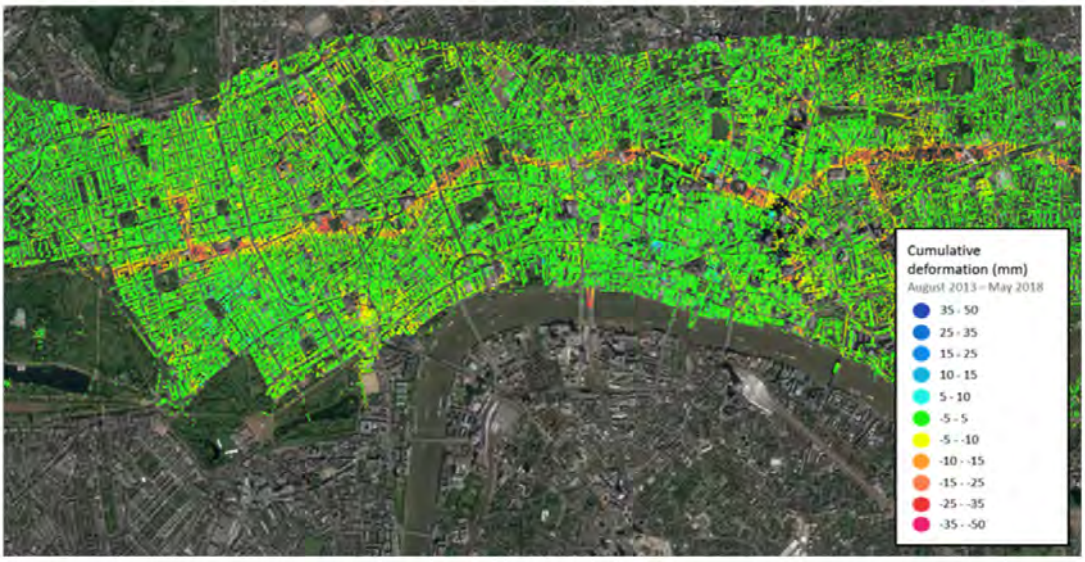

Figure 8:Accumulated deformation map over the tunnel alignment of Crossrail project (London, UK)

have been shown for infrastructure monitoring, more precisely road monitoring, and soil reclamation monitoring. The maps exposed above illustrate the advantages provided by the InSAR technique.

In the Crossrail tunnelling activities, in London, 42 km of tunnel alignment have been monitored with ATLAS InSAR using high-resolution TerraSAR-X imagery from August 2013. Velocity of deformation maps and deformation time series showing settlement in the tunnel length and dewatering areas show how the technique was used for monitoring while the construction activities were ongoing and is still used during the post-construction stage.

Digital Twin for Geotechnical Engineering Applications

I.S. Haryono, A.L. Saw, S.W. Lee
Golder Associates (HK) Ltd., Hong Kong

Lewis C.K. Wong
Atkins China Ltd., Hong Kong

ABSTRACT

Engineers have been motivated to push boundaries and find better tools for a more efficient design process and innovative solutions in construction industry. Digital engineering is the synergistic application of electronic and software technologies. The ultimate goal is to produce digital twins which are digital replicas of real and potential physical assets. With the rise of Building Information Modelling (BIM), digital twin in geotechnical engineering focuses more on the data management. However, the inherent information in digital models can be further exploited for optimizing engineering works. In this paper, this process is illustrated from the viewpoint of geotechnical works. Examples on the use of digital twin to design complex deep excavation and earthwork projects in difficult ground conditions are presented. The geotechnical design process was streamlined and the estimated time saving was up to 50% compared with a traditional design method relying on 2D cross sections. There is also significant time saving for planning of other associated civil elements of works such as master planning as a result of efficient communication and early findings from geotechnical studies attributed to the digital models developed. This was done by combining the use of digital data to produce various models, including Digital Terrain Models and 3D geological models. Besides, innovative monitoring techniques in other case studies are also presented to demonstrate how they assist project stakeholders in monitoring different aspects of a project. The data are readily processed into different formats for monitoring ground movement, monitoring site progress, and controlling excavation and filling works. Overall, digital twin has great potential for geotechnical works.

1 INTRODUCTION

Digital twin (DT) has gained popularity and has been gradually adopted in many civil and geotechnical engineering projects. DT encompasses collection of digital data representing physical objects and it can be considered as virtual replicas of physical infrastructures or ground conditions that can be adopted to run simulations before actual works are executed (Lu et al, 2019). Through DT, different stakeholders can visualise, brainstorm, and communicate many different aspects of a project more efficiently.

In recent days, engineers have witnessed increasing complexity in projects combined with tight design and construction programmes. Large projects usually use abundant data from different sources, and these data are transformed to a format that can be used for design and construction. Traditionally, data transformation is carried out manually, involving production of various 2D cross sections and views. These 2D data are then adopted in various analysis and prediction works. This traditional process is also adopted in geotechnical works as illustrated in Figure 1.

The process is typically hierarchical and tedious. During the design period, design iterations and changes in any component shown in Figure 1 are always inevitable. One can immediately imagine that

changes in master layout plan will restart the entire design loop. Such rework will make some processes redundant and certainly induce a heavy cost to the project. On the other hand, demand for efficiency is only increasing rather than decreasing, regardless the situation. In such case, traditional approaches associated with manual data processing may no longer be feasible and new solutions are required.

To ensure successful delivery, streamlined and smooth data handling during design is required. DT has the potential to offer an alternative approach in expediting project execution. With the advancement of computing power and data processing algorithm, abundant data involved in a project can be processed quickly for the benefits of engineering process as early as possible. This paper aims to present a few practical examples to demonstrate the actual benefits of adopting DT in geotechnical works. It is built on two case studies involving design for deep shaft excavation and large-scale earthwork in a seismic region. Subsequently, innovative monitoring techniques used in other case studies are also presented.

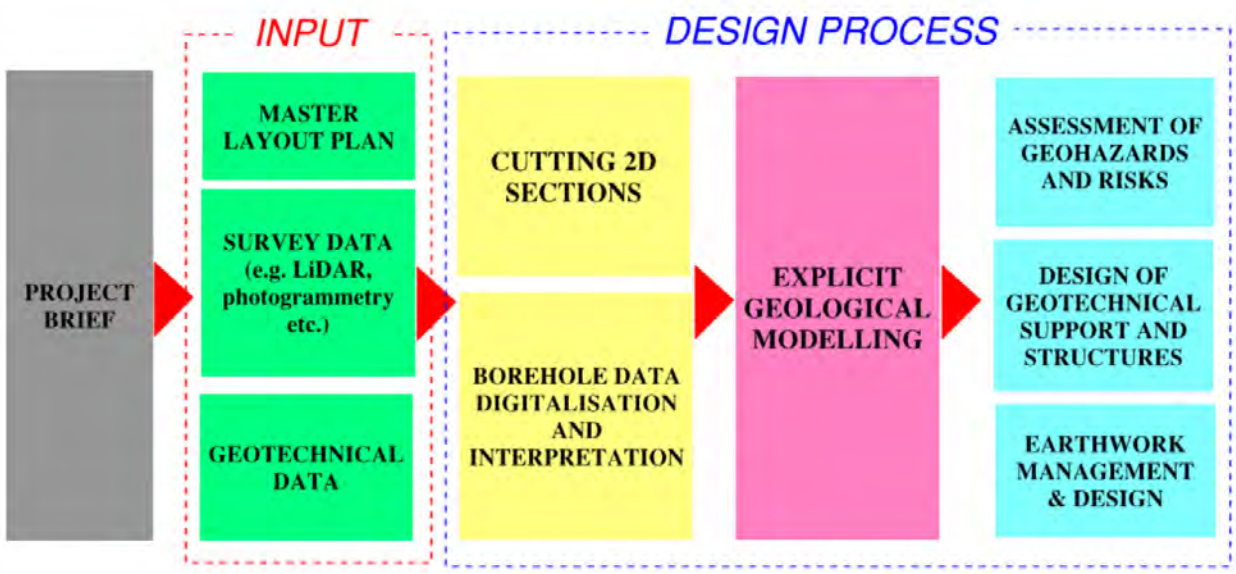

Figure 1: Traditional Design Approach in Geotechnical Works

2 DIGITAL TWIN FOR DESIGN

In geotechnical engineering, DT is adopted to predict and model ground profile in a more organized and accurate manner, compared with traditional methods, and to estimate risks associated with the ground conditions. Examples of DT applications have been demonstrated by Chan et al. (2019) and Mak et al. (2019). DT not only offers data management for ground models and integration with BIM, but also improves design engineering processes.

2.1 Digital Twin for Deep Shaft Excavation

Figure 2 shows a streamlined process from geological modelling to geotechnical analysis stages of a deep shaft excavation project. This example shows the shaft excavation in complex geological conditions. Based on preliminary review of the borehole data, it was identified that the soil layering and rockhead were highly non-uniform across the site. Leapfrog was employed to create a representative DT for design and assessment. The modelling process produces rich data, including thickness of various soil materials across the site. The Leapfrog model can be immediately used in other software packages for analysis. Subsequently, some potential effects on design and construction of the shafts arising from the geological conditions can be quickly identified, as follows:

- Due to non-uniform rockhead levels, unbalanced forces in the shaft walls can be expected. By adopting the Leapfrog model in 3D numerical modelling, unbalanced forces can be analysed. Subsequently, the shaft wall thickness and reinforcement can be designed accordingly.

- The situation above also influences dewatering design. Dewatering scheme for each shaft was specifically designed considering the soil units encountered and the rockhead profile.
- Based on the 3D geological model, the contractor can evaluate its construction methodologies, determine excavation sequence of the shafts and adits, and plan for contract programme.

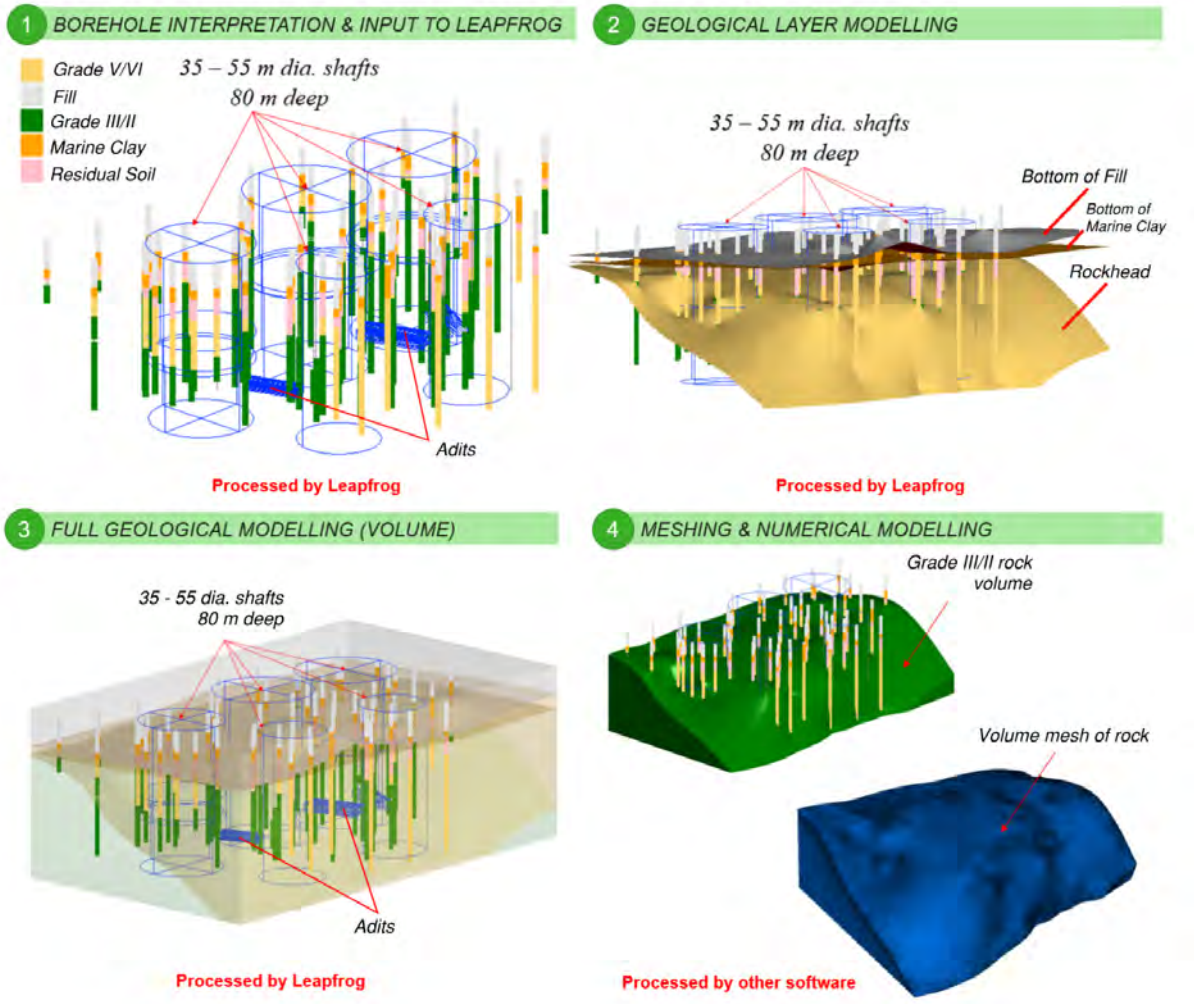

Figure 2: Streamlined Digital Twin Modelling for Deep Shaft Excavation

2.2 Digital Twin for Earthwork

DT is particularly useful when dealing with earthwork in complex terrain with different geological units. Such condition cannot be well handled in the 2D environment. Figure 3 shows a case study of large-scale infrastructure works involving 25.8 million m3 of earthwork volume in 400-ha land. It was planned for a public transportation hub. The earthwork was required to be finished within a 2-year period and this would be followed by construction of buildings and other structures for full operation two years later. As a result of this tight programme, the period of detailed design for the earthwork was squeezed to only 4 months.

In addition to the challenging timeframe, other challenges arose from its ground conditions. The site was situated in hilly terrain and in seismically active area at the toe of a dormant volcano. Cut and fill works were required, and in different areas the fill thickness or cut depth could reach 30 m (Figure 4). The ground conditions were mainly dominated by weathered tuff. Soft alluvial deposits were identified at some isolated locations, hence the risk of large settlement and differential settlement needs careful consideration. Considering these conditions, the components of detailed design for the earthwork comprise the following:

- Review and optimization of planning for additional ground investigation (GI) works;
- Slope stability analysis and design of slope stabilisation systems;
- Prediction for long term settlement and differential settlement;
- Earthwork management;
- Liquefaction assessment; and
- Ground improvement design.

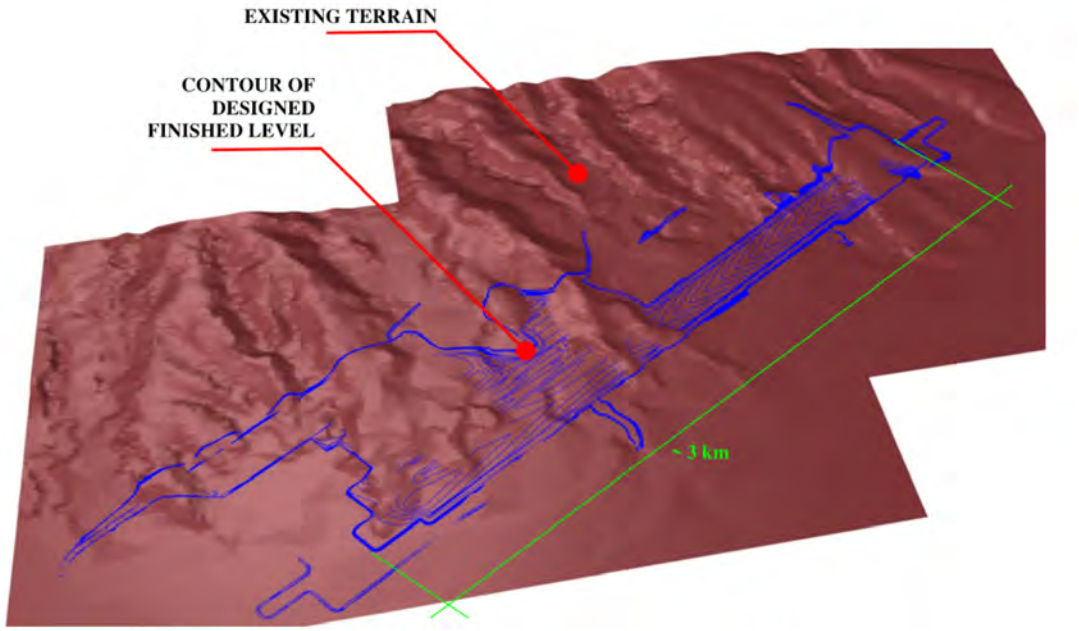

Figure 3: Isometric View of Existing Terrain and Finished Level

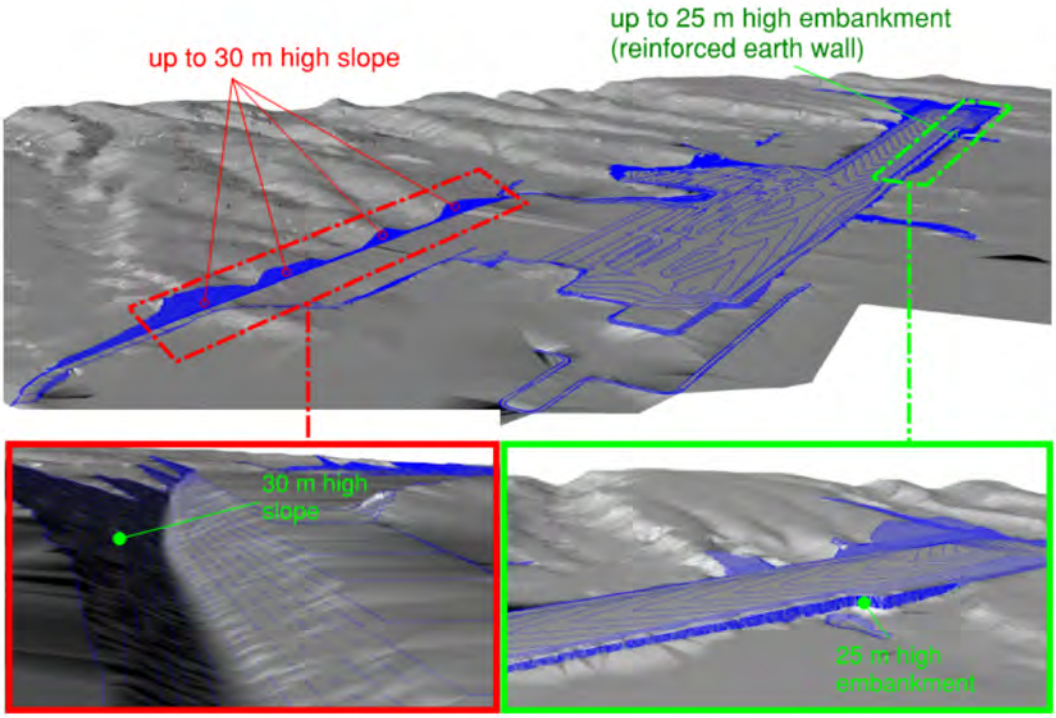

Figure 4: Illustration of Cut Slope and Fill Embankment

For a fast-track, large-scale infrastructure development project of significant geotechnical challenges in a developing country, planning of GI works needs to consider the technical, cost and programme factors. The ground risk could be managed by the digital 3D ground models developed, which are a useful visual tool to inform the project stakeholders of variability and uncertainty in geology across the site. Additional GI could be then focused in the high-risk areas.

During the earthwork design, the master layout plan was still being developed. Hence, iterations were expected in any stage of the earthwork design. This process required a seamless, automated design process overcoming the limitations of traditional approach relying on manual handling using 2D cross sections. A combination of digital terrain modelling, Geographical Information System (GIS) modelling, and implicit geological modelling (Leapfrog) was adopted together with standard geotechnical analysis packages. The key is the interoperability between the different digital platforms. As soon as this runs seamlessly, geotechnical engineers can focus on achieving a robust and optimised geotechnical design which can be incorporated in the development of master layout plan.

2.2.1 Site Reconnaissance and Geotechnical Hazard Assessment

Considering the site area of 400 ha, site reconnaissance was not a trivial task and site visits might not be able to capture a thorough condition of the site. In this situation, utilising digital data such as LiDAR, orthophotos, and borehole data provides an alternative way for site reconnaissance.

Figure 5 shows the orthophoto of the site presenting the complete existing surface conditions. Combined with borehole data, this photo indicates the approximate locations of critical geotechnical features which may affect the design, for example the extent of alluvial plain. This plain is associated with relatively soft deposits and when this area is loaded, it will be subject to long term settlement. This would induce potential problems to the infrastructures in terms of differential settlement due to variability in ground conditions.

The alluvial plain also poses seismic risk, because apart from soft clay it also consists of loose sand. An earthquake could trigger liquefaction that could induce large ground deformation and failure of the adjacent slopes. Figure 6 presents the geological model demarcating the alluvial plains at the site. This knowledge became the basis of settlement predictions, liquefaction assessment, ground improvement design and value engineering, which aimed to resolve any potential stability and serviceability/ground settlement problems during the operational life of the hub.

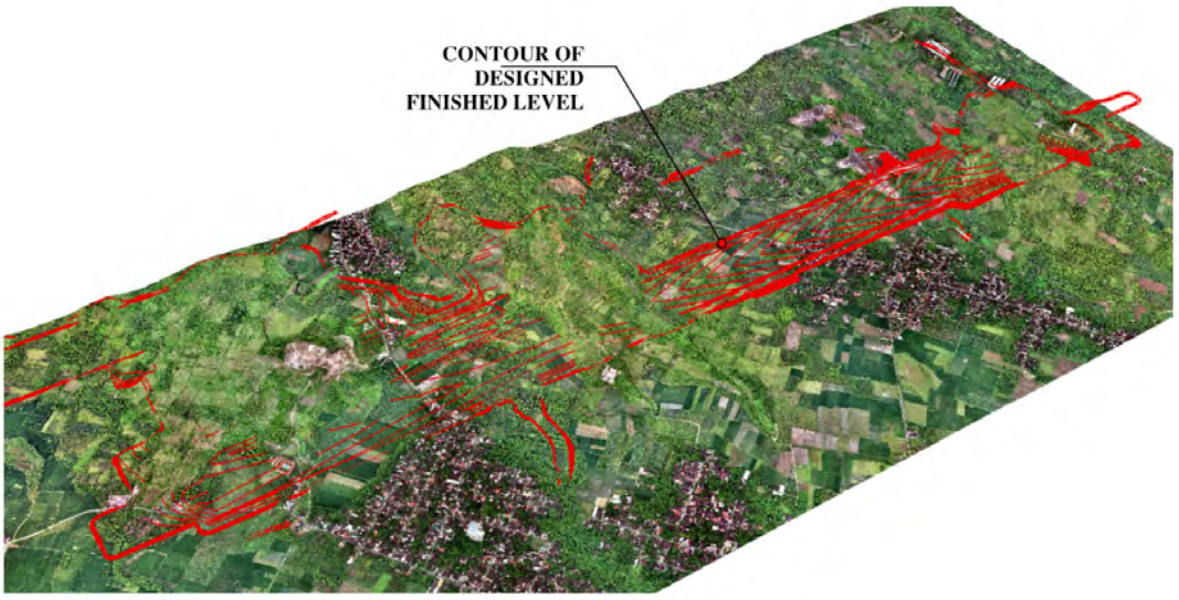

Figure 5: Orthophoto of the Site

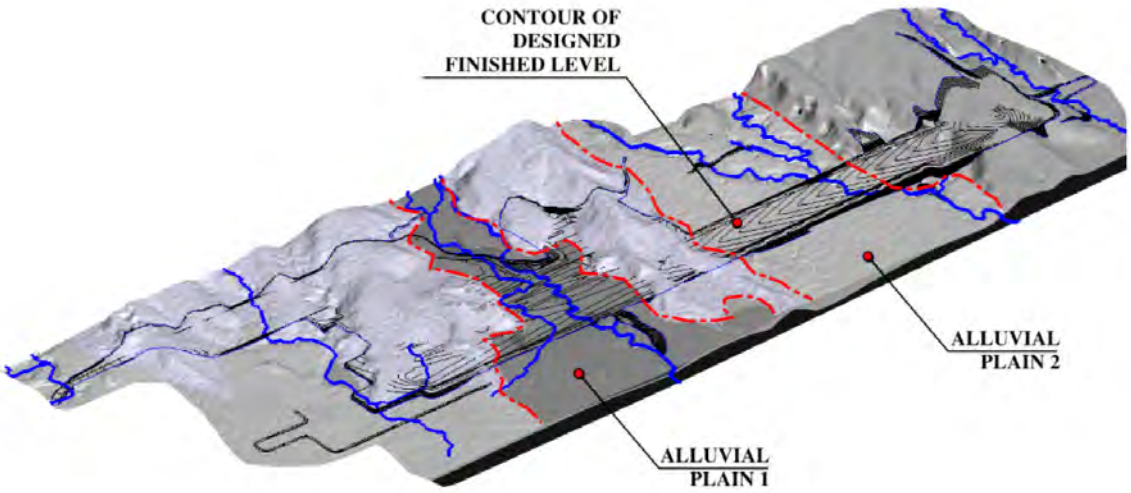

Figure 6: Ground Model with Identified Alluvial Plains

2.2.2 Managing Cut and Fill Balance

The site was in complex terrain. To prepare for a relatively flat grade for the hub, massive cut and fill volumes were required. This was a challenging issue considering limited material sources around the area. The use of sorted material from excavation works within the site was preferred to minimise the use of materials from borrow areas away from the site. Figure 7 shows the significant amounts of cut and fill thicknesses for the site. Figure 8 shows the changes in elevations from the existing conditions to the final grade. Therefore, earthwork sequencing was a critical component in the planning stage for achieving sustainable construction in terms of balancing the cut and fill volumes.

In the analysis of cut and fill thicknesses and volumes, available digital data such as LiDAR data and digital data of the master layout plan have been used. Digital Terrain Models (DTM) was created based on several LiDAR datasets taken in the previous years, and these models were compared with DTM for the final formation level.

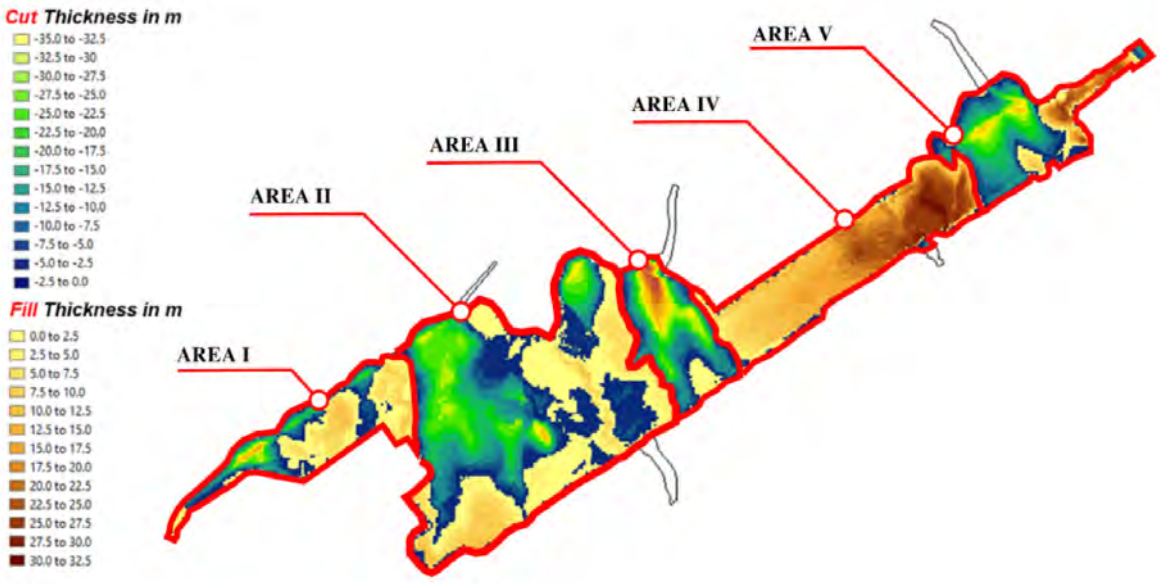

Figure 7: Plan View Showing Works Areas and Cut and Fill Thicknesses

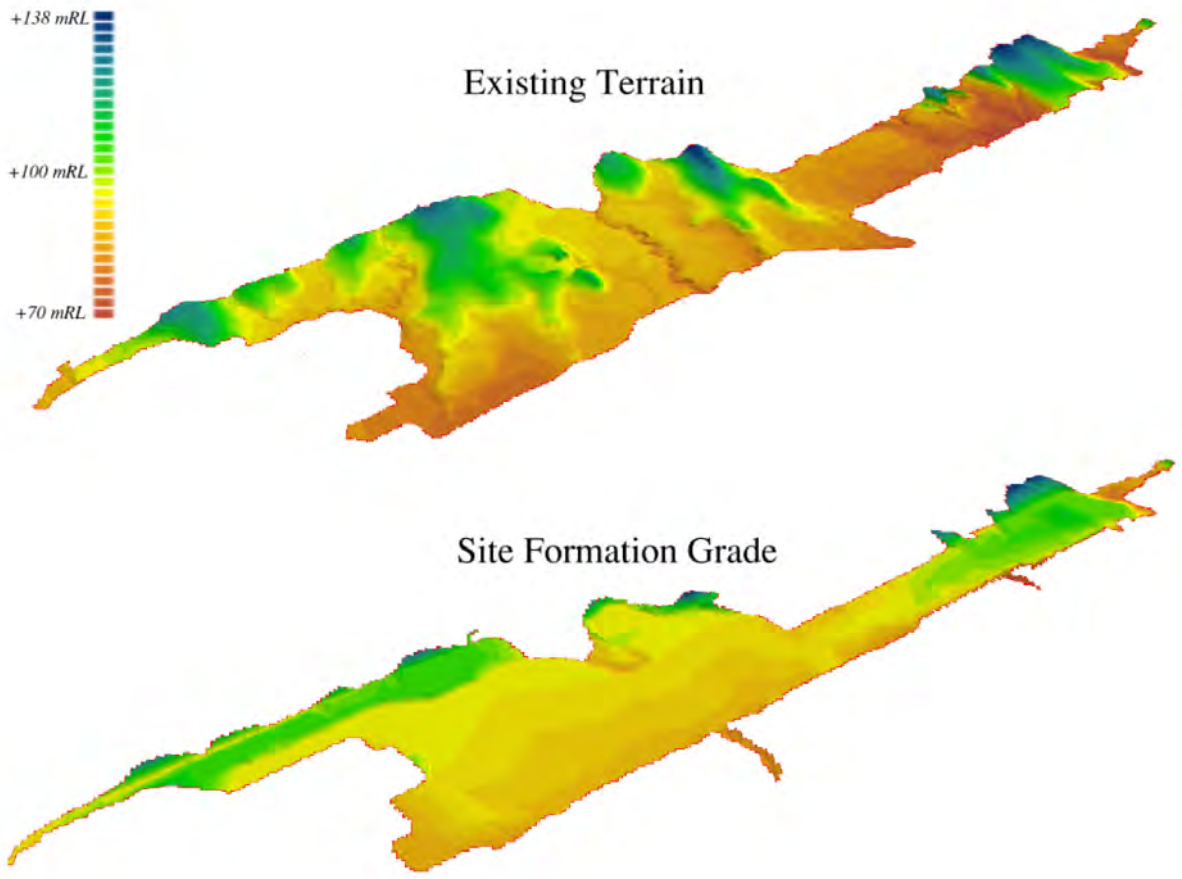

Figure 8: Isometric View of Existing and Site Formation Grades

These results were then combined with the existing 3D ground model data to check the existing material types. Subsequently, assessment of the material characteristics was carried out to determine their suitability as a fill material. Thickness of each material can also be mapped and subsequently, the use of excavated materials available at each area can be optimised. A total cut volume of 13.0 million m^3 and fill volume of 12.8 million m^3 were immediately identified. Table 1 presents the results of cut and fill balance for each area, which are valuable for the contractor to plan its earthwork sequence.

Table 1: Typical Cut & Fill Balance for the Project

Work Area	Cut Volume [million m^3]	Fill Volume [million m^3]	Excess Volume (Cut – Fill) [million m^3]	Area [ha]
I	1.0	0.9	0.1	63.7
II	6.1	1.9	4.2	140.8
III	3.1	0.1	3.0	57.2
IV	–	8.7	-8.7	83.7
V	2.8	1.2	1.6	54.6
Total	13.0	12.8	0.2	400

This process was quickly repeated each time the master layout plan was updated, and the results were communicated immediately to the client and the contractor. For each iteration in the design, the DTM and geological models were integrated directly with the geotechnical design process. Had it been done using the traditional method relying on 2D cross sections, the entire process described above would take longer time and be less accurate. The current integrated process has reduced the time expended on design changes by up to 50%. The digital twin adopted has enabled the geotechnical designer to

quickly update the earthwork design for the area as soon as its additional GI is complete. This allows the contractor to immediately commence earthwork in this area, whilst additional GI is still in progress in other areas.

3 DIGITAL TWIN FOR MONITORING

Monitoring data is essential to evaluate the performance of the design and construction works. Monitoring works are traditionally carried out using manual systems. For a large-scale site formation works, monitoring works would be labour intensive and time consuming. Surveyors need to travel from one location to another and monitor each individual point (see Figure 9). Even then, the monitoring points are very limited / localised and sometimes inadequate to cover a meaningful area.

Figure 9: Typical Localised Monitoring Point Set Up for Manual Monitoring

With recent technological advances, monitoring works can be undertaken using digital monitoring techniques such as remote sensing technology, e.g. Unmanned Aerial Vehicle (UAV), InSAR, etc. While conventional monitoring instruments only represent localised points and are restricted by site access to install or take monitoring readings, digital monitoring techniques can overcome these two limitations. Moreover, digital monitoring techniques will record abundant data and they can be utilised for different purposes. This section presents some ideas on adopting digital twin in monitoring works.

Figure 10 shows a project site monitored by drones and the acquired photos were processed using photogrammetry techniques. DTM were generated based on the processed drone photos and these provide abundant useful information such as the true coordinates of a location. The use of this technique will benefit many stakeholders as it has capability in monitoring different components of a project. Photogrammetry data can be turned into a DTM and the designer can utilize the DTM in different periods to monitor ground movement of an area (Figure 11). Adopting the same DTM, progress of excavation or stockpiling works can be recorded and used for planning. The contractor or client can turn the monitoring data into 3D imageries such that site activities can be observed in different periods (Figures 10 and 11). The other benefit of taking the digital data is that the information can stored more easily and extracted quickly when they are required.

Other than capturing and building 3D imageries for monitoring the physical conditions of a site, UAV can also be used to monitor geo-environmental events, such as methane gas escaped from a landfill or rising temperature from an activity. A thermal camera or inlet nozzle (for gas) can be mounted on UAV to monitor temperature or surface emission. Figure 12 shows the monitored temperatures of a

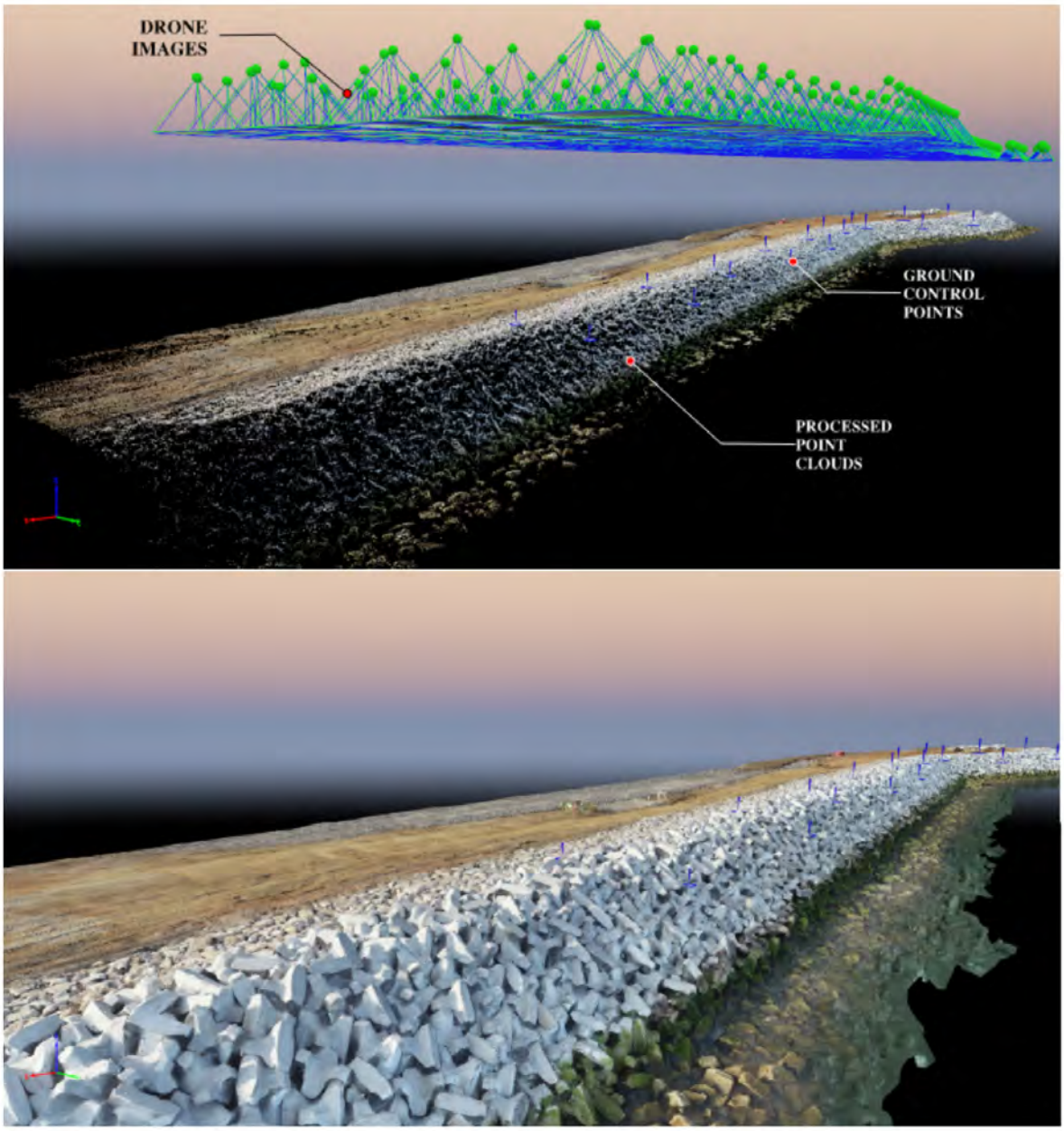

Figure 10: Photogrammetry Processing of Monitored Area (Above) and Constructed 3D Imagery (Below)

project site due to mudflow erupting from a gas well with an affected area of approximately 1 km2. The temperatures were monitored using a thermal camera mounted on a helicopter. The use of this remote sensing technique reduces health and safety risks to engineers when carrying out such difficulty duty. The same approach can be carried out for surface emission monitoring, e.g., gas emitted from a landfill or toxic gas in sewers.

4 CONCLUSION

Digital twin (DT) is bringing huge potential to the planning, design, construction, monitoring and maintenance of large-scale, complicated civil and geotechnical projects. This paper has used four case studies to demonstrate the benefits of DT in different project phases to the project stakeholders in terms of improving the efficiency of design process, handling of processing, presentation, and storage of a large amount of information, control and monitoring of construction activities, achievement of sustainable construction, and safeguarding the health, welfare and safety of construction personnel.

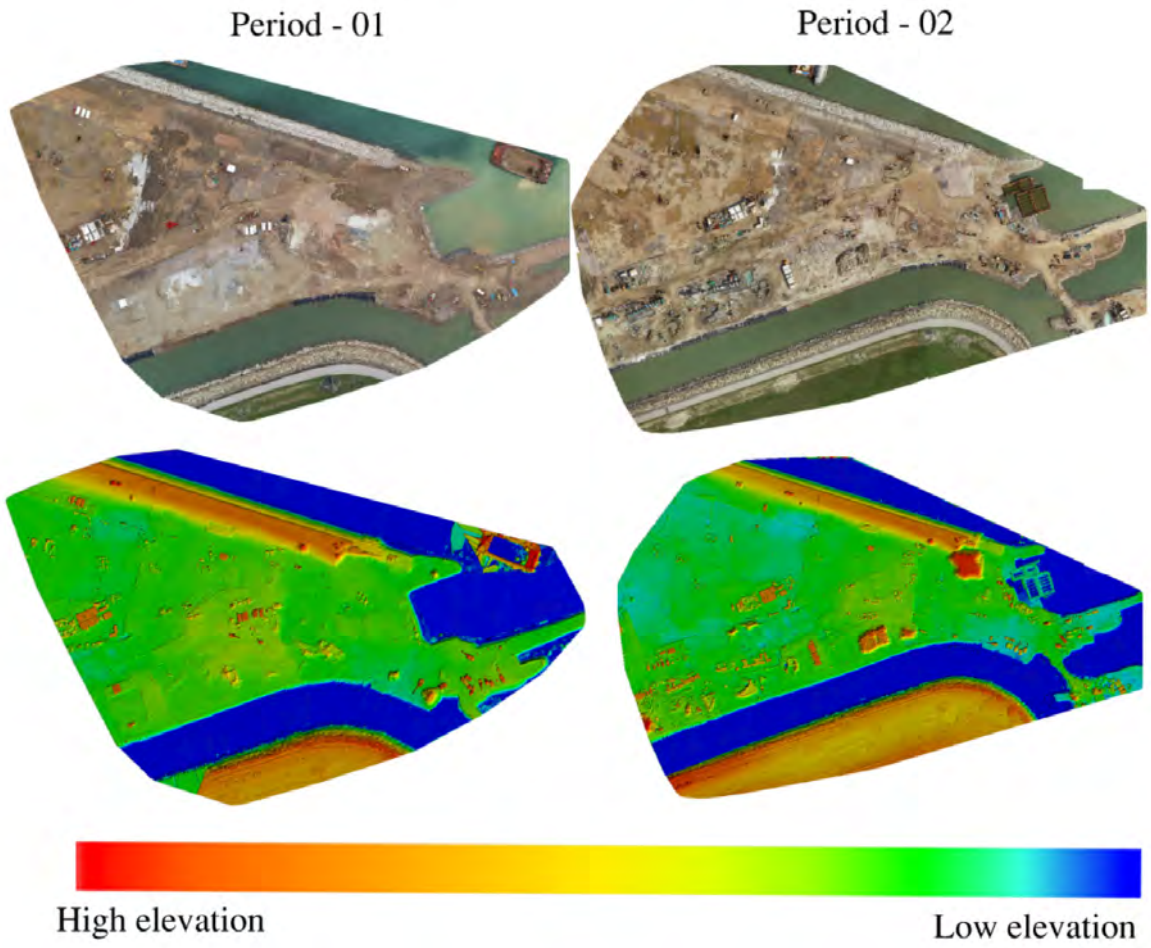

Figure 11: Plan View of Monitored Elevations by Photogrammetry: Orthophotos (Above) and Digital Elevation (Below)

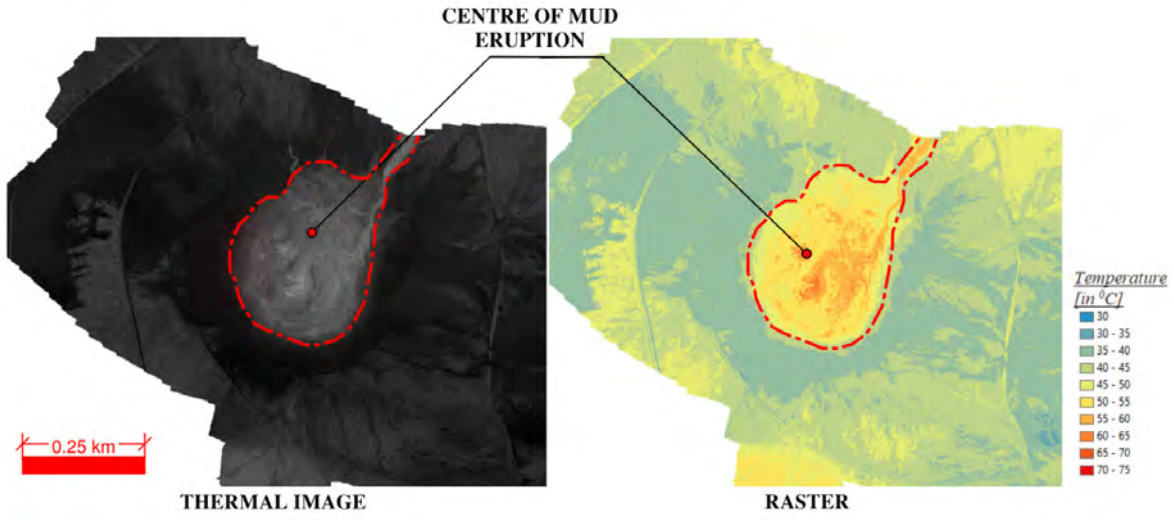

Figure 12: Plan View of Monitored Temperatures of Mudflow from a Gas Well

REFERENCES

Chan, T.H., Woodmansey, P., Suen, H.Y., Lee, S.W., Henderson, T. & Wu, K.K. 2019. Application of Digital Engineering to Geotechnical Tunnel Design. The Hong Kong Institution of Engineers Geotechnical Division 39th Annual Seminar 2019, pp.20-28.

Lu, V.Q.C., Parlikad, A.K., Woodall, P., Ranasinghe, G.D. & Heaton, J. 2019. Developing a Dynamic Digital Twin at a Building Level: Using Cambridge Campus as Case Study. In International Conference on Smart Infrastructure and Construction 2019 (ICSIC) Driving data-informed decision-making, ICE Publishing, pp.67-75.

Mak, D.Y.Y., Luk, F.W. & Chan, H.H.K. 2019. A New Approach to Modelling the Ground. The Hong Kong Institution of Engineers Geotechnical Division 39th Annual Seminar 2019, pp.150-159.

Using UAV-based Technology to Enhance Landslide Investigation – A Case Study in Fei Ngo Shan, Kowloon

W. Hou, J.R. Hart, R. Tsui, A. Ng & C. Cheung
GeoRisk Solutions Limited, Hong Kong

ABSTRACT

Establishing landslide models plays a critical role in Natural Terrain Hazard Studies (NTHS). Conventional approaches adopted by NTHS practitioners may be subject to temporal and spatial limitations. In particular, landslide volume estimations are prone to inaccuracies using conventional approaches including direct, field-based measurements due to time and access constraints. With the rapid advancement of unmanned aerial vehicle (UAV) and 'Structure from Motion' (SfM) technologies in recent years, digital methods are being developed to provide useful and practical tools, which can be applied quickly, to enhance the results of landslide mapping. In this paper, we present a natural terrain landslide case study from a cluster of landslides, which were probably triggered by an intense short-duration rainstorm on 6 June 2020 at Fei Ngo Shan, Kowloon. Following initial landslide inspections to establish a preliminary engineering geological model for the failure, a digital approach was applied using a UAV-SfM derived point cloud to construct a 3D spatial model of the scar. A key objective of the 'drone survey' was to provide an alternative and accurate method of landslide volume measurement. The results demonstrate that a combination of conventional mapping and digital modeling techniques using UAV-captured data, results in enhanced landslide models for investigations and NTHS.

1 INTRODUCTION

1.1 Background

The presence of a 'fresh' natural terrain landslide, i.e. a recently occurred landslide which is relatively clear of vegetation cover, is of great value to natural terrain hazard study (NTHS) practitioners, as it offers a unique opportunity to investigate, first-hand, active natural terrain failure mechanisms within a study catchment. Investigations on landslide failure scale, materials and mechanisms provide critical data for the derivation and discussion of future landslide design events and, therefore, for the subsequent development of appropriate hazard mitigation strategies. Conventional approaches to the investigation of natural terrain landslides involve direct field-based measurements (assuming safe field access), typically using hand-held tape measures, to estimate and record the extent and dimensions of the landslide scar. However, this approach has a number of significant limitations given the time and difficulties often involved in reaching the scar, together with the inherent challenges associated with the physical methods of accurately mapping the scar shape. In addition, there are further limitations with the use of the standard formula W_r x L_r x D_r x $\pi/6$ (IAEG, 1990), which is commonly adopted to calculate landslide source area volume. This formula, whilst extremely useful to estimate a range of possible landslide volumes, assumes a rotational sliding mechanism and is based on the assumption of ellipsoidal landslide geometry, assumptions which may not readily apply to natural terrain landslides commonly occurring in Hong Kong.

With the rapid advancement in unmanned aerial vehicle (UAV) technology in recent years, UAV-based photogrammetry has become a useful tool for landslide investigation. In conjunction with the previous territory-wide LiDAR survey in Hong Kong, this technology-driven approach can overcome a number of temporal and spatial limitations in conventional landslide investigations and provide accurate, relatively quick and cost-effective, 3D landslide models. In this paper, we present a case study from an investigation of recent landslides that occurred in June 2020 at Fei Ngo Shan, Kowloon, using digital measures, i.e. UAV-based photogrammetry, point cloud, GIS, LiDAR etc., to enhance the results of landslide field mapping.

1.2 Study area

The study area is located at the mid- to lower portion of southeast-facing hillside slopes below Fei Ngo Shan (Kowloon Peak) (Figure 1). Within the study area, a cluster of eight landslides, named as RC15-RC22, were observed in June 2020 (Figure 2). The landslides were most likely triggered by a heavy rainstorm between 2:00 am and 6:00 am on 6 June 2020 (based on detailed rainfall analysis). A Black Rainstorm Warning signal was issued on the same day by the Hong Kong Observatory due to incessant downpours across the territory at that time.

A preliminary UAV survey and field mapping were carried out in August 2020. According to the preliminary field work and interpretation on UAV-captured aerial photos, the landslides were debris avalanches with source widths and lengths ranging from 5 m to 13 m, source depths (perpendicular to the assumed original ground surface profile) ranging from 1 m to 2.5 m, and debris trail lengths ranging from 24 m to 70 m. The estimated source volumes range from 13 m^3 to 144 m^3. The landslides typically involved the failure of bouldery colluvium overlying tuff saprolite (i.e. predominantly completely decomposed tuff) and locally moderately decomposed coarse ash tuff. Details are provided in Table 1. Among these eight landslides, the largest, RC15, was selected for detailed field mapping and further analysis.

Table 1: Inventory of 2020 landslide cluster

Landslide No.	Type*	Width of source (m)	Length of source (m)	Depth of source (m)	Estimated source volume (m^3)**	Length of debris trail (m)***	Main materials involved in the failure****
RC15	DA	11	10	2.5	144	70	Colluvium
RC16	DA	12	13	1.5	81.6	55	Bouldery colluvium overlying CDT
RC17	DA	8.5	10.5	1.5	70	40	Colluvium
RC18	DA	5	5	1	13.1	10	–
RC19	DA	7.5	7	1.5	41.2	32	–
RC20	DA	13	8.5	1	57.8	24	Thin colluvium overlying CDT (& HDT)
RC21	DA	5	6	1	15.7	35	–
RC22	DA	7.5	10.5	1.5	61.8	70	Thin colluvium overlying HDT & MDT

* DA refers to Debris avalanche; ** Source volume is based on W × L × D × π/6 (IAEG, 1990); dimensions of landslide source (i.e. W, L & D) of RC15 are from field mapping, and for others they are from UAV photograph based API; *** Length of debris trial of RC15 is from field mapping, and for others they are from UAV photograph based API; **** CDT, HDT and MDT refer to completely (C), highly (H) and moderately (M) decomposed (D), coarse ash tuff (T)

1.3 Published geology

According to the 1:20,000-scale geological map of Hong Kong (Sheet 11, Edition II) (GEO, 2012), the study area is underlain by the Mount Davis Formation, forming part of the Lower Cretaceous Repulse Bay Volcanic Group (Figure 3).

The Mount Davis Formation is at least 500 m thick and comprises variably lapilli-bearing, coarse ash

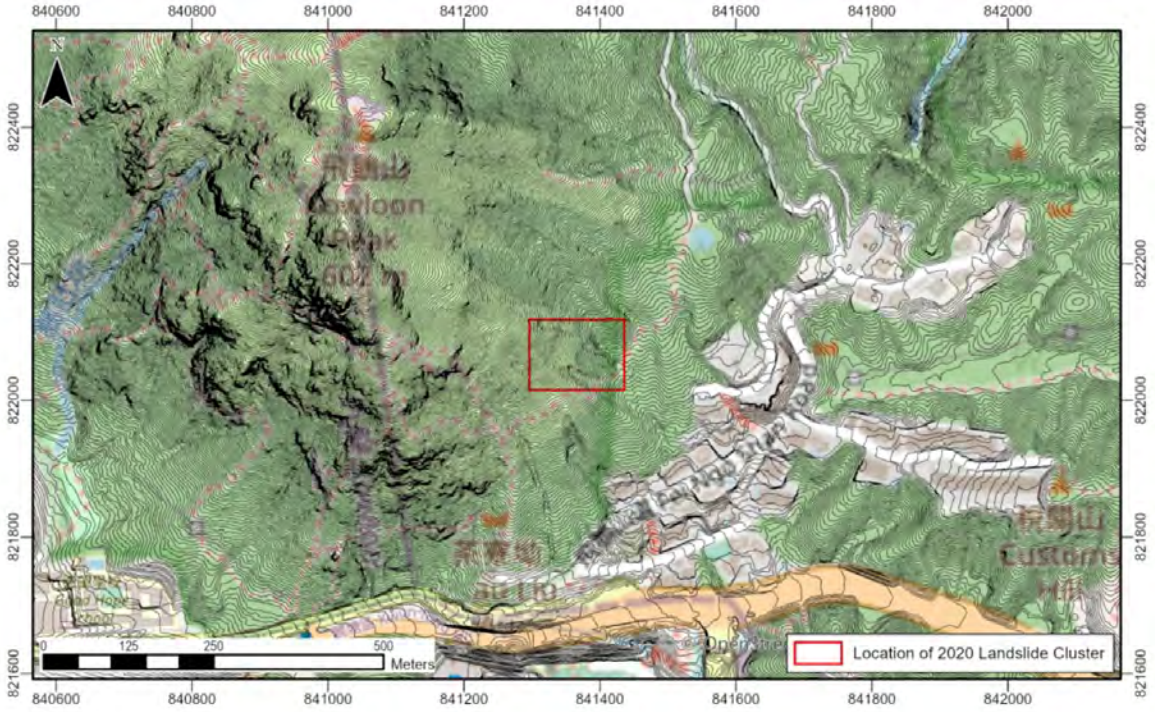

Figure 1: Location of the recent landslide cluster (June 2020). Basemap is taken from Esri OpenStreetMap (OSM contributors, 2015); contour is taken from the 2010 LiDAR survey of Hong Kong (AAM Pty Ltd, 2012)

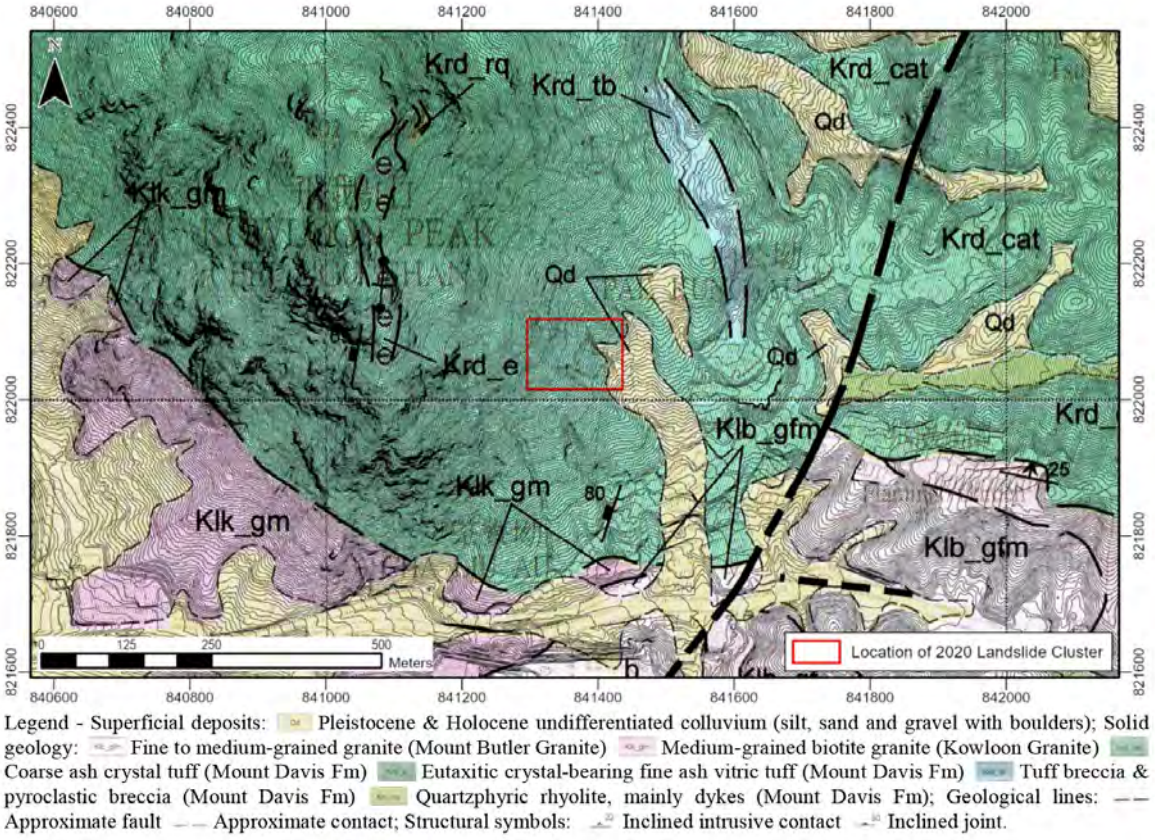

Figure 2: Overview of the recent landslide cluster (June 2020). Left: UAV photograph showing an overview of the landslide cluster. Right: a plan showing the source area and debris trail of each landslide in the cluster. Note: basemap contours are taken from the 2010 LiDAR survey of Hong Kong (AAM Pty Ltd, 2012)

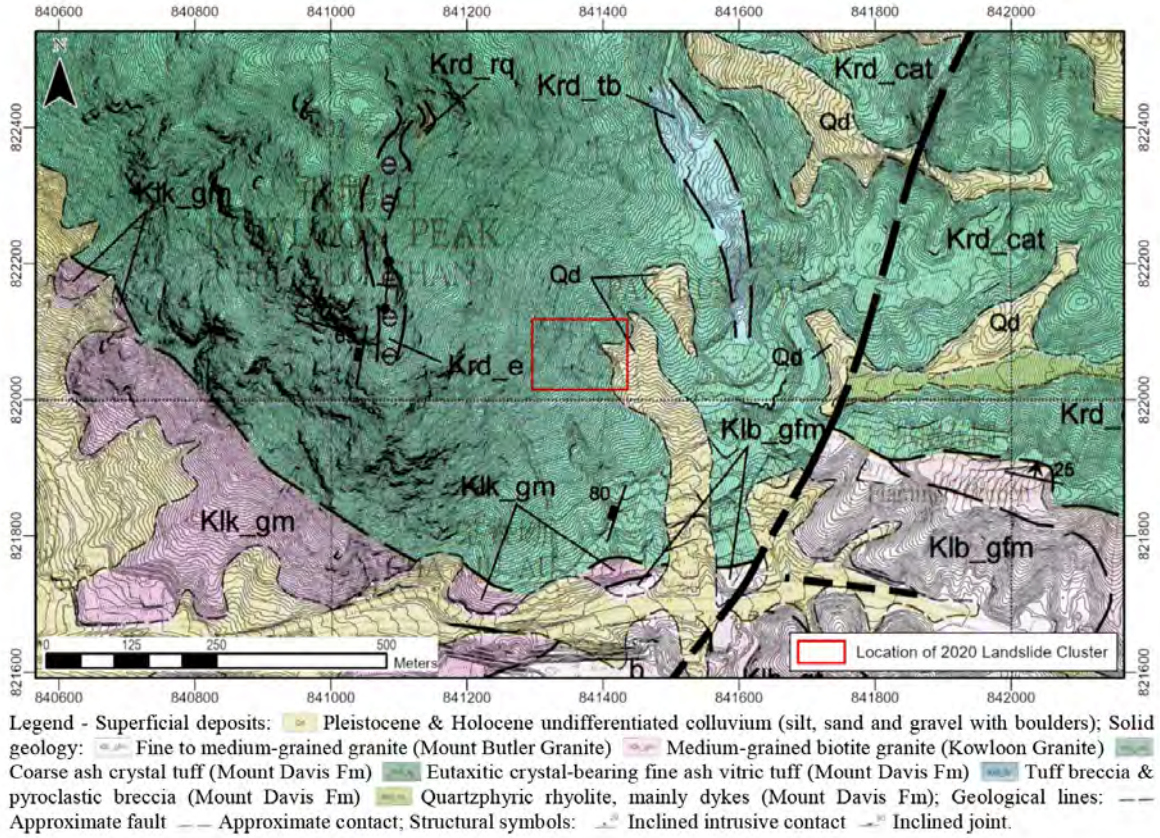

Figure 3: Geological map. Extracted from GEO (2012) and overlaid with 2010 LiDAR-derived contours (AAM Pty Ltd, 2012)

crystal tuff, with some eutaxite and sandstone beds at the type locality (GEO, 2000). In eastern Kowloon, this formation is approximately 950 m thick and includes several thick eutaxite units (GEO, 2000).

A band of eutaxitic crystal-bearing fine ash vitric tuff and a thin band of quartzphyric rhyolite dykes are present at the crest of the hillside above the study area, and these are aligned sub-parallel to the strike of the volcanic strata. An approximately N-S striking layer of tuff breccia and pyroclastic breccia is present on the slopes to the northeast of the study area. Granite of the Mount Butler Formation is present at approximately 250 m to the south of the study area.

A NE-SW aligned fault is inferred to the east of the study area. Major regional faults are mostly orientated NE-SW and NW-SE, and occasionally E-W. However, there are no faults indicated within the study area. The study area comprises an area of undifferentiated colluvium present along the valley floor.

Legend - Superficial deposits: Pleistocene & Holocene undifferentiated colluvium (silt, sand and gravel with boulders); Solid geology: Fine to medium-grained granite (Mount Butler Granite) Medium-grained biotite granite (Kowloon Granite) Coarse ash crystal tuff (Mount Davis Fm) Eutaxitic crystal-bearing fine ash vitric tuff (Mount Davis Fm) Tuff breccia & pyroclastic breccia (Mount Davis Fm) Quartzphyric rhyolite, mainly dykes (Mount Davis Fm); Geological lines: Approximate fault Approximate contact; Structural symbols: Inclined intrusive contact Inclined joint.

1.4 Geomorphology and hydrology

Along with detailed aerial photograph interpretation (API), digital analysis of the 2010 LiDAR data (AAM Pty Ltd, 2012) was carried out to identify and map prominent geomorphological features within and in close proximity of the study area. A Digital Elevation Model (DEM) of 0.5 m resolution for the study area and adjacent terrain was generated from the LiDAR data. This LiDAR-derived DEM is used to: (1) establish a digital 3D ground model; (2) investigate topographic, hydrological and geomorphological

features; and, (3) assist in determining geomorphological units by automated landform classification as part of the development of a geomorphological model for the study area.

According to the slope angle map derived from the DEM (Figure 4), the study area is characterised by three sub-horizontal bands of steeply (i.e. >45°) slopes at 350 mPD to 360 mPD (Upper band), 330 mPD to 340 mPD (middle band) and 300 mPD to 310 mPD (lower band). The upper band is the location of the source area of RC22, the middle band is the location of the source areas of RC16 and RC17, and the lower band is the location of the source areas of RC15 and RC18 to RC21. Other slopes in the vicinity are moderately inclined (i.e. 25° to 35°) to gently inclined (i.e. 15° to 25°). Flatter slopes (i.e. <15°) are present locally along the valley floor below.

The valley floor at the study site is shaped by both ephemeral and perennial streams. A stream network was generated from the DEM-based hydrological modeling (using various ArcGIS tools, e.g. flow direction, flow accumulation, stream order etc.) and is shown in Figures 4 and 5. The main streamcourse at the study site had flowing water during the entire observation period of May to December 2020 although water levels were observed to be minimal in May (i.e. at the start of the 'wet' season) and in December (i.e. within the 'dry' season). More significant stream flows were observed in August to September (i.e. within the 'wet' season). However, the subsidiary streams across the areas covered by debris from RC15 and RC21 (Figures 4 & 5) were dry during the observational period. This indicates the transient nature of surface water runoff after rainstorms. Nonetheless, these ephemeral streams provide channels for post-failure erosion of landslide scars.

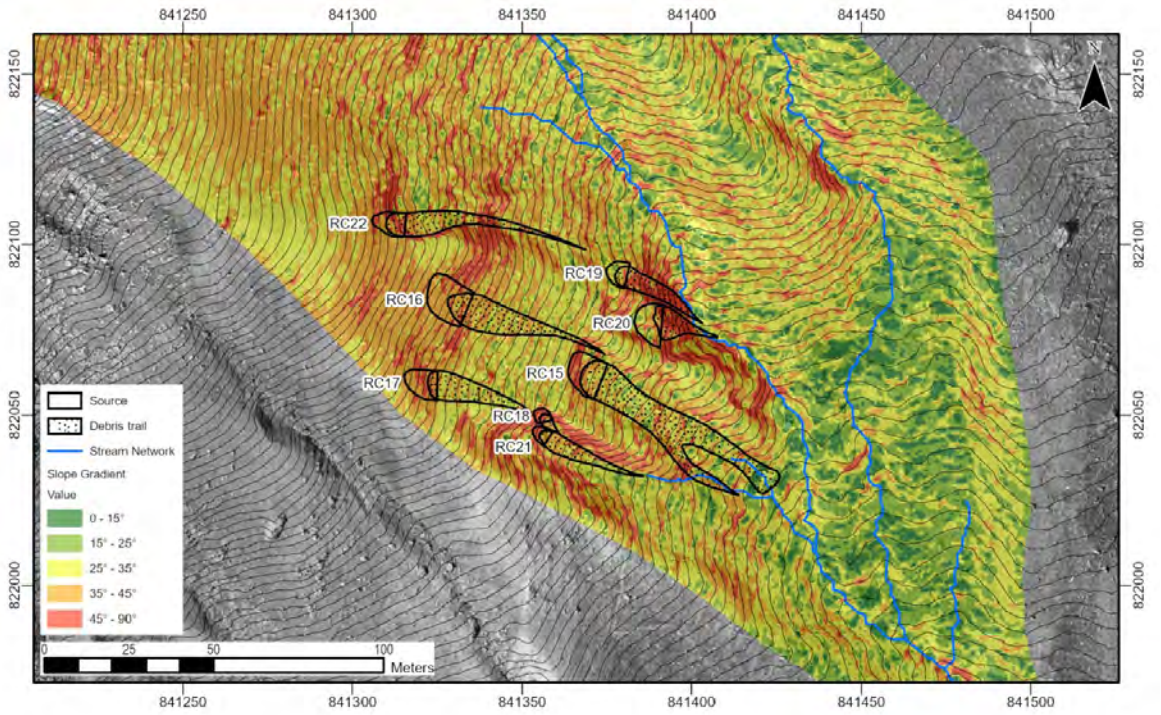

Figure 4: Slope angle map of the study area and its adjacent area and overlaid with an ortho-rectified 1963 aerial photo

An automated approach for landform classification is applied on the LiDAR-derived DEM concerning two parameters. One parameter is the Topographic Position Index (TPI), which considers the difference between each DEM pixel and the mean elevation of its surrounding pixels (Jenness, 2006). The other parameter is the ground roughness, which considers the deviation of each DEM pixel from the mean elevation. Detailed methodology is described by De Reu et al. (2013). According to the automated landform classification (Figure 5), four geomorphological units can be determined in and adjacent to the study area. These units are valley floor, valley slope, interfluvial slope and spurline. The landform classification model shows that the source areas of RC16, RC17 and RC22 are located at the boundary between spurline and interfluvial slope. Source areas of RC18, RC19, RC20 and RC21 are located at the boundary between interfluvial slope and valley slope. RC15 occurred within the interfluvial slope.

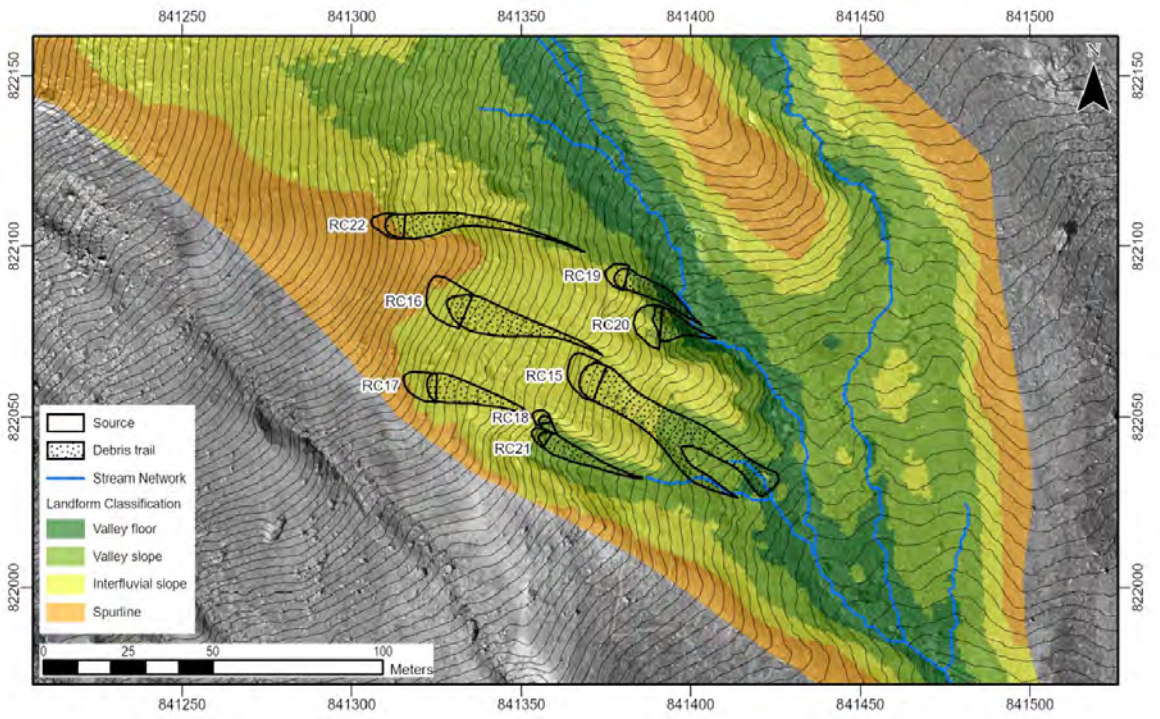

Figure 5: Automated landform classification for the study area and its adjacent area and overlaid with an ortho-rectified 1963 aerial photo

2 LANDSLIDE MAPPING

2.1 Field mapping of RC15

2.1.1 General

Detailed field mapping of RC15 (i.e. the largest landslide within the cluster) was carried out in mid-late 2020. Field photographs illustrating the key observations are presented in Figure 6. Mapping results including a plan and three section profiles are presented in Figure 7.

2.1.2 Main scarp

The main scarp was up to 4 m high in the central portion and was steeply inclined at 80° (Figure 7c). Bouldery colluvium was exposed in the main scarp. The colluvium was composed of stiff, orangeish brown, slightly clayey sandy silt with many cobbles and boulders. A soil pipe of approximately 0.7 m diameter and > 0.8 m long was present at the base of the main scarp (Figure 6b). The soil pipe was dry, approximately horizontal and partly infilled with cobbles. A 1.5 m high and 0.2-0.3 m wide tension crack was present at the lower end of the south flank of the main scarp (Figure 6c).

2.1.3 Source Area (CH0m to CH10m)

The source area of RC15 was approximately 11 m wide, 10 m long and 2.5 m deep with an estimated source volume of 144 m^3 (Table 1, Figure 6a & Figure 7b). Material exposed on the surface of rupture was similar to that on the main scarp, i.e. bouldery colluvium. The upper portion of the surface of rupture is moderately steeply inclined at 45°, becoming more gently inclined at approximately 20° in the lower portion (Figure 7c).

The surface of rupture was covered intermittently by displaced boulders and debris rafts with some relatively intact topsoil and vegetation (Figure 6d). Large boulders predominantly rested on gently inclined slopes at the lower part of the surface of rupture. Bouldery landslide debris was locally clast-

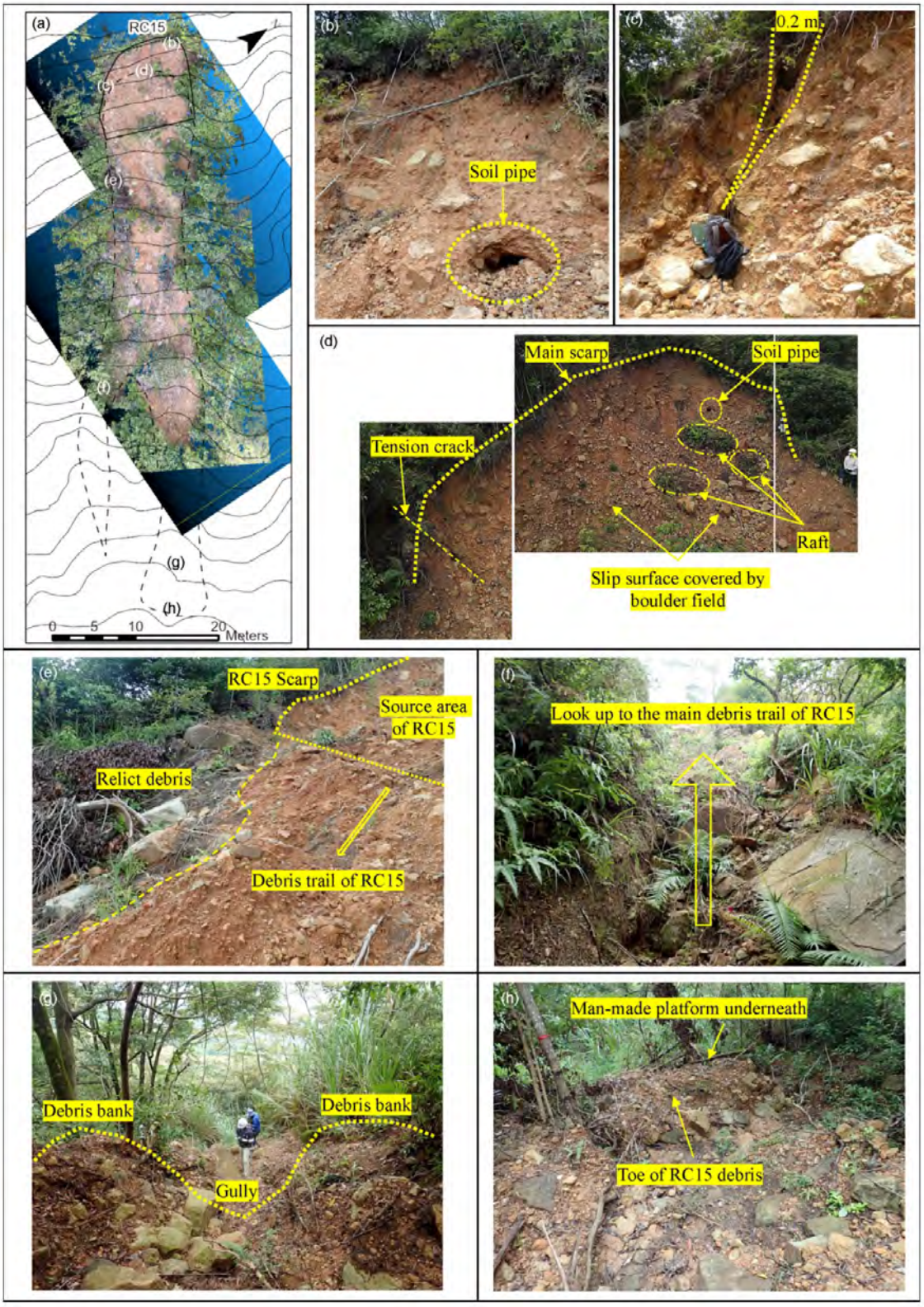

Figure 6: Photographs of RC15. (a) a plan with 2010 LiDAR contour and point cloud image showing the extent of RC15 and the locations of (b) to (h); point cloud image for the lower portion of RC15 was not available due to dense vegetation coverage; (b) soil pipe at the main scarp, approximately 0.7 m across and > 0.8 m deep; (c) minor scarp with tension crack at the south portion of main scarp, approximately 1.5 m high and up to 0.2 m wide at its widest portion near the ground surface; (d) main scarp, approximately 4 m high, inclined at 80°, with the presence of rafts and boulders below; (e) older, relict, debris below recent debris of RC15; (f) bifurcated debris trail; (g) post-failure erosion with the presence of debris banks (levees) and an incised gully within the debris; (h) debris deposited on a man-made platform at the toe.

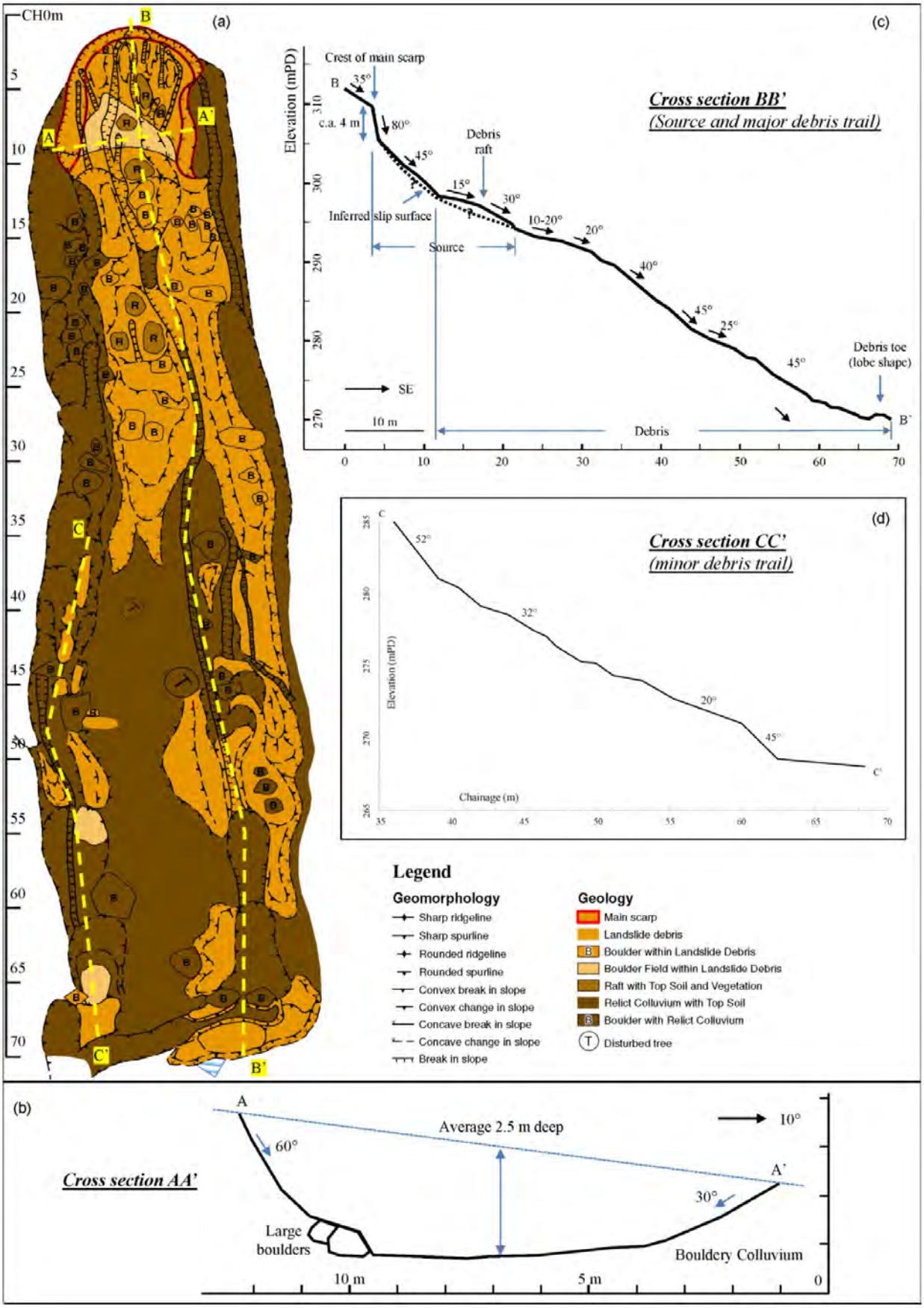

Figure 7: Field mapping of RC15. (a) mapping proforma showing the geomorphology and material of RC15; (b) cross section AA' at source area; (c) cross section BB' from crest to debris toe; (d) cross section CC' of the split debris trail.

supported and voided, probably due to post-failure erosion of finer grained materials. A thin layer of finer grained landslide debris was also present on the lower part of the surface of rupture.

2.1.4 Debris trail

Below the source area the debris trail width reduced slightly to 9 m to 10 m wide with slopes inclined at 20° to 45°. The landslide debris was thin (< 0.2 m) overlying colluvial topsoil (Figure 6e), which probably represents the top of the older, relict, landslide debris. Lobe-shaped debris deposits were present locally and up to 0.6 m thick. The estimated volume of the debris deposited in the upper 35 m long section of the trail is approximately 50 m^3.

The debris trail bifurcated at approximately 35 m distance from the main scarp (Figure 6f; Figure 7a), forming two separate trails, i.e. a major trail (Figure 7c) and a minor trail (Figure 7d). The width of the major trail reduced to approximately 5 m.

An erosion gully was present along the major trail exposing pre-existing colluvial top soil. Landslide debris within the gully was approximately 0.1 m thick. Debris levees of approximately 0.6 m thick and 0.5 m wide were present along and above the two sides of the gully (Figure 6g), indicating significant post-failure erosion, which had probably removed a significant amount of debris from this part of the trail.

The toe of the landslide debris was present at approximately 70 m distance along the major debris trail, with a lobe-shaped debris deposit resting on top of a man-made concrete platform (Figure 6h).

The minor trail followed an existing drainage depression sub-parallel to the major trail. Small amounts of debris were present sporadically along the minor trail, overlying older, relict, landslide debris (Figure 7a).

The slopes in this section varied from 10° to 52° (Figure 7c & d). The overall average slope gradient through this section was 35°. The estimated volume of debris deposited in this section is approximately 45 m^3.

2.1.6 Summary

The mapped landslide (i.e. RC15) most likely involved a debris slide in relatively thick bouldery colluvium, which transformed into a debris avalanche. The landslide debris was partially confined within an existing topographic depression, and bifurcated at 35m distance, forming two separate trails. These debris trials were confined within existing drainage depressions which have been previously affected by relict and recent landslides. Both the source area and the overall debris trail had similar widths.

According to a conventional calculation (refer to Table 1), the estimated source volume is 144 m^3. The estimated volume of the debris which was mapped along the debris trails is 95 m^3. The difference between these volumes suggests that 49 m^3 of debris (i.e. 34% of the source volume) had been removed by post-landslide erosion prior to mapping.

2.2 Photogrammetry model of RC15

2.2.1 Methodology

In order to construct a landslide 3D model, a digital method using a UAV-based Structure from Motion (SfM) photogrammetry was applied. Using this method, a high resolution point cloud and a high accuracy DEM for the study feature, i.e. RC15, were constructed. Some researchers have demonstrated that DEMs acquired via UAV-SfM technology are comparable with those acquired via Terrestrial Laser Scanning (Tsunetaka et al., 2020), and in recent years, this method has been used in some landslide studies (Fernández et al., 2017; Cahyono and Zayd, 2018). Relevant digital tools used in this study are summarised in Table 2.

Under the current study, the point cloud for RC15 was constructed using the software Agisoft Metashape Professional (Agisoft, 2020), which generated a point cloud with accurate longitude and latitude coordinates (i.e. x and y values). However, the accuracy of the z value (i.e. elevation) of each point is limited by our UAV equipment and the relevant aerial photos. Therefore, the z value must be adjusted

before calculating the landslide source volume. The adjustment of the z value in this study was carried out in ArcMap at a later stage, i.e. after point cloud data cleansing. Methods for data cleansing and z value adjustment are elaborated in the following paragraphs. It should be noted that a 3D georeferencing for all x, y and z values might be required if the Agisoft Metashape Standard version or other equivalent software is used. In this case, at least four ground control points covering the area of the study feature would be required. These can be either study-specific topographic survey points (often not available) or easily recognizable, pre-existing landmarks. For the latter method, establishing a regional model covering a larger area for georeferencing is probably needed.

Table 2: Digital tools used in this study

Digital tools	Objective / product	Notes
UAV equipped with a camera	Systematically take aerial photos for building the 3D model of the study feature RC15.	DJI Mavic Air 2 was used.
Agisoft Pro*	Produce the point cloud.	Low quality cloud was used and was sufficient for this study.
CloudCompare	Carry out point cloud data cleansing and georeferencing*.	Vegetation was removed using ERGBVEI, density and SOR.
ArcGIS	Produce DEM from the point cloud, and carry out other relevant analysis, e.g. section profiles, source volume calculation, 3D presentation etc.	Useful tools include Las to TIN, interpolate shape, raster calculator, raster to point etc.
Python	Handle large dataset calculation, particularly for testing point cloud data cleansing scalars.	Or other preferred programming language.

* Agisoft Pro version produces correct x y coordinates and incorrect z coordinate (if standard version is used, extra georeferencing of the x y values is required); adjusting z value in this study was carried out in ArcGIS.

The initial point cloud of RC15 generated by Agisoft Meashape comprises a high amount of vegetation signals (Figure 8a), which must be removed before producing the DEM (Figure 8b). In this study, the data cleansing process was carried out mainly using the software CloudCompare (2015) in the following steps. Firstly, an RGB index was calculated for all points in order to effectively classify ground features. A number of RGB-based indices have been developed by previous researchers for different purposes (Lussem et al., 2018; Wan et al., 2018; Sancho-Adamson et al., 2019). For the purpose of this study, an appropriate index was needed to effectively classify the exposed landslide scar (i.e. yellowish soil and boulders) and vegetation (greenish trees, bushes and grass). Our adopted index is the Enhanced RGB Vegetation Index (ERGBVI) introduced by Themistocleous (2019). The calculation of ERGBVI is through equation (1).

$$ERGBVI = \pi * (R_G^2 - (R_R * R_B)) / (R_G^2 + (R_R * R_B)) \quad (1)$$

where R_G = Green, R_R = Red and R_B = Blue.

The ERGBVI was then used as a scalar field in CloudCompare to filter out the vegetation. The histogram of the ERGBVI shows a bimodal pattern indicating a satisfactory result in classifying exposed ground and vegetation (Figure 8 c & d).

After applying ERGBVI index scalar filter, a substantial amount of the vegetation signals was removed. The remnant vegetation signals became evidently sparse such that they could be removed by the density scalar in CloudCompare. The final remnant vegetation signals were extremely low in amount and were removed using the Statistical Outlier Removal (SOR) tool.

The cleaned point cloud was then processed to generate a DEM of 0.1 m resolution in ArcMap (Figure 8e). The generation of this DEM underwent two steps. Firstly, due to the incorrect z value (refer to the second paragraph of this section) of the point cloud, the initial DEM generated directly from the point cloud data was bearing incorrect elevation values. Here we call it fake-DEM. In this fake-DEM, landslide crown can be easily identified based on the steep slopes of the landslide scarp. Given that the

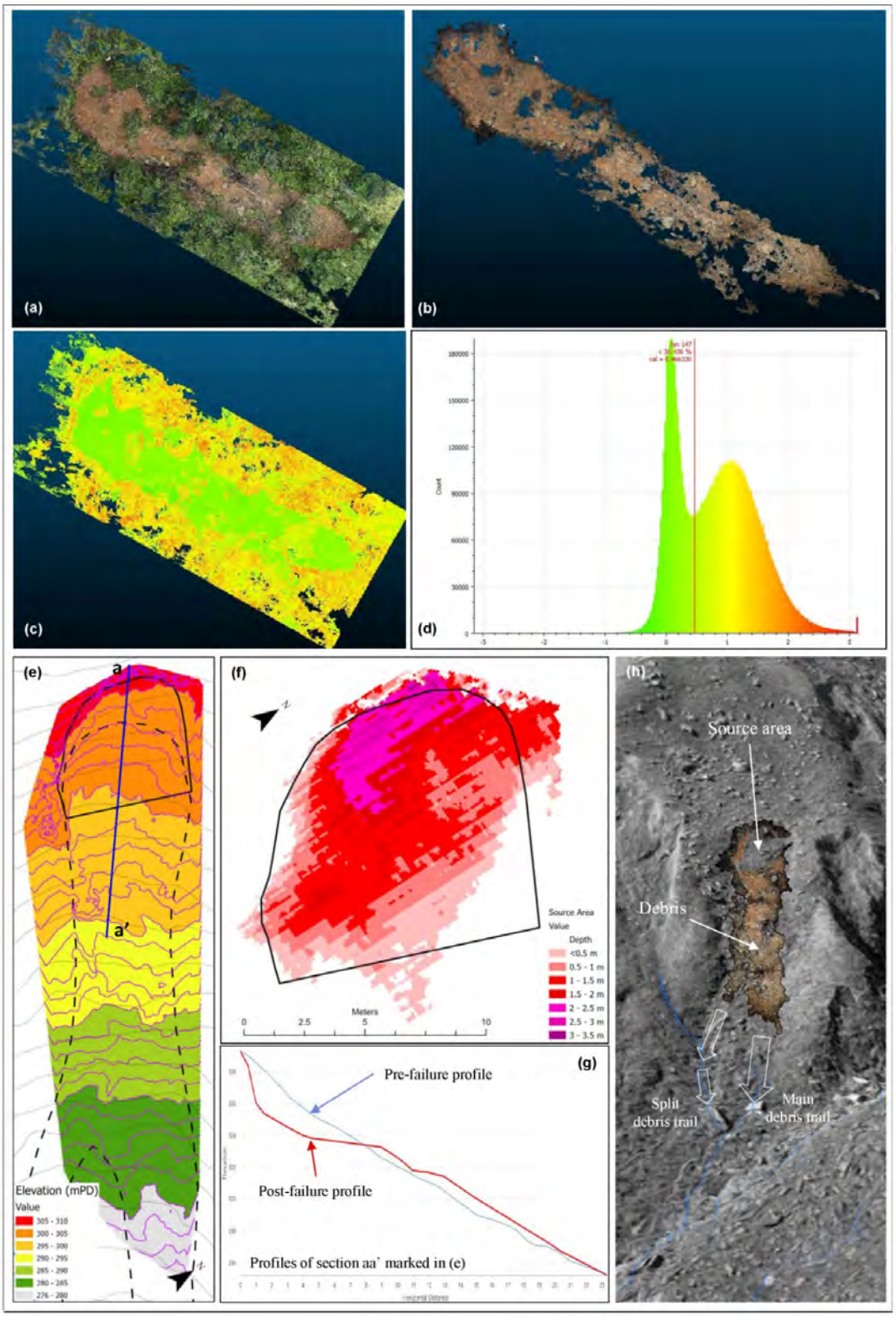

Figure 8: Photogrammetry model of RC15. (a) point cloud before data cleansing; (b) point cloud after data cleansing using firstly Enhanced RGB Vegetation Index (ERGBVI) scalar, secondly Volume Density scalar, and finally Statistical Outlier Removal tool; (c) visualisation of applying ERGBVI; (d) bimodal distribution histogram of ERGBVI showing well differentiated features (i.e. ground and vegetation); (e) DEM derived from processed point cloud showing 1 m interval post-failure contour; (f) calculation of source volume from the difference of post- and pre-failure DEMs; (g) post- and pre-failure profiles of section aa' as marked in (e); (h) 3D view of RC15 overlay 1963 aerial photograph.

elevation of the landslide crown is considered unchanged compared to the pre-failure ground profile, an adjusting parameter, z', can be derived by comparing the fake-DEM and the pre-failure ground profile (i.e. the 2010 LiDAR-derived DEM) at the landslide crown area. Each pixel of the fake-DEM was then added by z' to generate the final (i.e. the correct) DEM. In brief, these two steps used the landslide crown as the georeferencing area to adjust the z value.

The pre-failure DEM, i.e. derived from 2010 LiDAR, and the post-failure DEM, i.e. derived from the cleaned point cloud with the z value adjustment, were then used for calculating the failure volume (Figure 8f & g) and for 3D visualisation (Figure 8h).

2.2.2 Source volume of RC15

To validate the reliability of the RC15 model, two steps were taken. Firstly, 1 m interval contours were generated for RC15 using the point cloud derived DEM (Figure 8e) and the result shows the typical landslide depression contour pattern. Secondly, the RC15 model was embedded in the 2010 LiDAR-derived DEM with the 1963 aerial photo overlay (Figure 8h) with the result indicating a very close fit. After the validation, the failure volume of RC15 was calculated by comparing the pre-failure and post-failure ground profiles. The calculation process was carried out in ArcMap (Figure 8f). The source volume of RC15 calculated by this method is 115 m^3.

2.2.3 Summary

The final result shows that construction of a 3D model for the 'fresh' landslide with UAV and SfM technology is feasible and practical. The 3D model also provides more accurate scarp and debris morphology as compared to conventional field mapping. The source volume of RC15 calculated based on the pre-failure and post-failure 3D models is slightly smaller than that calculated based on field-based measurements under the conventional approach. This smaller volume is considered more reliable given that RC15 is located within an existing depression. However, this volume may have slightly underestimated the true volume given that the calculated volume was not adjusted to take account of a small amount of debris present locally on the surface of rupture.

3 CONCLUSIONS AND FUTURE USES

The case study shows that this UAV-based, digital method is a useful and practical tool to assist engineering geologists in natural terrain landslide investigations. It produces time-efficient and cost-effective spatial model for landslides, and provide more accurate data on failure scale, such as source area dimensions and failure volume. Our case study also shows that the conventional field mapping produces an engineering geological/geomorphological model to serve a discussion of the mechanism, aftermath and possible pattern of landslides. A combination of these methods is able to provide a more comprehensive portrait for landslide events.

In addition to the successful practice, we also suggest some practices for future improvement. Firstly, it is noticed that our 3D model does not cover the lower part of RC15 due to dense vegetation. Therefore, either the handheld laser scanner or the LiDAR sensor mounted on a UAV (Huang et al., 2019; Pfeiffer et al., 2019) could be used to fill this gap. Secondly, with the advent of new territory-wide LiDAR survey (2020) in Hong Kong, and the possible DEMs derived from historical aerial photographs (Deane et al., 2020), e.g. 1963 photos in Hong Kong (our unpublished data), multi-temporal terrain models could be used to detect terrain changes and to provide valued backgrounds for landslide studies.

ACKNOWLEDGEMENTS

We would like to thank Ms Yan Au Yeng in assistance of the field mapping, and Mr. Jaime Anselmo Jr. Glemao for assistance in the GIS digitization of field notes. The 2010 LiDAR survey data has been used with the consent of the Geotechnical Engineering Office of the Civil Engineering and Development Department, of the Government of the Hong Kong SAR.

REFERENCES

AAM Pty Ltd 2012. *Territory-Wide Airborne Light Detection and Ranging (LiDAR) Survey*. The Government of the Hong Kong Special Administration Region, Civil Engineering and Development Department (Contract No. GE/2008/28), 14 p.

Agisoft, L. L. C. 2020. Agisoft metashape user manual, Professional edition, Version 1.6. *Agisoft LLC, St. Petersburg, Russia, from https://www.agisoft.com/pdf/metashape-pro_1_6_en.pdf, accessed March, 2021*.

Cahyono, A. B., & Zayd, R. A. March 2018. Rapid mapping of landslide disaster using UAV-photogrammetry. In *Journal of Physics: Conference Series*. Vol. 974, No. 1, p. 012046. IOP Publishing.

CloudCompare 2015. CloudCompare User Manual Version 2.6.1. *From http://www.cloudcompare.org/doc/ qCC/ CloudCompare%20v2.6.1%20-%20User%20manual.pdf, accessed March, 2021*.

De Reu, J., Bourgeois, J., Bats, M., Zwertvaegher, A., Gelorini, V., De Smedt, P., Chu, W., Antrop, M., De Maeyer, P., Finke, P. and Van Meirvenne, M. 2013. Application of the topographic position index to heterogeneous landscapes. *Geomorphology,* 186, pp.39-49.

Deane, E., Macciotta, R., Hendry, M., Gräpel, C., & Skirrow, R. September 2020. Historical aerial photographs and digital photogrammetry techniques to investigate the development and evolution of the Chin Coulee landslide in Alberta. In *GeoVirtual 2020*.

Fernández, T., Pérez, J. L., Colomo, C., Cardenal, J., Delgado, J., Palenzuela, J. A., Irigaray, C. & Chacón, J. 2017. Assessment of the evolution of a landslide using digital photogrammetry and LiDAR techniques in the Alpujarras region (Granada, southeastern Spain). *Geosciences, 7*(2), 32.

Geotechnical Engineering Office (GEO) 2000. *The Pre-Quaternary Geology of Hong Kong*. Geotechnical Engineering Office, Civil Engineering and Development Department, Hong Kong Government.

Geotechnical Engineering Office (GEO) 2012. *1:20,000-scale Solid & Superficial Geology. Sheet 11, Edition II, Hong Kong and Kowloon*. Geotechnical Engineering Office. Civil Engineering and Development Department, Hong Kong Government.

Hung, C. L. J., Tseng, C. W., Huang, M. J., Tseng, C. M., & Chang, K. J. 2019. Multi-Temporal High-Resolution Landslide Monitoring Based on Uas Photogrammetry and Uas LIDAR Geoinformation. *International Archives of the Photogrammetry, Remote Sensing and Spatial Information Sciences, 42*(3/W8).

International Association of Engineering Geology (IAEG) Commission on Landslides 1990. Suggested Nomenclature for Landslides. *Bulletin of the International Association of Engineering Geology,* No. 41, pp. 13-16.

Jenness, J. 2006. *Topographic Position Index extension for ArcView 3.x, v.1.2*. Jenness Enterprises.

Lussem, U., Bolten, A., Gnyp, M. L., Jasper, J., & Bareth, G. 2018. Evaluation of RGB-based vegetation indices from UAV imagery to estimate forage yield in grassland. *Int. Arch. Photogramm. Remote Sens. Spatial Inf. Sci, 42*(3), 1215-1219.

OpenStreetMap (OSM) contributors 2015. *Retrieved from https://planet.openstreetmap.org.*

Pfeiffer, J., Zieher, T., Rutzinger, M., Bremer, M., & Wichmann, V. 2019. Comparison and time-series analysis of landslide displacement mapped by airborne, terrestrial and unmanned aerial vehicle based platforms. *ISPRS Annals of the Photogrammetry, Remote Sensing and Spatial Information Sciences.* Vol. IV-2/W5.

Sancho-Adamson, M., Trillas, M. I., Bort, J., Fernandez-Gallego, J. A., & Romanyà, J. 2019. Use of RGB vegetation indexes in assessing early effects of Verticillium wilt of olive in asymptomatic plants in high and low fertility scenarios. *Remote Sensing, 11*(6), 607.

Themistocleous, K. June 2019. DEM modeling using RGB-based vegetation indices from UAV images. In *Seventh International Conference on Remote Sensing and Geoinformation of the Environment (RSCy2019)* (Vol. 11174, p. 111741J). International Society for Optics and Photonics.

Tsunetaka, H., Hotta, N., Hayakawa, Y. S., & Imaizumi, F. 2020. Spatial accuracy assessment of unmanned aerial vehicle-based structures from motion multi-view stereo photogrammetry for geomorphic observations in initiation zones of debris flows, Ohya landslide, Japan. *Progress in Earth and Planetary Science, 7,* 1-14.

Wan, L., Li, Y., Cen, H., Zhu, J., Yin, W., Wu, W., Zhu, H., Sun, D., Zhou, W. & He, Y. 2018. Combining UAV-based vegetation indices and image classification to estimate flower number in oilseed rape. *Remote Sensing, 10*(9), 1484.

Application of BIM in Deep Excavation Projects

H.C. Hung, Y.Y. Liu, J.F. Chang, C.R. Chou
Moh and Associates, Inc., Taipei

ABSTRACT

This paper presents a Taipei MRT project as an example to illustrate the process and benefit of using BIM in a deep excavation case. The BIM concepts that are being used in this project include, (1) transforming and integrating soil boring information and soil profiles data into a comprehensive 3D models, (2) establishing 3D BIM for excavation and its strutting system, (3) detecting conflicts between interfaces, such as support and hoist systems, and creating a 4D construction simulation model by integrating construction schedule into the original 3D BIM model, and (4) creating and displaying the structure model, design and construction drawings, and quantity calculation sheets with the support of other compatible software. BIM is expected to bring a more direct and visual display and presentation of information for construction progress, and to make construction control and management simpler and more efficient. The project in the paper could be a reference for other geotechnical design and construction cases.

1 INTRODUCTION

The development of integrating Building Information Model (BIM) into the life cycle of construction projects has been grown rapidly in recent years. Many infrastructure projects have started to require and include BIM in the contracts for almost every stage, for example planning, basic design, detail design, construction, and operation and maintenance. In the traditional 2D design, conflicts among different professional disciplines were difficult to discover. Many errors were omitted even with regular meetings between each party. With the introduction of BIM, and its 3D object model and database, it becomes possible to detect conflicts in a 3D model and to simulate construction sequence in a 4D scheme. Its application has been widespread from building, pipeline, drainage/sewage, land development, structure, bridge, mechanical and electrical projects, to geotechnical engineering. There is also an array of commercial software that has been developed to support BIM platform and make integration of analyses and database possible. The visualized presentation of 3D BIM model, along with its supporting software and APIs, and 4D scheduling, the use and development of BIM in engineering projects can be far beyond imagination. This paper presents a deep excavation case in a Taipei MRT project where the application of BIM in geotechnical engineering is demonstrated. The BIM concepts were implemented to (1) create 3D borehole model and fence diagram to present soil layers in a 3D environment, (2) build 3D excavation and support system model, (3) detect conflicts between support system, plates, and drainage culverts, and (4) simulate construction progress with (4D). The background of the project is first overviewed followed by the BIM application. Concluding remarks are made at the end of the paper.

2 PROJECT OVERVIEW

This project is the extension of an existing MRT line, as shown in Figure 1. It begins from the working shaft of the end track of the operating red line, goes along Xin-Yi Road and Fu-De Street, then follows Zhong-Po South Road to the end-track working shaft in Yu-Cheng Park. The total length of the extension

project is about 1.42 km, which includes tracks, an underground station with cross-passage, two sections of TBM tunnels, and an end-track shaft. The net length of the underground station is about 330 m. The station, together with the ventilation shafts and exits, would be constructed using the cut-and-cover method. The two sections of the TBM tunnels include one from west end of the cross-passage to the east end of existing working shaft with an average length of about 490 m, and the other from east end of the station to the west end of end-track working shaft with an average length of about 520 m. Both tunnel sections consist of two single-tube tunnels for up- and down-track lines.

The geotechnical issues and conflicts that are encountered in the project include connection to an operating line, pipelines and culverts distributing over the designed station, TBM under passing existing buildings, and proximity of TBM tunnels (MAA, 2015b).

Furthermore, since most of the Taipei MRT network within the central downtown area is already completed, the project is the one that was planned to extend to the edge of the Taipei basin where rock depths vary significantly. The geological formation along the project alignment is thus rather complex and it would be quite beneficial to adopt BIM to create a visual and integrated platform for every professional discipline. The BIM model was created during the design stage (MAA, 2015a) to detail the complicate interaction between underground structure and soil layers, as shown in Figure 2.

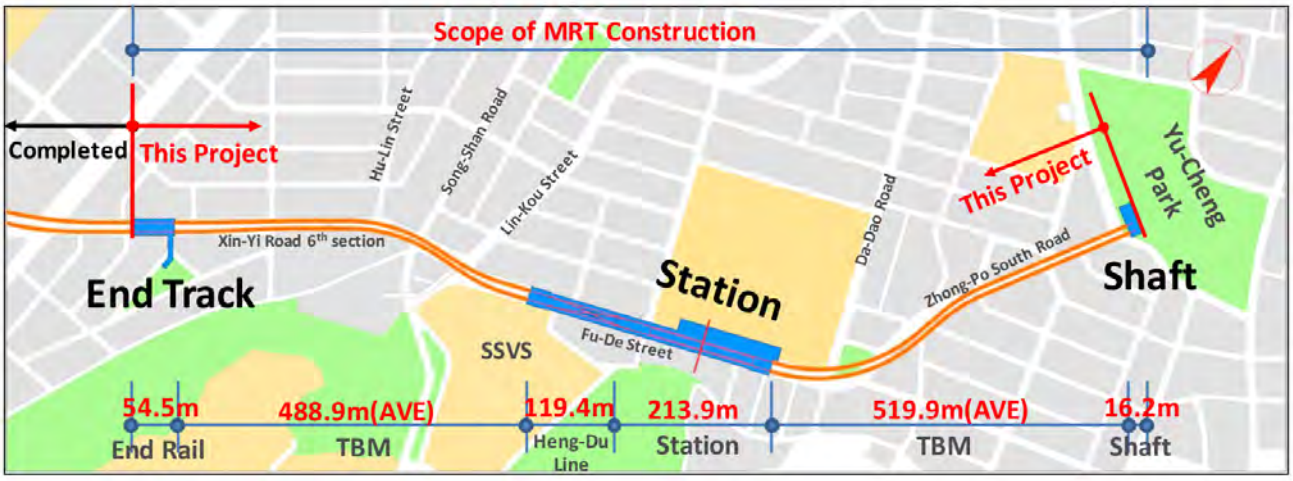

Figure 1: Project map

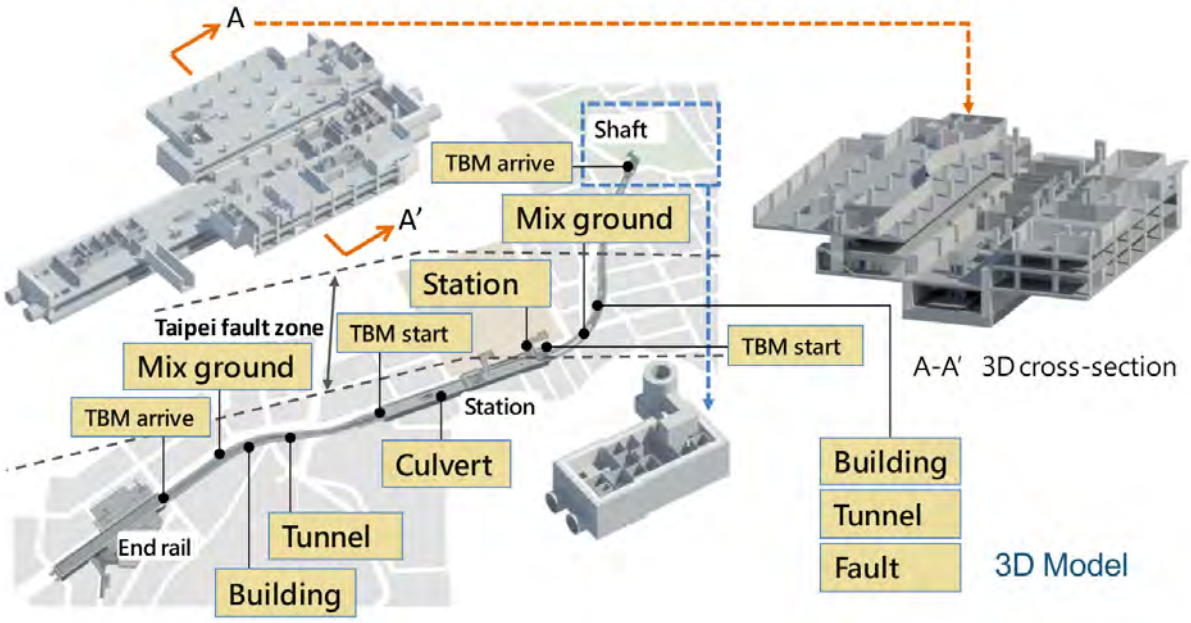

Figure 2: BIM model of the Project

2.1 Ground layer and groundwater

The project site is located on the edge of Taipei basin. The basin was formed by the collapse of several thrust faults at the foothills region in the northern Taiwan. It was formed roughly two to three million years ago during the Pliocene and Pleistocene Epoch. The geological formation of the site is mainly the Holocene alluvium, which consists of gravel, sand, and clay. The surface layer along the alignment belongs to the Song-Shan Formation, which consists of 6 interbedded clayey and sandy soils. Its engineering properties can be referred to Chin et al., (2006).

Taipei Fault, a non-active fault classified by the Central Geological Survey, is the closest fault near the project site, as shown in Figure 3. It is a thrust fault that goes in the direction of east-south with a 70 degree dip to the south-east direction. The width of the fault is about 70 m, and about 170 m in total if its fracture zone is included (eg., Lee at el, 1999; MAA, 2013b).

The project is in Xin-Yi District. According to the geological analysis report of the region (MAA, 2013a), the site is consisted of mainly silty clay, sandstone, shale, and their interbedding. The project site is located at the plan region adjacent to foothills region, with Xiang Shan (Elephant Mountain) on the east. The depth of bedrock ranges from 17 m to 31 m, and the depth of the groundwater table from 1.3 m to 2.8 m. The water pressure measured is similar to the static water pressure, as shown in Figure 4.

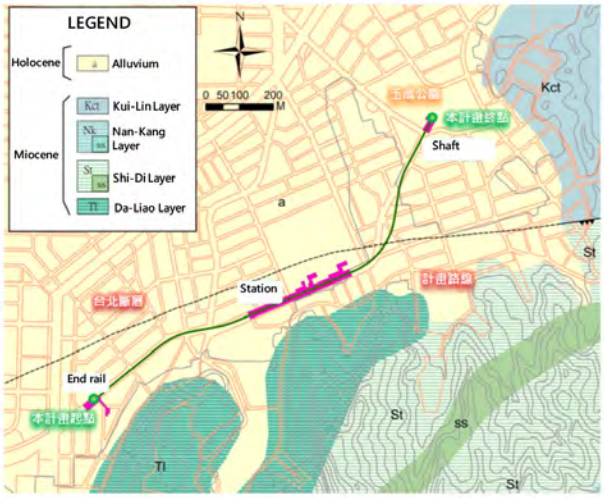

Figure 3: Geological map of project site

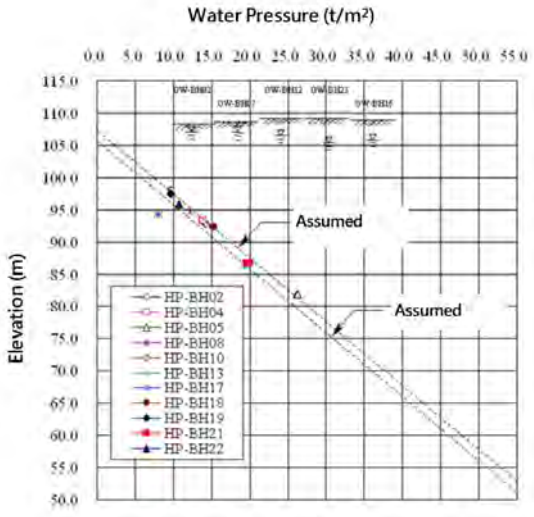

Figure 4: Water pressure plot

2.2 Deep Excavation of Station

The cut-and-cover method was employed for constructing the station where diaphragm wall (D-wall) was selected as the retaining wall that was constructed using MHL (Masago Hydraulic Long-bucket) accompanied by pilot-hole method for facilitating excavation in rock layers. After excavation of one panel trench was finished, the rebar cage was installed and concrete was then poured via tremie pipe to complete the D-wall panel. Once the D-wall work was finished, the following construction sequence included king-post installation, decking, and sequential station excavation and strutting to the designed depth.

The major issue of using cut-and-fill method was its impact to the traffic, which required a sophisticated traffic control plan that took into account of environmental limits, such as ground condition, road width, adjacent buildings, and pipeline distribution (MAA, 2015c). The contractor should select appropriate equipment accordingly to keep up with the schedule.

One of the largest issues that may be encountered at a MRT deep excavation project is conflicts with existing underground pipeline that would affect the construction layout and thus traffic control plan. However, these challenges can be mitigated by insuring good scheduling, construction quality control, and planning (MAA, 2015c; 2016).

This study chose deep excavation of the underground station in the project to demonstrate how BIM

resolved geotechnical issues involving significantly varying depths of rock layers, D-wall excavation, king-post layout, conflicts between strut system and drainage culvert, and traffic control planning. The application of BIM in geotechnical engineering included: (1) creating 3D ground layer and fence diagram from borehole data, (2) setting D-wall, king-post, and strut layout in 3D BIM model, (3) applying commercial software Revit to detect conflicts with existing drainage culverts and 4D scheduling, and (4) applying graphical programming software Dynamo to generate 3D strut system model automatically in Revit.

3 APPLICATION OF BIM IN GEOTECHNICAL ENGINEERING

3.1 3D borehole logging

Normally, borehole information is presented in plan layout and cross-section logging for geotechnical engineers to evaluate ground condition for future analysis and design. However, for projects that cover larger area, it is difficult to picture the overall geological condition. Therefore, it is preferable to use commercial software to organize and create a 3D model of the layers. The detail procedure implemented in this study is shown in Figure 5, and explained as follows.

(1) gINT data
Establish borehole database, including NE coordinates, elevation, and profile in Microsoft EXCEL files (.xls).

(2) GMS (Groundwater Modeling System) software
This software is able to read input borehole data in .xls format and create 3D ground layer model, as shown in Figure 6. Cross-section profile can be taken from the model at any chosen place as shown in Figure 7 for the selected cross-section A-A' and B-B'. The 3D fence diagram of boreholes and that along the project alignment is as shown in Figure 8 and 9, respectively.

(3) ArcGIS 3D software
Since GMS is also able to read shapefiles, a vector data type file generated by ArcGIS, the GIS software can be used to process the model, such as stratifying the model with topography map, contour, and aerial photos.

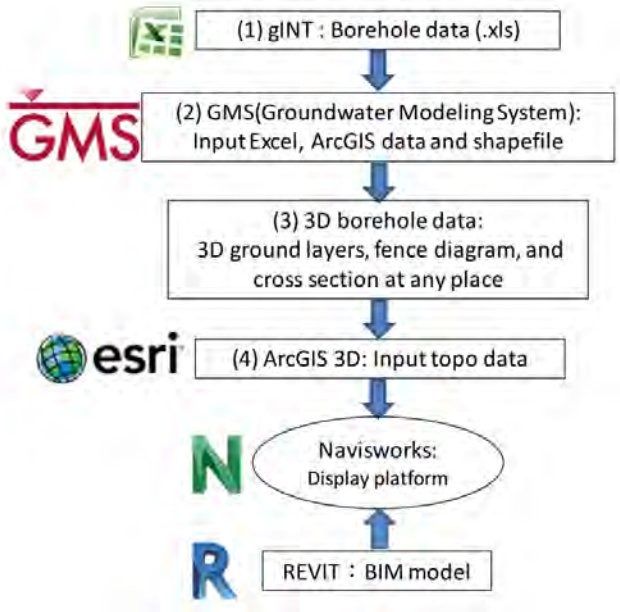

Figure 5: Flow chart for building BIM model

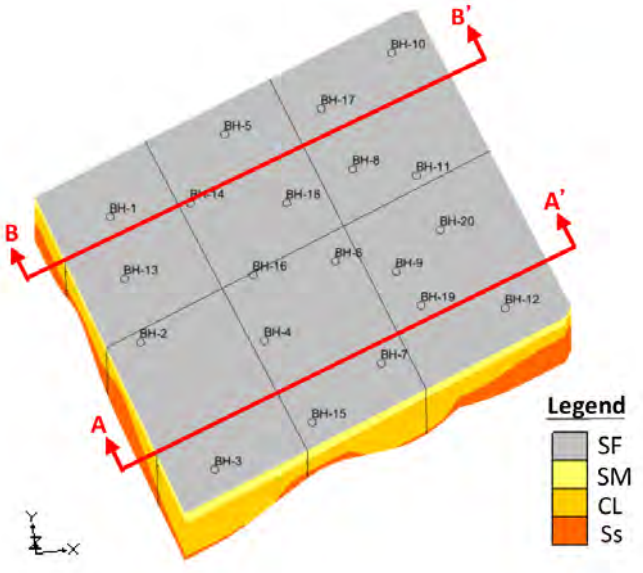

Figure 6: 3D ground layer

(4) Naviswork software
Naviswork supports a wide range of file types, which make it possible in the future for integrating and displaying models from different disciplines on one platform. However, there are still issues to be solved, such as data loss and trouble editing in the model when converting Revit files into Naviswork files.

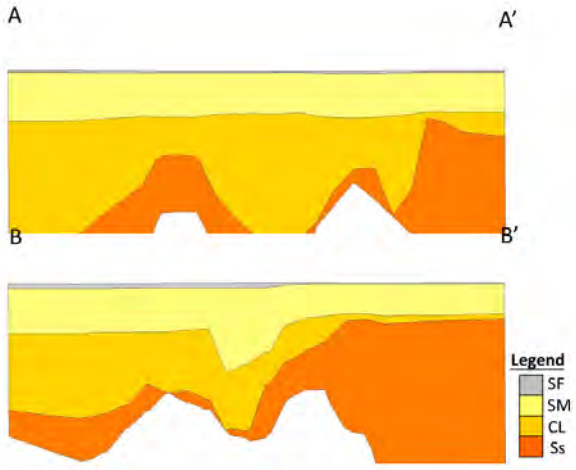

Figure 7: Profile of AA' and BB'

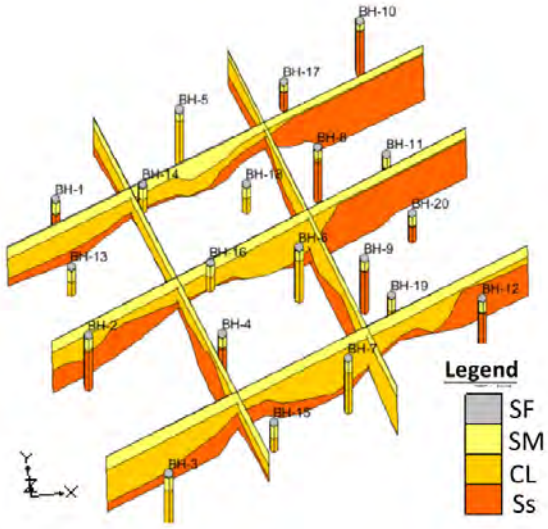

Figure 8: 3D fence diagram

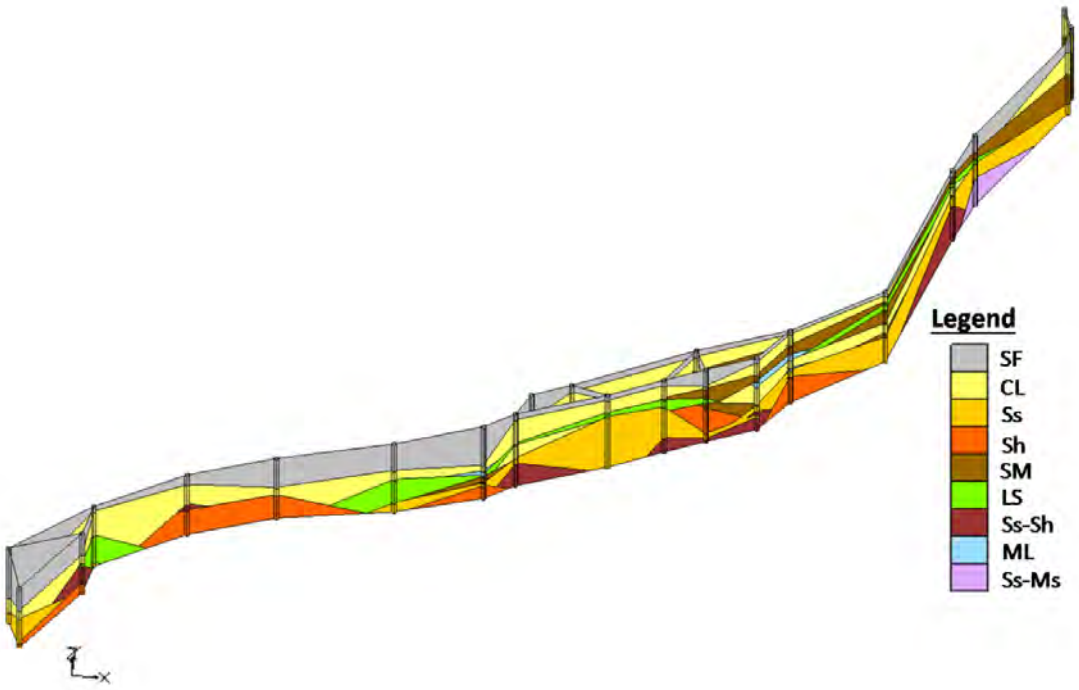

Figure 9: Strip 3D fence diagram

3.2 The 3D BIM model of strut system

Most of the strut systems in excavation works are temporary structures. Determination of king-post locations is a critical stage in design. Things to be considered during construction and determination of layout of king-post include conflicts with tracks, platform, pipelines, and other critical structures. The spacing of king-posts would further affect the spacing and size of struts, D-wall displacement, building protection measures, and monitoring plan.

This study created a 3D BIM model for deep excavation of the station. Design parameter can be extracted from the model, including length and thickness of D-wall, concrete strength, NE coordinates, size of strut and rebar, size of king-post, and etc. The BIM model is shown in Figure 10, and Figure 11 presents the in top view. Figure 12 shows the longitudinal section (ie., cross-section A-A') of the model, and Figure 13 shows the transverse section (ie., cross-section B-B') and its corresponding 3D view. In the future, the Navisworks software can be used to detect conflicts between king-posts and other structures, such as tracks and platforms. It enables each professional discipline to present their design on the same platform for discussion and coordination. However, the actual locations of pipeline are not often as shown on the shop drawings. Therefore, good construction management is still required for the quality and safety of work.

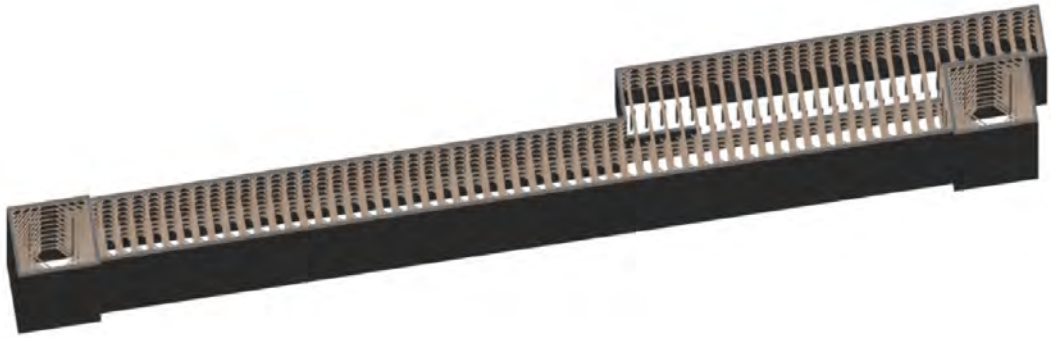

Figure 10: Strut system 3D model

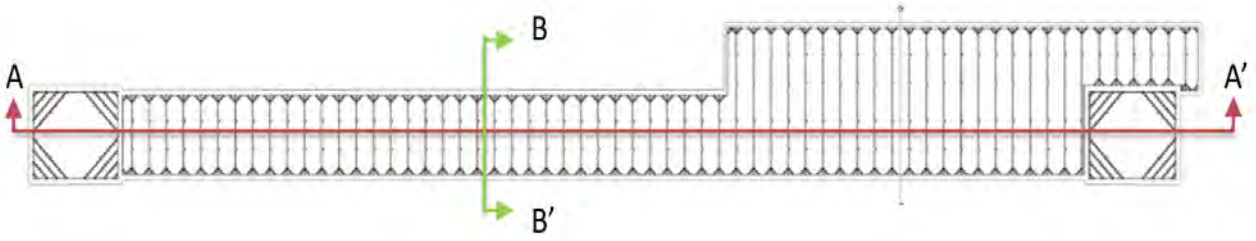

Figure 11: Strut system map

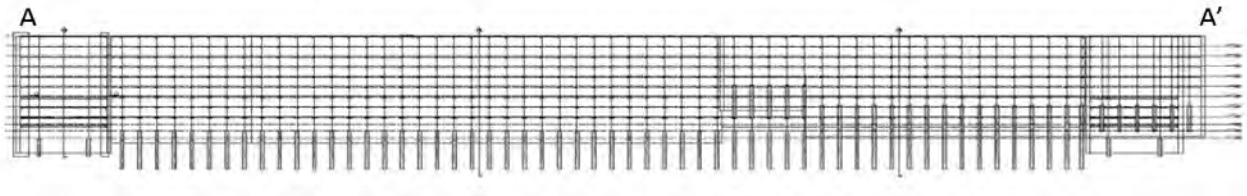

Figure 12: Strut system model A-A' profile

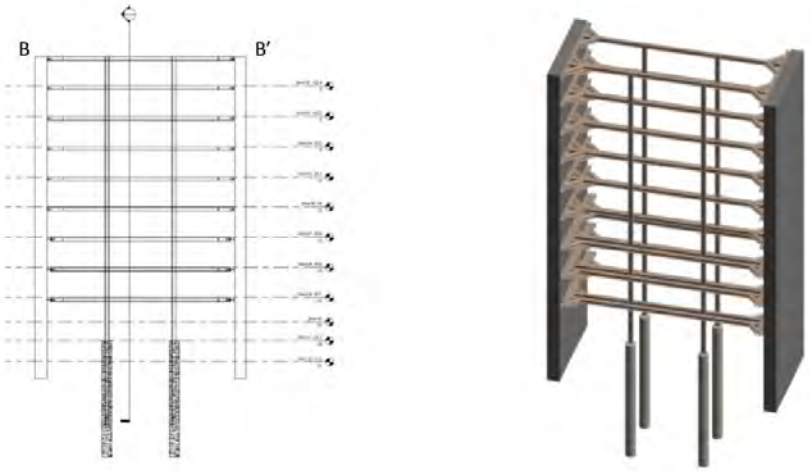

Figure 13: Strut system model B-B' profile

3.3 Conflict review and 4D scheduling

In the cut-and-cover excavation for the station, an inner strutting system was introduced. It includes horizontal support, lagging, bracket, bracing, king-post, and decking. Usually, conflicts would occur during the first stage of excavation between strut systems and existing pipelines. In order to maintain the function of these pipelines, they have to be either diverted or protected.

In this study, Revit was adopted to create the BIM model of the first-stage strut system with existing pipeline. The model is allowed to present the relative position of strut system and pipelines, and transform traditional 2D drawings into a more visualized 3D model. The BIM model creates a more convenient platform for communication among the contractor, engineers, and the client.

Once the BIM model is completed, one can employ Navisworks to simulate the construction sequence in 3D visualization and play 3D animation, as shown in Figure 14. The flow chart of producing 3D animation and 4D scheduling is shown in Figure 15. The 3D model allows users to review the locations of conflicts. The 3D simulation makes coordination easier by allowing engineers to prepare and present conflicts or issues to be discussed beforehand and make an interdisciplinary meeting run more effectively.

As shown in Figure 16, with the TimeLiner function in Navisworks, scheduling information can be integrated into the BIM model to create a 4D construction simulation.

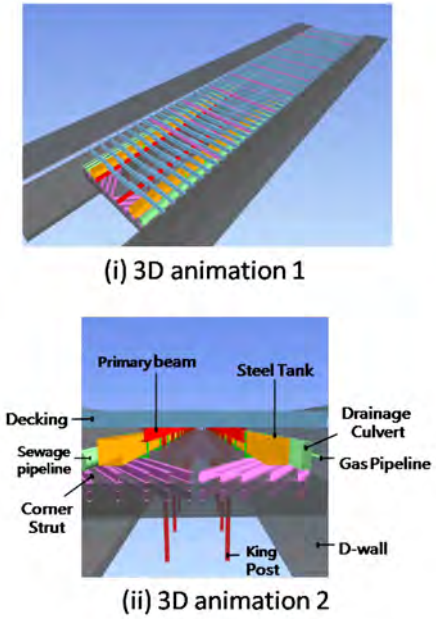

Figure 14: 3D animation

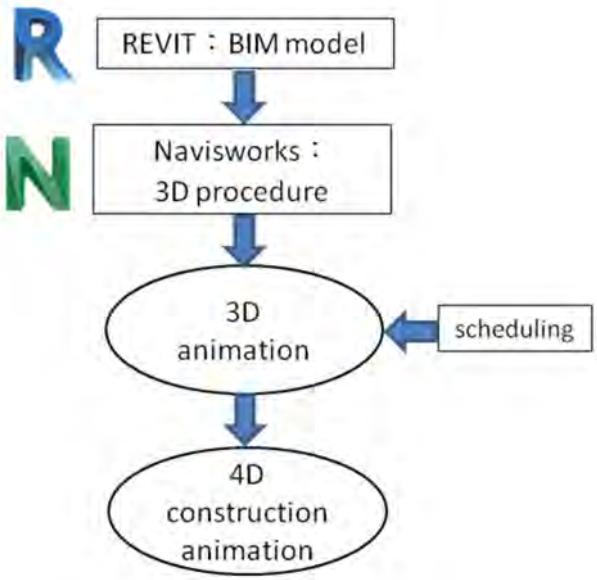

Figure 15: Flow chart for creating 3D animation

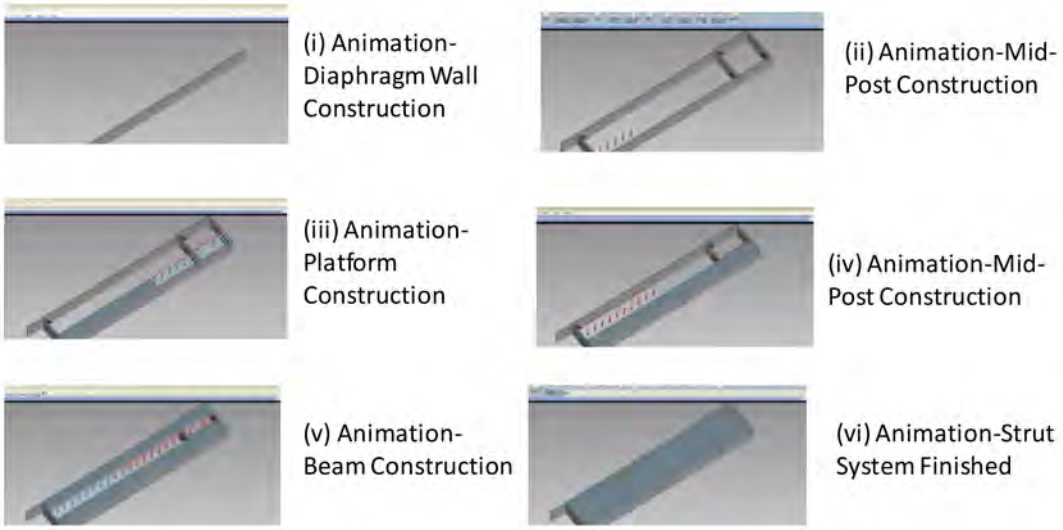

Figure 16: Construction 4D simulation of strut system

As for the strut system of the cut-and-cover sections, this study tried to use BIM model to perform 4D simulation of the project, including traffic control issues. The construction procedures are (a) traffic control and construction of D-wall, king-post, and strut system for the south of the road, (b) traffic control and construction of D-wall, king-post, and strut system for the north of the road, and (c) regular traffic control and construction of working platform.

3.4 Application of Revit and Dynamo software

BIM models are often subjected to change during planning and design stages where requirement and thus design are updated. Usually any changes to the model would involve modification of extensive amount of model elements, and mistakes are prone to happen. Dynamo, an easy-to-use and visualized programming tool, backed by many researches and studies, has been adopted to create BIM models. It allows users to automatically generate BIM models and perform analyses.

This study used Dynamo to create BIM model of strut systems, and produced drawings and quantity calculation sheets automatically. The strut system was designed and calculated, and organized in an Excel format. Dynamo was then employed to automatically generate BIM model by reading design data from the Excel file. The procedure is shown in Figure 17.

Dynamo is able to perform the repetitive task of creating 3D horizontal strut, waling, and corner bracing models automatically in Revit. Therefore, one could edit the model by merely adjusting the design parameters in Excel and rerun the program. The automatically generated model using Dynamo is shown in Figure 18.

This program is also able to perform data analyses and deliver selected information and list of requested element quantities in BIM model, as shown in Figure 19. Furthermore, design drawings could be generated from BIM model, as shown in Figure 20.

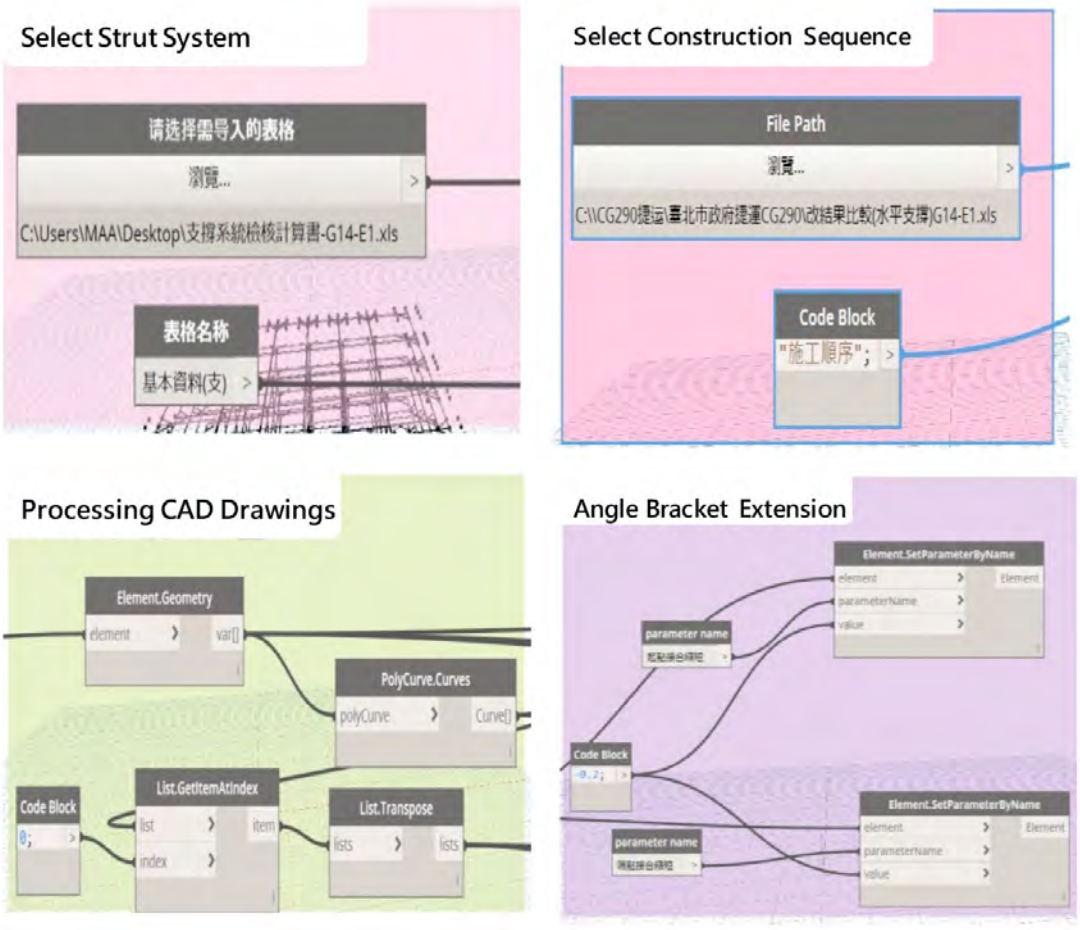

Figure 17: Dynamo programming procedure

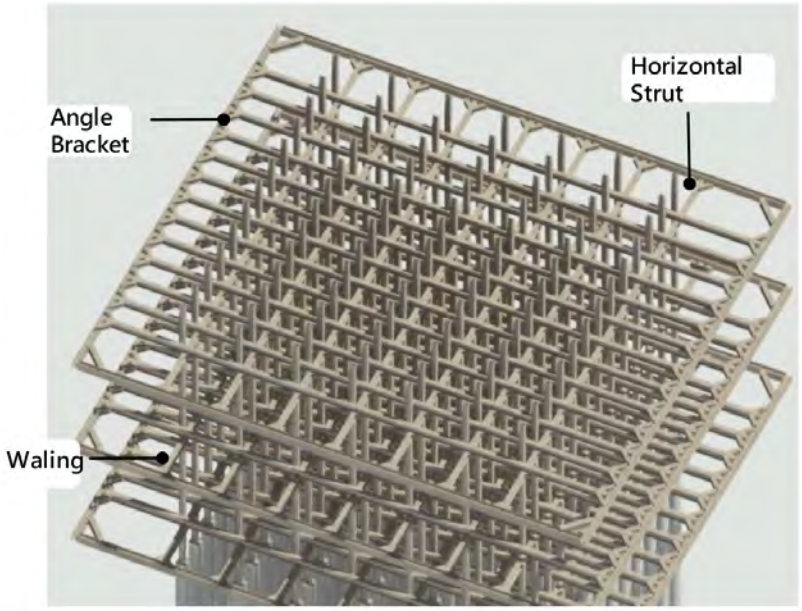

Figure 18: Model generated by Dynamo

Material List

A	B	C	D	E	F	G
Rotation	Types	Quantity	Material	Length	Unit Weight	Total Weight
0.00°	MAA大地部H型钢		金屬 - 鋼 43-27	1.1313	94.00 kgf/m	1.04 kN
0.00°	MAA大地部H型钢		金屬 - 鋼 43-27	1.1313	94.00 kgf/m	1.04 kN
0.00°	MAA大地部H型钢		金屬 - 鋼 43-27	1.1313	94.00 kgf/m	1.04 kN
0.00°	MAA大地部H型钢		金屬 - 鋼 43-27	1.1313	94.00 kgf/m	1.04 kN
0.00°	MAA大地部H型钢		金屬 - 鋼 43-27	1.1313	94.00 kgf/m	1.04 kN
0.00°	MAA大地部H型钢		金屬 - 鋼 43-27	1.1313	94.00 kgf/m	1.04 kN
0.00°	MAA大地部H型钢		金屬 - 鋼 43-27	1.1313	94.00 kgf/m	1.04 kN
0.00°	MAA大地部H型钢		金屬 - 鋼 43-27	1.1313	94.00 kgf/m	1.04 kN
0.00°	MAA大地部H型钢		金屬 - 鋼 43-27	1.1313	94.00 kgf/m	1.04 kN
0.00°	MAA大地部H型钢		金屬 - 鋼 43-27	1.1313	94.00 kgf/m	1.04 kN

Figure 19: Material quantity list

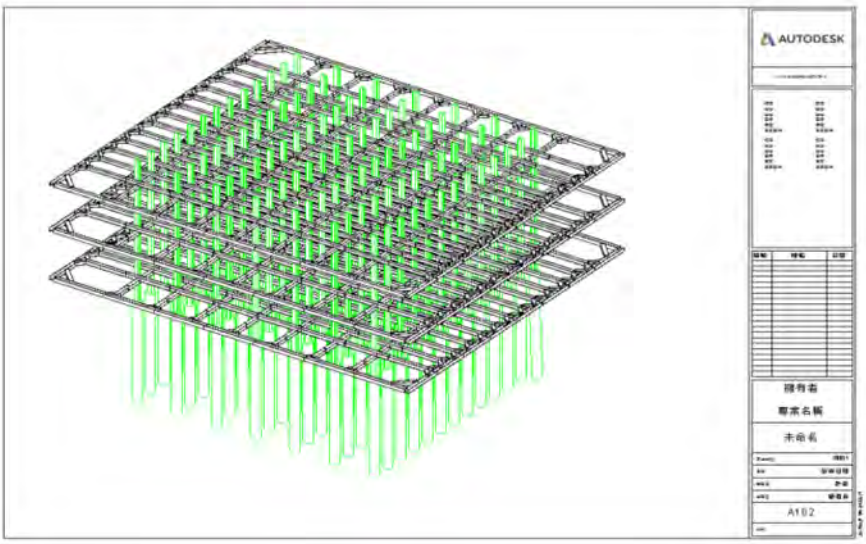

Figure 20: Design drawing generate by Dynamo

4 CONCLUDING REMARKS

Through combination of commercial software package, one is able to organize data, exchange files, produce quantity list, and detect 3D models via an integrated environment. The concept of 3D design has since been planted in construction and civil engineering industry, and may just change how designs are done in the future. As more and more BIM models are required by contracts in various construction projects, engineers are to equip with multiple new skill sets. This study introduces the application of BIM in geotechnical engineering, including (1) transform 2D boring log into 3D soil layer model, (2) create 3D model of excavation strut systems, (3) detect conflicts between strut systems and existing pipelines, and 4D scheduling, and (4) apply Dynamo to build BIM models automatically.

The early investment in developing BIM, including purchasing software, and enhancing engineers' programming skill, is significant. However, in the long term it can provide a convenient platform for discussion between various professional disciplines and reduce design and construction errors and possible penalties. In the future, it is expected that BIM is able to bring a more visualized 3D, and direct way into design, management, and construction supervision.

ACKNOWLEDGEMENTS

Permission for publishing this paper from Department of Taipei Rapid Transit Systems of Taipei City Government and Moh and Associates, Inc. is gratefully appreciated. Special thanks to Mr. C.R. Yu, manager of Numerical Development Department of Moh and Associates, who provided technical supports, and Mr. Jason Shen and Dr. J.F. Chang who helped prepare and review the manuscript, respectively.

REFERENCES

Chin, C.T., Chen, J.R., Hu, I.C., Yao, D.T.C. and Chao, H.C. 2006, "Engineering Characteristics of Taipei Clay," Proceedings, The 2nd International Workshop on Characterisation and Engineering Properties of Natural Soils, No. 3, pp.1755-1803.

Lee, J.C., Chang, J.C., and Chen, D.S. 1999, "Investigation of the Taipei Fault – A Case Study of Construction Site in Nankang," Special Publication of the Central Geological Survey, No.11, pp. 181-205.

MAA, 2013a, "Supplemental Site Investigation Report for Taipei Metropolitan area Rapid Transit System Xin Yi Line Extension Project Design Lot DR149 and Construction Lot CR285", Report, Moh and Associates, Inc. (In Chinese).

MAA, 2013b, "Taipei Fault's Activity and Impact Analysis Report for Taipei Metropolitan area Rapid Transit System Xin Yi Line Extension Project Design Lot DR149", Report, Moh and Associates, Inc. (In Chinese).

MAA, 2015a, "Design Report for Taipei Metropolitan Area Rapid Transit System Xin Yi Line Extension Project Detail Design Lot DR149 and Construction Lot CR285", Report, Moh and Associates, Inc. (In Chinese).

MAA, 2015b, "Geotechnical Design Summary Report for Taipei Metropolitan Area Rapid Transit System Xin Yi Line Extension Project Design Lot DR149 and Construction Lot CR285", Report, Moh and Associates, Inc. (In Chinese).

MAA, 2015c, "Report of Traffic Maintenance Plan for Taipei Metropolitan Area Rapid Transit System Xin Yi Line Extension Project Design Lot DR149 and Construction Lot CR285", Report, Moh and Associates, Inc. (In Chinese).

MAA, 2016, "Supplemental Utilities Survey Report for Taipei Metropolitan Area Rapid Transit System Xin Yi Line Extension Project Design Lot DR149 and Construction Lot CR285", Report, Moh and Associates, Inc. (In Chinese).

Use of Slurry and CSM Wall for Excavation and Lateral Support Works

Kenny Hung & Leo Lee
Intrafor Hong Kong Ltd., Hong Kong

Victor Li
Victor Li & Associates Ltd., Hong Kong

ABSTRACT

Steel beams embedded in soil cement columns or soil cement panels can be used for construction of embedded walls for excavation and lateral support works. The soil cement columns can be formed using the secant pile method or deep cement mixing while soil cement panels can be constructed using cutter soil mixing (CSM). Steel beam walls formed by CSM are called the CSM wall. Another method for forming a soil cement panel is by using the method for construction of diaphragm wall and such walls are known as slurry wall. In this paper, the design concepts and construction procedures of steel beam walls are discussed. Case histories of slurry walls and CSM walls are also presented to illustrate the use of steel beam walls in supporting deep excavations in Hong Kong.

1 INTRODUCTION

The scheme of using steel sections embedded in cement stabilized soils or hardened cement slurry as embedded walls for excavation and lateral works (ELS) is commonly used outside Hong Kong. There are many different names for such types of embedded walls in the literature. In this paper, this type of embedded walls will be referred to steel beam walls. If there is no space restriction, I-beams are usually preferred to other steel sections (e.g. universal column) for construction of steel beam walls as I-beams are usually more effective in resisting bending moment per unit weight of steel.

There are different methods for forming a steel beam wall. If the steel sections are inserted in cement stabilized soils mechanically mixed insitu, the steel beam walls so constructed are sometimes called the soil-mix walls (e.g. Denies & Huybrechts, 2017). If a steel beam wall is formed by placing steel sections inside excavated panels or trenches filled up with cement slurry, it is often called a slurry wall in Hong Kong.

The materials encasing the steel beams are collectively called the soil cement, although the cement slurry for constructing a slurry wall will normally contain only a small proportion of bentonite. The term 'cement slurry' will mean fluidic cement slurry when discussing an excavated panel and hardened cement slurry when discussing a completed steel beam wall.

Soil-mix walls are formed by inserting steel sections into soil cement columns constructed using the secant pile method or deep cement mixing method (DCM). Steel sections can also be inserted into soil cement panels constructed using the technique of cutter soil mixing (CSM) to form a CSM wall. Slurry walls are generally formed using similar construction techniques for diaphragm wall (D-wall).

This paper aims to discuss the design concepts of steel beam walls and present some case studies of CSM wall and slurry wall in Hong Kong.

2 STEEL BEAM WALLS

A steel beam wall is a composite wall with steel sections encased by cement stabilized soils or cement slurry. This is similar in concept to the soldier pile wall or pipe pile wall system for ELS works. The steel sections provide the structural strength to resist the bending moment and shear force induced by soil and water pressure behind the steel beam wall during bulk excavation while the soil cement between steel sections act as the lagging wall.

In Hong Kong, tube-a-manchette (TAM) grouting is commonly provided behind a soldier pile wall or pipe pile wall to serve two functions. First, it enhances stability of the soils to prevent soil collapse before installation of the lagging wall across adjacent soldier piles. Second, it provides an impermeable barrier below the excavation level to prevent excessive seepage flow into the cofferdam and hydraulic failure of the soils. These two functions are often not fulfilled because it is difficult to produce uniform grouted soils using TAM grouting.

It is not uncommon to see collapse of soils before the lagging wall is installed in time to seal the exposed face of excavation even when the exposed vertical cut face of soils is often limited to a small area. Also, the grouted soils formed by TAM grouting may not be sufficiently uniform to provide a water-tight barrier below the excavation level for limiting the drawdown of water level outside the cofferdam during excavation.

Steel beam walls offer a much more robust system of embedded walls than soldier pile walls or pipe pile walls in reducing the risk of soil collapse during excavation and providing a reliable water-tight barrier for the cofferdam. Soil cement is a much more uniform material than soils treated by TAM grouting. The strength of soil cement can be suitably adjusted such that it is strong enough to resist the soil and water pressure without the use of lagging walls. Being a more uniform material, the soil cement in a steel beam wall is a much more reliable impermeable barrier than soils treated by TAM grouting in providing a water-tight cofferdam.

The choice of a suitable embedded wall for ELS works depends on many factors. For deep excavations with adequate space for storage and maneuvering of construction plants, the option of steel beam walls offers distinct advantages in terms of overall costs and construction programme than soldier pile walls or pipe pile walls when one takes account of the cost and time needed for installation of the lagging wall.

3 CONSTRUCTION OF STEEL BEAM WALLS

Steel beam walls can be constructed using different construction techniques as discussed below.

3.1 Secant pile construction technique

Contiguous soil cement columns can be formed using the same techniques for construction of secant piles as shown in Figure 1. The soil cement columns are first formed by mixing the soil and cement insitu using augers. If there are underground obstructions, bored piling equipment can be used for forming the soil cement columns. The steel sections are inserted into the secondary columns before the soil cement has hardened. This method of construction is generally less efficient than other techniques described below and hence less common.

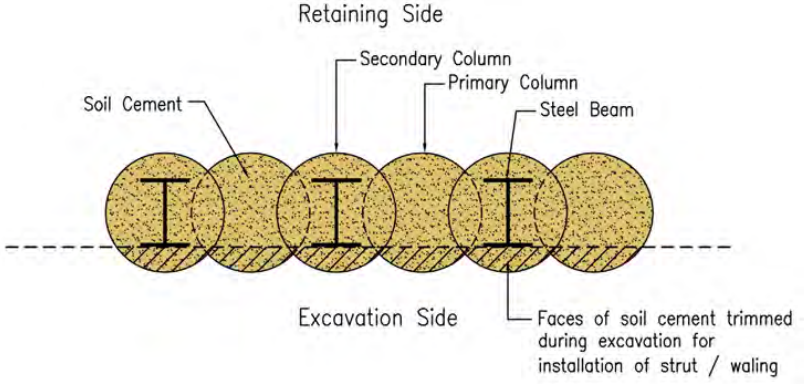

Figure 1: Steel beam columns constructed using secant pile technique

3.2 Deep cement mixing

Different techniques of DCM involving multiple auger-based or blade-based tools as described in Bruce et al (2013) can be used as an alternative means for forming contiguous soil cement columns. The method is generally more efficient than the secant pile method as two or more soil cement columns can be constructed by DCM at the same time. The technique of DCM is not suitable for soil profiles with obstructions. After the soil cement columns have been formed, the steel sections are exerted into the soil cement to form a steel beam wall. Figure 2 shows the procedures for constructing a steel beam wall using DCM. This technique is commonly used in many parts of the world including the Mainland China for constructing steel beam walls.

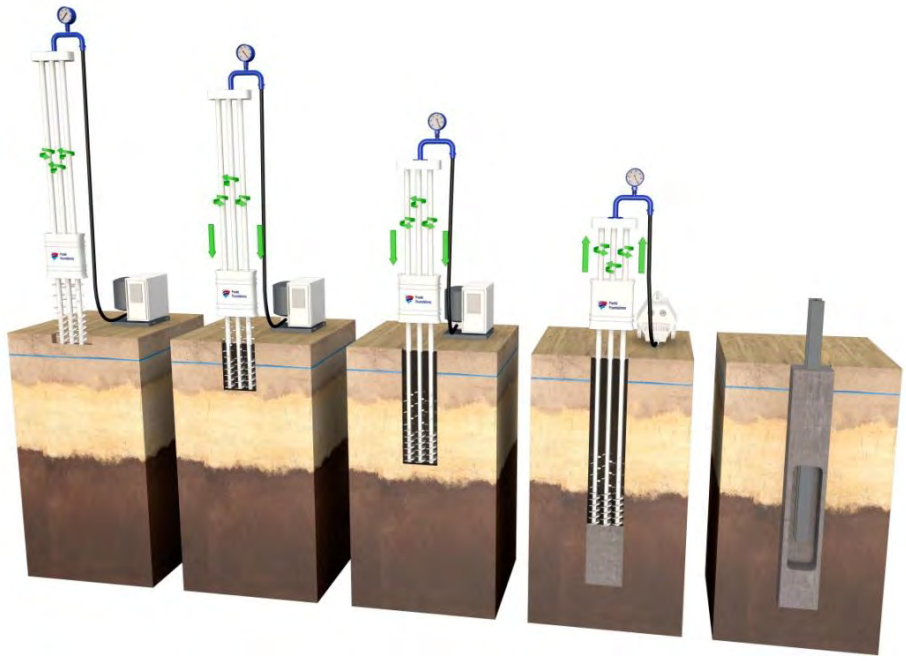

Figure 2: Steel beam wall constructed using DCM technique (Franki Foundations, 2021)

3.3 Diaphragm walling technique

A steel beam wall can also be formed using a similar technique for construction of D-wall. A panel is to be excavated using a grab or cutters to form a trench for placement of steel sections. The trench will be supported initially by bentonite slurry. When the excavated panel has reached the required depth, a cement slurry is then pumped into the trench to displace and completely replace the lighter bentonite slurry. This is called the substitution method of placement. The cement slurry will fully encase the steel section. With time, the cement slurry will harden to form a composite embedded wall.

The cement slurry can be placed into the excavated trench before or after insertion of the steel sections depending on the contractor's preference and the design mix of cement slurry. If the design strength is high, the cement slurry will be thicker and may harden more quickly. Under this situation, it may be preferable to place the steel section before placing the cement slurry into the excavated panel.

If the steel beam wall is purely designed as an embedded wall for ELS works and not a load bearing wall, it may not be necessary to spend too much efforts to reduce the sand content of bentonite slurry in the excavated panel as long as the contractor is confident that the bentonite slurry can be displaced by the cement slurry. If the steel beam wall is designed to also perform as a load bearing wall, it is preferable to de-sand the bentonite slurry and to clear the soil debris accumulated at the base of the excavated panel before placement of cement slurry to avoid reduction in load bearing capacity due to the presence of loose soil debris at the bottom of the wall.

3.4 Cutter soil mixing

CSM can be used as an alternative to the D-wall method for forming the steel beam wall. Figure 3 shows the procedures for constructing a CSM wall. The rotating soil cutters are sunk progressively to slurrify the soils. Depending on the soil conditions, bentonite slurry may need to be fed into panel through the feeder pipe connected to the cutters to help maintain stability of the panel when cutting in sand. When the soil cutters reach the required depth, cement slurry will be fed to the rising cutters. The rotating cutters will mix the cement slurry with the slurrified soils to form a soil cement mixture. Unlike the D-wall technique, the steel section can only be inserted into the soil cement panel after it is completed. The strength of soil cement can be adjusted by varying the design mix of cement slurry and more importantly by controlling the rate of upward movement of the cutter during soil mixing.

CSM is usually more efficient and less costly than the D-wall technique because CSM is faster and consumes less cement. In addition, CSM tends to induce less settlement of adjacent ground than the D-wall method as the soil cement panel is at all time supported by disturbed soil mixture or soil cement during construction. CSM has difficulties in overcoming large stones or boulders and is hence not suitable for ground profile with large obstruction materials. Perhaps, the D-wall remains the only choice for constructing a steel beam wall when there are underground obstructions.

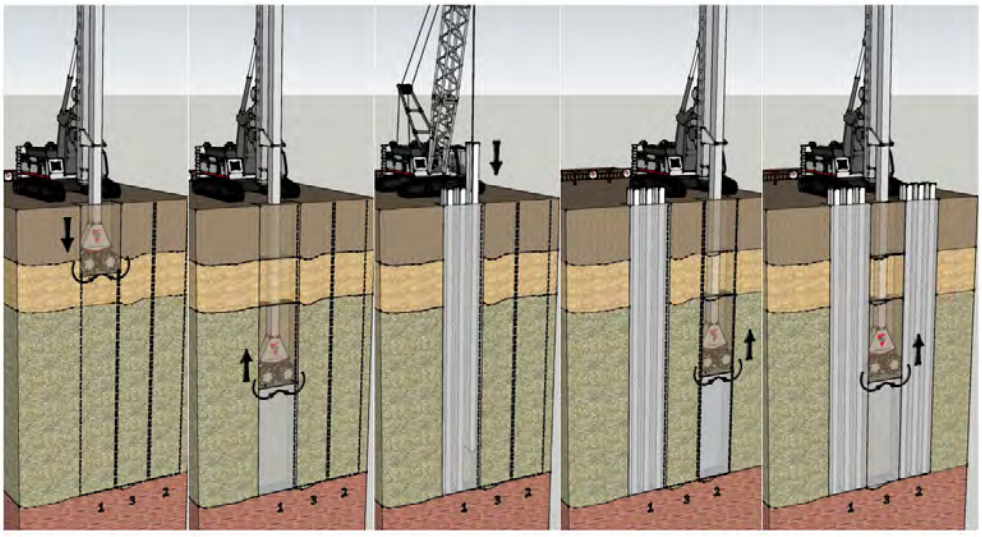

Figure 3: Steel beam wall constructed using CSM

3.5 Other details of construction

When constructing a steel beam wall using the D-wall method, a steel guiding frame is often provided to facilitate accurate placement of the steel sections at their designated positions. The guiding frame restrains and supports the steel beams before the cement slurry has hardened. Plate 1 shows an example of a guiding frame used for the project of Site A to be described later.

In the Mainland China, bituminous paint is often applied onto the surface of steel sections to reduce the interface friction to allow the steel sections to be extracted by jacking upon completion of ELS works and re-used for other purposes. If the steel beams are to be extracted later, they should be spliced by butt welding without the provision of splicing plates.

4 DESIGN ASPECTS OF STEEL BEAM WALLS

The design principles for a steel beam wall are well established in the literature. Figure 4 taken from Denies & Huybrechts (2017) depicts the load transfer mechanism of a steel beam wall. Arching effects will develop in the soil cement to withstand the soil and water pressure behind the steel beam wall. The stress arch transfers the load to the flanges of the steel section near the excavation side, and in turn to the walings/struts supporting the steel beam wall. The arching effect can also develop to a lesser extent

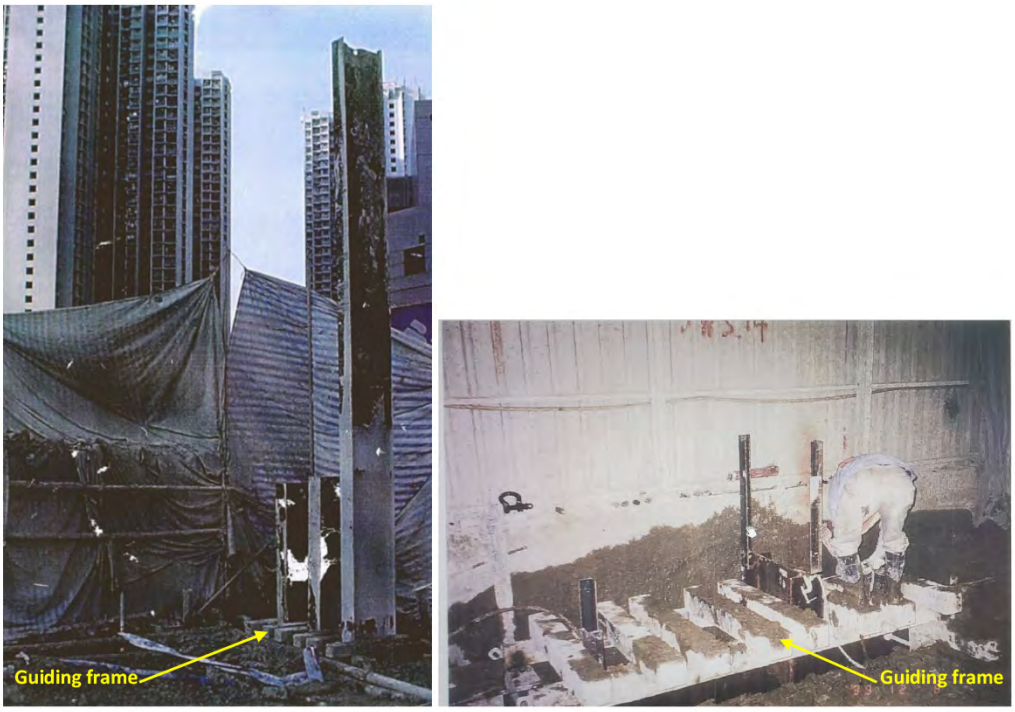

Plate 1: An example of guiding system for placement of steel section

in the soils behind the wall in helping to transfer part of the earth and water pressure directly onto the steel sections. This will reduce the soil and water loads transferred to the soil cement sandwiched between adjacent steel sections. As long as the soil cement has adequate compressive and shear strength to resist the induced stress, failure of the material will not occur and it will not be necessary to provide steel lagging walls between adjacent steel sections.

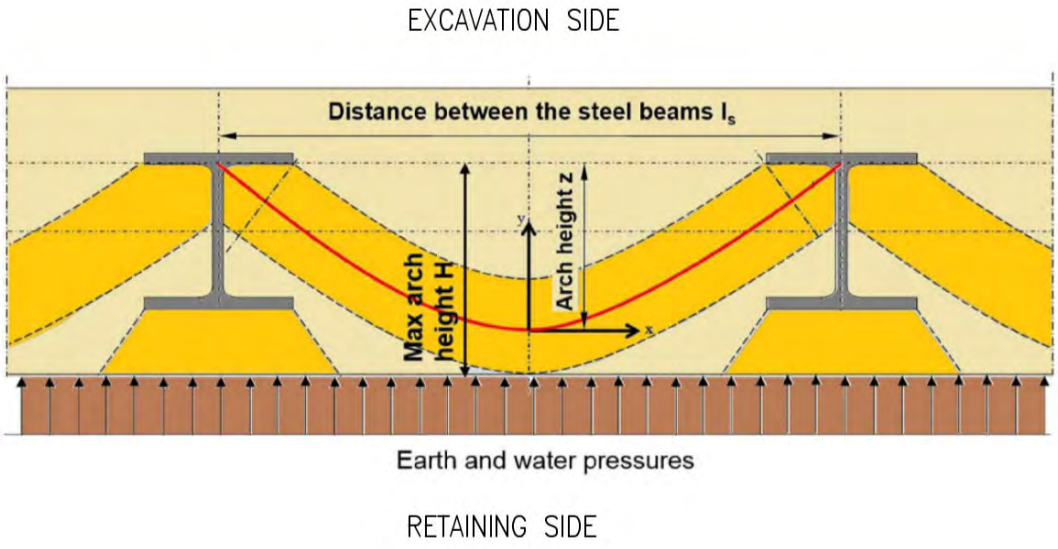

Figure 4: Load transfer mechanism of a soil cement wall (after Denies & Huybrechts, 2017)

The stability of soil cement can be easily analyzed using a geotechnical software such as Plaxis, FLAC or SIGMA/W in which the material is modelled as a geo-material with shear strength c. For a material with design unconfined compressive strength U, the design shear strength can be taken as c = U/2. If the calculated compressive and shear stress within the soil cement do not exceed their design strength, stability of the soil cement in the steel beam wall will be assured.

Structural engineers familiar with reinforced concrete design may find it uncomfortable to accept the idea that soil cement can be stable without reinforcement or lagging wall and may require a designer to justify that bending failure of the material will not occur. This may be a reasonable concern because the arching effect can only develop effectively when the spacing of steel sections is small relative to the thickness of the soil cement. As the spacing increases, a higher tensile stress will develop in the soil cement to cause failure of the material similar to bending failure. Based on a series of finite element analyses, Taki & Yang (1991) have developed a design rule as presented in Figure 5 for checking the likelihood of bending failure. If D is taken to be depth of the steel section h (i.e. D = h) and the steel sections are assumed to be placed centrally in the steel beam wall (i.e. e = 0), the criterion in Figure 5 will reduce to a simple rule that bending failure will not be a problem if the clear spacing between steel beams is less than twice the beam depth (i.e. L_2 / h < 2).

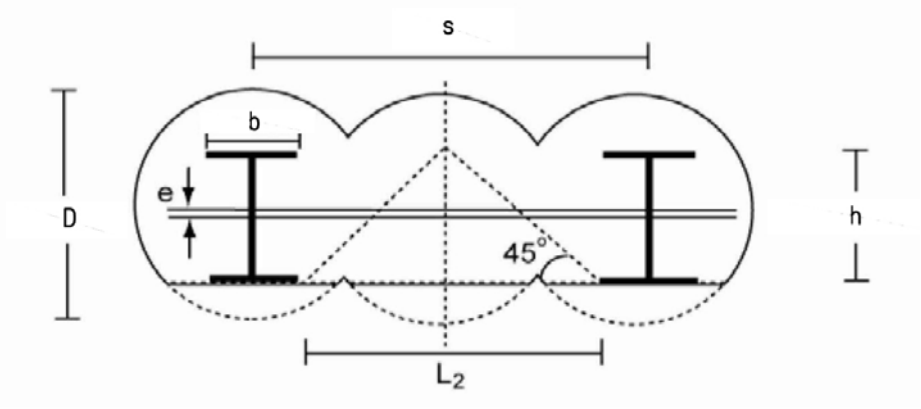

Figure 5: Structural checking of soil cement wall against bending failure (after Taki & Yang, 1991)

5 CASE HISTORIES

Three case histories are described for Site A, B and C in this section. Table 1 shows information of the clear spacing and beam depth of the steel sections for these sites. In all cases, I-beams were used with the L_2/h ratio less than 2. The criterion shown in Figure 5 was met and bending failure of the sol cement was therefore not a concern for the steel beam walls, rendering steel lagging walls unnecessary for all these projects. Figure 6 shows the layout of steel beam walls for Site A and Site B.

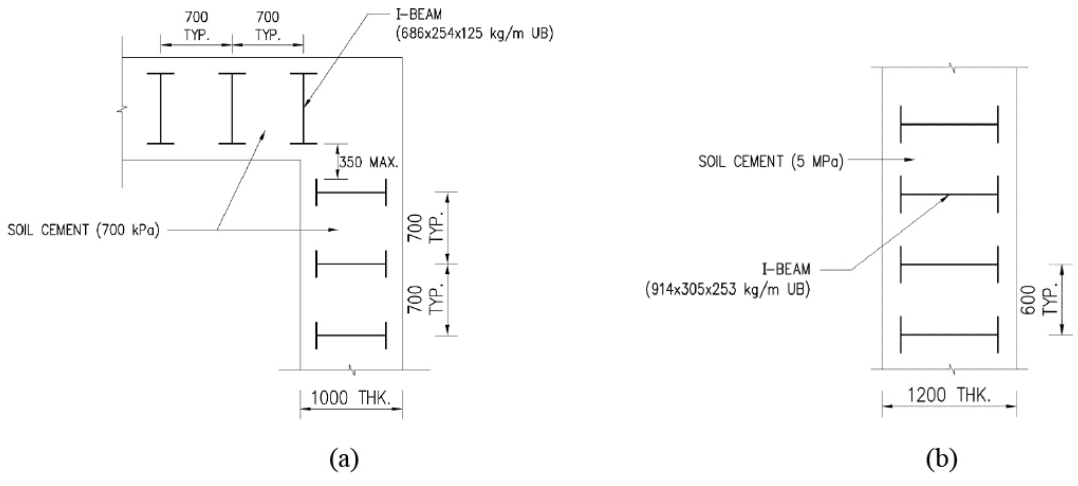

Figure 6: Layout of steel beam walls for (a) Site A and (b) Site B

Table 1: Details of steel beam walls

Site	Clear spacing between steel beams, L_2 (mm)	Beam depth, h (mm)	L_2/h ratio
A	446	686	0.65
B	295	914	0.32
C	970	914	1.06

5.1 Site A

The design of ELS works for Site A required formal approval by the Buildings Department as the ELS works formed part of the substructure works for a private project development in Tseung Kwan O, New Territories. The soil profile comprised a stratigraphy of fill, marine deposit, alluvial deposit and decomposed tuff with increasing depth. The fill comprised some rockfill which made the driving of sheetpiles difficult. The ELS works involved an excavation with a general excavation depth of about 14m. The original design scheme developed by the Engineer involved forming an excavated trench using the D-wall method and filling it up with weak plastic concrete. Lassen 6 sheetpiles were then installed by driving through the plastic concrete to form the embedded wall. The sheetpile walls were to be supported by up to 7 layers of steel struts.

The contractor considered the Engineer's design scheme difficult to implement as driving of sheetpiles through plastic concrete would be impractical if not infeasible. The contractor then proposed an alternative scheme of using a steel beam wall for the ELS works. As the fill layer comprised rockfill which might be difficult to overcome using other construction methods, it was decided to use slurry walls to replace the sheetpile walls.

The I-beams for the steel beam walls were of 686×254×125 kg/m UB placed at 0.7m spacings inside 1.0m wide panels. The guide frame used for facilitating the placement of I-beams is shown in Plate 1. The I-beams were hung onto the guide frame after placement. The hung I-beams would maintain a vertical alignment due to their own weight. After the cement slurry had hardened, a composite soil-cement wall would be formed.

The design 28-day unconfined compressive cube strength of the cement bentonite was 700 kPa, giving a design shear strength of 350 kPa. The design mix proportion for the soil cement was:

Cement	450 kg
Bentonite	20 kg
Water	878 litre
Additive (retarder)	1.5 litre

The design mix was based on results of trial mixes collected from past job references. It was predominantly a cement slurry, but with some bentonite and retarder added to improve the performance and setting time of the material. As the design strength of the soil cement for this project was not high, the cement slurry was not thick. This allowed the contractor to make the decision of using cement slurry directly for supporting the trench excavation. Once trench excavation had been completed, I-beams could be immediately placed into the cement slurry to complete the construction of steel beam walls without the need of using the substitution method to replace the bentonite slurry. For this project, trench excavation and placement of I-beams for each panel could all be completed within the same day resulting in a very efficient operation for construction of the slurry walls.

Plate 2 shows a photograph of the soil cement wall during excavation and Plate 3 a close-up view of the excavated face of soil cement. The soil cement was soft enough to be excavated easily by a backhoe but strong enough to resist the soil and water pressure behind the wall without the need of steel lagging wall.

Quality control of the soil cement was implemented by testing of cube samples prepared in a similar manner for quality control of concrete for private development projects. In addition, core samples were taken in top 3m of specified panels for compression test for further verification of strength parameters. Due to self-compaction under its own weight, the density of soil cement is expected to increase with

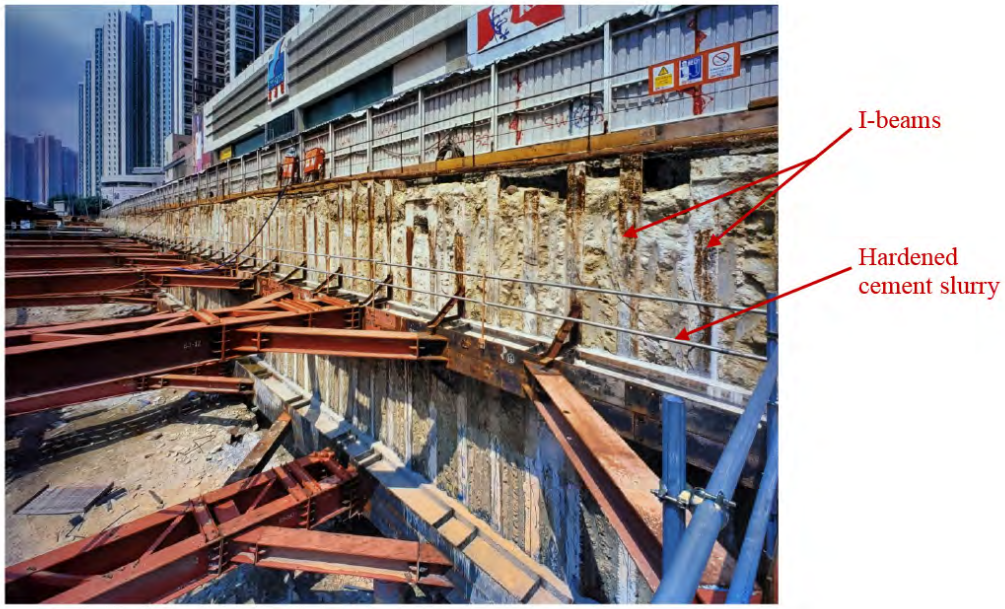

Plate 2: Photograph of soil cement wall during excavation

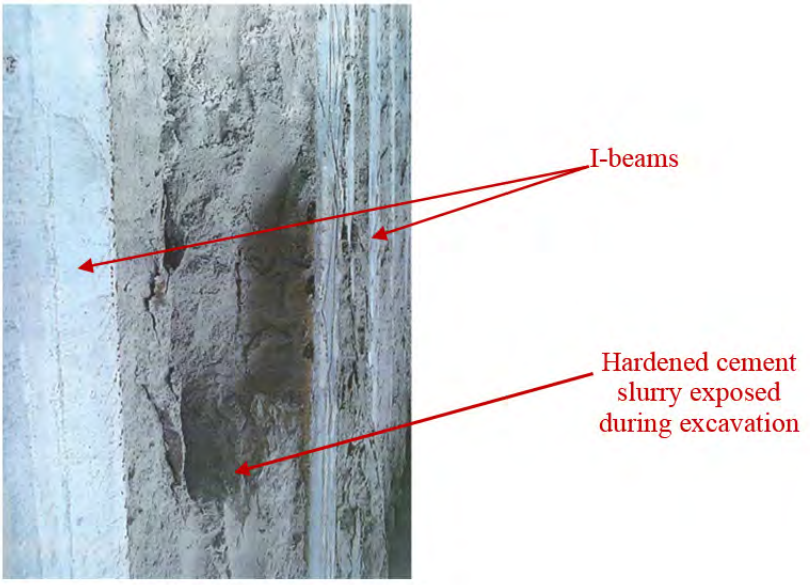

Plate 3: Exposed face of soil cement

depth. Therefore, taking the core samples within the top 3m of soil cement should give a conservative indication of the insitu strength of soil cement in the panel.

Adequacy of the soil cement was confirmed by performing analysis of a typical unit of the steel beam wall using the program SIGMA/W under the anticipated maximum applied water and earth pressure acting behind the embedded wall. The calculated maximum principal stress and shear stress were both within the design compressive and shear strength of the soil cement with a factor of safety exceeding 2.0.

The ELS works for this project were carried out over 20 years ago. Although the scheme of soil cement wall was not even something new in other parts of the world at that time, it was one of early projects if not the first project involving the use of steel beam walls in Hong Kong. It is also the first such design approved by the Buildings Department. The steel beam wall scheme had proven to be a big success for this project. With the higher stiffness and structural capacity of the I-beams than sheetpiles, it was able to reduce the struts from 7 to 3 layers. As steel lagging wall was not necessary for the ELS works, the progress of ELS works could be greatly enhanced. The soil cement had proven to be a uniform material

and impermeable during bulk excavation, providing an extremely good water-tight barrier against seepage flow across the soil cement wall throughout the entire excavation.

5.2 Site B

In Site B, a temporary slurry wall was used for construction of a cut-and-cover tunnel. The slurry wall was designed to support an excavation of over 50m deep. Figure 6(b) shows the layout of the slurry wall for this project. The wall was formed using I-beams of 914×305×253 kg/m UB placed at 0.6m spacings inside 1.2m wide excavated panels. The design compressive strength of the soil cement was 5 MPa necessary for resisting the relatively high water and soil pressure behind the slurry wall. A lower water/cement ratio as compared with Site A was required to achieve this higher design strength.

The rockhead profile for Site B was not deep below the final excavation level. Shear pins were used to enhance the stability of the slurry wall against kickout failure. The installation of shear pins was carried out by welding reservation pipes to the full length of selected I-beams during construction of the steel beam walls. When the slurry wall had been completed, drilling would be carried inside the reservation pipes to required depths in rock for installation of the shear pins. The drillholes would then be filled up by cement grout.

5.3 Site C

The third case history involved using CSM walls as temporary embedded walls for supporting a 20m deep excavation. The site was located in a reclamation formed by hydraulic sand fill which made the CSM technique most suitable for constructing the steel beam wall. The I-beams were of similar size as that of Site B. As the excavation depth is shallower for Site C, a larger spacing of the I-beams and a lower design strength of 3 MPa for the soil cement were found to be sufficient. The cement slurry used for constructing the CSM wall had a water/cement ratio of about 1.5. Again, no lagging wall was needed for Site C.

6 CONCLUSIONS

The design principles of steel beam walls are discussed. Although steel beam walls are commonly used in other parts of the world for ELS works, it is still not common in Hong Kong. It may be due to engineers in Hong Kong not familiar with this scheme of embedded wall and perhaps due to the engineers not being comfortable in accepting the fact that unreinforced soil cement can be strong enough to resist the soil and water pressure even without steel lagging walls. The main purpose of this paper is to encourage wider use of steel beam walls, particularly slurry walls and CSM walls, for ELS works by sharing the successful experiences gained from some case histories in Hong Kong.

REFERENCES

Bruce, E.C, Berg, R.R. Collin, J.G., Filz, G.M., Terashi, M. and Yang, D.S. 2013. *Federal Highway Administration Design Manual: Deep Mixing for Embankment and Foundation Support – Chapter 11. Report No. FHWA-HRT-13-036*. US Department of Transportation.

Denies, N. and Huybrechts, N. 2017. Deep mixing method for the construction of earth and water retaining walls, *RILEM Technical Letters*, Vol.2, 1-9.

Franki Foundations (2021). http://cogeco.be/Business-Units/Retaining-Walls---Utilities/Mixed-in-place-wand.aspx?lang=en-US. Accessed on 24 March 2021).

Taki, O. and Yang, D.S. 1991. Soil-cement mixed wall technique, *Geotechnical Special Publication No. 27,* ASCE, Vol.1: 298-309.

Geotechnical Design and Performance of a Jacked-in-Place Subway in the First Application of the Rectangular Tunnel Boring Machine Technology in Hong Kong

H.S. Kan
East Development Office, Civil Engineering and Development Department, HKSAR

Wilfred So
Build King – Richwell Engineering Joint Venture

K.M. Chiang & Willie Ang
Shanghai Tunnel (HK) Co., Ltd.

Davis Lee
Ove Arup & Partners Hong Kong Limited

ABSTRACT

The construction of a 140 m long subway at the Kai Tak Development was faced with aggravated constraints of urban settings – including congested utilities, lack of space, traffic concerns, proximity to structural foundations and existing facilities, etc. Combined use of the rectangular tunnel boring machine (RTBM) technology and segmental jacking techniques provided an innovative solution. This paper gives an overview of the design and construction process, the geotechnical challenges encountered and the measures to tackle them. Specifically, earth pressure balance (EPB) underlying the technology and jacking force assessment will be discussed. The successful completion of this project demonstrated the feasibility of the RTBM technology in typical geological conditions of Hong Kong, and the potential for routine applications for tunnel-type underground facilities particularly in congested urban areas.

1 INTRODUCTION

With the airport at Kai Tak relocated to Chek Lap Kok in July 1998, the vacated site constituted a good opportunity for a major re-development in the heart of Hong Kong. The resulting Kai Tak Development (KTD), more than 320 hectares in size, is being transformed into a vibrant new community. As part of the infrastructure of the KTD, a pedestrian subway SW4 is constructed to provide connectivity with the Choi Hung area.

Subway SW4 is of internal dimensions 4 m wide by 3 m high. About 140 m in length, it passes underneath several major roads as indicated in Plate 1. In particular, it has to be routed through closely-packed piled foundations of the Kwun Tong Bypass viaducts, with clearances as small as 2.7 m. Vertically, it is constrained by a number of major utilities, including in particular several water-bearing culverts and conduits on top.

A trenchless tunnelling method using, for the first time in Hong Kong, a rectangular tunnel boring machine (RTBM) was adopted for the construction. This paper focuses on the geotechnical aspects of the works. Challenges encountered during design and construction are also discussed.

Plate 1: Subway SW4

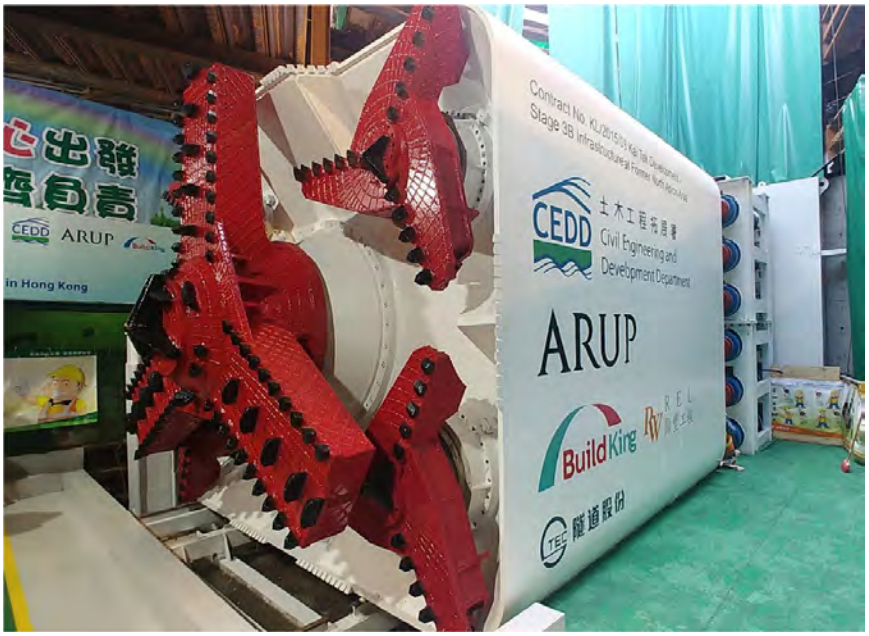

Figure 1: General view of the RTBM

2 GEOTECHNICAL DESIGN

2.1 Geology and soil properties

For evaluating the viability of the technology, additional ground investigation was conducted, comprising drillholes PS-1, PS-3 and PS-4 and inclinometers I3, I4, I5 and I6, as shown in Figure 2. The geological conditions revealed matched the previous ground investigation from drillholes DH15, DH16 to DH18 and 11521-PE-16 and 17. Generally, the site comprises fill, alluvium and completely decomposed granite (CDG), with average thicknesses of 6 m, 14 m and 33 m respectively. The tunnel alignment is located partly in fill and mostly alluvium. The ground condition was complex owing to the presence of many boulders, especially the location closely underneath the 4-cell box culvert where gravel or cobble fill material was found.

2.2 Potential underground obstructions

The presence of large underground obstructions would directly affect the viability of RTBM tunneling. Borehole investigation information alone might not be adequate as it only gave discrete geological information at certain locations. While machine was designed to cope with gravel fill material with cobbles size up to 150 mm in diameter, the potential presence of larger sized boulders, left-in structures

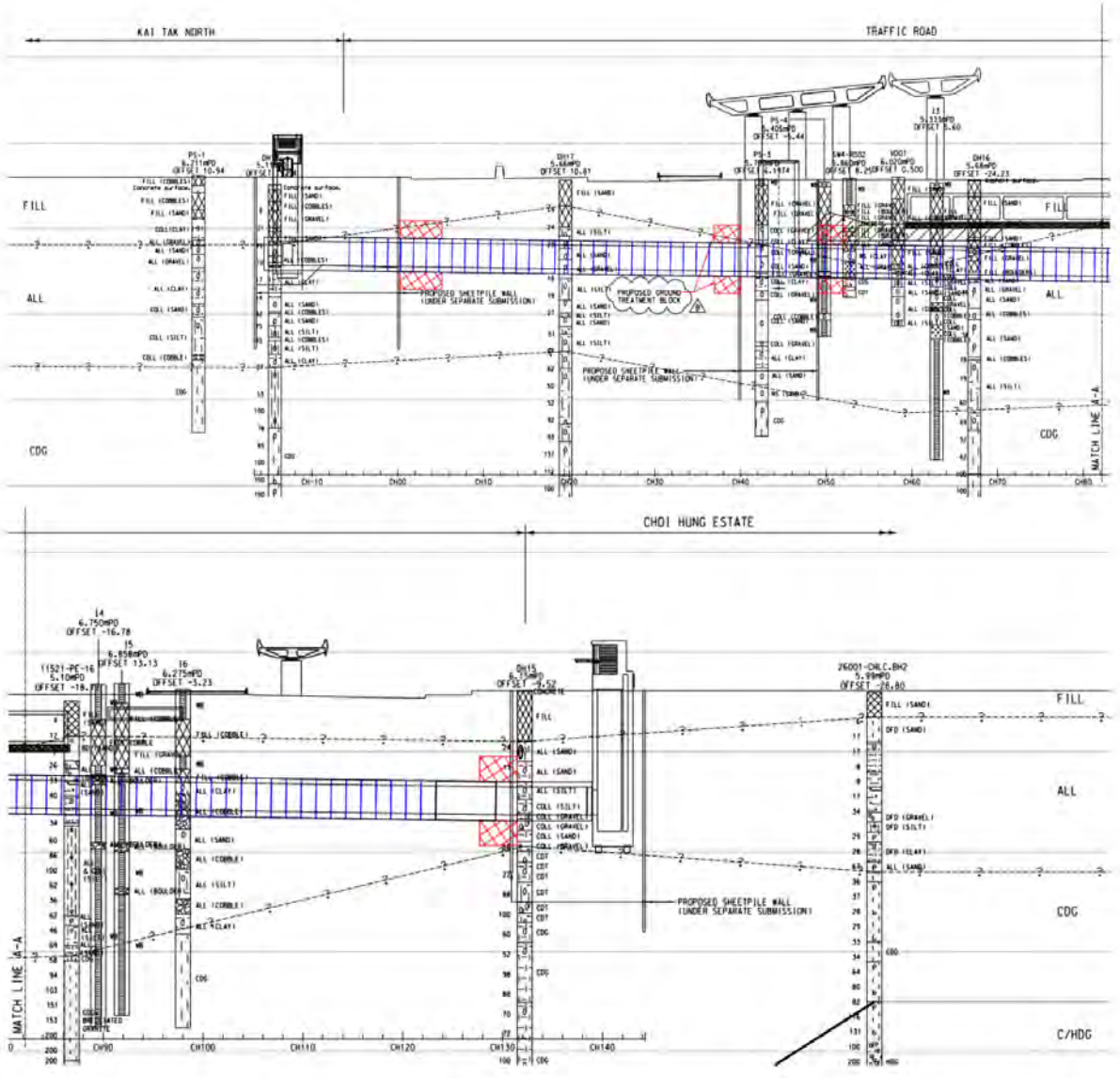

Figure 2: Geological profile interpreted from boreholes

etc, was a concern. A geophysical survey along the proposed tunnel alignment was therefore conducted, adopting the multichannel analysis of surface waves (MASW) method, which assessed the elastic condition, or stiffness, of the ground. By interpreting the velocities of surface waves, the shear wave velocity (Vs) below the surveyed area was derived, which could be related to stiffness of the ground. The result from the geophysical survey was verified by the borehole logs to determine the soil stratum distribution along the tunnel alignment. The survey revealed no major underground obstructions.

2.3 Soil properties and soil conditioning

Soil strength parameters were determined from consolidated undrained triaxial tests with pore water pressure measurement. Stiffness parameters were deduced from empirical correlation with SPT-N values.

Table 1: Design parameters for soils

Soil type	Bulk Unit Weight (kN/m^3)	Cohesion, c' (kPa)	Friction Angle, f' (degree)	Elastic Modulus, E' (kPa)
Fill	19	0	33	9000
Alluvium	19	4	33	20400
CDG	19	4	33	39895

Geological profile and soil parameters were important information for the mechanical design of the RTBM including the cutterhead and cutting tools, as well as the tunnelling operation. The choice of soil conditioners and details of conditioning were determined based on the soil parameters and assessed by on-site tests. The soil in front of the cutterhead was mixed with bentonite, water and additives to form a slurry material for RTBM excavation followed by disposal through a screw conveyer. Soil conditioning assisted in establishing a positive balance pressure and hence reduced water permeability. The conditioned soil had better flowability, plasticity and consistency. This would consequently contribute to more smooth execution and productivity of the tunnelling works.

Figure 3: Soil before and after conditioning

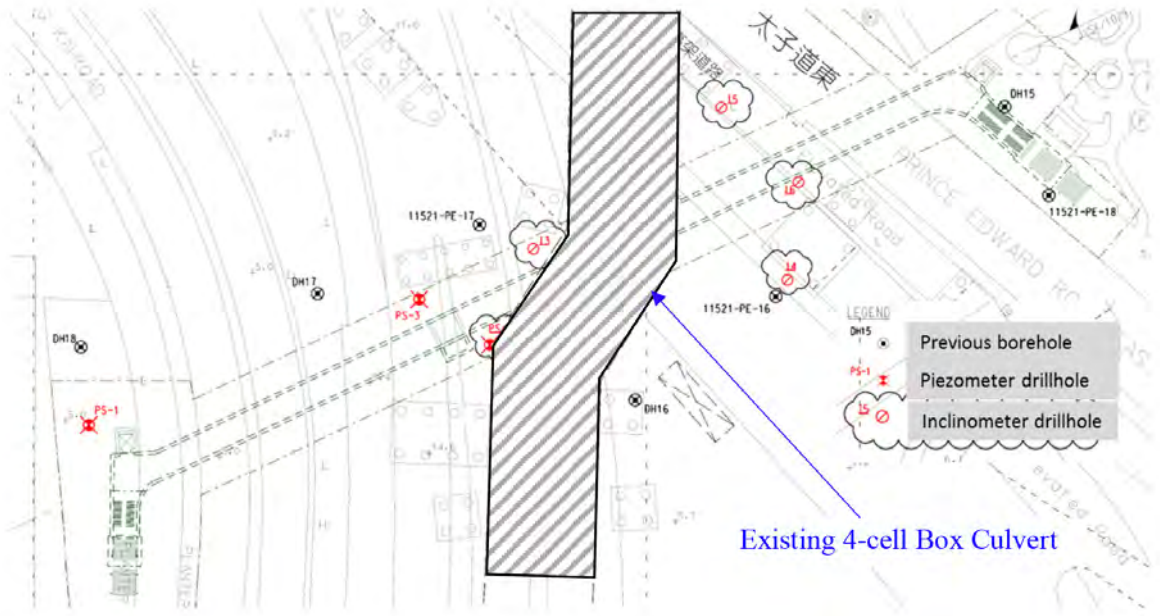

Figure 4: Locations of ground investigation boreholes

2.4 Hydrology

Groundwater monitoring has been carried out on site since June 2017, covering both wet and dry seasons. As shown in Figure 5, the highest measured groundwater level was +3.2 mPD. A design groundwater level at +3.5 mPD was adopted. It is noted this high groundwater table can pose severe risks for traditional mined tunnel construction methods involving manual underground excavation or in-situ structural construction.

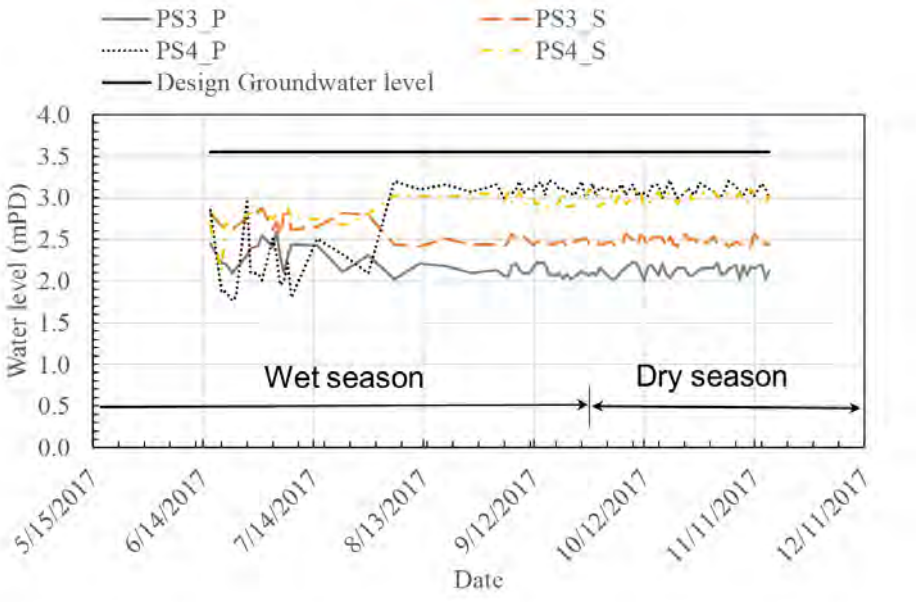

Figure 5: Groundwater monitoring records during design stage

3 DESIGN OF THE RTBM

3.1 Cutterhead and cutting tools

For soft soil ground conditions, a full-face cutting profile is preferable as this reduces over-excavation and squeezing of the soil, and therefore the impact to underground. It will also help control the face

pressure more smoothly, and both short-term and long-term settlement will be mitigated. To this end, the cutterhead design should be aimed at minimizing blind spots not covered by the cutting tools as far as possible.

In the case of Subway SW4, a large central cutting tools was adopted to cover the majority of the rectangular tunnel cross section. The rest of the area within the cutting profile is catered for by four eccentric cutting tools. The cutting profile of small cutting tools follow a rectangular path in order to reduce blind area. The overall coverage of this configuration is 92% of the face area, which is considered sufficient for the project.

Another important design aspect is ensuring that the cutting tools are strong enough to overcome the high friction and torque during tunnelling. Selected based on the project ground condition, two categories of cutting tools were utilised, namely rippers and scrapers. Rippers are of high strength and anti-wear capacity. They are used for breaking dense soil strata or hard materials such as cobbles. Scrapers mainly serve to move the excavated soil into the RTBM excavation chamber. Their cutting tracks need to fully cover the whole cutting profile to ensure the efficiency of soil collection.

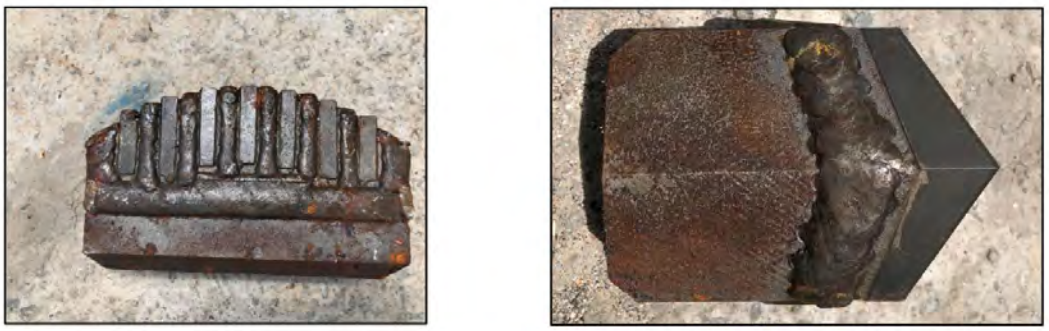

Figure 6: Rippers and Scrappers

3.2 RTBM face pressure

The RTBM used in the project worked on the earth pressure balance (EPB) principle. For operation safety, it was important to establish and maintain an appropriate face support pressure. An inadequate pressure would lead to instability with excessive ground movement or even collapse of the tunnel face. On the other hand, an excessive pressure might result in ground heave.

Tunneling in urban areas required particularly stringent control of ground movements to minimize the effect on overlying and nearby buildings, structures and utilities. Reference was made to GEO Report No. 298 in determining the design target and maximum face pressures, on the basis of the soil parameters described in section 2 above.

Maintaining the face pressure at the target value during the tunnel boring required the combined actions of adjusting the thrust force applied, the cutterhead rotation speed and direction, the excavated soil discharge rate and the injection of soil conditioners. It was a dynamic process and varied with geological conditions and site conditions being encountered. Making reference to past projects and the site specific geological characteristics, the project team established a set of control parameters for the RTBM operation.

3.3 Ground improvement for RTBM break-in and break-out

Along the RTBM tunnel alignment there were three shafts – a launching shaft, an intermediate ventilation shaft, and a receiving shaft. At the RTBM break-in and break-out locations, vertical openings had to be made in the shafts. To ensure ground stability, ground improvement works were designed and undertaken. Stability analyses using the SLOPE/W software was carried out for designing the grouting extent and grout strength. The design grout uniaxial compressive strength (UCS) strength adopted for this project was 1.0 MPa.

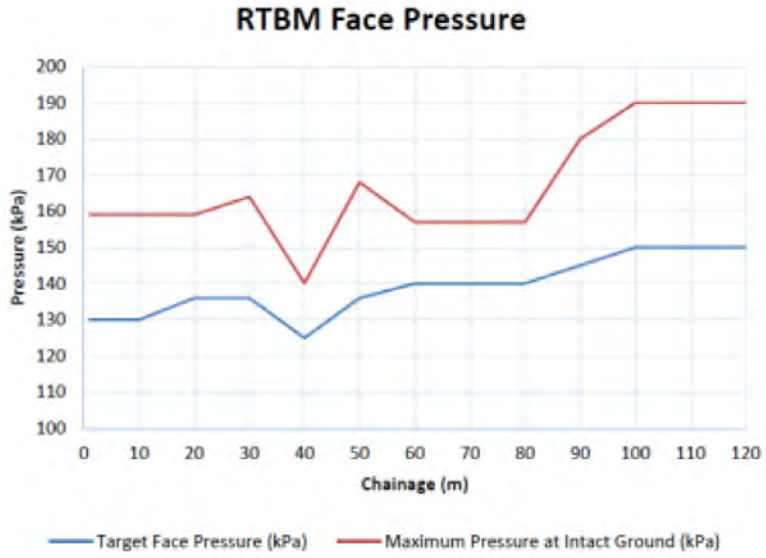

Figure 7: Target operation face pressure

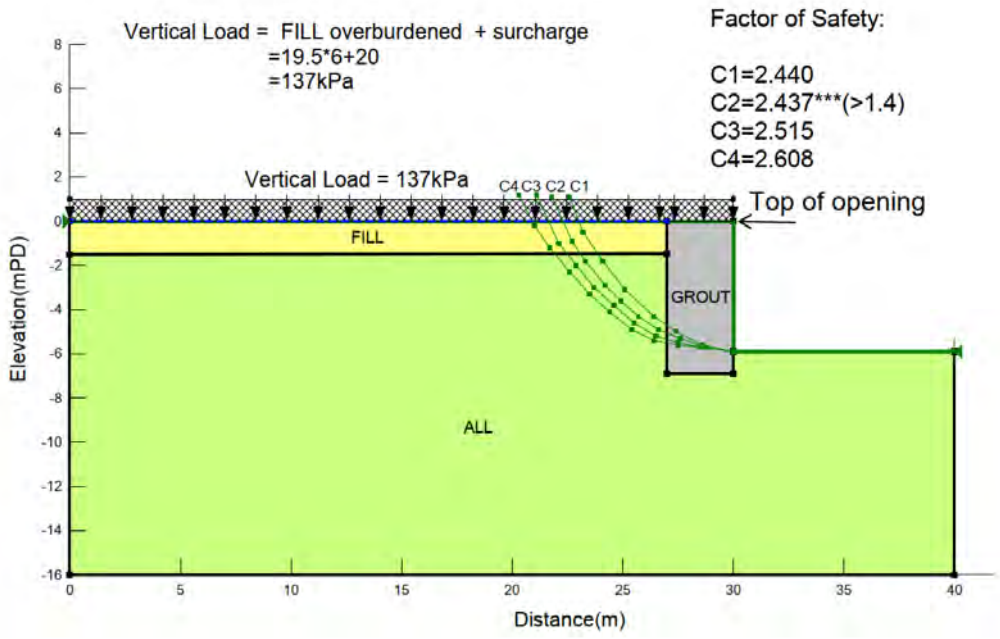

Figure 8: Ground improvement design for RTBM break-in and break-out

3.4 Jacking force estimation

Jacking force was applied to balance two types of resistance. The first was the frictional force between the jacked-in-place segments and the surrounding soil. The second was the reaction between the RTBM cutterhead and the soil in front of it. An accurate estimation of the jacking force was a challenging task.

A variety of methods have been put forward for estimating the jacking force internationally. Peng (2015) and Sterling (2020) provided comprehensive reviews on the subject. Many of the methods, however, are not specifically related to segment jacking using RTBM. In recent years, there were a number of segment jacking projects undertaken using RTBM in Mainland China, and several design codes and references have been published. The design of this project made reference to China Municipal Engineering Association (CMEA) (2020).

$$P = 2(B+H)Lf + B'H'Pc \quad (1)$$

where P = jacking force, B = segment width, H = segment height, L = jacking distance, f = friction force per unit area, B′ = width of the RTBM cutterhead, H′ = height of the RTBM cutterhead, and Pc = passive earth pressure in front of the cutterhead.

$$Pc = K_0\gamma\,(h + 2H/3) + \gamma_w h_w \quad (2)$$

where K_0 = earth pressure coefficient at rest (1-sinϕ′), h = cover depth of the tunnel, γ = unit weight of soil, γ_w = unit weight of water, h_w = height between groundwater level and one-third of RTBM cutterhead height (calculated from invert level).

The most challenging part of the estimation was the friction force per unit area f. Extensive experience has shown that where lubricants are applied between the annulus between the segments and the soil during jacking and are functioning, the value of f is in the range of 8.0 to 11.0 kN/m^2 (CMEA (2020) – Table 4.4.3 Silty SAND). Following a review of the geological condition, (SPT-N value in the range of 12 to 32), a value of 10.0 kN/m^2 was adopted for the project.

4 CONSTRUCTION PERFORMANCE

4.1 Face pressure during RTBM advancement

The project team maneuvered the machine by adjusting the advancement and mucking out speeds to control the real-time face pressure during excavation to match within the target face pressure. There were four pressure sensors installed in the bulk head of the machine for monitoring the actual face pressure developed during RTBM advancement.

Figure 9 presented the actual face pressure measured during tunnel excavation in relation to the design target pressure. It can be observed that the measured pressure was controlled to be fairly constant throughout the operation.

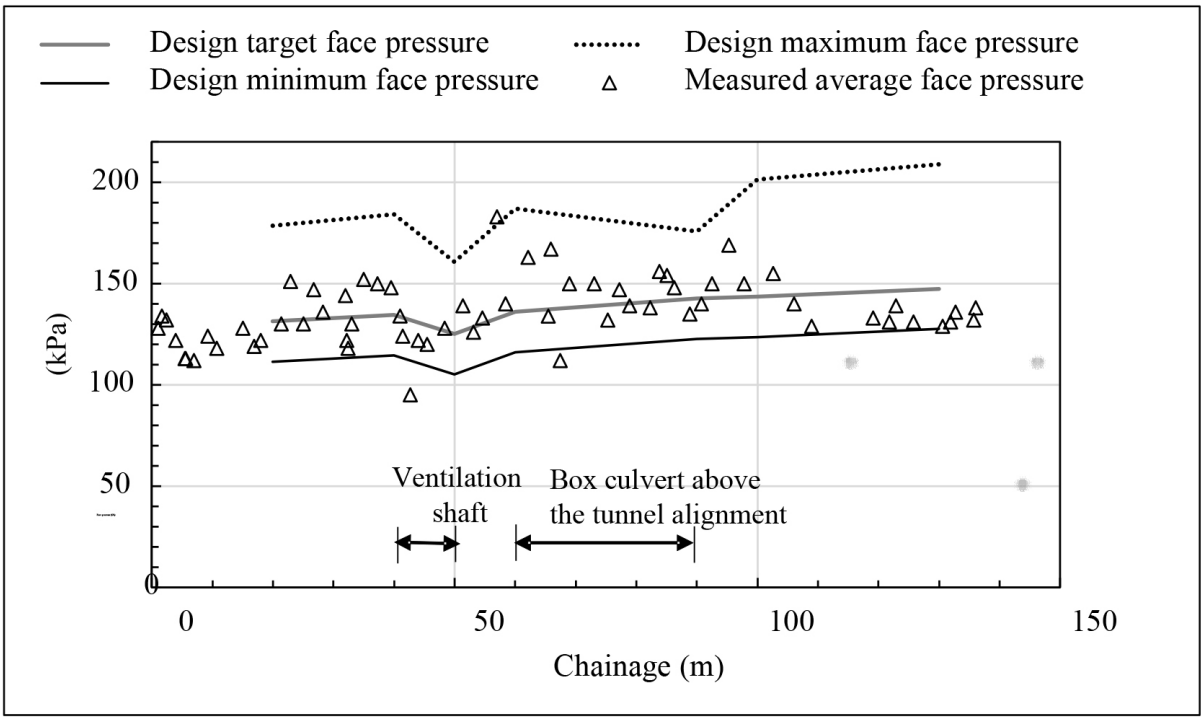

Figure 9: Comparison between design and measured face pressure

4.2 Recorded jacking force

Based on the jacking force estimation method, the maximum jacking force required for completion of the tunnel was 2858 tonnes at a jacking length of 130 m. A main jacking system with a capacity of 3600 tonnes was used for this project. In addition, an intermediate jacking station was incorporated in the machine as a contingency jacking capacity. A comparison between the estimated and the recorded jacking forces during RTBM advancement is shown in Figure 10. It is evident that when RTBM advanced though the grouted zones, the jacking force increased. Another observation is the increase of jacking force from Chainage 80 m to 100 m where the machine was passing underneath the 4-cell box culvert below Prince Edward Road East. Ground investigation records show that the presence of gravel or cobble fill material within this region, and higher torque and thrust force were required for the machine to pass through.

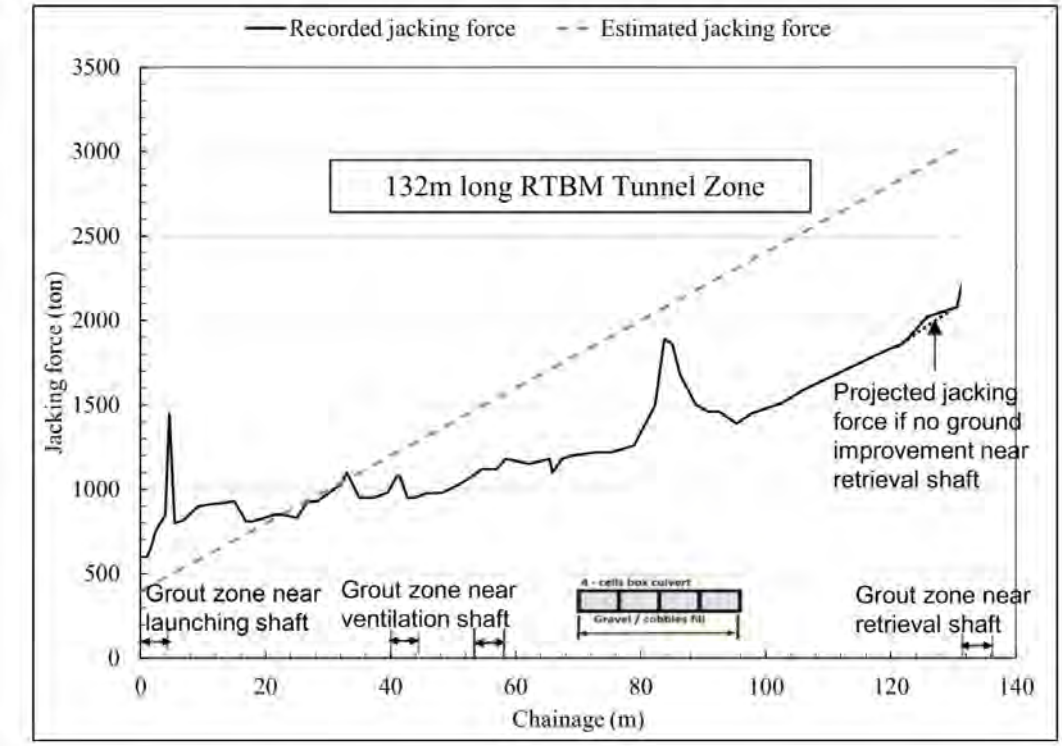

Figure 10: Comparison between estimated and recorded jacking force

Based on the measured face pressure and jacking force, the friction force per unit area f between the segments and soil could be back-calculated. Based on the CMEA formula in section 3.4 above, the maximum jacking force required to overcome the passive earth pressure in front of the cutterhead is 465 ton and the recorded maximum jacking force for the whole operation is approximate 2300 - 2400 ton, thus, a friction force per unit area f is derived to be approximately 7.5 kN/m^2 based on the formula, which corresponded to the lower bound of the design assumption.

4.3 Ground settlement monitoring

Ground surface settlement monitoring points were installed along the tunnel alignment. Some were installed above the tunnel center line and some at 1 m offsets , as shown in Figure 11. Assuming 1% volume loss, the predicted maximum settlement due to the tunnelling is 12mm based on the geotechnical impact assessment report. The measured settlement was well within 12mm prediction. The well-controlled settlement serves to demonstrate that the applied face pressure has been appropriate.

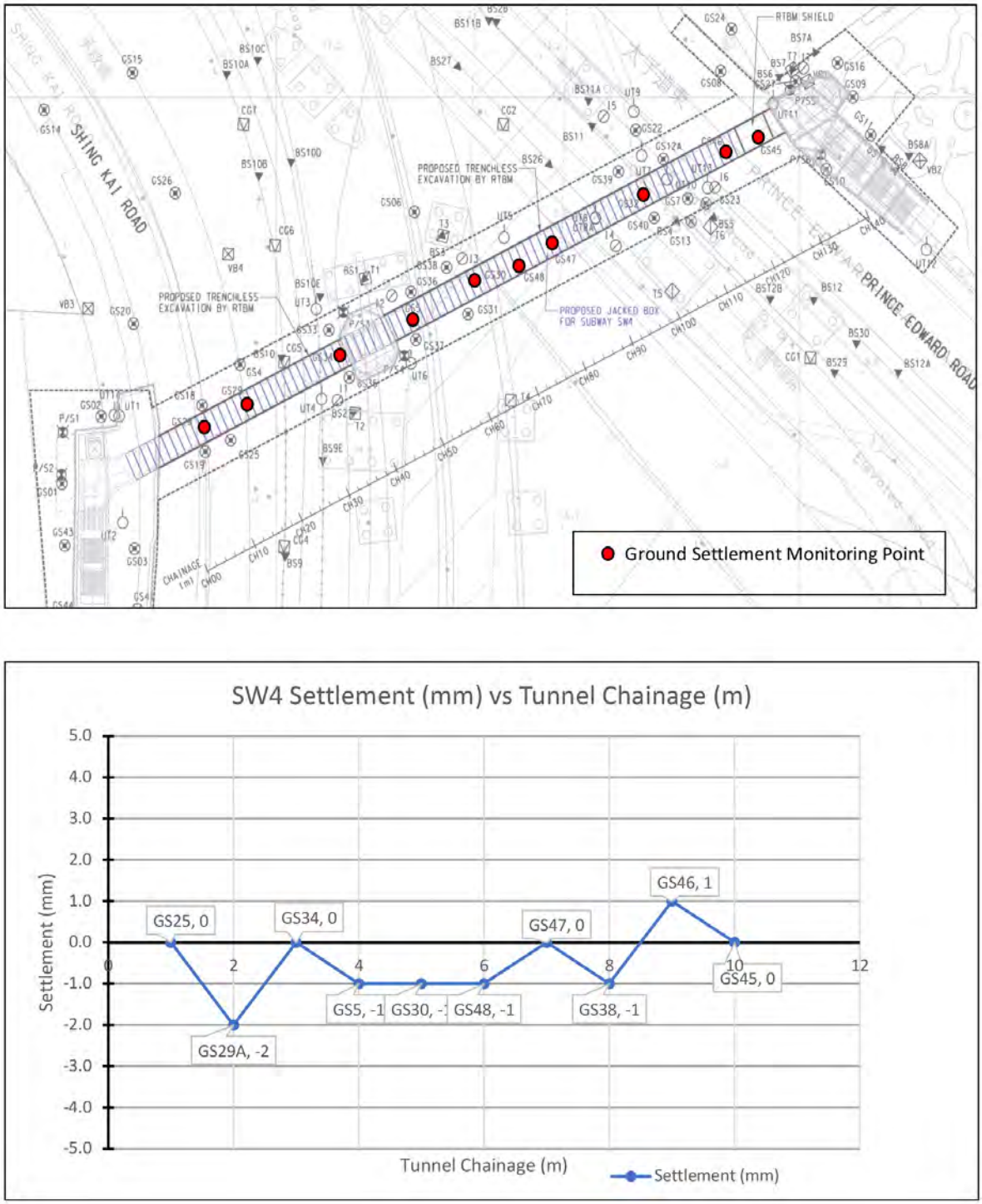

Figure 11: Measured ground surface settlement along the tunnel alignment

5 CONCLUSIONS

The project Subway SW4 saw the successful implementation of a jacked-in-place pedestrian subway using the first RTBM in Hong Kong. Albeit the technology has been commonly applied in Mainland China and Japan, the geological conditions of this project and the characteristics of Hong Kong soils presented unique challenges. Employing fully-mechanized excavation and precasting of tunnel segments, the RTBM technology has brought about a multitude of benefits, including enhanced works safety and working environment, effective management and control of construction risks, raising construction quality, and promoting sustainability.

The technology has good potential for application in delivering tunnel-type facilities particularly in congested urban areas. In the geotechnical aspect, the following conclusions can be drawn:

(a) Geophysical survey provides very important supplementary information to borehole investigation for RTBM cutterhead and screw conveyor design to minimize the risks arising from complex geological conditions.

(b) The friction force per unit area f back calculated in this project is approximately 7.5 kN/m^2. For future designs in similar geological conditions, a value of, say, 10 kN/m^2 can be considered.

(c) Face pressure estimation in accordance with GEO Report No. 298 gave satisfactory outcome in the RTBM operation.

(d) The resulting measured settlement is well within that corresponding to a 1% volume loss assumption.

REFERENCES

Chen, X., Ma, B., Najafi, M. & Zhang, P. 2020. Long rectangular box jacking project: A case study, *Underground Space,* https://doi.org/10.1016/j.undsp.2019.08.003.

China Municipal Engineering Association. 2020. *Technical standard for rectangular pipe jacking of comprehensive pipe gallery.* (in Chinese)

GEO. 2014. *Ground control for EPB TBM Tunneling – GEO Report No.298*. Geotechnical Engineering Office, Civil Engineering and Development Department.

Eurocode 8. 2003. *Design of structures for earthquake resistance*. European Committee for Standardization.

Peng, L., Wang, Z., Ye, Y. & Yang, W. 2015. Technological development and research status of rectangular pipe jacking method. *Tunnel Construction,* 35(1): 1-8. (in Chinese)

Sterling, R.L. 2020. Developments and research directions in pipe jacking and microtunneling. *Underground Space,* 5 (2020): 1-19.

Study of Creep Settlement of Driven H-piles in Loading Tests

Joley Lam
JL Engineering Ltd., Hong Kong

Kenneth Pak
Laboratory Specialist Co. Ltd., Hong Kong

Victor Li
Victor Li & Associates Ltd., Hong Kong

ABSTRACT

In Hong Kong, the maximum test load is required to be maintained constant for 72 hours during loading tests of piles according to the loading test procedures in the Code of Practice for Foundations 2017. Such a long duration of maintained loading is uncommon in pile loading tests overseas. In the paper, the behaviour of driven H-piles under maintained loading will be studied using creep settlements measured during the 72 hours of maintained loading of piles from various sites in Hong Kong. The reason for such a long period of maintained loading is not discussed in the literature. The paper aims to address the more fundamental issues of (a) usefulness of maintained loading if any, (b) whether it is meaningful to conduct maintained loading at peak test load and (b) whether the period of maintained loading can be reduced the time needed for loading test.

1 INTRODUCTION

In Hong Kong, quality assurance of pile foundation is usually implemented by means of loading tests, except for bored piles with pile diameter exceeding 750mm. According to the Code of Practice for Foundations issued by the Buildings Department (BD) (BD, 2017), loading tests for pile foundations are to be carried out based on the following steps, where WL denotes the design allowable capacity of the pile.

1st loading cycle: 0 → 0.5 WL → WL → 0
2nd loading cycle: 0 → 0.5 WL → WL → 1.5 WL → 2WL (72 hours) → 0

For each load increment, the pile settlement rate has to attain a certain threshold value before the next load increment and likewise for a load decrement. In the first loading cycle, the maximum test load is equal to WL. In the second loading cycle, the maximum test load is twice the design allowable capacity and will be maintained constant for 72 hours before release of loading at the end of loading test. Because of the requirement of a long period of maintained loading, loading tests for private projects in Hong Kong are commonly started on Monday, Tuesday or Friday to allow representatives from the BD to witness the application of loading to peak test load and final release of loading on a working day on weekdays. The Architectural Services Department (ArchSD) also adopts the same procedure as the BD for pile loading test (ArchSD, 2020).

According to the Code of Practice for Foundations (BD, 2017), a pile will pass a compression loading test if the measured settlements at pile head do not exceed the following two limits.

Total settlement (in mm):	2WL/AE + D/120 + 4
Residual settlement (in mm):	D/120 + 4 or 25% of maximum pile head settlement during the test, whichever is larger

where A, E and D are the cross-sectional area of the pile, Young's modulus of the pile material and the least dimension of the pile, respectively. The ArchSD adopts the same pile acceptance criteria except that D is taken as the least dimension of a driven H-pile, the outer diameter of steel casing of a mini-pile or the diagonal of rectangle enclosing the H-section of a rock-socketed steel H-pile. The maximum settlement criterion for the total settlement is often called the Davisson's criterion because it is based on an old publication by Davisson (1967).

The Civil Engineering Development Department (CEDD) adopts a loading test procedure different from that of the BD and ArchSD. For preliminary piles, the maximum test load is P = 2WL. For working piles, the maximum test load should not be less than P = 1.8 WL. As described in CEDD (2020), the test loads are applied in three increments to reach the maximum test load P as follows:

$0 \rightarrow 0.25$ P (24 hours) $\rightarrow 0 \rightarrow 0.5$ P (24 hours) $\rightarrow 0 \rightarrow$ P (24 hours) $\rightarrow 0$

For each stage of loading, the maintained loading will last for at least 24 hours until the settlement rate has reduced to less than 0.1mm/hour. The total duration of maintained loading will also be 72 hours, but divided into three periods of 24 hours. The CEDD adopts the Brinch Hansen's criteria (CEDD, 2020) in lieu of the Davisson's criterion for pile loading test, and there is no settlement criterion for the residual settlement.

This paper aims to discuss the following basic questions related to pile loading tests:

a. Is maintained loading necessary?

b. At which stage should the maintained loading be applied?

c. What is the suitable duration for maintained loading?

In this paper, discussion will only be focused on driven steel H-piles under maintained loading under compression in loading tests.

2 FUNCTION OF MAINTAINED LOADING

When a constant load P is applied to a stable pile, the pile settlement δ will not stop immediately after loading application, but gradually reduces with time. For practical purpose, some criteria need to be specified for defining the pile settlement corresponding to the applied load P at equilibrium condition. These criteria are usually in the form of a minimum holding time T_h and/or a threshold settlement rate r.

For a load increment, the BD and ArchSD specify a holding time of 10 minutes and a threshold settlement rate of 0.05mm in 10 minutes, whichever takes a longer time to attain (BD, 2017; ArchSD, 2020). For a load decrement, the holding time is increased to 15 minutes and the threshold recovery rate is 0.1mm/hour. The CEDD specifies a threshold settlement rate of 0.1mm in 20 minutes for load increment only (CEDD, 2020).

In Singapore, a threshold settlement rate of 0.25mm/hour for loading increment is recommended in their Code of Practice for Foundations CP4:2003 (2012) (Singapore Standards Council, 2012). A similar threshold settlement rate seems to be also used in Malaysia (G&P, 2005; Foundtest, 2021). Figure 1 shows the schematic diagram of pile settlement under a constant applied load.

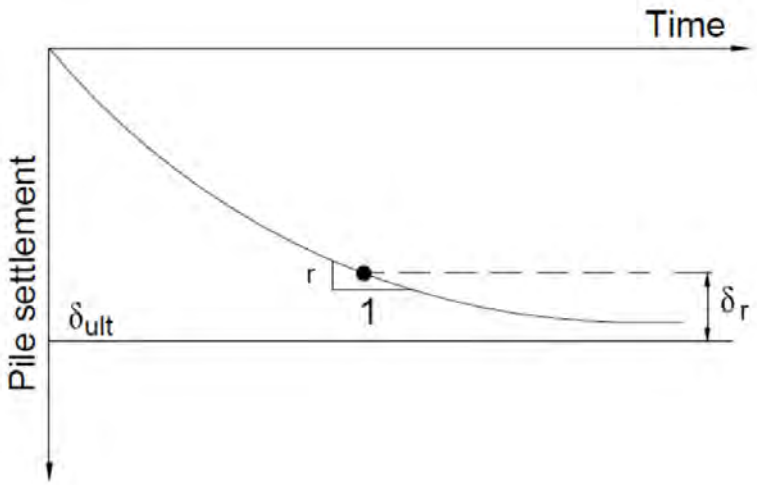

Figure 1: Pile settlement under constant loading

For a pile deriving its resistance mainly from sandy soils, dissipation of pore-water pressures is expected to occur quickly and the pile settlement during constant applied load may be attributed to creep movement of soils. For piles embedded in softer soils, such as continuous flight auger piles which have now become uncommon in Hong Kong, the pile settlement under constant loading may be a combination of consolidation and creep settlement.

In Hong Kong, driven piles are usually founded in dense sandy soils. Therefore, pile settlement under constant applied loading is expected to be dominated by creep settlement. Based on the experiences gained from jacked piles (Li et al., 2003), creep settlement tends to approach an asymptotic value δ_{ult} as indicated in Figure 1. Similar behaviour is expected to also occur for driven piles in sands. If the settlement has reached a small enough threshold settlement rate r, it is expected that remaining or residual settlement δ_r as indicated in Figure 1 will be small.

According the loading test procedures specified by BD and ArchSD, maintained loading has to be applied for 72 hours at the test load of 2WL. The practice of maintained loading for loading tests in Hong Kong for private development projects dates back to at least 60 years ago (Philcox, 1962). Maintained loading are not uncommon in loading tests in other parts of the world, but the holding time of applied load usually ranges from a few hours to one day. Hong Kong is perhaps the only example in which the duration of maintained loading is as much as 72 hours.

The question then arises as to the purpose of maintained loading. What is to be gained by spending the time on such a practice? If there is a good reason for such a practice, one will expect that the rationale for it should have been well discussed in the literature. To date, the authors are unaware of any publication that describes the advantage of maintained loading. It was neither discussed in Philcox (1962), nor even required by Davisson (1970) as part of his proposed pile acceptance criterion for total settlement. Perhaps, Fellenius & Nguyen (2019) have rightly remarked that "for tests employing unequal load increments, unequal load-holding, and unloading-reloading events, the attitude seems to be: we did it last time, so why not keep on doing it?" and that "no useful information is obtained from prolonging the holding time for the maximum load".

In our opinion, there appears to be little sound technical justification for imposing the requirement of maintaining the applied load for a long period of time in a loading test. If there is a concern that ultimate creep settlement of a pile is excessive, the best strategy is to use suitable threshold settlement rate r as alternative to prolonged maintained loading for assessing the ultimate creep settlement of pile. If the specified magnitude of r is sufficiently small, the total pile settlement that will occur upon reaching threshold the settlement rate will be for all practical purposes a close estimate of the ultimate creep settlement. It is much more efficient and rational than performing a prolonged maintained loading of 72 hours for assessing the residual creep.

The use of a threshold settlement rate has proven to be a practical tool for controlling the creep settlement of jacked piles (Lam, 2007) and the same is expected to be equally feasible for driven piles.

3 WHEN TO CONDUCT MAINTAINED LOADING

As discussed in the preceding section, there is no sound justification for the requirement of maintained loading. If such a requirement has to be imposed by the regulatory authority, the question then is at what load level should the maintained loading be preferably applied?

Figure 2(a) shows a schematic load-settlement response of a driven pile under normal condition. When a driven pile is installed, the pile will be subjected to virgin loading from zero to 2WL or perhaps higher due to the transient driving force of the hammer. The load path is described by the line O-A-B. After installation, the applied loading will drop to zero, represented by the load path B-C. When the structure supported by the pile foundation is gradually built, the pile will undergo reloading due to the dead load of the structure, causing the load path to change from point C to D upon completion of the building as depicted in Figure 2(a). During the life span of the building, the pile load will fluctuate between point D and point E in response to fluctuations in loading due to temporal variations of superimposed dead loads, live loads and etc., but the maximum load is expected to be within the design working load of the pile.

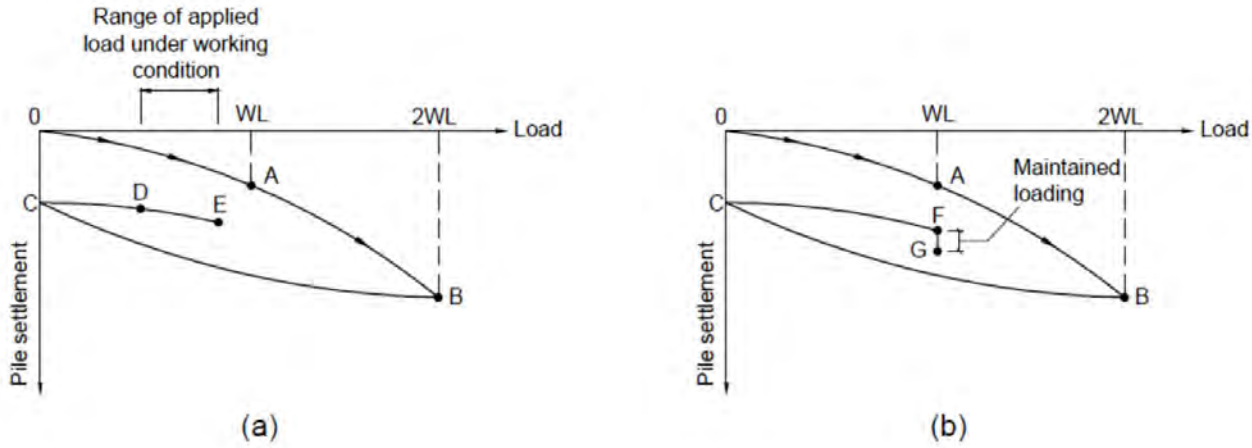

Figure 2: Load-settlement of pile (a) anticipated response under working condition
(b) preferred load cycle for maintained loading

The loadings applied to the pile during installation from point O, A and B are transient loading. Maintained loading will not occur in reality in this load path for a working pile. Only when the building is being constructed or has been completed under a load path from point C to E in Figure 2(a) will slow or maintained load be applied to the pile foundation. More importantly, the maintained load experienced by the piles under working condition will not exceed the design working load of the pile, WL. Because of this observation, it is theoretically not justifiable to impose a maintained loading at 2WL in a loading test.

If a maintained loading has to be imposed on a loading test to observe the behavior of the test pile under long-term load at working condition, it is more logical to conduct such a test at WL represented by point F to G in Figure 2(b). Based on this suggestion, the BD's loading test procedures can be modified as:

1st loading cycle: 0 → 0.5 WL → WL (maintained loading) → 0
2nd loading cycle: 0 → 0.5 WL → WL → 1.5 WL → 2 WL → 0

Similarly, the CEDD's loading test procedure can be modified as:

0 → 0.25 P → 0 → 0.5 P (maintained loading) → 0 → P → 0

4 WHAT IS SUITABLE DURATION OF MAINTAINED LOADING

If the requirement for maintained loading has to be imposed in a loading test, what is a suitable holding time for the maintained loading? To address this question, data on pile settlement obtained during the 72 hours of maintained loading in loading tests conducted according to the BD's loading test procedures is analyzed. Such data will be useful for making a suitable recommendation for the duration of load-holding.

In Hong Kong, it has now become a common practice to measure the pile settlement using both dial gauges and LVDTs. However, formal records of pile settlement are still based on dial gauge readings whereas the LVDT readings are often treated as backup data. The dial gauge readings are usually taken at less frequent intervals, but the LVDT readings are commonly taken much more frequently and automatically by data loggers.

Although the technology of servo-control for regulating the applied load is well established, it is not a mandatory requirement and not often used in pile loading tests. Manual control of applied load is usually preferred by contractors, whereby the jacking pressure of the hydraulic jacks is adjusted manually before the dial gauge readings are taken. If the hydraulic pressure of the loading jack is not held constant by servo-control and not adjusted frequently, the hydraulic pressure may drop leading to drop in applied load and reduction in creep settlement of the pile.

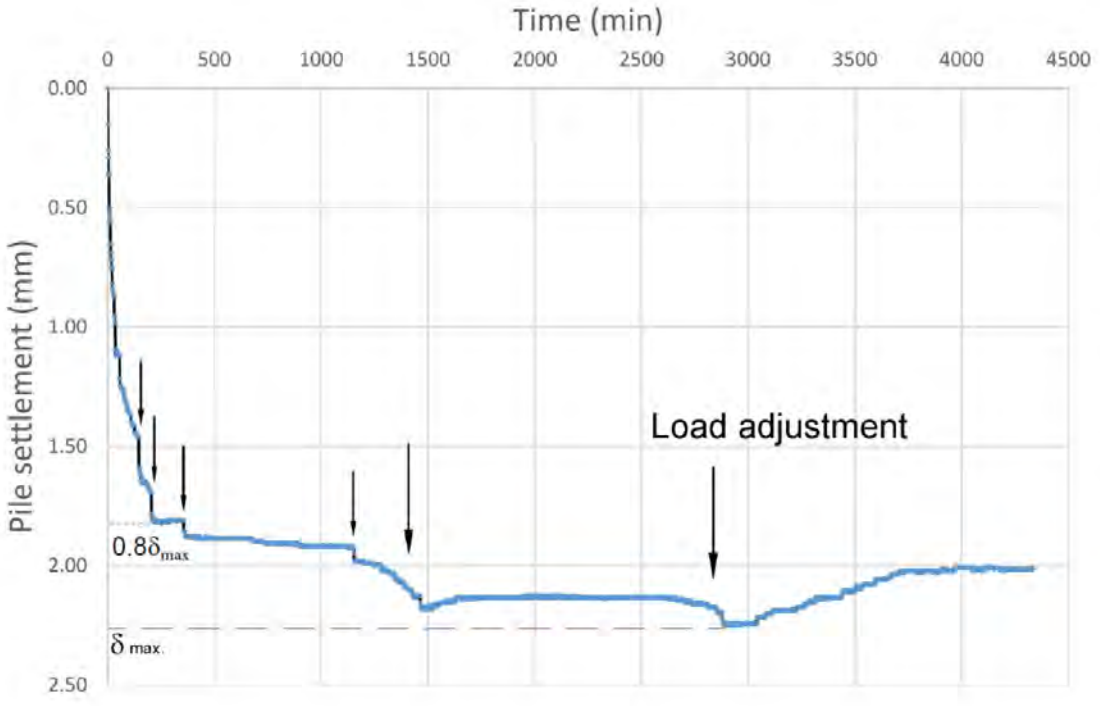

Figure 3: Setlement curve of a driven pile during maintained loading

Figure 3 shows the settlement curve for a Grade S460 305x305x223 kg/m UBP subjected to maintained loading of 7100 kN for 72 hours. The settlement readings were recorded by LVDTs every minute while the applied load adjusted manually. The following general observations can be made.

- The settlement increases rapidly at the early stage of the maintained loading, a large percentage of the total pile settlement measured during the 72-hour period has occurred within the first few hours of maintained loading;
- The rate of settlement reduces with time and tend to approach an asymptotic value.
- There are perturbations in the load-settlement curve.

If the constant applied load is achieved by manual adjustment, small adjustments are close time intervals will be necessary to maintain the load at a reasonably uniform level. This will be a very demanding task for the technicians conducting the loading test. More often, larger load adjustments are carried out at long time intervals to reduce the effort of load adjustment, resulting in larger perturbations in the load settlement curve as illustrated by Figure 3. If the time elapsed between load adjustment is long, significant recovery of pile movement may be observed during "maintained loading" causing the pile to rebound as exemplified by the data in Figure 3. Fellenius & Nguyen (2019) have reported similar observations from case histories of pile loading tests in which the applied loading for maintained loading was adjusted manually.

The above observations are quite typical of the results of maintained loading test for driven piles in Hong Kong. Figure 4 compiles settlement curves of some other driven piles showing a range of typical settlement curves under 72 hours of maintained loading, with some showing distinct perturbations similar to that of Figure 3.

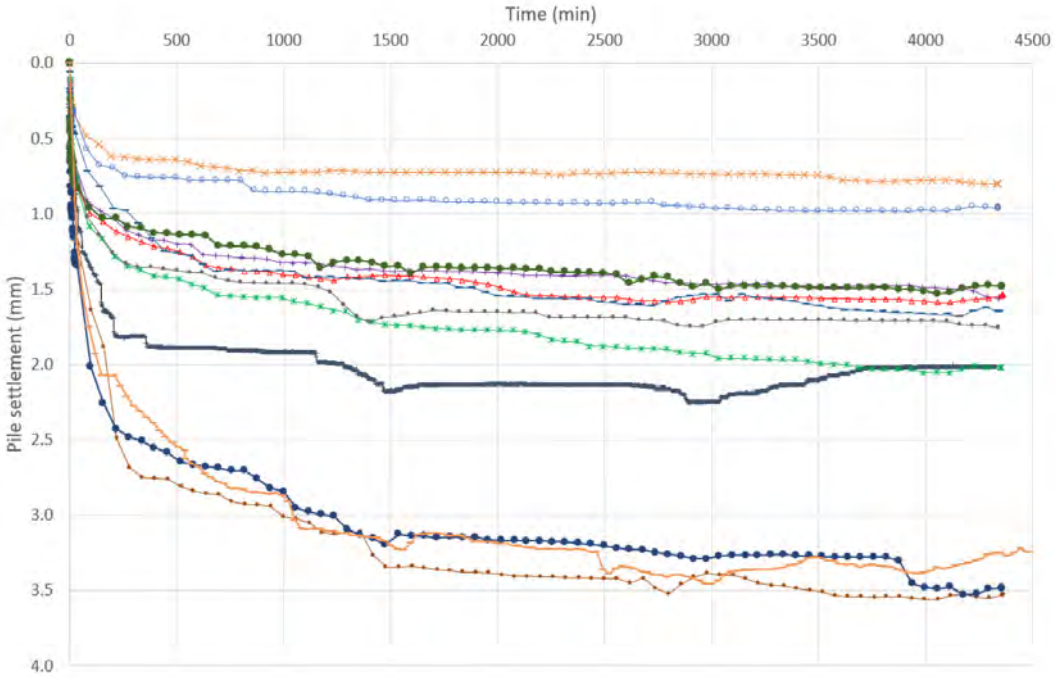

Figure 4: Typical settlement curves of driven piles from various sites in Hong Kong during maintained loading

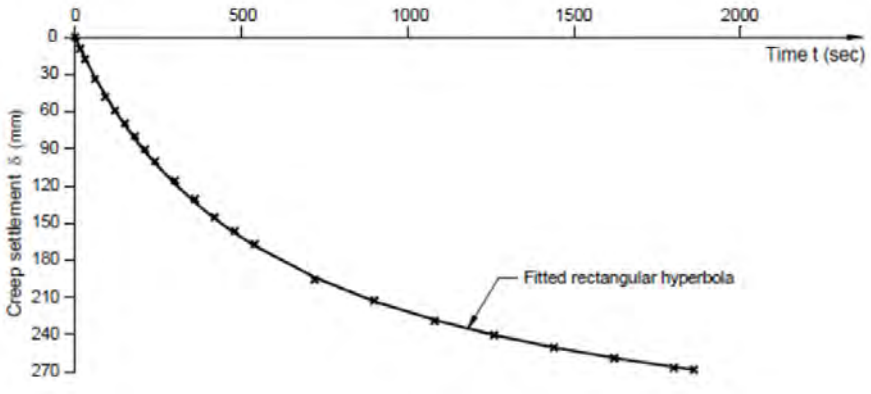

Figure 5: Setlement curve of a jacked pile under maintained load (Lam, 2007)

If servo-control is employed for regulating the applied load, it is expected that a smoother settlement curve will be obtained for maintained loading. Figure 5 shows the load-settlement curve of a jacked pile under constant loading reported by Lam (2007). The applied load had been controlled and maintained at a reasonable constant level by servo-control. As a result, a much smoother settlement curve could be obtained for the creep settlement of the jacked pile and the settlement curve can be well fitted by a rectangular hyperbola. A similar settlement curve is expected for driven piles if servo control is used to maintain the applied load to a constant level throughout the load holding period.

Figure 6 shows an example of a settlement curve of driven H-pile which does not exhibit large perturbations during the 72 hours of maintained loading at 2WL. It manifests that creep settlement curves can to a certain extent be reasonably fitted by a rectangular hyperbola or an exponential curve of the following form:

rectangular hyperbola: $\delta = at/(b + t)$
exponential curve: $\delta = a(1 - e^{-bt})$

where a and b are parameters to be fitted. However, the goodness of fit can be significantly affected by perturbations in the pile settlement curve caused by load adjustment.

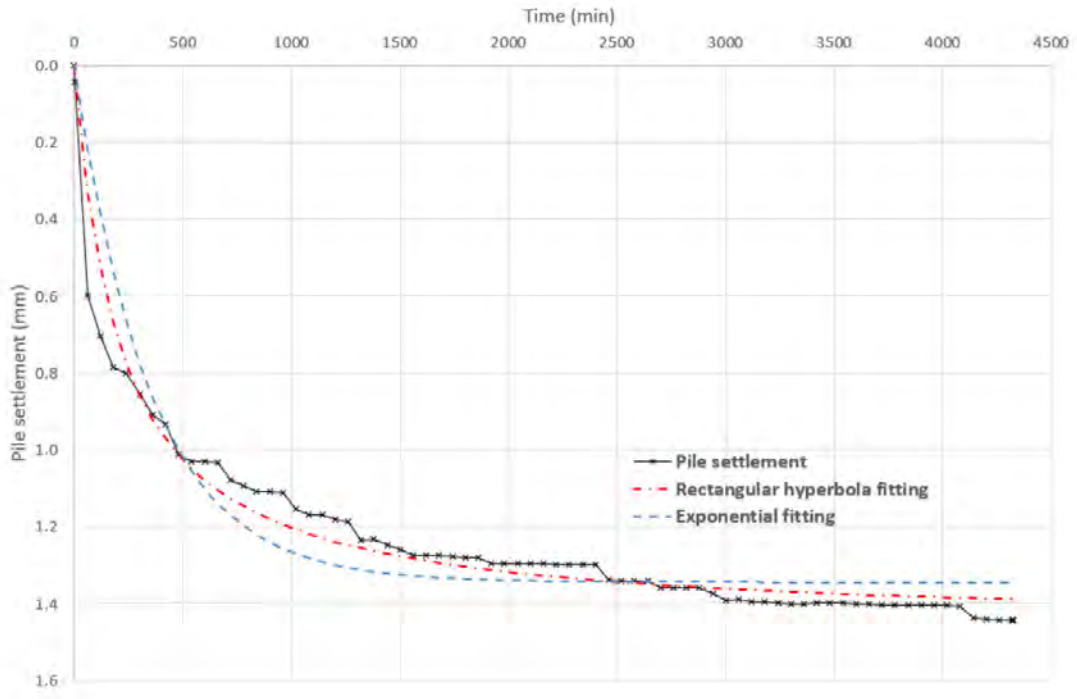

Figure 6: Curve fitting of a setlement curve of a driven pile under maintained load

To assess whether there is room for reducing the duration of maintained loading, the settlement curves during the 72 hour of loading at 2WL for 20 loading tests conducted on driven piles at different sites in Hong Kong using the BD's loading test procedures are studied. Referring to Figure 3, the maximum settlement δ_{max} recorded during the 72 hours of maintained loading is identified. The settlement corresponding to 80% of δ_{max}, denoted by δ_{80}, is then read directly from the settlement curve. The following table summarizes the results of δ_{80} for settlement curves presented in Figure 4.

Table 1: Summary of δ_{80} for maintained loading test

Pile no.	δ_{80} (mm)	Time to reach δ_{80} (hr.)	Pile no.	δ_{80} (mm)	Time to reach δ_{80} (hr.)
1	1.3	10	11	1.2	15.1
2	1.3	9.1	12	2.9	17.1
3	1.6	20.8	13	0.5	3.0
4	1.3	10.4	14	1.4	12.0
5	1.7	4.7	15	0.7	23.6
6	1.3	28.4	16	1.8	3.5
7	1.4	10.5	17	1.6	20.8
8	2.8	10.2	18	0.9	23.3
9	1.8	7.5	19	0.8	45.3
10	2.8	15.6	20	1.2	20.2
The above piles are Grade S450J0 305x305x 223 kg/m UBP with design capacity ranging from 2950 kN to 3670 kN founded in soil profile consisting of fill, alluvium overlying completely decomposed granite.					

The following observations can be made from the results of Table 1.

a. The settlement that occurred during maintained loading is small, mostly within 2mm for the data presented in Table 1.

b. 80% of creep settlement that occurred during the 72 hours of maintained loading will generally within the first 24 hours.

The results of creep settlement presented in Table 1 were collected during maintained loading at 2WL. As explained earlier, the magnitude of maintained loading acting on the piles under working condition will not exceed WL.

It is well established in soil mechanics that preloading will contribute to a significant reduction in creep settlement of soils and an increase in soil stiffness. This is the guiding principle used for installation of jacked piles (Lam, 2007). When jacked piles are installed, they are preloaded to a higher load level than 2WL so that the creep settlement will be sufficiently small to pass the loading test conducted at 2WL both in terms of total and residual settlement criteria.

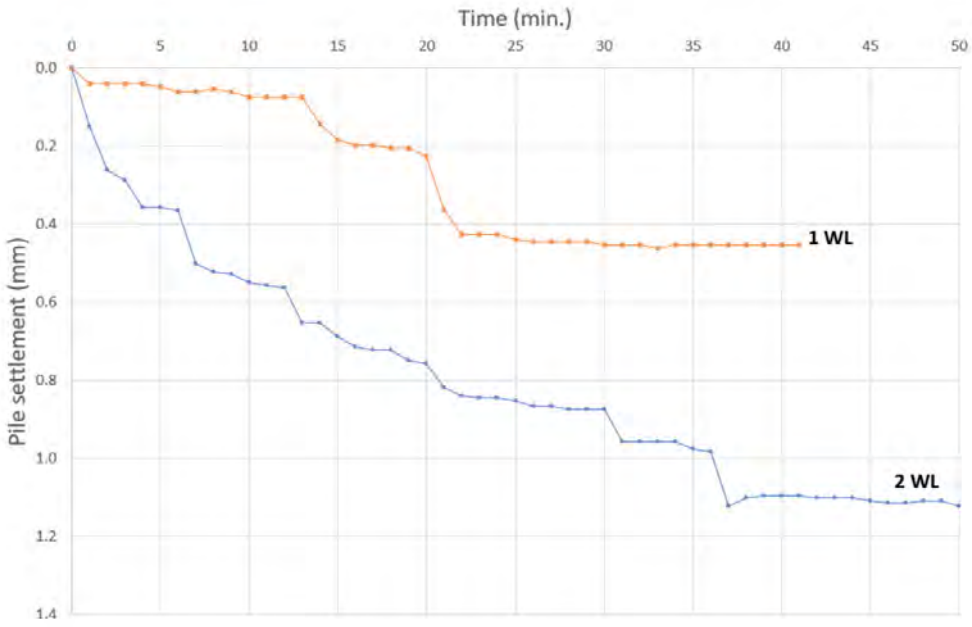

Figure 7: Setlement curves of a driven pile under constant loading of WL and 2WL

Similarly, driven piles will be preloaded by driving force of the hammer to a load level equal to or higher than 2WL during installation. It is therefore expected that the creep settlement of piles at a lower load level of WL under the working condition will be much smaller and occur much faster than that occurring under maximum test load at 2WL. Figure 7 shows the settlement curves of a driven pile measured in the first cycle of load-holding at WL and in the second load-holding cycle at 2WL in a pile loading test conducted according to the BD's procedures.

It is noticeable from Figure 7 that the creep settlement of the pile at WL is smaller and approaches the asymptotic value much more quickly than that at 2WL, in a matter of few tens of minutes.

5 CONCLUSIONS

A review of the practice of imposing maintained loading during a load test is presented. The following suggestions are made.

a. Servo-control is recommended for maintained loading to enable the applied loading to be held constant. This will reduce the occurrence of perturbations in the load settlement curve.

b. There is no good reason for a requirement of maintained loading. If there is a concern that the residual creep settlement may be significant, a more rational and efficient approach of loading test is to specify a suitable threshold settlement rate instead of spending days on performing maintained loading in a loading test.

c. It is also not logical to conduct the maintained loading test at maximum test load as required in the BD's or CEDD's loading test procedures. The installed piles will only be subjected to slow increase in loading during construction and service life of the structure and the applied loading under working condition will not exceed WL. If maintained loading has to be conducted as a statutory requirement, it is more logical to conduct maintained loading at the load level of WL instead of the maximum test load. Based on the results of Table 1, the creep settlement at 2WL is typically small. It is expected that the creep settlement under maintained loading at WL is insignificant.

d. Based on the settlement data of driven piles from maintained loading conducted at 2WL, it is found that creep settlement of pile will mostly be completed in one day. Further creep settlement occurring between 24 hours and 72 hours is relatively small, and typically less than 0.5mm. If maintained loading has to be conducted as a statutory requirement, there is room for reducing the holding time to 24 hours or less and/or specifying a suitable threshold settlement rate for terminating the maintained loading to reduce the total time needed for loading test without any significant effect on results of loading test as compared with the current practice. If the maintained loading can be conducted at WL, creep settlement is expected to smaller and occur much more quickly and perhaps a holding time of a few hours will be more than sufficient.

REFERENCES

Buildings Department (BD). 2017. *Code of Practice for Foundations*.

Architectural Services Department (ArchSD). 2020. *General Specification for Buildings*. 2017 Edition Incorporating Corrigendum No. GS 2017-02 (effective from 1 April 2020).

Civil Engineering Development Department (CEDD). 2020. *General Specification for Civil Engineering Works.* 2020 Edition issued on 1 December 2020.

Davison, M.T. 1970. High capacity piles. *Proceedings, Lecture Series, Innovations in Foundation Construction*. ASCE, Illinois Section, Chicago, 81-112.

Fellenius, B.H. and Nguyen, B.N. 2019. Common mistakes in static loading-test procedures and results analysis. *Geotechnical Engineering Journal of SEAGS & AGSSEA.* 50(3):20-31.

Foundtest Services (Fundtest) 2021. *Pile Maintain Load Test (MLT)*. (downloaded from http://www.foundtest.com.my/services/mlt.html on 18 April 2021).

G&P Geotechnics Sdn. Bhd. (G&P). 2015. *Pile Testing Specification for Driven Piles* (13 December 2005). (downloaded from https://gnpgroup.com.my/wp-content/uploads/2017/03/SP006.pdf on 18 April 2021).

Lam, J. 2007. *Termination Criteria for High-Capacity Jacked and Driven Steel H-piles in Hong Kong*. PhD. Thesis, The University of Hong Kong, 576pp.

Li, K. S., Lee, P. K. K. and Lam, J. 2003. Chapter 3 – Pile settlement behavior. *Case Studies of Jacked Piling in Hong Kong*. In K. S. Li, N. C. L. Ho, L. G. Tham, P. K. K. Lee (eds.). The University of Hong Kong and Centre for Research & Professional Development, 71-114.

Philcox, K.T. 1962. Some recent developments in the design of high buildings in Hong Kong. *The Structural Engineer,* IStrutE, October, 303-323.

Singapore Standards Council. 2012. *Singapore Standard – Code of Practice for Foundations CP4:2003(2012)*. Enterprise Singapore.

Application of landscape architecture to the rehabilitation of quarry in Hong Kong and an overseas case study

W.H. Lee
Ka Shing Management Consultant Limited, Hong Kong

L.M.K. Fung & C.K. Lai
Hong Kong

ABSTRACT

Background: The objective of this study is to explore the application of landscape architecture in quarries via a case study. The findings of our imitations in this study could have significant positive implications to inspire readers to more comprehensive thoughts and inspirations. Methodology: Desktop research is preliminarily adopted. Two case studies (Shek O Quarry in Hong Kong and Serra da Arrabida Natural Park in Portugal) have been selected. Findings: There are perceptible benefits from Shek O Quarry and Serra da Arrabida Natural Park on the use of landscaping in quarry. Benefits include the creation of diversity in ecology, vegetation, landscape visual impacts and the nesting areas that have been created. The disbenefits include immeasurable results of negative environmental impacts and high initial costs. Conclusion: Based on the research undertaken, it can be ascertained that the benefits of using landscaping in quarry outnumber the disbenefits. This can be perceived through the two case study analyses.

1 INTRODUCTION

Landscaping is delineated as any activity that alters the perceptible features of an expanse of land. The application of landscape in quarry rehabilitation is of great importance as there will be significant impacts on the environment [1]. There are, however, numerous disbenefits of employing landscape in quarry rehabilitation. This is linked to the aspect of adverse ecological impacts since there would continue to be extensive negative implications on the habitats of flora and fauna, deterioration of water quality, spoiled erosion in addition to the loss of land. In the long run, it will also result in greater costs incurred in the rehabilitation and reclamation of such land [2]. On the other hand, however, the use of landscape in quarry rehabilitation does generate numerous benefits. To begin with, it signifies a sustainable fiscal model for quarrying that facilitates, in an assimilated manner, the rehabilitation of the site in a way that is cost-effective. The use of landscape efficaciously amalgamates the landform with the beautiful adjoining and surrounding landscape and improves ecological habitats and generates an engineered side for land uses in the future. As of now, there are limited studies in Hong Kong regarding the application of landscape in quarry rehabilitation. Therefore, there is a need for a relevant study to explore the application of landscape in quarry rehabilitation via local and overseas empirical cases. The objective of this study is to find out whether landscaping is an ideal approach to apply to quarry rehabilitation. This study could have significant positive implications to inspire readers to more comprehensive thought as they will be inspired from the oversea quarry rehabilitation of our imitations.

2 LITERATURE REVIEW

More often than not, quarry rehabilitation projects take into account large-scale remodeling of the topography. Within the process of quarry rehabilitation as a whole, appropriate kinds of plants are selected and massively planted on slopes in order to accomplish the objective of the compatibility of the quarries to the nearby green environment [3]. Disbenefits of using landscape in quarrying involve high initial costs and immeasurable results of negative environmental impacts. The use of landscape to facilitate integration with surrounding areas through the restringing of the natural floristic conformation of the area and the use of native flora species is quite costly [2]. On the other hand, however, the benefits of using landscape in quarrying include diversity of ecology created, a decrease in carbon dioxide and the creation of visual impacts. Through landscaping the scenic quality is deemed to have improved with progressively more diversity of vegetation patterns and also topographic ruggedness. In addition, the landscaped parts are designed to minimize the usage of water and also to facilitate visual impacts [4]. It can be perceived that the benefits of using landscape in quarry for rehabilitation will outnumber the disbenefits.

3 METHODOLOGY

Desktop research has been adopted for this study. The research study collects existent relevant documents and related information from various sources [5]. Efforts have been made to ensure that the collections are based on the best available information that is impartial. Data and information have been collected in three steps. The first step is the selection criteria. Relevant documents and related information are selected in relation to the application of landscape to quarry rehabilitation. The second step concerns the language. All documents and information are in English only. The third step analyses the sources and relevant documents that have been collected. A considerable amount of documents and cases have been collected and identified as useful sources. However, sources without systematical analysis in relation to the objective of this study will be considered meaningless. From documents and information review, a local case and an oversea one (Shek O Quarry in Hong Kong and Serra da Arrabida Natural Park in Portugal) have been identified and considered suitable to illustrate the application of landscape in quarry rehabilitation.

4 A CASE STUDY FOR REHABILITATION OF SHEK O QUARRY IN HONG KONG

Shek O Quarry is situated on the south-eastern region of Hong Kong Island on the western part of D'Aguila Peninsula adjacent to Shek O County Park. The operations of the quarry began in 1964 (Figure 1) and 16 years later a major alteration on the landform on the western part was created. Thereafter, after consultation with the government, an agreement resulted in a sanctioned landscape master plan (Figure 2) for the Shek O Quarry rehabilitation. The engineering approach is the creation

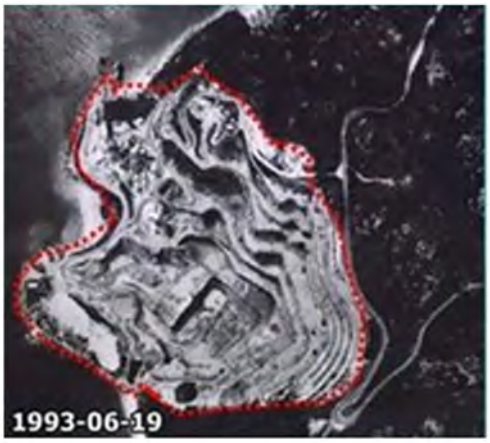

Figure 1: Top-up view of Shek O Quarry where there were no / few trees or plants. Retrieved from https://www.concrete.hk/system/files_force/assets/document/hkila_2012_soq4_low_res.pdf?download=1

Figure 2: The project was divided into five phases e.g. Area E (1998), Area B (1999), Area A (1998), Area C 2003) and Area D (2011). Retrieved from https://www.concrete.hk/system/files_force/assets/document/hkila_2012_soq4_low_res.pdf?download=1

of restored slopes from quarry benches. A scree slope (Figure 3) was placed over blasted rocks scree for the growth of vegetation on a safe slope angle. Stream courses were excavated in bedrock to avoid landslip (Figure 4). The rationale for this rehabilitation is to generate a landscape that can evolve into a sort of progressive ecological community found on the surrounding native slopes with the same flora and fauna. The rehabilitation of Shek O quarry has exemplified the prospect of taking advantage of natural resources without excessively compromising the natural habitat.

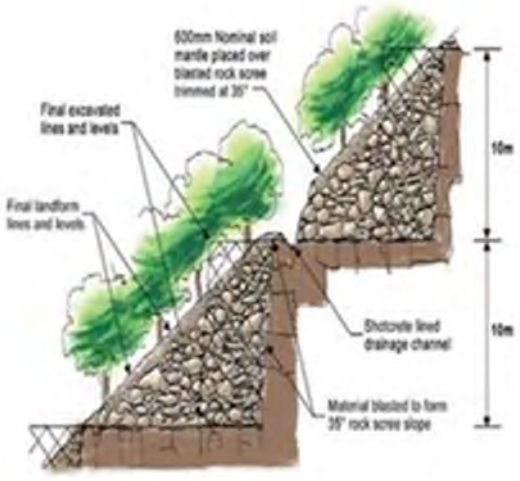

Figure 3: Side view of the formation of scree slope. Retrieved from https://www.concrete.hk/system/files_force/assets/document/hkila_2012_soq4_low_res.pdf?download=1

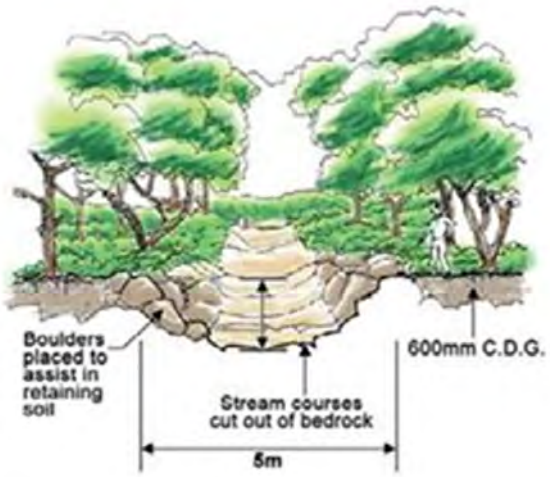

Figure 4: Front view of stream courses. Retrieved from https://www.concrete.hk/system/files_force/assets/document/hkila_2012_soq4_low_res.pdf?download=1

5 A CASE STUDY OF REHABILITATION AT SERRA DA ARRABIDA NATURAL PARK IN PORTUGAL

Quarrying activities, for instance the extraction of limestone, encompass major visual effects and degradation issues due to the depletion of the soil and extensive changes to the original topography. The increasing demands for limestone result in an intensification of quarrying which has significant impacts on the landscapes. In earlier times, quarries were basically abandoned subsequent to extraction. Nonetheless, natural colonization of disused limestone quarries is sluggish. The time periods involved in the formation of new communities are not deemed acceptable for the purposes of restoration or

reclamation. A rehabilitation quarrying project undertaken in another county is the rehabilitation of a limestone quarry within the Serra da Arrabida Natural Park in Portugal [6]. The area has a longstanding tradition of limestone quarrying. This case study delineates the significant benefits of landscape quarrying. The rehabilitation process took a period of 15 years, during which container grown plants were introduced by Portugal's mining industry in order to recover the floor of the quarry subsequent to the exploitation of the quarry. At the end of the project, there was a comparison of the revegetation of five abandoned platforms successively revegetated over the past 15 years at intervals of three years each [7]. This rehabilitation of the quarry resulted in distinctive plant communities, varying in age as well as cover. This permitted the evaluation of establishment and growth of instigated species in addition to the succession of natural species and stabilization of natural vegetation. There was also an evaluation of soil that added to the formation of different species on the platforms [6].

There are perceptible similar benefits between Shek O Quarry of Hong Kong and Serra da Arrabida Natural Park of Portugal for the use of landscaping in quarry. One of the benefits is the creation of diversity in ecology. For instance, in Serra da Arrabida Natural Park, the rehabilitation resulted in distinctive plant communities and different species of flora and fauna and natural vegetation. The same case can be perceived in Shek O Quarry in the sense that ecological regions and vegetation for nesting areas were created to benefit peregrine falcons.

CONCLUSIONS

The objective of this study explores the application of landscape in quarry rehabilitation in terms of their benefits and disbenefits. The benefits of using landscape in quarry include the diversity of the ecology created, the provision of visual impacts, blending with the surrounding landscape, and the ecological habitats facilitated as well as an engineered location for future uses. Nonetheless, the disbenefits of using landscape in quarry include the issue of immeasurable results and high initial costs. Based on the research undertaken, it can be ascertained that the benefits for using landscape in quarry outnumber the disbenefits. This can be perceived through the case study analysis of the rehabilitation of Shek O Quarry in Hong Kong and that of Serra da Arrabida Natural Park in Portugal.

REFERENCES

[1] Omosanya, K. O., & Ajibade, O. M. Environmental impact of quarrying on Otere village, Odeda, Southwestern Nigeria. Ozean Journal of Applied Sciences, 4(1), 75-82.

[2] Corry, R. C., Lafortezza, R., Brown, R. D., Kenny, N., & Robertson, P. J. Using landscape context to guide ecological restoration: an approach for pits and quarries in Ontario. Ecological Restoration, 26(2), 120-127.

[3] Greening Development Bureau. Landscape Rehabilitation. Retrieved 15 October, 2018 from: https://www.greening.gov.hk/en/departments_greening_efforts/rehabilitation.html.

[4] Holcim Pty Limited. Lynwood Quarry: Rehabilitation and Landscape Management Plan. Retrieved 16 October, 2018 from: https://www.holcim.com.au/sites/australia/files/documents/EMP02_REHAB.pdf.

[5] Crouch; Sunny Crouch; Matthew Housden (2003). Marketing research for managers; The Marketing Series; Chartered Institute of Marketing. Butterworth-Heinemann. p. 22.

[6] Villacampa, Y., Brebbia, C. A., Uso, L. J. (2001). Ecosystems and Sustainable Development. New York: WIT Press.

[7] Correia, O., Clemente, A. S., Correia, A. I., Máguas, C., Carolino, M., Afonso, A. C., & Martins-Louçao, M. A. (2001). Quarry rehabilitation: a case study. Ecosystems and Sustainable Development III (Villacampa Esteve Y., Universidad de Alicante, Spain, Brebbia CA, eds.), United Kingdom and JL. USO, Universitat Jaume I, Spain: Wessex Institute of Technology Press, 331-346.

The Sustainability of Concrete for Use under Different Loading and Environmental Conditions

W.H. Lee
Ka Shing Management Consultant Limited, Hong Kong

M.T. Wong
Technological and Higher Education Institute of Hong Kong, Hong Kong

L.M.K. Fung & C.K. Lai
Hong Kong

ABSTRACT

The objective of this study explores the sustainability of different concretes for use under different loading and environmental conditions in the construction and civil engineering industries. This study could have significant positive implications to inspire readers' more comprehensive thought and inspirations obtained from findings for our imitations. Desktop research is preliminarily adopted and an experiment is used. Thirty percent recycled coarse aggregate generally provides superior results compared to 30% recycled fine aggregate. Based on the research undertaken, it can be concluded that using recycled coarse aggregate in new construction and civil engineering projects just makes good sense.

Keywords: Concrete, Sustainability

1 INTRODUCTION

Although concretes made from gypsum and limestone have been used for thousands of years, modern concrete was only introduced 200 years ago (Winter 2012). Since that time, concrete has become ubiquitous in virtually all construction and civil engineering projects. This extensive usage has provided a growing body of scholarship concerning concrete's optimal applications in various scenarios including differences in loading and environmental conditions. The purpose of this paper is to identify the sustainability of different concretes for use under different loading and environmental conditions in the construction and civil engineering industries today. The paper first provides a review of the relevant literature concerning these issues, followed by a description of the experimental methodology used, and the results obtained thereby. Finally, a discussion concerning these issues is followed by a summary concerning the optimal concrete that should be used for sustainability under different loading and environmental conditions in the construction and civil engineering industries today.

2 LITERATURE REVIEW

The respective properties and applications of the three concretes of interest (i.e., partial cement replacements, recycled fine aggregate, and recycled coarse aggregate) mean that these materials have different optimal uses depending on the construction or civil engineering setting. There is a growing body

of scholarship, though, that indicates recycled fine and coarse aggregates represent a viable alternative for many applications. For example, a study by Hmar (2017) found that there are increasing quantities of waste materials that are generated by the construction industry, and identifying opportunities to recycle these materials represents an important step towards developing sustainable building practices. In this regard, Hmar (2017) advises that, "Recycling of these construction waste aggregate (recycled aggregate) can play a vital role in economical as well as natural resources". In fact, recycled aggregates are playing an increasing vital role in reducing the environmental impact of major public works projects and additional applications continue to be identified (Booker 2011).

The production processes for fine and coarse aggregates are essentially the same, differing only in the extent to which the former is processed more than the latter (Hmar 2017). In either case, the use of recycled aggregates just makes good business and environmental sense because both are produced from "aged concrete that has been demolished and removed from foundations, pavements, bridges or buildings [and] crushed and processed into various size fractions" (Hmar 2017).

Moreover, the use of recycled aggregates has also assumed growing importance in recent years because the global supply of natural aggregates for concrete applications is finite and is diminishing rapidly (Nili et al. 2019). In this regard, Nili et al. (2019) emphasize that, "Today, the use of recycled aggregates as a substitute for a part of the natural aggregates in concrete production is increasing. This approach is essential because the resources for natural aggregates are decreasing in the world." Using recycled aggregates for new concrete applications is also more cost effective, making their use a win-win for the construction and civil engineering industries today.

Assuming that using partial cement replacements for new building projects results in the same carbon footprint as the original manufacturing and transportation processes that were involved, it is therefore also important to determine which type of recycled aggregate is best suited for different applications and these issues are discussed in the experimental methodology section that follows below.

3 METHODOLOGY

Drawing on the seminal work by Hmar (2017) who investigated the respective properties of recycled aggregates, the experimental method involved analyzing the percentages of recycled aggregates obtained from a nearby demolished building that could partially or completely replace natural aggregates in terms of their weights (in this case, 0%, 30%, and 100%). In addition, the cast concrete cylinders and cubes use the various percentages of aggregates which were then subjected to laboratory testing with respect to, water absorption, aggregate impact and aggregate abrasion values.

The respective properties of natural aggregate concrete (NAC) versus recycled fine and coarse aggregate concrete were evaluated with respect to their compressive strength, workability, and tensile strength. The experimental methodology also compared various properties of the coarse and fine aggregates with respect to particle size distribution and compressive testing.

4 RESULTS

The results of this analysis showed that concrete that contained as much as 30% recycled aggregates exhibited the same strength as conventional concrete; however, additions of recycled aggregates beyond this limit is not recommended since it would make the resulting material nonconforming to specifications for water absorption and impact value. The respective cube compression strength of natural aggregate compared to 30% replacement and 100% replacement of coarse aggregate is depicted in Figure 1.

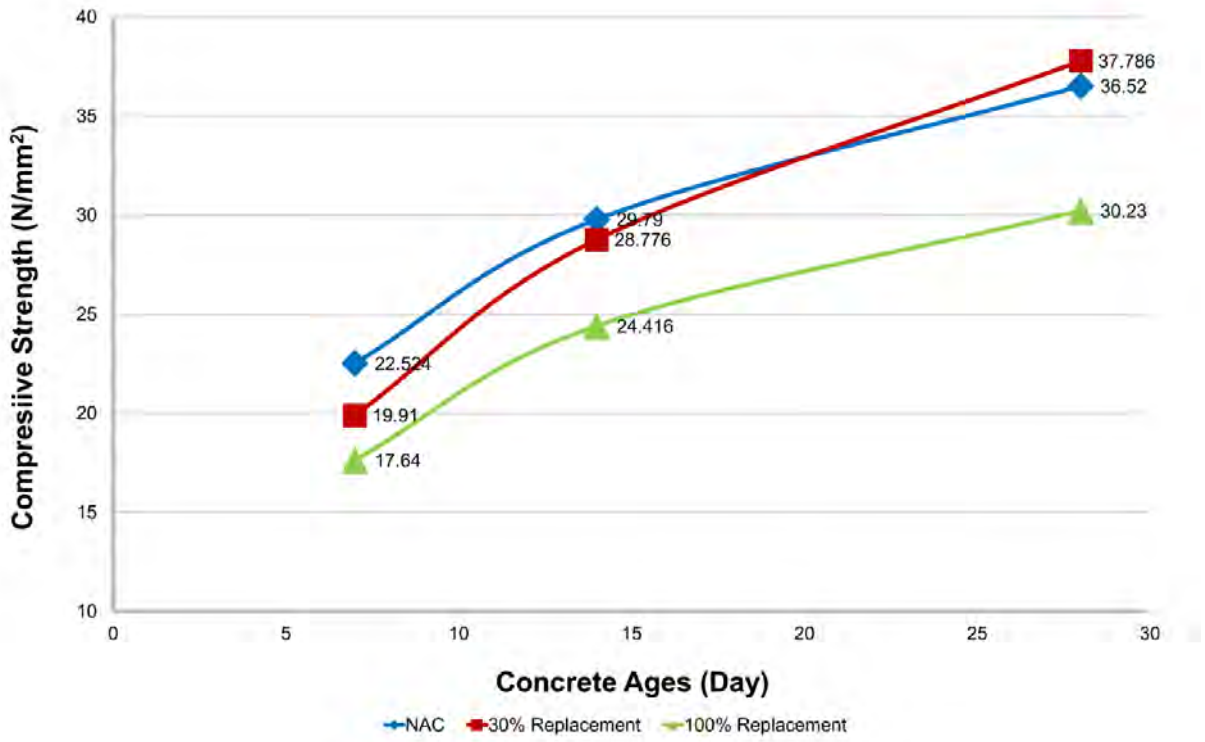

Figure 1: Comparison of cube compression strength of NAC (blue line) versus 30% replacement (red line) and 100% replacement (green line) with recycled coarse aggregate.

Likewise, the respective split tensile strength of natural aggregate compared to 30% replacement and 100% replacement of recycled coarse aggregate is depicted in Figure 2.

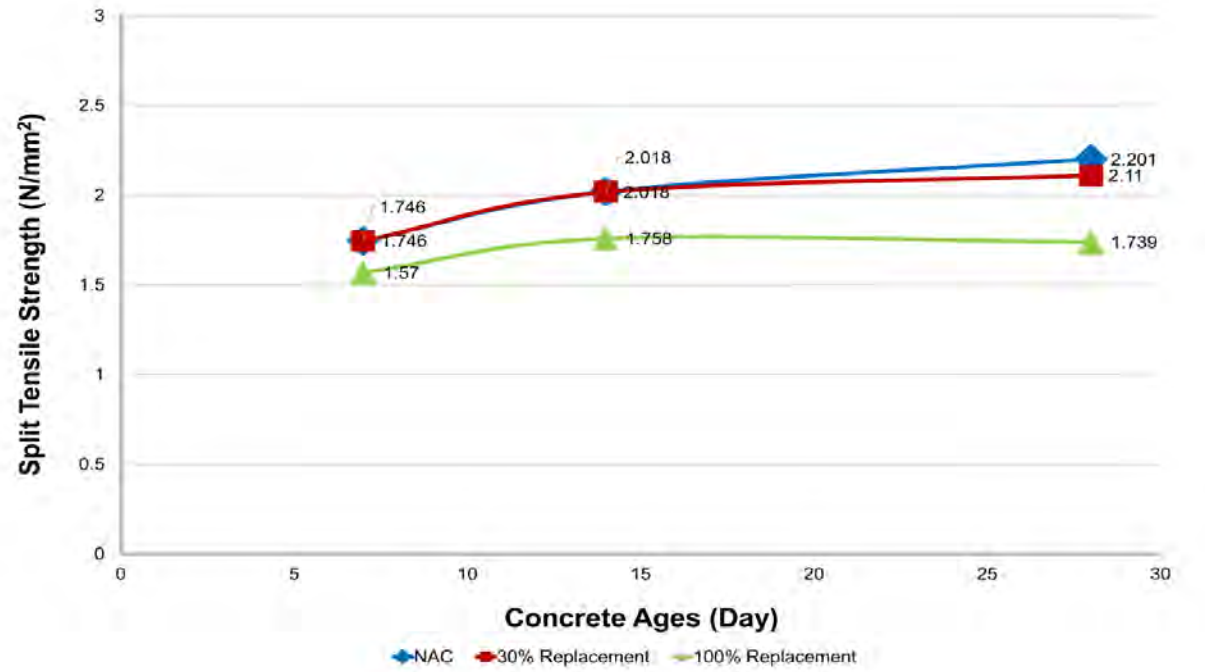

Figure 2: Comparison of split tensile strength of NAC (blue line) versus 30% replacement (red line) and 100% replacement (green line) with recycled coarse aggregate.

5 DISCUSSION

Based on the assumption that partial cement replacements require the same amount of resources with the corresponding carbon footprint as the original materials that were used in a construction or civil engineering initiative, the question then moves to whether recycled fine aggregate or recycled coarse aggregate represents the optimal solution for most projects. Based on the findings that emerged from the experimental methodology that was described above, a 30% recycled coarse aggregate generally provides superior results compared to a 30% recycled fine aggregate (results not shown). This finding, however, is situation-, resource- and time-dependent and other approaches, including partial cement replacements, may be required.

6 CONCLUSIONS

This paper shows that the use of recycled aggregates for cement applications has assumed new importance and relevance in recent years as the environmental impact of producing new concrete has become more apparent. In addition, the research also showed that properly manufactured and applied, recycled aggregates can not only reduce this environmental impact, they can also provide the same attributes as conventional concrete as a fraction of the original cost. Finally, although every engineering setting is unique in some fashion and partial cement replacements or recycled fine aggregates may be required, the research also showed that recycled coarse aggregates generally provides superior results compared to recycled fine aggregates and as much as 30% of conventional concrete can be replaced using this technique, especially if there are demolition projects underway nearby. For example, a significant percentage of the waste concrete that is generated by demolishing an office building can be recycled into public work projects such as highways or private enterprises including a new office building on the same site. In summary, using recycled coarse aggregates in new construction and civil engineering projects just makes good sense.

REFERENCES

Booker, S.M. 2011. The Road to Greener Blacktop. *Environmental Health Perspectives,* 109(4): A177.

Hmar, L. 2017. Study of Partial Replacement of Natural Aggregate by Recycled Aggregate on Concrete. *International Journal of Latest Engineering and Management Research,* 2(11): 1-6.

Nili, M., Sasanipour, H., and Aslani, F. 2019. The Effect of Fine and Coarse Recycled Aggregates on Fresh and Mechanical Properties of Self-Compacting Concrete. *Materials,* 12(7): 1120-1124.

Winter N.B. 2012. *Understanding Cement.* WHD Microanalysis Consultants Ltd.

A Note on Design of Rock-socketed Embedded Wall

Victor Li
Victor Li & Associates Ltd. Hong Kong

ABSTRACT

The design of excavation and lateral support works in Hong Kong generally follows the guidelines of GCO Publication No. 1/90. The document provides guidelines for determining the overall factor of safety against kickout failure of embedded walls in soil. There is limited discussion in this document for embedded walls partially socketed in rock. A method is proposed in this paper for determining the required socket length of a rock socketed embedded wall. The method allows the overall factor of safety to be applied consistently to resisting forces in soils and in the rock socket.

1 INTRODUCTION

When performing design of excavation and lateral support (ELS) works in Hong Kong, it is a common practice to check the factor of safety of the embedded wall against the so-called kickout failure. The design procedures for checking the kickout stability of an embedded wall fully installed in soils usually follow the guidelines described in GCO Publication No. 1/1990 (GCO, 1990), but there is no guideline in this publication for design checking of embedded wall socketed in rock. Guidelines for design checking the stability of a rock-socketed retaining wall are provided in the second edition of Geoguide 1 (GEO, 1982), hereafter referred simply as Geoguide 1 for brevity. The two guidance documents are not fully compatible with each other. The former is based on a hybrid of the overall factor of safety (FOS) and working stress approach and the latter is a combination of the partial factor approach. This paper presents a method of combining the two guidelines to produce a consistent design procedure for checking of the kickout stability of an embedded wall partially embedded in rock for the design of ELS works based on the overall factor of safety approach.

2 CURRENT DESIGN PRACTICE

The design equations and procedures for checking of cantilever and propped embedded walls are only slightly different. Only the principles for checking a propped embedded wall will be discussed in detail in this paper.

Geotechnical engineers usually follow the guidelines of GCO Publication 1/90 in their design of ELS works in Hong Kong. This publication is based on the overall FOS approach. Figure 1 shows the definition of the overall FOS for kickout failure for a propped retaining wall embedded in soils based on GCO Publication No. 1/1990.

According to the design equation in Figure 1, the overall FOS is applied to the resultant forces due to effective passive pressure and water pressure on the excavation side. The definition of overall FOS in Figure 1 can be re-written as:

$$F = \frac{P_p \times L_p + P_{wp} \times L_{wp}}{(P_a \times L_a + P_{wa} \times L_{wa}) - M_R} \quad (1)$$

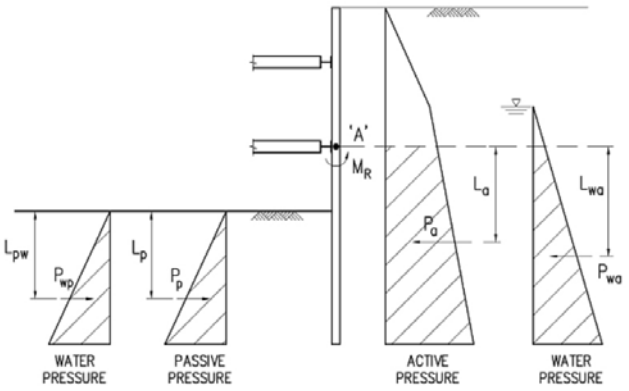

Legend

P_a = Resultant force due to effective active pressure below point 'A'

P_p = Resultant force due to effective passive pressure below point 'A'

P_{wa} = Resultant force due to water pressure on retaining side below point 'A'

P_{wp} = Resultant force due to water pressure on excavation side below point 'A'

L_a = Moment arm of P_a

L_p = Moment arm of P_p

L_{wa} = Moment arm of P_{wa}

L_{wp} = Moment arm of P_{wp}

M_R = allowable moment capacity of embedded wall

Equation based on limiting equilibrium:

$$P_a \times L_a + P_{wa} \times L_{wa} - \frac{P_p \times L_p + P_{wp} \times L_{wp}}{F} - M_R = 0$$

Figure 1: Design equations for checking of overall FOS for kickout failure based on GCO Publication 1/90

As discussed by Li & Lee (1993), the overall FOS approach is a 'variant' measure of geotechnical safety because the calculated value of overall FOS depends on its definition. In Eq.1, MR is treated as a reduction of disturbing moment and hence it appears in the denominator of the equation. If MR is treated as another component of the resisting moment, it should appear in the numerator and the calculated value of F will then be different.

Eq.1 is not a reasonable definition of F in dealing with water pressures. The forces due to water pressures appear both in the numerator and denominator of Eq. 1. Consider a somewhat extreme condition of an embedded wall immersed in a pool of still water for which the water pressures on both sides of the embedded wall are fully balanced. If the wall is hung at the wall top, MR is zero and Eq.1 will always be equal to unity. One cannot achieve a factor of safety higher than unity no matter how deep the wall is dipped into the water.

In Hong Kong, the structural moment capacity of the embedded wall MR is usually based on the allowable capacity under working condition. Eq.1 may therefore regarded as a hybrid of overall FOS and working stress approach.

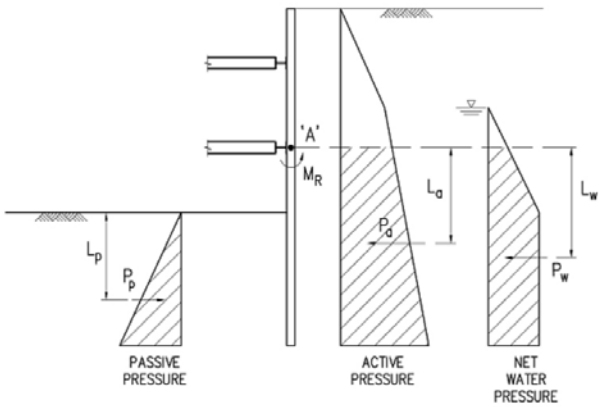

Legend

P_a = Resultant force due to effective active pressure below point 'A'

P_p = Resultant force due to effective passive pressure below point 'A'

P_w = Resultant force due to net water pressure on retaining side below point 'A'

L_a = Moment arm of P_a

L_p = Moment arm of P_p

L_w = Moment arm of P_w

M_R = allowable moment capacity of embedded wall

Equation based on limiting equilibrium:

$$P_a \times L_a + P_w \times L_w - \frac{P_p \times L_p}{F} - M_R = 0$$

Figure 2: Revised definition for the overall FOS for kickout failure based on TGN41

The definition of the overall FOS has recently been modified by GEO (2014) in TGN41. Net water pressure is now used in the definition of F as described in Figure 2. This gives a more reasonable definition and, as discussed by Li (2010), a less conservative design. The revised definition for overall FOS can be expressed as:

$$F = \frac{P_p \times L_p}{(P_a \times L_a + P_w \times L_w) - M_R} \qquad (2)$$

If the embedded wall is socketed in rock, guidelines for determining the required rock socket length can be obtained from Geoguide 1 as depicted in Figure 3 for a cantilever wall.

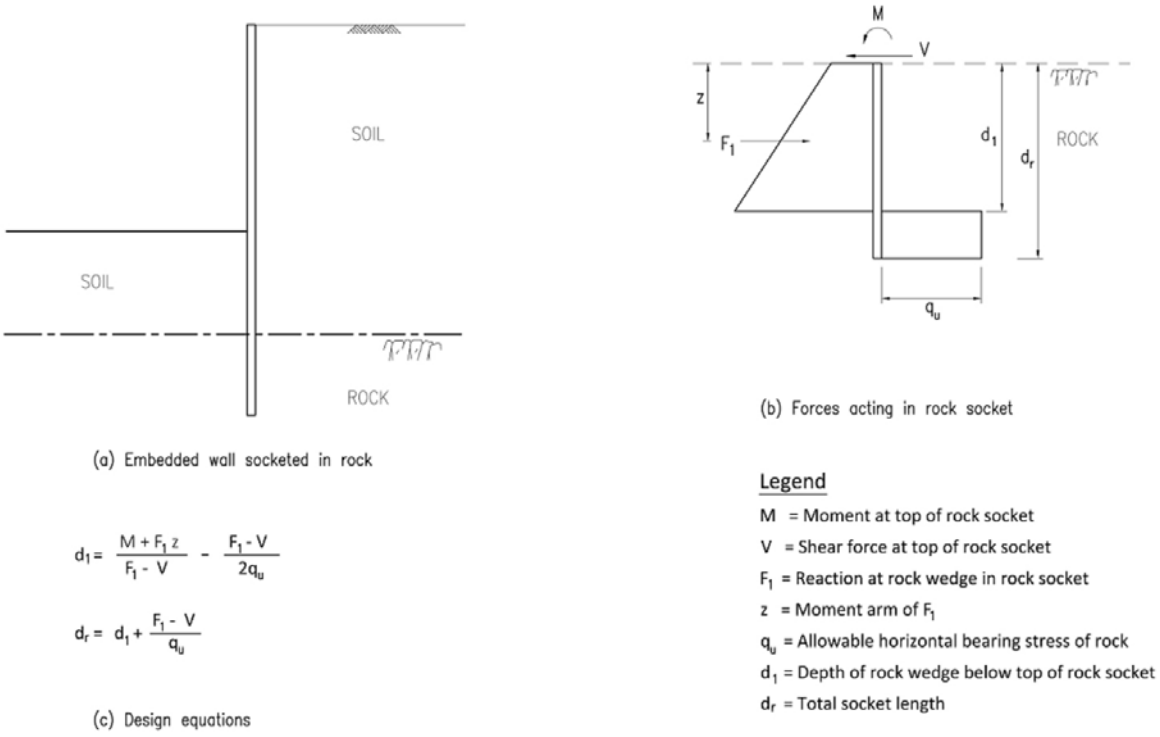

Figure 3: Design equations for determination of rock socket length based on Geoguide 1 (2nd Edition)

If the limit state approach based on partial factors is used for design of ELS works as described in Practice Note PNAP APP-57 (BD, 2012) for analysis, the calculated values of moment M, shear force V and passive resistance of rock in the rock socket F_1 will all be consistently obtained based on factored parameters. It will then be appropriate to use the "allowable" horizontal bearing stress capacity of rock as input value for q_u. In Hong Kong, the allowable value q_u is usually taken as 1/3 of allowable vertical bearing capacity of rock recommended in the Code of Practice for Foundations, although it is unclear about the origin of the factor.

Geoguide 1 gives no guideline on what appropriate distribution of water pressure should be used when applying the formulas in Figure 3, but designers commonly adopt the submerged unit weight of rock in the determination of rock socket length. This assumption may be inaccurate, but is considered a practical simplification given that the approach in Geoguide 1 for estimation of rock socket is itself conservative.

Based on the sign conventions shown in Figure 3(b), the bending moment M is expected to be a positive value when the embedded wall is acting as a cantilever wall before installation of first layer of struts. After struts are installed as shown in Figure 4(a), the situation will be different. If the portion of wall embedded in soil kicks out about point 'A' at the strut level, it will rotate in a clockwise direction at limiting equilibrium. To restrain the clockwise rotation of the embedded wall in soil, the resisting force V and moment M should be acting in the directions shown in Figure 4(b).

The directions of moment M and shear force V with respect the rock socketed portion of the embedded wall will be as shown in Figure 4(b). The direction of moment M in Figure 4(b) for a propped embedded wall is different from that shown in Figure 3(b) for a cantilever wall. If the sign convention in Geoguide 1 as described in Figure 3 is to be kept consistently for all analyses, negative values should be used for the input value of bending moment M when using the design equations in Figure 3 for calculation of the required rock socket length of a propped embedded wall.

When checking the stability of an embedded wall partially socketed in rock, the following procedures of analysis are commonly adopted by geotechnical engineers in Hong Kong:

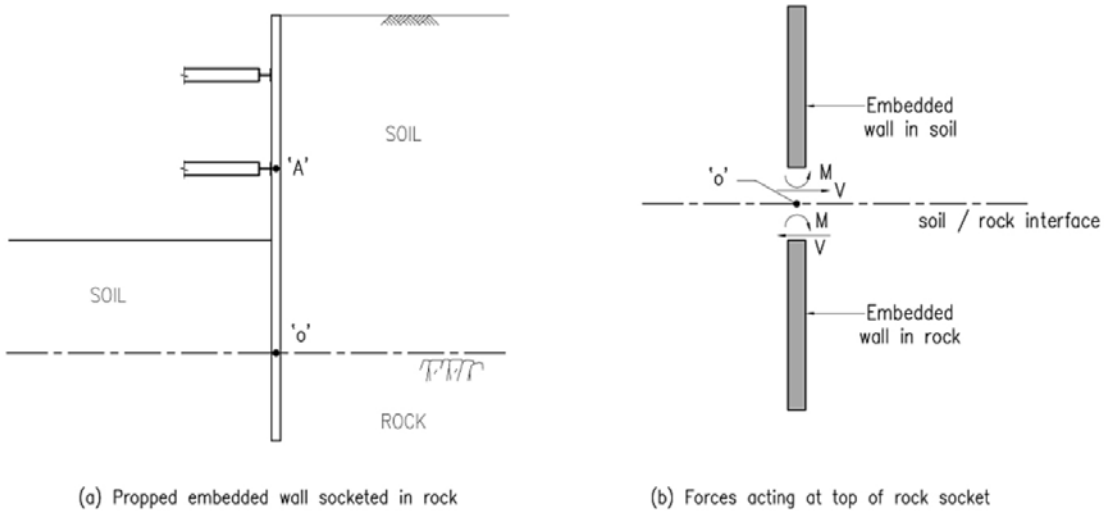

(a) Propped embedded wall socketed in rock (b) Forces acting at top of rock socket

Figure 4: Analysis of a propped embedded wall partially embedded in rock

a. A geotechnical program such as Plaxis is used to analyze the ELS works and obtain the shear force V and bending moment M of the embedded wall at the rockhead level. Unfactored parameters are usually used for the analysis.

b. Once the values of M and V at the top of the rock socket have been obtained, the required rock socket length is estimated using the design equations of Geoguide 1 shown in Figure 3. When performing this design checking, an overall FOS will be applied to the passive resistance of rock F_1 while the horizontal bearing capacity q_u will be based on the allowable value.

Although the above procedures based on the overall FOS approach for checking of embedded walls partially socketed in rock is popular in Hong Kong, it is subject to a strong criticism that unfactored parameters are used for obtaining the values of M and V in Step (a). This is equivalent to not applying a factor of safety to the passive resistance of the soils above the rock socket. It is not conservative and will lead to underestimation of the required rock socket length.

3 A SUGGESTED METHOD

To overcome the limitation of the analysis procedures described in the preceding section, a method for design checking of an embedded wall partially rocketed in rock based on the overall FOS approach is suggested as depicted in Figure 5. The meanings of the symbols in Figure 5 are same as those in Figure 2 and Figure 3.

Figure 5(a) shows the forces acting on the embedded wall. In line with the design guidelines of GCO Publication No. 1/90, an overall FOS (F) is applied to passive resistance of soils P_p above the rock socket. To be consistent, the same overall FOS is also applied to the passive resistance of the rock wedge F_1 within the rock socket. The sign conventions of Geoguide 1 for M and V in Figure 3 are consistently used throughout the analyses.

Figure 5(b) shows the forces and moments acting at the portion of embedded wall in soils between point 'A' at the strut level and point 'O" at the rock socket. The following equation relating M and V can be established by taking moment of the forces under the state of limiting equilibrium about point 'A' at the strut level.

$$V = \frac{M + P_a L_a + P_w L_w - \left(\frac{P_p L_p}{F} + M_R\right)}{h} \qquad (3)$$

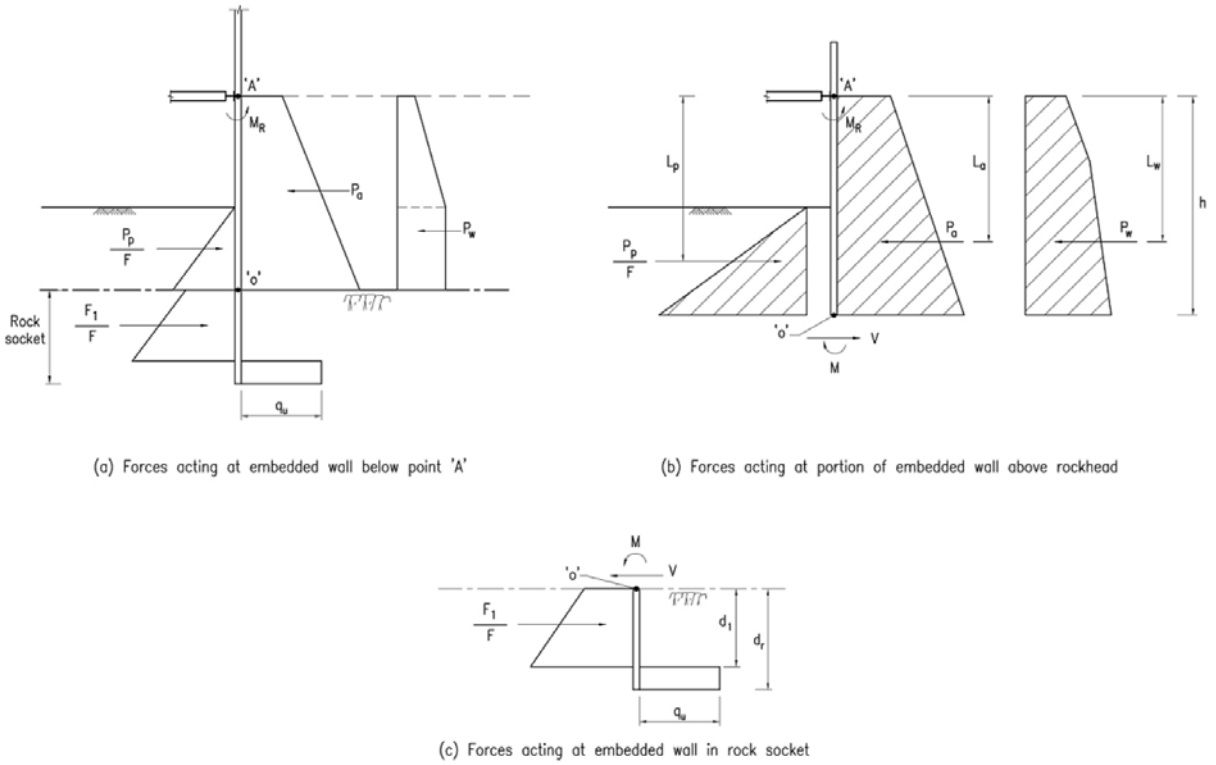

Figure 5: A suggested method for checking kickout failure of rock socketed embedded wall

Figure 5(c) shows the free-body diagram for the rock socketed portion of the embedded wall. For a selected value of V, the magnitude of M required to achieve limiting equilibrium is obtained by Eq.3. For this combination of M and V, the required rock socket length d_r can be obtained using the formulas in Geoguide 1 as described in Figure 3. The procedures can be repeated for other combinations of M and V and the longest calculated rock socket length based on the most critical combination of M and V will be adopted as the design rock socket for the propped embedded wall.

4 A WORKED EXAMPLE

A worked example is presented in this section to illustrate the analysis procedures of the suggested method. The input parameters for the worked example are shown in Figure 6. For simplicity of analysis, the following assumptions are made and parameters are used in this example:

- Wall friction angle is taken to be zero;
- Dry condition in soils;
- Submerged condition is assumed for rock, taking unit weight of water = 10 kN/m^3
- The coefficients of earth pressure are calculated based on the Rankine's theory of earth pressure
- The structural bending moment capacity M_R of the embedded wall is ignored, i.e. $M_R = 0$
- Design overall factor of safety is 2.0.
- Allowable horizontal bearing capacity of rock q_u = 1500 kPa

For this worked example, a closed-form solution can be derived for calculating the rock socket length, although it is beyond the scope of this paper. The analyses for two stages of excavation are considered. Stage 1 involves excavation to a depth of 1.5m before installing the strut at a depth of 1m. Stage 2 relates to excavation to a depth of 6m after installation of strut. The rockhead is assumed to be at the depth of 8.5m. The embedded wall acts a cantilever wall in Stage 1 and a propped embedded wall in Stage 2.

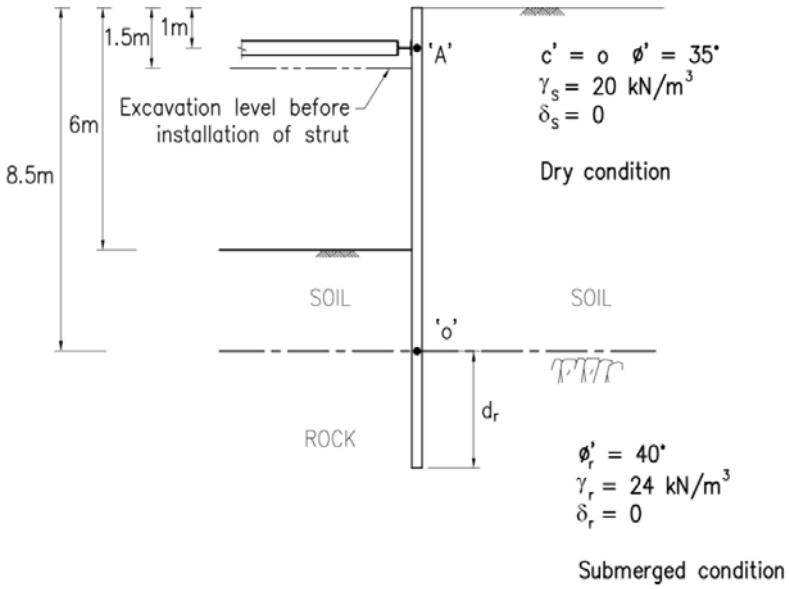

Figure 6: Details of worked example

4.1 Stage 1 – Cantilever stage

To assess the rock socket length required for this cantilever stage of excavation, the magnitude of M and V at the rock head can be obtained by considering force and moment equilibrium of soil pressures above point 'O'. An overall factor of safety of 2 is applied to the passive resistance of soil on the excavation side. By considering limiting force equilibrium, the magnitude of V is calculated to be –46.5 kN. By considering limit moment equilibrium about point 'O', the value of M is obtained as –44.9 kNm.

Since there are two equations available based on limiting force and moment equilibrium for solving V and M, the solution is unique. As the calculated values of V and M are both negative, the passive resistance offered by the soils on the excavation side will be sufficient to achieve the required factor of safety without a rock socket for Stage 1 excavation.

4.2 Stage 2 – Excavation after installation of strut

By taking moment about point 'A' at the strut level, the relation between M and V can be obtained using Eq.3 and the results are presented in Figure 7. As explained earlier, negative values of M should be

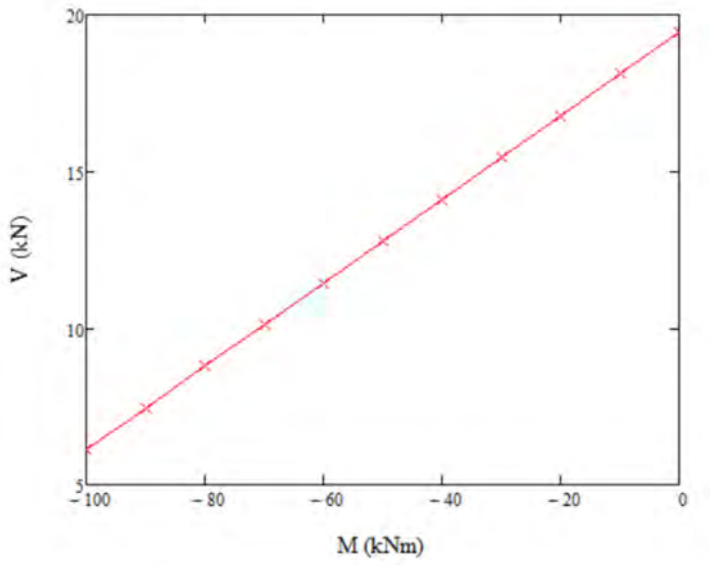

Figure 7: Relationship between M and V

selected for calculating the corresponding values of V because the sign conventions in Geoguide 1 as described in Figure 3 are adopted. When the restoring moment for preventing kickout failure is smaller (i.e. M being less negative), the shear force V needed to maintain limiting equilibrium will naturally be higher.

Using the selected value of M and calculated value of V shown in Figure 7, the required rock socket length for each of these pairs of M and V can be obtained using the formulas in Figure 3. The results are presented in Figure 8 with the calculated values of required rock socket length dr plotted against the selected values of M.

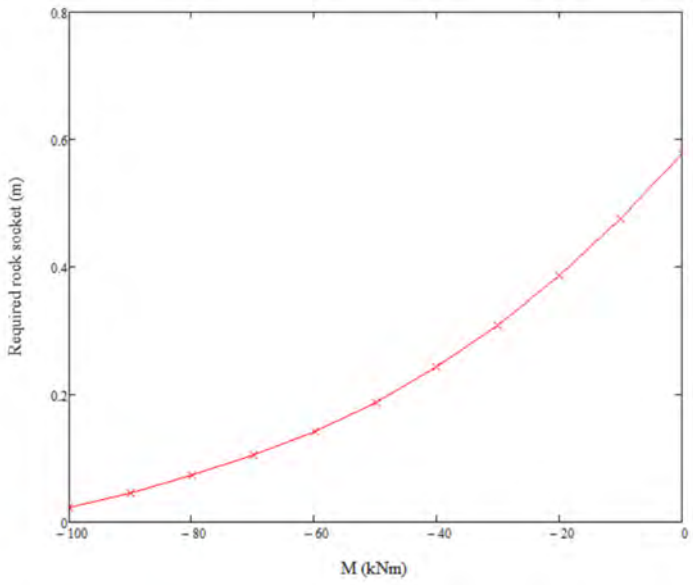

Figure 8: Required socket length for selected combinations of M and V for Stage 2 works

The required socket length is larger when the resisting moment is lower (i.e M being less negative). For design purpose, M can be taken as zero for simplicity of analysis and to be conservative. This gives a required socket length of 0.58m for this worked example for Stage 2 excavation. As the required rock socket for Stage 2 works is more critical than Stage 1 works, the design rock socket for the entire ELS works should be taken as 0.58m for this worked example.

5 DISCUSSIONS

The design checking for kickout stability of embedded wall is routinely performed by geotechnical engineers in Hong Kong when designing ELS works. The proposed method provides a consistent way in which the overall FOS (F) is applied to both the passive resistance in soils and in rock for an embedded wall partially socketed in rock.

The paper will end by presenting some Author's views regarding the current practice of ELS design in Hong Kong.

- The procedures for design checking in the current practice or the modified procedures discussed in this paper may be regarded as complex rules to force designers to provide a certain minimum embedment length for the embedded wall. The soil pressure distributions based on full active and passive pressure under limiting equilibrium state considered in the analyses are purely assumptions. They do not reflect the real distributions of earth pressure for propped embedded walls.
- The required minimum overall FOS for ELS design used in Hong Kong is high, particularly for private development projects regulated by the BD. The GCO Publication No.1/90 recommends a factor of safety of higher than 1.5 while the BD tends to prefer a higher overall FOS of 2.0. The author has compiled the following summary of percentages of BD approved ELS designs prepared by his firm for private development projects between year 2000 and 2009.

Table 1: Summary of overall FOS used for ELS design

Year	Proportion of designs based on overall FOS =1.5	Proportion of designs based on overall FOS =2.0
2000	0	100%
2001	10%	90%
2002	24%	76%
2003	0	100%
2004	15%	85%
2005	0	100%
2006	74%	26%
2007	37%	63%
2008	17%	83%
2009	0	100%

It can be observed from the above table that a design overall FOS of 1.5 was still acceptable to the BD for a reasonable percentage of ELS designs until the late 2000s. The requirement of an overall FOS of 2.0 was formally stated in Practice Note APP-57 issued by the BD in 2012 (BD, 2012). Limit state structural codes generally recommend load factors between 1.4 and 1.6. For checking of embedment length against hydraulic failure, the design factor of safety is commonly taken as 1.5. Such values are significantly less the minimum overall FOS of 2.0 required for kickout failure. Collapse of ELS works is controlled by the weakest link which is likely to be structural failure of the embedded wall or struts rather than insufficient passive resistance of soil/rock to prevent kickout failure.

As discussed by Li (2010), construction problems arising from ELS works are often caused by over-conservatism in design requiring long embedment length to be provided to achieve the required FOS against kickout failure. Perhaps, reviewing the minimum overall FOS required for ELS design is more critical than developing a consistent procedure for determining the socket length of rock-socketed embedded walls.

REFERENCES

Buildings Department (BD) (2012). *Practice Notes for Authorized Person, Registered Structural Engineer and Registered Geotechnical Engineer, PNAP APP-47*.

Geotechnical Control Office (GCO). 1990. *GCO Publication 1/90 - Review of Design Methods for Excavations*.

Geotechnical Engineering Office (GEO). 1982. *Geoguide 1 – Guide to Retaining Wall Design* (2nd Edition).

Geotechnical Engineering Office (GEO). 2014. *GEO Technical Guidance Note No.41 (TGN 41) - Annex A8. Issue No. 1.*

Li, K.S. and Lee, I.K. 1993. The assessment of geotechnical safety. *Selected Topics in Geotechnical Engineering – Lumb Volume* (Editor: K.S. Li). Department of Civil and Maritime Engineering, University College, UNSW, 195-229.

Li, V. 2010. A review of current practice for deep excavations in Hong Kong. *Proc. HKIE Geotechnical Division Annual Seminar*, 55-59.

Geotechnical Design from the Inside Out – Development of Automation Design Platform and BIM of MRT Geotechnical Engineering

Chih-Min Liou, Chen-Wei Hung & Cheng-Hsien Chang
Engineer, Mass Transit Engineering Department, Sinotech Engineering Consultants, Ltd

Chien-Ming Lai
Technical Manager, Mass Transit Engineering Department, Sinotech Engineering Consultants, Ltd.

ABSTRACT

Since 2011, countries around the world have started digital transformation after industrial revolution through automation and intelligentization. MRT engineering should also be transformed to automated and intelligent design. Owing to the complexity and huge amount of work within a limited time, MRT engineering design usually produces an inferior quality. Besides, geotechnical engineer design is placed at the end of whole MRT design process, so the tight schedule and heavy workload always trouble geotechnical engineers. Therefore, improving work efficiency and design quality by digital methods, preserving technical data, and checking the design accuracy become the main motivations for SINOTECH to develop design platforms. To put the digital transformation into practice, SINOTECH has developed three user-friendly website platforms, which are SinoExcavation, SinoTunnel, and SinoPipe. The standardize interface of input, output, and data validation reduce human errors. Furthermore, NTU BIM Research Center assisted SINOTECH in developing APIs to transform design parameters into BIM models automatically. In addition, the quantity calculations and conflict evaluation can be done by utilizing BIM model.

1 INTRODUCTION

Since 2011, as the advancement of science and technology, the Industry 4.0 has redefined the Manufacturing Industry. However, in the Construction Industry, management consulting McKinsey & Company published a paper titled "Imagining construction's digital future." It pointed out that due to the complexities of large-scale constructions, the delayed projects, low margins, and poor business processes were reasons to be changed. According to the digital transformation defined by International Data Corporation (IDC), digital transformation is a method to improve work efficiency, lower the cost, and optimize the customers' feeling by digital tools. Hence, the digital transformation seems like the solution to transform large-scale constructions.

From 2017, SINOTECH has started to wonder what is the best way for a Consultant Company to do a digital transformation. Therefore, SINOTECH established a BIM & Innovation Committee in 2018, and involved intelligence and automation to revolutionize all design tasks (standardize, automatize, and platformize the design process). Since then, SINOTECH has developed SinoExcavation, SinoTunnel, and SinoPipe website platform, and collaborated NTU BIM Research Center on Application Programming Interface (API) development. These APIs can link up analysis software and BIM software with Sino-platforms, and with user-friendly interfaces, this tool is able to reduce human errors and increase work

effectivity. The auto-generated BIM models from standard worksheets have many other applications that can improve our design quality. Additionally, all design parameter and all empirical references are well preserved in Sino-platforms can also provide the database for future designers to check their results.

2 SINO-PLATFORMS AND APPLICATIONS

The SINO-Platforms is the compilation of several platforms that was already planned by SINOTECH. Currently, from its plan there are 3 platforms that have been developed, which are Sino Excavation, SinoTunnel and Sinopipe. Each platform is specialized in one design scenario and targeted to increase work effectiveness and reduce errors.

2.1 Deep excavation engineering assisted by BIM automatic design (SinoExcavation)

In the traditional design process of deep excavation, designers needed to go through multiple Excel sheets to calculate, and managed each version were difficult. Moreover, the analysis results and the experiences might not be well preserved for the future use; also, the quantity calculation and quality control were time-consuming process. Therefore, SINOTECH has redefined the 3D design process to prevent these circumstances in the future. The design stages: (1) Automatic deep excavation design and analysis, (2) Automatic BIM generation, (3) BIM applications, (4) Data base and feedbacks.

(1) Automatic deep excavation design and analysis
Instead of using multiple Excel sheets, all the calculations are done inside the SinoExcavation platform. This can help to organize each calculation. The platform provide a user-friendly interface that guides its user on step-by-step deep excavation analysis, started from inputting soil strata parameters and ground water levels, computing excavation safety (toe stability analysis and excavation surface stability), determining construction sequence, and finally analyzing wall and supporting system stresses.

To analyze retaining wall and supporting system stresses, SINOTECH usually employs geotechnical calculation software for excavation purposes, i.e. RIDO. This process is very time consuming, since the analysis need to be optimized. To ease this cycle, SINOTECH has developed a Windows Forms (Winform), which can iterate RIDO analysis automatically. In each iteration, both strut section and its preload forces are check and adjust automatically. The optimized RIDO results are uploaded to SinoExcavation platform, and the important results are presented in the platform pages, which are shown in Figure 1. Based on these results, designer can design the retaining wall and other supporting system. After doing all the calculation, SinoExcavation can automatically generate design report for this retaining wall type.

Figure 1: (Left) The Winform interface, which can automatically call RIDO to conduct the iteration itself (Right) The analytical results will be kept in SinoExcavation platform

(2) Automatic BIM generation
After concluding the stage (1), SinoExcavation also can generate standard sheet, containing all excavation model information, including diaphragm wall and all supporting system members. Then input the sheet and diaphragm wall 2D drawing plan into SinoExcavation REVIT API to automatically build the BIM model, which is shown in Figure 2.

Figure 2: The process and interfaces of SinoExcavation auto-generate BIM models

(3) BIM applications
From the generated BIM model in Stage (2), we can the same use API to draw 2D drawing. Furthermore, it can also generate a quantity calculation report base on the current model. This automated program has helped reducing errors. Moreover, this BIM model can help to do conflict management and 4D simulations, which is shown in Figure 3.

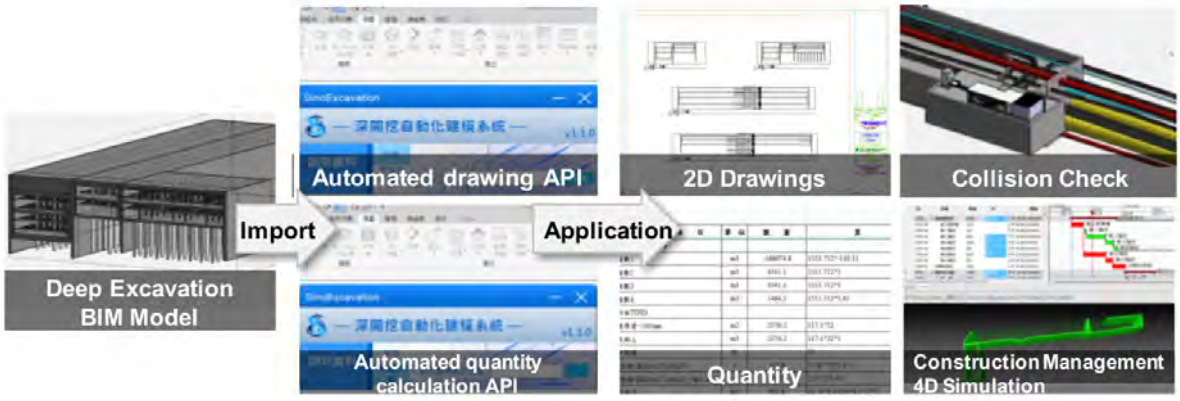

Figure 3: Applications of BIM models

(4) Data base and feedbacks
Since all workflows are done within SinoExcavation platform, every design parameters, analytical results, and reports from a project is automatically archived in the platform. Furthermore, all the previous projects that was designed by SINOTECH can be inputted into the platform to further broaden its database. This excavation database can be used as training tools for the future designer. Also, the past study about deep excavation design and analysis from Zhan (1992), Ou et al. (1993), Hsieh et al. (1996), Ji et al. (1999), Wang and Hsieh (2007) has been included into the platform which can help to verify our design, please see Figure 4.

2.2 Shield tunnel engineering assisted by BIM automatic design (SinoTunnel)

There are the same difficulties as deep excavation when it comes to shield tunneling design, such as: multiple Excel sheets, all previous design parameters need to be collected manually and hard to make use as a reference. Similar to deep excavation, there are 4 stages on how SinoTunnel can improve design workflows.

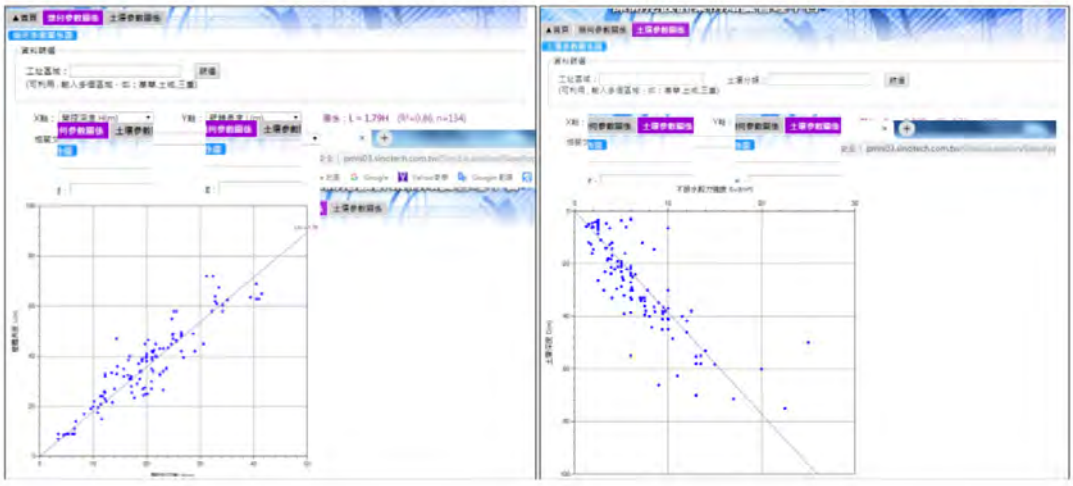

Figure 4: Past study and project data about deep excavation design are included into the platform

(1) Automatic shield tunneling design and analysis

Before inputting into the SinoTunnel, The dynamic envelope and vehicle clearance envelope are needed to firstly generated, which is based on each alignment and Metro planning manual. This procedure is done to confirm whether the tunnel internal space is sufficient. Only then, process to design shield tunnel lining can be carried out. In the design phase, the stress analysis by simulating several different load conditions on to lining was done in the structural analysis software, SAP2000. To simplify the iteration process, SINOTECH has also developed a Winform interface, which can automatically call SAP 2000 to conduct iteration, which is shown in Figure 5. Lastly, the final convergence results will be kept on SinoTunnel platform (Figure 6), to provide data for further safety analysis and section design.

Figure 5: The Winform interface, which can automatically call SAP 2000 to conduct the iteration itself

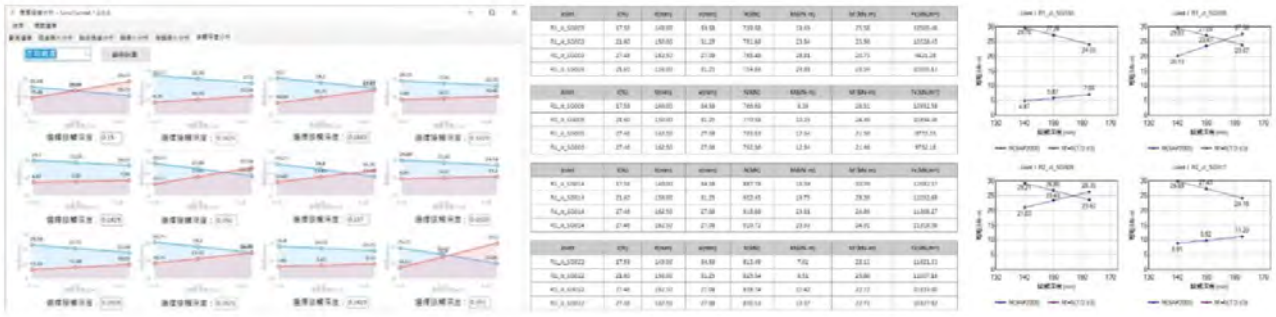

Figure 6: The analytical results will be kept on SinoTunnel platform

(2) Automatic BIM generation
From stage (1), SinoTunnel platform records all design parameters (i.e. tunnel lining's diameter, width, thickness, etc.) from analytical results. The supplementary information, such as alignment, cant, invert, walkway, track bed, etc also need to be inputted into the platform. Only then, the standard sheets, containing shield tunnel model information, can be downloaded from SinoTunnel platform as the main input for REVIT API to build BIM Model. All of these processes are summarized in Figure 7.

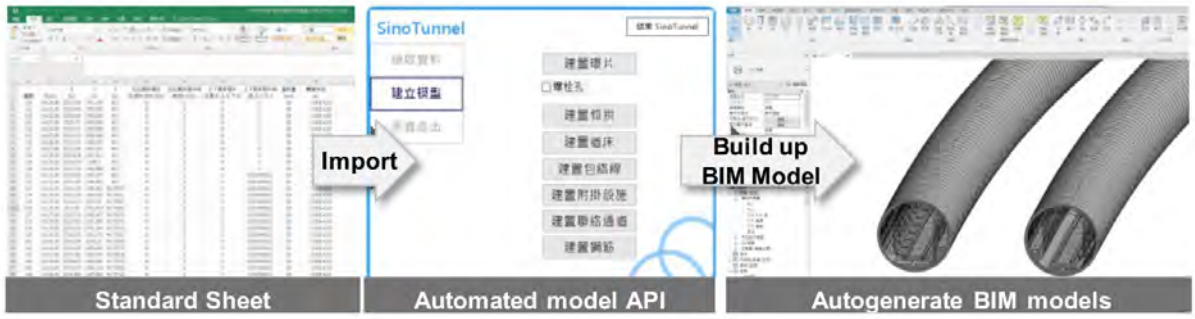

Figure 7: The process and interfaces of SinoTunnel auto-generate BIM models

Numbers of tunnel BIM elements generated by the API are enormous and complex. In summary, the items and models are listed below and shown in Figure 8:

A. Segments and invert: FST invert, standard track invert, ditch, and walkway
B. Track bed: floating slab track (FST), standard track, rails, and conductor rail
C. Envelopes: dynamic envelope, vehicle clearance envelope, and conductor rail envelope
D. Tunnel ancillaries, cross passage, and rebar

Besides, if some design components need to be revised, the relations between envelopes and the shield tunnel need to be examined all over again. Through the auto-generated envelopes, designers can check the conflict at all times, which make this workflow much more efficient.

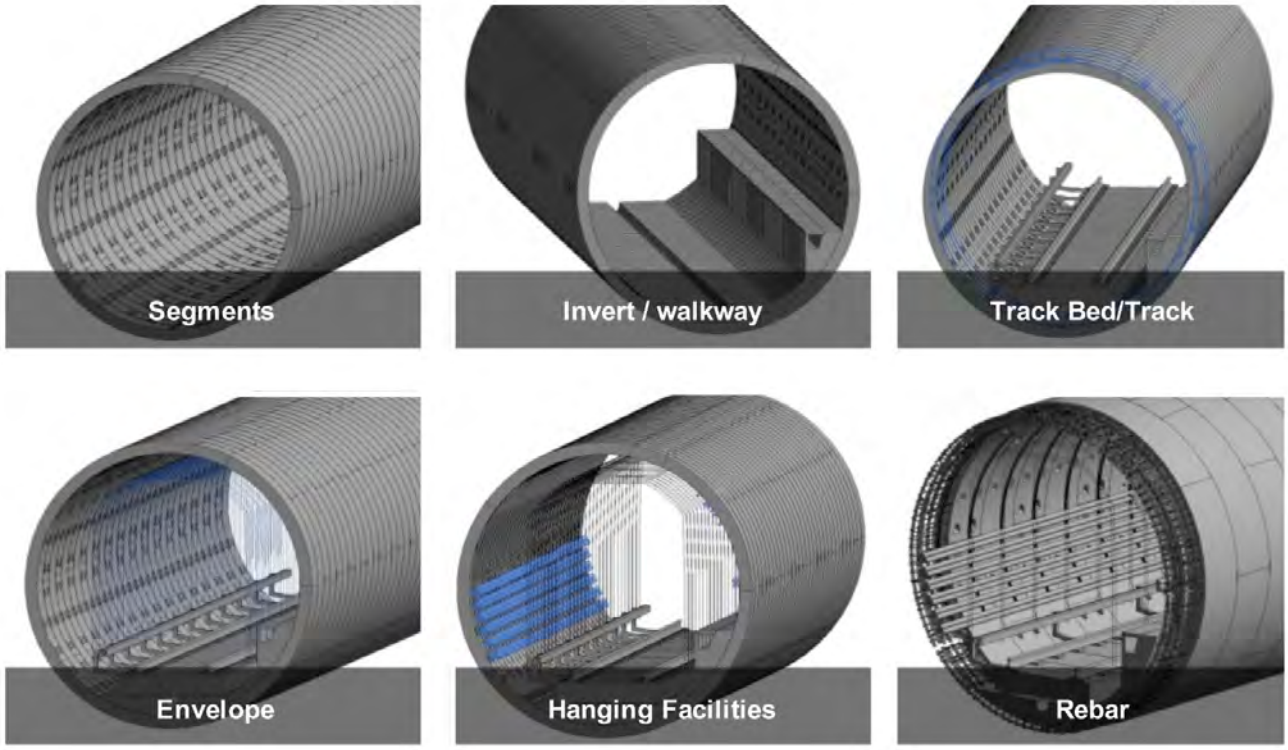

Figure 8: All kinds of tunnel BIM elements

(3) BIM applications
After we finished building BIM models in stage (2), BIM models can be transferred into 2D drawings by using the API. Moreover, the quantity calculation reports can also be generated through the API (Figure 9). When there are some modifications in the design, all the corresponding data will be revised instantly, which can efficiently assist designers to examine their results.

Figure 9: The process and interfaces of SinoTunnel auto-generated quantity calculation

(4) Data base and feedbacks
With the assistance from SinoTunnel, all the design information involves envelope data, shield tunnel data, and BIM data, can be well preserved on the platform. Similar to SinoExcavation, the SinoTunnel contains analysis references and specifications that are carried out according to AFTES (2005), JSCE (2007), DAUB (2013), ACI (2016), etc. Therefore, designers can apply the analysis precisely based on these experiences and feedbacks (Figure 10).

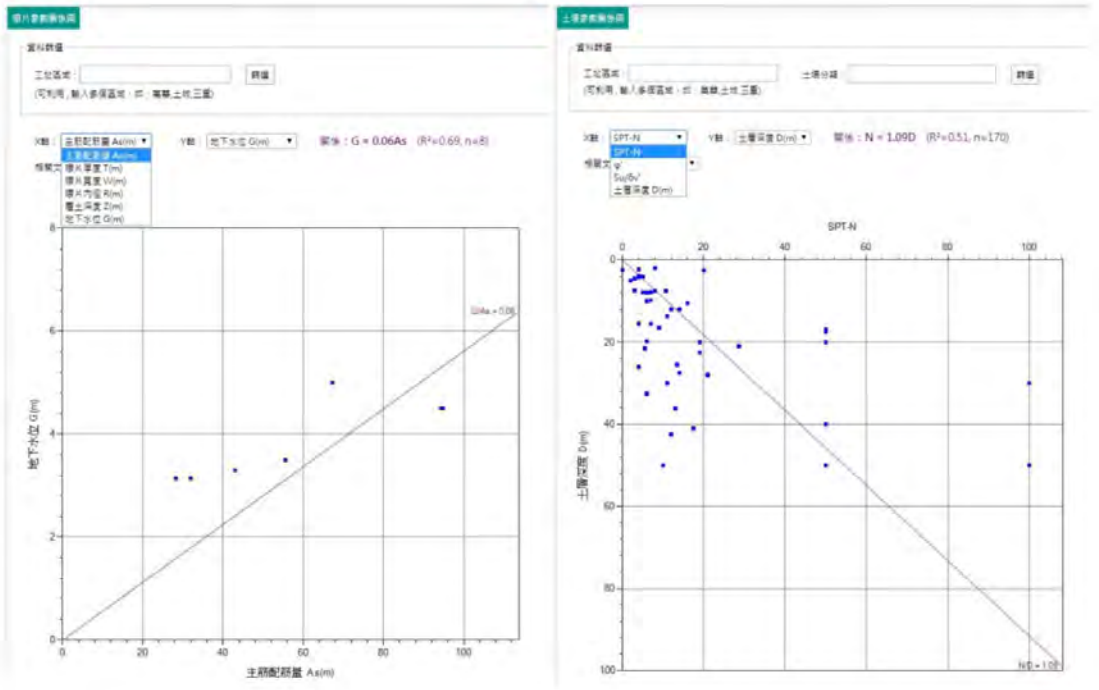

Figure 10: Past project data and specifications about shield tunneling design are included into the platform

2.3 Pipeline engineering assisted by BIM automatic design (SinoPipe)

There are multiple underground pipes like sanitary sewer, foul sewer, rainwater drains, etc, which are our daily life necessity. However, with the increasing amount of pipes and the underground space is limited, the spatial relations and database creation of pipes become urgent and essential. Hence, SINOTECH has evolved into a 3D automatic system named SinoPipe. We replace the old procedure with

new concept to shorten the design period. More importantly, the considerable database can be well organized on the platform, and allow designers to integrate in their design.

The SinoPipe working stages are as follows: (1) Input pipe database, (2) Automatic BIM generation, (3) BIM applications.

(1) Input pipe database

We start up a series of standard sheets, and each sheet contains the identities of pipes and manholes. The sources of these identities can be divided into two types, survey data and 2D CAD drawings (see Figure 11).

Figure 11: The process from input data to standard sheets

(2) Automatic BIM generation

Through the API, the sheets can be transfer into BIM models, like tubes, box culverts, manholes, and valves. After that, we can import the existing pipes models into BIM to evaluate overall status (see Figure 12).

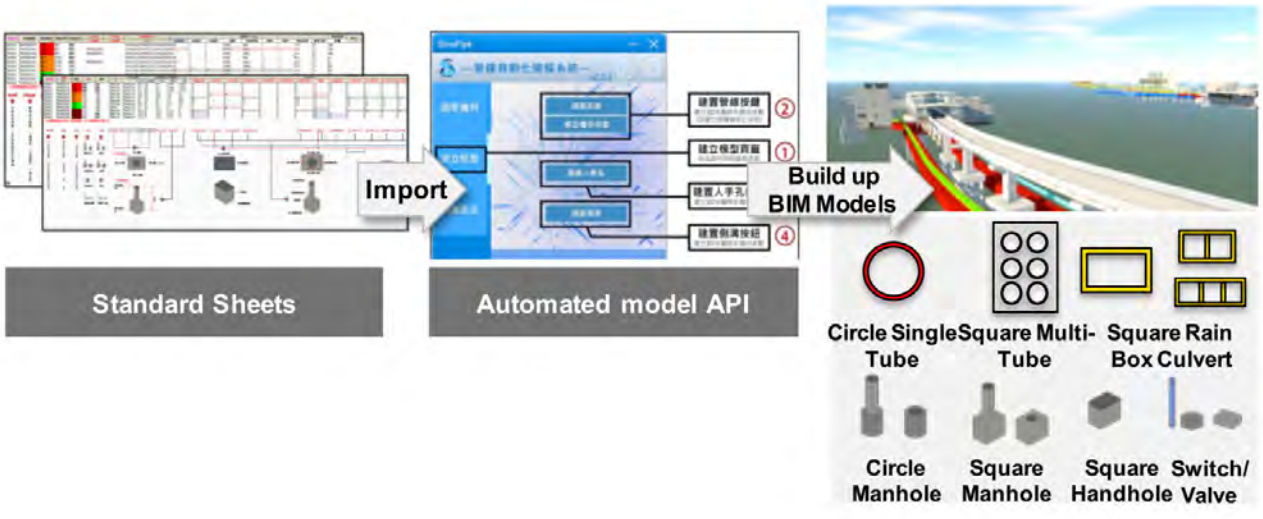

Figure 12: The process from standard sheets to BIM model

(3) BIM applications

When we finished building BIM models from stage (2), we can then apply many other advance functions including collision check, 2D drawings, and quantity calculation. Moreover, we can combine tunnel models (from SinoTunnel) and pipe models (from SinoPipe) to come up with the composite cross section diagram, which can save more time of integrating different professions (see Figure 13).

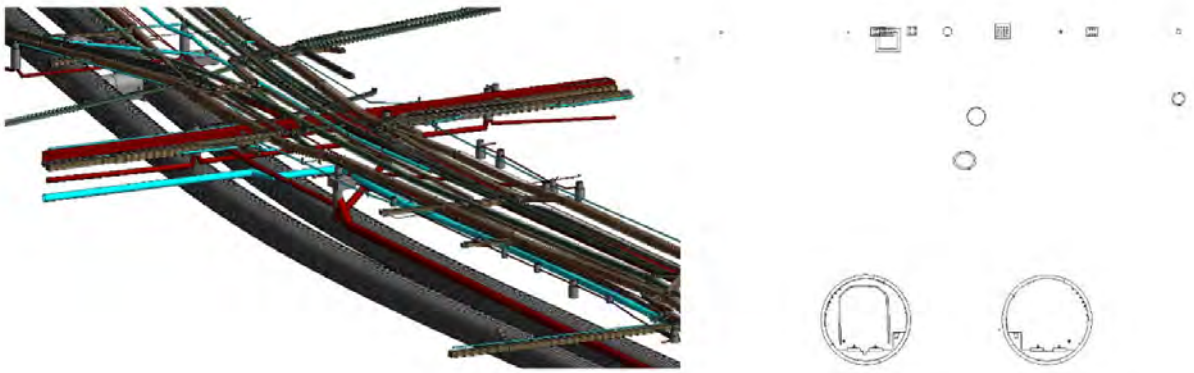

Figure 13: (Left) Tunnel models and pipe models, (Right) The composite cross section diagram

3 CASE STUDY

SINOTECH has put these Sino-platforms into practice, that is, we utilized these three platforms to fully design Taipei MRT detail design project. These platforms have significantly reduced the iteration time in comparison to the traditional design work flow. Furthermore, the automatic BIM model generation has also proved reduce all drawing and quantity computation time. Since all of these works has done in Sino-platforms, all data and experience were all recorded inside the platform, which can be used as references for other project.

In this project, the database has proven to be powerful tools when designing underground station's retaining wall system. These assessments from the previous projects has assisted us to reasonably

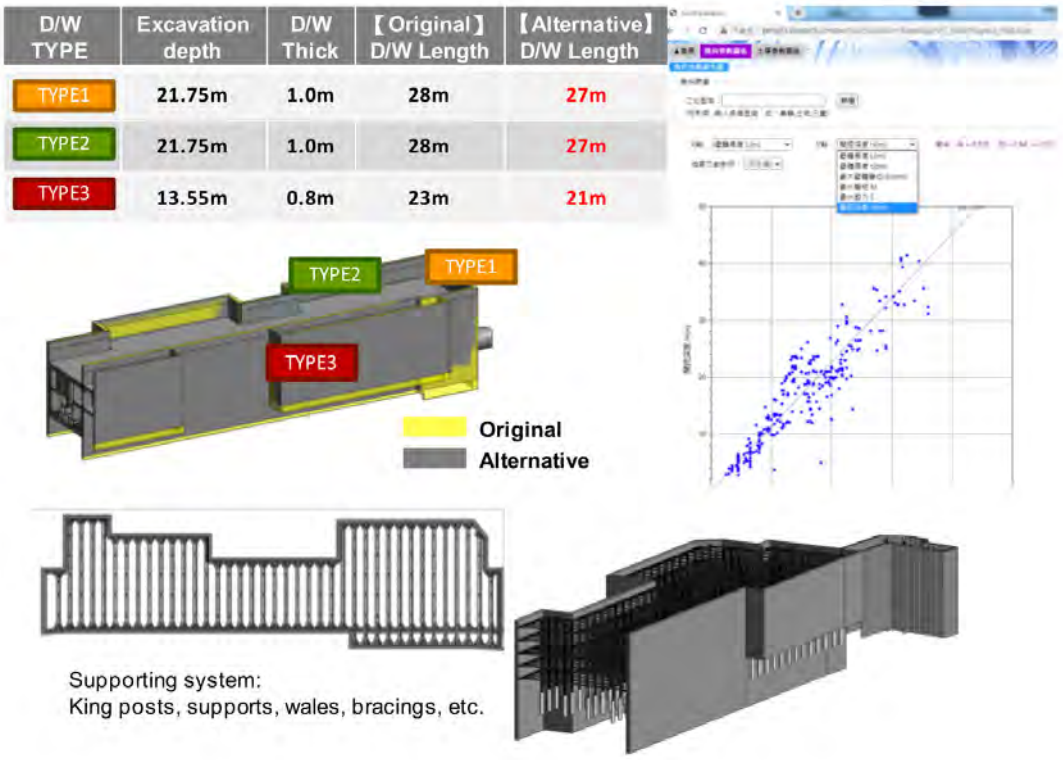

Figure 14: Use past design feedbacks to revise the diaphragm wall parameters

shorten the wall length, and re-adjusted the strut spacing based on in-situ geological condition (see Figure 14). Additionally, the combined BIM models, from three platforms, has facilitated engineers to check conflict and lower the construction risk (see Figure 15).

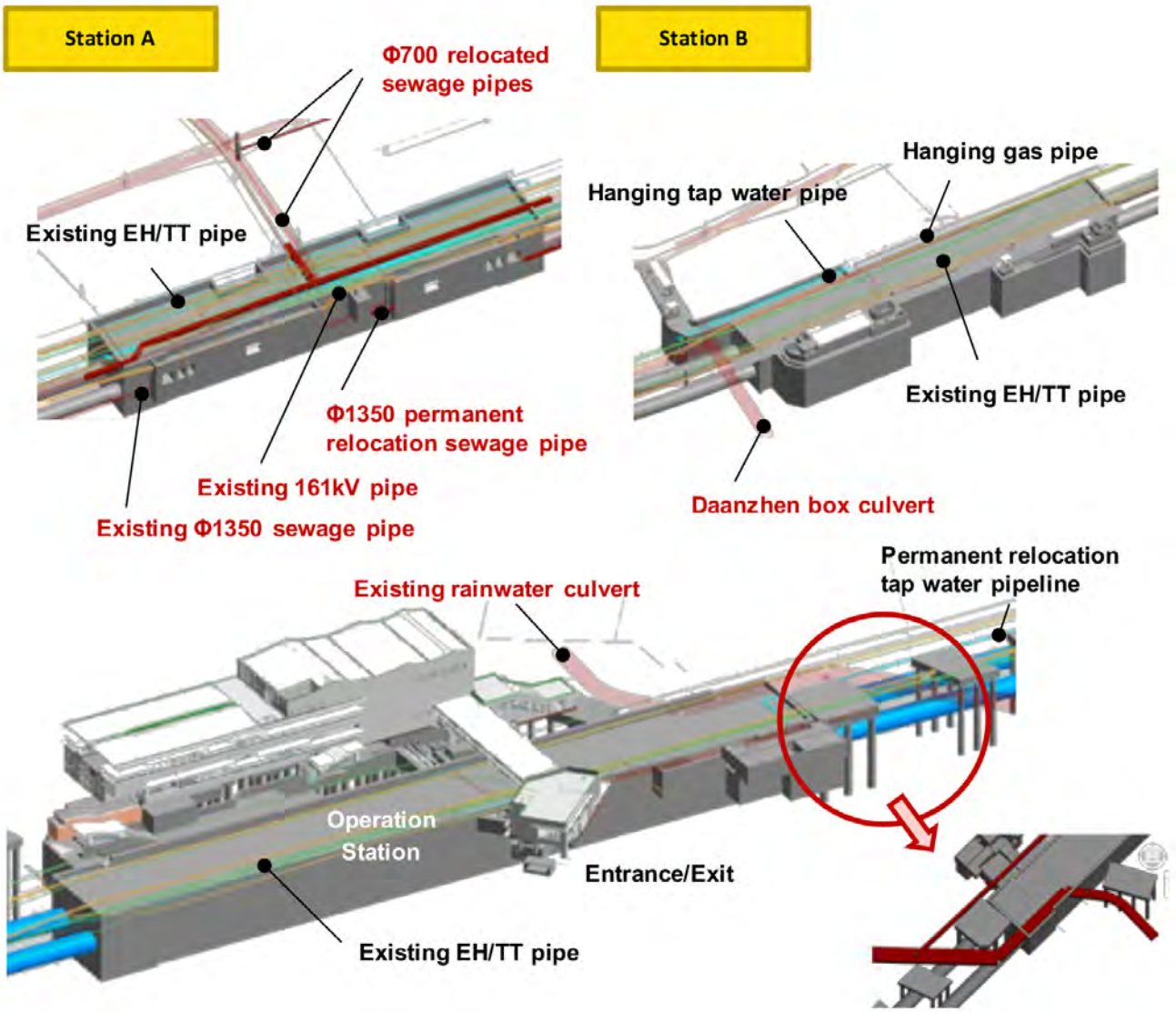

Figure 15: Collision check between structures and pipes

4 CONCLUSIONS

SINOTECH has led toward digital transformation by revolutionize the traditional 2D design, and using 3D digital simulation to redefine the construction design task. As mentioned, SINOTECH has been committed to reinvent whole design process by standardizing, automatizing, and platformizing.

First, standardizing makes our work more efficient by using a user-friendly interfaces platform. Secondly, with the automatizing, we can automatically generate 3D BIM models once the results are done analysis.Furthermore, each BIM element contains its own information, which can assist designers to analyze more effectively. Thirdly, due to the great amount of analytical data, we need a space to archive it. So we built website platforms and input all the previous project data onto them, which can provide valuable references for future engineers. To do so, we expect that we can apply it into analysis precisely based on these experiences and feedbacks in the upcoming projects.

International Data Corporation (IDC) has predicted that the global digital transformation would enter into “Transform 2.0 generation” in 2020. The enterprise would focus on “Data-Driven” instead of

previously “Digital-Led”. Through the rapid growth of information and technology in 21st century, all works of life start to have the awareness of digital transformation, and propose to digitize the data and automatize all the operation. With the preserved data and information all these years, this database can be used as the basis of intelligence in the future. Apparently, the digital transformation also becomes the vital task to the civil engineering market. Hence, SINOTECH published this paper to introduce our progress as a breakthrough into digital transformation in construction industry.

REFERENCES

ACI 544.7R(2016). Report on Design and Construction of Fiber Reinforced Precast Concrete Tunnel Segments. American Concrete Institute (ACI).

AFTES (2005). Recommendation for the design, sizing and construction of precast concrete segments installed at the rear of a tunnel boring machine (TBM). French Tunneling and Underground Space Association (AFTES). Paris, France.

Clough, G.W. and O’Rourke, T.D. (1990), Construction induced Movements of Insitu Walls, Design and Performance of Earth Retainings Structure, ASCE Special Conference, p.439-470.

DAUB (2013). Lining segment design: Recommendations for the design, production, and installation of segmental rings.

Ou, C.Y., et al. (1993), Characteristics of Ground Surface Settlement during Excavation, Canadian Geotechnical Journal, Vol. 30, No. 5, p.758-767.

Chi, S.Y., Cherng, J.C., and Wang, C.C. (1999), Information Construction Approach for Deep Excavation, Proc., Int. Symposium Geotechnical Aspects of Underground Construction in Soft Ground, Balkema, Rotterdam, The Netherlands, p.471–476.

Jan, J.C., Chi, S.Y. and Cherng J.C. (2001), Prediction of Diaphragm Wall Deflection in Deep Excavation Using Artificial Neural Networks, Computer Methods and Advances in Geomechanics.

Jan, J.C., Hung, S.L., Chi, S.Y., and Cherng, J.C. (2002), Neural Network Forecast Model in Deep Excavation, Journal of Computing in Civil Engineering, Vol. 16, No. 1.

JSCE (2007). Standard specifications for tunneling-2006: Shield tunnels. Japan Society of Civil Engineers (JSCE).

Zhan, S.H. (1992), Deep Excavation Numerical Analysis in Taipei City, Master's Thesis, National Taiwan University of Science and Technology. [詹尚宏(1992), 臺北市區深開挖之數值分析, 臺灣工業技術學院碩士論文]

Hsieh, H.S., Cherng, J.C., Tsai, T.H., Yang, M.J. (1996), Practical Considerations on Diaphragm Wall Analysis, Sino-Geotechnics, Vol. 53, p.35-p.44. [謝旭昇、程日晟、蔡宗鍠、楊明洲(1996), 連續壁設計分析之實務考慮, 地工技術, 第 53 期, p.35-44]

Ji, S.Y., Wang, C.C., Chen, J.Q., Lin, J.C., Tsai, M.H. (1999), Case Study and Feedback analysis of Deep Excavation in Taipei Basin, Study Report of Sinotech Engineering Consultants, Inc. [冀樹勇、王建智、陳錦清、林金成、蔡明欣(1999), 台北盆地深開挖案例資料蒐集與參數之回饋分析, 財團法人中興工程顧問社研究報告]

Construction and Planning Agency (2001), Design Code and Specifications of Building Foundations, Construction and Planning Agency. [內政部營建署(2001), 建築物基礎構造設計規範, 內政部營建署]

Wang, C.C., Hsieh, K.H. (2007), A Study of Engineering Characteristics and Optimized Soil Parameters of Deep Excavation in Kaohsiung Area, Journal of Kaohsiung University of Applied Sciences, Vol. 36, p.309-320. [王建智、謝坤宏(2007), 高雄深開挖工程行為特性與土層參數最佳化分析, 高雄應用科技大學學報, 第36期, p.309-320.]

Department of Rapid Transit Systems, Taipei City Government (2014), Civil Engineering Design Guidelines of Taipei Mass Rapid Transit Systems, Chinese Version No. 1. [臺北市政府捷運工程局(2014), 臺北都會區大眾捷運系統土木工程設計準則, 臺北市政府捷運工程局, 中文版第01版]

Design of Protection Measures for Deep Excavation of A New Underground Station Closely Adjacent to Viaduct of MRT System in Operation

Liu, Cheng, Lee, Yi-Ting, Sung, Shang-Ping, Tsai, Yuan-Yao, Lin, Heng-Tzu
CECI Engineering Consultants, Inc., Taiwan

ABSTRACT

Due to limited land space in urban area, interchange MRT stations have to be constructed closely adjacent to existing system. Geotechnical design of new station has to ensure the safe operation of existing line. This paper presents a new underground MRT station located within 1 m of the foundation of viaduct of MRT line in operation with ridership more than 200,000 persons per day. Deformations inducted by deep excavation have to be controlled Deformations induced by deep excavation have to be controlled carefully to meet the rigorous limit values set up by Regulation of Building Restrictions along MRT Facilities. Sophisticated 2D/3D finite element (hereafter FEM) analyses have been performed to simulate the sequence of diaphragm wall constructions and Bottom-up deep excavation with pre-stress strut system. Deformation behaviors of adjacent viaduct foundation and pier are evaluated carefully. Various protection measures such as ground improvement of double packer grouting, buttress wall to enforced diaphragm wall and enlargement of existing pile caps are simulated and studied. The results demonstrate that combination of pile cap enlargement and grouting provide best protection of existing pile foundations.

1 INTRODUCTION

A new underground interchange station is located close to the viaducts of MRT line in operation to provide platform-to-platform transformation services. Excavation of the new station has to ensure the safe operation of the existing MRT line which provide more than 200,000 daily ridership.

Dimitrios Iliadelis (2006) indicated that in dense urban environments where land is scarce and buildings are closely spaced, cut-and-cover excavations are widely used for basement construction and development of underground transit facilities. Maruf and Darjanto (2015) indicated the excavation next to existing building or structure is one of the most problems in geotechnical practices. Research and investigation in this area had been conducted till recent time. Mandy Korff et al. (2016) indicated that underground construction supports the quality of life in cities by improving the availability and quality of the space above ground. Tunnels and deep excavations can, however, not be realized without affecting adjacent structures.

This paper presents the analysis and design of various protection measures for deep excavation around 24m adjacent to the foundations of viaducts in operation. This study conducted with 2D/3D FEM methods to simulate the ground condition, engineering properties of two systems, construction arrangements and processes.

2 GEOTECHNICAL PROPERTIES

Information about the soil conditions along this area was interpreted from geotechnical investigation results at site and laboratory. Three geological bore holes with depths around 30 m have been conducted in this area. The geotechnical properties and design parameters are listed in Table 1. The ground formation in this area are divided into five layers, which includes backfill sand, silty clay, silty sand, boulders, and soft sand stone and shale interbedded, respectively. Ground water table is around 5m to 11m below ground surface.

Table 1: Geotechnical Parameters for Design

Layer	Soil type	Depth (m)	γ_t (t/m^3)	S_u (t/m^2)	C' (t/m^2)	ϕ' (degree)	E (kN/m^2)
1	SF	6	2	–	2	30	15385
2	CL	9	1.85	3	–	–	15000
3	SM	14	1.9	–	0	30	15385
4	GM	17	2	–	0	33	76923
5	SS/SH	40	2.47	–	5.6	35	104710

where γ_t: total unit weight of soil, S_u: undrained shear strength of soil, C': drained shear strength of soil, ϕ': drained friction angle, E: modulus of elasticity of soil.

3 STRUCTURAL INFORMATION OF RETAINING WALL SYSTEM AND EXISTING FOUNDATIONS OF VIADUCT

The depth of excavation of the new underground interchange station is 24 m. To minimize the impact of exist MRT line in operation, high stiffness and water tight diaphragm wall system is adopted. The thickness of diaphragm wall is 1.0 m to ensure the safety, constructability and economy of retaining wall system. Due to the rigorous rail deformation limits, displacement less than 15 mm, inclination less than 1/750, set by Regulation of Building Restrictions along MRT Facilities, additional protection measures are required to install around the adjacent foundation of viaducts.

The location of the new underground station and the existing viaduct foundations is shown in Figure 1. The foundations of viaducts (number 01, 02 and 03) located close to the new underground station. The distance between the existing foundations to the diaphragm wall is about 1 m. The foundation type is concrete bore piles with diameter of 1.2 m and length varied from 13.5 m to 16.0 m. The thickness of the concrete pile caps are 1.2 m and the overburden is about 2.0 m. The configuration profile of existing foundations of viaduct is shown in Figure 1.

4 DESIGN OF PROTECTION MEASURES

Protecting the existing foundation adjacent to new underground station is studied with FEM method to simulate the construction arrangements and processes. Both two dimensional and three dimensional FEM modeling have been performed.

4.1 Numerical analysis in FEM for simulating various methods to protect adjacent foundations

4.1.1 Two dimensional model

The advantage of two dimensional analysis is time efficient and resources saving. Various construction schemes and alternatives can be studies quickly. Sensitive parameters and critical deformations can be identified through parametric studies. It is observed that ground improvement at greater depths, more than 6 m below ground surface provide better control of lateral deformation induced by excavation of underground station.

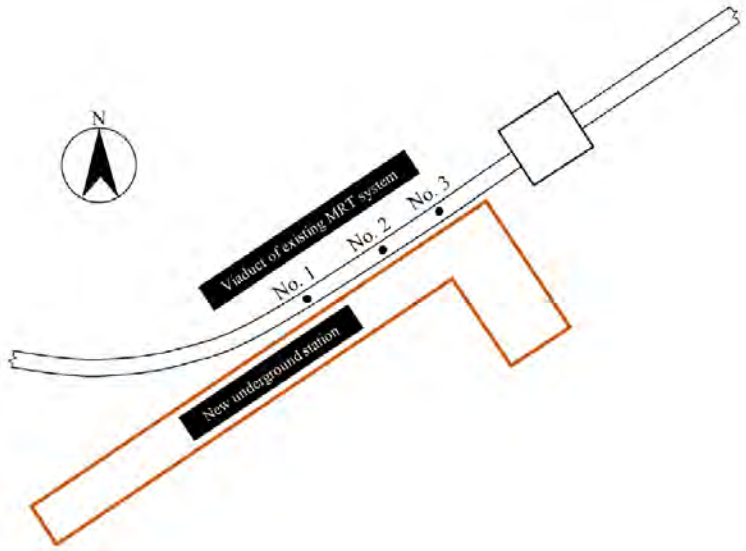

Figure 1: Relative position of the new station and existing viaduct foundations

Figure 2 shows the sections of 2D FEM model and Table 2 shows the geometric characteristics of the numerical model. The fine element generation mesh as shown in Figure 3. Diaphragm walls were constructed to 26 m below the ground surface with six levels of bracing systems and 16 construction steps to simulate the actual construction processes. The ground water level was set at 8 m below the ground surface. Two schemes of double-packer low pressure grouting ground improvement protection measures have been studied as shown in Table 3. The grouting material properties show in Table 4. Due to the new station close to existing foundations, high grouting pressure would disturb the soil around the existing foundations. The grouting with high pressure is not feasible. Low pressure double packer grouting in silty sand and boulder formation (9 m below ground surface) is adopted as major grout improvement measures.

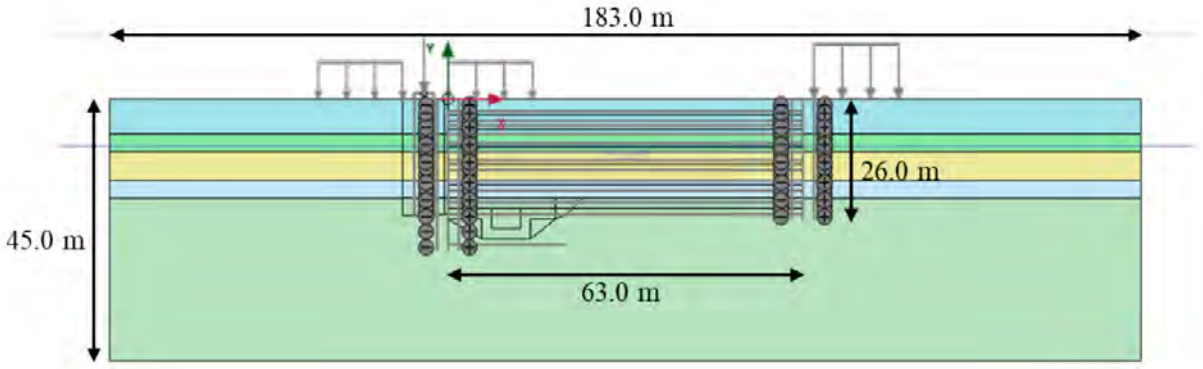

Figure 2: Model geometry in FEM 2D

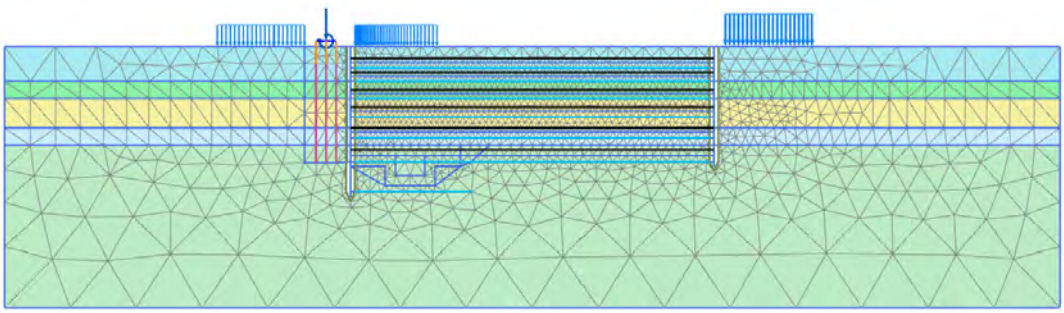

Figure 3: Fine element generation in FEM 2D

Table 2: Geometry characteristics of FEM 2D model

Geometry characteristics	Values
Dimension of the model	183.0 x 45.0 m
Depth of excavation	24.0 m
Width of excavation	63.0 m
Thickness of diaphragm wall	1.0 m
Depth of diaphragm wall	26.0 m

Table 3: Schemes of ground improvement for 2D simulation

Scheme	Methods	Contents
1	Ground improvement below pile cap	Grouting from 9 m below ground surface to bottom of pile to strength the pile foundation
2	Ground improvement between pile foundation and diaphragm wall	Grouting between pile cap and diaphragm wall from 9 m below ground surface to bottom of pile

Table 4: Grouting material properties

γ_t (t/m^3)	S_u (t/m^2)	C' (t/m^2)	ϕ' (degree)	E (kN/m^2)
22.0	50	–	–	20000

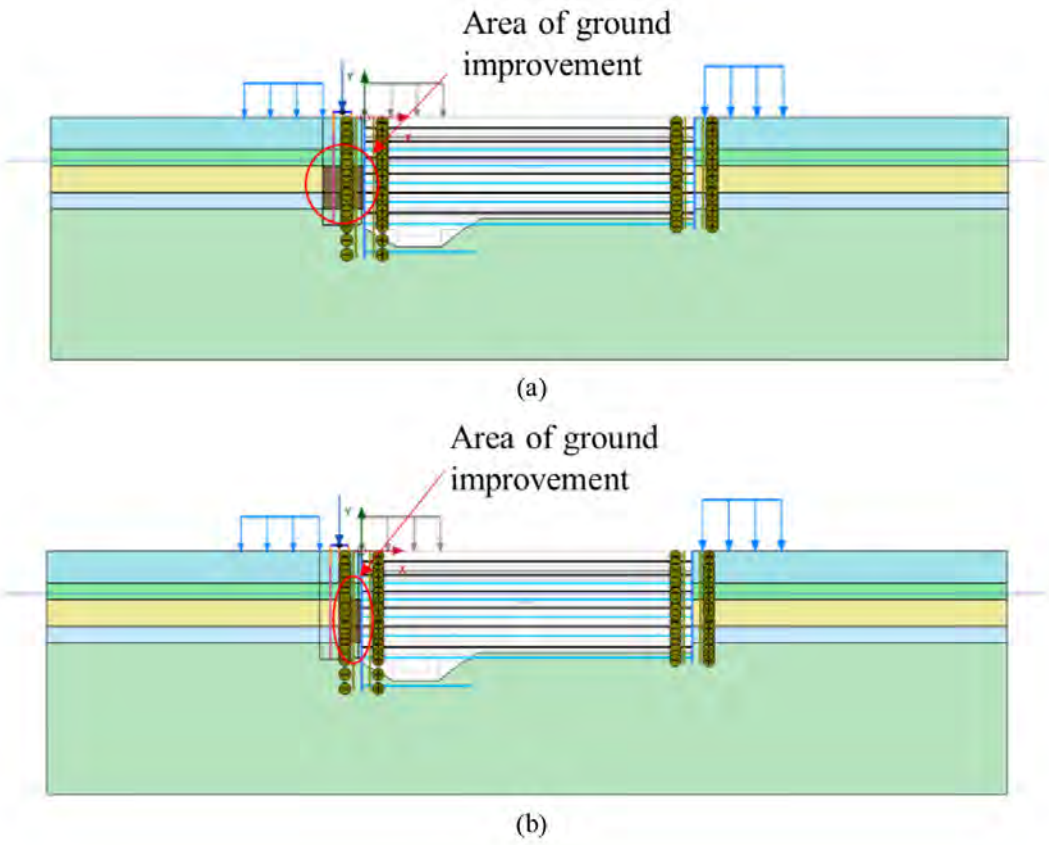

Figure 4: Foundation improvement with double packer low pressure grouting

Scheme 1 is to study the performance of grouting to pile group from 9 m below ground surface to bottom of pile and Scheme 2 is to simulate the effects of grouting between the existing piles and new diaphragm wall as shown in Figure 4 (a) and (b), respectively. Results of numerical analysis of Scheme 1 show maximum horizontal displacement of existing pile is 10.7 mm and the inclination value is 1/614. Both deformation values are exceeding the limit values of 15 mm and 1/750 specified in the regulation. Results of numerical analysis of scheme 2 yield the maximum horizontal displacement of 12.2 mm and inclination value of 1/685. Obviously, the performance of scheme 2 is much better, but the inclination amount is exceeding the limit value of regulation.

Both of the results of 2D FEM analysis cannot fulfill the limit values specified by the regulations. Part of the reasons is because the two dimensional analysis has simplified the three dimensional behavior into plan strain model which will yield too conservative results and costly solutions.

4.1.2 Three dimensional model

Based on the results of parametric studies of two dimension analysis, three protection schemes have been established to consider the effects of ground improvement and strengthening of existing pile foundation by three dimensional FEM analyses methods. The geometric characteristics of 3D model are shown in Table 5. The fine element generation mesh is shown in Figure 5. Ground improvement, cross walls installation and pile caps enlargements are simulated and evaluated as summarized in Table 6.

Scheme 1 utilize double packer grouting 9 m below ground surface to bottom of piles as shown in Figure 6(a). Scheme 2 provide buttress walls and cross walls to integrate with diaphragm wall of new underground station to minimize the deformation induced by excavation as shown in 6(b). Scheme 3 is to expand the existing pile caps and installed the pre-packed piles to confine the foundation as illustrated in Figure 6(c). Figure 7 illustrated the dimension of existing pile caps expanded. The diameter and length of each pre-packed pile bent installed around the pillars is 0.6 m and 15.8 m, respectively.

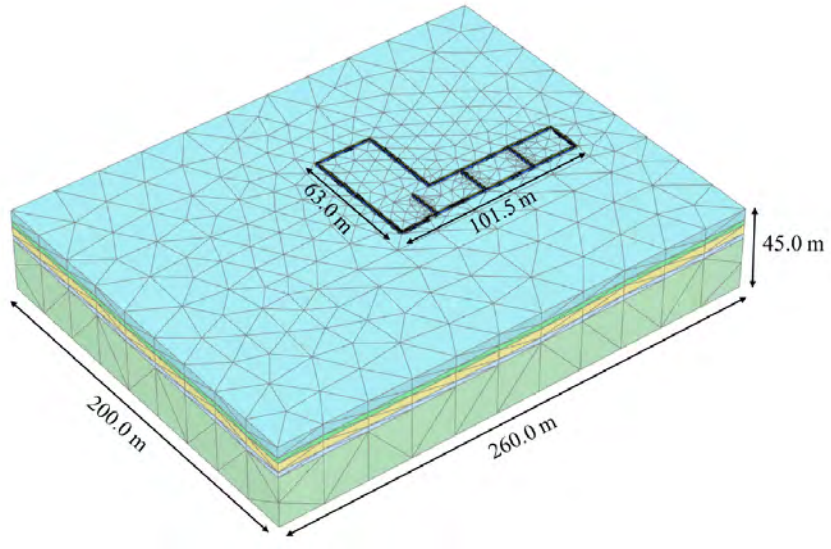

Figure 5: Fine element generation in FEM 3D

Table 5: Geometry characteristics of FEM 3D model

Geometry characteristics	Values
Dimension of the model	260.0 x 200.0 x 45.0 m
Depth of excavation	24.0 m
Width of excavation	63.0 m
Length of excavation	101.5 m
Thickness of diaphragm wall	1.0 m
Depth of diaphragm wall	26.0 m

Table 6: Schemes of Protection Measures for 3D Simulation

Scheme	Method	Content
1	Double packer grouting	Grouting from 9 m below ground surface to bottom of pile to strengthen the pile foundation
2	Buttress walls and cross walls	Installation of Buttress walls and cross walls adjacent to existing viaduct foundation
3	Pile caps enlargement and pre-packed piles	Enlargement of existing pile caps to 8.1* 8.1 m and installation of pre-packed piles to confine the pile foundation

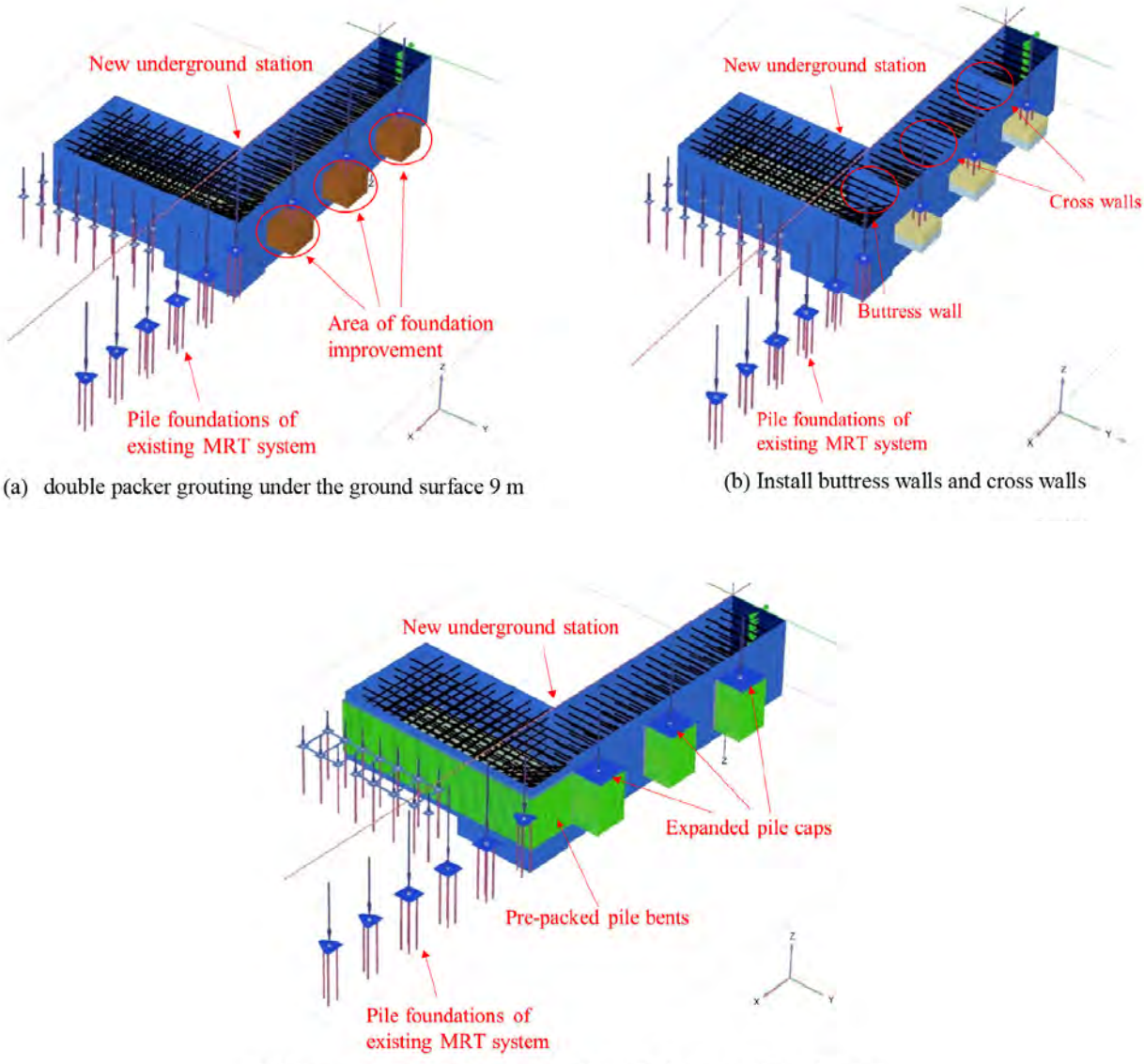

Figure 6: Existing foundations protecting methods

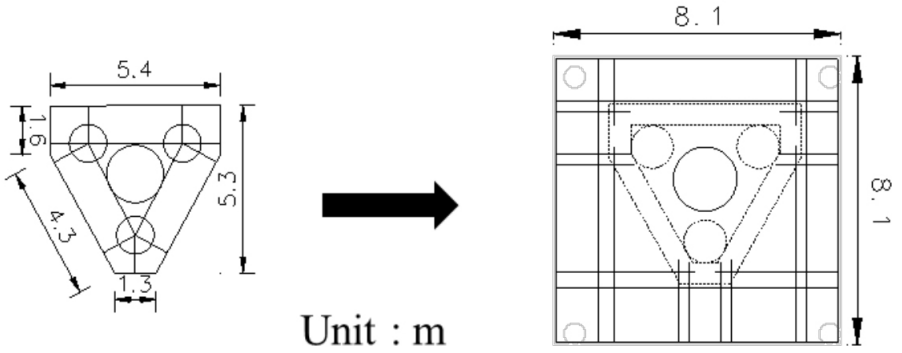

Figure 7: Existing pile caps enlargement

4.2 Results of 3D FEM analysis

Scheme 1 utilize deep grouting to strengthen the ground around exist pile foundation. Due to three dimensional effects, both displacement and inclination values of pile foundation have been reduced significantly compared with the results of two dimensional analysis. However, it is concerned that the quality of deep grouting is difficult to control especially in mix-ground conditions.

Scheme 2 adopted cross walls and buttress walls to connect with diaphragm wall adjacent to existing pile foundation. Displacements of existing pile foundation have been control effectively. However, the inclination value cannot fulfill the limit value required. Uncertainties due to densely allocated utilities below the road have increased the difficult and risk of this approach. Quality control of the interfaces between cross/buttress walls and diaphragm walls is another critical issue.

Scheme 3 focus on the structure strengthening of existing pile foundations with enlargement of pile cap and installation of pre-packed piles around the pile caps. Both displacements and inclination values are less than the limit values as shown in Figure 8 to 10. Performance of these strengthening works can be ensured with reasonable construction management and quality control.

Based on the above evaluations, Scheme 3 has been adopted as final design option and the comparison of these three schemes have been summarized in Table 7.

Table 7: Comparisons of protection measures

Scheme	Method	Max. horizontal displacement (mm)	Max. inclination value	Construability and quality control	Overall performance
1	Double packer grouting	12.63	1/728, NG	Difficult to control the quality of grouting	Fair
2	Buttress walls and cross walls	7.61	1/494, NG	Significant conflicting with existing utilities, Need careful control of the interface b/w cross walls and diaphragm walls	Poor
3	Pile caps enlargement and pre-packed piles	8.02	1/793	Better control of the performance and quality of strengthening works	Best

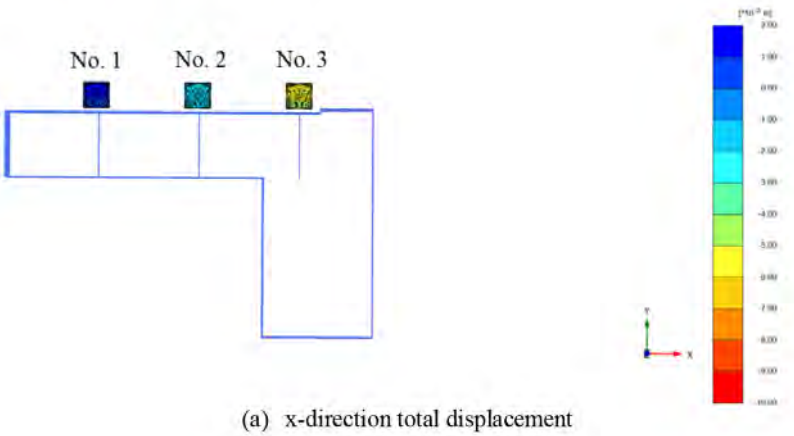

(a) x-direction total displacement

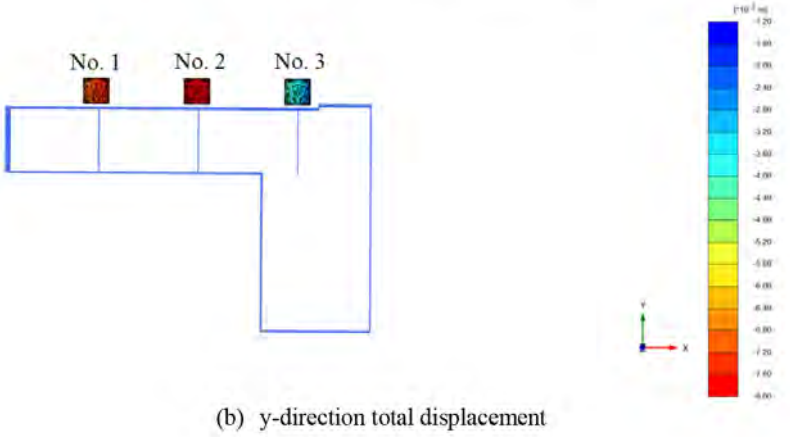

(b) y-direction total displacement

Figure 8: Existing foundations horizontal displacement due to the new station deep excavation for scheme 3

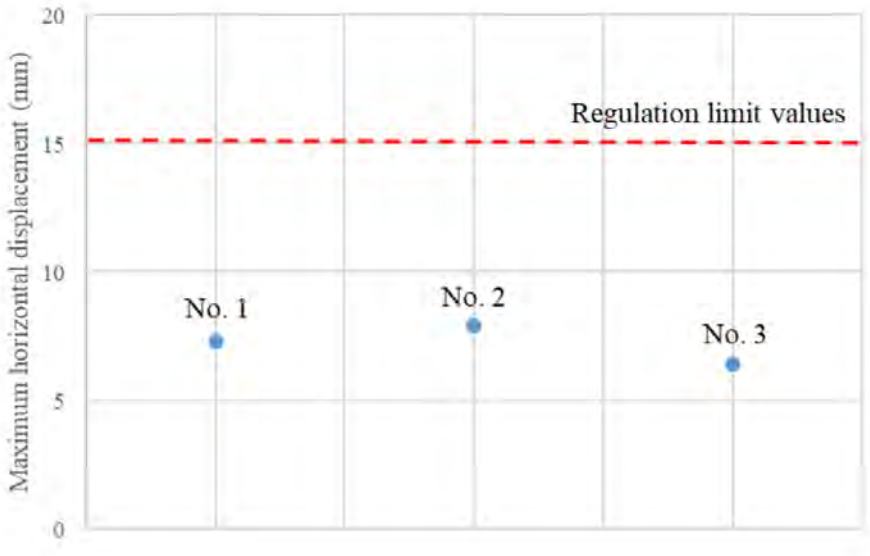

Figure 9: Existing foundations maximum horizontal displacement due to deep excavation for scheme 3

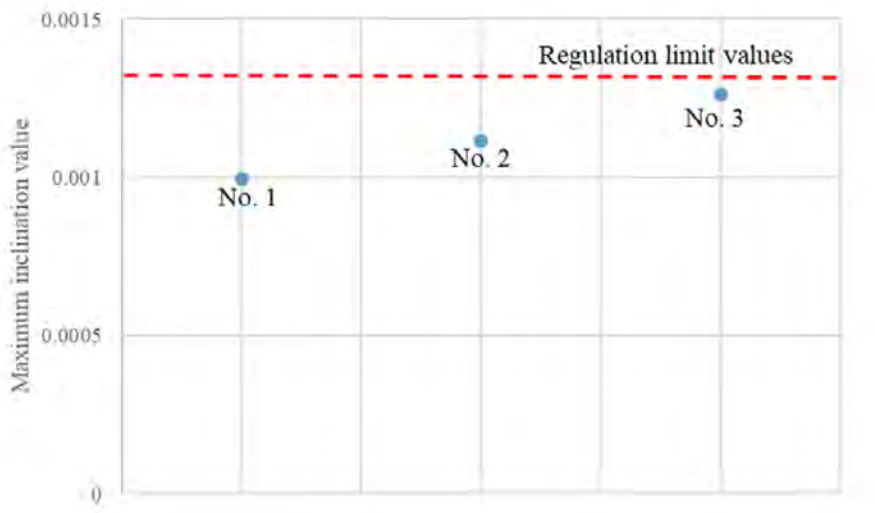

Figure 10: Existing foundations maximum inclination value due to deep excavation for scheme 3

5 CONCLUSION

In this paper, the displacements and the inclination values of the existing foundations induced by the excavation of a new underground station have been studied with various protection measures. Two dimensional analyses have been performed to identify the sensitivities of parameters and arrangement of ground improvement. Preliminary results of two dimensional analysis have been evaluated and additional three protection meres have been developed and studied with more accurate three dimensional numerical models. According to the results of three dimensional numerical analyses, strengthened existing pile foundation with enlargement pile cap and installation of pre-packed piles provide best protection of MRT line in operation.

REFERENCES

Iliadelis, D. 2006. Effect of deep excavation on an adjacent pile foundation. PhD thesis, USA: Massachusetts Institute of Technology.

Maruf, M.F. 2015. Excavation adjacent to the existing building: a study case. In Darjanto, H, *Proc of the 2nd Makassar International Conference e on Civil Engineering. Indonesia, 11-12 August 2015*.

Korff, M., Mair, R. J. & Van Tol, F. A. F. 2016. Pile-soil interaction and settlement effects induced by deep excavations. *Journal of Geotechnical and Geoenvironmental Engineering*, 142(8): 04016034.

A BIM-based Ground Information Management (GIM) Framework to Manage Ground Risk for Construction Projects

D.Y.Y. Mak, S.W. Millis & P. Li
Ove Arup & Partners Hong Kong Limited, Hong Kong

L.C.M. Tang
The University of Hong Kong, Hong Kong

ABSTRACT

Infrastructure design and construction in Hong Kong typically adopt a project-based process that is highly siloed and labour intensive. However, the successful delivery of construction projects in the digital age demands effective communication of the geological and geotechnical conditions through seamless ground information management and transfer. The requirements for Level 2 Building Information Modelling (BIM) approaches on engineering projects have driven a large-scale digitalization of the construction industry in recent years. However, geotechnical aspects have often remained neglected. To address this, mechanisms are proposed to incorporate ground information in BIM and ensure better ground risk management throughout the project life cycle. This paper reviews the current geotechnical context in terms of existing BIM standards and introduces a BIM-based ground information management (GIM) framework through Common Data Environments (CDE). This allows information-driven ground knowledge and management by clearly defining information requirements, adopting local classification systems, and developing project-specific level of information needs (LOIN). Through the BIM approach, ground uncertainty and risks are conveyed by introducing Level of Certainty (LOC) and Risk Registers linked through geometric information, LOIN, and metadata.

1 INTRODUCTION

1.1 Introduction of Ground Modelling for AECO Industry

Ground modelling plays an indispensable role in engineering projects, directing downstream planning, design, and construction and having significant bearing on overall costs. Indeed, several studies have shown that "unforeseen ground conditions" resulted in over a third of construction project overruns or failures due to the incorrect use or development of ground models (Morin, 2019). Based on The next normal in construction (McKinsey Global Institute, 2020), the construction ecosystem will be reshaped by digitalization of products and processes to form a more standardized and integrated system. This echoes the recent emergence and mandate for adopting Building Information Modelling (BIM) in the local construction industry. However, although gaining traction through widespread adoption, the sector still lacks a well-defined framework for the management of ground information in a BIM environment. This is particularly so regarding data standards, technology, and information layers.

The successful deployment of construction projects requires models that have been built through

the seamless integration of knowledge and data between both geology and engineering. Such models are described as Engineering Geological Models (EGM) (Baynes et al., 2020) [or Ground Model (GM) in this paper]. The GM can be seen as a critical knowledge hub for risk management, solving engineering problems, aiding engineering decision-making, and identify project opportunities throughout the project lifetime (Baynes et al., 2010; Parry et al., 2014; Kessler et al., 2015; Daly et al., 2019; Baynes et al., 2020).

1.2 Existing Ground Information Management (GIM) System

Holistic modelling of the ground involves interpreting data from various sources and formats (GEO 2007; Pan et al. 2012). These can be categorized into i) direct data from site mapping, ground investigation (GI), or laboratory tests, ii) indirect data from the interpretations made by others, including technical reports and geological maps, and iii) auxiliary data that aids the inference of available ground information such as satellite images, aerial photographs, topographic maps, historical maps, as-built drawings, etc. (Mak et al., 2019).

In Hong Kong, much of the above-ground data has been centralized within a cloud-based national database, namely the "Geotechnical Information Infrastructure (GInfo)" managed by Geotechnical Engineering Office (GEO) (Lai et al., 2019). Similar practices to this are also adopted in places like the UK and the US, where GI data can be downloaded in unstructured formats such as PDF as well as structured formats like AGS or DIGGS (Daly et al., 2019; Gilder et al., 2020). The AGS and DIGGS formats comprise standardized geospatial schemas for the electronic exchange of geotechnical data developed in 1992 and 2006, respectively. Their use allows the transfer of geotechnical data across borders in a manageable and structured manner and unleashes potentials for reusing digital data.

1.3 Current Issues in Ground Information Transfer

The increasing use of BIM means that the significance of GIM has come to the forefront once again, in particularly regarding the incorporation of both factual and interpreted geotechnical data (Antoljak, 2015; Kessler et al., 2015; Tawlian & Mickovski, 2016; Chadwick et al., 2019; Baynes et al., 2020). In this respect, several key issues and challenges have been identified.

While electronic transfer formats are available for GI data, a vast amount of ground information is still commonly transferred as unstructured data in the form of paper records, PDF files, or Computer-Aided Design (CAD) files (Antojak, 2015; Daly et al., 2019; Gilder et al., 2020). These formats are all static, imposing limitations on their transmission and re-use, and forming silo workflows (Antoljak, 2015). To overcome this, the data within the files must be re-processed through data re-entry and reworking to more versatile and standardised formats (Antojak, 2015; Daly et al., 2019; Gilder et al., 2020).

Although the AGS format enables the transfer and reuse of data, the current format is limited to factual data. This diverges from the BIM environment, where geometric and interpreted information is hosted (Kessler et al., 2015; Chadwick et al., 2019). This limitation is being addressed to some degree by recent computational advancements in geological modelling like 3D implicit ground modelling using algorithms. However, such 'algorithmic geometries' are often regarded as the 'truth' without conveying any of the underlying uncertainty associated with them (Baynes et al., 2020). There is also no standard schema currently available for geological models to facilitate the digital transfer of both the geometries and attributes in a consistent manner (Chadwick et al., 2019), which is one of the keys to successful BIM implementation. To address this, this paper proposes a GIM framework that will help maximize the value of ground data and enrich the wealth of ground knowledge in a BIM environment.

1.4 BIM Implementation in Hong Kong

According to ISO 19650-1:2018, BIM is defined as the use of a shared digital representation of a built asset to facilitate design, construction and operation processes to form a reliable basis for decisions (BSI, 2018). It aims to support the project or organization objectives using information management processes initiated by information requirements (Figure 1).

Since 2013, the Hong Kong Government has explored BIM technology for both public works and asset

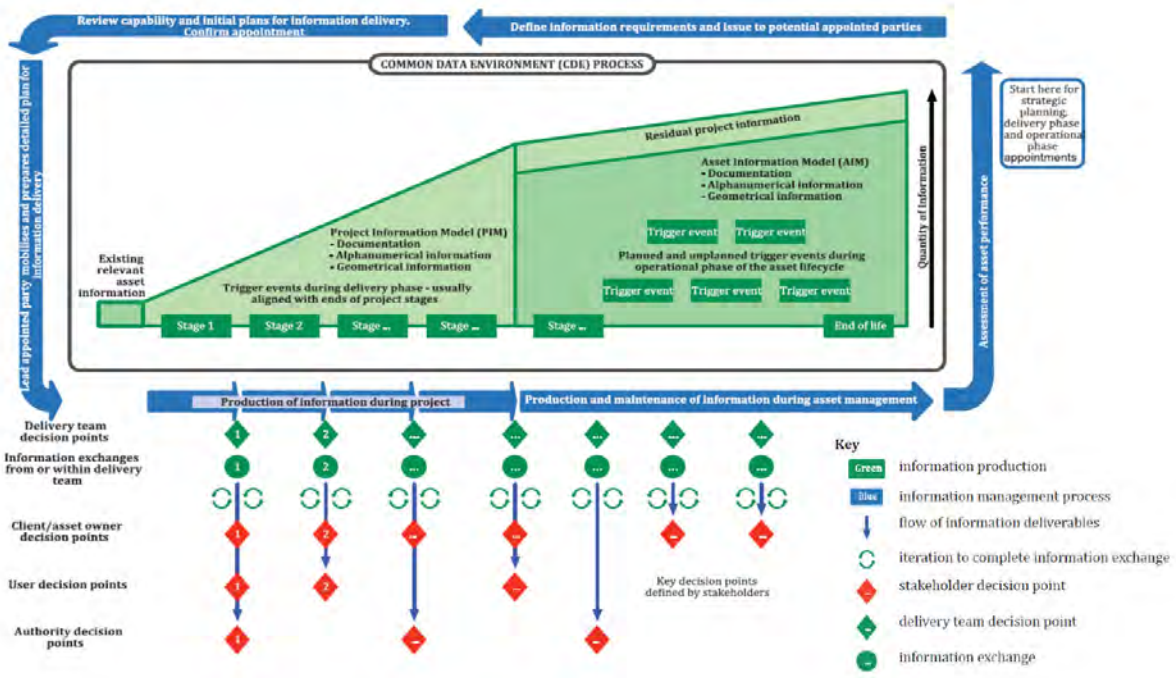

Figure 1: Process of BIM according to ISO 19650-1:2018 (BSI, 2018)

management. In the latest Technical Circular (Works) No. 12/2020 by the Development Bureau (DEVB), most BIM uses have become mandatory throughout all design and construction stages of a project. As a result, various BIM-related task groups have been established within the government departments and institutes such as the Construction Industry Council (CIC). The drive for BIM implementation by the government has been promising and has resulted in the development of the BIM Data Repository Platforms prototype by Lands Department (LandsD), BIM Integration with GInfo by CEDD, and the Electronic Submission Hub (ESH) by the Building Department (BD). In this respect, it is noted that Stage 2 of the ESH development will accept plans for geotechnical works, including foundation, site formation and excavation lateral support (ELS) in 2022 to 2023.

2 Principles of BIM-based GIM for Construction Project

2.1 Introduction

While there has been a recent surge in BIM use in the AEC industry, subsurface information remains somewhat neglected and lags behind data for other construction aspects (Kessler et al., 2015; Morin, 2019). However, the emergence of advanced technologies is disruptively transforming ground modelling practice through digitalization, opening up its potential for an enhanced BIM-based GIM (Antoljak, 2015; Kessler et al., 2015; Tawlian & Mickovski, 2016; Daly et al., 2019; Baynes et al., 2020; Gilder, 2020). This will provide notable benefits to the industry, yielding a whole-life ground risk management tool that complies with the existing BIM processes and better manages ground data as an asset.

2.2 BIM as a Whole-life Ground Risk Management Tool

The ground model is a key knowledge hub for the management of ground related risks that allow engineers to solve engineering problems, aid engineering decision-making, and identify project opportunities (Baynes et al., 2020). The benefits of a fully integrated GM-BIM approach have been successfully demonstrated by recent projects adopting a BIM-based and data-driven ground modelling, such as Crossrail 2 in London (Ting et al., 2020). For projects such as these, the 3D ground model acts as the engine to integrate and accumulate ground knowledge throughout all project stages in a 3D geological modelling environment (Figure 2). Through iterative modelling, the model continually evolves

with an increasing degree of certainty and the aid of 3D visualization (Ting et al., 2020). The ground model is also a vital mechanism for contractors to understand what ground risks can reasonably be foreseen before construction commences (Baynes et al., 2020). Hence, it is recommended to incorporate the ground model in the project management system, from procurement to decommissioning (Harding, 2004; Parry et al., 2014; Baynes et al., 2020), to minimise contractual risks from claims for unforeseen ground conditions (Baynes et al., 2020).

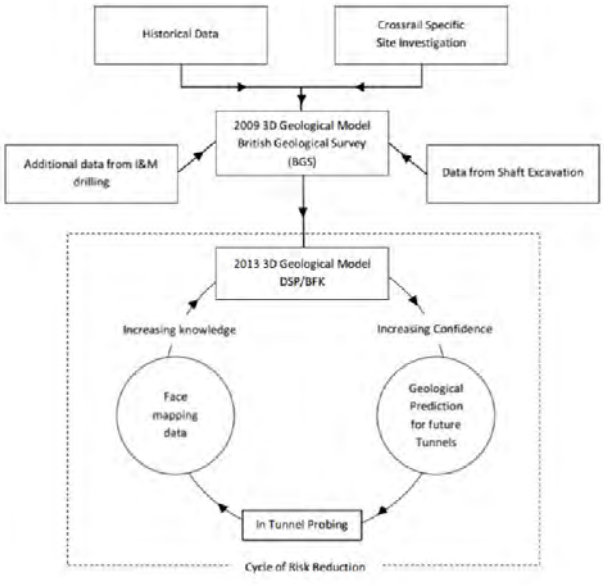

Figure 2: The cycle of risk reduction (adapted from Gakis et al., 2014)

2.3 Adopting BIM-based Information Management Processes

Although a number of workflows for ground modelling have been proposed over decades, whole-life ground risk management has been challenging due to the aforementioned issues of ground information transfer. This section highlights the interconnection between BIM (Figure 1) and GIM (an example is presented in Figure 3) needed to achieve whole-life ground risk management. These workflows indicate that ground models are the backbone for the assessment of ground risks and decreasing uncertainty as a project progresses (GEO, 2007 and Gilder et al., 2020). Recently, Baynes et al. (2020) has defined a new workflow for ground risk management in civil engineering based on the IAEG Commission 25 Report (Figure 3). By comparing the BIM and examples of GIM, the interconnectivity between BIM and GIM are summarized as follows:

- Ground modelling is initiated with a review of existing relevant asset information during desk study.
- Within Project Information Management (PIM), ground model, data and information are generated (i.e. information production) from various stages, which includes documentation (technical reports), non-graphical information (geotechnical parameters, etc.), and graphical information (ground model).
- Discrepancies between the predicted ground model and new ground information act as the trigger events during the delivery and operational phases to refine the ground model. Further ground information may appear in all stages, including the construction phase and post-construction ground monitoring.
- In the operation or maintenance stage, the ground model may enter a repository of Asset Information Management (AIM), where it is continuously assessed and updated, if necessary.
- PIM and AIM may be managed within CDE.

This contrasts with the BIM uses of ground information suggested in the BIM standards, which is limited to the feasibility and design stages only.

2.4 Adopting BIM-based Ground Asset Management

Key to incorporation of geotechnical data within BIM for whole-life ground risk management is treatment of geotechnical data as an asset for decision-making in future projects (Antoljak, 2015; Kessler et al., 2015). Managing data in a data respiratory requires well-structured, reusable and interoperable data (Antoljak, 2015; Daly et al., 2019). This provides room for the transfer of ground information amongst different asset environments. This concept is currently adopted by Highways England using the Highways Agency Geotechnical Data Management System (HAGDMS). The system is an open web-based enterprise-level database for i) reusing geotechnical data and ii) facilitating informed decisions based on risk-based documentation and prioritization (Daly et al., 2019). Such usage demonstrates the benefits of structured, fragmented, and open data as valuable information for risk analysis which complies with the BIM principles.

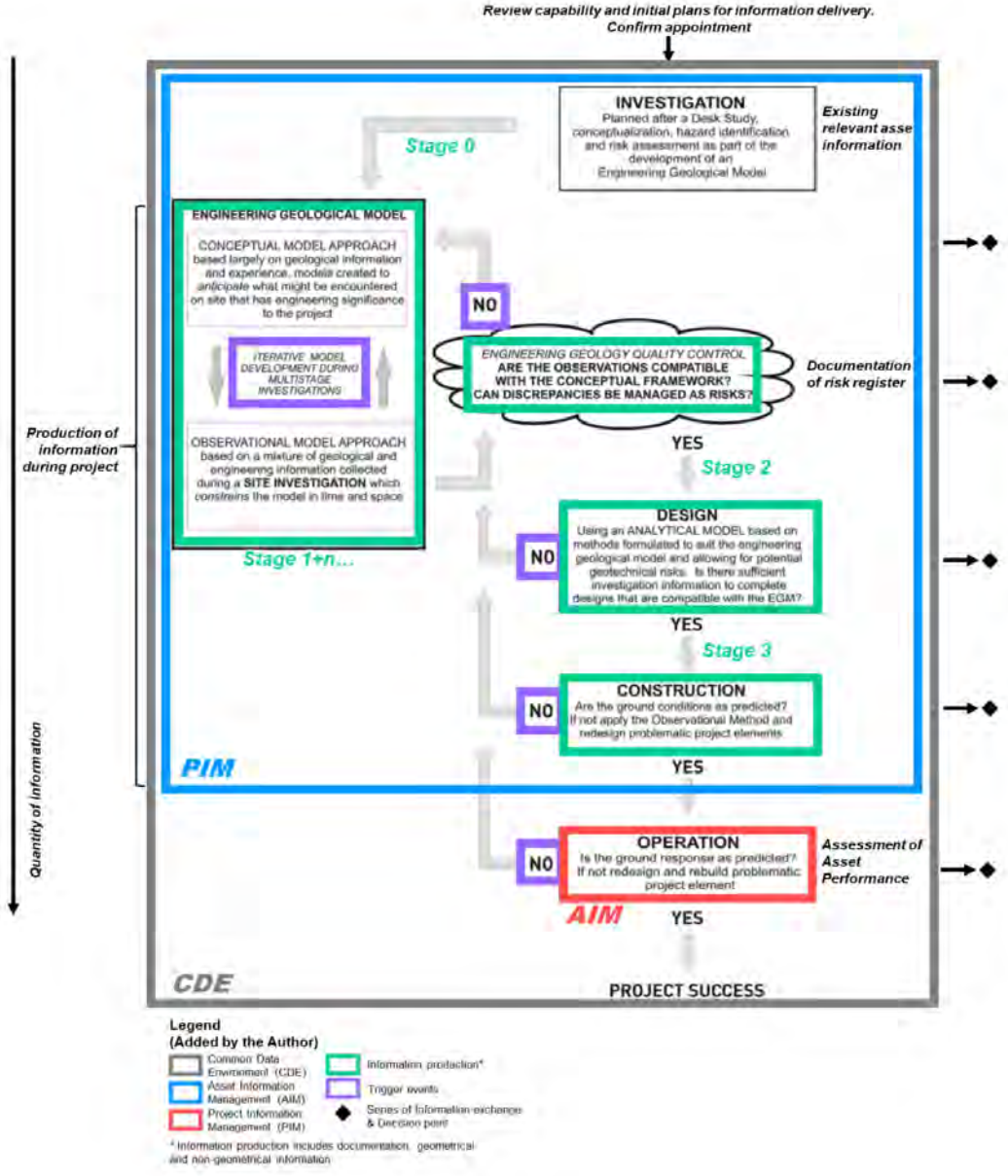

Figure 3: Workflow of using EGM for decision-making and risk management and its relationship with the BIM approach. Modified from Baynes et al. (2020)

3 Proposed BIM-based GIM for Ground Risk Knowledge and Uncertainty Transfer

3.1 Introduction

An information requirement-driven management system for ground information and knowledge (GKIM) is proposed to elevate the transfer of the data-information-knowledge (D-I-K) model for the ground within the BIM ecosystem in a digital and structured manner. A suggested framework of an IR-driven GKIM is illustrated in Figure 9. This covers the Business Layer, Standard Layer, and Information Layer of the Project Information Model (PIM) and Asset Information Model (AIM). AIM represents a national ground data repository that feeds the PIM throughout a project life cycle, and is fed back to by the PIM at the project close-out. Since it is unrealistic to formulate a global or national standard that caters for all disciplines, the following suggestions were considered when formulating discipline-or corporate-specific BIM standards, local BIM annexes, and IRs.

3.2 Business Layer – Information Requirements (IRs)

IRs, including Organisational Information Requirements (OIR), Project Information Requirements (PIR), Exchange Information Requirements (EIR), and Asset Information Requirements (AIR), act as the drivers of GIM to facilitate the maintenance of the ground model and procure high-value ground risk data and information. Tang et al. (2019) stressed the importance of a proper procurement of IRs to maximize knowledge reuse and minimize the construction cost due to fragmented information. As illustrated in Figure 4., IRs drive a cross-industry integration of digital twin (Tang et al., 2019) for the development of smart city.

The CIC BIM Adoption Survey 2020 concluded that 'Hong Kong client requirements' and 'Government policy' are the top BIM motivations (CIC, 2021). Given this, the recommendations herein are for the formulation of Project Information Protocol and National Geotechnical BIM-AM Standard as references for organizations to customize their IRs that fit national and organizational maintenance of the ground model.

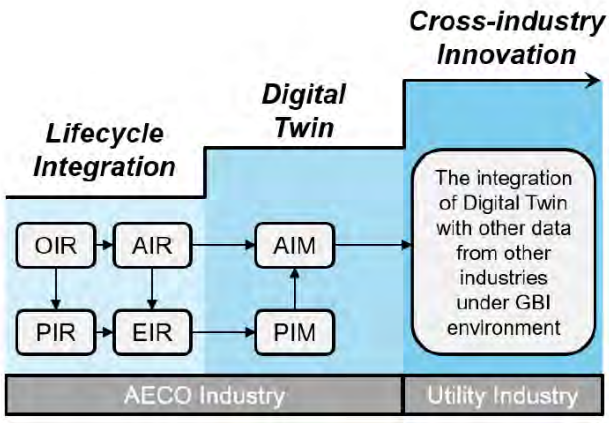

Figure 4: The impact of ISO19650 on the HK AECO Industry (Tang et al., 2019)

3.3 Standard Layer – Open Formats

Currently, the GIM is served as a standalone tool for the geotechnical expert due to its incompatibility with BIM formats and modelling methods. However, knowledge of ground data is essential during the initial design stage for both engineers and architects, meaning that GIM and BIM should not be independent aspects. The flow of data between GIM and BIM can be integrated for better collaboration through the use of OpenBIM formats (e.g. IFC), OpenGIS formats (e.g. CityGML), and BIM-GIS CDE platforms (Herlé et al., 2020). In this system, GIM can be linked to the native BIM platform to maximize the data sharing among all parties during the design stage. For instance, structural engineers may better understand the ground conditions and thus optimize their basement design when using a single source of information (CDE). The proposed information exchange and BIM-GIS integration are presented below.

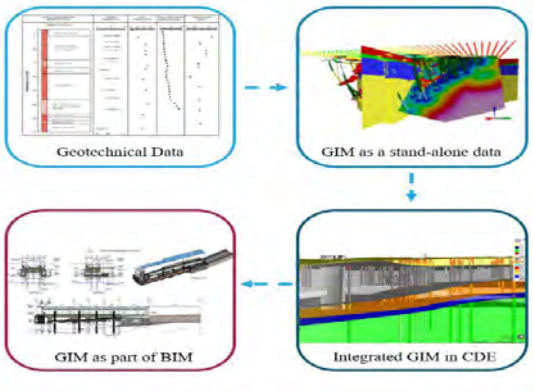

Figure 5: Integration of GIM and BIM through CDE

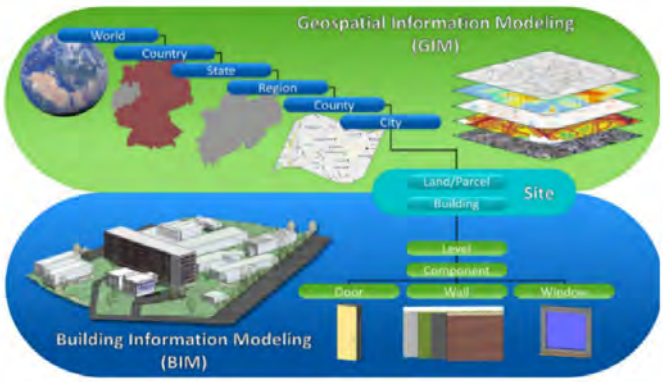

Figure 6: Information Exchange within BIM-GIS Integration

Storing a territory-wide GIM and BIM data in the form of OpenBIM format with standardized structures is the milestone towards developing automation in ground modelling and evaluation for urban planning.

3.4 Standard Layer – National-/ Project-specific Classification Systems

The classification system is the backbone needed to structure data and ease data extraction in the future. OmniClass and GEO's BIM Project Execution Plan Template present current requirements for geotechnical information, particularly the physical assets for foundation and excavation lateral support (ELS). This includes the ground information (Table 36: Information of OmniClass), geotechnical characteristics of the ground (Table 49: Properties of OmniClass), and geological model (CAT codes given by GEO's template). However, these are not available within ISO 12006-2:2020 and Uniformat. They are fundamental information for ground risk assessments and design and hence should be adhered to geometrical data for the downstream construction and operation.

However, the ground information and risks of concern to design engineers can be highly variable depending on the nature of the proposed works and ground characteristics. It is thus recommended to formulate a national classification system for geotechnical parameters and geological strata that comply with the local practice and standards of design and construction. Although GEO suggests some CAT codes for geotechnical projects in Hong Kong, it is impractical to cover all materials that would impact the geotechnical works. Therefore, in an early stage, the project engineering geologists should review the classifications of geological units and formulate a project-specific classification, if necessary.

3.5 Standard Layer – Project-specific Level of Information Needed (LOIN)

The LOD specifications by BIMForum, CIC, and GEO include geotechnical structures and the interacting geological strata (i.e. the profiles of bearing strata and rockhead), without stressing their intrinsic characteristics. According to BIMForum (2019), geotechnical regions are shown for context and not required to be modelled as part of this element at most LOD. However, this information is essential for geotechnical designs and construction. A project-specific LOIN should be established to fit the project needs, rather than adopting LOD as described in some of the standards. For instance, a reclamation site would require a preliminary model on the thickness and locality of soft clay to assess the risk of settlement in feasibility or design phases. In this case, low LOD suggested in the BIM standards would not be sufficient for preliminary study.

To transfer the ground knowledge and uncertainty through BIM, it is proposed to include the 1) raw data, 2) proceeded (standardized) data, and 3) interpreted data as the LOIN, where the interpreted data includes the delivery of the level of certainty (LOC) (See Section 3.5.1) and ground risk (See Section 3.5.2).

3.5.1 Level of Certainty (LOC)

While there has been a long history of quantitative and qualitative studies relating to ground model uncertainty, this paper focuses on a simple solution for a BIM-based transfer of semantic and geometric model uncertainty. This provides auxiliary information for model users to be aware and comprehends the uncertainty inherent in the ground model. The framework comprises geometric information (LOD-G), non-geometric information (LOD-I and metadata), and reports (DOC).

Digitalization of Knowledge

Ground knowledge is usually inherent implicitly in the ground model, making it hard to locate the uncertainty from subjective judgements. Modellers' interpretations and assumptions should be digitized and separately stored as explicit geometries (polylines, points, or meshes) or information (numbers or notes), which are then holistically modelled with the raw data (Mak et al., 2019). The digitized knowledge can then be transferred to the downstream project stages as LOD-G and LOC-I for model users and operators to visualize and reuse.

To maximize the value of information and avail the reuse of information, open or common formats should be used. This promotes compatibility with end-users' software programme or devices and aid to extract the right information at an appropriate time by the right person.

Type of Engineering Geological Model

The ground model is often taken as an absolute truth by engineers and stakeholders. It is imperative to convey to model users that every ground model is just an approximation of the ground conditions at varying scales (Baynes et al., 2020; Parry et al., 2014). Indeed, the concept of LOD in BIM is an analogue of LOC that presents uncertainty geometrically and semantically.

To convey ground-related uncertainty, the types of geological engineering model defined by IAEG Commission 25 can be adopted to represent the LOC of a model developed at different stages of a project (Figure 3 and Table 1) (Parry et al., 2014; Baynes et al., 2020). Being one of the most widely accepted standards for ground models, this can be a universal indicator of the uncertainty of a ground model stored as metadata.

Table 1: Types of EG Model for LOC

Type of EG Model*	**Description***	**Level of Certainty**
Conceptual Model	Anticipation based on geological information from knowledge, experience, and relevant references	
Observational Model	A model refined from conceptual model based on the surface or sub-surface observations and measurements of geological and engineering information	
Analytical Model	A model refined from observational model for engineering analysis on ground behaviour	

* Development stage models defined by IAEG Commission 25 (Parry et al., 2014)

Auxiliary Information of LOC

Some of the model information can reflect the LOC to a certain extent, namely 'auxiliary information of LOC'. Access to this information through metadata or parameters of the model provides a cost-effective and straightforward way to indirectly enhance model users' understanding of LOC. Examples of the auxiliary information of LOC are provided in Table 2. They may also be the indicators of evaluating the value of information for ground information managers to control the cost of data storage.

Table 2: Examples of Auxiliary Information of LOC

Auxiliary Information of LOC	Description	Example
Project Stage	Stage of the project when the ground model was formed	• Feasibility Stage • Investigation Stage • Design & Construction Stage • Post-construction Stage
Modelling Use	Usage of modelling aligning with BIM uses. For Engineering Analysis, type of geotechnical work should be provided	• Refer to BIM standards for BIM uses • Driven pile design
Resolution or Scale	Resolution or scale of the ground model	• 10m • 1:5,000
Development Stage of the Ground Model	See Section "Type of Engineering Geological Model" above	• Conceptual Model • Observational Model • Analytical Model
Type of Knowledge	Type of interpreted data, linked with the corresponding digitized user knowledge. See Section "Type of Engineering Geological Model" above	• Hypothesized ■ Assumptions based on experience only without technical support • Interpreted ■ Interpretations based on the available information (i.e. maps, reports) • Observed ■ Direct observations (i.e. mapping, intrusive ground investigation)

3.5.2 Ground Risk Registry

For BIM-based knowledge management of ground risks, it is proposed to establish a digital risk registry that links the geometrical information (e.g. locality of hazardous ground materials) and non-geometrical information (e.g. the type of ground hazards and their risks to the proposed engineering works). Communication of ground risk is recommended by Baynes et al. (2020) to present the locations where geology could adversely influence engineering using a graph (Figure 7) and risk register table. Applying the same concept in BIM, the graph can be stored as 3D BIM models [LOD-Graphical (LOD-G)] which are "tagged" with the risk register table stored as metadata [LOD-Information (LOD-I)] and technical reports as [Documentation (DOC)]. The 3D geometries are essential for clash detection, considering the spatial relationship between hazardous ground materials (i.e. corestones) and proposed works (i.e. driven pile foundation) as a 'clash' in construction to minimize rework. Utilising CDE technologies, GKIM

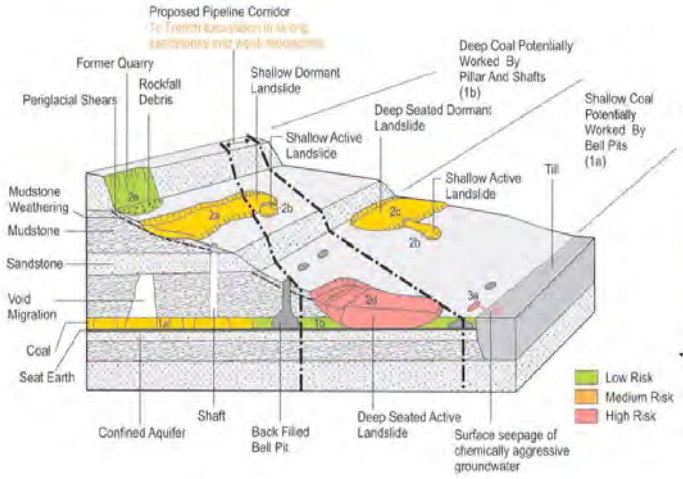

Figure 7: Visualization of Baildon engineering geological model used to communicate the qualitative risk assessment. (adapted from Baynes et al., 2020)

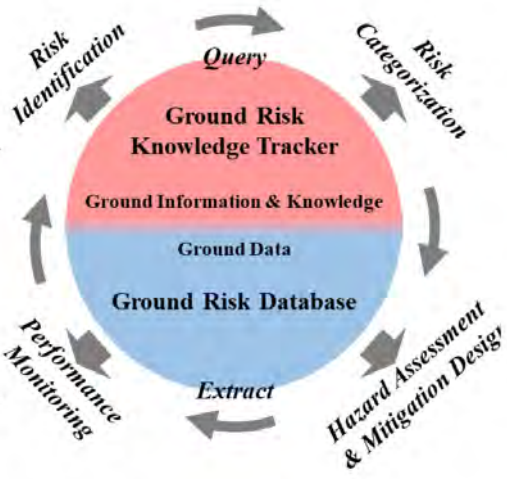

Figure 8: Ground Risk Management Process through GKIM

serves as a ground risk knowledge tracker for risk identification and categorization through knowledge query, and ground risk database for hazard assessment, mitigation design and performance monitoring (Figure 9).

INSPIRE Data Theme: Natural Risk Zones by European Commission could be adopted in data specification. Metadata tagging should be enabled to query ground risk information and incorporate ground risks in 4D and 5D BIM modelling for procurement of on-site mitigation materials.

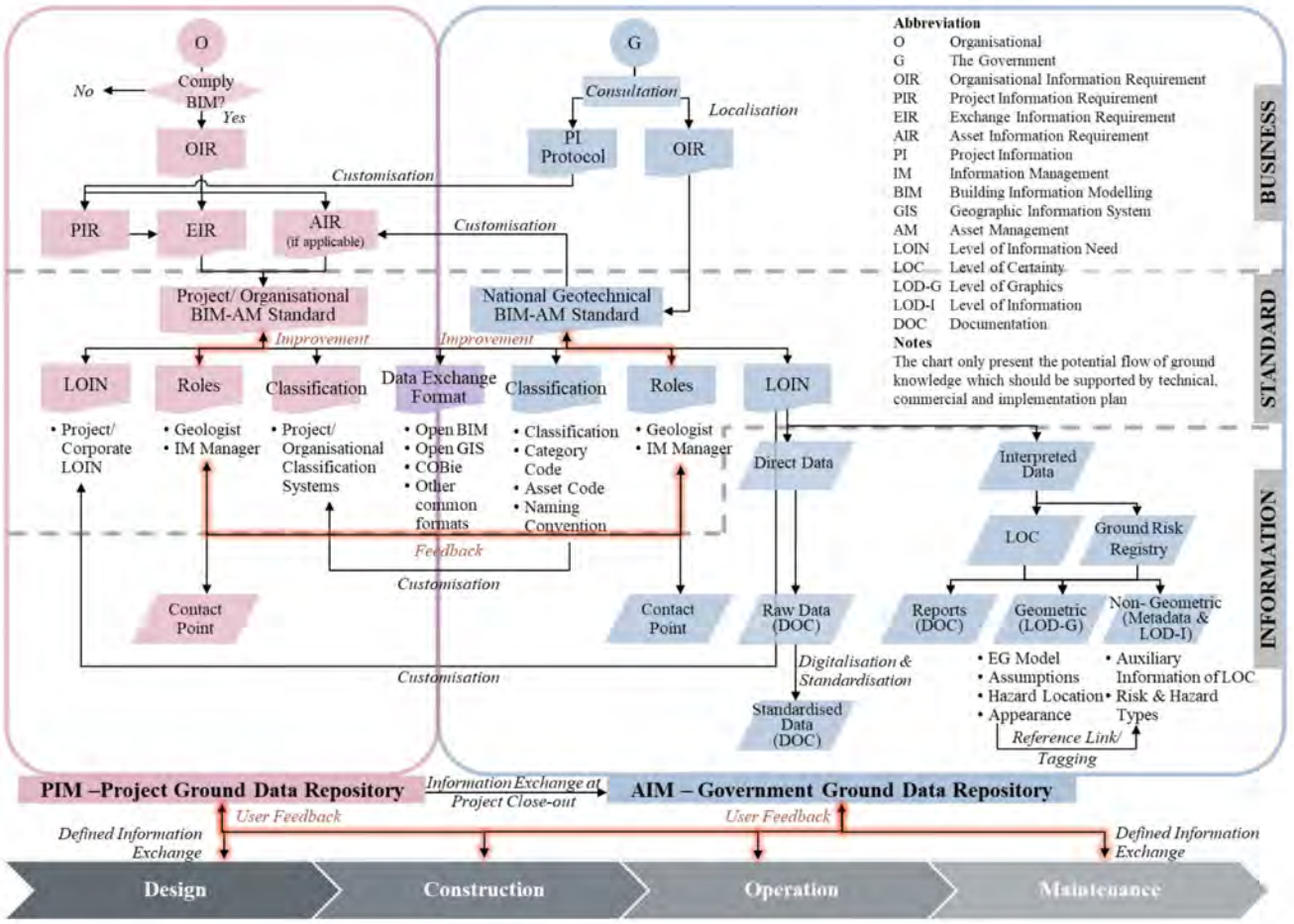

Figure 9: Proposed Framework of Information Requirement-Driven Ground Knowledge and Information Management

3.6 Feedback & Improvement

Continuous communication is critical in any projects for continual improvement of the BIM-AM standards and information requirements. This should be done among stakeholders, mainly the government, ground information management managers, project geologists, and the end-users of the ground model to maintain the information quality and effectively of information transfer within the ecosystem.

4 WAYS FORWARD

To enable the digital transfer of ground models and interpreted data, a beta version of the schema extension 'AGSi' has been launched by a sub-group AGS DMWG in November 2020 (Chadwick et al., 2019). It adopts an object model-based schema to which fits GIS and BIM like IFC and OGC standards. The draft schema carries simple geometrical elements and linked attributes, including reporting. Coincidently, IDBE, a collaborative group between buildingSMART and OGC, is also developing a conceptual schema for ground models within the IFC and OGC standards. The recent emergence of a cloud-based collaborative

platform for geotechnical data management like OpenGround also allows cloud-based integration with databases like gINT and HoleBase.

However, the development of a BIM-complicit software is crucial to achieving the integration of GIM and BIM. Overall, there is a pressing need in the Technical Layer – i) ISO-compliant integrated asset information system designated for supplementing the existing BIM software deficiencies in standard compliance and ii) open format for the ground model, and Standard layer – iii) formulation of a BIM-based GIM through IR. Furthermore, there is a lack of guidance or methodology on evaluating the information being retained. A method for information evaluation would be critical in the digital future to avoid overloading low-value information and maintaining the quality of information (Tang et al., 2010).

REFERENCES

Antoljak, S. 2015, September 20-23. *Subsurface Modeling and BIM. Subsurface Modeling and BIM*. GEOQuebec 2015, Quebec City, Canada.

Baynes, F.J. 2010. Sources of geotechnical risk. Quarterly Journal of Engineering Geology and Hydrogeology, 43: 321-331. https://doi.org/10.1144/1470-9236/08-003

Chadwick N., Farmer D., Chamfray J., Miles S. 2020. Extension of the AGS Format to Incorporate Ground Model and Interpreted Data. In: A. Correia, J. Tinoco, P. Cortez, L. Lamas. *Information Technology in Geo-Engineering*. ICITG 2019. Springer Series in Geomechanics and Geoengineering. Springer, Cham.

Daly, T., Carluccio, S., Bhanderi, D. & Patterson, D., Power, C., & Codd, J. 2020. Use of Geotechnical Asset Data Within Highways England: The Journey so Far and the Future. In: A. Correia, J. Tinoco, P. Cortez, L. Lamas. *Information Technology in Geo-Engineering*. ICITG 2019. Springer Series in Geomechanics and Geoengineering. Springer, Cham. 10.1007/978-3-030-32029-4_68.

Herlé, S., Becker, R., Wollenberg, R. & Blankenbach, J. 2020. GIM and BIM: How to Obtain Interoperability Between Geospatial and Building Information Modelling?. PFG – Journal of Photogrammetry Remote Sensing and Geoinformation Science. 88(8). 10.1007/s41064-020-00090-4.

GEO. 2007. GEO Publication No. 1/2007 Engineering Geological Practice in Hong Kong. Civil Engineering and Development Department, Hong Kong SAR Government.

Gilder, C. E. L.; Geach, M., Vardanega, P. J., Holcombe, E. A., & Nowak, P. 2020. Capturing the views of geoscientists on data sharing_A focus on the Geotechnical Community. Quarterly Journal of Engineering Geology and Hydrogeology. 2019. 138. https://doi.org/10.1144/qjegh2019-138

Harding, C. 2004. Site investigation and site conceptual models. The link between geology and engineering. In: Jardine, R. J., Potts, D. M., Higgins, K. G. *Advances in geotechnical engineering.: the Skempton conference*. The Skempton Conference. Thomas Telford. London. 1304-1315

Kessler, H., Wood, B., Morin, G., Gakis, A., McArdle, G., Dabson, O. J., Fitzgerald, R., & Dearden, R. (2015, November 1-4). Building Information Modelling (BIM): a route for geological models to have real world impact. In: K.E. MacCormack, L.H. Thorleifson, R.C. Berg. Three-Dimensional Geological Mapping: Workshop Extended Abstracts. Geological Society of America.

Mak, D. Y. Y., Luk, F. W., & Chan, H. H. K. 2019. A New Approach to Modelling the Ground. In B.C. Editor & C.D. Editor (ed.), The HKIE Geotechnical Division 39th Annual Seminar 2019 Transformation in Geotechnical Engineering – Technology, Digital and Innovation. Hong Kong, 11 April 2019. HKIE.

Morin, G. 2019. Geotechnical BIM: Applying BIM Principles to the Subsurface. Autodesk University. Retrieved from https://www.autodesk.com/autodesk-university/article/Geotechnical-BIM-Applying-BIM-Principles-Subsurface-2019

Pan, M., Li, Z. L., Gao, Z. B., Yang, Y. & Wu, G. Y. 2012. 3-D Geological Modeling-Concept, Methods and Key Techniques. Acta Geologica Sinica English Edition, 864, 1031-1036.

Parry, S., Baynes, F.J., Culshaw, M.G., Eggers, M., Keaton, J. F., Lentfer, K., Novotny, J. & Paul, D. 2014. Engineering geological models: an introduction: IAEG commission 25. Bulletin of Engineering Geology and the Environment. 73, 689-706. https://doi.org/10.1007/s10064-014-0576-x

Tang, L. C. M., Zhao, Y., Austin, S. Darlington, M., and Culley, S. 2010. Codification vs personalizationpersonalisation: A study of the information evaluation practice between aerospace and construction industries. International Journal of Information Management, 30(2010), 315-325.

Tang, L., Bew, M., Wen, Y. and Lee, Y.S. 2019. ISO19650-An international approach to the journey of industry integration, digitalizationdigitalization and innovation. In B.C. Editor & C.D. Editor (ed.), The HKIE Geotechnical Division 39th Annual Seminar 2019 Transformation in Geotechnical Engineering – Technology, Digital and Innovation. Hong Kong, 11 April 2019. HKIE.

Tang, L.C.M., Chan, G., Chan, C., Zhang, Z., Zheng, Y., Yi, X., Mok, A., Mak, D. 2021. BIM Adoption Survey 2020, CIC HK.

Design and Construction of Ground Improvement for TMCLKL Southern Ventilation Building

A. Martucci & A. Pickles
Golder Associates (HK) Ltd.

ABSTRACT

The Southern Ventilation Building (SVB) is located on newly reclaimed land where 15-20 m of Sand Fill overly 15m of soft to firm silty clay Marine Deposit which was improved with prefabricated band drains. The SVB sits directly above the Tuen-Mun Chek Lap Kok Tunnels (TMCLKL).

The original design required installation of over 330 number of shaft grouted piles. Due to the presence of the tunnels the pile design was relatively inefficient and required 3m thick pilecaps.

An alternative design was developed to delete the piled foundations by carrying out additional ground improvement within the soft soil layer using a combination of Jet Grouting and Deep Cement Mix using Cutter Soil Mix (CSM) and support the building on a raft foundation. The ground improvement scheme was also leveraged to reduce the temporary wall depth and shoring quantities. In order to rationalise and minimise the ground improvement quantities, the CSM panels formed a grid of orthogonal underground beams which allowed an efficient Area Replacement Ratio to be achieved.

The excavation and building construction has been successfully completed with excellent performance in terms of both ongoing settlement of the permanent works and lateral movement of the excavation retaining walls during the temporary works.

1 INTRODUCTION

The Tuen Mun – Chek Lap Kok Link (TMCLKL) is a new transportation route that provides a strategic connection between North West New Territories, North Lantau, the Hong Kong – Zhuhai – Macao Bridge Hong Kong Boundary Crossing Facilities (HKBCF) and the Hong Kong International Airport (HKIA) at Chek Lap Kok.

The Southern Ventilation Building (SVB) is located at the northern tip of the HKBCF ('Southern Landfall') as shown in Figure 1 and Figure 2. The SVB provides ventilation facilities to the twin 14m diameter tunnels, which are approximately 40m below ground at this location.

The ground conditions include Fill overlying soft marine clay, stiff/dense alluvial deposits and completely decomposed metasiltstone.

The original design required a piled foundation with over 330 shaft grouted piles connected to 3m thick pilecaps. An alternative design was developed which involved founding the SVB on a shallow foundation sitting directly on ground improved by Deep Cement Mixing and Jet Grouting, thereby allowing all the piles to be deleted.

In addition, the ground improvement was also used to enhance the stability of the temporary works, allowing a rationalization and quantity reduction for both the vertical retaining wall and the horizontal shoring system.

This paper describes the design philosophy adopted for foundations and lateral support works. The

ground improvement performance is illustrated by a comparison of predicted soil movements against monitoring data both in temporary and permanent stages.

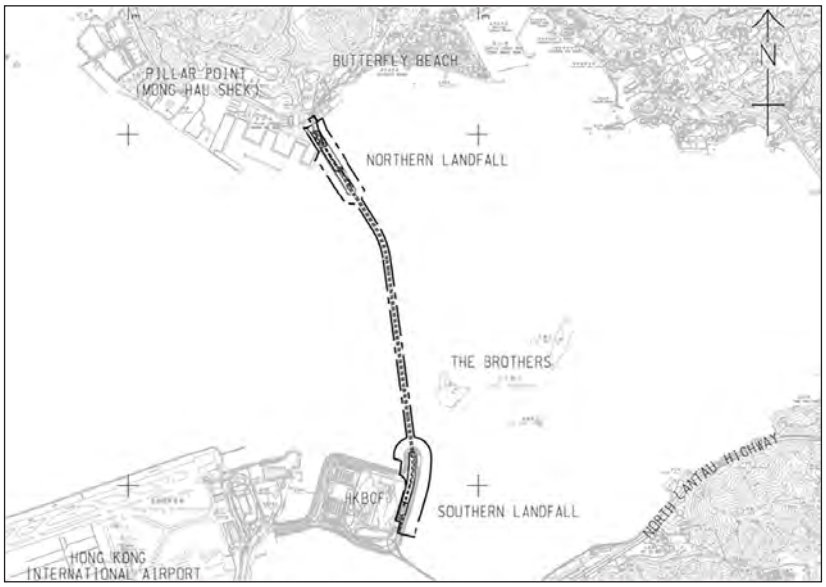

Figure 1: Site Location Plan

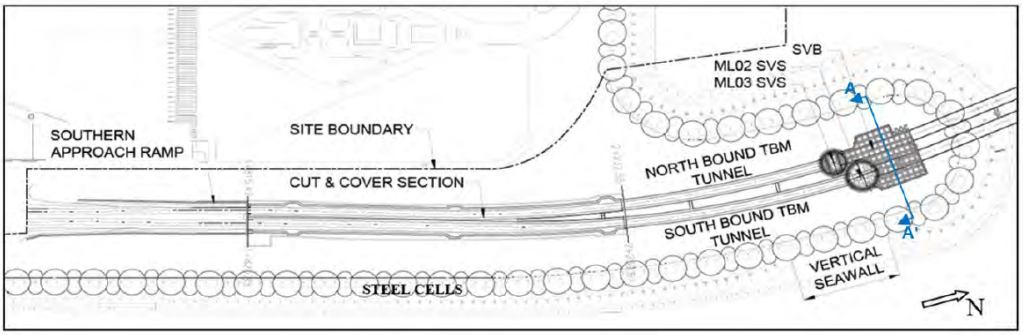

Figure 2: Southern Landfall Plan

2 PROJECT DESCRIPTION

The SVB comprises 2 levels of basement and a 3 story superstructure, with a footprint of approximately 65m x 47m, housing the tunnel ventilation systems as well as electrical systems, fire services provisions and drainage system. As shown in Figure 2, the SVB is adjacent to two circular shafts MLO2 SVS and MLO3 SVS, which connect the ventilation system to the 40m deep tunnels.

Due to the presence of the twin tunnels, the original foundations design required construction of 3 large 3m thick pile caps, connected by a relatively thick slab to span over the two tunnel footprints, see Figure 3.

Grade III rock of founding quality was identified to be at a depth of over 100m below ground level over this area. As a result of the depth to rock head, 330 shaft grouted H-piles approximately 70m deep were initially proposed to support the building.

The foundation redesign using ground improvement allowed the building to be founded on an at-grade slab of variable thickness between 1.5 and 2.5 m. The underside of the basement slab is between -8.5 to -9.5 mPD, which is approximately 15m below existing ground level, as shown in Figure 4.

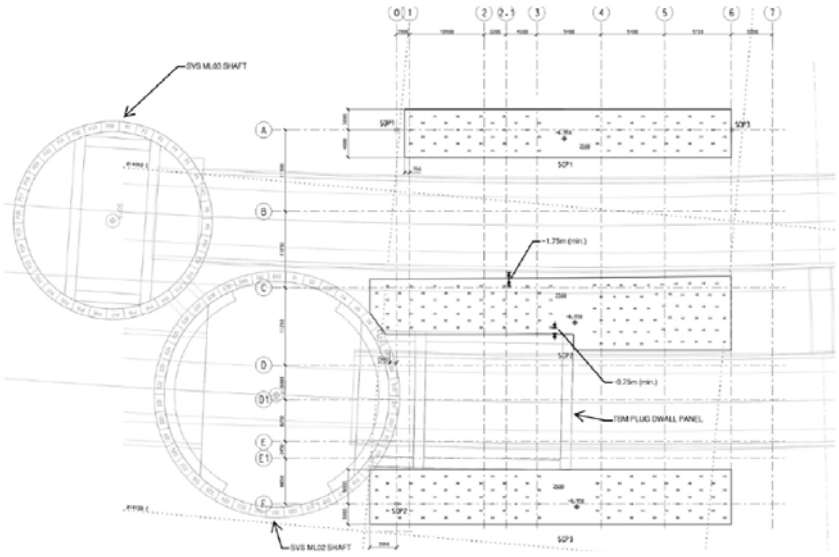

Figure 3: Layout Plan of Original Piling Scheme

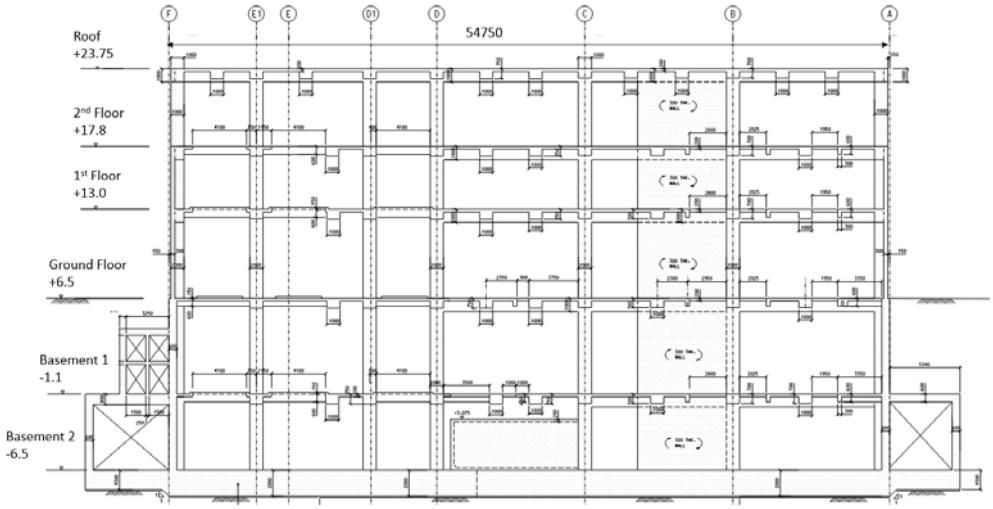

Figure 4: Cross-Section of Raft Foundation Scheme

2 GROUND CONDITIONS

The geological profile across the site has been altered by the reclamation works undertaken in the area to form the HKBCF island. The site formation level is at +5.5 mPD. The reclaimed land was constructed using sand fill placed directly over soft marine clay improved with Prefabricated Vertical Drains (PVD). The geological profile after reclamation consists of 4 main layers above engineering rock head:

a) Fill – typically medium dense to dense sand, with isolated pockets of soft disturbed clay towards the bottom of the layer

b) Marine Deposit – typically very soft to firm silty clay

c) Alluvial Deposit – typically interbedded layers of firm to stiff silty clay and medium dense to very dense silty clayey sand

d) Completely and Highly Decomposed Metasiltstone (MSLSTN)

No grade III or better rock was identified in any of the boreholes at the SVB which were drilled to a depth of approximately 100 m below ground level. The typical groundwater level is between +2 and +3 mPD, which is slightly higher than mean sea level. A geological section is shown in Figure 5. Refer to Figure 2 for the location of the geological section.

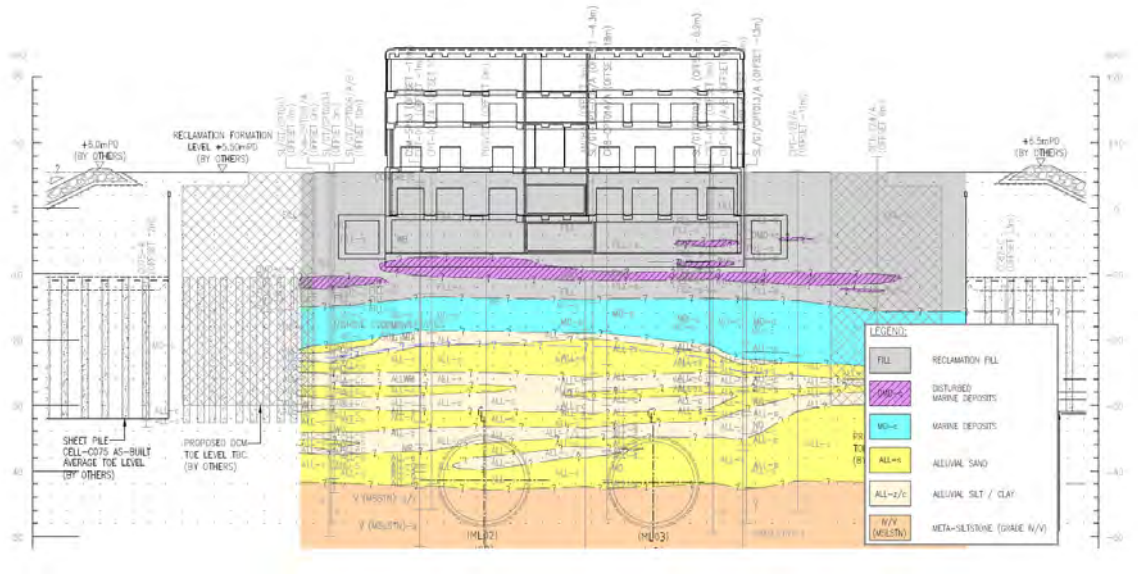

Figure 5: Geological Section

Soil parameters adopted for ELS and raft foundation design are presented in Table 1 and Table 2 respectively.

Table 1: Soil Parameters Adopted for ELS Design

Geological Stratum	γ_{sat} (γ_{unsat}) [kN/m^3]	Cu [kPa]		c' [kPa]	φ' [^{0}]	Eu [kPa]	E' [MPa]	
Fill	20.0 (17.5)	–		0	33	–	10	
Marine Deposits	16.0	22 + 2.5 x (-15 -z)		0	25	300 x Cu	–	
Alluvial Clay (C1/C2)	18.5	60 60 + 2.0 x (-27 -z)	z ≥ -27 z < -27	0	28	350 x Cu	–	
Alluvial Sand	18.5	–		0	28	–	20 20 + 4.0 x (-30 -z)	z ≥ -30 z < -30
Metasiltstone	20.0	–		3	30	–	40 40 + 2.0 x (-45 -z)	z ≥ -45 z < -45

z is elevation in mPD

Table 2: Additional Soil Parameters Adopted for Foundations Design

Geological Stratum	e_0	C_c	C_r	$C_{\alpha e}$	Ch – Cv (m^2/year)	OCR
Marine Deposits	N/A, soil improved with DCM					
Alluvial Clay (C1)	0.85	0.25	0.045	0.36	5.0 – 3.0	1.2
Alluvial Clay (C2)	1.1	0.6	0.045	0.86	5.0 – 3.0	1.0

3 GROUND IMPROVEMENT DESIGN

The ground improvement was designed to fulfil a dual function of vertical support for the permanent works raft foundation and lateral support for the temporary works retaining wall.

The depth of ground improvement is primarily driven by the foundation requirements, as treatment of the entire Marine Deposit was necessary to reduce long term settlements to acceptable levels. The ground improvement was therefore installed between a cut-off level of -8.0 mPD to a toe level typically between 20.0 mPD to -24.0 mPD. as shown in Figure 6. The toe level was designed to achieve a 2 m minimum embedment below the top of Alluvial Deposit, in order to cater for potential local variability of the ground profile and ensure that the ground improvement is founded on competent soil.

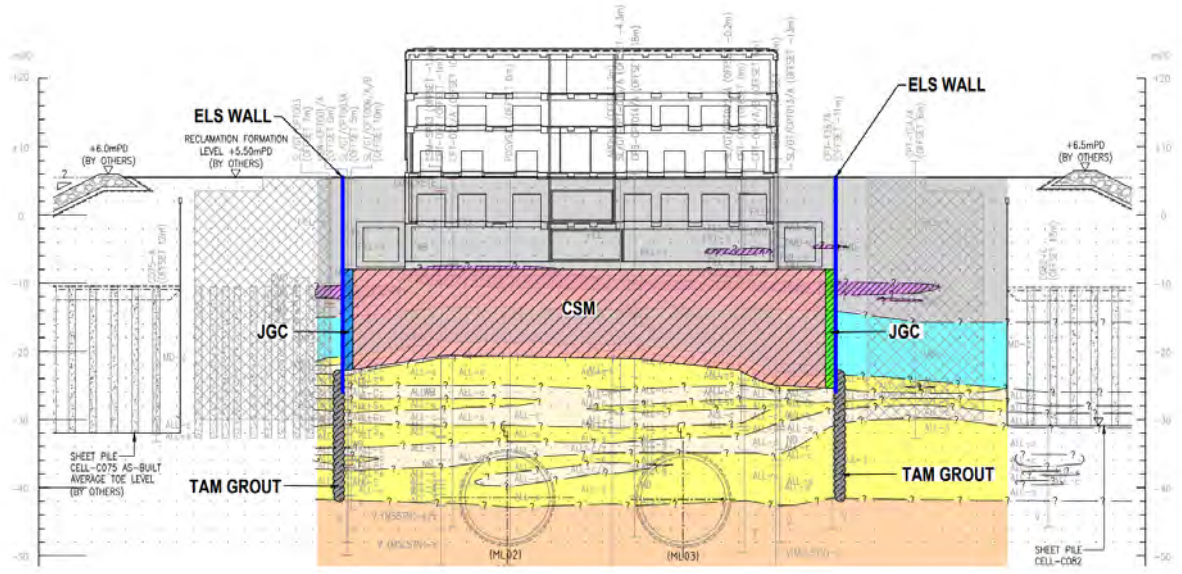

Figure 6: Ground Improvement Section

The ground improvement geometry replacement ratio was instead driven primarily by the excavation requirements. An orthogonal grid formed primarily of contiguous Cutter Soil Mix (CSM) panels was formed with an approximate replacement ratio of 55%, as shown in Figure 7. The dimensions of each panel are 1.2 x 2.4 m2. After completion of the CSM and installation of the ELS walls, an outer ring of Jet Grout Columns (JGC) of 1.5 to 1.8m diameter was installed between the CSM and the retaining walls to ensure adequate connection between the wall and the CSM grid for toe stability.

A number of CSM panels were previously installed for the construction of the circular shaft diaphragm walls and a parking plug for the tunnel boring machine to the north of the larger shaft. The ground improvement design for the SVB therefore incorporated these existing panels.

The ground improvement grids are formed by a pair of adjacent panels and are spaced at 7.2 m. Therefore, for the purpose of ground improvement passive pressure and toe stability, the effective replacement ratio of ground improvement grids orthogonal to the retaining wall is 33% (=2.4/7.2).

Typical ground improvement solutions for retaining wall design include relatively thin underground slabs with high replacement ratio, close to 100% (Page et al.2005, Wen 2005). For the SVB case, due to the dual function requirements, deep panels of 10 to 14m thickness below excavation level with relatively low replacement ratio were instead adopted. Due to the low replacement ratio, passive pressure is concentrated into the grids in orthogonal direction to the retaining walls, therefore a minimum UCS of 1.5 MPa was specified to provide sufficient lateral capacity. A summary of minimum required ground improvement parameters is provided in Table 3.

Table 3: Ground Improvement Minimum Required Parameters

Ground Improvement	γ_{sat} [kN/m^3]	UCS [MPa]	E [MPa]	SCR [%]
CSM and JGC	15.0	1.5	200	90

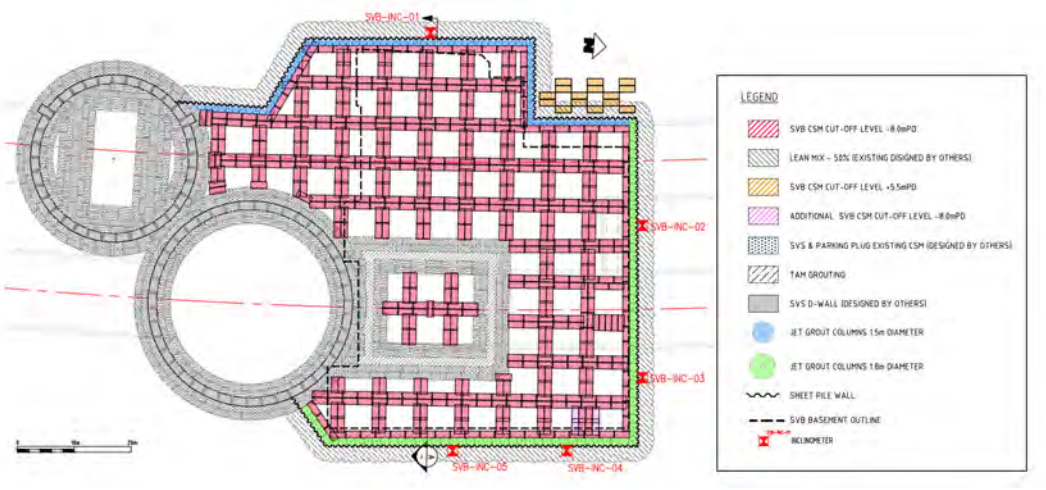

Figure 7: Ground Improvement Layout Plan

4 TEMPORARY EXCAVATION DESIGN

The basement construction required a 15 m deep excavation from ground level of +5.5 mPD to final excavation level of -9.5 mPD.

The ground improvement grid provides a stiff passive support to the retaining wall below ground level. This allowed optimisation of the shoring design quantities in comparison to the original excavation design which had been previously developed for the piled foundation scheme. The original design included a combi-wall of 1.2 m diameter pipe piles connected with double AZ18 sheet piles, embedded to a toe level of -30 mPD and supported by four levels of struts.

For the alternative design with ground improvement, the retaining wall size was reduced to FSP-V sheet-piles embedded to a toe level of -26 mPD. It should be noted that the toe level for the alternative design was driven by the need to form a water cut-off in the relatively thick Alluvial Sand layer identified below the Marine Deposit, in order to mitigate the risk of hydraulic uplift of the improved Marine Deposit layer and to reduce the groundwater inflow during the excavation works.

In addition, the number of strut levels was reduced from 4 to 3 levels. The strut quantities were further optimised by aligning the struts centerline in an orthogonal grid and connecting them at their intersection points. This configuration avoided using very long corner struts to deal with the particular geometry of the cofferdam and minimised the requirements for cross-bracing. The interaction between the different struts and walers generated by the grid alignment requires special consideration and therefore 3D analyses were carried out to assess the shoring performance, as shown in Figure 8.

The structural forces acting on the retaining wall and struts were assessed using both 2D and 3D Finite Element analyses, as shown in Figure 9. 3D analyses were required in particular to verify that the ground improvement capacity would be adequate to resist the horizontal stress concentration into the grids perpendicular to the retaining wall.

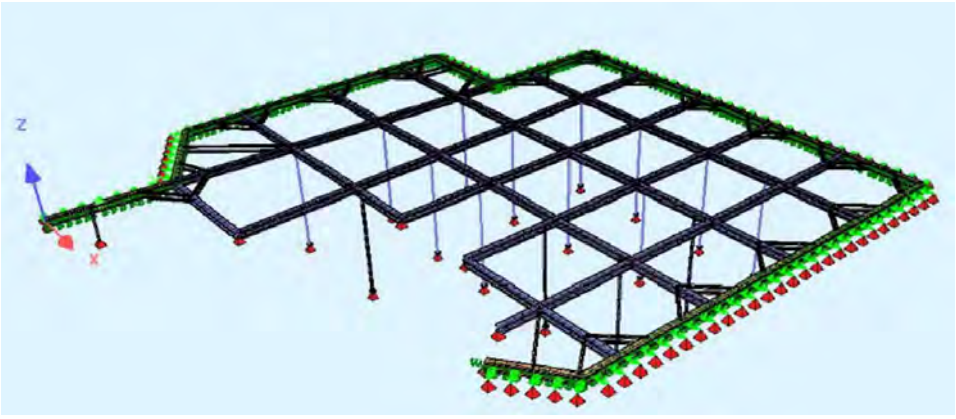

Figure 8: 3D Structural Model for Strut Design

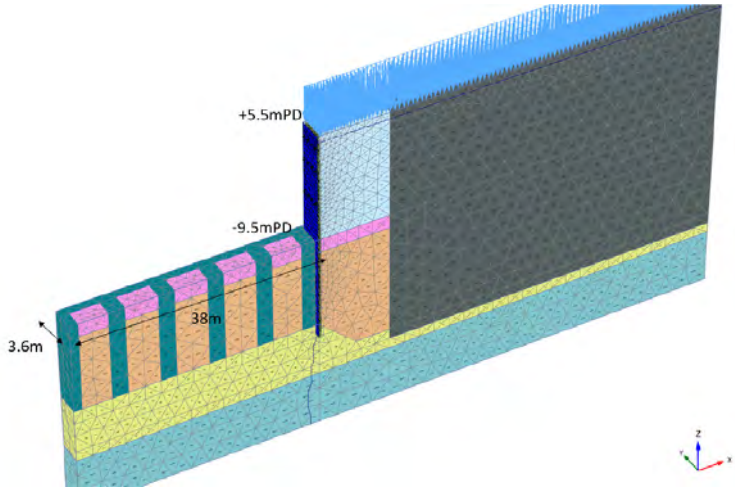

Figure 9: 3D FE Model for Temporary Excavation Design

5 RAFT FOUNDATION DESIGN

The SVB is founded on a continuous RC slab with top level generally of -6.95 mPD and thickness varying between 1.5 and 2.5 m.

The load-settlement behaviour of the building was modelled using 3D Finite Element soil-structure interaction analyses. The slab detailed geometry with variable thickness is modelled using continuum elements. As shown in Figure 10, the loads from each column, load bearing wall, and the distributed loads on the base slab are modelled individually in order to determine a realistic load distribution at the underside of the slab. The bearing pressure is typically between 100 and 250 kPa, as shown in Figure 11.

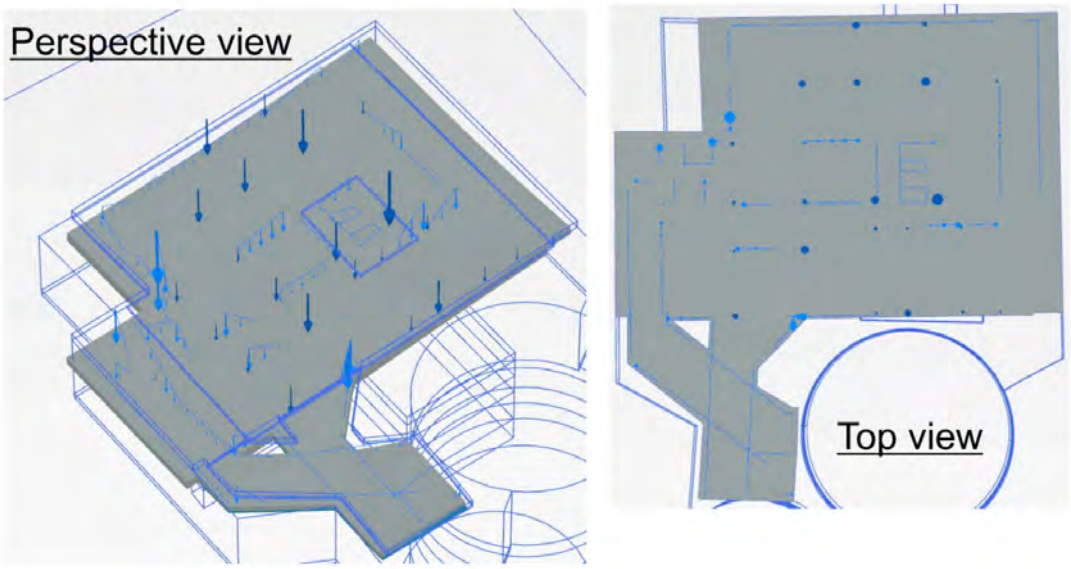

Figure 10: 3D FE Model for Foundations Design

The Alluvial Sand and CDM materials are modelled using the Mohr-Coulomb soil model, whilst the Alluvial Clays C1 and C2 are modelled with the 'Soft Soil Creep' model (Stolle et al. 1999). The effects of the reclamation additional overburden and unloading caused by the temporary excavation are considered in order to estimate a realistic vertical stress distribution within the underlying Alluvial Clays. For long term settlement assessment, the beneficial contribution of the groundwater uplift pressure at the underside of the slab was considered assuming a mean low water level of +0.3 mPD.

The analyses predicted a long term settlement of approximately 110 to 190 mm over 120 years design life. Approximately 50 mm of the total settlement were expected to occur in short term during construction.

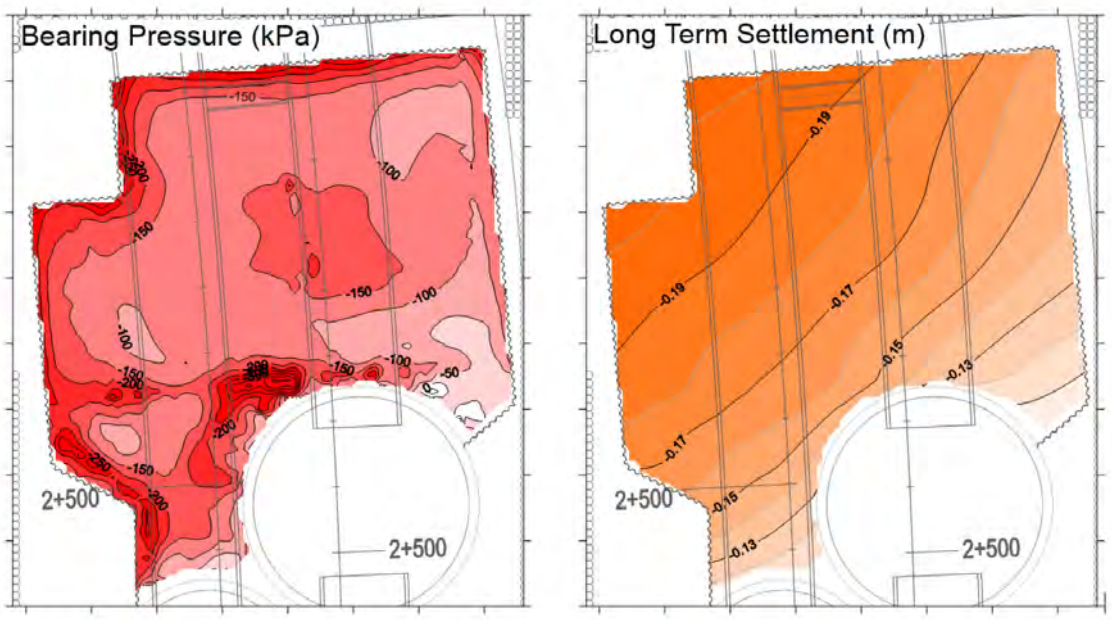

Figure 11: Raft Foundation Bearing Pressure and Predicted Long Term Settlement

6 GROUND IMPROVEMENT PERFORMANCE REVIEW

6.1 Ground Improvement Quality Control

Over 600 CSM panels and 150 JGCs were installed under the SVB. The strength and quality of the ground treatment was verified by carrying out a total of 30 and 8 cores in the CSM and JGCs respectively. For each core, four samples were selected for UCS testing. The test results are summarised in Figure 12. Approximately 98% and 92% of the tests demonstrated higher UCS than the minimum specified 1.5

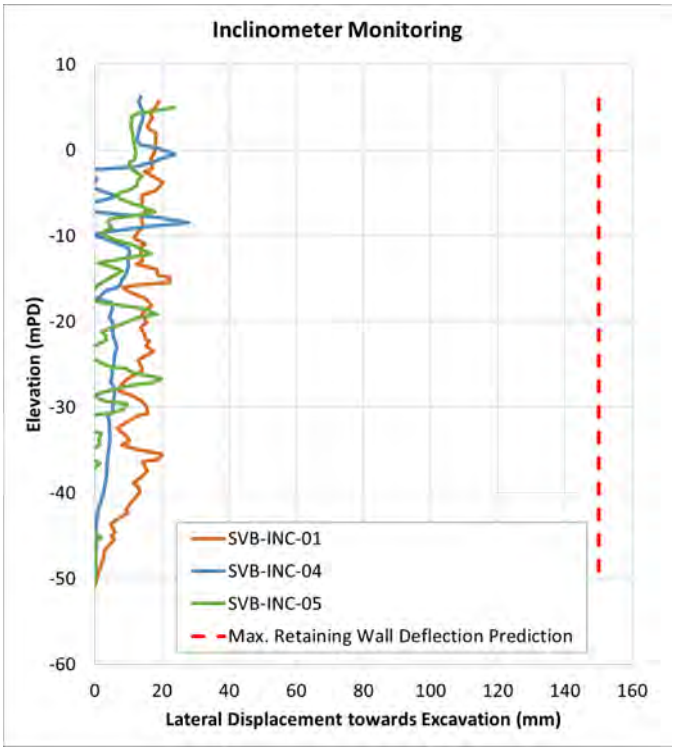

Figure 12: UCS and Young's Modulus QC Testing Results

MPa for the CSM and JGC respectively, which met the minimum 90% passing criterion. The mean UCS is approximately 4.6 MPa for both CSM and JGC, whilst the standard deviation is 1.3 MPa and 1.9 MPa for the CSM and JGC respectively.

It is considered that the ground improvement strength achieved in-situ exceeded the design requirement, in particular for the CSM panels which form the critical grid at a lower replacement ratio within the footprint of the excavation.

6.2 Excavation Performance

A total of 5 inclinometers were installed directly behind the sheet pile wall to monitor the lateral movements during the excavation and construction of the basement, as shown in Figure 7. A plot of available data after completion of the basement is presented in Figure 13. Typically less than 20 mm lateral movement was measured, which is significantly smaller than the predicted 150 mm maximum retaining wall deflections, indicating that the ground improvement and strutting system was very effective in supporting the 15m deep cofferdam excavation.

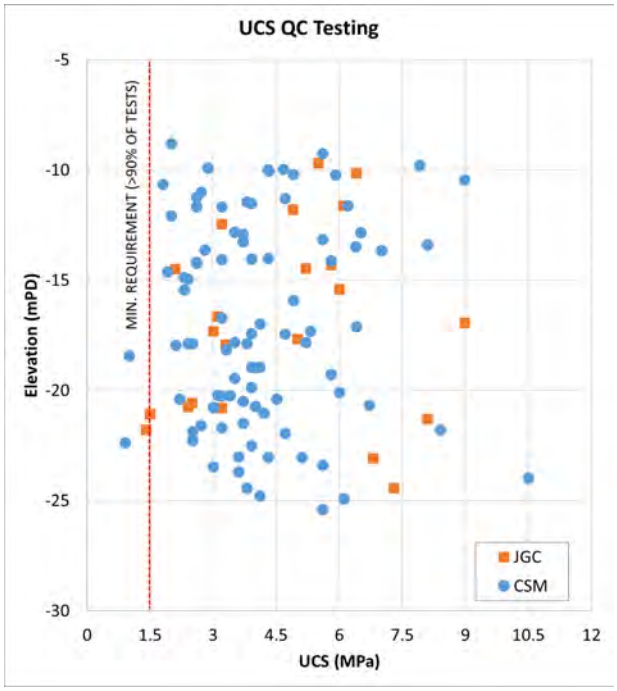

Figure 13: Inclinometer Monitoring

6.3 Foundations Settlement Performance

A total of four building settlement markers were installed at the ground level slab to verify the long-term performance of the raft foundations. The available data is presented in Figure 14. Less than 10 mm settlement were recorded over approximately 18 months between January 2019 and May 2020, with a stable trend of negligible settlement after October 2019. As the building main reinforced concrete works were completed in August 2019, the data indicates that the settlement performance is satisfactory and likely to be within the 190 mm predicted long term settlement over 120 years design life.

6 CONCLUSIONS

The construction of the Southern Ventilation Building provided a challenge due to the presence of a layer of soft clay directly underlying the basement slab, depth of rockhead exceeding 100m below ground level and construction of two large diameter twin tunnels at approximately 20m below the basement.

An effective solution was developed to found the building on a raft sitting directly on deep soil mixing ground improvement. This alternative design replaced over 300 shaft grouted piles. In addition,

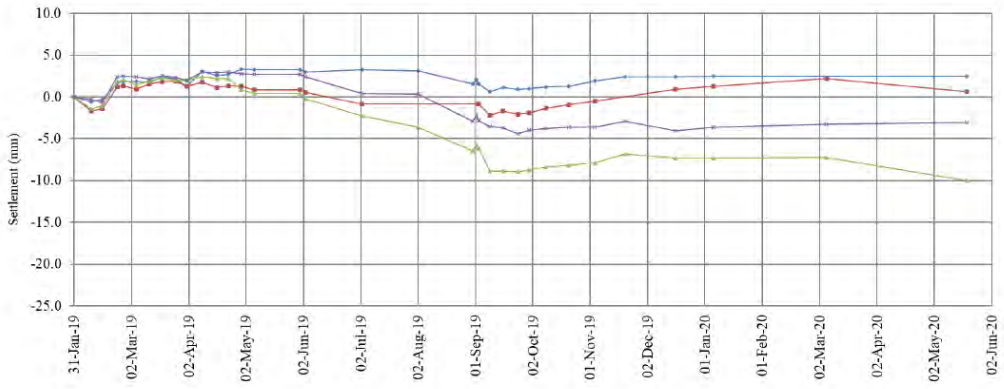

Figure 14: Building Settlement Monitoring

the ground improvement was leveraged to significantly optimise the shoring design for the 15m deep excavation, deleting one level of struts and reducing the size of the retaining wall from combi-wall to FSP V sheet pile.

The installation of the ground improvement on the field was successful. The minimum design criteria in terms of unconfined compressive strength have been achieved with more than 90% of the tested samples exceeding the required 1.5 MPa strength with an average exceeding 4 MPa.

Very limited lateral movement during excavation and post-construction settlement of the buildings have been measured, indicating that the performance ground improvement scheme has been highly satisfactory.

REFERENCES

Page, R.J., Ong, J.C.W. Osborne, N. & Shirlaw, J.N. 2005. Jet Grouting for Excavations in Soft Clay – Design and Construction Issues. Conference: International Conference on Deep Excavations (ICDE) 2006.

Stolle, D.F.E., Vermeer, P.A., and Bonnier, P.G. 1999. A consolidation model for a creeping clay. *Canadian Geotechnical Journal,* Volume 36, Number 4, 22 November 1999.

Wen, D. 2005. Use of Jet Grouting in Deep Excavations. *Elsevier Geo-Engineering Book Series,* Volume 3, 2005, Pages 357-370.

Open Cut Excavation Observational Method Associated with 3D Analysis for HKBCF PCB

A. Martucci & A. Pickles
Golder Associates (HK) Ltd.

ABSTRACT

The design of open cut excavations in newly reclaimed land overlying soft soils is often highly sensitive to the undrained strength parameter values. Under such circumstances, the use of the Observational Method may introduce significant programme and quantity savings by allowing the designer to adopt best estimate, rather than moderately conservative parameters.

The Hong Kong Boundary Crossing Facilities (HKBCF) is located on newly reclaimed land located to the East of Chek Lap Kok Island. The Passenger Clearance Building (PCB) is located in the middle of the HKBCF and provides the customs and immigration facilities for passengers entering Hong Kong from the Hong Kong-Zhuhai-Macau Bridge and the Tuen Mun-Chek Lap Kok Link.

The construction of the PCB basement required an excavation of approximately 10 m depth over an area of approximately 200 by 200 m. The typical soil profile consists of 15 m of sand fill overlying 20 m of very soft to soft Marine Clay. Ground improvement with prefabricated drains and surcharge was adopted by the reclamation Contractor to improve the Marine Clay strength. Extensive ground investigations indicated that the Marine Clays had not been fully consolidated at the time of the excavation work and the majority of the clays were still significantly weaker than anticipated. The low strength of the Marine Clays posed a stability related challenge to the design of the basement excavation.

The standard design approach based on 2D stability analyses would have required extensive ground treatment to be carried out to improve the clay by, for example, cement injection (i.e. jet grouting or deep soil mixing). However, an innovative open cut solution was developed, using 3D modelling associated with observational method, taking advantage of the particular basement geometry to fully account for the 'edge effects', which increase the excavation stability when the excavation is of limited extent.

The design provided an effective and sustainable solution compared to the ground improvement option, which would have required injection of over 14 thousand tons of cement in the soft soils and would cost approximately 12 million US$. The observational method implementation further saved over 2 months of programme. To the authors' knowledge, this project marks the first successful implementation of a combination of 3D stability analyses and the observational method on a large scale infrastructure project in Hong Kong.

1 INTRODUCTION

The infrastructure for the Hong Kong Boundary Crossing Facilities (HKBCF) is constructed on newly reclaimed land located to the east of the Hong Kong International Airport at Chek Lap Kok island. The HKBCF serves as a transportation hub connecting Lantau Island and the Hong Kong International Airport (HKIA) with the Hong Kong-Zhuhai-Macau Bridge (HKZMB) and the Tuen Mun-Chek Lap Kok Link

(TMCLKL). The Passenger Clearance Building (PCB) provides the customs and immigration facilities for passengers entering Hong Kong from the HKZMB. Aerial view photo of the PCB and the HKBCF is presented in Figure 1.

Construction of the PCB basement required a 9.5 m deep excavation in Fill overlying very soft to firm Marine Clay. The design of the excavation was optimised using the observational method, associated with detailed 3D modelling of the excavation sequence.

This paper describes the design philosophy adopted for the open cut observational method adopted. The excavation performance is assessed with reference to the benefits achieved with the implementation of the observational method and comparison of predicted soil movement against monitoring data.

Figure 1: Aerial View of PCB (https://www.hzmb.gov.hk/en/info/photo-hkbcf.html)

2 PROJECT DESCRIPTION

The PCB comprises of a 2 level high podium structure with a roof cladding system and basement, occupying a footprint of approximately 200mx200m in plan. The building is founded on a system of reinforced concrete pilecaps and beams, supported by large diameter bored piles founded on rock.

The construction of the foundations required an excavation of approximately 9.5 m depth to a final formation level of approximately -4 mPD. This paper focuses on the excavation of the western portion of the basement, where very soft Marine Clay was encountered below the reclamation fill.

3 SUBSOIL CONDITIONS

The geological profile across the site has been altered by the reclamation works undertaken in the area to form the HKBCF island. The site formation level after surcharge removal is at +5.5 mPD. The reclaimed land was constructed using sand fill placed directly over soft marine clay improved with Prefabricated Vertical Drains (PVD). Surcharging was applied to accelerate consolidation. The geological profile after reclamation consists of 5 main layers:

a) Fill – typically medium dense to dense sand

b) Marine Deposit – typically very soft to firm silty clay

c) Alluvial Deposit – typically interbedded layers of firm to stiff silty clay and medium dense to very dense silty clayey sand

d) Completely and Highly Decomposed Granite (C/HDG)

e) Moderately Decomposed Granite (MDG) or better

A simplified geological section is shown in Figure 2

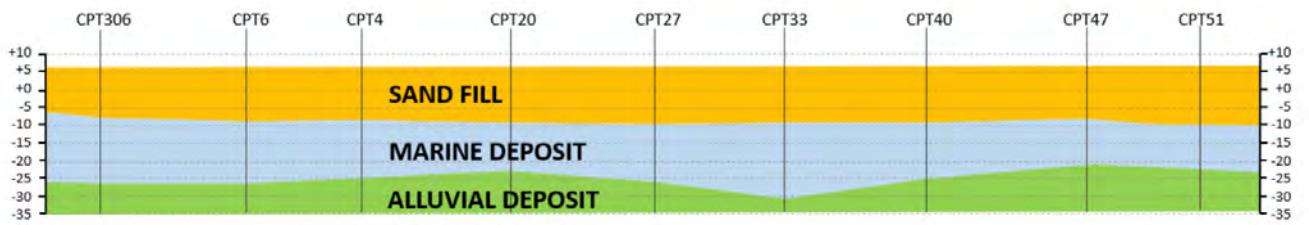

Figure 2: Geological Section

Traditional open cut design is based on adoption of moderately conservative parameters. For the observational method, a second set of most probable parameters is also required. The two sets of parameters adopted for the observational approach are summarised in Tables 1 and 2. It can be seen from Tables 1 and 2 that the differences between the moderately conservative and most probable parameters are limited to the strength and stiffness of the marine clay and the stiffness of the fill and alluvial deposits, as these are the parameters that control both the stability of the excavation and the predicted movements of the ground.

Table 1: Summary of Moderately Conservative Soil Parameters

Geological Stratum	γ_{sat} (γ_{unsat}) [kN/m^3]	Cu [kPa]	c' [kPa]	φ' [^{0}]	Eu [kPa]	E' [MPa]
Vibrocompacted Fill above + 1.0 mPD	20.0 (17.5)	–	0	37	–	15
Uncompacted Fill below + 1.0 mPD	19.5 (16.5)	–	0	35	–	15
Marine Deposits	16.5	Refer to Figure 4	0	25	350 x Cu	–
Alluvial Deposits	18.5	60 + 5.0 x d	0	28	350 x Cu	–

d is depth below -34 mPD

Table 2: Summary of Most Probable Soil Parameters

Geological Stratum	γ_{sat} (γ_{unsat}) [kN/m^3]	Cu [kPa]	c' [kPa]	φ' [^{0}]	Eu [kPa]	E' [MPa]
Vibrocompacted Fill above + 1.0 mPD	20.0 (17.5)	–	0	37	–	25
Uncompacted Fill below + 1.0 mPD	19.5 (16.5)	–	0	35	–	25
Marine Deposits	16.5	Refer to Figure 4	0	25	460 x Cu	–
Alluvial Deposits	18.5	60 + 5.0 x d	0	28	200 x 10^3	–

d is depth below -34 mPD

3.1 Marine Deposits Undrained Shear Strength

The undrained shear strength (Cu) of the Marine Deposits is the critical parameter with regards to the stability of the open cut. Extensive ground investigations were carried out to determine the nature and variability of the clay across the site, mainly by boreholes, Cone Penetration Tests (CPT) and Vane Shear Tests (VST), as shown in Figure 3.

The western portion of the basement (denominated Area W in Figure 3) is where the weakest Marine Deposits were encountered, with typical values between 10 and 50 kPa. A significant degree of variability is identified from the available GI. The moderately conservative and most probable design lines were determined based on CIRIA C580 definition, corresponding approximately to values with approximately 75% and 50% probability of exceedance, respectively. Figure 4 shows the adopted strength profiles.

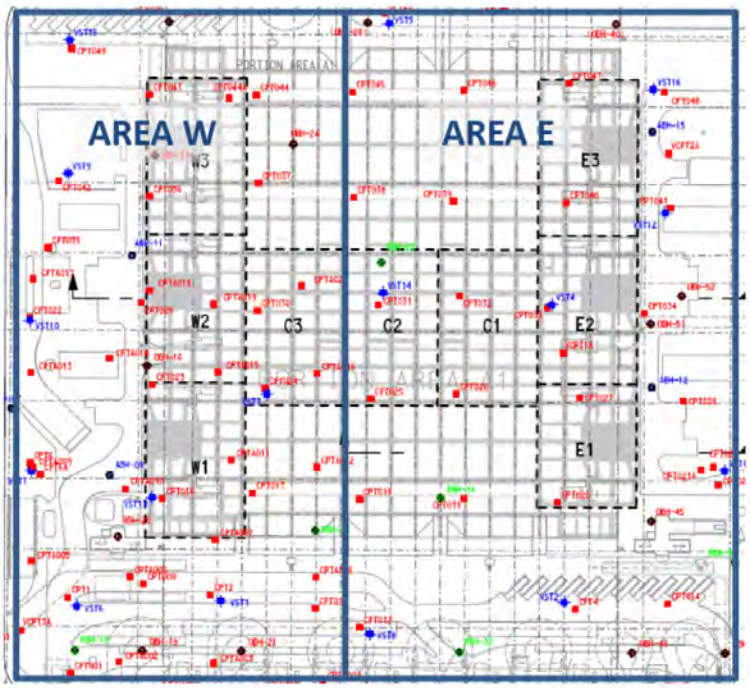

Figure 3: Marine Deposits Strength Zoning

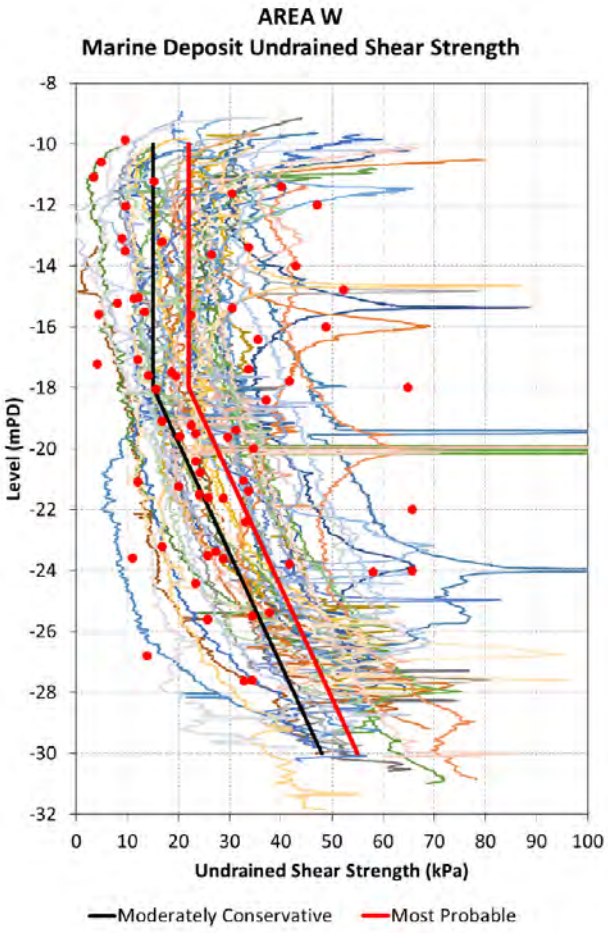

Figure 4: Marine Deposits Undrained Shear Strength at Area W

4 OPEN CUT EXCAVATION DESIGN

4.1 Introduction

The basement excavation was carried out in a staged manner starting from the south-east corner and progressing towards the north-west. The eastern portion (Area E) of the basement was located over an area with stronger Marine Deposits, whilst the most challenging conditions were encountered at the western portion.

Traditional design using moderately conservative parameters and 2D stability analysis was found to be adequate for Area E. 3D analyses associated with the observational method using most probable parameters were instead implemented to optimise the excavation design at Area W. The overall excavation sequence is presented in Figure 5, this paper focuses on Stages 5 to 12 for the western half of the basement.

Adoption of 3D analyses allows for consideration of three-dimensional failure modes which, in most cases, results in more realistic and less conservative FoS than 2D analyses (Zhang 1988; Michalowski 2010) . This is because 3D failure surfaces typically have so-called spoon or bowl shape failure mechanisms, whilst 2D surfaces extend in one dimension (i.e. plane strain) and therefore there is no contribution from shear resistance in the orthogonal direction.

The three-dimensional analyses took advantage of the particular geometry of the basement. The contribution of three-dimensional effects was further enhanced by developing a sequence to limit the excavation front extents.

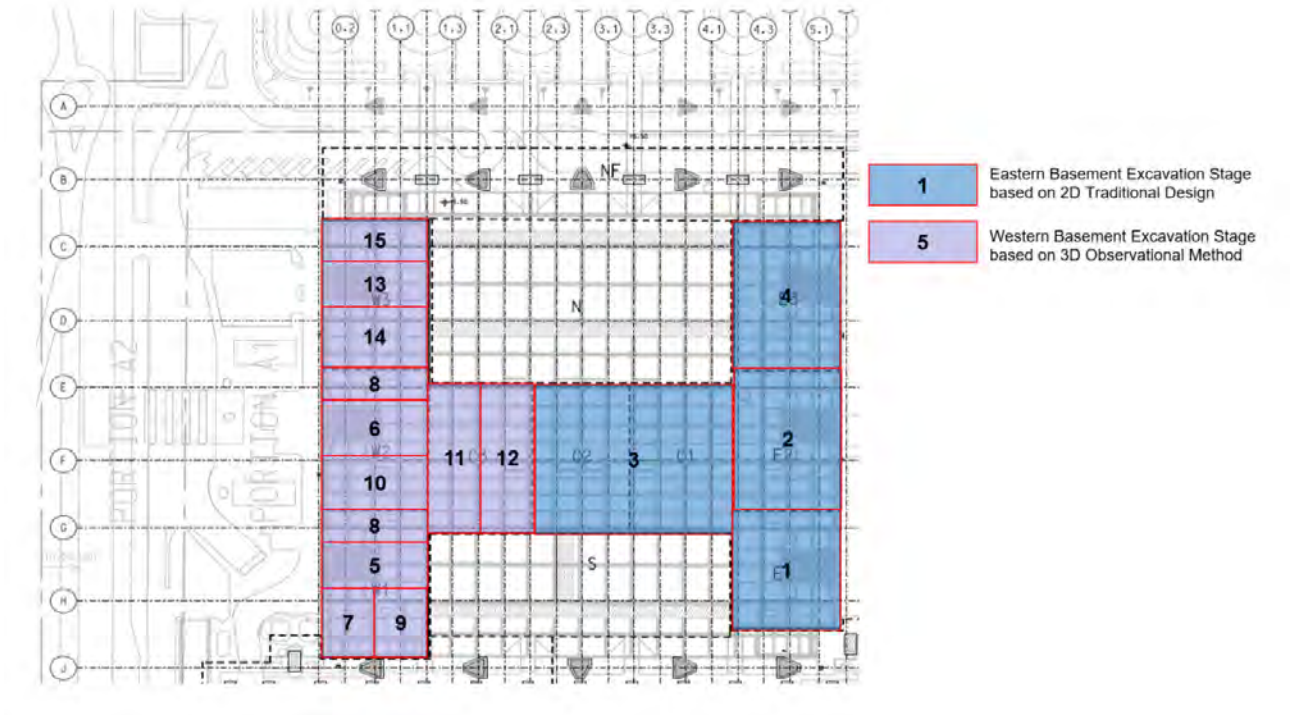

Figure 5: Excavation Sequence

The observational method was implemented based on the recommendations set out in CIRIA 185 (Nicholson et al. 1999) and CIRIA C580 (Gaba et al. 2003). At its core, the observational method involves the adoption of most probable soil parameters, associated with a strong emphasis on monitoring of the excavation performance, to continuously compare predicted with measured soil movements.

The Observational Method is a more rational design and construction method than the traditional approach for a number of reasons as follows:

- The Observational Method allows for a more efficient and cost-saving design proposal to be adopted which is less wasteful and not designed to an overly conservative factor of safety.

- The Observational Method requires risk-sharing, integration and cooperation between the supervising officer, designer and site construction team. This is necessary to reach agreement to change the construction sequence in response to the observed soil movement and excavation performance.
- Typically, a more extensive monitoring programme is required compared with traditional design, which requires increased density of instrumentation to be installed. However, greater attention is paid towards the monitoring works on site which results in improved control of design uncertainties. This inevitably leads to greater understanding of the design requirements and fosters a safer working environment.
- The use of the observational approach does involve additional costs for monitoring works but these are more than offset by the construction cost and time savings. As the observational approach requires some flexibility in the construction program, it is usually more appropriate for the contractor to propose and adopt such an approach, otherwise fairly significant changes may be required to contract documents.

A minimum global FoS > 1.3 was adopted. This value is somewhat higher than required by the HK Ports Works Manual but is more appropriate for conditions which are controlled by the undrained strength of the ground.

4.2 Implementation of 3D Analyses

Preliminary design analyses for the Area W open cut were carried out with standard 2D Finite Element methodology. The analyses indicated that two intermediate benches of 60 and 40m width would be required between the formation level at +5.5 mPD and the final excavation level at -4.0 mPD to achieve the minimum required FoS. A typical failure surface determined from 2D analyses is presented in Figure 6. The failure mode involves an extensive horizontal surface of the order of 100m length with the Fill sliding on top of the soft Marine Clay. This slope profile was considered impractical as the width of the required benches would significantly increase the excavation volumes and the crest of the slope would extend beyond the site boundary.

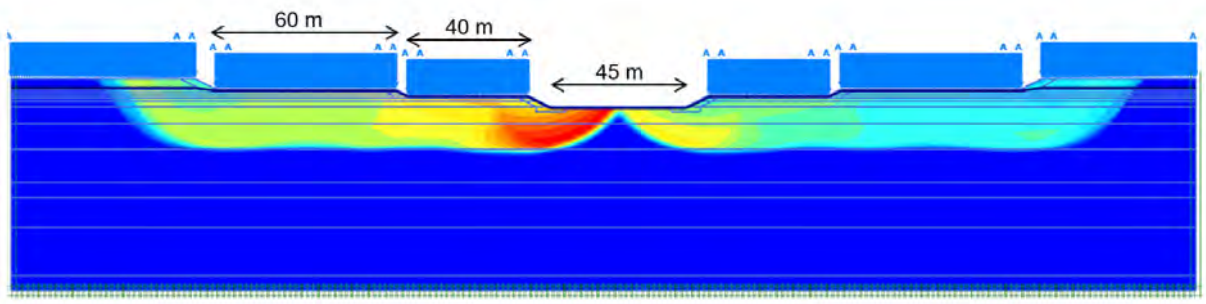

Figure 6: Failure Surface for 2D analysis at Area W

A ground improvement solution was then studied to minimise the excavation volumes. Figure 7 shows the extent of ground improvement, using deep cement mixing or equivalent method, required to achieve a sufficient FoS using 2D analyses and moderately conservative parameters. The scheme would have required continuous ground improvement 'panels' embedded into Alluvial Deposits beneath the slope toes, connected by a thinner ground improvement 'slab' across the basement, enabling a 1:2 single slope from formation to final excavation level. A replacement ratio (ratio between the treated soil plan area and the total plan area) of approximately 50% was envisaged. Whilst a ground improvement solution would have been effective in optimising the excavation volumes, the extent of required ground improvement would have been significant, given the size of the basement.

Therefore, in order to achieve a more rational and sustainable design, an innovative open cut design based purely on three-dimensional stability considerations, without requirement for any additional ground improvement, was developed. By using 3D analyses it was possible to significantly reduce the

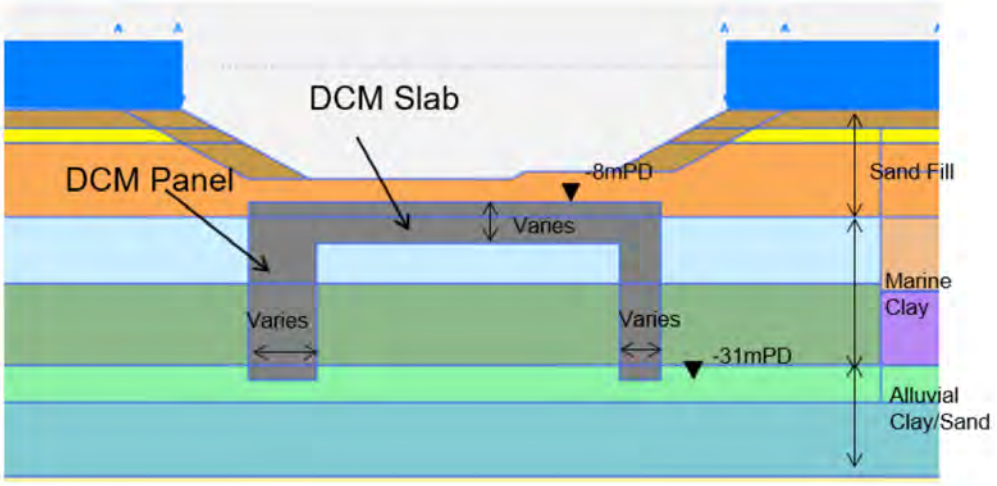

Figure 7: Potential Ground Improvement Solution

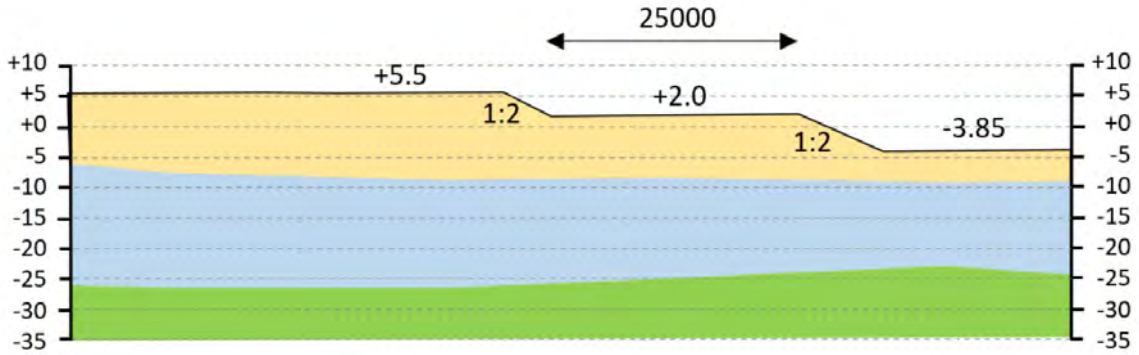

Figure 8: Open Cut Profile for Area W

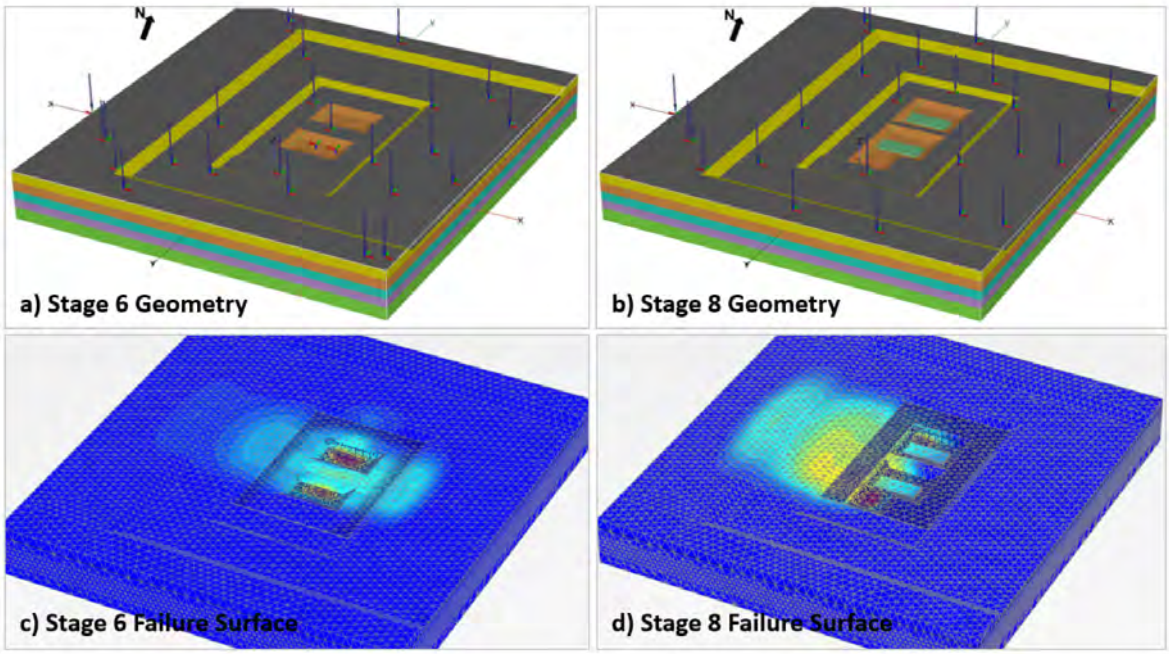

Figure 9: 3D Analysis for Stages 2D and 3D Based on Moderately Conservative Parameters

excavation volumes, adopting a single intermediate bench of 25 m width at +2.0 mPD and 1:2 gradient slopes, as shown in Figure 8. This design was based on moderately conservative parameters.

The open cut stability in a three-dimensional analysis is sensitive to the extent of the excavation, therefore a specific sequence was developed, dictated by the objective to limit the extent of the open cut front in order to maximise the three-dimensional effects.

As the excavation front progresses, portions of the basement foundations are required to be installed, as the pilecaps and beams provide additional constraints to the potential failure surfaces, thereby increasing the stability of the excavation.

As an example, with reference to the sequence shown in Figure 5, the excavation in Area W commenced at the two Zones 5 and 6 first. Before the adjacent Zones 7 and 8 could be excavated, it was required to install the foundations in both Zones 5 and 6. Similar constraints were necessary for the remainder of the excavations sequence, as summarised in Table 3.

Table 3. Comparison of Foundations Construction Requirements

Excavation Area	Foundation Construction Requirements Moderately Conservative Parameters – Areas	Foundation Construction Requirements Most Probable Parameters – Areas
5	None	None
6	None	None
7	5	None
8	5, 6	None
9	5, 6, 7	None
10	5, 6, 7, 8	5
11	5, 6, 7, 8	5
12	5, 6, 7, 8, 10	5, 6
13	5, 6, 7, 8, 9, 10, 11, 12	5, 6, 8
14	5, 6, 7, 8, 9, 10, 11, 12, 13	5, 6, 8
15	5, 6, 7, 8, 9, 10, 11, 12, 13, 14	5, 6, 8

4.3 Implementation of Observational Method

The observational method was developed for the Area W excavation before the commencement of the excavation in these areas ('Ab Initio' approach).

Application of the 'Ab Initio' approach was possible because sufficient data on the performance of the Area E excavation was available from inclinometers and ground movement markers was available as Stages 1 and 2 of the sequence, which correspond to the south-east corner of the basement had been completed.

The available monitoring data was used to carry out a back-analysis using 3D modelling and most probable soil parameters based on available GI data. Figure 10 presents the ground movements predicted by the Plaxis 3D model against the lateral movement monitored by the inclinometer adjacent to the slope crest after completion of the excavation to final formation level within Stages 1 and 2 zones.

One of the key findings of the back-analysis was that the Alluvium behaved in a stiffer manner than expected, likely because this layer is outside the influence depth of soil movements induced by the excavation unloading. In order to match the measured movements, the Young's modulus of the Alluvium was increased from approximately 20 MPa to 200 MPa, which is representative of a small strain stiffness of the alluvium.

The stiffness of the Marine Deposits and the Fill were also slightly increased by 30% and 67% respectively.

In accordance with the observational method framework, an optimised sequence was developed using most probable parameters to accelerate the programme with comparison with the sequence determined using moderately conservative parameters. Both sequences followed the same excavation stages, generally progressing from the south towards the north from Stage 5 to 15 (stages 1 to 4 refer to Area E) and the same open cut profile with 25m wide bench at +2.0 mPD. The key difference introduced

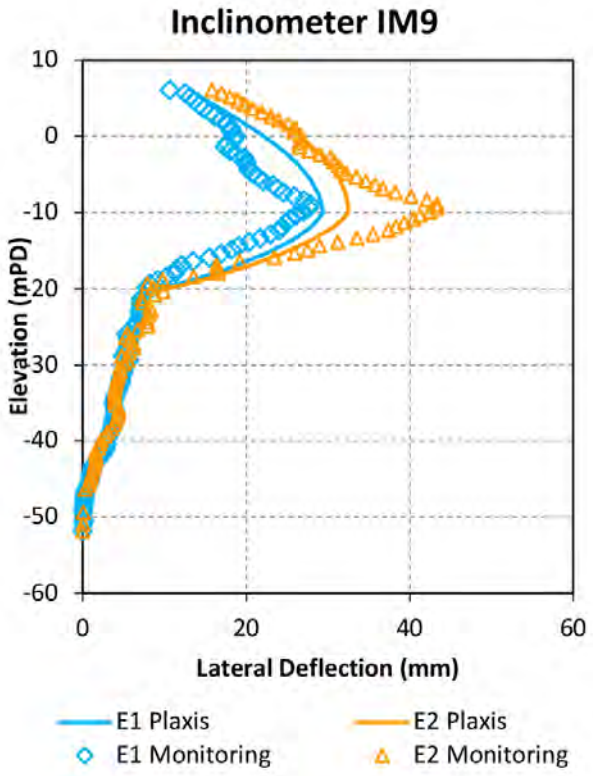

Figure 10: Results of Open Cut Back Analysis for Movement after Completion of Stages 1 and 2 Excavation

in the Observational Method sequence is a significant reduction in the requirements for construction of foundations pilecaps and beams, in order to speed up the temporary excavation progress. Table 3 shows a comparison of foundation construction requirements according to the moderately conservative and most probable sequences.

It is clear how the successful implementation of the observational method would enable the contractor to delete the majority of basement construction requirements and speed up the excavation programme.

A relatively extensive set of monitoring instrumentation was proposed to control the observational approach. In order to target the instrumentation work in the most efficient manner, the instruments were split into three categories:

- Critical – a limited number of instruments which are directly adjacent to the area being excavated. These instruments were considered the most relevant to assess the excavation safety and performance and were monitored twice a day.
- Primary – the rest of the instruments surrounding the basement and located close to the open cut slope crest. These instruments were monitored on a daily basis.
- Secondary – all other instruments within 50 m of the ongoing excavation work. These instruments were monitored at least two times per week.

A plan of the proposed instrumentation to monitor the excavation performance is shown in Figure 11. A total of 23 inclinometers at approximately 15m spacing and 24 soil movement markers were installed for the Area W observational method monitoring.

The excavation performance was assessed with reference to Trigger Levels for soil lateral movement and soil shear strain levels measured from the inclinometer data.

Soil movements Trigger Levels were based on design predictions at each stage and at each inclinometer location for both most probable and moderately conservative sequences as follows:

a) Amber Trigger – Corresponds to the ground movement prediction using most probable parameters, 10 kPa surcharge load and a groundwater level of -1.0 mPD which was based on the measured levels in observation wells in Area W. The low water level is a result of the ongoing dewatering.

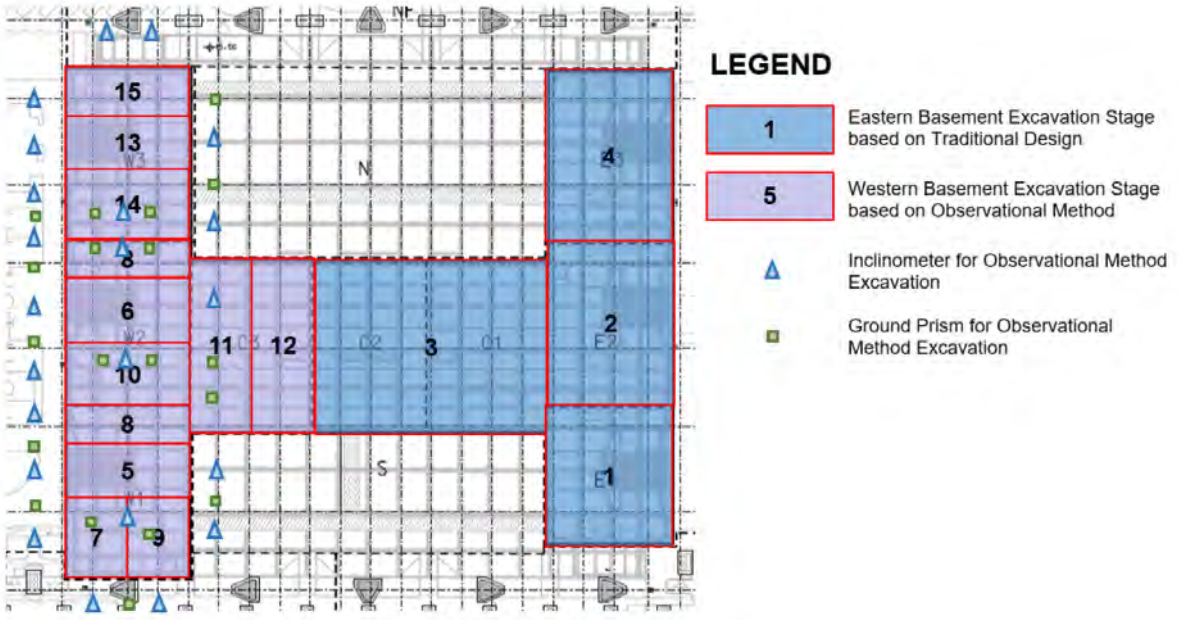

Figure 11: Monitoring Plan

b) Red Trigger – Corresponds to 80% of the ground movement prediction using moderately conservative parameters, 10 kPa surcharge load and a robust groundwater level of +1.5 mPD.

The factor of 80% applied for the red trigger is to take into account the condition that the soil movements may not occur instantaneously during the excavation works due to the presence of soft undrained material. The ground may instead exhibit 'creep behaviour' with increase in movements over time, even if no further excavation works are carried out.

Shear strain trigger levels, determined from the inclinometer profiles, were also adopted in order to overcome the uncertainty caused by variations of the ground profile and soil stiffness, which may affect the magnitude of predicted movements, as follows:

- Amber Trigger – Maximum shear strain of 1%
- Red Trigger – Maximum shear strain of 2%

Soft clays are considered to reach approximately 80 to 90% of peak stress capacity at shear strain levels of the order of 3 to 4%, therefore it is considered prudent to monitor the stability of the excavation against a maximum allowable shear strain of 2%. These shear strain Trigger levels are considered to represent the most objective way of determining the stability of the excavation, as they are not sensitive to the soil strength and stiffness design assumptions.

The observational method framework required that whenever an Amber Trigger is exceeded, a thorough review of the monitoring data is carried out in order to review the movement trends and assess the stability. Ad-hoc actions such as increased monitoring frequency would be required on a case by case basis.

If a Red Trigger is exceeded, any further excavation work would be stopped and contingency measures requiring construction of the foundations in accordance with the moderately conservative design sequence would be applied.

Furthermore, should the ground continue to creep and movements exceed 120% of predicted values, emergency measures would be applied to mitigate the risk of deep seated slope failure. Emergency measures typically required the contractor to backfill the excavation with a minimum of 2 m soil, or until the movements stabilise.

5 PERFORMANCE REVIEW

Continuous monitoring was carried out to verify the stability and safety of the excavation. The excavation lateral movement measured by the inclinometers were generally in agreement with the design predictions using most probable parameters, which had been used to set the Amber Triggers.

Figure 12 shows the movement profiles for the inclinometers installed at the west of the excavation. The maximum movement occurs towards the top of the Marine clays and was typically of the order of 100 mm, which is slightly larger than the predicted movements.

As indicated from the back-analysis at the eastern portion, the Alluvial Deposits behaved in a relatively stiff manner also for the excavation in the western portion. Above the alluvial deposits, the Marine Deposits exhibit a sharp increase of lateral movement due to shear strains necessary to mobilise the required shear stresses and achieve equilibrium due to the excavation works. Typically, maximum shear strains of approximately 1 to 1.5% (below the red triggers) were determined from the inclinometer profiles.

Of interest is the analysis of the development of the soil movements as the staged excavation progresses. Figure 13 shows the cumulative movement at the top of the Marine Deposits for Inclinometer IM21, which is located at the west of the Stage 5 area, as shown in Figure 14. The plot also includes the Amber and Red triggers determined at this inclinometer location for the different stages based on the design analyses. The largest movement contribution at this location is due to the excavation of the adjacent Stage 5 area, however further incremental movements are predicted as the excavation progresses and, in particular, when the adjacent Stage 6 and 7 areas were completed.

The inclinometer data indicates relatively good agreement with the Amber Trigger. However, the soil response appears to initially lag behind the excavation (Stages 5 to 6). After Stages 7/8, ongoing movement is measured after the excavation of all adjacent areas had been completed, albeit with a slower rate. This movement is considered to be due to creep of the soft Marine Deposits as this soil responds to the unloading caused by the excavation.

Similar relatively small rates of creep movement were measured generally in all inclinometers, however this tended to stabilise over time as the construction of the basement foundations progressed.

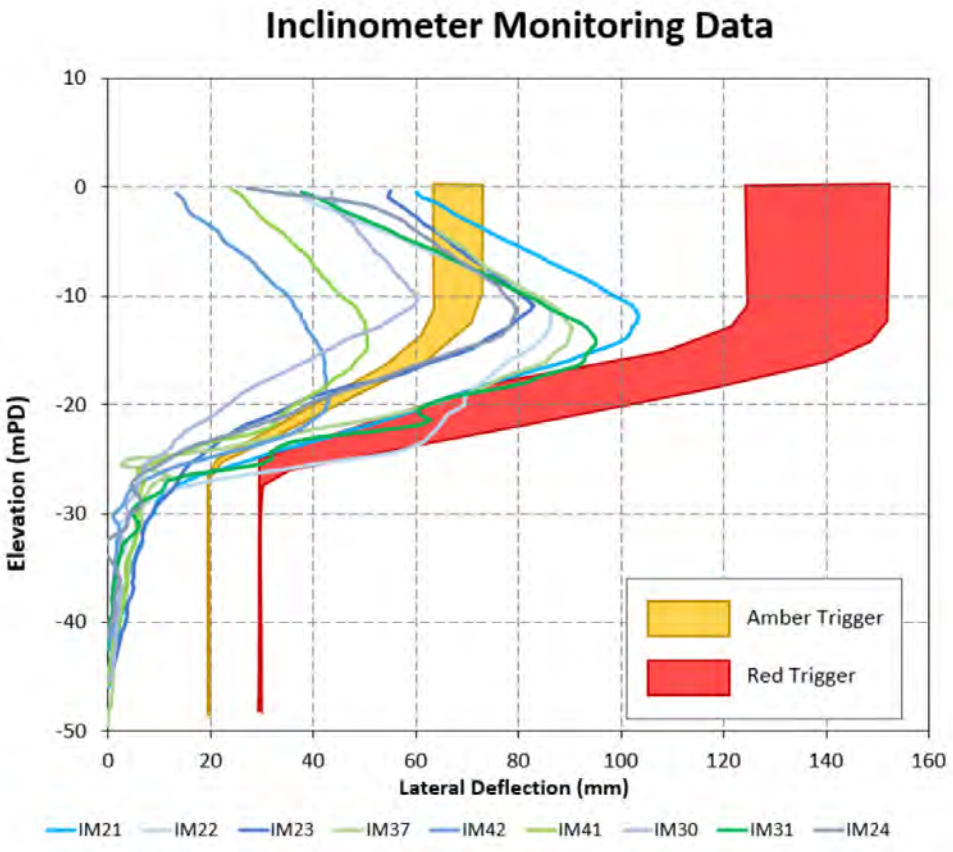

Figure 12: Inclinometer Movement Profiles at West of the Area W Excavation vs Trigger Levels

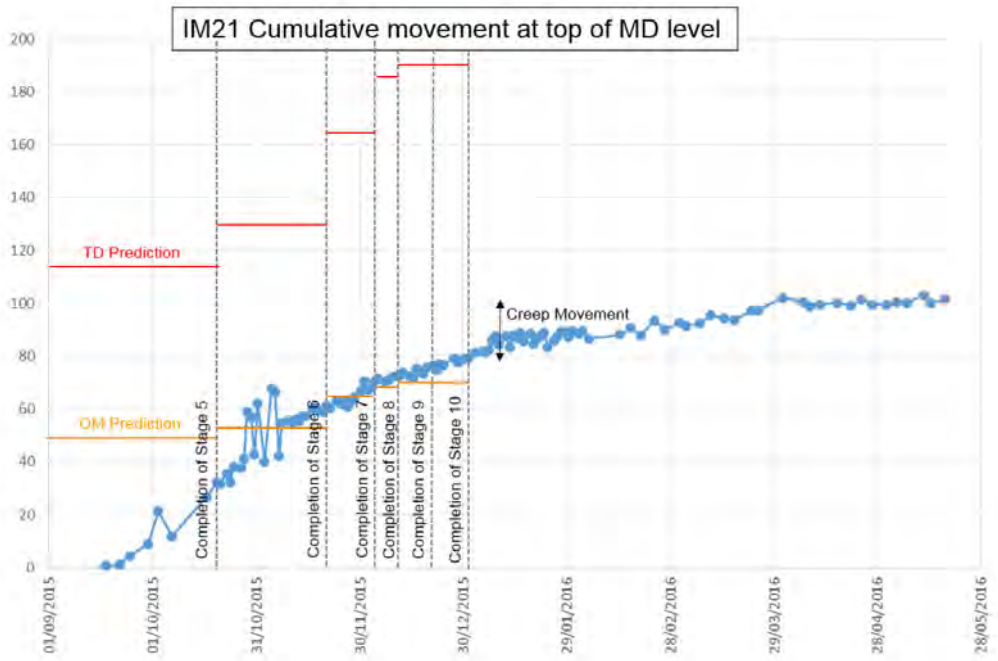

Figure 13: Maximum Inclinometer Movement vs Time

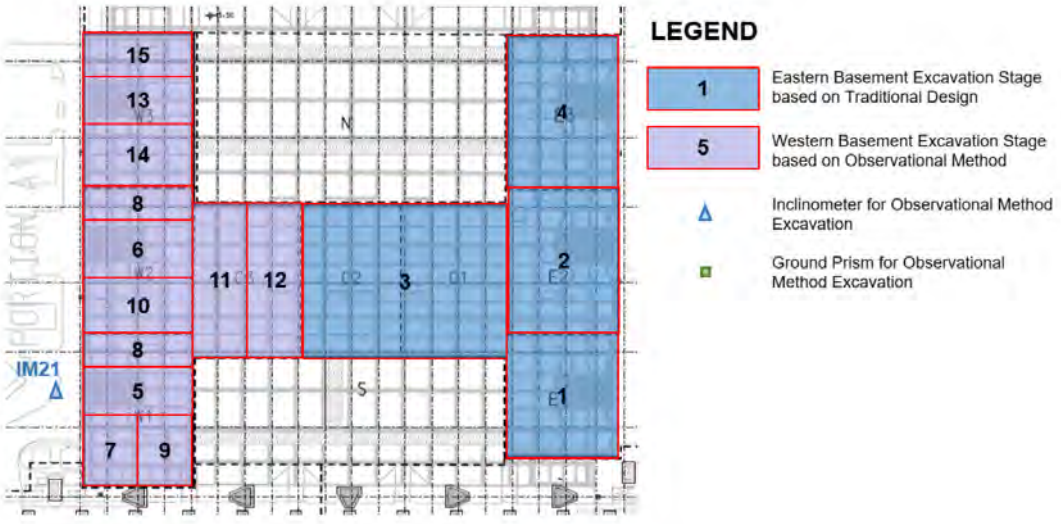

Figure 14: Location of Inclinometer IM21

At the end of each excavation stage, an ad-hoc meeting was held between Designer, Contractor, Independent Reviewer and Client's Engineer to review the stability of the excavation and agree on whether the excavation could progress according to the optimised observational method sequence. The successful implementation of the observational method was only possible thanks to the commitment of all parties to develop and follow the framework, hold timely reviews and promptly reach agreement on whether the most probable sequence could be followed after completion of each excavation stage.

As the performance of the excavation was generally in line with the predicted most probable movement and all the monitoring data was within the red triggers, no contingency measures had to be implemented throughout the works and all the observational method objectives to reduce the extent of foundations construction were achieved. It was estimated that a 2 month saving in excavation programme was achieved by implementing the observational method with comparison to the sequence required if the traditional design had been followed.

6 SUMMARY AND CONCLUSIONS

The adoption of the observational method associated with 3D stability analyses has allowed the contractor to efficiently complete a large scale open cut excavation in difficult ground conditions where thick very soft clay was present underlying a newly reclaimed land.

The standard design approach based on 2D stability analyses would have required extensive ground treatment to be carried out to improve the clay by cement injection (i.e. jet grouting or deep soil mixing). The 3D excavation design provided an effective and sustainable solution compared to the ground improvement option, which would have required injection of over 14 thousand tons of cement in the soft soils and would cost approximately 12 million US$.

The 3D excavation sequence using moderately conservative design parameters required staged excavation with the pilecaps and ground beams completed before the next stage of excavation could be commenced. This requirement was fairly onerous in terms of construction timing. The observational approach using best estimate parameters demonstrated that the requirement to construct pilecaps and ground beams could be relaxed assuming that the ground performed as expected. This would save a significant amount of construction time.

The performance of the excavation was very close to the best estimate design assumptions, with the majority of the inclinometers indicating lateral movement magnitude between the most probable and moderately conservative predictions. Therefore, by adopting the observational approach, the excavation was successfully completed achieving all the observational method objectives, with a further saving of over 2 months of programme.

REFERENCES

Gaba, A. R., Simpson, B., Powrie, W. & Beadman, D. R. 1999. Embedded retaining walls – guidance for economic design. *Construction Industry Research and Information Association,* CIRIA C580

Nicholson, D., Tse, C.M., Penny, C., 2003, The Observational Method in ground engineering: principles and applications. *Construction Industry Research and Information Association,* CIRIA Report 185

Michalowski, R. L. 2010. Limit Analysis and Stability Charts for 3D Slope Failures. *Journal of Geotechnical and Geoenvironmental Engineering*, 136:583-593.

Zhang, X. 1988. Three-dimensional stability analysis of concave slopes in plan view. *Journal of Geotechnical Engneering,* 1988.114:658-671.

Development of 3D Subsurface Models for Landslide Investigation using Spatial Interpolation Technique

S.M. Ng
Heriot-Watt University Malaysia

M.A.M Ismail
Universiti Sains Malaysia

ABSTRACT

Landslides events in Malaysia are often triggered by rainfall due to the tropical climate which has resulted in large numbers of casualties and massive economic losses. To prevent this disastrous events, subsurface investigation is essential to facilitate slope characterization and establish effective slope stabilization measures. This paper presents the integration of borehole drilling, electrical resistivity and seismic refraction method to characterize a residual soil slope in Malaysia. Borehole drilling was used to obtain soil stratigraphy, to locate groundwater level and to obtain undisturbed soil samples for geotechnical laboratory testing. The electrical resistivity method was adopted to measure resistivity distribution of the subsurface materials while seismic refraction method was used to measure the travel time of seismic waves refracted at the interfaces between subsurface layers of different velocities. A deterministic spatial interpolation technique was applied to develop three-dimensional (3D) subsurface models from the available two-dimensional (2D) data. The outcome from this study produced valuable subsurface information of the slope that enables potential failure zone and effective slope stabilization measure to be identified.

Keywords: Rainfall induced landslide, subsurface characterization, slope stabilization, spatial interpolation, 3D subsurface model.

1 INTRODUCTION

The National Slope Master Plan of Malaysia has reported that rainfall has been recognized as the major triggering factor of slope failure worldwide and also in Malaysia (Public Works Department of Malaysia 2008). The tropical climate in Malaysia that experiences Southwest monsoon from May to September and Northeast monsoon from November to March contributes to the abundant rainfall annually. Therefore, it is not uncommon for steep soil slopes to remain stable for a long period, whereas some gentle slopes may fail after several heavy rainfalls (Li et al. 2005). Rainfall induced landslides are commonly triggered by rainwater infiltration that increases the groundwater table or degree of saturation in the soil mass. This increases the pore water pressure subsequently loss of shear resistance in the soil mass leading to landslide. Slope stability analysis is carried out regularly to assess the level of safety of the slope.

Site characteristics such as subsurface and groundwater information are essentially utilized as important input for stability analysis. Borehole drilling is a conventional and widely used method to obtain subsurface information such as stratigraphy, groundwater level and sampling of the study area. However, borehole drilling only offers a single point well data and is invasive to the surrounding. For a large area, additional boreholes are required and this will incur additional cost to obtain representative

data. Therefore, geophysical methods such as electrical resistivity and seismic refraction can be the integral approaches to characterize the slope due to the advantages of being non-invasive, able to cover a large study area and less time consuming. The objective of this study is to enhance the conventional approach in developing subsurface models for slope stability assessment and the stabilization measures. Subsurface models in the form of 3D perspective were developed based on the results from borehole drilling, electrical resistivity and seismic refraction methods respectively.

2 GEOLOGICAL INFORMATION AND SUBSURFACE INVESTIGATION

The study area is generally underlain by graphitic quartz mica schist from Kajang Formation that mainly consists of dark grey to black carbonaceous quartz–muscovite schist interlayer with thin bands and lenses of orange to buff quartz–muscovite with minor intercalation of marble and phyllite (Manap et al., 2014). Observation on the outcrops indicates that intense weathering processes have taken place with weathering grades ranging from Grade III to VI. Based on the historical core samples obtained at the depths of 9m to 20m, the rocks in this area consist of interbedded sandstone, shale and actinolite schist (Ahmed et al. 2011).

Figure 1 shows the location of the borehole drilling, electrical resistivity and seismic refraction survey carried out at the site. A total of 17 boreholes drilling were conducted to determine the geological structure such as the thickness, sequence and extent of the soil strata, to determine groundwater conditions, to conduct in-site test such as standard penetration test (SPT) and to obtain disturbed and undisturbed soil samples for laboratory tests (e.g. particle size distribution, Atterberg limits test and consolidated undrained triaxial test). Rock coring was carried out when a rock layer was encountered. Total recovery ratio (TCR) and rock quality designation (RQD) were recorded for each core run to determine the quality of the rock samples.

Nine resistivity survey lines were performed to measure the resistivity distribution of the subsurface material. The principle that lies behind this method is by injecting electrical current into the ground through two electrodes and the potential difference is then measured through two potential electrodes. From the results of current and potential difference measurements, the variations of electrical resistivity value for the measurement point can be obtained. Since the ground resistivity is related to various geological parameters such as fluid content, degree of saturation and porosity, the variations in electrical resistivity may indicate the variations in composition, layer and contaminant levels. Table 1 shows the resistivity values of some type of common rocks and soil materials.

Six seismic refraction survey lines were carried out to map the seismic velocity of the subsurface geology. The seismic refraction method is based on the measurement of travel time of seismic waves

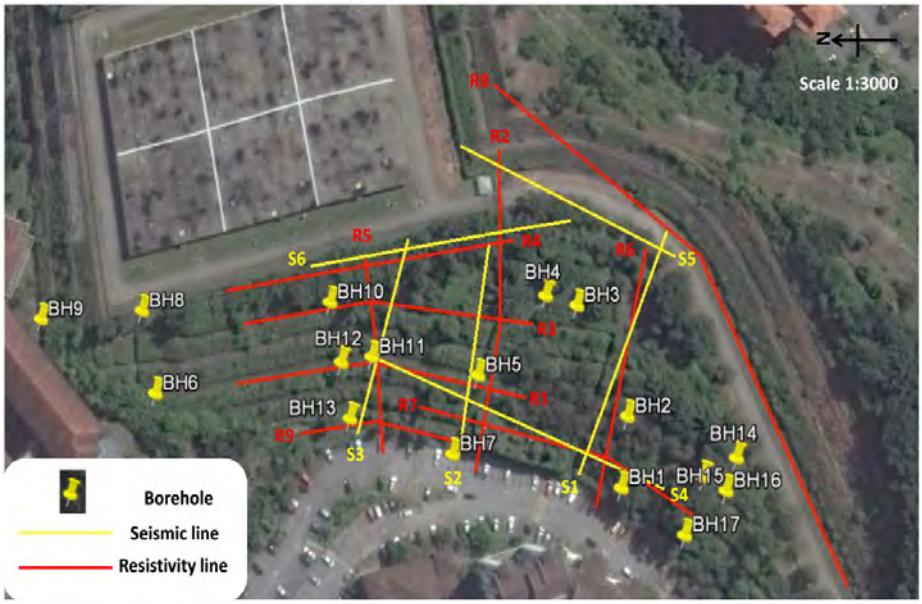

Figure 1: Location of boreholes, resistivity lines and seismic lines

refracted at the interfaces between subsurface layers of different velocity (Burger, 1992). Seismic energy is provided by a source generated by the sledgehammer impacting a metallic plate located on the ground surface. Energy radiates out from the shot point, either travelling directly through the upper layer, or travelling down to and then laterally along higher velocity layers before returning to the surface. This energy is detected on surface using a linear array of receivers known as geophones spaced at regular intervals (Redpath, 1973). Data are recorded on a seismograph and the first-arrival times for each shot position are analyzed. Table 2 shows the typical vp for various types of earth materials which is useful as a guide for results interpretation.

Table 1: Resistivity of some common rocks and soil materials (Keller and Frischknecht 1966)

Material	Resistivity (Ωm)
Alluvium	10 to 800
Sand	60 to1000
Clay	1 to 100
Groundwater (fresh)	10 to 100
Sandstone	$8 - 4 \times 10^3$
Shale	$20 - 2 \times 10^3$
Limestone	$50 - 4 \times 10^3$
Granite	5000 to 1,000,000

Table 2: Typical propagation velocities of seismic waves through different types of geological media (Reynolds, 2011)

Medium	Velocity min (m/s)	Velocity max (m/s)
Air depending on temperature	310	360
Weather soil	100	500
Gravel, dry sand	100	600
Loam	300	900
Wet sand	200	1800
Sand loose	200	2000
Clay	1200	2500
Water depending on temperature	1430	1590
Sand and gravel (near surface)	400	2300
Sandstone friable	1500	2500
Sandstone dense	1800	4000
Sandstone (medium to strong)	1400	4500
Chalk	1800	3500
Shale	2000	4100
Limestone	2500	6000
Marl	2000	3500
Gypsum	4500	6500
Ice	3100	4200
Granite	4000	5700
Metamorphosed rock	4310	6360

3 DEVELOPMENT OF 3D SUBSURFACE MODEL

Three different 3D subsurface models presenting the stratigraphy, P-waves velocity (v_p) and electrical resistivity were developed based on the results from boreholes drilling, electrical resistivity and seismic refraction. 3D models are able to present the spatial variation in the vertical, lateral and perpendicular directions along the survey line. However, 3D geophysical surveys are still a subject of active research at the present time thus not routinely used compared to the 2D survey (Loke, 1999). The cost for 3D geophysical survey is relatively higher and more time consuming due to the data acquisition for a large study area. Therefore, a simplified and less time-consuming approach is adopted in this study to develop the 3D models from the available 2D survey data.

The 3D stratigraphy, resistivity and v_p models were developed by using a solid modelling algorithm where the resistivity and v_p values were interpolated for fixed X, Y and Z coordinates. Numerous spatial interpolation methods have been developed and applied to various disciplines especially for meteorological data (Chai et al., 2011). Some of the examples are inverse distance weighting (IDW), kriging, nearest neighbour (NN), trend surface analysis (TSA), local polynomial (LP), etc. Each method has its own advantages and disadvantages and thus the optimal interpolation method is selected depending on the objectives of the study (Chen and Liu, 2012). The technique utilized in this study to perform spatial interpolation is the IDW method. This method assumes things that are close to one another are more similar than those that are farther apart and the local influence will diminish with distance (Li, 2008). The values of the unknown points are calculated with a weighted average of the values available at the known points. Hence, greater weights are assigned to points closest to the prediction location. A computer program named RockWorks15 was used to perform the IDW spatial interpolation to produce the 3D models. To evaluate the performance of the computed IDW model, coefficient correlation (R) was also determined. R value of 1 indicates a perfect correlation while a value of 0 indicates no correlation between the measured and computed data.

4 RESULTS AND DISCUSSION

This section presents the results of the subsurface investigation by borehole drilling, electrical resistivity and seismic refraction. Figure 2 shows the results of the multi borehole logs plotted in 3D according to their positions on site. This result is further interpolated into a solid 3D stratigraphy model using the IDW method as presented in Figure 3. The 3D stratigraphy model indicates that the types of soil encountered at the site are silt, gravelly silt, clay, and sand. However, silt appears to be the dominant soil that is present. Sand exists at the top layer for about 1m from the surface while traces of gravelly silt and clay are also randomly encountered at the study area. In addition, rock was encountered at five boreholes namely BH3, BH5, BH6, BH9 and BH16 at the depth of 7.5m, 11m, 12m, 4m and 8.4m respectively.

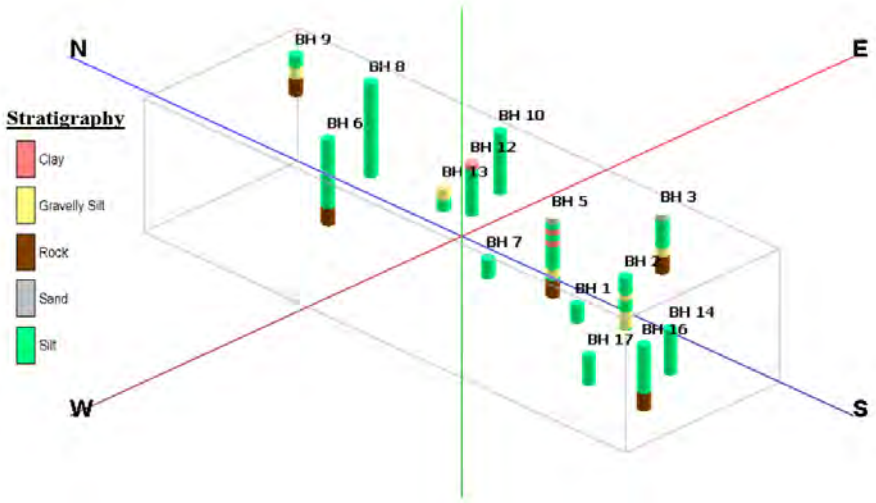

Figure 2: 3D multi boreholes log model

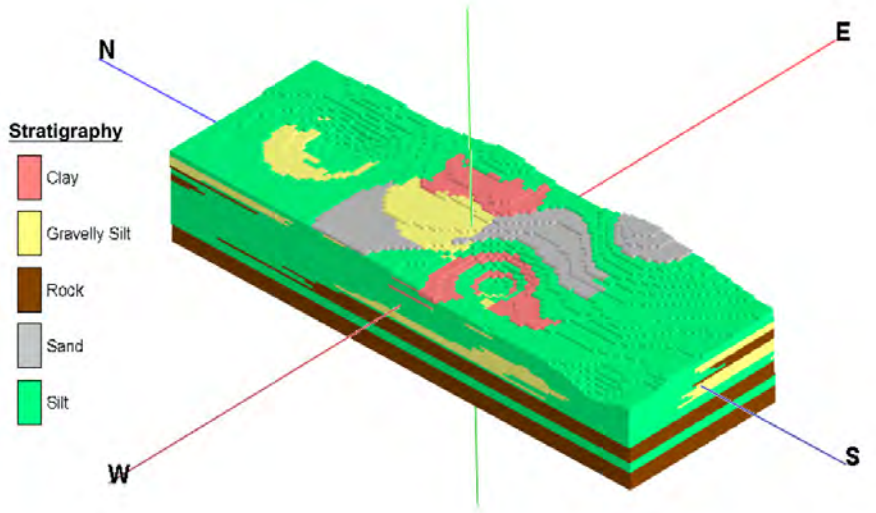

Figure 3: 3D stratigraphy model

Figure 4 shows the 3D resistivity model developed using the IDW spatial interpolation method. It can be observed that the model can be divided into two zones namely wet and dry zone. The wet zone indicated by blue colour scheme exhibits low resistivity values ranging from 10Ωm to 300Ωm and may indicate the presence of high water content or high seepage activities. The dry zone has higher resistivity values ranging from 300Ωm to 100000Ωm and this indicates that the soil within this zone is relatively dry with no seepage flow activities. Due to the high water content in the wet zone, rainfall events may increase the existing pore water pressure subsequently trigger failure. Hence, this area can be delineated as the potential failure zone. The robustness of the developed 3D resistivity model was measured through the correlation coefficient between the observed and computed resistivity. The correlation coefficient obtained was 0.791 and this indicates a satisfactory performance between the observed and computed resistivity values. Hence, the 3D resistivity model has a reliable accuracy to provide the indication for potential failure zone with high water bearing.

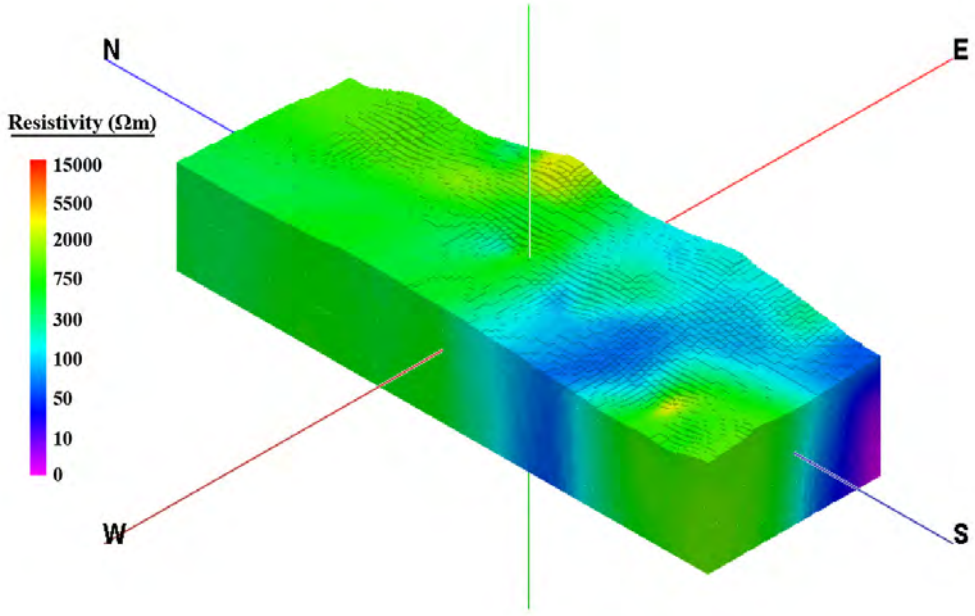

Figure 4: 3D resistivity model of the study area

The 3D v_p model presents seismic velocity distribution of the site is shown in Figure 5. The accuracy of the model is considered good indicated by the correlation coefficient value of 0.872. Generally, the site possesses the v_p value of approximately 1500m/s. In comparison with the 3D resistivity model, the water bearing zone coincides with the intermediate v_p zone of 500m/s to 1000m/s. This suggests that the identified zone consists of lower density or high porosity materials thus is prone to slope failure. Based on this subsurface investigation and developed 3D models, horizontal drains are proposed to be installed at the toe of the slope within the delineated high water bearing zone. This stabilization measure aims to discharge the high groundwater table subsequently reducing pore water pressure build-up. The flowrate measurements recorded the value of 115 ml/s during the dry season demonstrating the effectiveness of the horizontal drains as shown in Plate 1. This study has shown that the integration of borehole drilling, electrical resistivity and seismic refraction has provided useful information to characterize and remediate landslides.

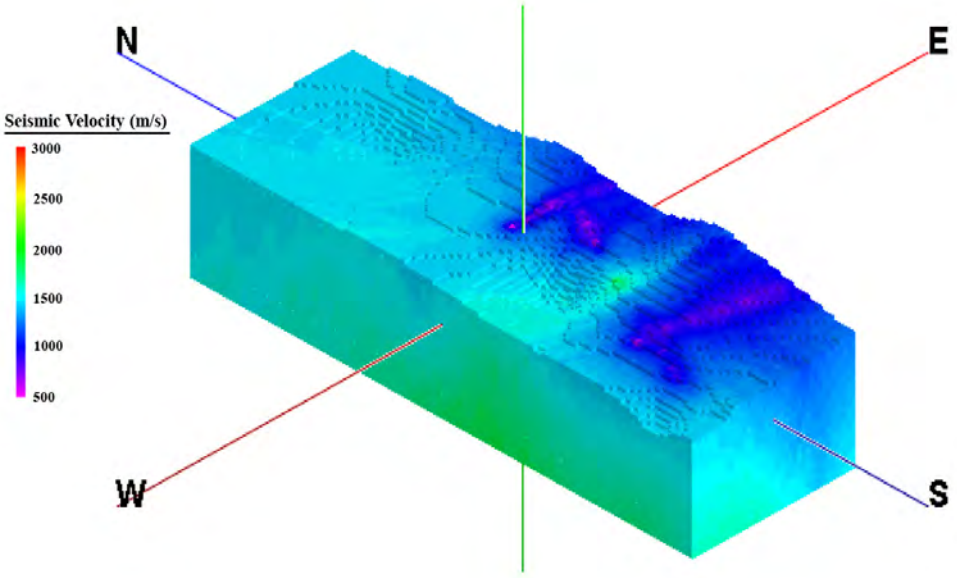

Figure 5: 3D v_p model of the study area

Plate 1: Continuous discharge of groundwater from the horizontal drains on site

5 CONCLUSIONS

3D subsurface models of the stratigraphy, electrical resistivity and seismic velocity were successfully developed to characterize the study area using IDW spatial interpolation technique. The 3D stratigraphy model shows that the study area generally consists of silt with plasticity ranging from intermediate to very high plasticity. The 3D resistivity model indicates a high water content zone with the resistivity values ranging from 10Ωm to 300Ωm. The seismic velocity zone of 500m/s to 1000m/s in the 3D seismic velocity model also indicates low density and high porosity soil layer. These results demonstrated that the areas which consist of both characteristics of high water content and intermediate seismic velocity are prone to slope failure. Hence, an effective remediation measure can be proposed with such comprehensive subsurface investigation.

REFERENCES

Ahmed, J., Ghazali, M. A., Mukhlisin, M., Alias, M. N., and Taha, M. R. 2011. Effectiveness of horizontal drains in improving slope stability: A case study of landslide event in Putra Jaya Precinct 9, Malaysia. *Unsaturated soils: theory and practice,* pp.753–758.

Burger, H. R. 1992. *Exploration geophysics of the shallow subsurface.* Prentice Hall PTR, Upper Saddle River, NJ.

Chai, H., Cheng, W., Zhou, C., Chen, X., Ma, X., and Zhao, S. 2011. Analysis and comparison of spatial interpolation methods for temperature data in Xinjiang Uygur Autonomous Region , China. *Natural Science,* 3(12), pp.999–1010.

Chen, F. W., and Liu, C. W. 2012. Estimation of the spatial rainfall distribution using inverse distance weighting (IDW) in the middle of Taiwan. *Paddy and Water Environment,* 10(3), pp.209–222.

Keller, G. V., and Frischknecht, F. C. 1966. *Electrical methods in geophysical prospecting*. Pergamon Press Inc., Oxford.

Li, A. G., Yue, Z. Q., Tham, L. G., Lee, C. F., and Law, K. T. 2005. Field-monitored variations of soil moisture and matric suction in a saprolite slope. *Canadian Geotechnical Journal,* 42(1), pp.13–26.

Li, J. 2008. *A Review of Spatial Interpolation Methods for Environmental Scientists.* Canberra: Geoscience Australia.

Loke, M.H., 1999. Electrical imaging surveys for environmental and engineering studies. *A practical guide to 2-D and 3-D surveys 2,* 67.

Manap, M. A., Nampak, H., Pradhan, B., Lee, S., Sulaiman, W. N. A., and Ramli, M. F. 2014. Application of probabilistic-based frequency ratio model in groundwater potential mapping using remote sensing data and GIS. *Arabian Journal of Geosciences,* 7(2), pp.711–724.

Public Works Department of Malaysia, P. 2008. *National Slope Master Plan of Malaysia.*

Redpath, B. B. 1973. Seismic refraction exploration for engineering site investigations: *US Army Engineer Waterway Experiment Station Explosive Excavation Research Laboratory, Livermore.* Technical Report E, 73(4), pp.51.

Reynolds, J. M. 2011. *An introduction to applied and environmental geophysics.* John Wiley & Sons, New York.

Reinforced Earth Wall – A Sustainable Alternative to a Piled Vehicular Abutment Ramp

Dimitri Plantier & Norman M.H. Lee
Reinforced Earth Pacific Limited

Gavin S.H. Toh & Sai Shun To
Lambeth Associates Limited

Kim C.H. Kwan
Meinhardt (C&S) Limited

ABSTRACT

A vehicular ramp was proposed to replace the existing elevated road (which has been planned for future demolition) connecting to existing podium deck of the Building for vehicular circulation.

In the original design, socket H-piles with pile cap and reinforced concrete wall would be constructed as the abutment for supporting the replacement ramp in form of steel girders. In order to minimize the construction time and to fit in the tight construction schedule, a Reinforced Earth Wall was proposed as an alternative. This Reinforced Earth Wall was designed as a true abutment with no piling required and the steel girder was supported by a reinforced concrete seating which was located directly on the backfill of the Reinforced Earth Wall. This vehicular ramp was designed as a permanent structure and would be used as a new access to replace the existing elevated road until the commencement of the next phase of development. It would be much easier to demolish in comparison with the original design of socket H-piles and reinforced concrete wall, and significantly reduce the construction wastage.

1 INTRODUCTION

Reinforced Earth is a composite material formed by the association of granular earth and flexible reinforcement. The friction which is developed between the earth and the reinforcement strips mobilizes and binds all particles within the Reinforced Earth block into a monolithic, yet flexible mass gravity structure capable of retaining and supporting large applied loads on top.

With over 50 years of research and development, this technology has been refined and is widely used all over the world. These include roads and slope retaining walls, bridge abutments and railway embankment; hydraulic structures such as sea walls, river walls, flood protection structures and dams; industrial structures including material processing and storage facilities; containment dikes for crude oil and liquefied natural gas storage; protective bund walls against fire and explosion in military application, to mitigate against natural terrain landslide and boulder fall hazards.

This project is going to demonstrate the use of Reinforced Earth Wall as a "true abutment" (Figure 1). A "true abutment" is a Reinforced Earth retaining wall with a bridge abutment footing bearing directly on top of the reinforced soil volume. The footing is directly supported by the Reinforced Earth structure

Figure 1: True abutment

below without the need of piles or columns. The design considers the heavy concentrated vertical and horizontal loading imposed by the bridge superstructure and traffic loading together with horizontal earth pressure acting behind the abutment footing.

2 PRINCIPLE OF REINFORCED EARTH

A Reinforced Earth structures has three essential components, which are defined as:

2.1 Selected backfill material

Selected backfill materials which extends from facing to the end of the reinforced strips is commonly called the "reinforced volume". The selected fill material must be cohesionless, granular material and contains not more than 10% particles smaller than 63μm. This is to ensure that the material has little plasticity and is relatively free draining so that a sufficient and predictable friction is achieved under saturated or dry conditions.

2.2 Reinforcing strips

Reinforcing strips are fastened only to the facing. The dimension of the strips will depend on the external loading and height of structure. These material strips are hot-dip galvanized (to protect against the corrosion) with ribbed surfaces (to increase the friction with the backfill).

2.3 Facing

The facing which acts essentially as a skin to protect the exposed surface of the Reinforced Earth block. The facing system adopted must be flexible and may not restrict the movement of the block itself. A precast concrete facing system is commonly used to provide an easy and rapid erection procedure and a very pleasing appearance.

3 GROUND PROFILE AND DESIGN PARAMETER

Based on the ground investigation information, the general ground profile in the area comprises of a reclaimed fill layer at the surface, followed by marine deposit, alluvium and decomposed quartz monzonite. The summary of soil stratum is shown in Table 1.

Table 1: Soil stratum

Stratum	Thickness (m)	Typical SPT 'N' Value
Fill (FILL)	4.5 - 8	9 - >35
Marine Deposits (MD)	2.5 – 10	3 - >30
Alluvium (ALL)	0.5 – 5.5	9 - >45
Completely Decomposed Quartz Monzonite (CDM)	10.19 – 31.13	20 - >200

The shear strength parameters for different soils are determined according to the results of laboratory tests (Triaxial compression test, determination of bulk & dry density test and unconfined uniaxial compressive strength test) carried out for the soil samples retrieved during ground investigation works. The effective friction angles are obtained from the s'-t' plot for different soil types. The design parameters are summarised in Table 2 as shown below.

Table 2: Design parameter

Soil Type	Bulk Density (kN/m^3)	Effective Friction Angle Ø (°)	Effective Cohesion c' (kPa)
FILL	19	33	0
MD (SAND)	19	30	0
ALL (SAND)	19	33	0
CDM	19	35	5
SELECTED FILL	19	36	0

3 EXTERNAL DESIGN AND INTERNAL DESIGN

The vehicular ramp is a plate girder bridge with 109m span supported by two steel truss towers and an abutment. The original design of abutment is a Reinforced Concrete (R.C.) retaining wall supported by socketed H-pile with 1.5m combined pile cap (Figure 2). The design has been revised to Reinforced Earth True abutment with a L-shape R.C. seating as an alternative (Figure 3).

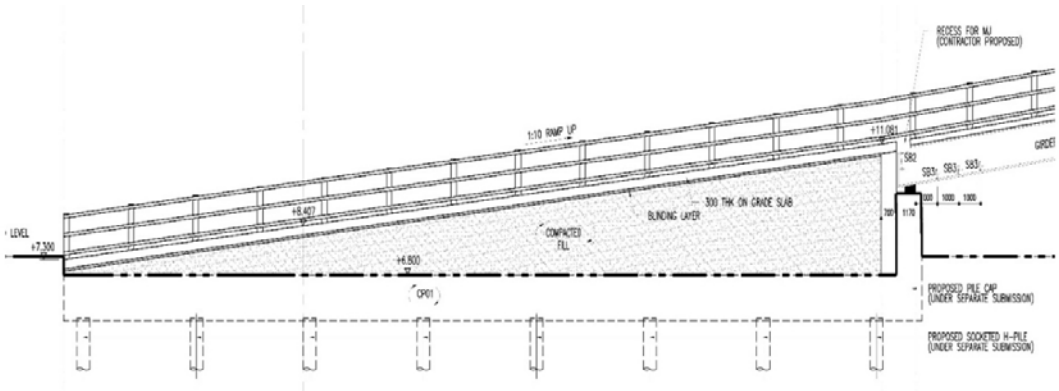

Figure 2: Original Design

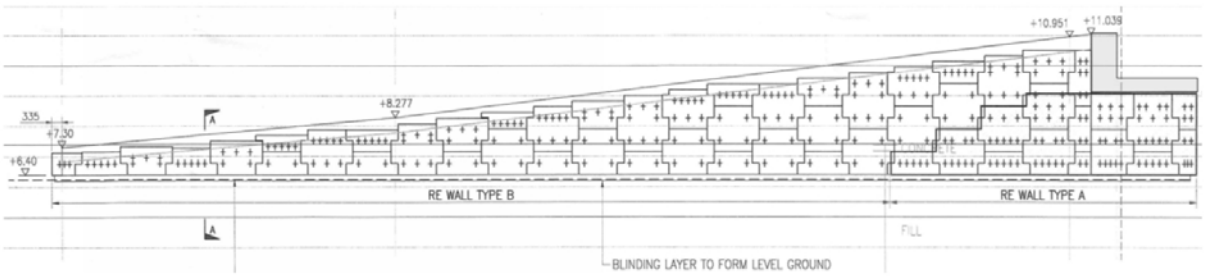

Figure 3: Reinforced Earth Wall Design

3.1 External design

For the external stability, the load from the vehicular ramp to soil need to be checked. Adequate frictional resistance between the L-shape R.C. seating and Reinforced Earth retaining wall should be provided to resist the sliding force from the ramp above while dead weight of the R.C. seating should provide adequate moment resistance to resist overturning moment. Apart, bearing of Reinforced Earth retaining wall to be considered to ensure the load from the R.C. seating will not fail the foundation.

Load path of gravity load is as below: Vertical load from vehicular ramp will be transferred to R.C. seating through bearings and then to Reinforced Earth (R.E.) retaining wall which is directly on grade. Horizontal load from bearings will be transferred to R.C. seating and then to R.E. retaining wall by frictional resistance.

3.2 Internal design

The stability of reinforced fill relies upon the mechanism of load transfer between the selected fill material and the reinforcing element. When a load is applied to the reinforced fill feature, tensile strains can develop within the reinforced fill. The internal stability of a reinforced fill structure relates to the tensile and pullout failure of reinforcing elements. Both failure modes may lead to large movements or possible collapse of the structure. Tensile failure occurs when the tensile forces in the reinforcing elements become larger than the tensile strength, so that they elongate excessively or break. The pullout failure occurs when the tensile forces become larger than the force required pulling the reinforcing elements out of the soil mass. The internal design is based upon the principles in Geoguide 6 published by Geotechnical Engineering Office. In common with other codes for the design of civil engineering structures, this code of practice adopts limit state principles. These principles involve the application of partial material and load factors for various structure types; design lives and load combinations to ensure sufficient safety margins.

The internal stability design is used to determine the amount of soil reinforcement required to maintain the structural integrity of the reinforced soil mass. The following modes of instability should be considered in the design.

(a) Rupture of reinforcement
(b) Pullout of reinforcement
(c) Failure of connections
(d) Rupture of facing panels

The design life of the structure is used to determine the thickness of reinforcing strip which will be lost due to corrosion. This is referred to as the sacrificial thickness and is used to calculate the strength of the reinforcing elements at the end of the design life.

4 COMPARISON OF ORIGINAL PILING DESIGN VS REINFORCED EARTH RETAINING WALL DESIGN

The benefit of using the Reinforced Earth retaining wall by comparing with the R.C. retaining wall is not only the cost saving, but also the environment friendliness. Table 3 illustrated the material used in the two systems.

Table 3: Comparison of Material Used

Scheme	Element	No. of pile (nos.)	Concrete (m^3)	Structural Steel / Rebar / Strip (ton)
Piling Scheme	Foundation	24	–	245
	Cap	–	535	130
	Wall	–	100	6
Total		**24**	**635**	**381**

Scheme	Element	No. of pile (nos.)	Concrete (m^3)	Structural Steel / Rebar / Strip (ton)
Reinforced Earth Wall Scheme	Panel	–	33	2
	Levelling Pad	–	6	0
	L-shape RC wall	–	35	4
Total			**74**	**6**

The table above reveals that the consumption of concrete, structural steel, and reinforcement / steel strip of Reinforced Earth retaining wall with L-shape R.C. seating is far below than the original piling and pile cap with R.C. retaining wall scheme. Carbon footprint could be reduced by this proposal. By eliminating the piling, construction waste can further be reduced and clean underground could be allowed for future development in case.

5 CONSTRUCTION SEQUENCE

The construction of the Reinforced Earth retaining wall can be done by one team of 5 workers with the backhoe and vibratory roller. The construction sequence of the Reinforced Earth retaining wall is straightforward and as shown below.

5.1 Excavation

Excavate to the level and alignment as stated in the drawings, except during excavations in rock and in areas of fill formed of rock fill material, formations shall be compacted to obtain a relative compaction of at least 98% to a depth of 200mm below the formation by main contractor. (Figure 4a)

Figure 4a: Formation level

5.2 Leveling Pad

Pour concrete leveling pad (Figure 4b). The leveling pad should be of concrete grade 20/20, cured for 12 hours. The concrete finish must be smooth and flat. The size of the leveling pad is 350mm width with 200mm thick.

Figure 4b: Leveling Pad

5.3 Installation of first layer of panel and laying the filter material

The alignment of the first layer of first layer of panel (Figure 4c) should be checked. Use the timber to fix the position of the panel to make sure the alignment is maintained and place the filter material.

Figure 4c: First layer of panel

5.4 Placing the selected backfill and compaction

Place approved selected fill material (Figure 4d) up to the bottom row of panels tie strips and each layer is around 300mm thick and compact by vibratory roller.

Figure 4d: Placing selected backfill

5.5 Placing of reinforcement

Place reinforcing strips on the compacted backfill (Figure 4e). Position strip end into the tie strip gap and match the holes. Push a bolt through the holes from below, put a washer on top and thread on a nut (Figure 4f). Tighten the nut with a socket wrench to complete the connection.

Figure 4e: Placing reinforcing strip

Figure 4f: Thread on a nut

5.6 Erection of the pre-cast L-shape wall

When the selected backfill is laid to the bottom level of the precast L-shape seating, it is placed on the Reinforced Earth retaining wall (Figure 4g).

Figure 4g: Erection of the precast L-shaped R.C. seating

By repeating the construction sequence of section 5.3 to 5.5, the construction of Reinforced Earth Wall is completed (Figure 4h and Figure 4j).

Figure 4h: Completion of Reinforced Earth wall

Figure 4j: Completion of Reinforced Earth wall with L-shape R.C. seating with steel girder ramp erected

6 OTHER TRUE ABUEMENT PROJECT REFERENCE

The first Reinforced Earth True Abutment Wall was built more than 50 years ago (Figure 5) and more than 1,000 Reinforced Earth True Abutment Wall were completed to date. Suncor Steepbank River Bridge (Figure 6 and 7) is a heavily loaded true abutment in Canada. The wall height is around 15m with 20m long reinforcing strip. The loading is more than 1300ton. Another example of the Reinforced Earth True Abutment with wire mesh facing is shown in Figure 8. A TerraTrel wire mesh facing Reinforced Earth True Abutment can provide a cost effective solution when the facing appearance is not a critical requirement. It can also be used as a permanent structure or temporary structure as requested by the client. Another application of the TerraTrel wire mesh facing is for two-stage construction (Figure 9, 10 & 11) which enables the Reinforced Earth retaining wall to allow traffic during construction. Concrete panel facing is used in one side and the wire mesh facing is used in the middle to support the ramp. After stage 1 is completed and the traffic is transferred to the new ramp, the stage 2 can start to complete the other half of the ramp.

Figure 5: 1969 Strasbourg, France

Figure 6: Suncor Steepbank River Bridge

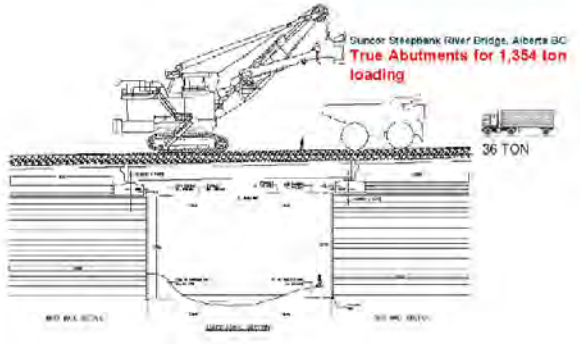

Figure 7: Suncor Steepbank River Bridge

Figure 8: TerraTrel Reinforced Earth True Abutment

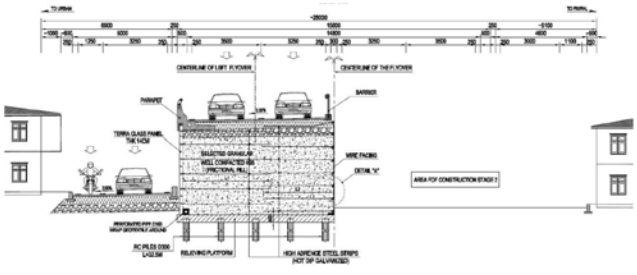

Figure 9: Section of stage 1 of a two-stage construction of Reinforced Earth

Figure 10: Two-stage construction of Reinforced Earth

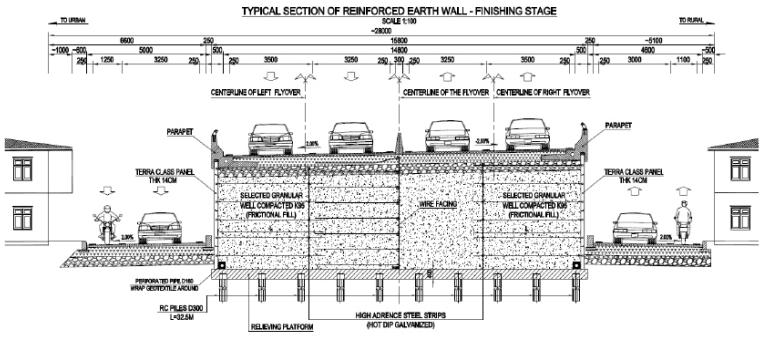

Figure 11: Section of stage 2 of a two-stage construction of Reinforced Earth

7 CONCLUSION

Reinforced Earth structures provide great strength and flexibility. The precast concrete facing system adopted provides an attractive appearance and a simple and rapid construction procedure. The procedure is repetitive and mainly consists of panel erection, filter and selected fill backfilling, and reinforcing strips laying.

Moreover, the ecological advantages of Reinforced Earth retaining wall are undeniable. The use of the technique results in saving materials and energy, reducing nuisance associated with the construction of a structure such as air pollution and traffic congestion and also reducing disturbances to the foundation soil.

In this project, the use of Reinforced Earth retaining wall for the construction of true abutment offer numerous technical and economical advantages including savings made on the foundation works, on the cost of materials, on the skillfulness of the labour and also on the total duration of works.

REFERENCES

GEO, CEDD, 2002, Geoguide 6 Guide to Reinforced Fill Structure and slope design.

Diaphragm Wall Trench Stability in Recently Reclaimed Land, a Case Study Review

T.M.S. Sacadura & L. Lee & O. Haye
Intrafor Hong Kong Limited, Hong Kong

ABSTRACT

This paper focuses on the design and review of diaphragm wall trench stability using bentonite as the stabilizing fluid on a reclaimed site in Hong Kong SAR, Hong Kong Boundary Crossing Facilities. The site geological conditions were challenging for construction of long diaphragm wall panels due to the presence of considerable thickness of soft Marine Deposit and Alluvium Clays. In addition, a special type of diaphragm wall panel (Y-panel) was required for a multi circular cell cofferdam. The applicability of three-dimensional finite element methods software, Plaxis 3D, to model the trench stability is discussed through a comparison with other analytical trench design methods. Two site trials were undertaken, one for a triple-bite panel, 6.8m long and 1.5m thick, and another for the 5-bite panel (Y-panel), 3.6m x 6.5m. The latter required ground improvement, Cutter Soil Mixing, works to ensure both a satisfactory factor of safety against failure and acceptable lateral movements of the trench. The ground treatment extended for 1.0m around the perimeter of the trench with two different degrees of improvement in terms of strength and deformability. The shallower deposits, Fill, disturbed and natural Marine Deposit (approximately 20.5m) were treated with nominal ground improvement (UCS = 0.5 MPa) while the underlying Marine Deposit and Alluvium (approximately 20.7m) were fully treated to achieve an UCS of 1.0 MPa. Both site trials were instrumented, and the results are compared against the design predictions from the Plaxis 3D model.

1 INTRODUCTION

The Tuen Mun – Chek Lap Kok Link (TMCLKL) project will provide a strategic link connecting the Northwest New Territories with the Hong Kong Zhuhai Macau Bridge Hong Kong Boundary Crossing Facilities (HKBCF), North Lantau and the Hong Kong International Airport. The overall project consists of a dual 2-lane 5 km long subsea tunnel, a northern and southern landfall with the respective reclamation and associated works. The southern landfall approach ramp is located on the reclaimed site of the HKBCF. The site was reclaimed between 2011 and 2015 and was subject to extensive ground investigation, which revealed a range of ground conditions at the site. This included Alluvium Clays and Sand overlain by soft Marine Deposit (MD) with significant thickness overlain by Fill materials. The Fill materials comprise man-made Fill and pockets of disturbed MD.

The lowest formation level for the approach ramp of TMCLKL was at -37.5mPD, which equated to an excavation of about 43m since the existing ground level was at +5.5mPD. Design development of the southern landfall approach ramp saw a typical multi-propped straight cofferdam transform into a temporary hybrid Excavation and Lateral Support (ELS) scheme with 15 consecutive cells. This ELS scheme allowed for a strut free construction within the cells, with cross walls and localized struts at the panels connecting adjacent cells, Y-Panels. It was also a stiffer ELS solution, which minimized lateral movements and associated settlements.

Due to the challenging ground conditions and to ensure proper trench stability, single bite, 2.8m long x 1.5m thick, diaphragm wall panels were adopted in the initial panel layout design of the ELS. Special 5-bite diaphragm wall panels, Y-Panel, 3.6m x 6.5m, were required adjacent to each cell to transfer the hoop stress loads through the struts and cross wall to the opposite side of the cofferdam. Ground improvement works using Cutter Soil Mixing (CSM) were required to ensure both a satisfactory factor of safety against failure as well as an acceptable lateral ground movement of the trench. Two site trials were undertaken to confirm the trench stability design and confirm lateral movements, one for a straight 6.8m long x 1.5m and another for the Y-Panel.

2 SITE DESCRIPTION AND GROUND CONDITIONS

2.1 Site Description

The southern landfall approach ramp of TMCLKL, which is approximately 20 hectares, is located on the recently reclaimed site of the HKBCF, see Figure 1. The 150 hectares artificial island was reclaimed between 2011 and 2015 using 31m diameter steel cells as the inner perimeter seawalls combined with sloping rockfill in the outer perimeter. The reclamation was non-dredged leaving in place soft MD, which was subject to a number of different methods of ground improvement, e.g. stone columns, prefabricated vertical drains with surcharge. The ground level prior to the cut-and-cover tunnel excavation was generally at +5.5mPD. The 550m long cut-and-cover tunnel adopted a temporary hybrid ELS scheme with 15 consecutive circular cells, see Figure 1. The circular cell radius varied from approximately 21.9m to 28.5m with the minimum and maximum cell radius occurring at cells 1 and 15, respectively. A total number of 424 diaphragm wall panels, including the arch and the cross walls, together with 30 nos. of Y-Panels were required. The maximum excavation depth within the cut-and-cover tunnel was approximately 43m, formation level of -37.5mPD.

Figure 1: a) Tuen Mun Chek Lap Kok Link Project Location, adapted from www.hzmb.hk/eng/about_tmclkl.html (Accessed on the 31/03/2021); b) Hybrid ELS Scheme, courtesy of Dragages Bouygues Travaux Public JV

2.2 Ground Conditions

The site was subject to extensive ground investigation campaigns with one occurring pre-reclamation works and another four campaigns post-reclamation. The site investigation confirmed the highly variable geological conditions. The reclamation Fill is predominantly loose to dense silty fine to coarse sand with occasional gravel and cobbles. Possibly during fill placement some of the underlying natural

soft to firm silty clay MD was displaced and formed localized pockets of disturbed MD (DMD) within the fill. The variable Alluvium deposits, which range from silty clay to silty fine to coarse sand, underlie the MD and overlie completely decomposed rock, which in turn overlies engineering rockhead. Depending on location, bedrock can either be granite or meta-sedimentary rock (siltstone / sandstone). Soil parameters were derived from the ground investigation and subsequent insitu and laboratory testing. Moderately conservative geotechnical design parameters adopted in this study were based on the suggested parameters determined by the main contractor's ELS designer, Atkins, and are shown below in Table 1. Table 2 summarizes the range of stratum thicknesses.

Table 1: Summary of Design Soil Parameters (Moderately Conservative Values)

Stratum	Bulk Unit Weight (kN/m^3) (unsaturated)	Poison's Ratio ν	Cohesion, c' (kPa)	Angle of Internal Friction, ϕ' (o)	Undrained Shear Strength, c_u (kPa) (z' refers to mPD)	Drained Young's Modulus E' (MPa) (z' refers to mPD)	Undrained Young's Modulus Eu (kPa)	Typical Permeability k (m/s)
Reclamation Fill	20/(19)	0.25	0	33	–	15	–	$5x10^{-4}$
Rock Fill (Working Platform)	20	0.30	0	40	–	80	–	$5x10^{-4}$ to $1x10^{-3}$
Marine Deposit Clay (Natural)	16	0.50	0	28	30+1.5(-z-10)	–	$300c_u$	$1 x10^{-8}$ to $1x10^{-9}$
Marine Deposits Clay (Disturbed)	16	0.50	0	28	0.22 s'v	–	$300c_u$	$1 x10^{-8}$ to $1x10^{-9}$
Alluvium Silt/Clay	19	0.50	0	28	Cat1: z ≥-35: 80 z ≤-35: 80+2(-z-35) Cat2: z ≥-35: 60 z ≤-35: 60+2(-z-35)	–	$400c_u$	$1x10^{-8}$ to $1x10^{-9}$
Alluvium Sand	19	0.25	0	35	–	z ≥-30: 30 -30>z≥-40:30+3(-z-30) z ≤-40: 60	–	$8x10^{-5}$ to $8x10^{-6}$
Completely Decomposed Granite	19	0.50	5	32	–	z ≥-50: 60 z <-50: 60+11.2(-z-50)	–	$1x10^{-6}$ to $1x10^{-8}$

Table 2: Range of Stratum Thickness

	Fill (Including DMD Pockets)	Marine Deposit Clay	Alluvium (Silt / Clay / Sand)	Completely Decomposed Granite
Range of Stratum Thickness	~20m	6m – 14m	18m – 32m	4m – 41m

3 TRENCH STABILITY CALCULATION METHODS

An excavated trench relies on the soil arching and the stabilizing fluid, e.g. bentonite, polymer, to maintain its stability. Bentonite was the stabilizing fluid used in this project. It has the advantage of effectively creating a filter cake on the excavation faces, which restricts fluid loss into the soil. The presence of the filter cake, combined with the fact that bentonite's bulk unit weight is larger than that of groundwater, allows for a positive hydrostatic head to be maintained within the excavation. At surface where the bentonite pressure is insufficient or the acting loads from plant / equipment are high, a guide

wall protects the trench against failure. The presence of fine-grained soils such as silts and clays usually present in Marine and Alluvium strata combined with the short-term nature of diaphragm wall trench excavation benefit trench stability analysis methods that can consider the undrained behavior of soils. In addition, the applicability of these methods also needs to consider if complex geometries or specific loading conditions can be addressed in the analysis.

3.1 Soil Pressure Balance on Trench Walls

Huder (1972) and Schneebeli (1964) developed trench stability methods based on the theory of soil arching, Terzaghi's and Caquot's, respectively. Wong (1984) concluded that Schneebeli's method was the least conservative of the two methods and had the advantage of excluding from the input the earth pressure parameter. However, it also found the Schneebeli method to be conservative in Hong Kong historical case studies with presence of Fill, Marine Deposit, Colluvium and Completely Decomposed Granite. Wong (1984) states that a possible cause is Hong Kong's local practice of ignoring soil cohesion in the design and that when it's considered the results from the method are closer to the one's he observed in the test panels. Wong (1984) suggests calculating the horizontal earth pressure acting on the trench using formula (1), adapted to include the cohesion of the soil, which considers a surcharge load located at least half of the trench's length away.

$$\sigma'_3(z) = K_a \frac{\gamma L}{\sin 2\emptyset}\left[1 - e^{-\sin 2\emptyset \frac{z}{L}} + \frac{q \sin 2\emptyset}{\gamma L} e^{-\sin 2\emptyset \frac{z}{L}}\right] - 2c' \sqrt{K_a} \quad (1)$$

where s'3 (z) = effective horizontal earth pressure at depth z, K_a = active earth pressure, γ = soil's density, L = length of trench, F = soil's angle of friction, z = depth, q = surcharge load, when load is applied at a depth equal to z.

The Factor of Safety (FS) would then be calculated in accordance with equation (2) below and a value of 1.2 was quoted by Wong (1984) as adequate.

$$Fs = \frac{(p_s - p_w)}{p} \quad (2)$$

where FS = factor of safety, p_s = bentonite pressure acting on the wall of the trench, p_w = water pressure acting on the wall of the trench, p = s'_3 = effective horizontal earth pressure.

3.2 Limit Equilibrium

Several methods were developed to determine the stability of trenches, using bentonite as the stabilizing fluid, based on limit equilibrium analysis. Morgenstern (1965) proposed a method for cohesionless soils which considered the stability of a 2D wedge, see Figure 2. A 3D limit equilibrium method proposed by Aas (1976) applicable to soft clay was developed based on the experience gained from full scale field tests carried-out on Norwegian soft clays. The method assumed two separate blocks that could create the failure of the soil mass. The upper block was assumed to move vertically and at the same time the lower block would move horizontally towards the trench, see Figure 3.

Aas (1976) proposed formula (3) below to calculate the factor of safety. Other methods considering different shapes of wedges / failure conditions were developed throughout the years and some of these methods consider local stability in addition to the overall stability of the trench. However, all limit equilibrium methods require an iterative process to identify the possible failure wedge / block that leads to the minimum Factor of Safety, which can be time consuming.

$$F = \frac{\tau_{VD}}{D(\gamma - \beta^2 \gamma_f)}\left[2\frac{\tau_{TD}}{\tau_{VD}} + 0.86\frac{D}{L} + 0.6\right] \quad (3)$$

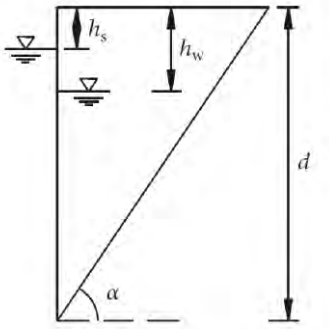

Figure 2: Morgenstern (1965) Stability of Sliding Wedge

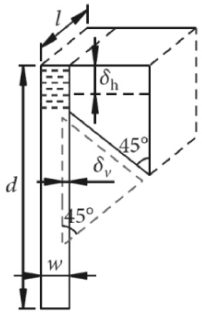

Figure 3: Aas (1976) Assumed Failure Condition in Trench

where D = depth to lowest point of failure surfaces, L = length of trench panel, β = slurry depth as a fraction of failure depth, γ = unit weight of clay, γ_f = unit weight of trench slurry, τ_{TD} = triaxial compression strength at depth, D and τ_{VD} = vane shear strength at depth D.

3.3 Finite Element Analysis (Plaxis 3D)

The use of Finite Element Analysis (FEA) software in trench stability problems is not recent. Wong (1984), used a 2D FEA analysis to demonstrate the soil arching effect through the stress distribution adjacent to the trench. Brzakala (2008) used Plaxis 3D Foundations software to analyze the stability of trenches, Grandas-Tavera (2012) analyzed the stability of corner panels using ABAQUS while Wei Li (2019) used FLAC 3D to compare numerical simulations with analytical models.

Plaxis is a commercial Finite Element Analysis software that allows users to accurately model the construction process and obtain realistic assessment of stresses and displacements for every node. The 3D package allows for problems that cannot be solved by the 2D software to be calculated. In addition, the software allows for undrained behavior to be modelled using pre-defined material models such as the Mohr-Coulomb, Hardening Soil, Soft Soil models. A realistic calculation of stress / strain allows the software to define a failure mechanism more accurately than assuming a certain shape of wedge or a soil arching extent. In addition, actual earth pressures are calculated rather than assuming limit equilibrium values.

The safety calculation (phi/c reduction) was adopted as a calculation stage in Plaxis 3D to compute global safety factors. In this calculation stage the shear strength parameters (tan ϕ' and c (either c' or cu)) are successively reduced until failure occurs. The total multiplier ∑Msf is used to define the value of the soil strength parameters at a given stage in the analysis as per formula (4) below.

$$\sum \text{Msf} = \frac{\tan\phi_{input}}{\tan\phi_{reduced}} = \frac{c_{input}}{c_{reduced}} = \frac{s_{u,input}}{s_{u,reduced}} = \frac{\text{Tensile strength}_{input}}{\text{Tensile strength}_{reduced}} = \frac{\text{available strength}}{\text{strength at failure}} \quad (4)$$

where the strength parameters with the subscript "input" refer to the properties entered in the material sets and parameters with the subscript "reduced" refer to the reduced values used in the analysis.

The ∑Msf is set to 1.0 at the start of a calculation to set all material strengths to their input values. It must always be checked whether the final step has resulted in a fully developed failure mechanism. If that is the case, the ∑Msf represents the factor of safety as calculated by equation (4) above.

4 TRENCH STABILITY DESIGN AND SITE IMPLEMENTATION

The initial panel layout for the 15 consecutive cell cofferdam was based on single bite diaphragm wall panels, 2.8m long, because of trench stability concerns associated with the adverse geological/ geotechnical conditions discussed in Section 2 above. An alternative panel layout with triple bite diaphragm wall panels, maximum 6.8m long, was studied concurrently with the physical works on site.

Figure 4 below shows two adjacent cells, one with short panels, primary / closing arrangement, and another already incorporating long panels, primary / successive / closing arrangement. Since the works were ongoing at the time of the trial the long panel layout was adopted in 8 circular cells out of the 15 and to the final straight portion of the ELS. The alternative reduced the number of diaphragm wall panels by about half, which meant reducing the associated time consuming "milled joints" between primary / closing panels. The construction programme was reduced by approximately 15% with obvious beneficial impacts to cost, environment, and quality. The final total number of diaphragm wall panels constructed in the hybrid 15 circular cell ELS scheme was 424 nos.

Y-Panels are located between circular cells and are required to transfer the hoop stresses from the arch panels of each cell through the cross walls and reinforced concrete struts to the cofferdam's opposite side, see Figure 4, Figure 5 and Plate 1. Trench stability and lateral ground movement were of concern for these 5 bite-panels due to their size, 3.6m x 6.5m, and therefore, it was envisaged that ground improvement using Cutter Soil Mixing was required, see Plate 2. A total of 30 nos. of Y-Panels were required for the successful execution of the hybrid ELS Scheme.

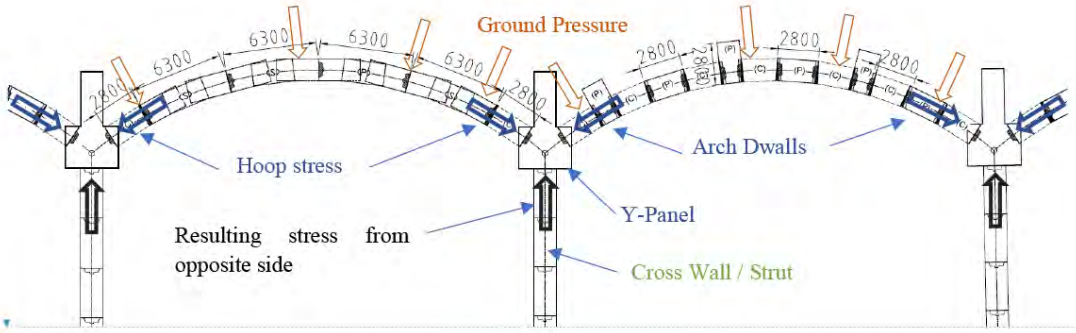

Figure 4: Adjacent cells, left-hand side with the long panels alternative incorporated and right-hand side wit short panels

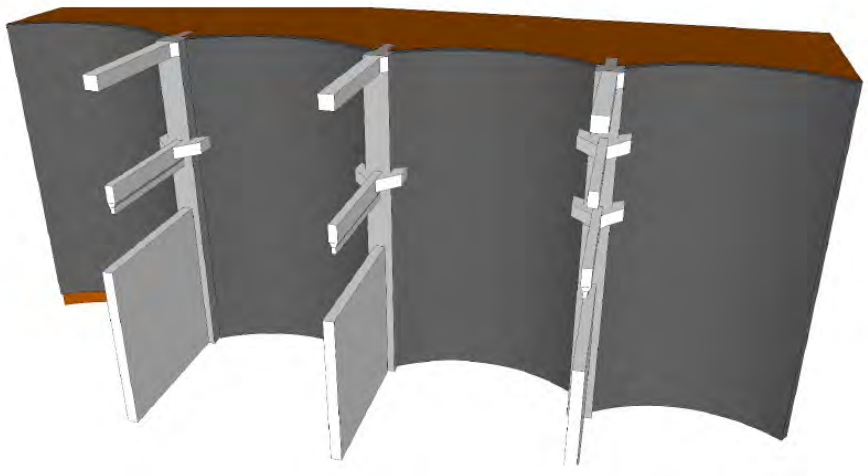

Figure 5: Simplified 3D View of ELS System

The most common methods for trench stability design were reviewed in terms of their applicability to this project. The methods highlighted in Sections 3.1 and 3.2 above, rely on empirical assumptions to define the extent of soil arching and the failure wedge / block slip failures. In addition, the limit equilibrium methods require an iterative process to ensure that all possible failure mechanisms are studied, which can be time consuming if not automated. The presence of fine-grained soil, i.e. MD and Alluvium Silt / Clay, at TMCLKL site and the fact that diaphragm wall panel trench excavation is a

Plate 1 – Exposed Y-Panel with Struts and Arch Cells

Plate 2 – Cutter Soil Mixing for Y-Panel

short-term loading, benefit a method that can consider the undrained behavior of these soils. The soil pressure balance methods ignore the undrained behavior of cohesive materials, which is one of the known limitations. This is even more critical in soft cohesive materials like the ones present on site due to the inherent difficulty to determine accurately the drained parameters. Moreover, these parameters generally govern design when compared to the undrained parameters. The analytical methods were devised based on a straight panel and therefore, could not accurately consider the complex geometry of the Y-Panel. Plaxis 3D was the chosen method for the design of trench stability; however, trench stability was also calculated using the pressure balance method for the long panel for comparison and due to its historical significance in Hong Kong.

To validate the trench stability design and access expected lateral ground movements, fully instrumented site trials, one for each kind, long panel and Y-panel, were undertaken. The site trials were done outside of the footprint of the future ELS but at a location where the geological / geotechnical conditions were most adverse. This way the trials are considered conservatively representative for the whole site. For both the long and Y-Panel trials, bentonite properties were checked as per normal operational procedures, that were also followed during the construction works. A fresh mixture was checked twice per shift while during excavation the bentonite properties were checked three times per panel every 24h. When recycled bentonite was being used its properties were checked once per bentonite poll per 24h with a minimum of two tests. The monitoring plan specified that the inclinometers were checked every 8h during the whole trial period. Koden tests were done once per shift and once a day during excavation and the extended monitoring period, respectively. The inclinometer readings, and to a lesser degree the Koden test results, allowed determining if excessive ground lateral movement or trench necking was occurring. The trench's depth was measured every shift during the extended monitoring period to ensure that no collapse was occurring, which would cause material to accumulate at the bottom of the trench.

4.1 Loading Conditions

Different plant / equipment was used to excavate the diaphragm wall trench. Five loading conditions were studied and detailed as follows, general 20kPa, mechanical grab, hydraulic grab, BC40 cutter mounted both on a MC96 and a MC64 base machines. The plant properties and loading conditions are summarized in Table 3 below.

For the method detailed in Section 3.1 the load from the plant was distributed through the plant's footprint (AxB), and a load spread of 45 degrees was considered until the load reached the face of the panel (A' x B'), see Figure 6. The surcharge from the plant was then added at the determined depth while at the surface a nominal 5kPa load was considered. In Plaxis 3D, the load case assuming that the load is spread through the whole plant's footprint (AxB) was analyzed; however, additional load cases were

considered by applying the plant's load directly on its tracks. In addition, another load case considered there was an unbalanced load, which was added to the track load of the track closest to the trench, q1, and subtracted from the other, q2. These originated different loading conditions, both in terms of load and distance to the trench, see Table 3, and Figure 7 and Figure 8.

Table 3: Summary of Plant Properties and Loading Conditions

Plant	Track Width (m)	Track Length, A (m)	Length, B (m)	Distance to face of trench, D (m)	Plant Load (kN)	Unbalanced Load on Track (kN)
B: Mechanical Grab	0.8	5.36	4.90	3.50	1400	+/- 344
C: Hydraulic Grab	0.8	4.70	4.47	2.50	1150	+/- 399
D: BC40 & MC96	1.0	6.10	5.31	2.90	2070	+/- 586
E: BC40 & MC64	0.9	5.75	5.05	2.90	1700	+/- 593

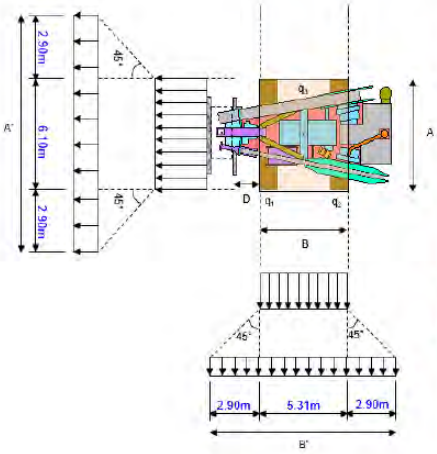

Figure 6: Load Case D for Pressure Balance Method

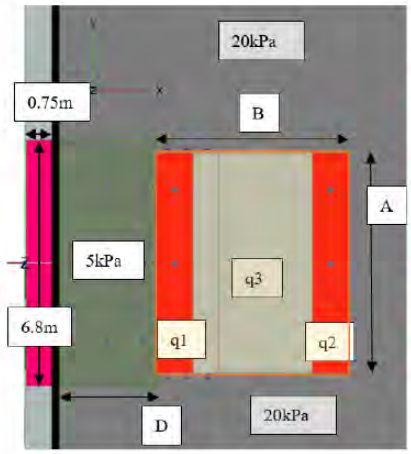

Figure 7: Typical scheme for Plant Load Cases (Long Panel), Plaxis 3D

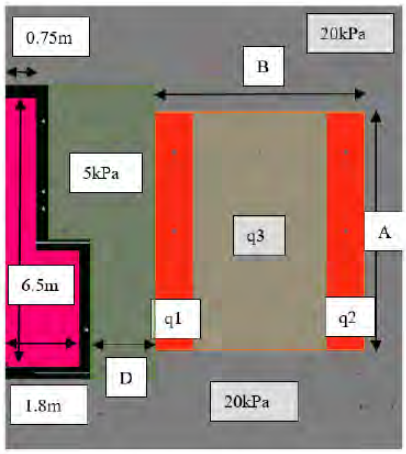

Figure 8: Typical scheme for Plant Load Cases (Y-Panel), Plaxis 3D

4.2 Long Panel

Trench stability calculations were carried out using the soil pressure balance method, Section 3.1, as well as the finite element analysis method, Section 3.3, for a 6.8m long, 1.5m thick and 56m deep panel. The calculations assumed that the existing ground level was at +5.5mPD and that the ground water table was 2.0m below ground (+3.50mPD). The 0.2m thick guide wall protrudes 0.2m from the ground and is 1.2m below ground, which means it has a total length of 1.4m. The bentonite slurry level was maintained 0.2m below the guide wall level (+5.5mPD) with a bulk density of 10.6 kN/m^3.

The trench stability factor of safety using the soil pressure balance method for the several plant load cases and the overall 20kPa load are summarized below in Table 4. The method considered the drained propertied of fine-grained soil (DMD, MD and Alluvium Clay). Figure 9 shows the effective horizontal stress and the bentonite pressure versus depth. From Table 4 and Figure 9 it is possible to determine that the pressure balance method estimates failure to occur, FS < 1.2, at two different locations. All load cases show a possible failure mechanism developing at the interface between the Fill and the Disturbed Marine Deposit while load case no. 1 (20kPa) also indicates a possible failure just below the guide wall.

Table 4: Summary of Trench Stability FS Using the Soil Pressure Balance

Load Case \ Plant		A: 20kPa	B: Mechanical Grab	C: Hydraulic Grab	D: BC40 & MC96	E: BC40 & MC64
1	20kPa	1.13	–	–	–	–
2	Load Distributed by Plant's Footprint (A'xB')	–	1.14	1.14	1.12	1.13

Based on symmetry conditions the panel was modelled in Plaxis 3D as a 0.75m thick and 6.8m long trench, see Figure 7 and Figure 12. The model was extended in all three directions for at least 20m beyond the trench to ensure that deformations and stresses could develop. The load cases and plant considered in this analysis as well as the calculated FS is summarized in Table 5 below. Safety calculations were undertaken for all loading cases and Figure 10 shows the determined failure mechanism per load case. The minimum FS to prevent failure was maintained at 1.2, similarly to what was assumed for the balance pressure method. From Table 5 only the load case no. 4, unbalanced load towards the front track is under the 1.2 threshold. However, after inspection of the safety calculation output, see Figure 10, and the FS plot vs displacement, see Figure 11, it can be determined that the failure mechanism that drives the FS occurs under the track. Since the objective of the study is the trench stability a new load case no. 5 assumes that a typical 6.0m long, 2.4m wide and 30mm thick steel plate is placed centered to the front track to spread the load. Other methods could have been considered, e.g. replacing the top

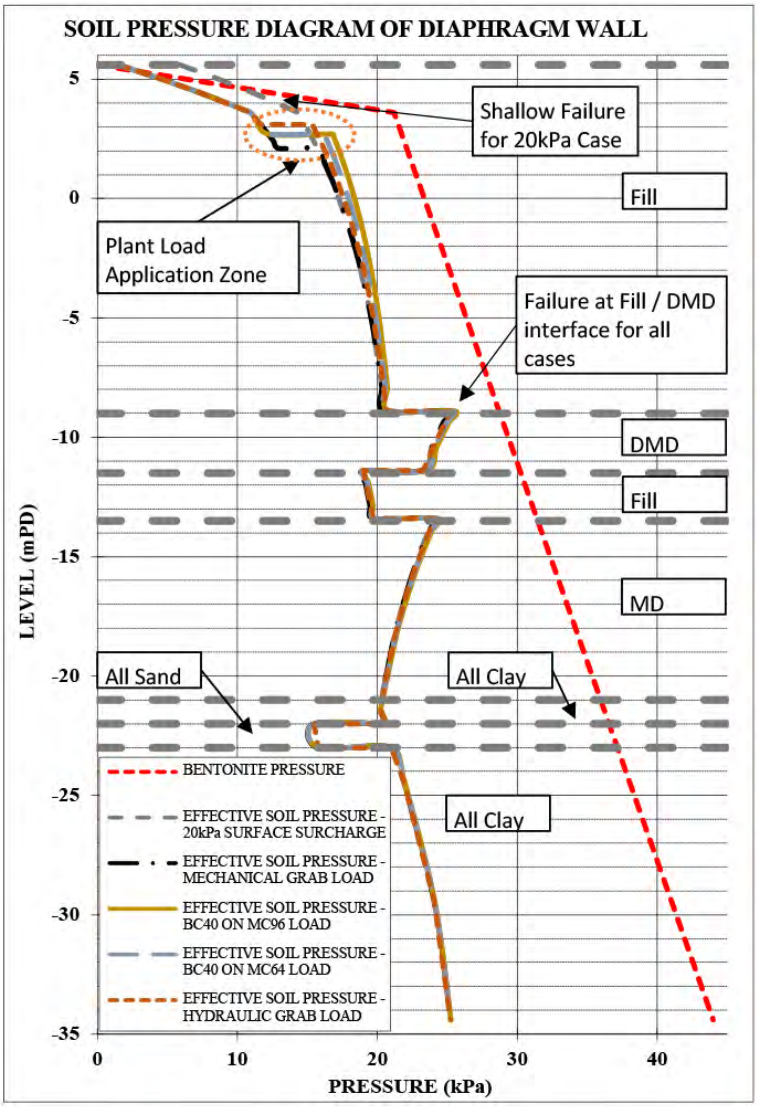

Figure 9: Pressure Diagram of Diaphragm Wall Trench

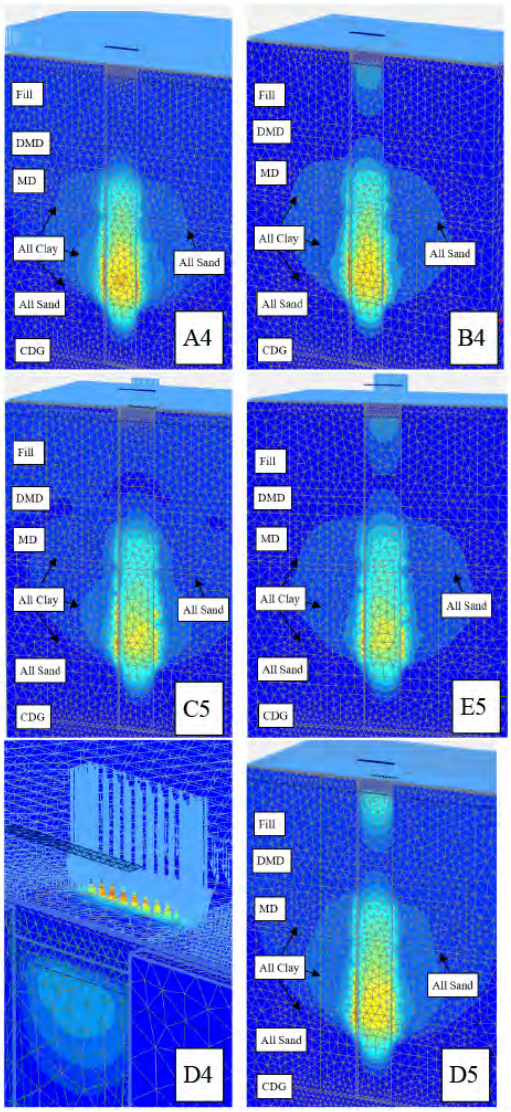

Figure 10: Failure Mechanism for all Load Cases

of the Fill with a more competent working / piling platform. The calculated FS for the new load case 5 is in line with the FS determined for load cases no. 1 to 3, which indicated a deeper failure within the MD and Alluvium Clay, see Figure 10. However, due to the increased pressure at the surface, the safety stage shows increased movement at the trench located at the underside of the guide wall. Although Plaxis 3D confirmed the stability of the trench the estimated soil lateral movements in the plastic stages, approximately 200mm, would be unacceptable. Therefore, a site trial was deemed required to confirm if trench squeezing could occur. The findings of the site trial and comparison with Plaxis 3D results are further discussed in Section 5 below.

Table 5 – Summary of Long Panel's Trench Stability FS Using Plaxis 3D

Load Case \ Plant		A: 20kPa	B: Mechanical Grab	C: Hydraulic Grab	D: BC40 & MC96	E: BC40 & MC64
1	20kPa	1.45	–	–	–	–
2	Load Distributed by Plant's Footprint (AxB)	–	1.44	1.45	1.44	1.45
3	Equal Load on Each Track	–	1.44	1.45	1.43	1.44
4	Unbalanced Load on Tracks	–	1.44	1.12	1.16	1.17
5	Unbalanced Load on Tracks with Plate	–	–	1.45	1.43	1.44

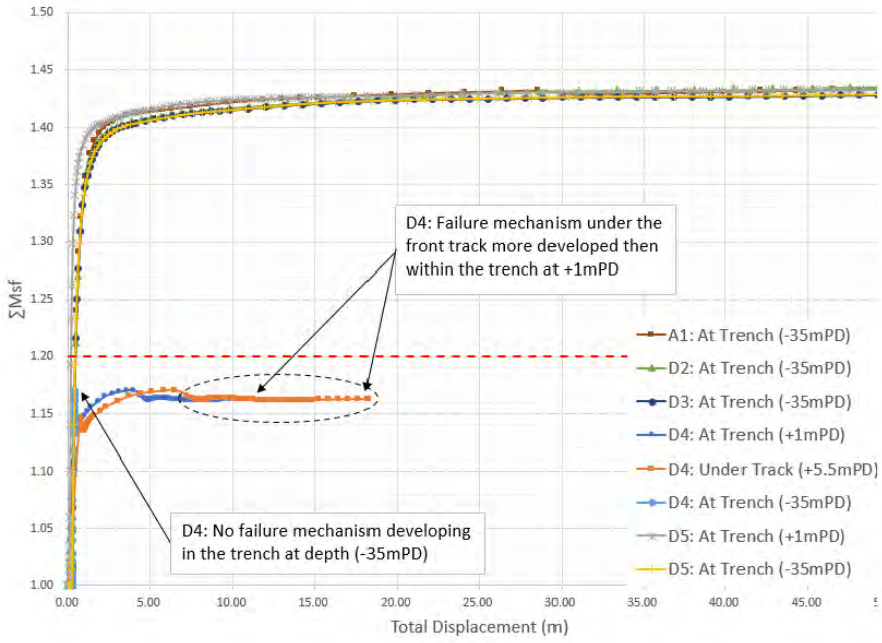

Figure 11 – Plaxis 3D Safety Stages: Calculated FS vs Displacement

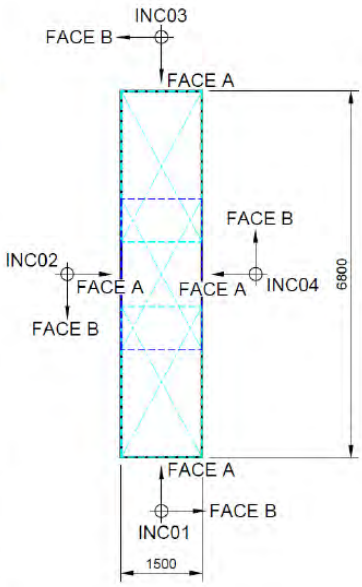

Figure 12 – Inclinometer Location at Long Panel

4.3 Y-Panel

The Y-Panel is a 56m deep, 5-bite panel, 3.6m x 6.5m, see Figure 13, and due to its geometry the pressure balance method and the limit equilibrium methods are not suitable to accurately calculate the trench stability. Therefore, the Y-Panel's trench stability was only calculated using finite element analysis, Plaxis 3D. The guide wall's allowable bearing capacity had to be increased due to the heavy weight of the steel reinforcement cages, up to 140 tons. Its thickness increased to 0.3m and horizontal sections of reinforced concrete around the whole perimeter of the Y-Panel were added, 0.7m to 1.0m long. To increase the stability at the top of the trench and ensure a better load distribution from the plant the top 0.7m of Fill was replaced by compacted working platform, soil properties as shown in Table 1. Remaining

assumptions, i.e. bentonite level and density, guide wall depth below ground, remained the same as per what was described for the long panel.

Four load cases were considered in this calculation, A1, E2, E3 and E4 as shown in Table 6. The calculated factor of safety for the Y-Panel was initially unsatisfactory for load case E4 with no ground improvement, FS inferior to 1.2, see Table 6. Similarly, to the long panel the model showed that a failure mechanism was developing under the track; however, for the Y-panel case the failure mechanism developed through the track to the underside of the guide wall as the model showed similar ground movement at both locations. In addition, this failure mechanism occurred even when a more competent piling / working platform was provided instead of the Fill. The plastic calculation stages were also showing unacceptable ground lateral movement (in excess of 250mm) for all the load cases, see Figure 14. Therefore, a solution to ensure both adequate trench stability and limit lateral movements was required.

Table 6: Summary of Trench Stability FS Using Plaxis 3D

Load Case \ Plant (E: BC40 & MC64)		Unimproved Ground		Ground Improvement with CSM	
		A: 20kPa	E: BC40 & MC64	A: 20kPa	E: BC40 & MC64
1	20kPa	1.37	–	1.70	
2	Load Distributed by Plant's Footprint (AxB)	–	1.37	–	1.70
3	Equal Load on Each Track	–	1.37	–	1.70
4	Unbalanced Load on Tracks	–	1.14	–	1.70

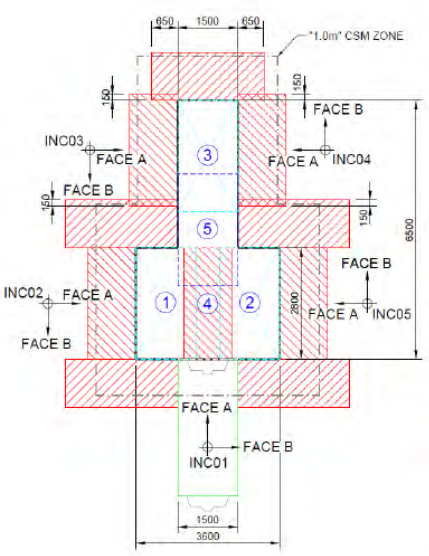

Figure 13: Y-Panel diaphragm wall excavation sequence and CSM ground treatment on plan and section views

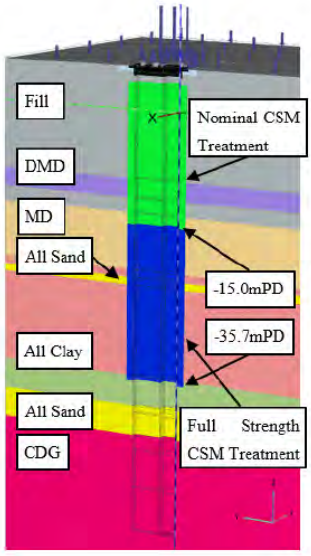

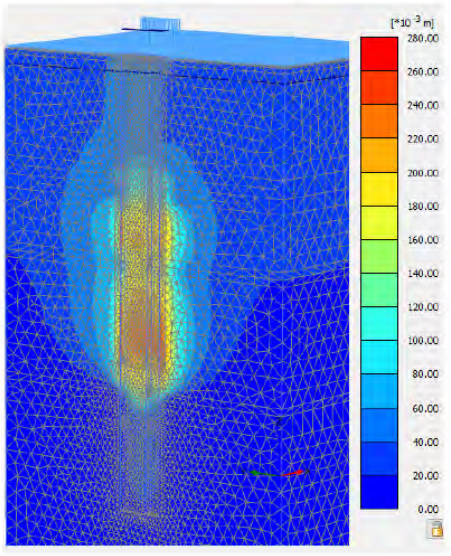

Figure 14: Ground Lateral Movement for Y-Panel Excavation without CSM

Cutter Soil Mixing (CSM) was chosen as the ground improvement method to enhance trench stability and limit lateral ground movements, due to both the applicability and availability of equipment on site. Through the design development stage, it was determined that a 1.0m perimeter ground treatment was required to ensure trench stability and limit lateral movements, see Figure 13. To achieve this treatment envelope 9 nos. of 1.2m x 2.8m CSM bites were required with an extra CSM bite in the middle of the panel so that the required verticality limit, 1/400, could be achieved. The ground improvement had two target strength requirements, the shallower Fill, Disturbed MD and upper part of the natural Marine Deposit (approximately 20.5m) were treated with a nominal ground improvement (UCS = 0.5 MPa). The underlaying Marine Deposit and Alluvium (approximately 20.7m) were fully treated to achieve an UCS of 1.0 MPa. The ground improvement was modelled using the Mohr-Coulomb material model with

undrained behavior and conservatively it neglected any tension cut-off resistance. Figure 15 and Figure 16 show the failure mechanisms (safety calculation) without ground improvement and with the CSM treatment, respectively. Table 6 abovebelow summarizes the Y-Panel's trench stability factor of safety for both treated and untreated ground conditions for all load cases.

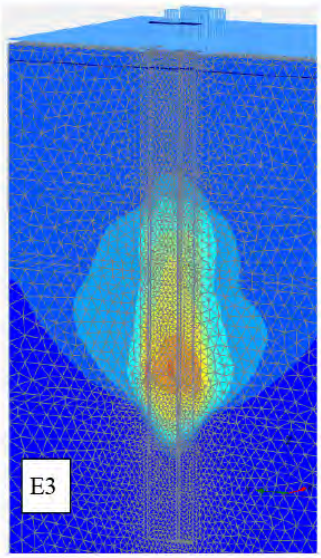

Figure 15 – Y-Panel Failure Mechanisms without CSM

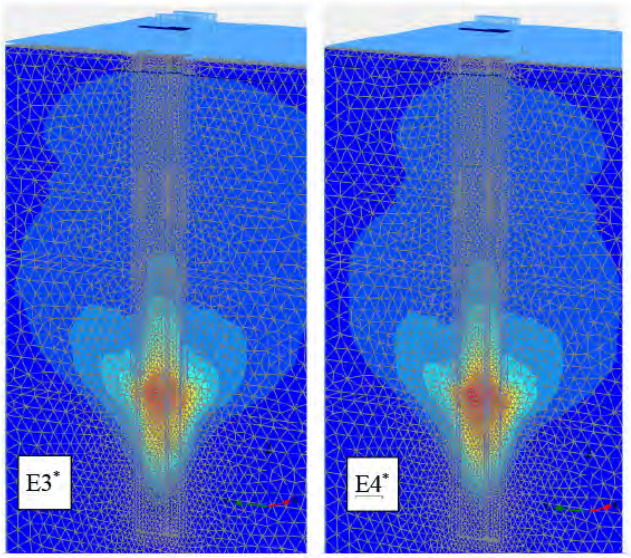

Figure 16 – Y-Panel Failure Mechanisms with CSM*

5 TRENCH STABILITY LATERAL GROUND MOVEMENT REVIEW

A total of four inclinometers, one at each side of the panel, see Figure 12, were installed to monitor the ground's lateral response of the long / triple bite panel's trench excavation. The panel excavation ended on the 24 of January 2018 with a recorded maximum ground movement at INC02 Face A of less than 10mm towards the excavation, INC02 Face A. Considering the same plan location as the inclinometer, Plaxis 3D estimated a maximum lateral movement of about 200mm towards the excavation. Figure 17 below shows a comparison between the two and while Plaxis 3D gave a reasonably accurate lateral ground movement profile with the maximum occurring within the Alluvium Clay the magnitude of this movement was greatly overestimated, Face A direction. Plaxis 3D calculated negligible movement along the perpendicular direction, (Face B). Four days after the excavation, timeframe considered for preparation works to be done prior to casting the diaphragm wall panel, the recorded displacement in INC02 Face A had increased to about 22mm, . The panel was left open for an additional two weeks to study its behavior and the maximum ground lateral movement recorded by the inclinometerINC02 Face As was less than 35mm. Recorded displacement in the perpendicular direction (Face B) was about 21mm. The inclinometer in the opposite side, INC04, recorded less movement towards the excavation, 24mm, but similar movement in the perpendicular direction. The most likely scenario is that a combination of reasons is responsible for the over-estimation of lateral ground movement calculated by Plaxis 3D rather than a particular one. One reason, e.g. might be the use of the Mohr-Coulomb material models rather than more advanced models. In addition,, the deformability parameters might be excessively conservative, deformability parameters particularly when used for trench excavation modeling. This latest reason might have been exacerbated by ongoing ground improvement effectss, which might have been exacerbated by ongoing ground improvement effects.

Similarly, the Y-Panel was instrumented with five inclinometers to register the ground's lateral response to the trench excavation, see Figure 13. The Y-Panel excavation ended on the 14 of February 2018 with a recorded maximum ground movement at INC03 Face A of less than 10mm towards the excavation. This movement was recorded, INC03 Face A, approximately 5m below the CSM treatment. The recorded ground movement towards Face B of the same inclinometer was well under 5mm. The ground lateral movement prediction from Plaxis 3D towards the excavation (Face A) and at the same plan location as the inclinometer was just under the 45mm mark. This movement was estimated to occur at the interface between the toe of the CSM treatment and the natural Alluvium Clay. Plaxis 3D estimated

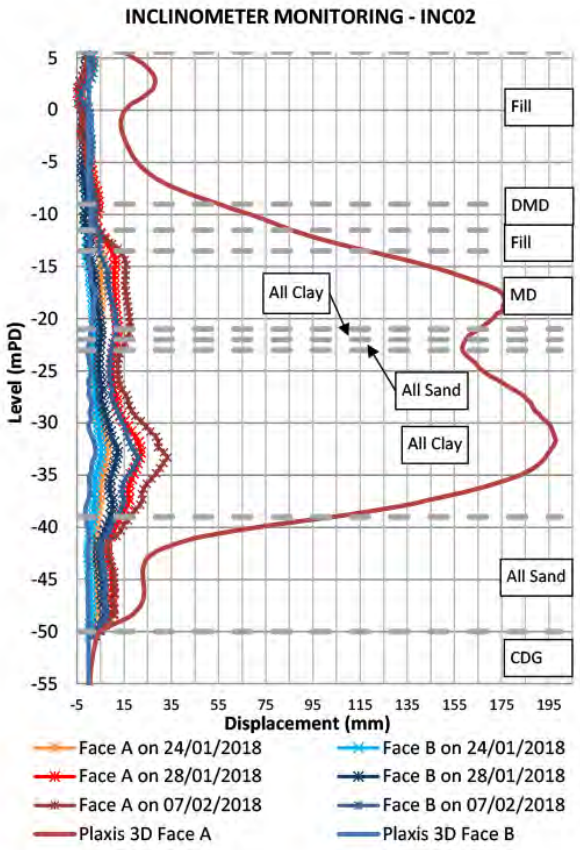

Figure 17: Long Panel Inclinometer Monitoring Results

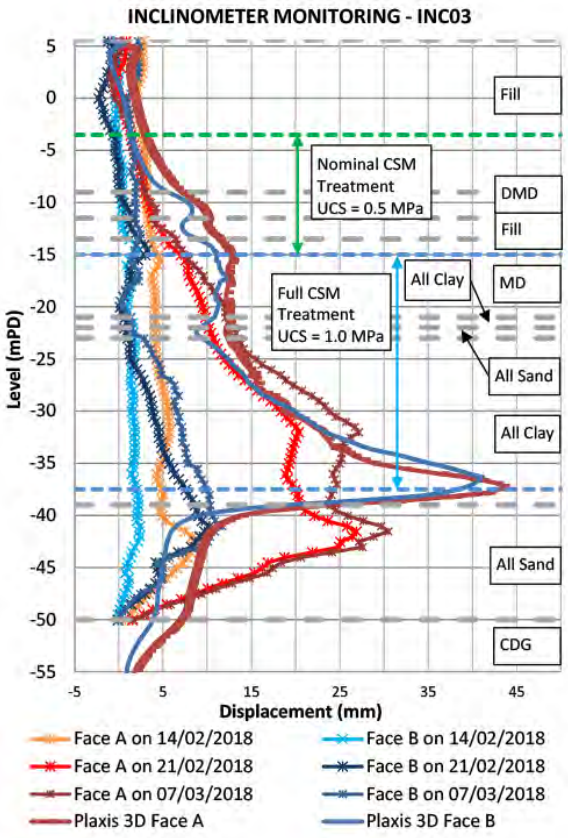

Figure 18: Y-Panel Inclinometer Monitoring Results

a similar lateral ground movement in both magnitude and profile when comparing the movement occurring in the direction towards the excavation (Face A) with its perpendicular direction (Face B). Assembling the Y-Panel cages is a more complex procedure and therefore, the timeframe from excavation to casting was increased to 7 days. The recorded displacement at INC03 Face A by the inclinometers in this time step increased to just under 30mm. Similarly to the long panel, the Y-Panel was left open for another two weeks at which stage the maximum ground lateral movement recorded by INC03 Face A the inclinometers was approximately 32mm, Face A. The final recorded movement by INC03 towards the perpendicular direction (Face B) was about 12mm. The Plaxis 3D analysis overestimated the ground movements, especially in the perpendicular direction to the closest excavation face, Face B.

6 CONCLUSIONS

The trench stability design for the long / triple bite panel using the pressure balance method proved to be too conservative for the TMCLKL ground conditions, when compared to the results obtained from both the site trials and Plaxis 3D. It identified two failure mechanisms, a shallow failure for the 20kPa general surcharge and a deeper failure at the interface of the Fill and Disturbed Marine Deposit for the other load cases. Plaxis 3D requires the user to have experience in identifying the governing failure mechanism and to ensure that these are both fully developed and relevant to the analysis. The Plaxis 3D trench stability design was validated by the site trials as no failure mechanism was identified in either. Despite this the FEA greatly overestimated the predicted lateral movement of the trench when compared to the monitored results from the trial. Based on the findings of the long panel trial the panel layout was updated in 8 circular cells, which lead to a saving of half the number of panels for those cells. This change represented a construction programme saving of about 15%.

The FEA allowed for the trench stability of the Y-Panel to be calculated since the other referenced methods could not accommodate its complex geometry. Initial analysis determined that the estimated lateral movement and the trench stability were not satisfactory. Therefore, a ground improvement

scheme using CSM was analyzed. Plaxis 3D was used to refine the required strength of the CSM that was divided into two zones, a nominal treatment and full treatment with UCS values of 0.5 MPa and 1.0 MPa, respectively. The extent of treatment was also determined, 1.0m perimeter along the trench and about 41m deep. The site trial of the 5-bite panel confirmed the stability of the trench as per the design; however, the calculated lateral ground movement was overestimated, especially in the direction perpendicular to the closest excavation face. The Y-Panel was essential for the successful execution of the hybrid ELS scheme with 15 consecutive circular cells.

REFERENCES

Huder, J. "Stability of Bentonite Slurry Trenches with some Experiences in Swiss Practice," in Proceedings of the 5th European Conference on Soil Mechanics and Foundation Engineering, Vol. 1, Madrid, Spain, 1972.

Schneebeli, G, "La Stabilite Des Tranchees Profondes Forees en Presence de Bour," La Houille Blanche, N. 7, 1964.

G. C. Y. Wong, "Stability analysis of slurry trenches," Journal of Geotechnical Engineering, vol 110, no. 11, pp 1577-1590, 1984.

N. Morgenstern and I. Amir-Tahmasseb, "The Stability of a slurry trench in cohesionless soils," Geotechnique, vol. 15, no. 4, pp 387-395, 1965.

G. Aas, "Stability of slurry trench excavations in soft clay," in Proceedings of the 6th European Conference on Soil Mechanics and Foundation Engineering, pp 103-110, International Society of Soil Mechanics and Foundation Engineering, Vienna, Austria, March 1976.

W. Brzakala, K. Gorska, "On Stability Analysis of Slurry-Wall Trenches", Institute of Geotechnical and Hydroengineering, Faculty of Civil Engineering Wroclaw University of Technology Wybrzeze Wyspianskiego 27, 50-370 Wroclaw, Poland, 2008 .

Grands-Tavera C E, Triantafyllidis T. "Simulation of a corner slurry trench failure in clay" [J]. Computers and Geotechnics, 2012, 45: 107–117.

Li Wei, Zhang Chengping "Stability Analysis of a Slurry Trench in Cohesive-Frictional Soils" Open Geosciences, Vol 11, Iss 1, Pp 888-900, 2019.

On the Application of Mechanical Reinforcement of Tree Roots to Slope Stabilization

Arthur K.O. So & Ricky Y.S. Choi
Meinhardt Infrastructure and Environment Limited

ABSTRACT

The root strengthening effects on soil behind retaining walls may be quantified by a simplified equation $\Delta S = 1.2T_R(A_R/A)$ where ΔS, T_R and A_R/A are the shear strength increase, tensile strength of root and root area ratio respectively. However, this effect is ignored during stability analysis due to the possible significant variability of the potential beneficial effect and extreme difficulty in fully characterizing the tree roots and quantifying their effects. In this paper, advancements in the last few decades in biotechnical slope stability are reviewed. Representative models to quantify the mechanical effects of tree roots are studied. If other potential beneficial effects due to existence of roots and suction effect due to transpiration of tree are ignored, the term 1.2, root tensile strength and root area ratio may still be the three key parameters to the root strengthening effect in slope stability. However, for plants with larger structural roots where root bending rather than axial breakage is dominant, the roots may be considered using beam bending or p-y models. Based on the information commonly used for slope design and obtained from literatures, presumed values of two key parameters and a simple insitu measurement method invented by other are recommended

Keywords: Biotechnical Slope Stabilization, Root-Soil-Slope Interactions, Mechanical or Root Reinforcement, Predictive Models, Root Architecture, Presumed Values, Parametric Studies

1 INTRODUCTION

Vegetation had been used as foundations, retaining walls and to stabilize slopes and embankments 4,000 years ago in ancient China (Smith and Snow 2008) and ancient Rome (Partov et al. 2016). The design and utilization at that time were basically empirical in nature. Despite the incorporation of vegetation effects onto slope stability analysis was introduced in 1960s (Greenway 1987), current practice in most part of the world still considers vegetation mainly for aesthetic purposes and erosion control. The engineering functions of plant roots have been generally ignored in the scientific analysis and design of slope stability. As in the GEO Report No. 257 (GEO 2011), the root strengthening effects on the soil behind retaining walls was quantified following a simplified equation $\Delta S = 1.2\ T_R\ (A_R/A)$ by Wu et al. (1979) where ΔS, T_R and A_R/A are the shear strength increase, tensile strength of root and the root area ratio (RAR) respectively. However, the Report concluded that this equation may be conservatively ignored during stability analysis due to the possible significant variability of the potential beneficial effect and the extreme difficulty in fully characterizing the tree roots and quantifying the strengthening effects of tree roots.

In this paper, the root reinforcement model by Wu et al. (1979) is examined. Advancements in the last few decades in the biotechnical slope stability, and in particular the soil variability and effect of vegetation are reviewed. Other representative models to quantify the mechanical effects of tree roots

are studied. The key design parameters to the root strengthening effect in slope stability are identified. Based on the information commonly used for slope design and obtained from literatures, presumed values of two key parameters and a simple insitu measurement method invented by Meijer et al. (2019) are suggested. Hypothetical slope analyses and parametric studies are carried out.

2 LITERATURES REVIEW

2.1 The Root Reinforcement Model of Wu et al. (1979)

The model is based on the Mohr-Coulomb equation

$$S = c + \sigma_N \tan\phi \quad (1)$$

where S = soil shearing resistance, c = cohesion, σ_N = normal stress on the shear plane and ϕ = soil friction angle. Waldron (1977) first assumed that all roots extended vertically across a horizontal shear zones and the roots act like laterally loaded piles so that tension is transferred to the roots as the soil is sheared. The equation is therefore modified as

$$S = \Delta S + c + \sigma_N \tan\phi \quad (2)$$

and

$$\Delta S = T_R(\sin\theta + \cos\theta\tan\phi) \quad (3)$$

where ΔS = increased shear strength due to the roots, T_R = tensile strength of roots and θ = angle to the shear plane. Gray (1974) reported that the results of several studies on root permeated soil showed that ϕ appeared to be affected little by the presence of roots. ΔS may therefore be considered as an increase in c or the apparent cohesion c_r. Sensitivity analysis by Wu et al. (1979) showed that the bracket ($\sin\theta + \cos\theta\tan\phi$), or k' as termed by some researchers, is fairly insensitive to the normal variations in θ and ϕ with values ranging from 1.0 to 1.3. A value of 1.2 was therefore selected and the equation became

$$\Delta S = 1.2T_R(A_R/A) \quad (4)$$

where A_R/A is the root area ratio RAR. Thus, the root reinforcement simply depends on RAR and T_R. Despite this model is simple to use, it may be over-simplified as it assumes that: i) the roots are well anchored and do not pull out when tensioned (fibre break), ii) the roots are perpendicular to the slip plane (perpendicular root), iii) the full tensile strength of all roots is mobilized when the soil shears, and therefore considers the forces acting in the root-soil matrix when all roots reach their maximum tensile stress. Furthermore, the variability in vegetations and effects of root architecture might have imposed uncertainty in the predictions. In order to have a better understanding of the biotechnical slope stability, advancements in the knowledge and technology in the last few decades are reviewed.

2.2 Slope Stabilization Function of Plants

Ng et al. (2019) and Bordoloi and Ng (2020) have attempted to provide a state-of-the-art for the vegetation in engineered slope stability by viewing the effect of inherent plant traits/parameters with that of its slope stability and protection functions. Their work reviews can be distinguished into three areas: 1) the plant-soil-atmosphere continuum, 2) an overview of the major stability functions provided by plant in slope, and 3) a new gap area and function scope in engineered vegetated slopes. Figure 1 is a schematic representation of the stabilization functions provided by plant in slope which includes; namely, a) the root reinforcement, b) the hydrological reinforcement, and c) the interception. Both the root and shoot architecture affect these functions. The root reinforcement in turn includes: i) the tensile force mobilization and anchorage upon hard stratum, ii) the soil aggregation by root growth, and iii) the secretion of cohesive enzymes called mucilage.

For the purpose of this paper, only the mechanical reinforcement of root (shaded in Figure 1) is focused, but not other potential beneficial effects, such as the increase in soil aggregate stability by roots interweaving in the soil matrix, roots exudating organic matters to increase the soil structure, root caps secreting mucilage to bind the soil particles, and micro-organisms producing polysaccharides to enhaunce the formation of soil aggregates (Vannoppen et al. 2015). Suction effect due to transpiration of the tree is also ignored.

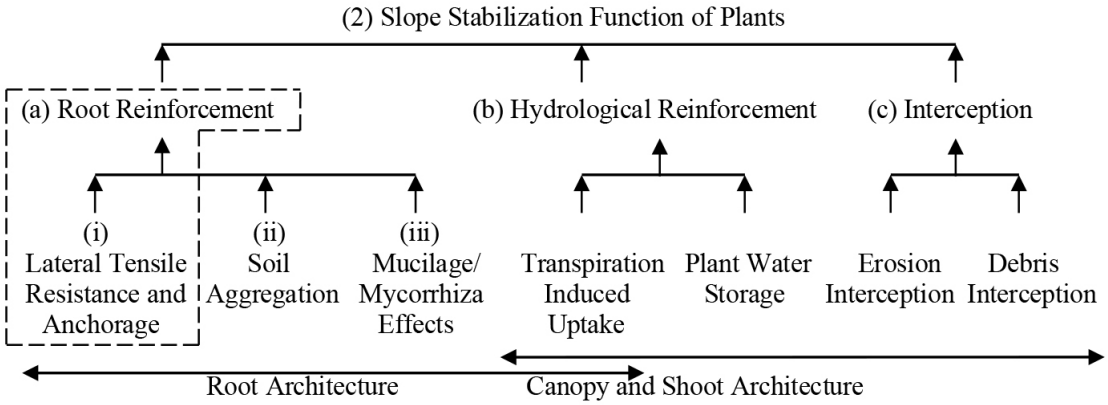

Figure 1: Schematic Representation of the Major Slope Stabilization Functions of Plants (modified after Bordoloi and Ng, 2020)

The incorporation of vegetation effects on slope stability resembles a reinforced soil slope analysis. It involves complicated interaction of two natural materials, unsaturated soils and plants, and crosses over the fields of unsaturated soil mechanics, plant science and ecological science. Table 1 is a summary of the basic parameters for the inter-dependent of the root-soil interactions to determine the mechanical strength (shear strength and Young's modulus) of rooted soil in slopes.

Root	Soil
Condition (Living/Dead)	Particle and Pore Size Distribution
Fine/Coarse Root Ratio	Matric Suction and Water Content
Micro-Fibrillary Angle	Stress History
Root Diameter	Density
Root Architecture (Sinuosity)	Mineralogical Content
Bio-Polymer Composition	Nitrogen Availability

Table 1: Root-Soil Interaction in Terms of Basic Parameters that Govern the Mechanical Strength of Rooted Soil (modified after Bordoloi and Ng, 2020)

2.3 Variability of Vegetation and Soil and their Effects to Roots

Vegetation may be classified as herbs (including grasses and ferns), climbers, shrubs, small trees (around 3m tall), medium trees (much taller than 3m with small crown) and large trees (taller than 10m with large crown) (GEO 2008). Different species have different root systems (tap root and fibrous root) and root architecture (uniform, triangular, exponential and parabolic), and properties of soil affect the spatial distribution and depth of the root system. Perry (1989) commented that the variation in root size from large woody to small non-woody, perennial to ephemeral, and absorbing to non-absorbing is continuous. This makes the sorting of roots into various category arbitrary, but classification and sorting are still essential to comprehending the pattern and integrated function of the total root system. Coppin and Richards (1990) reported that individual species vary in their rooting behaviour, but soil type and ground water regime strongly influence the root development. e.g. Roots in well-drained soils have to go deeper and exploit a much larger volume of soil than those in moister soils while a high groundwater level or a layer of densely compacted soil will force roots to spread laterally. The majority

of roots are usually found within 300-400mm depth in herbaceous vegetation and up to 3m deep in vegetation dominated by trees and shrubs. Dobson (1995) reported that most roots are found close to the soil surface with 90% or more of all roots located in the upper 600mm. It is uncommon for trees to have roots deeper than 2m though exceptionally some small roots (a few mm in diameter) can extend to 5m or more.

Of the mechanical properties of roots, many researchers (e.g. Coppin and Richards 1990, Abernethy and Rutherford 2001, Simon and Collison 2002, Pollen and Simon 2005, Stokes et al. 2008, Leung et al. 2015 and Ji et al. 2020) reported an exponential decrease in root tensile strength with increasing root diameter. Regarding the root-soil interaction, Abe and Ziemer (1991) used a large shear box to shear across a vertical plane and found that the amount of root deformation increases as the number and size of roots decrease. Tobin et al. (2007) found that roots can stretch by 10-20% of their length before failure whilst most soils fail at strain around 2%. Based on in-situ field shear tests for different tree species, Docker and Hubble (2009) showed two modes of root failure: type 1 failure which occurs after reaching maximum shear resistance and diminishes as the displacement increases, and type 2 failure which occurs before reaching a maximum resistance with continuous increasing shearing resistance. Thomas and Pollen-Bankhead (2010) found that the root architecture has a significant impact on the loading curve shape and the peak load supported by a root bundle. Based on triaxial tests, Meng et al. (2020) showed that roots under low confining pressure can play a greater role in resisting the failure of rooted soil, and its ability is affected by root geometry (number, diameter and length) and distribution characteristics (root angle).

2.4 Measurement of the Mechanical Behaviour of Roots

The measurement of mechanical behaviour of roots started in 1970s (Wu 2007, Giadrossich et al. 2017). They may be distinguished into two main types of test: 1) direct measurement of a specific behaviour of root and 2) combination of root and soil as a matrix. Tensile strength tests, compression test, buckling tests and pullout tests are in the former group and are for woody roots. They can be carried out on a single root or on a bundle of roots in the field or in the laboratory. Shearing of a block of rooted soil in field or a rooted soil column in the laboratory, direct shear test and rooted soil under compression are tests in the latter group. They are for finer roots of which the roots are part of the soil system and the effect of each one cannot be separated but can only be considered within a global behaviour. Some innovative methods are the X-ray computed tomography and digital volume correlation (Bull et al. 2019) and the Corkscrew extraction method (Meijer et al. 2019).

2.5 Predictive Root Reinforcement Models

The researches of root reinforcement began with direct shear tests performed on soil blocks containing roots, e.g. Endo and Tsuruta (1969), Wu (1976). Since then many models were developed which may be classified (e.g. Liang et al. 2020) into: 1) a continuum approach which considers root-soil matrix as a homogeneous material of increased strength or root cohesion, or 2) a root-soil interaction approach which considers roots as structural elements embedded in soil. The additional resistance in soil due to roots is introduced into stability calculations, which may be distinguished as: a) fibre pull out model, b) fibre break models, c) fibre bundle model, and d) beam bending or p-y model. Some representative models are given in Table 2.

	Authors	Models
Fibre Pull-Out Model		
1.	Endo and Tsuruta (1969)	$S = (c + r) = W \cos\alpha \tan\phi$ where S = shear strength of root-soil, c = cohesion of soil, r = apparent cohesion, W = effective weight of soil, α = slope of failure surface, and ϕ = friction angle.
Fibre Break Models		
Perpendicular Root Reinforcement Models		
1.	Wu (1976)	$\Delta S = \tau_r (\sin\theta + \cos\theta \tan\phi) = 1.2\ T_R$ where ΔS = increase in shear strength, τ_r = shear stress parallel to shear zone, θ = shear strain, ϕ = friction angle of soil, and T_R = tensile strength of root.
2.	Waldron (1977)	$\Delta S = T_R (\sin\theta + \cos\theta \tan\phi)$ where ΔS = increase in shear strength, T_R = tensile strength of roots, θ = angle to the shear plane, and ϕ = friction angle of soil.
3.	Wu et al. (1979)	$\Delta S = 1.2\ T_R (A_R/A)$ where ΔS = increase in shear stress, T_R = tensile strength of roots, and A_R/A = amount of roots present in soil.
4.	Waldron and Dakessian (1981)	$T_{RS} = (4z\tau_b E_R/d)^{1/2} (\sec\theta-1)^{1/2} (A_R/A)$ where T_{RS} = mobilized tensile strength of stretched roots, z = thickness of the shear zone, $z\tau_b$ = root-soil bond stress, E_R = tensile modulus of the root, D = root diameter θ = angle of shear distortion, and A_R/A = root area ratio.
5.	Abe and Ziemer (1991)	$\Delta S = \Delta S_t + \Delta S_p$ where ΔS_t = reinforced strength caused by tensile stress of root, and ΔS_p = shear strength applied to a root by earth pressure.
6.	Wu (2013)	T_R = breakage tensile strength or pull-out capacity, whichever the less.
Inclined Root Reinforcement Models		
1.	Gray and Leiser (1982)	$\Delta S\ \alpha\ A_R/A = \Delta c_r$ where ΔS = increase in shear strength, A_R/A = root area ratio, and Δc_r = increase in apparent cohesion of soil.
2.	Gray and Ohashi (1983)	$\Delta S = t_r [\sin\theta + \cos\theta \tan\phi]$ for perpendicular fibre $\Delta S = t_r [\sin(90-\psi) + \cos(90-\psi) \tan\phi]$ for inclined fibre where ΔS = increase in shear stress, $t_r = (A_R/A)\ \sigma_b$, A_R/A = root ratio area, σ_b = tensile stress developed in root at shear plane, θ = angle of shear distortion, ϕ = friction angle of soil, $\psi = \tan^{-1}\{1 / [k_1 + (\tan^{-1}\alpha)^{-1}]\}$, k_1 = shear distortion ratio = x/z x = horizontal component of shear displacement, z = thickness of shear zone.
3.	Gray and Barker (2004)	$\Delta S = k\ \beta(A_R/A) (\sin\theta + \cos\theta \tan\phi)$ where $k = (4z\ \tau_b\ E_R\ /d)^{1/2}$, z = thickness of shear zone, τ_b = bond stress of root-soil, E_R = tensile modulus of root, d = diameter of root, $\beta = (\sec\theta - 1)^{1/2}$, θ = angle of shear distortion, A_R/A = root ratio area, and ϕ = friction angle of soil.
Fibre Bundle Models (FBM)		
1.	Pollen and Simon (2005)	a) Comments to the assumptions and limitations of the Wu et al. (1979) model which could over-estimate up to 50%. Considered that when slopes fail, the root- b) soil matrix shears and the roots contained within the soil have different tensile strengths and thus break progressively with an associated redistribution of stress as each root breaks by iterations (see flow chart on the right). Laboratory test data showed that the root tensile strengths decreased nonlinearly c) with increasing root diameter.
2.	Thomas and Pollen-Bankhead (2010)	a) Used sensitivity analysis and fiber-bundle model (FBM) to examine assumptions underpinning root-reinforcement models. b) Different methods for apportioning load between intact roots. c) Monte Carlo approach to simulate plants growing on slopes and floodplains.

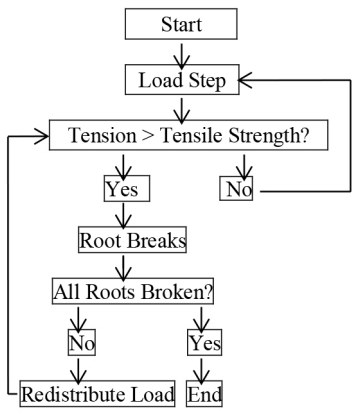

3.	Schwartz et al. (2010)	a) A more complicated pull-out based model by iterations, also named as the Root Bundle Model. b) It incorporated some features of the root geometry (root length, root diameter, root branching pattern and root tortuosity) and mechanics (maximum tensile strength, Young's modulus, root-soil interfacial friction, soil saturation) (see flow chart on the right). c) It contributed to the understanding the pull-out behavior of roots.	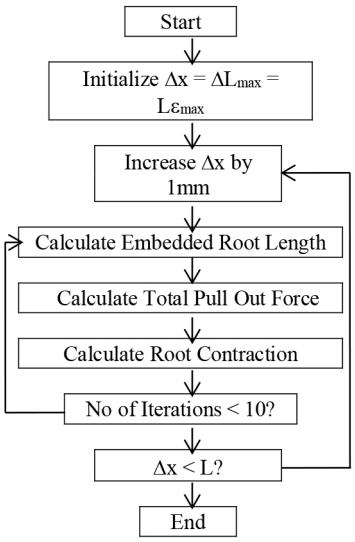
4.	Ji et al. (2020)	This model is based on an energy approach whereby the root breakage is driven by the work that is yielded in soil shear movement and is dissipated by roots. The criterion determining the rupture of a root is only dependent on whether the work that it receives is greater than the energy to break the root in tension. The work equation shows that the root breakage is dependent on the load and displacement.	
Beam Bending or p-y Models			
1. 2. 3. 4.	Duckett (2014) Mao et al. (2014) Liang et al. (2015) Meijer et al. (2019)	These models use a set of transverse force-displacement (p-y) springs, which may be highly non-linear, to model the root-soil interaction in bending. They are computationally efficient and implicitly incorporate the effects of soil properties as well; however, further development would be required to generalize such analyses into analytical or finite difference-based models which are simple to use in practice.	

Table 2: Some Representative Root Reinforcement Models

3 ON THE APPLICATION

3.1 Selection of Prediction Methods

The Wu and Waldron model (Wu 1976, Wu et al. 1977, Waldron 1977) and the RipRoot model (Pollen and Simon 2005) are widely used. They assume the roots being highly flexible with negligible bending stiffness. The roots will break in tension during shearing such that the additional strength provided by the roots is mainly a function of root properties, i.e. tensile strength of roots, root density and root orientations. However, the RipRoot model can model progressive failure as the weakest roots within the root system break first, with the load shared between different diameters of the roots. Thomas and Pollen-Bankhead (2010) permitted the load shared by: (i) equal load applied to individual roots regardless of root dimension, (ii) load apportioned by root diameter or (iii) load apportioned by root cross-sectional area. For plants with shallower, fine and fibrous root systems, the fibre breakage models are acceptable because the root diameters are more homogenous. However, it may not always work as roots are pulled out of the soil before breaking. Waldron and Dakessian (1981) proposed a pull-out-based model which is not widely adopted due to its dependence on root strain and is relatively difficult to estimate in practice. Schwarz et al. (2010) proposed a more complicated pull-out-based model or the Root Bundle Model, which incorporated some features of the root geometry and mechanics. Despite this, it is seldom used in engineering practice due to its complexity in the input parameters. Since most of these models assume root breaking such that the roots are well anchored and do not pull out when tensioned, the term "breaking" may be interpreted as by breakage, slippage or buckling. As such, the "interpreted breaking force" may be a more flexible term to consider other types of root failure depending on what the "ultimate" resistance is considered to be. For plants with larger structural roots where root bending rather than axial breakage may be more dominant, the roots may be considered as flexible cables for fine roots or bending beams for coarse/ structural roots subject to lateral loadings

using the beam bending or p-y models. The surcharge and wind effects of shoot to slope stability can refer to GEO Report No. 257 (GEO 2011). Recommendations on the estimation of root reinforcement are summarized in Table 3.

Vegetation	Root Diameters (mm)	Approaches	Predictive Methods	Field or Laboratory Tests	Recommended T_R (MPa)
Herbs (including Grasses and Ferns)	Generally thin or fine roots (<10mm)	Continuum approach combining root and soil as a matrix	Wu and Waldron model or RipRoot model k' = 1.15 to 1.18	Field: shear test, borehole shear test and vane shear test. Laboratory: shear test, triaxial test and compression test.	3 - 18MPa for 10mm diameter roots. Suggested 8MPa for all roots with diameter < 10mm in mixed species
Climbers					
Shrubs					
Small Trees (around 3m Tall)					
Medium Trees (much taller than 3m with Small Crown)	Fine and thin roots (<10mm) / Coarse roots (>10mm)	Root-soil interaction approach considering roots as structural elements embedded in soil	Beam bending or p-y models for coarse roots	Field: pullout test Laboratory: tensile test and compression test	Tree species specific.
Large Trees (Taller than 10m with Large Crown)					

Table 3: Summary of Suggestions based on Literature Reviews

3.2 Determination of the Three Key Parameters in the Wu and Waldron Model

Leung et al. (2015) may be the pioneers to study the root effects of Hong Kong native plants on enhauncing slope stability. Despite many sophisticated models have been developed, the Wu and Waldron model was adopted likely due to its simplicity. The term ($\sin\theta + \cos\theta\tan\phi$) or k', tensile strength of roots and root area ratio are therefore the three key parameters. Based on four young shrubs and trees with height ranging between 1m and 1.5m, k' was determined varying from 1.15 to 1.18. The root class distribution was found varying probably due to species genetics and environmental factors such as soil moisture, and the roots of the studied trees extending deeper into the ground (up to 0.8m) as compared with the shrubs (up to 0.4m). Figure 2(a) shows that the average RAR lied between 0.03% and 0.14% for the top 0.1m soil and decreased with depth when all roots were considered, but could lie below 0.05% even close to the ground if only the roots of 1 to 10mm diameter were considered. Figure 2(b) shows that the conventionally adopted power decay relationship between T_R and root diameter was applicable for the studied species. The T_R was found having no significant difference within the studied species, but significant difference between the studied species. Despite this, the consolidated figure shows that T_R appears to fall within a band irrespective of the studied species with an average T_R = 8MPa for a root diameter = 10mm.

As shown in Figure 3, the obtained T_R and root diameter relationship of all studied species (modified to natural scale) also falls into the order compared to some reported European species. This may suggest that 8MPa may be a conservative design assumption for an average T_R of the fine and thin roots for slope covered with mixed native species. Thus, presumed values of k' = 1.15 and T_R = 8MPa may be conservatively used for fine and thin roots of less than 10mm irrespective of species as recommended in Table 3.

The root depth and RAR are therefore the only significant variants which are unknown but can be determined by conventional field or laboratory tests (see Table 3). An innovative method invented by Meijer et al. (2019) using a corkscrew device to extract soil cores may also be considered as it can provide rapid estimation of T_R, root depth and RAR for mixed species on field. As shown in Figure 4, for each selected corkscrew sample, the total mass, volume and water content are measured. Root material is collected by careful washing of the extracted soil plug on a 2mm sieve. The root volume fraction can be calculated as the volume of roots over the measured volume of the extracted core. Assuming a uniform distribution of root orientations, RAR can be estimated as ½ of the measured root volume.

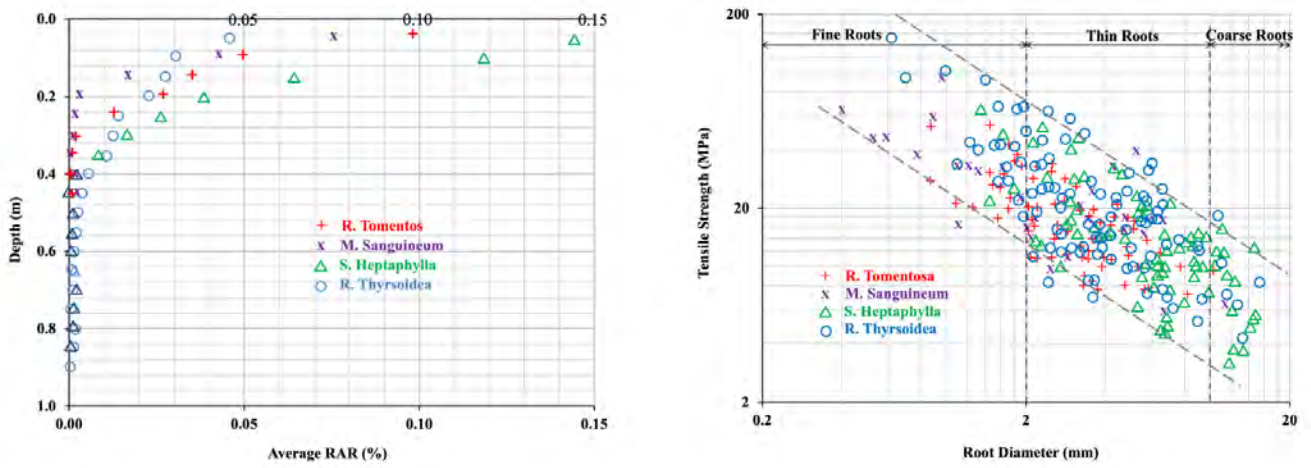

Figure 2: Variation of (a) Average RAR with Depth when All Roots are considered, and (b) Tensile Strength with Root Diameter of Four Native Species (after Leung et al. 2015)

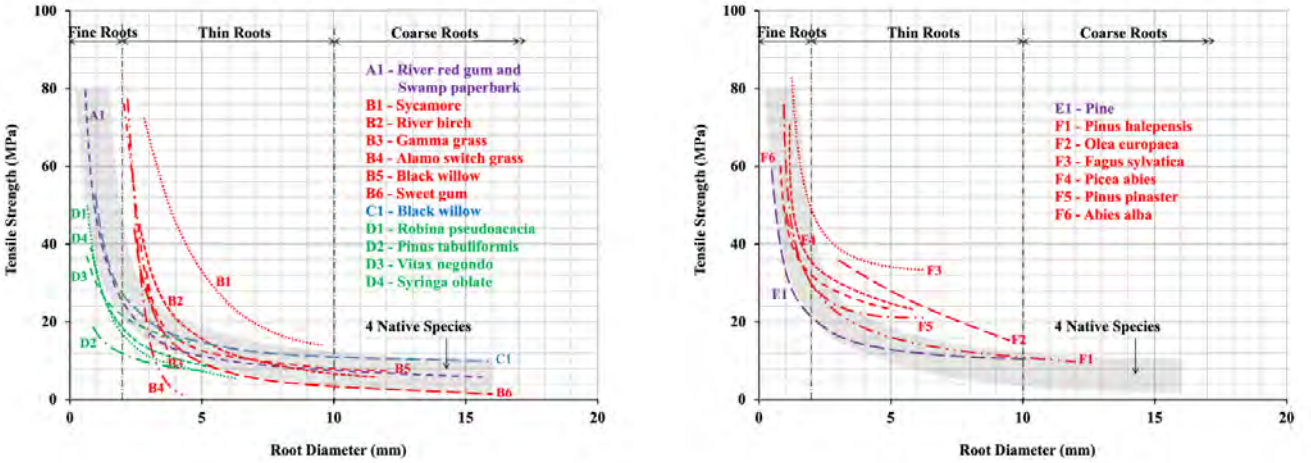

(a) Grasses to Medium Trees: A-series after Abernethy and Rutherford (2001), B-series after Simon and Collison (2002), C-series after Pollen and Simon (2005) and D-series after Ji et al. (2020)

(b) Large Trees: X-series after Pollen and Simon (2005) and Y-series after Stokes et al. (2008)

Figure 3: Variation of Tensile Strength T_R with Root Diameter of Four Native Species and Some European Species

3.3 Slope Stability Analysis

As shown in Figure 5, a hypothetical slope model of 7m high at 37° angle and composed of 3m colluviums fill on the top and completely decomposed granite at the bottom is set up for demonstration. Presumed values k' = 1.15 and T_R = 8MPa are adopted, and conservative values RAR = 0.1% and root depth = 0.4m are assumed. The ΔS or apparent cohesion c_r is calculated equal to 1.15 x 8MPa x 0.1% = 9.2kPa. The design parameters of the slope with and without roots are summarized in Table 4. Soils are modelled according to the Mohr-Coulomb theory. The hydraulic condition is assumed to be hydrostatic with a fixed groundwater table at 1/3 slope height and a perched water table at 1m below the surface of top soil. Stability analysis is carried out by Morgenstern and Price method using the computer software SLOPE/W 2012. For a slope without vegetation, shallow slip appears at the crest of the slope and extends to the toe of slope giving a FOS = 0.505. When vegetation is added, the apparent cohesion renders the slip surface moving away from the crest of the slope and deeper into the top soil, thus resisting by a larger volume of soil and giving larger FOS = 0.576.

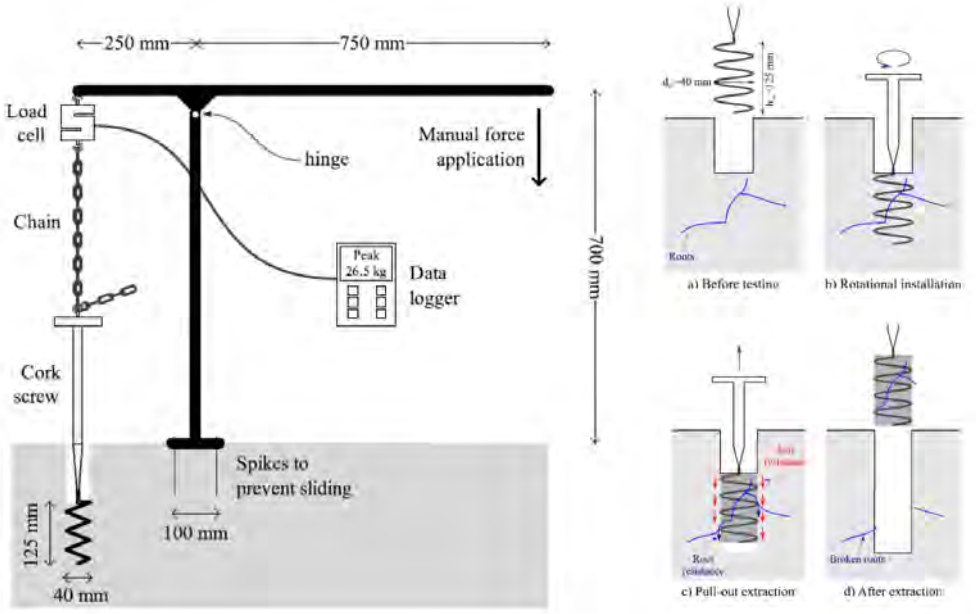

Figure 4: Schematic Corkscrew Measurement Setup and Test Procedures (after Meijer et al. 2019)

Soil Type	Thickness (m)	Unit Weight γ (kN/m³)	Cohesion c (kN/m²)	Friction Angle ϕ	Vegetation	Root Depth (m)	Average RAR (%)	ΔS (kN/m²)
Upper Soil (Fill)	3m	19.0	0	30°	Without	–	–	–
					With	0.4	0.1%	9.2
Lower Soil (CDG)	infinite	19.0	5	35°	–	–	–	–

Table 4: Design Parameters for Slope Analysis (using k' = 1.15, T_R = 8MPa and RAR = 0.1%)

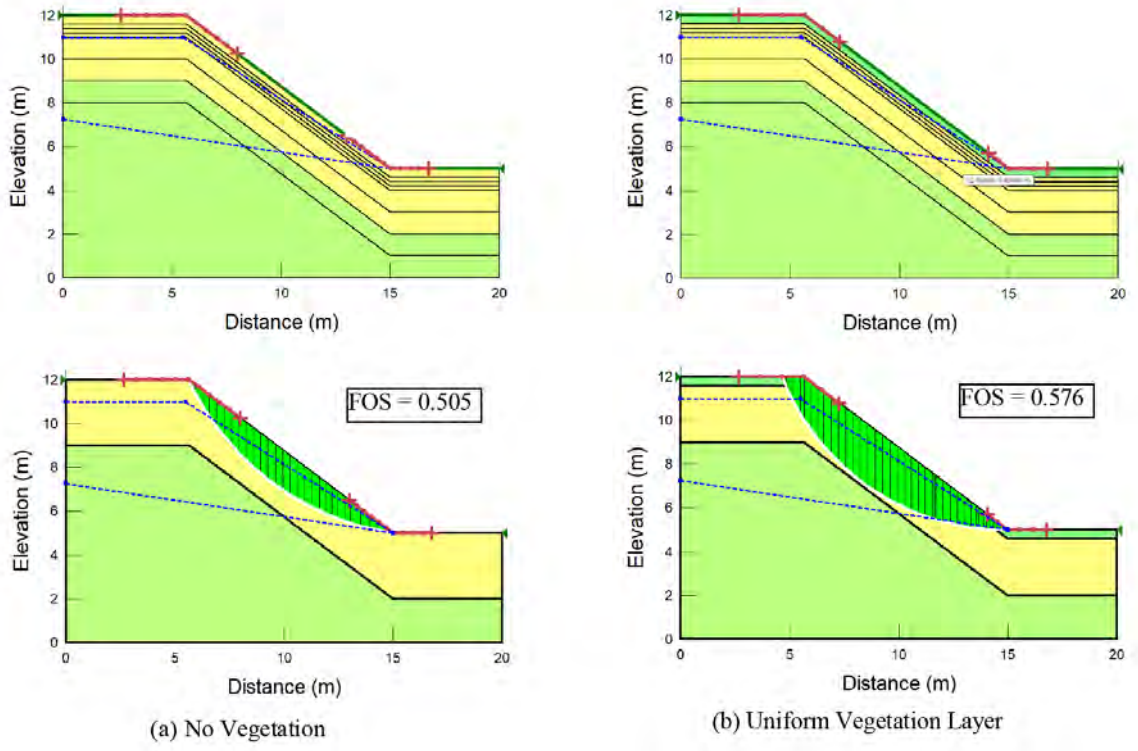

Figure 5: Hypothetical Infinite Slope Models

Sensitivity analyses are carried out for different RAR (0.125%, 0.15%, 0.175% and 0.2%), root depth (0.4m, 0.6m, 0.8m and 1m) and top fill thickness (1m, 2m and 4m). Figure 6(a) shows the effect of RAR to root strengthening with root depth = 0.4m. For RAR = 0.1%, the increase in FOS is 0.408 at fill thickness = 1m, and decreases markedly to 0.094 at fill thickness = 2m and then slightly to 0.072 at fill thickness = 3m and 4m. This is significant as it may imply that a marginally safe slope with shallow top soil can be upgraded to a safe slope with sufficient FOS even with RAR = 0.1%. Similar trends of increase in FOS are observed when RAR is increased from 0.1% to 0.2%. The increase in FOS and % increase corresponding to respective RAR for various fill thickness with root depth = 0.4m are summarized in Table 5. Largest increase in FOS with increased RAR occurs at fill thickness = 2m.

Top Fill	1m		2m		3m		4m	
RAR (%)	Increase in FOS	Increase in %	Increase in FOS	Increase in %	Increase in FOS	Increase in %	Increase in FOS	Increase in %
0.1	0.408	–	0.094	–	0.071	–	0.072	–
0.125	0.477	17%	0.116	23%	0.085	19%	0.086	19%
0.15	0.546	34%	0.138	47%	0.099	36%	0.098	36%
0.175	0.613	50%	0.160	70%	0.110	54%	0.111	54%
0.2	0.681	67%	0.182	94%	0.124	72%	0.124	72%

Table 5: Increase in FOS with increased RAR for Slope Model with Root Depth = 0.4m

Figures 6(b)-(d) show the effect of RAR to root strengthening with root depth increasing from 0.4m to 1.0m. Similar trends of increase in FOS are observed, of which a marked increase is observed at fill thickness = 1m. For RAR = 0.1% and fill thickness = 1m, the increase in FOS increases from 0.408 to 0.570, 0.962 and 0.992 when the root depth increases from 0.4m to 0.6m, 0.8m and 1.0m respectively, indicating the increase in strengthening effect is very prominent when the root depth about 0.4-0.6m, which is about half of the top soil thickness. Similar trends of increase in FOS with increased root depth are observed for different RAR.

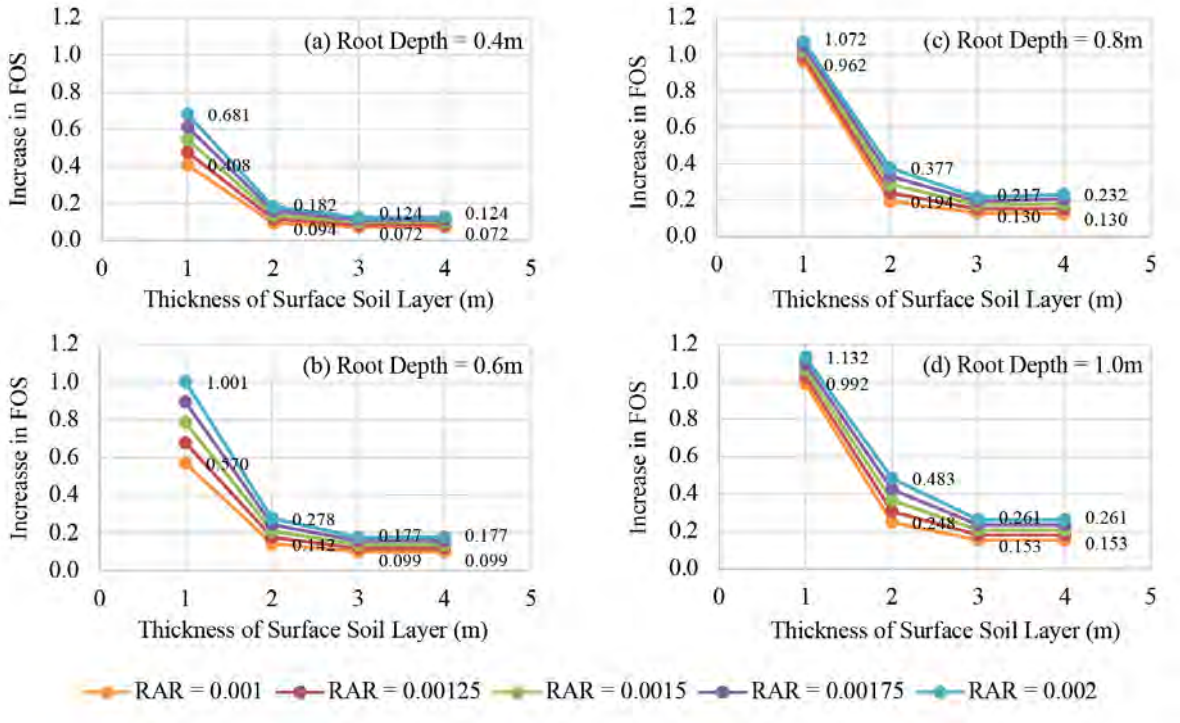

Figure 6: Sensitivity Analysis for Different RAR, Root Depths and Slope Heights

4 CONCLUSIONS

Current practice in most part of the world still considers vegetation mainly for aesthetic purposes and erosion control. The engineering functions of plant roots have been generally ignored in the scientific analysis and design of slope stability. This may be due to the lack of understanding of root functions and therefore the lack of confidence from engineers. The significant variability of the potential beneficial effect and the extreme difficulty in fully characterizing the tree roots and quantifying the strengthening effects of tree roots may be the crux. Despite many complicated and rigorous models are developed in the last decade to predict the root reinforcement, they are considered impractical to use due to the large number of inter-related controlling factors which resulted in low correlation coefficients, and mixed vegetations are always encountered in field.

An overview of the major stability functions provided by plant in slope is examined. Plant roots stabilize a soil slope by root reinforcement, hydrological reinforcement and interception. Root reinforcement can be in the form of lateral tensile resistance and anchorage, soil aggregation and mucilage effects. A lower bound approach is attempted such that it can provide an indication to the probability of the predicted strengthening likely exceeded. As such, only the mechanical reinforcement of root is considered but not other potential beneficial effects. Suction effect due to transpiration of the tree is also ignored. The Wu and Waldron model is recommended because of its simplicity. Root depth and RAR can vary largely and are therefore two key parameters dominating the strengthening effect. They can be determined on site. k' varies within a small range of 1.0 - 1.2 and is therefore not controlling. In the absence of test data, presumed value of 8MPa for TR is suggested. It is determined from the strengths of many European, Chinese and 4 native species for root diameter of 10mm or less, which show that the majority of roots of these sizes for a vast number of species in different soils and climates can exceed. The presumed value can be fine-tuned when more local data are obtained.

However, for plants with larger structural roots (say > 10mm) where root bending rather than axial breakage is dominant, more sophisticated beam bending or p-y models can be adopted which require more input parameters to execute. A hypothetical slope stability analysis is carried out to demonstrate the practicality of the presumed values. Sensitivity analyses show that root strengthening can be significant for slope with shallow top soil even with RAR = 0.1%. The root depth and thickness of top soil affects the locus of the slip surface, and the strengthening appears to be most effective when the root depth is about half of the thickness of the top soil.

REFERENCES

Abe, K. & Ziemer, R.R. 1991. Effect of tree roots on a shear zone: modeling reinforced shear stress. *Canadian Journal of Forest Research,* 21(7): 1012-1019.

Abernethy, B. & Rutherford, I.D. 2001. The distribution and strength of riparian tree roots in relation to riverbank reinforcement. *Hydrological Processes,* 15(1): 63-79.

Bordoloi, S. & Ng, C.W.W. 2020. The effects of vegetation traits and their stability functions in bio-engineered slopes: A perspective review. *Engineering Geology,* Elsevier.

Bull, D., Sinelair, I., Pierron, F., Roose, T. & Smethurst, J. 2019. Understanding the mechanisms of root-reinforcement in soils: soil shear tests using X-ray computed tomography and digital volume correlation. *7th International Symposium on Deformation Characteristics of Geomaterials,* E3S Web of Conferences 92, Glasgow, UK.

Coppin, N.J. & Richards, I.G. 1990. Use of vegetation in civil engineering. *CIRIA,* Butterworths Construction Industry research and Information Association, London.

Dobson, M.C. 1995. Tree root systems. *Arboriculture Research and Information Note 130/95/ARB*, Arboricultural Advisory and Information Service, Farnham, UK.

Docker, B.B. & Hubble, T.C. 2009. Modelling the distribution of enhaunced soil shear strength beneath riparian trees of south-eastern Australia. *Ecological Engineering,* 35: 921-924.

Duckett, N. 2013. Development of improved predictive tools for mechanical soil-root interaction. *PhD Thesis.* University of Dundee, UK.

Endo, T. & Tsuruta, T. 1969. The effect of tree roots upon the shear strength of soil. 18th *Annual Report,* Forest Experimental Station, Hokkaido, Japan. 167-179

GEO-SLOPE International Limited, 2012. Stability Modelling with SLOPE/W 2012. Calgary, Alberta, Canada.

Geotechnical Engineering Office, 2008. Guidelines for soil bioengineering applications on natural terrain landslide scars. *GEO Report No. 227,* Geotechnical Engineering Office, CEDD, The Government of HKSAR.

Geotechnical Engineering Office. 2011. Study on masonry walls with trees. *GEO Report No. 257,* Geotechnical Engineering Office, CEDD, The Government of HKSAR.

Giadrossich, F., Schwarz, M., Cohen, D., Cislaghi, A., Vergani, C., Hubble, T., Phillips, C. & Stokes, A. 2017. Methods to measure the mechanical behavior of tree roots: A review. *Ecological Engineering,* 109: 256-271.

Gray, D.H. 1974. Reinforcement and stabilization of soil by vegetation. *Journal of Geotechnical Engineering Division of ASCE,* 100: 695-699.

Gray, D.H. & Barker, D. 2004. Root-soil mechanics and interactions. Bennett, J.J. and Simon, A. Ed., *Riparian Vegetation and Fluvial Geomorphology,* Water Science and Applications, 8, American Geophysical Union, Washington DC, 113-123.

Gray, D.H. & Leiser, A.T. 1982. Biotechnical slope protection and erosion control. *van Nostrand Reinhold Company Inc., New York.*

Gray, D.H. & Ohashi, H. 1983. Mechanics of fibre reinforcement in sand. *Journal of Geotechnical Engineering,* 109(3): 335-353.

Greenway, D. R. 1987. Vegetation and slope stability. Slope Stability: *Geotechnical Engineering and Geomorphology,* Anderson, M.G., Richards, K.S. Eds., Wiley, USA.

Ji, J., Mao, Z., Qu, W. & Zhang, Z. 2020. Energy-based fibre bundle model algorithms to predict soil reinforcement by roots. *Plant Soil,* 446: 307-329.

Leung, F.T.Y., Yan, W.M., Hau, B.C.H. & Tham, L.G. 2015. Root systems of native shrubs and trees in Hong Kong and their effects on enhauncing slope stability. *Catena,* 125(February): 102-110.

Liang, T., Knappett, J.A. & Duckett, N. 2015. Modelling the seismic performance of rooted slopes from individual root-soil interaction to global slope behavior. *Geotechnique,* 65(12): 995-1009.

Liang, T., Knappett, J.A., Leung, A., Carnaghan, A., Bengough, A.G. & Zhao, R. 2020. A critical evaluation of predictive models for rooted soil strength with application to predicting the seimic deformation of rooted slopes. *Landslides,* 17: 93-109.

Mao, Z., Yang, M, Bourrier, F. & Fourcaud, T. 2014. Evaluation of root reinforcement models using numerical modeling approaches. *Plant Soil,* 381: 249-270.

Meijer, G.J., Bengough, A.G., Knappett, J.A., Loades, K.W. & Nicoll, B.C. 2019. In situ measurement of root-reinforcement using the cockscrew extraction method. *Canadian Geotechnical Journal,* 55(10): 1372-1370.

Meijer, G.J., Wood, M., Knappett, J.A., Bengough, A.G. & Liang, T. 2019. Analysis of coupled axial and lateral deformation of roots in soil. *International Journal for Numerical and Analytical Methods in Geomechanics,* 43(3): 684-707.

Meng, S., Zhao, G. & Yang, Y. 2020. Impact of plant root morphology on rooted-soil shear resistance using triaxial testing. *Advances in Civil Engineering,* Hindawi. 2020.

Ng, C.W.W., Leung, A.K. & Ni, J. 2019. Plant-soil slope interaction. *CRC Press,* Taylor and Francis Group.

Partov, D., Maslak, M., Ivannov, M., Sergeev, D. & Dimitrova, A. 2016. The development of wooden bridges through the ages: A review of selected examples of heritage objects, part 1 – The milestones. *Technical Transactions,* 2-B, 93-106.

Perry, T.O. 1989. Tree roots: facts and fallacies. *Arnoldia,* 49: 1-21.

Pollen, N & Simon, A. 2005. Estimating the mechanical effects of riparian vegetation on stream bank using a fibre bundle model. *Water Resources Research,* 41(7): 1-11.

Schwartz, M., Cohen, D. & Or, D. 2010. Root-soil mechanical interaction during pullout and failure of root bundles. *Journal of Geophysical Research,* 115: 1-19.

Simon, A. & Collison, A.J.C. 2002. Quantifying the mechanical and hydrologic effects of riparian vegetation on streambank stability. *Earth Surface Processes and Landforms,* 27(5): 527-546.

Smith, I. & Snow, M. 2008. Timber: An ancient construction material with a bright future. *Forestry Chronicle,* 4(84), 504-510.

Stokes, A., Norris, J.E., van Beek, L.P.H, Bogaard, T., Cammeraat, E. Mickovski, S.B., Jenner, A., Di lorio, A. & Fourcaud, T. 2008. How vegetation reinforces soil on slopes. *Slope Stability and Erosion Control, Ecotechonological Solutions,* 65-118.

Thomas, R.E. & Pollen-Bankhead, N. 2010. Modelling root-reinforcement with a fibre-bundle model and Monte-Carlo simulation. *Ecological Engineering*, 36: 47-61.

Tobin, B. Cermak, J., Chiatante, D., Danjon, F., di lorio, A. Duputy, A., Eshel, A., Jourdan, C., Kalliokoski, T., Laiho, R., Nadezhdina, N., Nicoll, B., Pages, L., Silva, J. & Spanos, I. 2007. Towards developmental modeling of tree root systems. *Plant Biosystems,* 141: 481-501.

Vannoppen, W., Vanmaercke, M., De Baets, S. & Poesen, J. 2015. A review of the mechanical effects of plant roots on concentrated flow erosion rates. Earth-Science Reviews 150: 666-678.

Waldron, L.J. 1977. The shear resistance of root-permeated homogeneous and stratified soil. *Soil Science Society America Journal,* 41(5): 843-849.

Waldron, L.J. & Dakessian, S. 1981. Soil reinforcement by roots: Calculation of increased soil shear resistance from root properties. *Soil Science,* 132(6): 427-435.

Wu, T.H. 1976. Investigation of landslides on Prince of Wales Island, Alaska. *Geotechical Engineering Report 5,* Civil Engineering Department, Ohio State University, Columbus, Ohio, USA.

Wu, T.H. 2007. Root reinforcement: analysis and experiments. *Eco- and Ground Bio-Engineering: The Use of Vegetation to Improve Slope Stability.* Springer, 103: 21-30.

Wu, T.H. 2013. Root reinforcement of soil: review of analytical models, test results, and applications to design. *Canadian Geotechnical Journal,* 50: 259-274.

Wu, T.H., Mckinnel, W.P. & Swanton, D.N. 1979. Strength of tree roots and landslides on Prince of Wales Island, Alaska. *Canadian Geotechnical Journal,* 16(1): 19-33.

A Comparison of Empirical and Numerical Approaches for Estimating Rock Support Pressure on Permanent Tunnel Lining

Franklin K.L. To
AECOM Asia Company Ltd., Hong Kong

ABSTRACT

In Hong Kong, the rock support pressure acting on the permanent tunnel lining is usually estimated using the empirical equations by Terzaghi's rock arching theory (1946) and Grimstad & Barton's Q support pressure (1993). However, with the advanced technologies, the assumptions behind these studies may become too conservative and subsequently lead to high construction cost and time. According to the Geoguide 4 (2018 Edition), it is suggested that the rock support pressure should be estimated either by an empirical method or an analytical/numerical assessment. By establishing different comparison models, this paper investigates the difference in estimated rock support pressure acting on the permanent lining using empirical approaches and finite element modelling. The influence of missing parameters in empirical equations and the rock mass behavior around the excavation profile are also studied.

1 INTRODUCTION

Only less than 25% of total land area in Hong Kong has been developed for the 7.5 million population. This is because the rest settings have been surrounded by hilly terrains, rural areas and statutory protected areas. Nevertheless, significant portions of these hilly terrain features are underlain by hard and massive igneous rocks such as granite and volcanic tuff. This brings favorable conditions to develop underground space such as rock tunnels and caverns as an alternative source for land supply. In recent years, the government has been playing a leading role to explore the feasibility and strategy for long-term underground development in Hong Kong.

In consideration of the consequence of life, durability and maintenance problems, temporary supports such as rock dowels and shotcrete are usually not taken to contribute any of the long-term ground stability. Most of the constructed rock tunnels in Hong Kong are permanently supported by conventional cast-in-situ concrete lining. If design optimization for lining (e.g. thickness and reinforcements) is achieved, the overall construction cost and time for excavating the rock, rebar fixing and casting the concrete lining will be significantly reduced.

From geotechnical design perspective, the estimation of rock support pressure acting on the permanent lining is very uncertain because it cannot be simply measured and well-proved. In Hong Kong, the rock support pressure has been estimated using the empirical equations by Terzaghi (1946) and Grimstad & Barton (1993) based on the back-analysis of installed support and field data collection. As suggested by GEO (2018), the source of loadings should be either accounted for by an empirical method or an analytical/numerical assessment. By establishing different comparison models, this paper investigates the difference in estimated rock support pressure on lining using empirical approaches and finite element modelling. The influence of missing parameters in empirical equations and the rock mass behavior around the excavation profile are also studied.

2 ROCK TUNNELLING WITH EMPIRICAL APPROACHES

2.1 Terzaghi's Rock Arching Theory (1946)

The rock arching theory developed by Terzaghi in 1946 was the first successful rock mass classification for tunnel engineering. The theoretical rock arch above crown is self-supporting and only the weight of loosened rock after excavation is acting on the tunnel supports. The support pressure was estimated based on the known strength of failed wooden blocks and back-analysis of a 5.5m wide tunnel supported by steel-arches.

He defined the term "arch action", which indicates the capacity of rock above the tunnel roof to transfer the major part of the total overburden weight to both sides of tunnel walls. The body of rock which transfers the load will briefly be referred to as the ground arch. The arch action is an inevitable consequence of the local stress relaxation produced by excavation operation. The mechanics of the arch action is illustrated in Figure 1. The ground arch is represented by the shaded area **a c d b** with a height of D and width of B_1. When the tunnel is being excavated and the support installed, the mass of crushed rock constituting the ground arch tends to move into the tunnel. This movement is resisted by the friction along the lateral boundaries **a c** and **b d** of this mass. The friction forces transfer the major part of the total overburden weight with height H onto the material located on both sides of the tunnel and the roof support carries only the balance, equivalent to a height $D=H_p$.

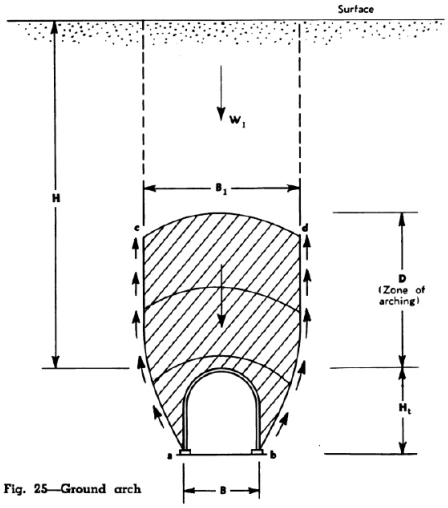

Figure 1: Ground Arch (Terzaghi, 1946)

Terzaghi combined his experiment results and the estimated rock loads from Alpine tunnels to compute rock load factors H_p of the loosened rock mass above the tunnel crown (as listed in Table 1) in terms of tunnel width B and tunnel height H_t. The vertical support pressure (P_v) is defined by Equation 1:

$$P_v = \gamma \times D = \gamma \times H_p \quad (1)$$

2.2 Grimstad & Barton's Q Support Pressure (1993)

The empirical Q-system for rock mass classification and its relationships to tunnel supports were first developed by Barton et al. (1974) and further updated by Grimstad & Barton (1993) at the Norwegian Geotechnical Institute (NGI), Norway by considering more than 1000 case histories from underground openings. The tunnel support pressure at crown (P_{roof}) and walls (P_{wall}) for different rock mass conditions are estimated using Equation 2 and Equation 3.

Table 1: Rock load in tunnels within different nine rock classes (Terzaghi, 1946)

Rock Condition	Rock Load Hp *	Remark
1. Hard and intact	Zero	Light lining required only if spalling or popping occurs
2. Hard stratified or schistose	0 to 0.5B	Light support.
3. Massive, moderately jointed ^	0 to 0.25B ^	Load may change erratically from point to point.
4. Moderately blocky and seamy	0.25B to 0.35 ($B + H_t$)	No side pressure
5. Very blocky and seamy	0.35 to 1.10 ($B + H_t$)	Little or no side pressure
6. Completely crushed but chemically intact	1.10 ($B + H_t$)	Considerable side pressure. Softening effects of seepage toward bottom of tunnel requires either continuous support for lower ends of ribs or circular ribs.
7. Squeezing rock – moderate depth	1.10 to 2.10 ($B + H_t$)	Heavy side pressure, invert struts required. Circular ribs are recommended.
8. Squeezing rock – great depth	2.10 to 4.50 ($B + H_t$)	
9. Swelling rock	Up to 250 ft (80 m), irrespective of the value of ($B + H_t$)	Circular ribs required. In extreme cases use yielding support.

Note:
* The roof of the tunnel is assumed to be located below the water table. If it is located permanently above the water table, the values given for types 4 to 6 can be reduced by fifty percent. However, this pressure reduction has not been considered in the study.
^ Rock Load H_p=0.25B is adopted for this study where the baselined Q-value is 10.

$$P_{roof} = \frac{0.2\ J_n^{1/2}\ Q^{-1/3}}{3\ J_r}\ (MPa) \quad (2)$$

$$P_{wall} = \frac{0.2\ J_n^{1/2}\ Q_w^{-1/3}}{3\ J_r}\ (MPa) \quad (3)$$

where Q = Tunnelling Quality Index
J_n = Joint Set Number
J_r = Joint Roughness Number

Q_w = 5.0 Q for Q > 10
2.5 Q for 10 ≥ Q ≥ 0.1
1.0 Q for Q < 0.1

2.3 Missing Parameters in Empirical Approaches

For a tunnel project, there are two major types of design parameters including the geotechnical parameters and tunnel arrangements. The considerations of these variables to the rock support pressure by each empirical study were very limited based on their specific engineering assumptions and field data as summarized in Table 2. Both studies have incorporated the importance of rock mass quality and only Terzaghi (1946) has considered the significance of tunnel width. However, none of these two approaches have considered the influence of varying uniaxial compressive strength, intact rock modulus, poisson's ratio, in-situ stress ratio and tunnel depth to the rock support pressure. Therefore, it is important to study whether engineers have been missing any governing parameters to estimate the rock support pressure throughout the years.

Table 2: Summary Table of Design Parameters Considered in Previous Empirical Approaches

Empirical Studies/ Rock Parameters	Uniaxial Compressive Strength σ_{ci}	Intact Rock Modulus E_i	Poisson's Ratio υ	In-situ Stress Ratio k	Rock Mass Quality	Tunnel Depth	Tunnel Width
Terzaghi (1946)					✓		✓
Grimstad & Barton (1993)					✓		

3 ROCK TUNNELLING WITH NUMERICAL MODELLING

3.1 Setting up the Comparison Models

Apart from empirical approaches, the rock support pressure can also be estimated using the numerical modelling such as the finite element method (FEM) and the discrete element method (DEM). They are powerful tools to handle complicate engineering problems such as complex geology, imposed loadings, influence from/to existing buildings and structures, excavation sequence, composite structures and 3-dimentional geometric problems.

There were total 57 numbers of finite element models established using the software Phase2 Version 8 developed by the Rocscience (BD Ref: G0179) for this study. The baseline geotechnical parameters and tunnel arrangements were adopted based on a highway tunnel project in Hong Kong. The excavation span (or tunnel width, D) was 13.5 m and the tunnel depth was approximately 110 m (8 times the tunnel width D) below ground level.

3.2 Rock Mass Failure Criteria

The strength of a jointed rock mass depends on both the mechanical properties of intact rock as well as the degree of freedom for the rock block to slide and rotate under different stress states. The yield mechanism is non-linear and the failure mechanisms are often brittle.

The Hoek-Brown Failure Criterion was first derived by Hoek and Brown (1980) from testing results of rock specimen to estimate the deformation and strength characteristic of jointed rock mass based on the interlocking effect and discontinuities conditions. Later in 2002, the modified Generalized Hoek-Brown (GHB) Failure Criterion was further developed as presented in Equations 4 to 7 to overcome the bias of data towards hard rock.

$$\sigma'_1 = \sigma'_3 + \sigma'_{ci}\left(m_b \frac{\sigma'_3}{\sigma'_{ci}} + s\right)^a \quad (4)$$

$$s = \exp\left(\frac{GSI - 100}{9 - 3D}\right) \quad (5)$$

$$m_b = m_i \exp\left(\frac{GSI - 100}{28 - 14D}\right) \quad (6)$$

$$a = \frac{1}{2} + \frac{1}{6}\left(e^{-GSI/15} - e^{-20/3}\right) \quad (7)$$

where σ'_1 = Major Effective Principal Stress
σ'_3 = Minor Effective Principal Stress
σ'_{ci} = Uniaxial Compressive Strength
m_i = Hoek-Brown Intact Constant
m_b = Hoek-Brown Constant
s = Rock Mass Materials Constant
a = Rock Mass Materials Constant
D = Blast Disturbance Factor

The Geological Strength Index (GSI) was introduced by Hoek (1994) and Hoek, Kaiser and Bawden (1995). It is used to estimate the rock mass strength by considering the reduction of the intact rock strength due to adverse rock structure and block surface conditions. It can be corelated to the NGI Q-system using Equation 8.

$$GSI = 9 \ln Q' + 44 \quad (8)$$

where $Q' = \frac{RQD}{J_n} \times \frac{J_r}{J_a}$

3.3 Geotechnical Parameters and Tunnel Arrangements

For each of the comparison model, there was only one varying parameter and the remaining numerical inputs were assigned in accordance with the baseline assumptions. These parameters consist of the geotechnical parameters and tunnel arrangements as summarized in Table 3 and were assumed based on a highway tunnel project in Hong Kong. The varying parameters in Table 4 were assigned at appropriate intervals within the common design ranges by considering the geology conditions in Hong Kong.

Table 3: Summary Table of Baseline Parameters

Baseline Parameters	Baseline Value			Descriptions
Unit Weight	γ	=	27 kN/m^3	–
Uniaxial Compressive Strength	σ_{ci}	=	75 MPa	–
Intact Rock Modulus	E_i	=	30000 MPa	Em estimated by Geoguide 4 Eq. 6.8
Poisson's Ratio	v	=	0.3	–
Tunnel Depth	Depth	=	8D = 108 m	Moderate Depth
Tunnel Width	D	=	13.5 m	Medium Span
Tunnel Height	H	=	9.5 m	–
Rock Quality Designation	RQD	=	80	Good
Joint Set Number	J_n	=	12	Three joint sets plus random joints
Joint Roughness Number	J_r	=	1.5	Rough, irregular, planar
Joint Alteration Number	J_a	=	1	Unaltered joint walls, surface staining only
Joint Water Reduction Factor	J_w	=	1	Dry excavations or minor inflow
Stress Reduction Factor	SRF	=	1	Medium stress, favorable stress condition
Q-value	Q	=	10	Fair/Good Rock
In-situ Stress Ratio	k	=	1.5	–
Material constants	m_i	=	32	Granite
Lining Thickness	T	=	350 mm	C40 plain concrete lining

Table 4: Summary Table of Varying Parameters

Varying Parameters	Ranges
Uniaxial Compressive Strength σ_{ci}	50, 75, 100, 125, 150, 175, 200 MPa
Intact Rock Modulus E_i	20000, 25000, 30000, 35000, 40000, 45000, 50000 MPa
Poisson's Ratio v	0.2, 0.25, 0.3, 0.35, 0.4
In-situ Stress Ratio k	0.5, 1, 1.5, 2, 2.5, 3, 3.5, 4
Q-value (assume Q=Q')	0.1, 0.4, 1, 4, 10, 25, 40
Tunnel Depth	1D to 15D (13.5 m to ~200 m), per D intervals
Tunnel Width D	5.5, 8, 13.5, 20, 30 m

3.4 Construction Sequence and Staged Analysis in FEM

There were 4 stages assigned to each of the finite element model as presented in Figure 2 for different construction sequence. Stage 1 calculated the original in-situ stress stage of the rock mass before excavation. Stage 2 simulated the ground relaxation with the core replacement method to consider the 3-dimensional effect of tunnel face supporting the surrounding rock mass. Stage 3 simulated further ground relaxation of rock mass due to advance excavation and the installation of permanent concrete lining support. Stage 4 modelled the complete excavation and all ground loadings were exerted to the permanent concrete lining.

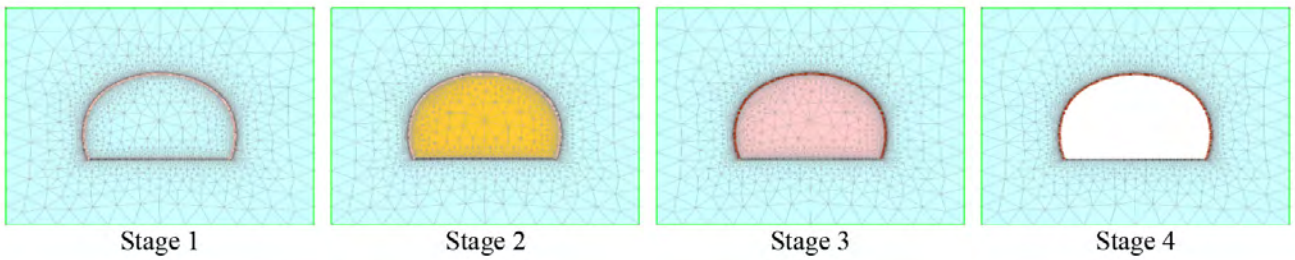

Figure 2: Staged Analysis in FEM

3.5 Assumptions and Limitations

The FEM comparison models have the following assumptions and limitations:

- Single parametric study was carried out where each comparison model only changed one parameter. Therefore, some of the observations and statements made under this paper may only be appliable for the condition of only one varying parameter adopted
- Rock mass was modelled as continuum element with rock mass modulus Em and GHB failure criterion instead of discontinuum element. Rock wedges should be considered separately using kinematic analysis
- In-situ stress was induced by gravity and the actual ground level in models
- No relaxation during temporary stage was considered. The permanent support was installed after tunnel excavation by assuming constant ground relaxation for varying rock mass quality and tunnel width
- Groundwater pressure should be considered separately
- Excellent and controlled blasting. No significant damage to surrounding rock mass.

4 RESULTS AND DISCUSSIONS

4.1 Rock Arching after Tunnel Excavation

Different rock arching zones were identified in Figure 3 by observing the principal stress orientation and rock mass strength factor after the removal of the original rock mass (i.e. tunnel excavation). The orientation of major principal stress (σ_1) rotated and became perpendicular to the excavated profile which provides the hoop force for rock arching. For the rock strength factor, which is calculated by dividing the rock strength (based on GHB failure criteria) by the induced stress at every point in the mesh, dropped significantly after excavation from about 4 to 1 near the excavation boundary and gradually increased away from the opening. These results from numerical modelling verified the rock arching theory proposed by Terzaghi in 1946.

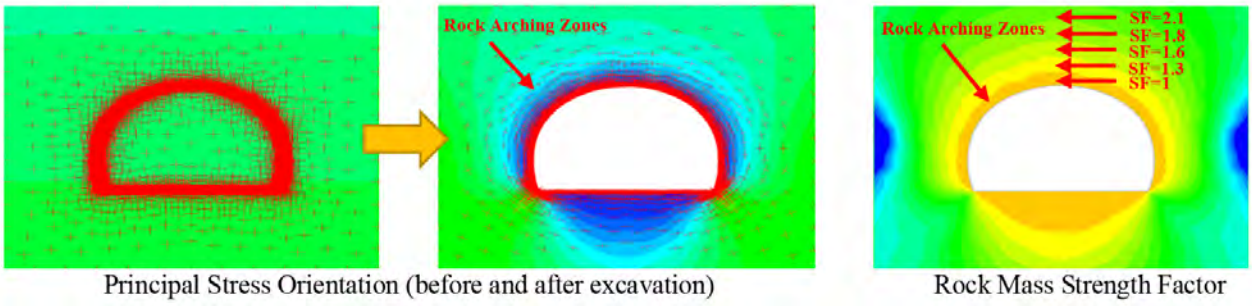

Figure 3: Rock Arching after Tunnel Excavation

Figure 4 shows the stress contours at different tunnel depths and Figure 5 presents the close-up views at depths of 1D (13.5 m), 4D (~55 m), 7D (~95 m), 8D (~110 m), 12D (~160 m) and 15D (~200 m). Similarly, the rock arching zones were observed in these comparison models. This implies that the permanent lining of a rock tunnel at moderate depth is only supporting the loosened rock mass after excavation instead of the full overburden pressure to the ground surface. However, a slow increasing trend of support pressure with increasing tunnel depth was observed by comparing the colour of stress contours around the excavation profile.

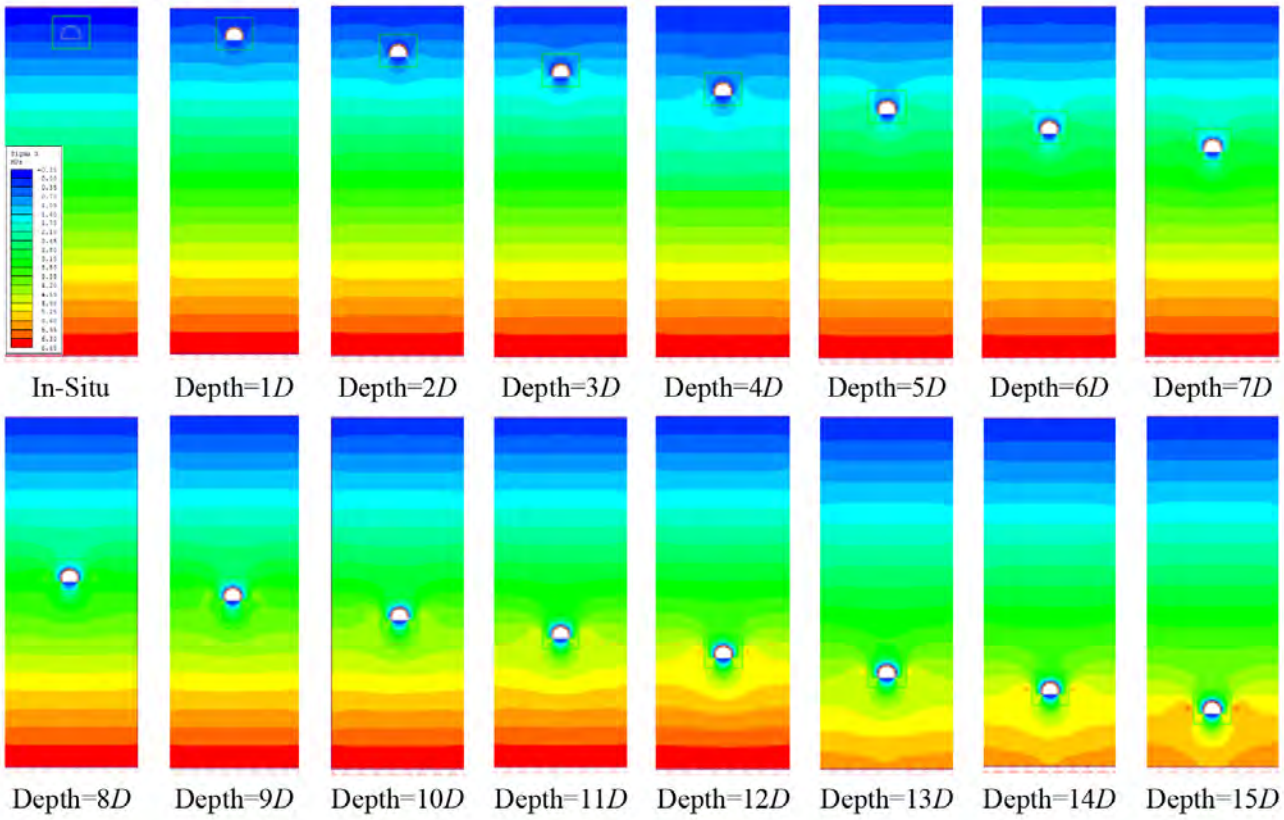

Figure 4: Stress Contours at different Tunnel Depths

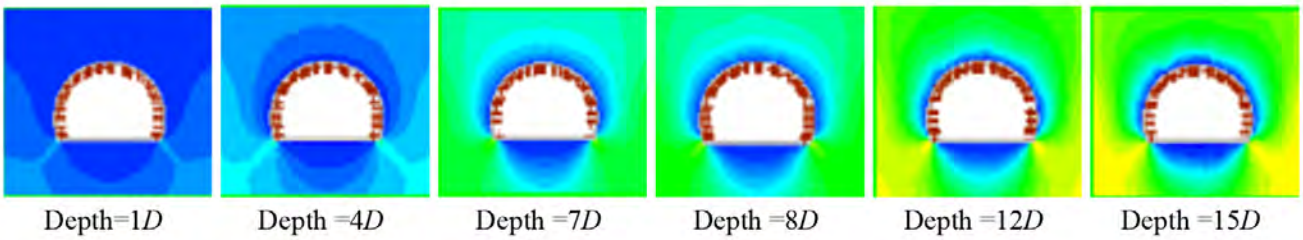

Figure 5: Stress Contours at different Tunnel Depths (Close-up Views)

4.2 Plastic Zone Development around Excavation Profile

The concept of loosened rock after excavation in empirical approaches can be correlated to the plastic zone in numerical modelling. Therefore, the influence of tunnel depth and rock mass quality to the plastic zone development around excavation profile were studied as shown in Figure 6 and Figure 7 below.

It was noted that the extent of plastic zone increased with overburden depth. At shallow depth, plastic zones were only observed at corners. With the increasing depth, the plastic zone extended to the tunnel crown, invert and further to the wall around the entire excavation profile. The thickness of plastic zone was approximately 1 to 2.5 m.

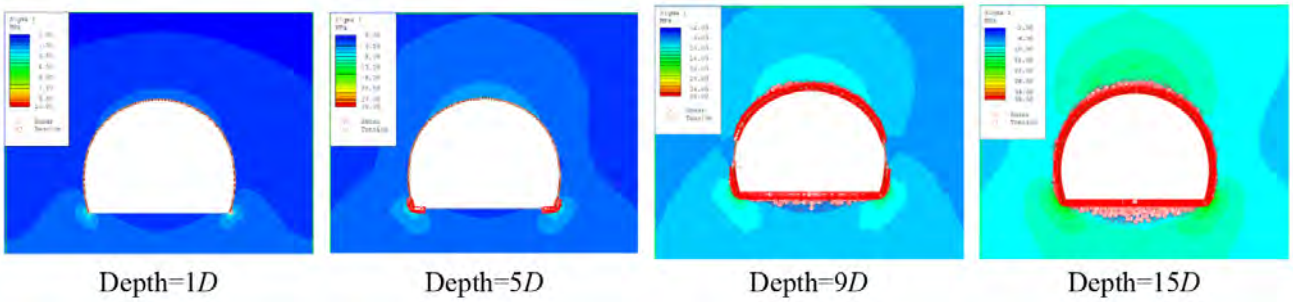

Figure 6: Plastic Zone around Excavation Profile at different Tunnel Depths

It was also observed that the plastic zone decreased significantly with better rock mass quality. For very poor rock (Q=0.1), the plastic zone developed all around the profile with thickness of about 1 to 2.5 m. For Q=1, the plastic zone started to decrease. For Q=4, the plastic zone only developed at crown and corners. For very good rock (Q=40), only small area of plastic zones at corners were observed.

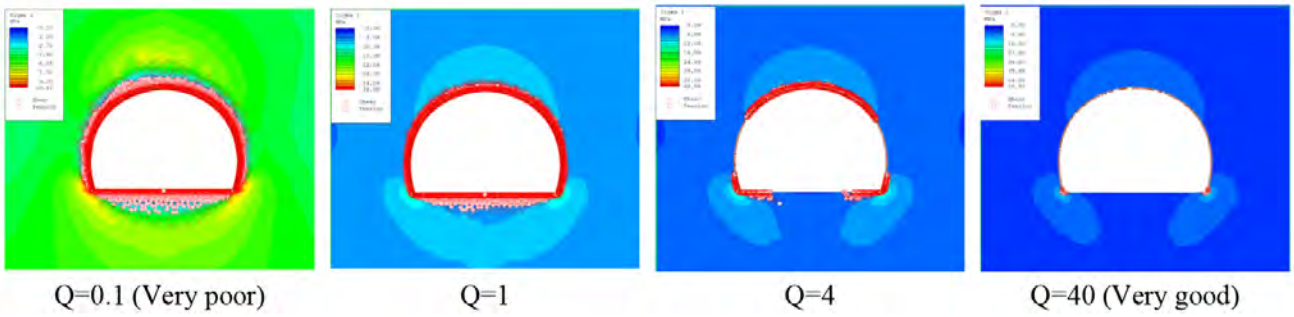

Figure 7: Plastic Zone around Excavation Profile for different Rock Mass Quality Q

4.3 Comparison of Estimated Rock Support Pressure

The comparison of estimated rock support pressure at tunnel crown from the empirical approaches and numerical modelling are summarized in Figure 8 to Figure 11.

For most of the cases, the support pressure at tunnel crown from numerical modelling was much smaller than that from empirical approaches. It was found that the estimation by Grimstad & Barton (1993) was the closer one to the numerical results than Terzaghi (1946) except for poor rock mass conditions.

In general, it was observed that the influence of in-situ stress ratio and rock mass quality were significant to the support pressure. Also, the support pressure increased slowly with increasing tunnel depth. However, the corresponding influence of uniaxial compressive strength, intact rock modulus, poisson's ratio and tunnel width were found to be negligible for tunnel lining design in hard rock.

After excavation, the in-situ stresses are redistributed around the tunnel profile. However, at moderate depth (around 100m), these induced stresses are very small when compare to the compressive strength of strong rock (the baseline UCS is 75 MPa). Same finding in Figure 8 (left) was observed where the uniaxial compressive strength was found to be insignificant to the support pressure for tunnel lining design in hard rock.

Also, Figure 8 (right) and Figure 9 (left) illustrate that the influence of deformation parameters including the intact rock modulus and poisson's ratio to the pressure were insignificant for tunnel lining design in hard rock.

According to GEO (2018), the in-situ stress ratio in Hong Kong at shallow depth ranges from 1.4 to 2.5 and drops to about 1 to 1.5 at a depth below 100 m. Within this common range of 1 to 2.5, the results from numerical results in Figure 9 (right) revealed that the rock support pressure at crown increased with the in-situ stress ratio.

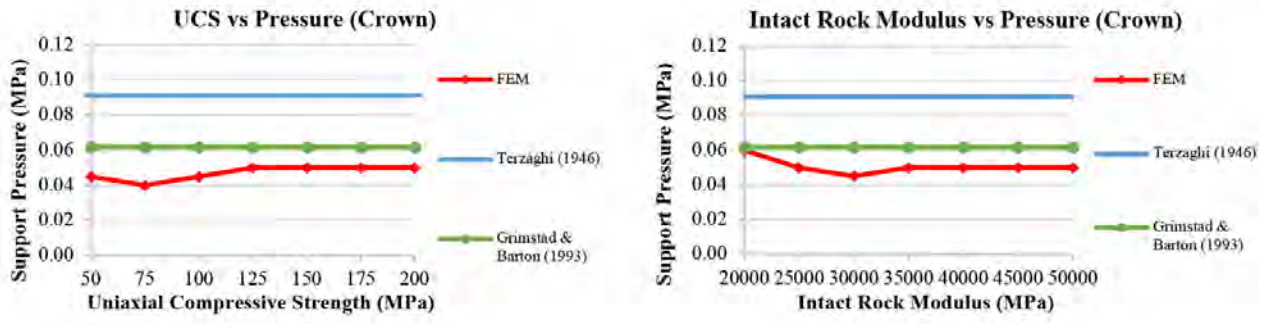

Figure 8: Influence of UCS (left) and Intact Rock Modulus (right) to Rock Support Pressure (Crown)

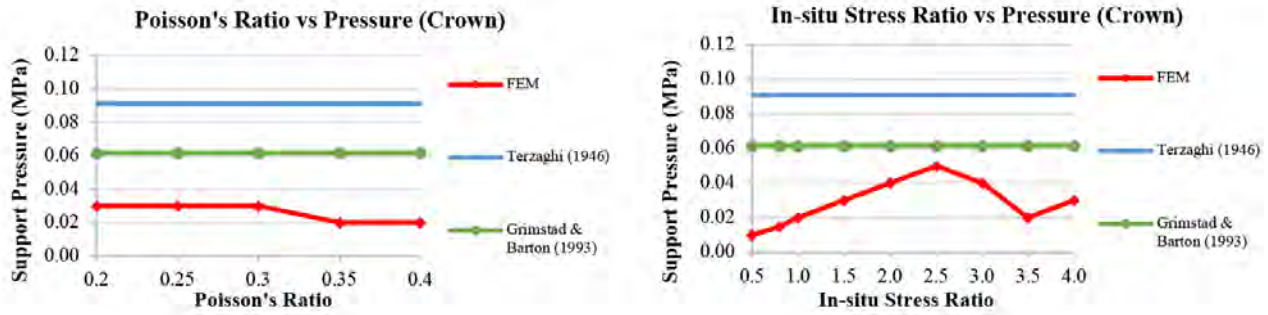

Figure 9: Influence of Poisson's Ratio (left) and In-situ Stress Ratio (right) to Rock Support Pressure (Crown)

Figure 10 below indicates an exponential decay function for the relationship of rock mass quality with support pressure at crown. For very poor rock, the estimated pressure by numerical modelling was larger than that by empirical approaches. This could probably be explained by the wrong application of same ground relaxation and lining stiffness for different ground conditions, which led to excessive ground deformation and yielding failure. This could be avoided if a stronger lining was assigned to support the ground. A detailed study could be carried out for further investigations.

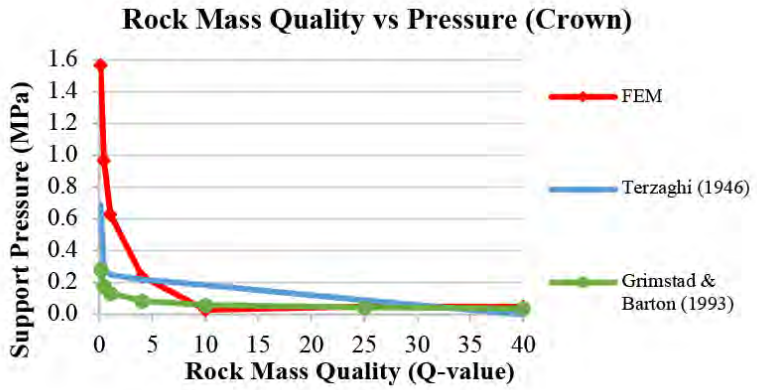

Figure 10: Influence of Rock Mass Quality to Rock Support Pressure (Crown)

A slow increasing trend of support pressure with tunnel depth has been discussed in Section 4.1. The same trend was observed from FEM results in Figure 11 (left). Nevertheless, the estimated pressure at tunnel depth of about 200 m was still smaller than all empirical approaches. The estimation by Grimstad & Barton (1993) is still conservative to be adopted for tunneling at moderate depth.

The influence of excavation width to support pressure has been a controversial topic in rock tunnelling. Some previous studies have confirmed the dependency when a flat tunnel roof was used or at very poor rock conditions. Figure 11 (right) presents that the influence of tunnel width for a horseshoe profile to support pressure at crown was negligible for tunnel lining design in hard rock.

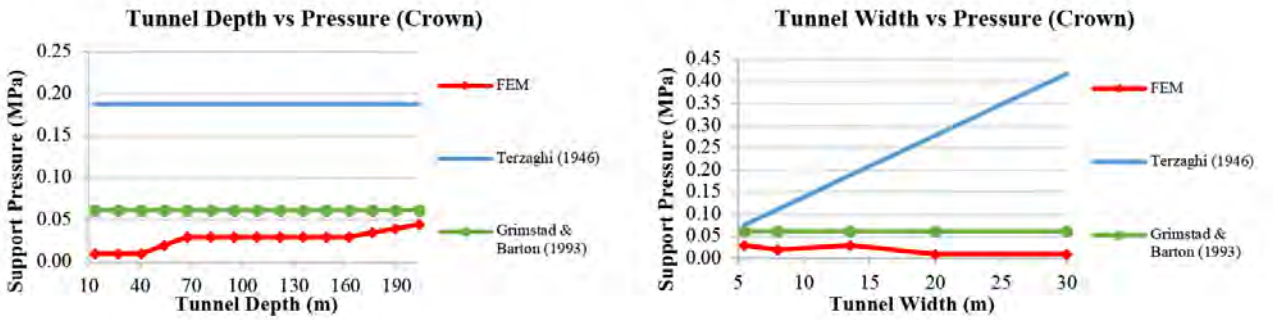

Figure 11: Influence of Tunnel Depth (left) and Tunnel Width (right) to Rock Support Pressure (Crown)

The detailed comparison for support pressure at walls are not discussed in this paper.

5 CONCLUSIONS AND RECOMMENDATIONS

Empirical approaches are conservative to estimate the rock support pressure acting on tunnel lining and therefore is very useful during the planning and preliminary design phases. However, it could be too conservative on certain occasions which cannot provide a cost-effective engineering solution. When more ground investigation data is available during the detailed design phase in later stage, the use of numerical modelling shall be explored for design optimisation in order to save construction cost and time.

Particular attention should be given when planning the ground investigation proposal for tunnel projects. For example, laboratory tests for uniaxial compressive strength, intact rock modulus & poisson's ratio are frequently ordered by geotechnical engineers, but they are not particularly useful to the design of permanent tunnel lining in hard rock, which dominant the solid geology in Hong Kong. Alternatively, other types of ground investigation such as the use of horizontal directional coring (HDC) should be explored to determine the representative rock mass conditions and details of inferred faults/ weakness zones along the proposed tunnel alignment in order to identify the locations of poor rock. Furthermore, although this paper states that larger-span excavation would experience the same support pressure, lining with larger-span will still sustain a much higher bending moment during structural design. Therefore, field tests for in-situ stress ratio measurement (such as hydraulic fracturing or over-coring) are recommended for projects where large-span tunnels and caverns are proposed.

REFERENCES

Barton N., Lien R. and Lunde J. 1974. *Engineering Classification of Rock Masses for the Design of Tunnel Support*. Rock Mechanics, vol. 6, pp 189-236.

GEO. 2007. GEO Publication No. 1/2007: *Engineering Geological Practice in Hong Kong*. Geotechnical Engineering Office, Hong Kong.

GEO. 2018. *Geoguide 4: Guide to Cavern Engineering, Second Edition (2018)*. Geotechnical Engineering Office, Hong Kong.

Grimstad E., and Barton N. 1993. *Updating of the Q-system for NMT*. Proceedings of the International Symposium on Sprayed Concrete, Fagernes, Oslo. pp46-66.

Hoek, E. 2007. *Practical Rock Engineering*. Rocscience.

Hoek, E., Carranza-Torres, C. & Corkum, B. (2002). *Hoek-Brown Failure Criterion – 2002 Edition*. Rocscience.

NGI. 2015. *Using the Q-system: Rock Mass Classifications and Support Design (handbook)*. Norwegian Geotechnical Institute, Oslo.

Singh B. & Goel R. K. 2006. *Tunnelling in Weak Rocks*. Elsevier Ltd, London.

Terzaghi, K. 1946. *Rock Defects and Load on Tunnel Supports - Introduction to Rock Tunnelling with Steel Supports*. Ed: R. V. Proctor, and T. L. White, Commercial Shearing and Stamping Co., Youngstown, Ohio, USA, 278.

Design Optimization of Permanent Systematic Rock Bolts and Shotcrete Lining for Large-Span Caverns in Hard Rock

Franklin K.L. To, Bridges, G.D.C. & Andrew K.W. Seto
AECOM Asia Company Ltd., Hong Kong

ABSTRACT

The hilly terrain in Hong Kong is underlain by hard and massive igneous rocks. This brings favorable conditions to develop underground space including rock caverns as an alternative source of land supply. In recent years, the government departments have been playing a leading role to study the feasibility of rock cavern development in Hong Kong. These studies include the relocation of existing sewage treatment works, service reservoirs, refuse transfer stations, archive centre and laboratory to rock caverns. After completion of the relocation, the previously occupied surface land can be released for other developments beneficial to the communities.

For an underground excavation in competent rock, the use of empirical design approaches is usually fast and straightforward to assess the rock mass conditions and determine the rock support systems. However, there are a number of limitations that empirical approaches cannot adequately address regarding the design of rock caverns, in particular the appropriateness for large-span excavation and influence of multiple parallel excavations. However, these limitations could be addressed appropriately by carrying out numerical modelling, which is a very powerful tool to handle ground and support material properties with greater complexity. It allows the designer to develop a more flexible and compatible range of possible supports.

This paper discusses some key technical components of rock engineering related to the design and modelling of large-span rock caverns in order to achieve a cost-effective permanent support system. A comparison is carried out between the rock support requirements for a range of cavern excavation spans and parallel excavations predicted by empirical approach and numerical modelling.

1 INTRODUCTION

1.1 Recent Rock Cavern Development in Hong Kong

Whilst being globally famous as a densely built environment with a population of over 7.4 million, less than 25% of the land area in Hong Kong has been developed out of the total area of about 1,100 km2. This is because much of Hong Kong comprises hilly terrain, rural areas and protected areas including country parks and special areas, restricted areas, conservation-related zonings and water gathering grounds. Development of these areas are prohibited under statutory protection.

Under such circumstance, the flat land available for development has become scarce in Hong Kong. Traditional approaches of land development including flat land, open-cut site formation of moderately hilly terrain and large-scale reclamation have been playing an important role in Hong Kong's continuous

land supply. However, these approaches have caused the built-up areas to be largely concentrated within the foothills of natural terrain extending towards the shoreline or the reclaimed land.

About 85% of the hilly terrain in Hong Kong is underlain by hard and massive igneous rocks such as granite and volcanic tuff. This brings favorable conditions to develop underground space including rock tunnels and caverns as an alternative source of land supply. In recent years, the government departments have been playing a leading role to study the feasibility of rock cavern development in Hong Kong. A territory-wide Cavern Master Plan (CMP) as shown in Figure 1 has been prepared to guide and facilitate the planning and implementation of long-term cavern development. The CMP delineates 48 numbers of Strategic Cavern Areas (SCVAs) that are suitable for cavern development in terms of geological considerations and the current planning perspectives.

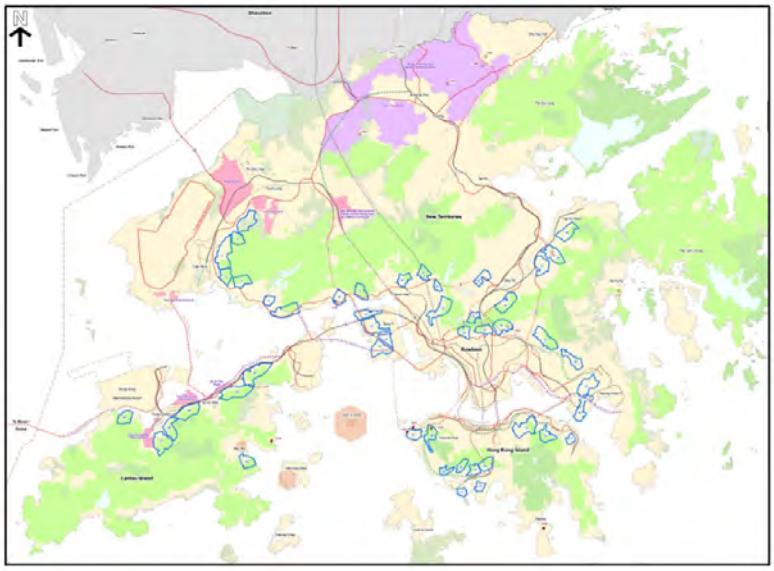

Figure 1: The Cavern Master Plan (CEDD and PlanD, 2017)

Recent on-going projects include the relocation of existing sewage treatment works, service reservoirs, refuse transfer stations, archive centre and laboratory to rock caverns. After completion of the relocation, the previously occupied surface land can be released for other developments beneficial to the communities.

2 EMPIRICAL APPROACHES FOR CAVERN EXCAVATIONS

2.1 General

The term “empirical” refers to the methodology to first gain information (directly or indirectly) then correlate relationships by testing, observation or experience. The simplest form is applying a best-fit line of y=mx+c for a sample group of data. Empirical approaches such as the Terzaghi’s Arching Theory (1946) and the Q-system developed by Barton et al. (1974) are the most common methods used for underground excavation in competent rock. They are fast and straightforward to assess the rock mass conditions and determine the rock support systems without spending high cost and time on carrying out sophisticated numerical modelling.

2.2 The Rock Arching Theory

The rock arching theory developed by Terzaghi (1946) was the first successful rock mass classification for tunnel engineering. The theoretical rock arch above crown is self-supporting and only the weight of loosened rock after excavation is acting on the tunnel supports as illustrated in Figure 2. The support pressure was estimated based on the known strength of failed wooden blocks and back-analysis of a 5.5m wide tunnel supported by steel-arches. Nine categories of pressure were developed for different rock mass conditions.

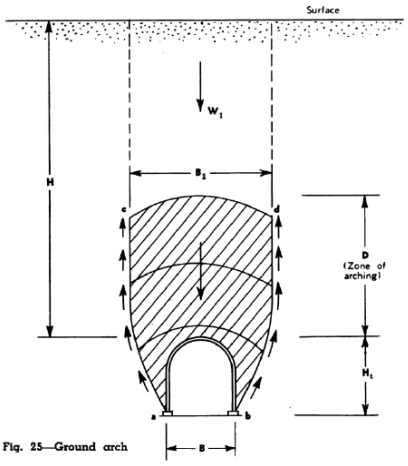

Figure 2: The rock arching theory (Terzaghi, 1946)

2.3 The NGI Q-System

The empirical Q-system for rock mass classification and its relationships to tunnel supports were first developed by Barton et al. (1974) and updated by Grimstad & Barton (1993) at the Norwegian Geotechnical Institute (NGI), Norway. It has been continuously updated since then with more than 2,000 case histories from underground openings, and takes into account the advancement in construction technology. The Q-value is formulated by the multiplier of six different rock mass parameters as presented in Equation 1:

$$Q = \frac{RQD}{J_n} \times \frac{J_r}{J_a} \times \frac{J_w}{SRF} \quad (1)$$

(i) Rock Quality Designation RQD
(ii) Joint Set Number J_n
(iii) Joint Roughness Number J_r
(iv) Joint Alteration Number J_a
(v) Joint Water Reduction Factor J_w
(vi) Stress Reduction Factor SRF

The first component (RQD/J_n) describes the relative size of rock blocks, or how fractured the rockmass is. The second component (J_r/J_a) describes the shear strength of inter-block discontinuities. The third component (J_w/SRF) describes the in-situ stress conditions and the active stress due to groundwater inflow in the rock joints surrounding the excavation boundary. These individual empirical parameters were developed from monitoring data and back-analysis of case histories from a large number of underground excavations, both stable and unstable.

The Q-value ranges from a minimum of 0.001 to a maximum of 1000, and is typically represented on a logarithmic scale. It gives a description of the stability of an underground opening in jointed rock masses. High Q-values indicate good stability and low values means poor stability. It has been widely adopted to assess the rock mass quality, estimate rock support pressure and determine the supports for hard rock underground excavation in Hong Kong.

In addition to the rock mass quality (Q-value), there are also two important factors governing the rock support design in underground openings. These include the safety requirement expressed by Excavation Support Ratio (ESR) and the size of excavation (span and height). In general, a wider excavation profile requires more rock support for stabilization than a smaller excavation profile. For the factor of safety, the ESR can be applied, for example a highway tunnel with heavy traffic would be assigned a lower ESR than an underground sewage tunnel with limited maintenance requirements (lower value being more conservative). The variable Equivalent Dimension is then given by span or height (in m) divided by ESR.

The formula proposed by Barton et al (1977) can be used to determine the initial systematic rock bolt length as presented in Equation 2. This is appropriate for systematic support, but may not be sufficient bolt length for potential rock wedges, which need to be assessed separately.

$$L = 2 + \frac{0.15B}{ESR} \quad (2)$$

where L = bolt length (in m)
B = cavern span for roof support (could use cavern height H for wall support) (in m)
ESR = excavation support ratio (safety requirement)

The Q-value and Equivalent Dimension are then used to determine the rock support design using the rock support chart by NGI (2015) as shown in Figure 3. For a given combination of Q-value and Equivalent Dimension, the support requirements such as the required shotcrete thickness and systematic rock bolt spacing for a given rock support class can be obtained. However, there are a number of limitations that empirical approaches cannot adequately address regarding the design of rock caverns, in particular the appropriateness for large-span excavation and influence of multiple parallel excavations.

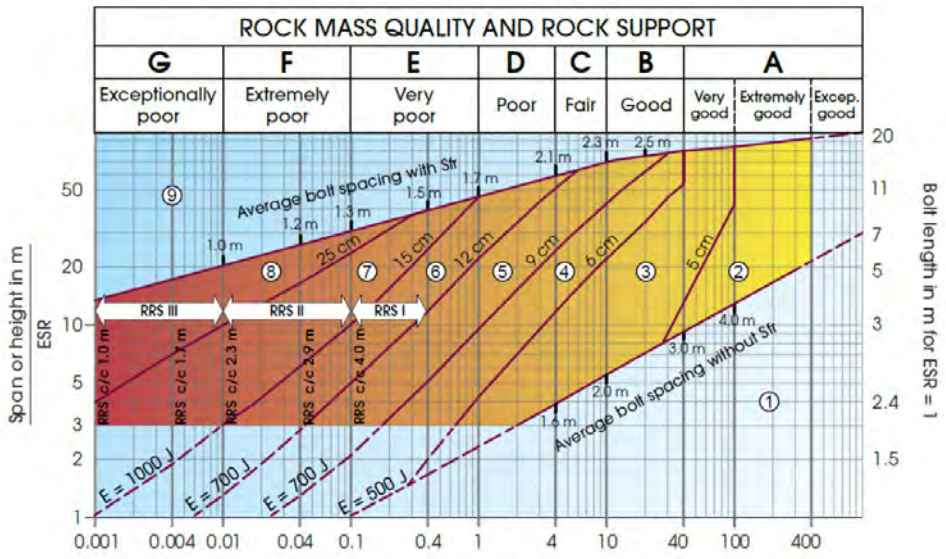

Figure 3: The Q-system rock support chart (NGI, 2015)

2.4 The Generalized Hoek-Brown Failure Criterion

The strength of a jointed rock mass depends on both the mechanical properties of intact rock as well as the degree of freedom for the rock block to slide and rotate under different stress states. The yield mechanism is non-linear and the failure mechanisms are often brittle.

The Hoek-Brown Failure Criterion was first derived by Hoek and Brown (1980) from testing results of rock specimens to estimate the deformation and strength characteristic of a jointed rock mass based on the interlocking effect and discontinuity conditions. Later in 2002, the modified Generalized Hoek-Brown (GHB) Failure Criterion was further developed as presented in Equations 3 to 6 to overcome the bias of data towards hard rock.

$$\sigma'_1 = \sigma'_3 + \sigma'_{ci}\left(m_b \frac{\sigma'_3}{\sigma'_{ci}} + s\right)^a \quad (3)$$

$$m_b = m_i \exp\left(\frac{GSI - 100}{28 - 14D}\right) \quad (4)$$

$$s = \exp\left(\frac{GSI - 100}{9 - 3D}\right) \quad (5)$$

$$a = \frac{1}{2} + \frac{1}{6}\left(e^{-GSI/15} - e^{-20/3}\right) \quad (6)$$

where σ'_1 = Major Effective Principal Stress
σ'_3 = Minor Effective Principal Stress
σ'_{ci} = Uniaxial Compressive Strength
m_i = Hoek-Brown Intact Constant
m_b = Hoek-Brown Constant
s = Rock Mass Materials Constant
a = Rock Mass Materials Constant
D = Blast Disturbance Factor

The Geological Strength Index (GSI) was introduced by Hoek (1994) and Hoek, Kaiser and Bawden (1995). It is used to estimate the rock mass strength by considering the reduction of the intact rock strength due to adverse rock structure and block surface conditions. It can be correlated to the NGI Q-system using Equation 7.

$$GSI = 9 \ln Q' + 44 \quad (7)$$

where $Q' = \frac{RQD}{J_n} \times \frac{J_r}{J_a}$

3 ROCK REINFORCEMENT APPROACHES FOR CAVERN EXCAVATIONS

3.1 Conventional Cast-in-situ Permanent Concrete Lining

Many highway and railway projects in Hong Kong were constructed in the form of rock tunnels and caverns. The temporary support includes rock dowels/bolts with a thin layer of shotcrete, and the permanent support mostly includes permanent cast-in-situ concrete lining as shown in Figure 4. The local design practice for temporary and permanent tunnel supports are different. Temporary supports are used to control the rock mass deformations and ensure a safe working environment, and they should be installed immediately after the excavation if required. Permanent supports are used to maintain stable rock mass conditions throughout the design life to meet the serviceability and durability requirements. According to Geoguide 4 (2018), temporary supports should not be taken to contribute any of the structural capacity of the permanent support unless satisfying the serviceability and durability requirements throughout the 100-120 years design life.

Figure 4: Conventional Cast-in-situ Permanent Concrete Lining

The use of permanent cast-in-situ concrete lining for large-span rock caverns has been successful in Hong Kong, such as the 24.2 m span cavern for MTR Island Line Tai Koo Station completed in 1985 and the 24.3 m span cavern for MTR South Island Line Admiralty Station completed in 2016. For permanent cast-in-situ concrete lining, the conventional “rock support” design approach is adopted in which concrete and reinforcement are used as structural materials to sustain all possible loadings. The design load involves an array of load combinations, including the overburden, groundwater and different internal facilities. They should be checked against the structural capacity of the lining such as axial, shear and bending moment accordingly.

3.2 Theoretical Rock Arch

The in-situ stress conditions existing in a rock mass at a specific depth below ground can have one or more origins. The major components usually comprise the gravitational stresses and tectonic stresses. According to GEO (2018), there is no evidence of high tectonic stresses in Hong Kong rocks. Local strong igneous rock has a typical uniaxial compressive strength (UCS) that ranges from 75 MPa to 200 MPa, which is much greater than structural concrete. Compared with the redistributed stresses after excavation, high stresses will not be a problem for local cavern construction at modest depths given the high strength of most of the rocks encountered.

An arched structural form has been widely used in civil engineering projects such as bridges and arched dams. This also applies to rock cavern engineering. After excavation, the overburden weight of loosened rock above the cavern crown is redistributed to the sidewalls. Hard rock is strong in compression but very weak in tension. With an arched roof, the best stress distribution is obtained to reduce the zone of tensile stresses in the cavern crown. This utilizes the "arching-effect" within the rock mass and therefore improves the ground stability, allows a more cost-effective support system and reduces the overbreak for excavation.

As such, the "rock reinforcement" design approach has been developed to offer a practical method to consider the hard rock as a structural material to self-support itself by utilizing the hoop stress within the arch of the rock above the roof of the cavern. Permanent rock bolts are installed as rock reinforcement to guarantee the formation of this arch, and permanent shotcrete supports rock wedges between bolts. The inherent strength of the rock mass is utilized by applying confining pressure from the rock bolts. The thrust capacity is therefore increased and the theoretical rock arch formed around the cavern is capable to resist the hoop force and can stabilise the opening by supporting the ground above the excavation. The design load involves the field stresses in rock mass. They should be checked against the individual failure modes.

The use of permanent rock bolts and shotcrete for large-span rock caverns has been successful in Hong Kong, such as the 15 m span cavern for DSD Stanley Sewage Treatment works completed in 1995 and the 27 m span cavern for EPD Island West Transfer Station completed in 1997. The on-going DSD project to relocate the Sha Tin Sewage Treatment Works to caverns in Figure 6 involves the construction of a cavern complex with 7 parallel rock caverns up to 32m width x 33m height in order to handle a large sewage treatment capacity. Upon completion, the relocated STSTW will be the biggest cavern sewage treatment works in Asia.

Figure 5: Rock bolt installation in hard rock

Figure 6: Relocation of Sha Tin Sewage Treatment Works (STSTW) to Caverns

4 NUMERICAL MODELLING FOR CAVERN EXCAVATIONS

4.1 General

Apart from empirical approaches, the design of permanent systematic rock bolts and shotcrete supports for large-span caverns can be carried out using the numerical modelling such as the finite element method (FEM) and the discrete element method (DEM). They are powerful tools to handle complicate engineering problems such as complex geology, imposed loadings, excavation sequence and 3-dimentional geometric problems.

As discussed in Section 2.3, there are a number of limitations that empirical approaches cannot adequately address regarding the design of rock caverns, in particular the appropriateness for large-span excavation and influence of multiple parallel excavations. However, these limitations could be addressed appropriately by carrying out numerical modelling. A total of six finite element models were established using the software Phase^2 Version 8 developed by the Rocscience (BD Ref: G0179). The adopted geotechnical parameters are listed in Table 1. The support requirements for systematic rock bolts and shotcrete were determined separately using the Q-system rock support chart and numerical models. Discussion and comparison were made.

The rock mass was modelled as continuum with considerations of rock mass modulus E_m and GHB failure criterion instead of discontinuum. A detailed comparison study could be further carried out.

Table 1: Summary Table of Geotechnical Parameters

Geotechnical Parameters	Adopted Value			Descriptions
Unit Weight	γ	=	27 kN/m^3	–
Uniaxial Compressive Strength	σ_{ci}	=	75 MPa	–
Young's Modulus	E_i	=	30000 MPa	–
Poisson's Ratio	v	=	0.3	–
Rock Cover	D	=	100 m	Moderate Depth
Rock Quality Designation	RQD	=	80	Good
Joint Set Number	J_n	=	12	Three joint sets plus random joints
Joint Roughness Number	J_r	=	1.5	Rough, irregular, planar
Joint Alteration Number	J_a	=	1	Unaltered joint walls, surface staining only
Joint Water Reduction Factor	J_w	=	1	Dry excavations or minor inflow
Stress Reduction Factor	SRF	=	1	Medium stress, favorable stress condition
Q-value (assume Q=Q')	Q	=	10	Fair/Good Rock
Material constants	m_i	=	32	Granite
In-situ Stress Ratio	k	=	1.5	–
Excavation Span Ratio	ESR	=	1	Type of excavation = E

4.2 Large-Span Excavation

The cavern profile should satisfy the spatial requirements for facilities accommodation. As summarized in Geoguide 4 (2018), the typical span of completed caverns in Hong Kong ranges from 15 m to 27 m. Clients usually prefer larger caverns for their projects, but this may not be cost-effective because a larger opening would require more permanent support and greater rock pillar width between adjacent excavations.

A hypothetical comparison was carried out among three different caverns with span of 15m, 25m and 35m and same height of 15m. The required supports in Table 2 were determined using the NGI rock support chart.

Table 2: Rock support requirements using the Q-system rock support chart by NGI (2015)

Cavern Size	Systematic rock bolts				Shotcrete lining	
	Crown		Wall		Crown	Wall
	Length	Spacing	Length	Spacing	Thickness	Thickness
15 m (W) x 15 m (H)	4.3 m	2.3 m c/c	4.3 m	2.5 m c/c	60 mm	60 mm
25 m (W) x 15 m (H)	5.8 m	2.3 m c/c	4.3 m	2.5 m c/c	70 mm	60 mm
35 m (W) x 15 m (H)	7.3 m	2.3 m c/c	4.3 m	2.5 m c/c	80 mm	60 mm

Based on empirical approaches, the rock bolt length and shotcrete thickness increased for caverns with larger span. Although there was no change in bolt spacing as the rock mass quality (Q=10) was baselined, the total number of systematic rock bolts indeed increased significantly following the perimeter of larger opening. There was no change in wall support requirements as the same cavern height of 15 m was provided.

Three finite element models were established for each of the cavern with different span as illustrated in Figure 7. The geological parameters in Table 1 and the rock supports in Table 2 were adopted. In compliance with the assumption in rock support chart by NGI (2015), fully-grouted high yield steel reinforcement with 20mm bar diameter and 157 kN ultimate tensile capacity was assigned for the permanent systematic rock bolt. For the permanent shotcrete lining, Grade 40 structural concrete (f_{cu}=40MPa) was used.

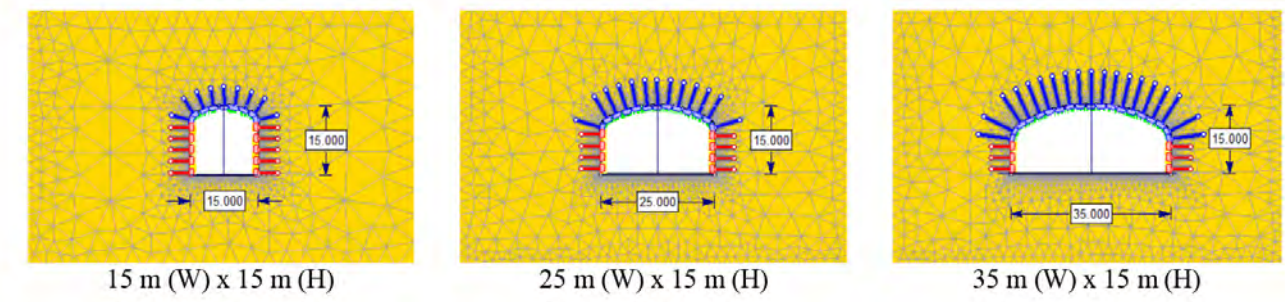

Figure 7: Finite element models for caverns with different span

The maximum mobilized bolt force in each numerical model and the utilization percentage of ultimate bolt tensile capacity were studied. In accordance with Geoguide 4 (2018), a minimum factor of safety 2.0 should be established on the ultimate tensile strength of permanent grouted rock bolt. This means a maximum of 50% utilization is allowed. For permanent shotcrete lining, the provided factor of safety in each numerical model based on the M-N interaction diagram was also studied. The results are summarized in Table 3.

Table 3: Results from finite element models for caverns with different span

Cavern Size	Systematic rock bolts				Shotcrete lining	
	Crown		Wall		Crown	Wall
	Max. bolt force	Utilization (157 kN)	Max. bolt force	Utilization (157 kN)	FOS	FOS
15 m (W) x 15 m (H)	12 kN	7.6 %	15 kN	9.6 %	2.8	3.4
25 m (W) x 15 m (H)	14 kN	8.9 %	21 kN	13.4 %	3	2.6
35 m (W) x 15 m (H)	18 kN	11.5 %	26 kN	16.6 %	3.4	2.4

Based on the numerical analysis, the maximum systematic bolt force increased with increasing cavern span. Higher bolt force at walls than at crown was observed. However, a very low utilization percentage of ultimate bolt tensile capacity was noted. This means the empirical rock support chart is a bit too conservative for cavern support design in hard rock (this paper does not cover poor rock mass conditions). Therefore, further design optimization to increase the bolt spacing and reduce the bolt length determined from empirical approach is technically feasible, subject to the approval from relevant checking authorities. For permanent shotcrete lining, increasing cavern span adversely affected the factor of safety in the wall. This result is different from the empirical approach.

4.3 Multiple Parallel Excavations

It is important to integrate the cavern development with surface facilities for capitalizing the strategic benefits and synergy effect. For example, connecting the underground supporting and recreational facilities with surface buildings and railway stations. This can be achieved by providing an access tunnel to connect the portal access with the cavern complex. A cavern complex usually comprises multiple parallel caverns with rock pillars between each opening which are interconnected by adits. As per Geoguide 4 (2018), the typical pillar widths between caverns should be at least half and full cavern span or height, whichever is the greater.

For concurrent excavations in multiple caverns, the interaction between adjacent opening such as excessive stress relaxation and excessive deformation in rock mass should be minimized. The stress redistribution and damage zone surrounding each opening will superimpose at the rock pillar location, and the global rock mass stability will be affected.

Three finite element models were established to study the influence of multiple parallel excavations to the design of permanent systematic rock bolts and shotcrete lining. A hypothetical comparison was carried out among three different scenarios of cavern arrangement: single, double and triple parallel excavations. Each cavern was 25 m (W) x 15 m (H) with 20 m rock pillar (80% of cavern span) between as illustrated in Figure 8.

Similarly, the maximum mobilized bolt force, the utilization percentage of ultimate bolt tensile capacity and the factor of safety on shotcrete lining were summarized in Table 4.

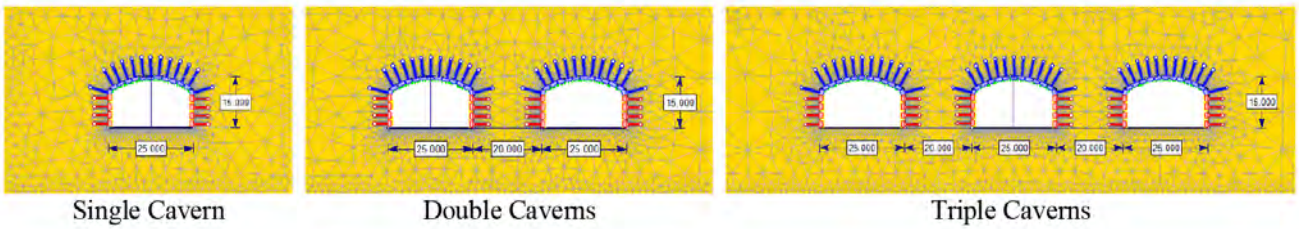

Figure 8: Finite element models for caverns with multiple parallel excavations

Table 4: Results from finite element models for caverns with multiple parallel excavations

Cavern Size	Systematic rock bolts				Shotcrete lining	
	Crown		Wall		Crown	Wall
	Max. bolt force	Utilization (157 kN)	Max. bolt force	Utilization (157 kN)	FOS	FOS
Single Cavern	14 kN	8.9 %	21 kN	13.4 %	3	2.6
Double Caverns	16 kN	10.2 %	29 kN	18.5 %	2.4	2.2
Triple Caverns (Excavate caverns at two sides first)	16 kN	10.2 %	30 kN	19.1 %	2.4	2
Triple Caverns (Excavate middle caverns first)	18 kN	11.5 %	35 kN	22.3 %	2.2	1.8

Based on the numerical analysis, the maximum systematic bolt force increased substantially due to multiple parallel excavations. Higher increment of bolt force at walls than at crown was observed, with almost doubled utilization percentage of ultimate bolt tensile capacity. The reason is due to the superimposed vertical stress concentration at the rock pillar location as shown in Figure 9.

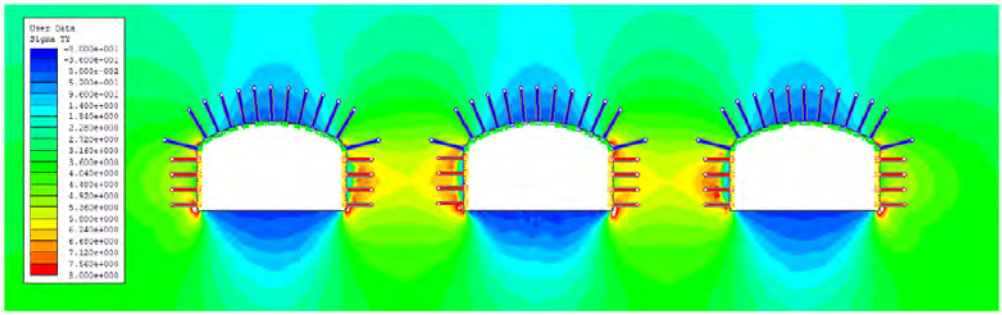

Figure 9: Superimposed vertical stress (σ_{yy}) concentration at rock pillars in FEM

In addition, it was observed that varying the excavation sequence will impose a slight impact on the final systematic rock bolt force and shotcrete lining support. The influence on adjacent excavation was more apparent when the middle cavern was excavated first followed by the caverns at two sides. Nevertheless, the empirical rock support chart is still conservative for cavern support design in hard rock and further design optimization is technically feasible.

5 CONCLUSIONS AND RECOMMENDATIONS

In consideration of technically feasibility, cost-effectiveness and sustainability, it is envisaged that the use of systematic rock bolts and shotcrete lining will become the dominant permanent support system for large-span caverns in Hong Kong, rather than conventional cast-in-situ concrete lining. However, there are a number of limitations that empirical approaches cannot adequately address regarding the design of rock caverns.

In this technical paper, a total six numbers of finite element models were established to investigate and validate the appropriateness of using empirical design for large-span excavation and influence of multiple parallel excavations. The results from numerical analysis have shown that the permanent support requirements are more stringent with increasing cavern span and multiple parallel excavations. a very low utilization percentage of ultimate bolt tensile capacity was observed. Therefore, it is successfully demonstrated that the use of empirical rock support chart by NGI (2015) is conservative for cavern support design in hard rock (this paper does not cover poor rock mass conditions). Further design optimization to increase the bolt spacing and reduce the bolt length determined from empirical approach is technically feasible, subject to the approval from relevant checking authorities.

REFERENCES

Barton N., Lien R. and Lunde J. 1974. *Engineering Classification of Rock Masses for the Design of Tunnel Support.* Rock Mechanics, vol. 6, pp 189-236.

Bischoff J.A. & Smart J.D. 1977. *A method of computing a rock reinforcement system which is structurally equivalent to an internal support system.* In Proceedings of the 16th US Symposium on Rock Mechanics, Minneapolis, MN, USA (Fairhurst C and Crouch SL (eds)). ASCE, New York, NY, USA, pp. 279–284

CEDD. 2017. *Cavern Master Plan*. Civil Engineering and Development Department, Hong Kong SAR. See https://www.cedd.gov.hk/eng/topics-in-focus/index-id-27.html

GEO. 2007. GEO Publication No. 1/2007: *Engineering Geological Practice in Hong Kong*. Geotechnical Engineering Office, Hong Kong SAR.

GEO. 2018. *Geoguide 4: Guide to Cavern Engineering, Second Edition (2018)*. Geotechnical Engineering Office, Hong Kong SAR.

Grimstad E., and Barton N. 1993. *Updating of the Q-system for NMT*. Proceedings of the International Symposium on Sprayed Concrete, Fagernes, Oslo. pp46-66.

Hoek, E., Carranza-Torres, C. & Corkum, B. 2002. *Hoek-Brown Failure Criterion – 2002 Edition*. Rocscience.

Hoek, E. 2007. *Practical Rock Engineering.* Rocscience.

Hoek, E. 2011. *Cavern Reinforcement and Lining Design*. See Cavern-Reinforcement-and-Lining-Design.pdf (rocscience.com)

Kong, K.W.K. & Garshol, K.F. 2015. *Rock Reinforcement Design for Underground Openings*. Proceedings of the Underground Design and Construction Conference 2015, The Institute of Materials, Minerals & Mining Hong Kong Branch, Hong Kong 2015. pp. 51-62.

Lang, T.A. 1961. *Theory and practice of rockbolting*. Transactions of the American Institute of Mining Engineering, Vol. 220.

NGI. 2015. *Using the Q-system: Rock Mass Classifications and Support Design (handbook).* Norwegian Geotechnical Institute, Oslo.

Singh B. & Goel R. K. 2006. *Tunnelling in Weak Rocks*. Elsevier Ltd, London.

Terzaghi, K. 1946. *Rock Defects and Load on Tunnel Supports - Introduction to Rock Tunnelling with Steel Supports*. Ed: R. V. Proctor, and T. L. White, Commercial Shearing and Stamping Co., Youngstown, Ohio, USA, 278.

Intersection-based potential plane failure detection on 3D meshes for rock slopes

R. Tsui, C. Cheung, J. Hart, W. Hou & A. Ng
GeoRisk Solutions Limited, Hong Kong

ABSTRACT

Plane failure, a major class of rock block failures, will be considered kinematically feasible on a rock discontinuity if it fulfills certain criteria when plotted and analysed on a stereonet. However, it is often the case that this approach does not consider if a block is present above the discontinuity. With significant advances in digital surveying techniques in recent years, high-resolution 3D meshes can be readily produced for rock slope stability assessments. A semi-automatic, intersection-based approach has been developed by the authors to detect potentially adverse planar discontinuities and their intersections with planar blocks on 3D meshes. The approach involves the detection of the necessary geometrical conditions for a rock block located above a planar discontinuity and in a potentially detachable condition. The approach is considered robust in that it does not require an assumption of slope face orientation, and is not limited to checking joints within major joint sets only. A region-growing joint extraction algorithm has also been developed and used in this study. The approach is demonstrated successfully for two case studies: (I) an old road cut in Colorado, USA; and, (II) a newly formed cut slope in Hong Kong. The approach can quickly alert engineering geologists of potentially unstable blocks at risk of plane failure, especially at an early project stage when access to the rock slope may be limited.

1 INTRODUCTION

One of the goals of rock slope mapping is to identify potentially unstable blocks, which are formed along rock joints (or other types of discontinuities). Conventionally, engineering geologists measure the dipping angles and orientations of joints on the slope manually, and plot the data on stereonets to assess the kinematic feasibility of structurally controlled rock block failures. Plane failure, a major class of rock block failures, will be considered kinematically feasible on a joint if it fulfills certain criteria when plotted and analysed on stereonets (Wyllie and Mah, 2004). However, as these criteria assume rock slope uniformity and do not consider intersection relationships between individual joints, it is often the case that some of the detected adverse joints are not actually associated with potentially unstable blocks. The analysis also has limitations for rock slopes with complex geometries. In addition, whilst on site observations and measurements are critical, measurements taken directly on the slope can be time-consuming and subjective, with data accuracy and relevance dependent on the skill and experience of the practitioners involved.

With significant recent advances in digital surveying techniques such as photogrammetry and laser scanning, high-resolution 3D meshes can be readily produced for rock slopes, and can be used to provide innovative solutions to these challenges. Numerous new software, algorithms and workflows have been developed or proposed in recent years for digital rock slope mapping (e.g. Assali et al., 2014; Riquelme et al. 2014, 2016; Buyer, 2020). While workflows for the kinematic analysis of data generated from 3D point clouds have been proposed (e.g. Matasci et al., 2018; Menegoni et al., 2019), these are based on traditional kinematic analysis approaches, or are limited to considering joints within major joint sets.

To overcome these issues, the authors propose an alternative and innovative, semi-automatic approach to detect potential plane failures using high-resolution 3D meshes, based on intersections between the planar joints and the associated blocks above. The approach does not require slope orientation assumptions or major joint set identification and assessment prior to the analysis.

1.1 Terminology

For readers less familiar with 3D data, terminology related to 3D data such as "point cloud", "mesh" and "faces" are provided in Figure 1. The term "normal" refers to a unit vector perpendicular to a planar entity, such as a joint plane or a mesh face (i.e. "poles" to planes plotted on stereonets). A point or a vertex can also have a normal which is perpendicular to its locally best-fit plane.

Figure 2 illustrates terms related to joint orientation. For convenience, the dip angle δ and the strike S of a joint used in our study are used slightly differently from conventions (for overhanging cases), and are related to the joint normal n_j as follows:

$$\delta = \cos^{-1}(n_j \cdot z) \text{ (note: } \delta < 90° \text{ for overhanging cases here)} \quad (1)$$

$$S = \frac{z \times n_j}{|z \times n_j|} \text{ (note: S is towards dip direction + 90° for overhanging cases here)} \quad (2)$$

where z is the unit vector along z-axis (upwards)

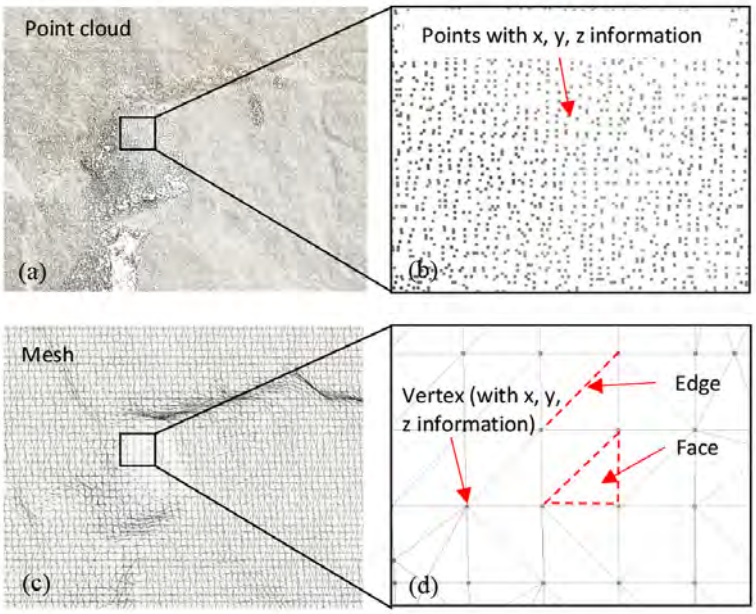

Figure 1: Terminology for 3D data

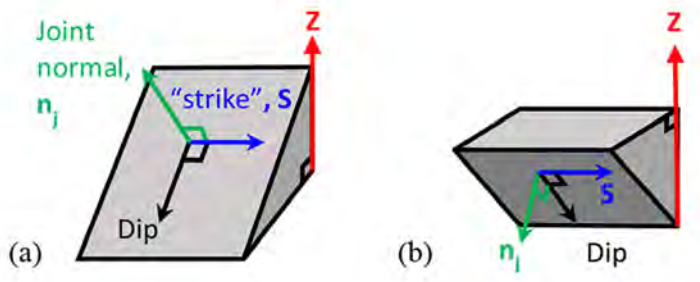

Figure 2: Terminology for joint orientation (slightly different from convention for overhanging case)

1.2 Proposed approach for the detection of potentially adverse planar joints

If a block can slide along a planar joint, its lowest, frontal face should be unobstructed. This means that the block's frontal face should intersect with the planar joint and form a concave rock edge. The joint in this case is daylighting. These intersections are referred to as "daylight-indicating intersections" for this approach.

As illustrated in Figure 3, suppose all intersections made by the daylighting planar joint (effectively these form its outline, if no isolated blocks are present on top) are arranged in a clockwise orientation, then we can measure the angle between the joint's strike S and an intersection as α. For an intersection between the planar joint and the front of the block, which cuts above the joint (Figure 3b), the α would be small. In contrast, if the joint only intersects with the lateral side of a block (Figure 3c), the α would be 90°. For cases in between, some sharp blocks may have a minimum α of 30° (Figure 3d). However, it would be rare that a detachable block does not have a side with α < 80° (Figure 3e). In this study, 60° is used as a cut-off value for α. In addition, if the intersection "cuts below" the joint (i.e. intersection with the rear of a block), α = 90° to 180° (Figure 3f).

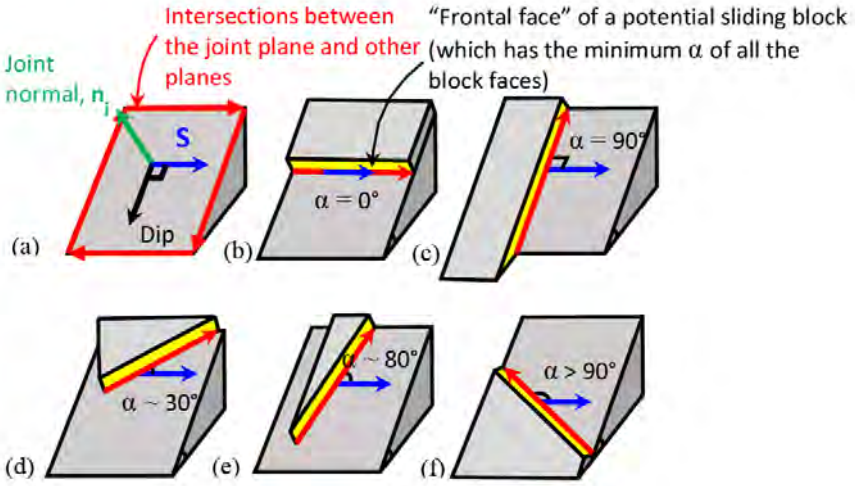

Figure 3: α in different configurations of a planar block and a planar joint

A daylight-indicating intersection therefore satisfies two conditions:

(i) it has α < αtol (angle of tolerance for α, set to 60° in this study), and

(ii) it is concave.

Considering natural undulations on the rock may create noises, it would be desirable to set a minimum length, L_{min}, for a daylight-indicating intersection to be flagged. In addition, the associated planar joint should be steeper than the friction angle along the joint surface to be regarded as adverse. However, as indicated earlier, this approach does not need to assume an overall orientation for the slope face.

2 METHODOLOGY

The proposed method comprises four main stages: (1) joint extraction; (2) estimation of joint orientations; (3) detection of daylight-indicating intersections; and, (4) consideration of minimum block width.

Prior to meshing, the point cloud of the rock slope is cleaned such that points not belonging to the rock mass (e.g. vegetation, man-made features, soil deposits, etc.) are removed. Meshing was carried out in CloudCompare (2017), using the Poisson Surface Reconstruction plugin. Section 2.7 provides a list of python packages used in our implementation.

2.1 Joint extraction

Since the outline of the exposed surface of the joint will be used to represent intersections made by the joint, the outline should be extracted accurately. In addition, random joints should also be evaluated.

Whilst a number of plane segmentation schemes have been developed for digital rock joint mapping, which have worked well for their intended purposes, there are a number of limitations when applying these schemes to our approach. For example, some only extract those joints within major joint sets (e.g. Riquelme et al. 2014), and some do not preserve the outline of the joints accurately (e.g. Dewez et al. 2016). Therefore, for the purpose of this study, we have adopted a region-growing approach similar to those described by Vöge et al. (2013) and Wang et al. (2017).

2.1.1 Edge removal

The first step for joint extraction is to remove edges of the rock mass, such that flat planes with different orientations can be segmented as isolated small meshes (i.e. "seed planes").

Mesh faces at rock edges can be identified by high surface curvature. To estimate the local curvature (σ) of a face, eigendecomposition is carried out on the covariance matrix of the centroids of its neighboring faces. This yields three pairs of orthogonal eigenvectors and eigenvalues (λ_1, λ_2 and λ_3, where $\lambda_1 \geq \lambda_2 \geq \lambda_3$). Curvature σ can be estimated by Pauli et al. (2002):

$$\sigma = \frac{\lambda_3}{\lambda_1 + \lambda_2 + \lambda_3} \tag{3}$$

The variation of σ on a simple object is illustrated on Figure 4a. In this study aggressive thresholds are used (e.g. removing 40-80% of the total mesh faces) to ensure that planes with different orientations can be completely separated. This step turns the original mesh into a "patchy" mesh, which is in fact a group of disconnected small meshes.

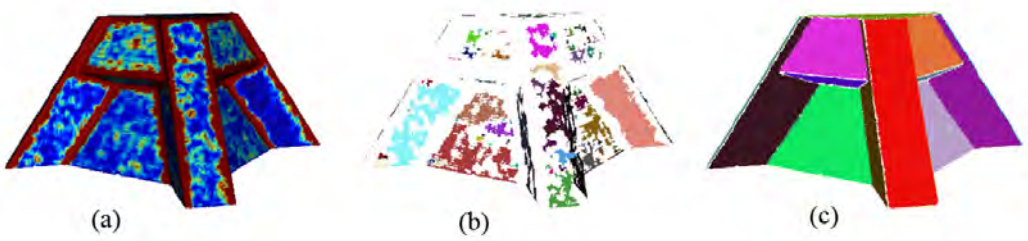

Figure 4: Region-growing joint extraction algorithm on a simple object

2.1.2 Seed planes

By analyzing mesh connectivity, each isolated small mesh in the "patchy" mesh is then labelled as a seed plane (Figure 4b). Initial plane-fitting by principal component analysis (i.e. PCA, further discussed in Section 2.2) is carried out on each seed plane (with face centroids) to derive its plane normal, n_s. The normals of all of the mesh faces on the seed plane are then uniformly re-orientated in the direction same as n_s. This is to ensure that in the later region-growing stage, mesh faces on the same seed plane can stay together.

2.1.3 Region-growing

In the previous two steps, a joint may be separated into two or more seed planes due to undulations. In addition, mesh faces close to the rock edges or corners are not preserved well during the aggressive edge removal process. The region-growing stage aims to grow the seed planes back to their full extents.

For each seed plane M_s, which has normal n_s, the angular difference θ_f between itself and a mesh face f in the original mesh M with face normal n_f is:

$$\theta_f = \cos^{-1}(n_s \cdot n_f) \tag{4}$$

If θ_f is small enough, f can be regarded as co-planar with Ms. In our study, the angle of tolerance, θ_{tol}, is set at 15°-30° based on rock mass characteristics. If $\theta_f < \theta_{tol}$, then f is added to a temporary mesh, M'. This is evaluated for every mesh face f in the original mesh M. All components connected to M_s in M', including previously unclassified mesh faces and other seed planes, will be combined into Ms. The normals of these newly added components will now also re-orient with n_s. This process is then iterated over all of the remaining seed planes. At the end of the stage, each grown seed plane is regarded as a joint plane (Figure 4c).

2.2 Estimation of joint orientation

After extracting the joints, the joint orientations are estimated by PCA, which can minimize the orthogonal distances between the input data and the fitted plane.

Each extracted joint is now represented by its mesh, M_j. For each joint, PCA is carried out by eigencomposition on the covariance matrix of the mesh vertices on M_j. which gives three pairs of orthogonal eigenvectors (e_1, e_2, e_3) and eigenvalues (λ_1, λ_2 and λ_3, where $\lambda_1 \geq \lambda_2 \geq \lambda_3$). The eigenvector e_3, associated with the smallest eigenvalue λ_3, represents the direction that accounts for the least variance in the scatter of the vertices on M_j. This is effectively the normal to the best-fit plane of M_j. In other words, joint normal $n_j = e_3$ (or $-e_3$ if e_3 is opposite to most of the face normals on M_j).

The dip angle δ and strike S for each extracted joint can then be obtained from equations (1) and (2).

2.3 Detection of daylight-indicating intersections

As mentioned in Section 1.2, a daylight-indicating intersection has (i) $\alpha < \alpha_{tol}$ and is (ii) concave. In the implementation, conditions (i) and (ii) are checked for each mesh edge on the outline of M_j. Since the outline of M_j may be ragged, spline smoothing is applied. In addition, edges which are also part of the outline of the original mesh M are excluded as they do not represent real intersections between planes (Figure 5b).

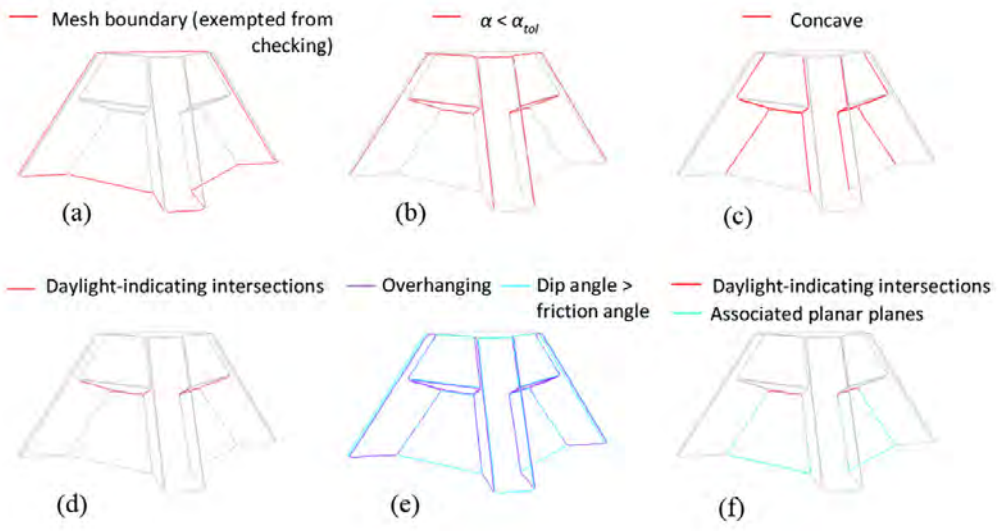

Figure 5: Plane failure detection on a simple object (same object as in Figure 4)

2.3.1 Identification of intersections "above" the joint

As illustrated in Figure 3(a), the mesh edges on the outline of M_j are first arranged in a clockwise direction around the joint normal n_j. The vertices on the outline are $[v_1, v_2, ..., v_n]$. An edge between two vertices v_i and v_{i+1} is represented by $E_i = v_{i+1} - v_i$. If the displacement from an edge E_i to the center of the mesh is l_i, the cross product $l_i \times E_i$ for most edges should roughly align with n_j if the edges are in a clockwise direction. If not, then the outline vertices need to be sorted in the opposite direction. After the ordering is fixed, the angle α_i between each edge E_i and the strike of the joint S_j, can be calculated by:

$$\sigma_i = \cos^{-1}\left(\frac{E_i}{|E_i|} \cdot S_j\right) \quad (5)$$

Based on discussion in Section 1.2, an angle of tolerance αtol is set at around 60°. If $\alpha i < \alpha_{tol}$, the edge will be regarded as "cutting above" the joint. Figure 6 demonstrates the effect of α < 60° on an object with circular holes.

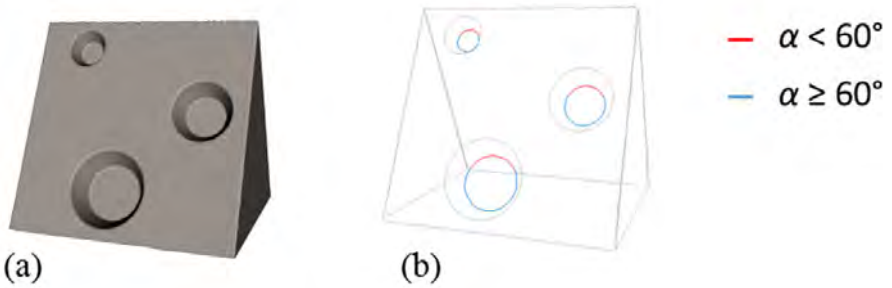

Figure 6: (a) A simple object with circular holes (b) α around the circular holes

2.3.2 Estimation of signed local curvature (concavity)

Whether a mesh edge E_i is concave or not can be estimated by the curvature of either one of its vertices, v_i. In this study, the "concavity" (c_i) of v_i is estimated by the mean positional differences between v_i and its k-nearest neighbors along n_v, i.e., the normal of v_i (Figure 7, equation (6)). c_i is positive for v_i at concave rock corner or edges, and is negative for convex cases. To reduce sensitivity, a threshold is set to ignore slightly positive c. Concave edges for a simple object is identified in Figure 5(c).

$$c_i = (\overline{v_k} - v_i) \cdot n_v \quad (6)$$

where $\overline{v_k}$ is the mean position of the nearest neighbors of v_i.

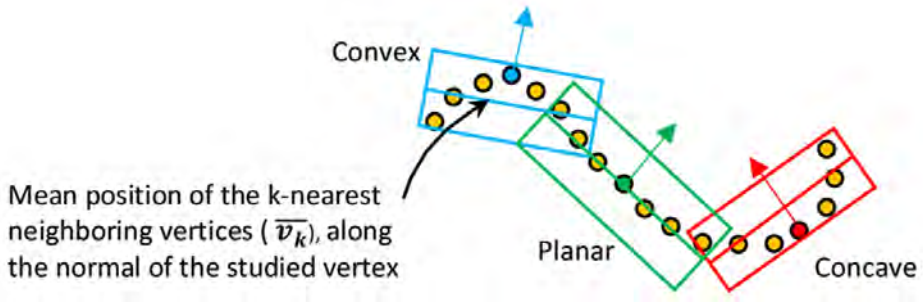

Figure 7: Estimation of signed local curvature

2.4 Minimum width of potential planar block

As mentioned in Section 1.2, daylight-indicating intersections are required to be longer than L_{min}, to be flagged. In our approach we evaluate the projected length along the joint's strike (S_j) against L_{mi}. In other words, a connected segment of N mesh edges [E_1, E_2, …, E_N] which satisfy conditions (i) and (ii) needs to further satisfy equation (7) below. On the other hand, mesh edges on daylight-indicating intersections might locally fail to satisfy conditions (i) and (ii). These are ignored if less than a certain length (0.1m used in the case studies).

$$\sum_{i=1}^{N} = E_i \cdot S_j > L_{min} \quad (7)$$

2.5 Special case

In rare cases, there may be an isolated "island block" on top of a planar joint. In such case, the intersections between the block and the joint will not be represented as part of the outline of the mesh M_j, but as a hole within M_j. The approach described above can still be applied to find daylight-indicating intersections in such holes, although in the procedures described in Sections 2.3.1, the edges should be orientated anticlockwise instead of clockwise. Case study II (Section 3.2) takes this special case into account. However, in most cases these holes are merely slightly elevated undulations instead of isolated blocks.

2.6 Presentation

If a joint contains any segments satisfying equation (7), and that the joint is steeper than the friction angle, it is flagged as a potentially adverse planar joint, or an overhanging joint if $\delta > 90°$. The polylines of the daylight-indicating intersections and the associated joint outlines are output as dxf files, which can be viewed in CAD and GIS.

2.7 Implementation in Python

Our approach is implemented in Python scripts. The overall analysis relies heavily on a number of widely used, well tested Python packages, as shown in Table 1:

Table 1: Python packages used in analysis

Python packages	Usage
Trimesh (Dawson-Haggerty et al. 2019)	Mesh input / output, general mesh manipulations
NumPy (Harris et al. 2020)	Eigendecomposition for PCA, and other operations on matrices
SciPy (Virtanen et al. 2020)	Finding connected components on meshes; spline smoothing for joint outline; k-nearest neighbor search
NetworkX (Hagberg et al. 2008)	Finding mesh outline and holes
ezdxf (2021)	Writing dxf files

3 APPLICATIONS

The approach described above is applied to two case studies to detect potentially adverse planar joints. The results are then compared to that obtained from traditional rock slope mapping and kinematic analysis. Case study I is a roadside cut slope in Ouray, Colorado, USA (Lato et al., 2013) (Figure 8a). Case study II is a newly-formed cut slope in Hong Kong (Figure 8b). Information of the datasets and key parameters used in the analyses are summarized in Tables 2 and 3.

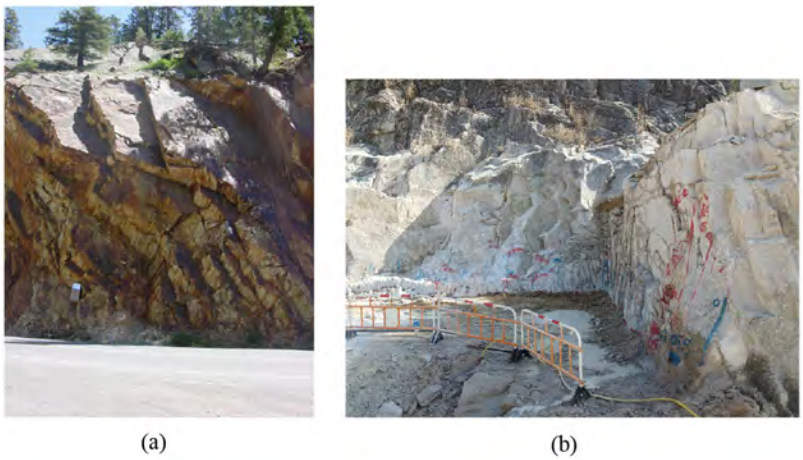

Figure 8: (a) Case study I – an existing roadside cut slope in Ouray, Colorado, USA;
(b) Case study II – a newly formed cut slope in Hong Kong

Table 2: Information of the analyzed datasets

	Case Study I	Case Study II
Lithology	Quartzite	Granite
Approximate slope dimensions	20m long × 15m high	16m long × 8m high (max.) (W-facing), 10 long × 3m high (N-facing)
Approximate slope orientation(s)	295º/75º	258º/80º, 348º/80
Method of data acquisition	Terrestrial laser scanning	Structure-from-Motion photogrammetry (from UAV photos)
Point spacing	< 20mm	< 5mm
Total No. of faces on analyzed mesh	2,533,930	1,105,468

Table 3: Key parameters used in potential planar sliding joint detection analyses

	% of mesh face removed based on σ	θ_{tol} (°)	α_{tol} (°)	% of positive c values ignored	Friction angle (º)	Lmin (m)
Case Study I	45	20	60	50	35	0.2
Case Study II	80	17	60	50	40	0.2

3.1 Case I: Roadside cut slope in Ouray, Colorado, USA

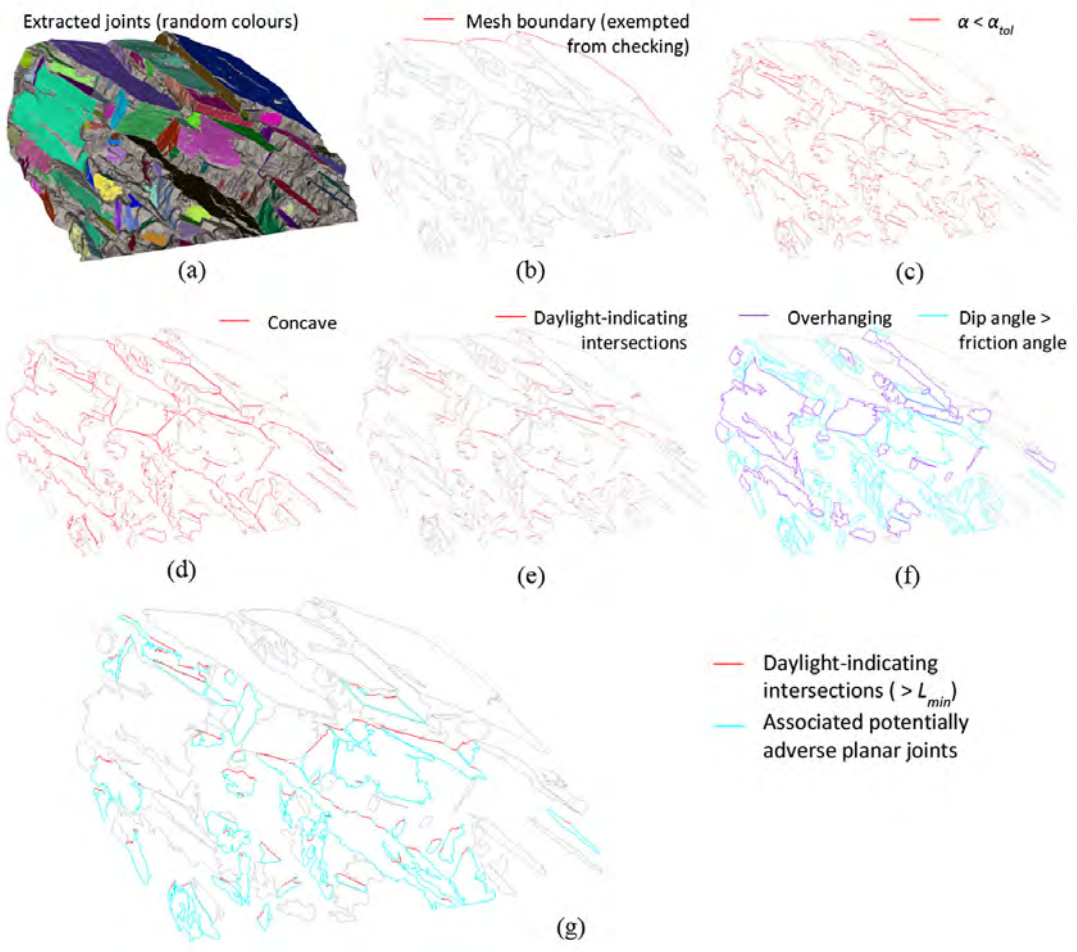

Figure 9: Results of plane failure detection for Case Study I

The dataset was originally hosted on the Rockbench open repository (Lato et al. 2012) and has been used in several digital rock joint mapping research (e.g., Riquelme et al. 2014; Chen et al. 2016; Zhang et al. 2020). The rock slope contains a set of persistent planar joints dipping at approximately 35°, obliquely towards the road. For testing purposes, the friction angle is set to 35° so that more joints within the set are included as potentially adverse.

In the joint extraction stage, a total of 90 joints were extracted. The results are reasonable based on visual inspection of the mesh. Applying our approach, 39 potentially adverse planar joints were identified, which contain a total of 68 daylight-indicating intersections. The intermediate and final outputs are displayed in Figures 9a-f and 9g respectively.

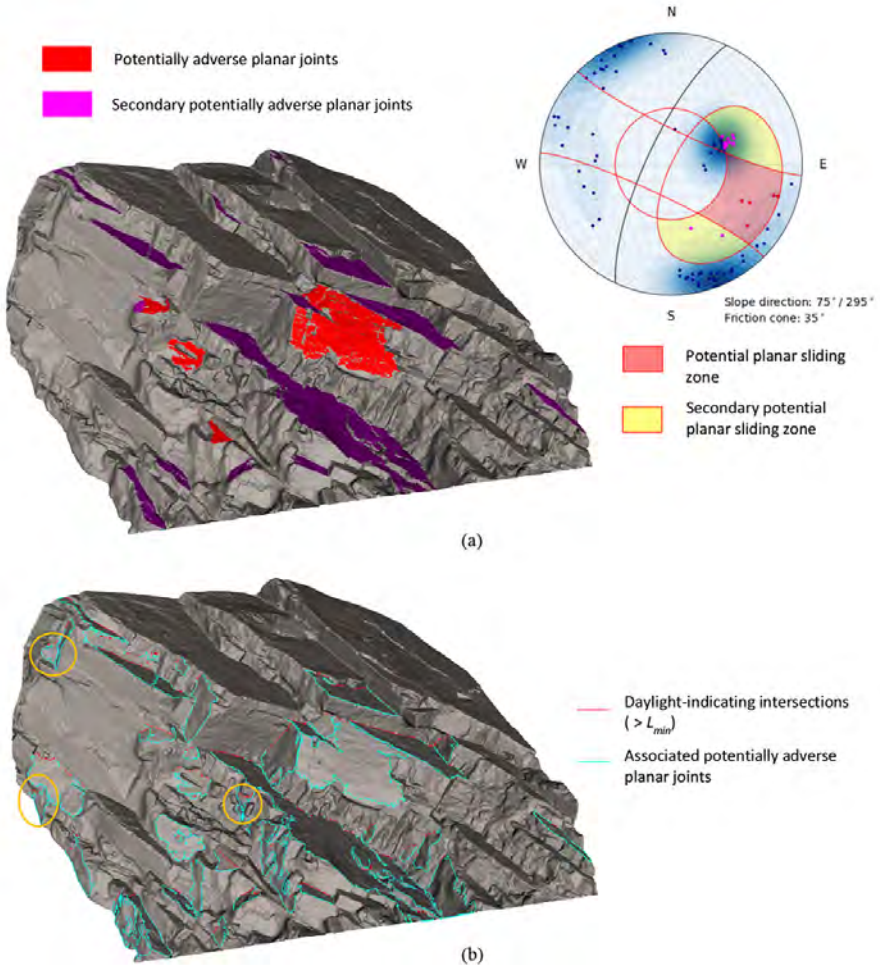

Figure 10: (a) Case Study I results – traditional kinematic analysis; (b) our results for comparison

Using the same extracted joint data, the traditional kinematic analysis identified 5 joints within the main planar sliding zone (± 20° lateral limits), and 15 joints within the secondary planar sliding zones (Figure 10a). Out of a total of 20 joints, 18 are also identified by our approach. The other 2 joints are not associated with blocks above. The majority of these 18 joints appear valid to be flagged (i.e. highlighted) as potentially adverse.

Among the joints which are only detected by our approach, some appear valid to be flagged but is missed by the traditional approach, although the potential blocks are rather small (three circled in Figure 10b). However, some are indeed irrelevant cases where the detected daylight-indicating intersections are merely undulations. In addition, a significant portion of the irrelevant cases are in fact associated with wedge-sliding mechanism.

The case study demonstrates that without considering the slope orientation, our approach can potentially yield more relevant results than the traditional kinematic analysis. In addition, some potential wedge joints are also flagged as potentially adverse.

3.2 Case II: A newly-formed cut slope in Hong Kong

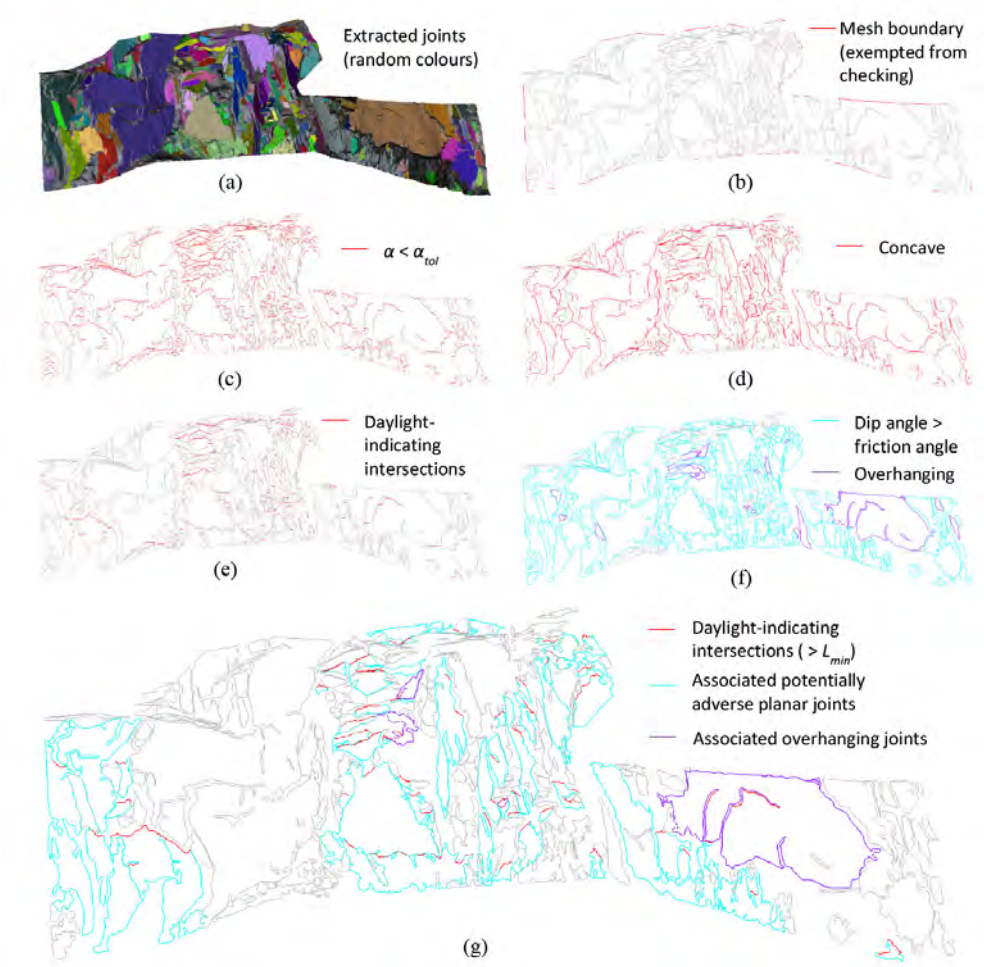

Figure 11: Results of plane failure detection for Case Study II

The cut slope was newly excavated at the time of the survey, which was completed prior to slope treatments. The cut slope contains a north-facing portion and a west-facing portion. This slope was selected for analysis for three reasons: (1) the lower part (< 4m high) has been mapped by the authors on site; and, (2) potentially unstable rock blocks were identified during this survey; and, (3) the geometry of the rock slope is not uniform, requiring multiple kinematic analyses using traditional methods.

In the joint extraction stage, a total of 279 joints were extracted. Applying our approach, 56 potentially adverse planar joints were identified, which contain a total of 75 daylight-indicating intersections. The intermediate and final outputs are displayed in Figures 11a-f and Figure 11g respectively.

As the slope contains two portions with two different orientations, it is required to be segmented into two parts for traditional kinematic analysis (Figure 12a). Using the same extracted joint data, the traditional kinematic analysis approach identifies a total of 83 joints within the main planar sliding zone, and 60 joints within the secondary planar sliding zones (Figure 12a). Out of a total of 143 joints, 38 are identified by our own approach.

Within <4m height of the analyzed slope area, our on-site mapping identified one potentially unstable planar block, two potentially unstable wedge blocks, and a small area of potentially raveling blocks. In both approaches, the potentially adverse planar joint and one of the potentially adverse wedge joints are detected (circled in black in Figure 12b). The other wedge sliding case is not detected since the associated joints have limited exposed area (i.e. traces) and are not extracted. For the raveling case, the blocks are not sitting on planar joints.

From the mapping results, it would appear that both methods produce a large number of false positives. However, some of the false positives are in fact valid to be flagged or highlighted, meaning it

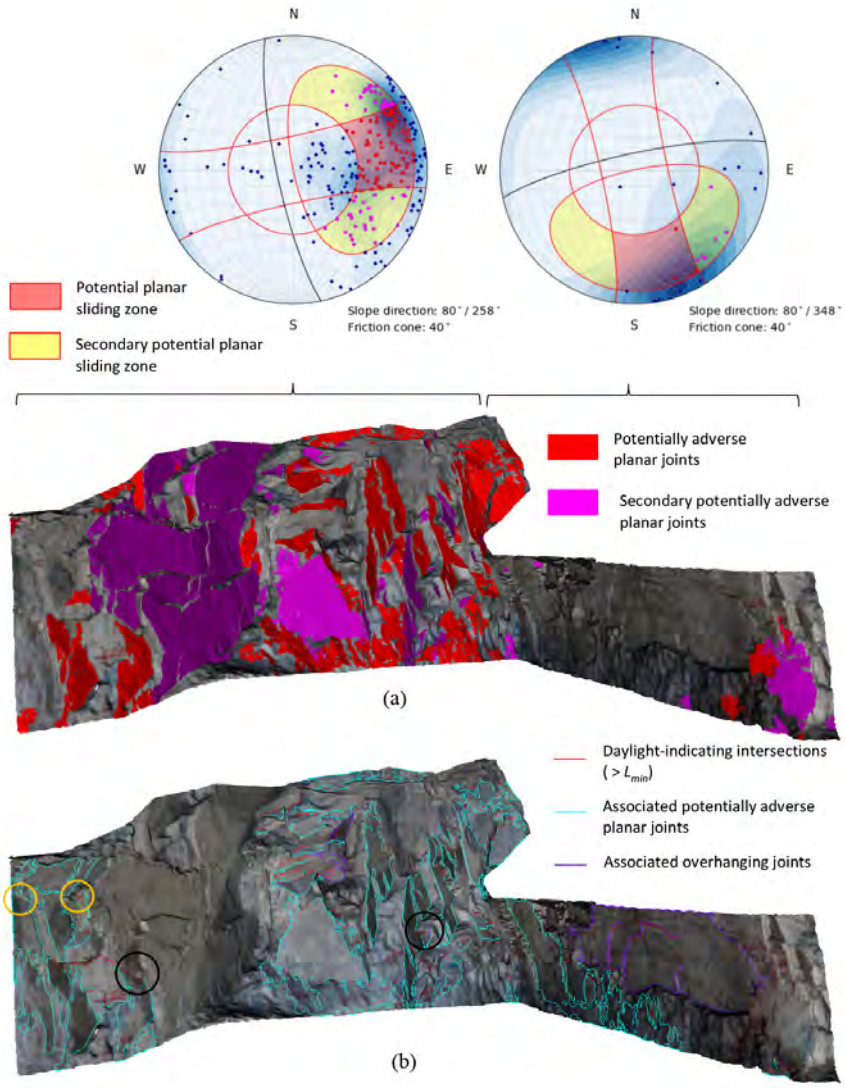

Figure 12: (a) Case Study II results – traditional kinematic analysis; (b) our results for comparison

would indeed require further checking to see if the block on the flagged joint is detachable. A significant portion of false positives identified in our approach belong to this case. Some of these cases are not detected by traditional kinematic analysis (circled in orange in Figure 12b). As for cases which are indeed irrelevant, the detected daylight-indicating intersections are mostly stepped undulations on closely spaced, persistent joints. In comparison, the traditional kinematic analysis approach produces more irrelevant cases (i.e., false alarms), which is expected given a large number of exposed joints are subvertical joints parallel to the slope face. It is also worth mentioning that slope angle and orientation estimation is somewhat subjective. If it was estimated at 70°, the potentially adverse planar joint identified on site (δ = 74°) would be too steep to be in the daylight envelope and will be missed.

4 DISCUSSION

4.1 Advantages of the approach

The case studies demonstrate that both the intersection-based approach and the traditional kinematic analysis are useful in highlighting joints susceptible to plane failure on 3D meshes.

Advantages of our approach over traditional kinematic analysis for plane failure are:

- The approach involves more flexibility as there is no need to estimate a slope orientation, which may be difficult for some slopes with complex geometry.

- It is not necessary to sub-divide the slope for every change in slope direction.
- It allows direct visualization of the potentially adverse planar joints alongside their intersection with the planar blocks, which is convenient for checking purposes.
- The widths of the potentially unstable planar blocks can be estimated at a glance.
- Fewer missed cases.
- Fewer false alarms, when a subvertical joint set parallel to the slope face is present.

4.2 Limitations

There are also a number of intrinsic limitations with the intersection-based approach. Firstly, joint traces (i.e. joints with limited exposed area, appearing as lines on the rock slope) are not considered. Secondly, similar to traditional kinematic analysis, the assumption that all joints have the same assumed friction angle is an over-simplification, given that joint-infilling can be present at some joints, which is not checked by our approach and requires field verification. Thirdly, our approach does not check the height of the potential sliding block, causing it to be sensitive to stepped undulations on joint planes. Fourthly, assuming all joints are accurately extracted and all have the same assumed friction angle, the conditions used in detection for detachable blocks on planar joints are in logic terms "necessary but not sufficient". This is because detachable blocks would also have side and back release mechanisms, which are not checked in our approach, meaning that there may be significant false positives with our approach.

4.3 Parameters and computation time

Although systematic sensitivity analysis is not available, the case studies show that using the same preset values for α_{tol}, c and L_{min} in our approach, yields reasonable results, requiring no mesh-specific parameter tuning. L_{min} is adjustable based on the project purpose. In comparison, our joint extraction algorithm is not as reliable and is rather sensitive to the σ and θ_{tol} parameters. Optimal values for these two parameters are mesh-specific and require trial-and-error tuning. The joint extraction algorithm proposed in this study can probably be replaced by other mesh-based plane segmentation algorithms of choice, as long as the outline of the extracted joints are reasonably accurate, and, ideally, random joints are extracted.

The total computation time is reasonably short since we leverage a number of high-performance Python packages (e.g., NumPy and SciPy). On a computer with Intel Core i7-9750H and 16 GB RAM, the total computation times (i.e. from loading pre-segmented mesh to exporting .dxf files) for both cases were < 3 minutes. Joint extraction took approximately 90% of total computation time. On segmented meshes, plane failure detection took under 20s for the two case studies. Further testing can be carried out to see how this scales to larger projects. Further optimization, such as rewriting some of the Python loops in C++, are also possible.

4.4 Potential useful applications and further investigations

Potential useful applications for this technique are:

- Slopes without sufficient access can be surveyed by remote sensing techniques first. Potentially adverse planer joints can be flagged before safe access becomes available for closer inspections and measurements.
- This method can supplement the results of direct mapping so that potentially adverse planar joints are not overlooked. This is especially useful when the rock mass is heavily fractured, and the chance of overlooking critical joints is increased.

Potential further investigations are:

- Estimation of the planar block's height for screening out the stepped undulations
- Extension to other rock slope failure modes, such as wedge and toppling failure

5 CONCLUSIONS

This study proposes and describes an alternative, semi-automatic, intersection-based approach to detect potentially adverse planar joints and their daylighting intersections on 3D meshes of rock slopes. A region-growing joint extraction approach is also proposed and used in this study. The proposed plane failure the detection of the necessary geometrical conditions for a rock block located above a planar discontinuity and in a potentially detachable condition. Our approach is demonstrated successfully for two case studies involving real rock slopes, one of which is a mapped rock slope in Hong Kong. Benchmarking against traditional kinematic analysis for planar sliding, our approach yields more relevant results and is more flexible and better suited for engineering needs. While these semi-automatic techniques cannot replace field verification by geologists, our approach can quickly alert engineering geologists of potentially unstable blocks at risk of plane failure, especially at an early project stage when access to the rock slope may be limited.

ACKNOWLEDGEMENTS

The laser scanner data from Case Study I was retrieved from Dr. Riquelme's personal website (https://personal.ua.es/en/ariquelme/a-new-approach-for-semi-automatic-rock-mass-joints-recognition-from-lidar-data.html). The dataset was formerly hosted on the Rockbench open repository (www.rockbench.org). Our approach was developed following a benchmarking exercise instigated by the GEO in 2020 and we would like to thanks the organizers.

REFERENCES

Assali, P., Grussenmeyer, P., Villemin, T., Pollet, N., & Viguier, F. 2014. Surveying and modeling of rock discontinuities by terrestrial laser scanning and photogrammetry: Semi-automatic approaches for linear outcrop inspection. *Journal of Structural Geology,* 66: 102-114.

Buyer, A., Aichinger, S., & Schubert, W. 2020. Applying photogrammetry and semi-automated joint mapping for rock mass characterization. *Engineering Geology,* 264: 105332.

Chen, J., Zhu, H., & Li, X. 2016. Automatic extraction of discontinuity orientation from rock mass surface 3D point cloud. *Computers & Geosciences,* 95: 18-31.

CloudCompare (version 2.9). 2017. Retrieved from http://www.cloudcompare.org/

Dewez, T.J., Girardeau-Montaut, D., Allanic, C., & Rohmer, J. 2016. Facets: A CloudCompare Plugin To Extract Geological Planes From Unstructured 3d Point Clouds. *Int. Arch. Photogramm. Remote Sens. Spatial Inf. Sci.*, XLI-B5: 799-804.

Dawson-Haggerty et al. 2019. Trimesh (version 3.2.0). https://trimsh.org/

ezdxf (version 0.16). 2021.ezdxf.mozman.at/

Hagberg, A. A., Schult, D. A., & Swart, P. J. 2008. Exploring Network Structure, Dynamics, and Function using NetworkX. In G. Varoquaux, T. Vaught, & J. Millman (ed.), *Proceedings of the 7th Python in Science Conference, Pasadena, 2008*.

Harris, C. R., Millman, K. J., van der Walt, S. J., Gommers, R., Virtanen, P., Cournapeau, D., . . . Oliphant, T. E. 2020. Array programming with NumPy. *Nature,* 585: 357–362.

Lato, M., Kemeny, J., Harrap, R.M., & Bevan, G. 2013. Rock bench: Establishing a common repository and standards for assessing rockmass characteristics using LiDAR and photogrammetry. *Computers & Geosciences,* 50: 106-114.

Pauly, M., Gross, M., & Kobbelt, L. P. 2002. Efficient simplification of point-sampled surfaces. In *IEEE Visualization, October 2002. VIS 2002*. IEEE.

Riquelme, A. J., Abellán, A., Tomás, R., & Jaboyedoff, M. 2014. A new approach for semi-automatic rock mass joints recognition from 3D point clouds. *Computers & Geosciences,* 68: 38-52.

Riquelme, A. J., Tomás, R., & Abellán, A. 2016. Characterization of rock slopes through slope mass rating using 3D point clouds. *International Journal of Rock Mechanics and Mining Sciences,* 84: 165-176.

Virtanen, P., Gommers, R., Oliphant, T.E., Haberland, M., Reddy, T., Cournapeau, D., . . .SciPy 1.0 Contributors. 2020. SciPy 1.0: Fundamental Algorithms for Scientific Computing in Python. *Nature Methods,* 17, 261–272.

Vöge, M., Lato, M.J., & Diederichs, M.S. 2013. Automated rockmass discontinuity mapping from 3-dimensional surface data. *Engineering Geology,* 164: 155-162.

Wyllie, D. C., & Mah, C. 2004. Rock slope engineering. CRC Press.

Wang, X., Zou, L., Shen, X., Ren, Y., & Qin, Y. 2017. A region-growing approach for automatic outcrop fracture extraction from a three-dimensional point cloud. *Computers & Geosciences,* 99: 100-106.

Application of "Big Data" to Engineering Properties of Hong Kong Soils

Dr Wong Hong-yau
Geotech Engineering Ltd, Hong Kong, China

ABSTRACT

In recent years, big data is becoming a very powerful tool in processing extremely large amount of data in such fields as finance, industry, engineering, etc. For geotechnical engineering, large number of laboratory and in-situ tests (mostly SPT) have been carried out in the past few decades. Laboratory testing includes soil classification and most importantly three major engineering properties: shear strength, compressibility and conductivity. In order that these data forming the big data can be useful in engineering design, a lot of processing/analysing works have been carried out and these indicate that soil type is the most dominant parameter affecting all engineering properties. Within each soil type, there are some secondary factors such as fines content, dry density, etc, which have only a secondary effect on these properties. Another dominant primary factor is SPT, which will affect most importantly the shear strength. A 2020 HKIE paper by the author has established that the relationship between shear strength and SPT is unique, irrespective of the soil type. As for compressibility, SPT is in general directly proportional to the elastic modulus. However, SPT has basically no effect on conductivity. Finally, the method of entering the processed data is proposed.

1 INTRODUCTION

Pioneering work on soil testing was carried out in the 1950s to 1960s by the late Professor Lumb in the soil laboratory of University of Hong Kong. In spite of the limited testing facilities and number of tests carried out in that period, these works do lay out a solid foundation for future testing works in Hong Kong.

Since the late 1970s, a lot of site investigation and laboratory testing have been carried out in various Hong Kong testing laboratories, following in general the guidelines set out by Professor Lumb. By that time, all the testing procedures and testing facilities have been basically standardized. Accordingly, data thus collected should be useful for big data analysis.

For big data analysis to be applicable to engineering properties of Hong Kong soils, the following problems have to be considered: firstly the types of soils to be considered in Hong Kong; secondly the major types of engineering properties to be considered for these soils; thirdly, the major primary and secondary parameters affecting these properties and their respective correlations and finally the type of processed data to be entered and methods of determining design parameters from such data.

2 HONG KONG SOILS: THEIR FORMATION AND MAJOR TYPES

2.1 General

To be exact from a geological point of view, the earth's crust consists of various types of rock materials. Soil materials are just some special types of rock materials formed as a result of weathering or erosion

of the parent rocks or other soils. Accordingly, there are only two general soil types: weathered soils and transported soils.

2.2 Weathered soils

These are formed as a result of weathering of the parent rocks in-situ. The two major rock types in Hong Kong are 'Granite' and 'Volcanic' which were formed from the large scale volcanic activities during the Middle Jurassic period to Early Cretaceous period (these two periods being formed respectively about 210 and 140 million years ago), thus forming the volcanic rock. This is followed by intrusion of the volcanic magma, thus forming the granitic rock. It is obvious from the above processes that these two have no significant difference in mineral content. The only difference is grain size, with granite minerals being coarse sand size and volcanic minerals in the ground-mass of medium to fine silt size as a result of faster rate of cooling in the outer volcanic rock.

2.3 Transported soils

These are formed as a result of the erosion of weathered soils (or rocks) or other transported soils by various erosion agents. During this erosion process, the soil particles are detached from each other, transported and finally re-deposited again to a soil layer with compactness and particle size depending on the extent of the above processes of detachment, transportation and re-deposition. In some cases, further weathering or chemical and physical changes might also take place after re-deposition. The extent of these processes of detachment, transportation and re-deposition is, in turn dependent entirely on the type of erosion agents, thus forming different types of transported soils.

2.4 General classification

In view of the above considerations, Hong Kong soils can be further classified into the following 6 major types:

Weathered soils	(1) Completely/highly decomposed granite (C/HDG)	
	(2) Completely/highly decomposed volcanic (C/HDV)	
Transported soils	(3) Fill/colluvium in granitic areas	(4) Fill/colluvium in volcanic areas
	(5) Marine deposit (MD)	(6) Alluvial deposit (ALL)

2.5 Classification in accordance to formation process

Finally, purely from the formation process, these soils should be classified into three distinct groups: (a) weathered soil comprising mostly C/HDG and C/HDV; (b) fill/colluvium in both granitic and volcanic areas; (c) MD and ALL. Each of these three groups has a different formation process, with the first one formed from in-situ weathering of the parent rocks and the other two being transported soils formed from erosion of the weathered soils (or rocks) or other transported soils.

The erosion process for fill/colluvium in both areas is vastly different from that of MD and ALL. Firstly MD and ALL have a longer period of dislocation, transportation, sorting and re-deposition, in particular the re-deposition period. In view of the above phenomena, MD and ALL have more intensive chemical and physical changes and weathering, the only exception being some of the more recently deposited ALL.

3 ENGINEERING PROPERTIES

3.1 General considerations

In general, there are three major engineering properties: shear strength, compressibility and conductivity.

Shear strength, in classical soil mechanics, concerns the determination of shear strength parameters: angle of internal friction (ϕ) and cohesion (c). Both parameters can be expressed in term of total or

effective stresses. Compressibility in its simplest form can be represented by the SPT value in-situ, or by the consolidation testing results in the laboratory. Conductivity is represented most directly by its permeability value (k). Another parameter is the coefficient of consolidation (c_v) introduced by Terzaghi but this also measures the soil compressibility.

Of the three major engineering properties, the dominant parameter affecting them is the soil type: weathered or transported soils. In view of the very different formation processes between weathered and transported soils as well as between various transported soils, the engineering properties of different soil types can vary very substantially, in particular the conductivity property, with c_v and k varying up to ten thousand times or more, as indicated in the paper by Wong (2020a).

Another dominant primary factor is the SPT value, which will affect most importantly the shear strength. In a recent paper by Wong (2020b), it has been established that for Hong Kong soils, there is a unique relationship between soil shear strength and SPT, irrespective of the soil type. Quite unlike conductivity, the variation in term of shear strength is at most a couple of times among different soil types.

As for compressibility, the more compressible the soil, the lower is the SPT. With SPT varying from less than 1.0 for MD to over 100 for C/HDG (see Tables 2 & 3 in Wong (2020b)), the variation in the worst case scenario might be up to several hundred times. However, the above trends do not hold for conductivity. Strictly speaking, there is in general no meaningful correlation between SPT and conductivity.

Within each soil type, there are some secondary factors such as fines content (F), dry density (τ_d), etc, which can also affect the soil engineering properties. However, these effects are of a more secondary nature as evidenced by the experimental fact that two soil types with similar fines content and dry density can have quite different engineering properties. The same applies to the other secondary factors.

So far research on soil engineering properties does indicate that these are dominated by the two primary factors: soil type and SPT. Accordingly these must be firstly identified in future processing work forming the big data. These together with other secondary factors can fine-tune the engineering properties for design. For large/important jobs, some confirmatory testing might be necessary.

3.2 Soil shear strength

3.2.1 Determination by laboratory testing

It should be noted that the earlier developed laboratory testing methods are for the undrained conditions. This is not surprising as at that time the effective stress principle has not yet been proposed. It is only in the triaxial compression testing (e.g. Bishop and Hankel, 1962) that both undrained and drained conditions can be adopted. As for in-situ testing, most of them are for the undrained conditions. Table 1 summarizes the various laboratory and in-situ testing methods for determining soil shear strength.

A very vital point to note in choosing the most appropriate testing method of analysis and interpretation is the type of soil: granular or cohesive. When first applying the triaxial testing by Bishop and Hankel (1962), this is mostly for saturated cohesive clay with only a single stage testing. According to Table 1, the type of testing will be CQP_S and CD_S for measuring ϕ' and c'. As for c_u this will be measured by UU or UC. For weathered soils and fill/colluvium in both areas, UU or UC testing is basically not applicable.

In view of the fairly large sample variation for Hong Kong soils, Lumb (1964) introduced the multi-stage testing and this was later further modified by Wong (1978). Alternatively, single stage testing (e.g. Beattie and Chau, 1978) has also been proposed and in this case the "Method of Least Squares" has been adopted to determine the most appropriate shear strength parameters. Wong (1982) summarised the various then existing triaxial consolidated testing methods, comprising: CQP_M, CQP_S, CD_M and CD_S as in Table 1. He concluded that CQPM being the most feasible one with respect to both the quality of the testing results as well as for testing cost.

Regarding method of analysis, Wong (1982) recommended that for basically granular materials soil shear strength parameters should be determined from the arithmetic mean of all individual CQP_M test results, each with modification to account for the decreasing cohesion with each stage of shearing as suggested by Wong (1978). As for basically cohesive materials, the undrained cohesion is directly measured from the test results and no further analysis is required.

Table 1. Laboratory and in-situ testing methods for determining soil shear strength parameters

	Testing method commonly adopted		Drainage condition	Soil shear strength parameter determined
Laboratory	Triaxial consolidation	(1) CQP_M CQP_S CD_M CD_S	Drained and undrained	ϕ' angle of internal friction c' cohesion
	Triaxial compression	(2) UU UC	Undrained	ϕ_u undrained friction angle c_u undrained cohesion
	Vane shear test		Undrained	c_u undrained cohesion
	Shear box	Robertson, Golder, Simple shear box	Undrained	ϕ friction angle along joint surface separating 2 soil/rock blocks
		Large shear box	(3) Drained and undrained	ϕ friction angle of rockfill
In-situ	SPT (Standard Penetration Test)		Undrained	Correlating with dry density and hence ϕ' & c'
	GCO probe test			Similar to SPT but limited to fill/colluvium for only a few metres.
	Vane shear test		Normally testing under undrained condition unless testing rate reducing to required low value	c_u undrained cohesion
	CPT (Cone Penetration test)			Theoretically ϕ' and c' can be determined, but accurate measurement & interpretation being difficult in practice.
	Plate loading test			
	Pressuremeter test			
	In-situ dry density		(4) (not applicable)	Correlating with ϕ' and c'

Notes: 1. CQP = Consolidated undrained with pore pressure measurement CD = Consolidated drained
M = Multi-stage S = Single stage
2. UU = Unconsolidated undrained UC = Unconfined compression
3. Drainage condition not as well controlled as in triaxial testing.
4. Operation involving mainly sampling and always above ground water table.

Since the late 1970s to early 1980s, most of the testing and analysing works are based more or less on the above papers. In addition, there is also a trend of plotting all the triaxial test results on a combined deviator stress (q) versus effective mean normal stress (p') plot to assess the most likely soil shear strength parameters (ϕ', c') visually, in which ϕ' is related to c' by the Mohr-Coulomb criterion.

It is not until 2020 then a new method other than those previously discussed has been introduced by Wong (2020b) to analyse the numerous triaxial testing results so far collected and processed in the past few decades. In contrast to most previous methods of analysis, it is the median (ϕ', c') values instead of the mean (ϕ', c') values that will be adopted. By definition, any design line specified by the set of (ϕ', c') values will have these (ϕ', c') values as the median values if, within the range of p′ considered, the number of test points above this design line is equal (or nearly equal) to the number of test points below it.

The above new method is most suitable for application of "big data" analysis. By inputting the coordinates of the test results as well as those of a number of probable design median (ϕ', c') lines into the computor, the true median values can be determined with successive trial of different deign lines. It sould be noted that different sets of (ϕ', c') values are to be assigned to different types of soil. Different places might require different sets.

Nevertheless, before "big data" can be applied and when only a limited amount of data is involved, the manual fitting method as proposed by Wong (2020b) can be adopted.

There are certain distinct advantages of this new method:

(1) It is simple to use as no advance statistical analysis is involved and it also avoids the problem of the results being affected by a few extraordinarily high values.

(2) The triaxial test results together with the design envelope provide a very good visual view and hence more engineering judgement can be carried out. Moreover, if a conservative design

is necessary, the number of test points above the proposed design line can be increased to say 60% or more of the total number.

(3) It takes into account the effect of ground condition on shear strength by introducing the p′ term as one of the soil shear strength parameters. Only with p′ and (ϕ', c') together, it is possible to estimate the soil shear strength at any site location, as discussed in details in Wong (2020b). The above paper also point out a very vital issue that (ϕ', c') are just shear strength parameters. Accordingly, any location with a lower p′ but higher (ϕ', c') does not necessarily have a higher shear strength than the location with higher p′ but lower (ϕ', c').

3.2.2 Determination by in-situ testing

To determine the soil shear strength in-situ will be much more involved. In theory according to Table 1, CPT, plate loading and pressuremeter can yield drained values (ϕ' and c') as well as undrained values. However in practice, measurement and interpretation of in-situ results will be extremely difficult, if not impossible. Moreover, some of these tests have high operating cost (e.g. plate loading), some difficult to mobilize to site (e.g. CPT) and some difficult to perform (e.g. pressuremeter)

An obvious choice is the SPT as this test is not only simple to operate in practically all soil types both above and below groundwater table. Moreover, the equipment required is relatively simple, rugged and permits frequent test. Lastly but not least, SPT can be correlated to the majority of the engineering properties, including shear strength and deformation characteristics.

Table 2 (which is basically reproduced from Table 6 and 7 of Wong 2020b) summarizes the effect of soil type on SPT, dry density and shear strength parameters. This table also demonstrates that with the same increase in dry density, weathered soil has a much larger increase in shear strength than fill/ colluvium. Moreover, for SPT value of the same order, the average shear strength is also of the same order, irrespective of the type of soil, which in this case is weathered soils and fill/colluvium.

Table 2: Variation of average soil shear strength with SPT for various soil types based on median (ϕ', c') values from Table 6 of Wong (2020b)

Soil type	SPT (In-situ dry density, Mg/m^3)	Median (ϕ′, c') values (ϕ' in degree & c' in kPa)	*Average soil shear strength kPa
Fill/ colluvium	3 – 6 (1.20 – 1.40)	34, 3	87.31
	6 – 12 (1.40 – 1.60)	35, 4	91.52
	12 – 24 (1.60 – 1.75)	36, 5	95.81
	24 – 42 (1.75 – 2.00)	38, 7	104.67
C/HDG	3 – 6 (1.20 – 1.40)	36, 5	95.82
	6 – 12 (1.40 – 1.60)	38.5, 6.5	105.93
	12 – 24 (1.60 – 1.75)	42, 9	121.35
	24 – 42 (1.75 – 2.00)	45, 10	135.00

* Average soil shear strength = Average mean effective normal stress x tan ϕ′ + c'
Average mean effective normal stress for p′ ranging from 0 to 250 MPa = (250 + 0)/2 = 125 MPa ,
(ϕ′, c') are median (ϕ', c') values for various SPT ranges as given in Table 6 of Wong (2020b)

3.3 Soil compressibility

3.3.1 Types of compressibility parameter and their respective definition

Soil compressibility parameters are normally defined in accordance with the testing conditions and there are the following three major types (see Head, 1986):

(1) Anisotropic stress condition defining the Young's modulus (E). This is commonly referred to as elastic modulus. In this anisotropic case E is just defined as

$E = (\delta\sigma_z - \delta\sigma_c)/\ \delta\varepsilon_z$ with σ_z = Vertical stress
σ_c = All round lateral stress
$\delta\varepsilon_z = \delta z/z$
z = Depth of specimen
or $E = \delta\sigma z/\delta\varepsilon z$ when $\delta\sigma_c = 0$

(2) Isotropic stress condition defining the bulk modulus (B). In this isotropic case in which an all round equal pressure δp is applied, B is defined as

$B = \delta p/\delta\varepsilon v$ with $\delta\varepsilon_V = \delta V/V$

V = Volume of specimen

In soils, however, it is the reciprocal of B that is commonly used,

$m_v = 1/B = \delta\varepsilon_v/\delta p$

and m_v is termed as coefficient of volume compressibility.

(3) Rigid lateral boundary condition defining the constrained modulus (D). In this case, only a vertical stress is applied and the lateral boundary is so rigid that there is no lateral deformation, thus yielding

$D = \delta p/(\delta h/h)$ with h = depth of specimen

In soils, it is again the reciprocal of D that is commonly used, and this is also termed as coefficient of volume compressibility

mv = 1/D

Nevertheless, it should be noted that with the lateral boundary fixed in this case, the vertical stress (p) applied in the later stages will be very high. Accordingly, a semi-log plot of void ratio (e) versus $\log_{10}$ p is normally adopted so that a new compressibility parameter termed: Compression Index, C_c, is introduced and this is defined as

$C_c = \delta e/\delta \log_{10} p$

In spite of the fact that 1/B and 1/D are both termed as coefficient of volume compressibility, it should be noted that these two terms are quite different as the testing conditions are also quite different. The relationship between the various mv compressibility parameters so far introduced has been further discussed in Wong (2020a).

3.3.2 Practical considerations and applications

So far the following compressibility parameters: E, B, m_v , D & C_c have been introduced and these are as summarised in Table 3.

Table 3. Compressibility parameters under different testing conditions

<table>
<tr><th>Testing Condition</th><th>Compressibility Parameter</th><th>Assumptions Required</th><th>Applications</th><th colspan="2">Testing method</th></tr>
<tr><td>Anisotropic stress Condition</td><td>Elastic modulus,
$E = \delta\sigma Z/\delta\varepsilon z$</td><td>Linear elastic normally required</td><td>Cases in which loading area small comparing with thickness of compressible layer</td><td rowspan="2">Triaxial consolidated compression testing, either one of the following:
CQPM CQPS
CDM CDS</td><td>Shearing stage</td></tr>
<tr><td rowspan="2">Isotropic stress condition</td><td>Bulk modulus
$B = \delta p/(\delta V/V)$</td><td rowspan="2">Not necessary required to be linear elastic</td><td rowspan="2">Practically no application in practice</td><td rowspan="2">Triaxial consolidation Stage</td></tr>
<tr><td>Coefficient of volume compressibility
$m_v = 1/B$</td></tr>
<tr><td rowspan="3">Rigid lateral boundary condition</td><td>Constrained modulus
$D = \delta p/(\delta h/h)$</td><td rowspan="3">Not necessary required to be linear elastic</td><td rowspan="3">Cases in which loading area large comparing with thickness of compressible layer</td><td colspan="2" rowspan="3">Oedometer testing</td></tr>
<tr><td>Coefficient of volume compressibility
$m_v = 1/D$</td></tr>
<tr><td>Compression index
$C_c = \delta e/\delta \log_{10} p$</td></tr>
</table>

Moreover, it can be seen that these parameters can be measured in practice as follows:

(1) E is equal to the slope of the deviator stress versus axial strain curve in the shearing stage of the triaxial consolidated compression test, either the tangent modulus (E_t) or secant modulus can be determined. In this case, the anisotropic stress condition applies.

(2) B can be determined from the triaxial consolidation stage of triaxial consolidated compression test and this is an isotropic stress condition, m_v being the slope of the volumetric strain versus consolidation pressure curve. Nevertheless, such loading condition can rarely happen in practice.

(3) D (or m_v) is equal to the slope of the vertical strain versus p curve and C_c is equal to the slope of the void ratio versus $\log_{10}$ p curve. It should be noted that both C_c and m_v have been determined from the same test and the difference is only because of the method of calculation. Moreover, C_c and mv are not necessarily for linear elastic materials. .

(4) As for in-situ testing, the most useful one is SPT. The other in-situ tests as in Table 1 in theory can provide the information for compressibility. However, those data have not yet been well documented, thus limiting their application. In practice, it is obvious from Table 3 that only the two parameters (E and C_c) are useful for engineering design, normally E for granular soils and C_c for the more cohesive ones. Moreover, the assumptions required and testing restraints for E and SPT are basically similar. Accordingly, E can be assumed to be proportional to SPT. In fact this is the current Hong Kong empirical design practice of assuming E (in Mpa) equal to SPT value. With consistency being an indication of its compressibility, the above assumption can be further justified in Table 4 which summarizes the classification of transported and weathered soils of different consistency.

Table 4. Classification of transported and weathered soils in accordance to SPT
(based on Table 4 of Wong, 2020b)

Dry density	Transported soil			Weathered soil		
	Soil Consistency	Soil type (1)	SPT (2)	Soil consistency	Weathered state	SPT (2)
< 0.8 0.8 – 1.2	Very soft Soft to very soft	MC MC, M-sandy clay M-clayey sand	N ≤ 1 1 < N ≤ 3	–	–	–
1.2 – 1.4	Medium firm or loose	ALL-C, MS, F ALL-Sandy clay	3 < N ≤ 6	Very loose to loose	Grade VI to Grade V	8 < N ≤ 20
1.4 – 1.6	Stiff to very stiff or medium	ALL-C, MS ALL-Clayey sand,	6 < N ≤ 12	Medium dense	Grade V	20 < N ≤ 50
1.6 – 1.75	dense	F, Re coll, CF	12 < N ≤ 24	Dense	Grade V to Grade IV	50 < N ≤ 100
1.75 – 2.0	Hard or dense	Old coll, MS, ALL-sand, CF	24 < N ≤ 42	Very dense	Grade IV	100 < N ≤ 200 (3)
> 2.0	Very dense	CF	42 < N			

Notes: 1. MC = Marine clay, M-sandy clay = Marine sandy clay, M-clayey sand – Marine clayey sand, MS = Marine sand; ALL-C = Alluvial clay, ALL-sandy clay = Alluvial sandy clay, ALL-clayey sand = Alluvial clayey sand, ALL-S = Alluvial sand; F = Normal filling without compaction except by its own weight, CF = Compacted fill; Re coll = Recent colluvium, Old coll = Old (or ancient) colluvium
2. SPT value corrected as in Skempton (1986).
3. Max SPT measurable is normally limited to 200.

The following special features can be observed:

(1) Firstly all transported soils (fill/colluvium in both areas, MD and ALL) can be further sub-divided as in Note (1) of Table 4.

(2) Weathered soils comprise mostly C/HDG and C/HDV and their respective classification is based only on the weathering state as the difference in engineering properties between these soils is not significant.

(3) The SPT value provides a more quantitative indication of the soil compressibility than such descriptive terms as loose, dense and hard, etc. From this table, SPT is related to compressibility.

As for C_c, this in theory can be applied to both granular and cohesive materials when the loading area is large in comparison with the thickness of the compressible layer. However, in practice, this is normally only applied to the more cohesive materials. From a detailed study of the marine and alluvial deposits in Hong Kong, Wong (1993) reckons that as far as Hong Kong soils are concerned, there is no correlation whatsoever between C_c and Atterberg limits. On the other hand, C_c is closely related to a parameter: corrected initial void ratio ($\hat{e}_o$), which is obtained by projecting the loading $\log_{10}$ p versus eo curve to cut the vertical line p = 10 kPa, the ordinate of this intersection point being the $\hat{e}_o$. Moreover, êo. can be estimated from e_o which can be quite simply calculated from a knowledge of water content (w) and particle density (G) of MD or ALL. Accordingly, the compression index (C_c) for these soils can be easily estimated.

3.4 Soil conductivity

3.4.1 Theoretical background

There are two types of hydraulic properties: coefficient of consolidation (c_v) and permeability (k). These can be measured indirectly at the same time in the laboratory either by oedometer testing or the consolidation stage of a triaxial consolidated compression test. The major difference between these two parameters is that c_v is a lumped parameter introduced by Terzaghi (1943) in deriving his one-dimensional consolidation theory whilst k is a parameter measuring directly the soil resistance to fluid (usually water) flow.

Theoretically speaking k is defined from the Law of Darcy (1856) for laminar flow, applying to any viscous fluid flow through any material under any temperature. This is related to an intrinsic (or absolute or specific) permeability K (in m^2) usually adopted in such fields as soil science and agriculture as follows:

$k = K g\gamma_w / \mu$ where g = Acceleration due to gravity (m/s^2)
γ_w = Water unit weight (kN/m^3)
μ = Dynamic viscosity ($kN\ m^{-1}s^{-1}$)

For most practical engineering problems, the definition adopted by Tschebotarioff (1973) is most useful: k of a soil is defined as the imaginarily average velocity of flow which will occur under the action of a hydraulic gradient of unity through the total cross-sectional area (voids + solids) of the soil..

On the other hand, c_v is just a derived parameter calculated from Terzaghi's consolidation equation:

$k = (\gamma_w)\ c_v\ m_v$ with c_v = Coefficient of consolidation (m^2/s)
m_w = Soil compressibility (m^2/kN).

It should be noted that quite unlike c_v, k can also be measured directly in the laboratory as well as in-situ, both being based on Darcy's Law. The equations for calculating k is fairly simple and detailed description being given in Section 10 of Head (1986). In case of in-situ testing, as the normal practice is to measure from a porous section in a vertical borehole, the measured k value will be affected quite considerably by the size and location of this porous section relative to the various soil/rock strata as well as the direction of flow.

3.4.2 Testing results

The test results processed in the past years are as indicated in Tables 5 and 6, with Table 5 summarizing the cv and k results for various major soil types for IC testing and Table 6 for in-situ k values. It should be noted that the measurement of cv in-situ is difficult, if not impossible. The same applies to measurement of k in-situ for MD and ALL as the testing time will be extremely long in view of their very low permeability.

Table 5: Consolidation coefficient, c_v and permeability, k determined by IC (isotropic consolidation in a triaxial cell) for various soil types

Soil type		Coefficient of consolidation, c_v (m^2/year)				Permeability, k (m/s)			
		No of test Results[1]	$(c_v)_{50}$	$(c_v)_{10}$ – $(c_v)_{90}$	[2]Dev c_v	No of test Results[1]	$(k)_{50}$	$(k)_{10}$ – $(k)_{90}$	[2]Dev k
C/HDG		509	13400	1160 – 43000	1.569	509	$9.25x10^{-7}$	$8.70x10^{-8}$ – $3.58x10^{-6}$	1.614
C/HDV		375	8450	614 – 39700	1.811	337	$4.10x10^{-7}$	$5.10x10^{-8}$ – $2.45x10^{-6}$	1.682
Fill/Coll Granitic areas		228	2399	111 – 30200	2.434	227	$3.92x10^{-7}$	$1.64x10^{-8}$ – $3.29x10^{-6}$	2.301
Fill/Coll Volcanic areas		159	2380	95 – 37000	2.590	185	$2.94x10^{-7}$	9.6510^{-9} – $3.55x10^{-6}$	2.565
MD	F > 20%	114	0.910	0.238 – 3.780	1.200	74	$1.82\ x10^{-10}$	$2.18x10^{-11}$ $8.20x10^{-10}$	1.593
ALL	F > 20%	104	1.220	0.470 – 9.700	1.315	70	$9.05\ x10^{-11}$	$2.28x10^{-11}$– $6.35x10^{-10}$	1.445
MD	F < 20%	24	3680	71.0 – 20000	2.450	18	$1.19\ x10^{-7}$	$8.65x10^{-9}$ $7.35x10^{-7}$	1.929
ALL	F < 20%		(too few test results for meaningful analysis)						

Notes: 1. Test results being from single & multi-stage triaxial testing, each stage representing one test result
2. Dev $(c_v) = \log_{10}\{(c_v)_{90}/(c_v)_{10}\}$ and Dev $(k) = \log_{10}\{(k)_{90}/(k)_{10}\}$

Table 6. Variation of median k, interdecile range of k and its deviation with SPT for various soil types as determined by various types of in-situ testing

Soil type	(1) No of test results	SPT range	Median k (m/s)	Interdecile range of k (m/s)	(2)Dev k
C/HDG	12 (10 FH + 2 RH)	< 20	8.50×10^{-7}	2.24×10^{-7} – 2.76×10^{-5}	2.091
	38 (30 FH + 8 RH)	20 – 50	1.15×10^{-6}	1.33×10^{-7} – 2.98×10^{-5}	2.350
	20 (20 FH + 3 RH)	50 – 100	2.00×10^{-6}	3.82×10^{-7} – 2.00×10^{-5}	1.719
	33 (24 FH + 9 RH)	> 100	1.15×10^{-6}	1.72×10^{-7} – 1.66×10^{-5}	1.985
	24 FH	> 100	1.00×10^{-6}	1.33×10^{-7} – 9.20×10^{-6}	1.840
	9 RH	> 100	1.12×10^{-6}	3.01×10^{-7} – 2.11×10^{-5}	1.846
	103 (81 FH + 22 RH)	< 20 to > 100	1.12×10^{-6}	1.88×10^{-7} – 1.92×10^{-5}	2.028
	81 FH	< 20 to > 100	1.02×10^{-6}	1.50×10^{-7} – 1.24×10^{-5}	1.917
	22 RH	< 20 to > 100	1.49×10^{-6}	3.94×10^{-7} – 3.50×10^{-5}	1.949
C/HDV	10 FH	< 20 to < 50	7.62×10^{-7}	5.00×10^{-8} – 2.00×10^{-6}	1.602
	18 FH	50 to > 100	1.33×10^{-6}	1.76×10^{-7} – 3.84×10^{-5}	2.339
	28 FH	< 20 to > 100	1.00×10^{-6}	8.80×10^{-8} – 3.65×10^{-6}	1.618
Fill/ colluvium	9 (8 FH + 1 RH)	< 6	5.62×10^{-6}	4.62×10^{-7} – 2.22×10^{-5}	1.682
	10 (7 FH + 2 RH+ 1 CH)	6 to 24	6.35×10^{-6}	3.20×10^{-7} – 5.00×10^{-5}	2.194
	22 (17FH+ 3 RH+ 2 CH)	<6 to > 24	5.00×10^{-6}	3.34×10^{-7} – 2.93×10^{-5}	1.943

Notes: 1. No. of test results is the summation of the following different test types
FH – Falling Head test, RH – Rising Head test and CH – Constant Head test
2. Dev (k) = $\log_{10}\{k_{90}/k_{10}\}$

Moreover, the following special features can be observed from these test results. Firstly, soil type has a dominant effect on the c_v and k values. In moving from MD and ALL to weathered soils, the increase in c_v and k can be up to ten thousand times or more. This is considerably larger than the variation within the same soil type as indicated by their respective dev (c_v) and dev (k) values.

It should be noted that as oedomer testing tends to under-estimate the c_v and k results for the more granular soils (see Wong, 2017), it follows that such results should be excluded in the future big data analysis.

4 METHODS OF DATA PROCESSING FOR APPLICATION OF "BIG DATA"

4.1 General considerations

As far as soil engineering properties are concerned, it is soil type classified in accordance to the formation process that is most vital. According to this classification, there are only three groups: (1) weathered soil (mostly C/HDG or C/HDV), (2) fill/colluvium in granitic or volcanic areas and (3) MD or ALL. This is quite different from classical soil mechanics in which fines content (F) and in-situ dry density (τ_d) are the controlling parameters affecting the soil engineering properties. As demonstrated by the test results in Wong (2020a), two soil types with similar F and τ_d can have their c_v and k values differing by more than thousand times. The same applies to the SPT values, but only at a lesser degree as demonstrated by Table 4.

4.2 Specific guidelines

In order that the data can be useful for big data applications, the following major guidelines have to be followed in the processing works.

Firstly, for every set of data with engineering properties, the soil type must be firstly identified as there is usually a tremendous difference between various soil types, in particular the conductivity parameters. For future use, soil type should be entered in the more specific pattern as follows;

(1) Weathered soil – C//HDG; Weathered soil – C//HDV; Weathered soil – (other weathered soil, e.g. granodiorite).

(2) Fill/colluvium – granitic area; Fill/colluvium – volcanic area; Fill/colluvium – (other unidentified areas).

(3) MD – Marine clay; MD – Marine sandy clay; MD – Marine clayey sand; MD – Marine sand.

(4) ALL – Alluvial clay; ALL – Alluvial sandy clay; ALL –Alluvial clayey sand; ALL – Alluvial sand.

Secondly, SPT might not be present in every set of soil data. This should be entered together with soil type, overburden depth and dry density range (should there be any). The location where each sample was taken should also be entered as this basically serves as a more secondary role to define the soil type and is useful when soil type was not identified in the original description.

Finally, other more secondary data to be entered comprises the following items: sampling date (d/m/y), testing date (d/m/y), sample depth (m), depth at which sample tested (m), etc.

4.3 Data entering for soil shear strength determination

As proposed in the recent paper by Wong (2020b), shear strength can be determined from either the data of (1) triaxial testing or (2) in-situ testing or by both. For data entering, there are two major types of data: (1) primary data and (2) secondary data.

(1) Primary data
For triaxial testing, this is q versus p' in CQPM/CQPS/CDM/CDS test at the critical state, in which $q = (\sigma_1 - \sigma_3)/2$, $p' = (\sigma_1' + \sigma_2' + \sigma_3')/3$ or $(\sigma_1' + \sigma_3')/2$ and the critical state is at which (σ_1'/σ_3') equal to a maximum. For multi-stage testing (CQP_M and CD_M), the specific stage number must be identified. In case of SPT, this must be identified if it is either below or above an in-situ sample in which triaxial testing has been carried out.

(2) Secondary data
Each set of primary data must be accompanied by the secondary data listed as follows. Secondary data are basically for identifying the respective samples in which shear strength testing (triaxial or SPT) has been carried out. These should be in the following sequence: Sample location, Date of testing, Hole No, Sample No, Sample depth, Fines content, In-situ dry density, testing laboratory and any other data relevant .to the specific data set.

4.4 Data entering for soil compressibility determination

In case of in-situ testing for each soil, collect the SPT and the τ_d value (should there be any). As a preliminary design the elastic modulus is assumed to be directly proportional to the SPT. In case of laboratory testing, it is only E and C_c that will be useful in practical engineering design. The B value will not be considered as an isotrpic case has no practical application. As for the D value, this derives from the same set of test results as C_c. However, the latter is more adaptable to mathematical evaluation. As in soil shear strength, the primary data and secondary data have to be entered. For E determination, enter the set of $(\sigma_z - \sigma_c)$ versus ε_z values for each σ_c value together with the F and τ_d values. For each set of data, the average E as in Section 3.3.1 (1) together with σ_c must be entered.

To determine C_c, the void ratio (e_o) versus $\log_{10}p$ values have to be entered for each oedometer test. In addition, the F and e_o of the in-situ sample have also to be entered. An alternative approach when no ooedomster testing is available is to estimate the corrected initial void ratio ($\hat{e}_o$.) from the water content (w) and particle density (G) values as proposed by Wong (1993). By assuming $\hat{e}_o$ to be approximately equal to e_o, a correlation between C_c and $\hat{e}_o$ can be established from the empirical relationship proposed in the above paper: for MD, $C_c = 0.39(\hat{e}_o - 0.4)$ and for ALL, $C_c = 0.325(\hat{e}_o - 0.3)$.

4.5 Data entering for soil conductivity

The most vital data to enter is soil type, then fines content (F) and finally in-situ dry density (τ_d). Unlike shear strength and compressibility, SPT is basically not required. A very special feature is that k for engineering design is normally measured in-situ. Moreover, for each soil type c_v and k appear to be not related to such parameters as F and τ_d , except in the case of MD and ALL. For these two soil types, c_v and k increase quite considerably for F < 20%. In entering in-situ k values, the types of additional data to be entered comprise: location and depth of testing, testing type (FH/RH/CH), soil layering (if any) and other special features relating to the particular site.

On e final vital point to note is that for design in soil types other than MD/ALL, it is normally the design for drainage in which only the in-situ k is required. The design for consolidation settlement as in MD/ALL is not applicable. In he latter case, it is the cv value that is controlling.

5 METHODS OF DETERMINING SOIL DESIGN PARAMETERS

5.1 General considerations

In order to evaluate the required design parameters (e.g. ϕ', c') from the original data processed, certain programmes are required to be keyed in first, as listed below. Moreover, these are required to be updated from time to time with the rapid development of modern technology.

5.2 Shear strength design parameters

The following two programmes are required: (1) for determining the (ϕ', c') from the p' – q data for p' within a certain range and (2) for correlating between average soil shear strength and SPT for a certain range of p'.

5.3 Compressibility parameters

Programmes are required for determining E and C_c To determine E, a programme for evaluating E from a set of ($\sigma_z - \sigma_c$) versus ε_z values within a certain range of σ_c, and another one for correlating the E value thus obtained with SPT.

For C_c, a programme based on the paper by Wong (1993) is required to calculate the C_c and hence the ($\hat{e}_o$) value for each set of oedometer testing. In case oedometer testing is not available, the programme can also provide an estimate of the ($\hat{e}_o$) value from the water content and particle density of the soil.

5.4 Conductivity parameters

In considering the conductivity parameters, a programme is required to be keyed in so as to list the c_v, k as well as the F and τ_d values of laboratory testing carried out within a certain specified area. The median and interdecile range of c_v and k values are then evaluated for each soil type within a certain range of F and τ_d values. The same operation can be applied for in-situ k values.

Nevertheless, the following special features should be taken into consideration. Firstly, because of the very permeable nature, c_v is practically not required for design for weathered soils and fill/colluvium. On the other hand, the very impermeable nature of MD/ALL also render their k values not useful in design. Secondly, the k value for design must be determined in-situ as the presence of local voids cannot be reproduced in the laboratory and these would have tremendous effect on the k value. Accordingly, the median and interdecile range of in-situ k values thus obtained are for reference only. Finally, except for MD/ALL with F < 20%, the effect of such secondary parameters as F and dry density is relatively insignificant in comparison with the effect of soil type.

6 CONCLUSIONS

The data processed in the past few decades has demonstrated quite conclusively that the major engineering properties are dominated by two primary parameters: soil type and SPT, in particular

soil type classified in accordance to the formation process. With this classification, Hong Kong soils are divided into three major groups: weathered soil, fill/colluvium and MD/ALL. Another important parameter is SPT.

The relative importance of these two parameters does vary. There is a tremendous increase up to ten thousand times or more for conductivity in moving from MD/ALL to weathered soils, but the effect of SPT is not to such an extent. For shear strength and compressibility, the effect of these two parameters is somewhat less significant. In both cases, the effect of in-situ dry density (τ_d) also plays a fairly important secondary role. Within each soil type, shear strength will increase but compressibility decrease with the increase in τ_d. However, in moving from one soil type to another, the above trend no longer holds. For example as indicated in Table 2, in moving from fill/volluvium to weathered soil, a higher τ_d sample in the former group might not necessarily have a higher shear strength than the one with a lower τ_d in the latter group. In general, the correlation between SPT and shear strength or as in Table 4 between SPT and compressibility is irrespective of soil type. It should be noted that as far as Hong Kong soils are concerned, this type of soil is weathered soils and fill/colluvium for shear strength and this includes MD/ALL for compressibility.

So far this paper has only outlined the basic principles for application of "big data" by identifying the major soil engineering properties for design and the major primary and secondary parameters affecting them. In order to ensure the usefulness of such data, this must be re-processed in a more orderly manner as proposed. Moreover, to obtain the required parameters for design, programmes must be keyed in to perform such operations.

Finally it must be pointed out that this paper has been dealing exclusively with soil materials (weathering state Grade IV to VI as in Table 4), not rock materials (weathering state Grade I to III). Nevertheless, as far as normal civil engineering works are concerned, it is the conductivity parameter that is most vital, then shear shear strength in case of rock slope and tunnelling. Moreover, laboratory testing is usually not required.

ACKNOWLEDGEMENTS

Lastly but not least, the author should like to thank his former colleagues in the Architectural Services Dept of HKSAR: Mr K L Wong and Mr K L Li for their useful and sometimes enlightening discussions.

REFERENCES

Beattie, A A and Chow, E P Y (1976), The assessment of landslide potential with recommendations for future research. Journal of Hong Kong Institution of Engineers, Vol 4, No 1, pp 27 – 44.

Bishop, A W and Hankel, D J (1962), The Measurement of Soil Properties in the Triaxial Cell (London : Edward Arnold Ltd, Second Edition).

Darcy, H P G (1856). Les fontaines publiques de la vilk deDijon, Paris Victor Dalmont, Editeur, pp 570, 590, 594.

Head, K H (1986), Manual of Soil Laboratory Testing, Volume 3, Effective Stress Tests (New York : Halsted Press).

Lumb, P (1964), The multi-stage testing of Hong Kong soils. Civil Engineering and Public Works Review.

Skempton, A W (1986), Standard penetration test procedures and the effects in sands of overburden pressure, relative density, particle size, ageing and over consolidation. Geotechnique, Vol.36, No. 3, pp 425-447,

Terzaghi, K (1943), Theoretical Soil Mechanics. (New York, John Wiley and Sons).

Tschabotarioff, G P (1973). Soil Mechanics, Foundations and Earth Structures. (2nd edition, McGraw Hill, New York).

Wong, H Y (1978). Soil Strength parameter determination. Journal of Hong Kong Institution of Engineers, Vol 6, No 6, pp 37-49.

Wong, H Y (1982). An evaluation of various methods of triaxxial testing testing analysis for residual soils in Hong Kong. Proceedings of the Seventh Southeast Asian Geotechnical Conference, Hong Kong, Vol 1, pp 901-913.

Wong, H Y (1993). Compression index from simple site operation and simple laboratory testing for some of the Hong Kong soils. International Conference on Soft Soil Engineering, Guangzhou, China.

Wong, H Y (2017). Limitation of measuring cv by oedometer in Hong Kong granitic soils. Proceedings of the Institution of Civil Engineering, Volume 170, Issue GE 1, pp 84-92.

Wong, H Y (2020a). Representative consolidation coefficient values in HK soils. Proceedings of Institution of Civil Engineers, Geotechnical Engineering, http://doi.org/10.1680/jgeen.18.00228.

Wong H Y (2020b). Shear strength properties of Hong Kong soils for slope stability. Institution of Engineering Transactions, Vol. 27, Issue 1, pp 48 – 54.

Effectiveness of Cross-Walls in Reducing Wall Deflections in Deep Excavations

L.W. Wong
Formerly Moh and Associates, Inc., Taipei

R.N. Hwang
Moh and Associates, Inc., Taipei

ABSTRACT

Three cross-walls were installed to brace the diaphragm walls prior to excavation for a cross-over tunnel of the Taipei Metro in front of the South Gate of the old Taipei City and has now been a National Heritage. The tunnel had the maximum excavation depth of 20.1 m. Three-dimensional finite element analyses have been performed to evaluate the effectiveness and the influence of the cross-walls in reducing the wall deflections. The nonlinear Hardening-Soil model has been adopted in the analyses. The results of the analyses indicate that the maximum wall deflections are much reduced as a result and the effectiveness of cross-walls is thus proved.

1 INTRODUCTION

Cross-walls is common construction method for protecting structures adjacent to deep excavations. Eide et al. (1972) developed the concept for improving bottom heave stability and limiting displacements in deep excavations using diaphragm walls to act as cross-walls below the final excavation level. Karlsrud and Andresen (2008) reported 4 case histories on using cross-walls to reduce displacements for excavation in soft normally consolidation Oslo clay. Ou et al. (2006) reported the use of cross-walls to reduce the displacements for a 32.5 m deep excavation in soft clay in Taipei. Although these case histories show that cross-walls are very effective in reducing lateral displacements of diaphragm wall, the design methodology has not been fully developed.

Presented herein is a study of the effectiveness of cross-walls in reducing the deflections of the diaphragm walls to reduce the potential damages to a historical monument, i.e., Lizhenmen, refer to Figure 1, which is the South Gate (the Gate, hereinafter) of the old Taipei City built in Ching Dynasty in 1884. The Gate was designated as a Class I heritage of the City in 1998. Since it is close to the excavation for constructing a cross-over tunnel of the Taipei Metro, three cross-walls were installed prior to the commencement of excavation to reduce the movements of the diaphragm walls.

While the 3 cross-walls are deployed symmetrically against the central axis of the Gate, two-dimensional (2D) finite element analysis could be conducted along the axis of the Gate to study the effectiveness of the cross-walls. The equivalent stiffness values for the soil and the cross-wall materials could be adopted to study the effects to wall deflections and to compare the performance with and without cross-walls. However, since the 2D model assumes that the cross-walls extend infinitely along the longitudinal direction, it could not analysis the variation in wall deflections with the distances to the cross-walls, nor to assess the wall deflections between 2 cross-walls. In order to study the influence of the cross-walls, the three-dimensional (3D) finite element analyses have been conducted in this study.

As soils are nonlinear materials, the Hardening-Soil (HS) constitutive model is adopted to simulate

Figure 1: Lizhengmen, South Gate of Old Taipei City

the non-linear stress-strain relationships of soils. The various parameters for the HS model are calibrated against the deflection profiles observed in Inclinometer SID-6, which is located far away from the end walls or from the cross-walls so that the 2D analysis could be adopted. The set of calibrated parameters is then applied for the 3D analysis for the cross-walls. The 3D analyzed deflection profiles are compared with those observed in 2 inclinometers, namely, SID-2 and SID-3 for validation. Since these inclinometers were installed to the same depths as the diaphragm walls, their readings were duly corrected to account for the movements at the wall toes.

2 CASE STUDIED

2.1 Cross-over tunnel

The cross-over tunnel, refer to Figure 2, running between Xiaonanmen Station and Chiang Kai Shek (CKS) Memorial Hall Station of the Taipei Metro, was constructed by using the cut-and-cover method. The length of the tunnel is 397 m and the widths of the tunnel vary from 13 m to 8 m. The depths of excavations increase from 16.5 m at the west end to 21.7 m at the east end. This section of the route could be considered as free-field for evaluating the influences of various parameters on wall deflections because there are only a few low-rise structures in the vicinity of the excavation with one-level basements under some of them. Therefore, wall deflections are in general unaffected by the presence of adjacent structures. As such, the readings obtained by Inclinometer SID-6, which is 210 m from the Gate, can be used to compare with the results obtained in the free-field analyses for calibrating the soil parameters adopted.

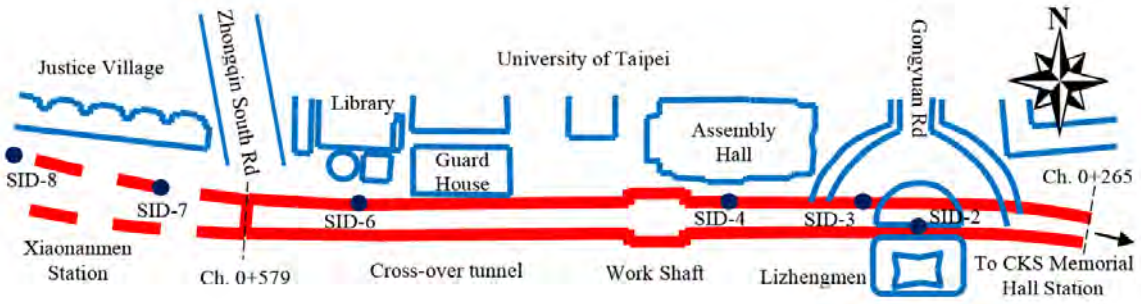

Figure 2: The cross-over between Xiaonanmen Station and Chiang Kai Shek Memorial Hall Station

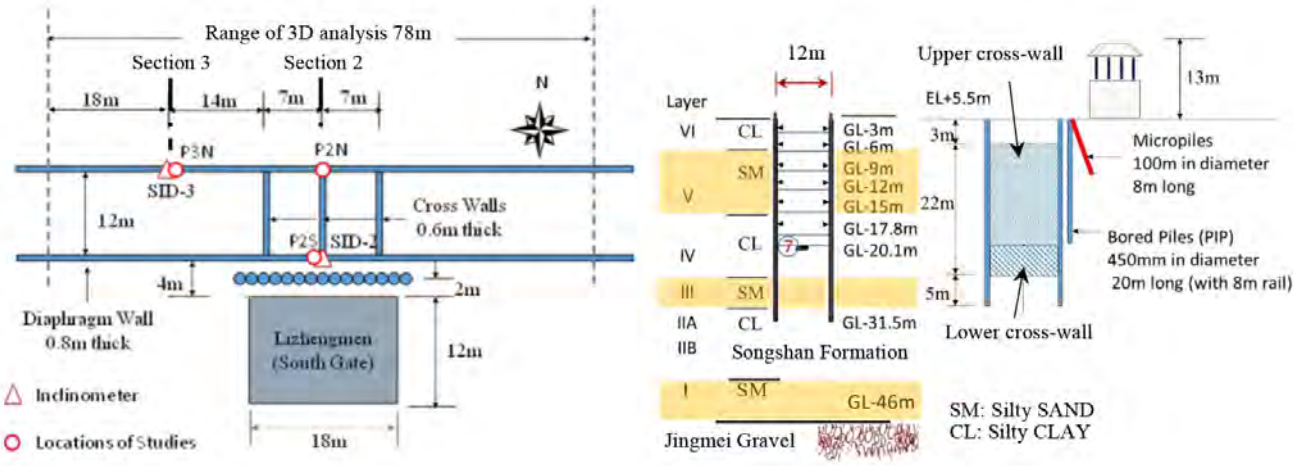

Figure 3: Layout and cross-section of the cross-walls for protecting Lizhenmen and locations of interest

Near the Gate, the excavation was carried out to a maximum depth of 20.1 m in 7 stages. The pit was retained by diaphragm walls of 0.8 m in thickness with the depths varying from 30 m to 32 m. The walls were braced by 6 levels of steel struts spaced at 3 m intervals. The un-reinforced cross-walls were built by the diaphragm walling technique along the transverse direction of the tunnel. Since the influences of the Gate and the cross-walls on the wall deflections are the main theme of the current study, the 3D analyses performed are limited to a section of the route of 78 m in length as depicted in Figure 3. It is considered that the influence of the excavation is approximately 1.5 times the excavation depth in the T2 Zone. The lateral extent of the numerical model along the east-west direction is taken as 30 m from each side of the Gate of 18 m in width. Along the north-south direction, the lateral extent is taken as 34 m each side from the excavation trench of 12 m in width. The model therefore has the dimension of 78 m by 80 m. Figure 9 depicted the western half of the 3D finite element model.

The readings obtained by Inclinometer SID-2 in front of the Gate are of primary interest and are compared with the results of the 3D analyses at the corresponding location, i.e., P2S. The results of the analyses obtained at Location P3N are also compared with the readings obtained by Inclinometer SID-3 to assess the influence of the cross-walls.

2.2 Ground conditions

This section of the tunnel route is located in the T2 Zone (MAA 1987; Lee 1996) in the central Taipei Basin. As depicted in the cross-section in Figure 3, the Songshan Formation at the surface comprises six alternating sand (SM) and clay (CL) layers i.e., sublayers I, III and V of sandy soils and sublayers II, IV and VI of clayey soils. Underlying the Songshan Formation is a water-rich gravelly (GM) stratum, i.e., the so-called Jingmei Formation. The properties of the six sublayers in the Songshan Formation have been well discussed in literatures (Moh and Ou 1979; MAA 1987).

The piezometric levels in the Jingmei Formation were lowered to a level near the bottom of the Songshan Formation in the 1970s due to excessive extraction of groundwater as the sole water supply for the city, leading to significant reductions of water pressures in the Songshan Formation and substantial ground settlements as a result. The piezometric levels in the Jingmei Formation did not recover till the mid-1970s although pumping had been banned since 1968. The subsoils in the Songshan Formation in the central city area are thus substantially over-consolidated. This is particularly true for the clayey sublayer II because the underlying sandy sublayer I is so permeable that the piezometric level in sublayer I essentially dropped by the same magnitudes as those in the Jingmei Formation.

An advanced study was conducted by Geotechnical Engineering Specialty Consultant engaged by the Department of Rapid Transit Systems of Taipei City Government in the very early stage of the metro construction. The Designated Task studied the characteristics of the soils in the Taipei basin to provide the basic information for the design and construction of metro facilities (Chin et al. 1994; Chin and Liu 1997). Soil samples of high quality were obtained and tested under stringent supervision. Hwang et al. (2013) summarized the results of the study and suggested Figure 4 be adopted for estimating the

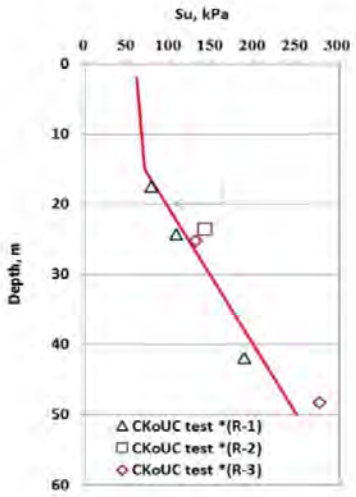

Figure 4: Estimated undrained shear strengths of clays in T2, TK2 and K1 Zones (Hwang et al. 2013)

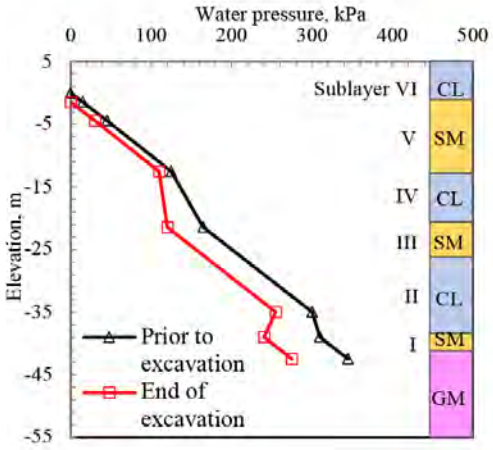

Figure 5: Groundwater pressures on the outer face of the diaphragm walls

undrained shear strengths of the clays in the central city areas, including the T2 Zone, for practical applications.

2.3 Soil Parameters for Hardening-Soil model

The PLAXIS-3D finite element software developed by PLAXIS BV (2013) has become a very popular tool in geotechnical analysis and design. The Hardening-Soil (HS) constitutive soil model (Schanz and Vermeer 1978; Schanz et al. 1989) introduced in the PLAXIS programme is adopted to simulate the non-linear behavior of soils under loading. In the HS model, different stiffness values are used to define the hyperbolic stress-strain relationship. The parameters for the HS soil model are:

E^{ref}_{50} is the reference secant stiffness from standard triaxial test,
E^{ref}_{oed} is the reference tangent stiffness for oedometer primary loading,
E^{ref}_{ur} is the reference unloading-reloading stiffness,
m is the exponential factor for stress-level dependency of stiffness,
R_f is the failure ratio, $R_f = q_a / q_f$,
q_f is the asymptotic value of the shear strength and q_a is the failure strength.

The stress-strain curves could be determined from laboratory tests such as the Ko-consolidated triaxial undrained compression and extension tests. In this study, the stiffness values of soils are related to the undrained shear strengths for clays and to the N values for sands. The empirical relationships expressed in Equations 1 to 4 are adopted in the analysis using the HS soil model:

$$E^{ref}_{50} = 250\ s_u \text{ (for clayey soils)} \quad (1)$$
$$E^{ref}_{50} = 2\ N \text{ (in MPa for sandy soils)} \quad (2)$$
$$E^{ref}_{ur} = 6\ E^{ref}_{50} \quad (3)$$
$$E^{ref}_{oed} = E^{ref}_{50} \quad (4)$$

in which s_u is the undrained shear strengths for clayey soils and N is the blow-counts in standard penetration tests for sandy soils. The soil parameters adopted in the finite element analyses are summarized in Table 1.

Equations 1 to 4 are basically obtained by back-analysis and by matching the deflection profiles observed in the inclinometers SID-2, SID-3 and SID-6. The effective shear strength parameters, i.e., the c' and ϕ' values, for the silty sand strata, are determined from laboratory tests conducted on thin-wall tube specimens. For the clayey layers, c' = s_u and ϕ' = 0° are assumed in the analyses. The dilation angle, ψ', of 2°, 0° and 5° are adopted for the sandy, the clayey and the gravelly soils respectively. The interface reduction factor, R-inter, of 1.0 is adopted.

Table 1: Soil parameters for the HS model adopted in the PLAXIS analyses

Depth m	Soil type	Unit weight γ' kN/m³	N value	Undrained shear strength s_u, kPa	Effective cohesion c' kPa	Effective friction angle ϕ' deg	Dilation angle ψ' deg	Reference stiffness, MPa		Poisson's ratio υ'
								Secant stiffness E^{ref}_{50}	Unload-reload stiffness E^{ref}_{ur}	
0-6	CL	18.8	4	50			0	12.5	37.5	0.35
6-17	SM	19.2	5		0	32	2	10	30	0.30
	SM	19.2	8				2	16	48	0.30
	SM	19.2	11				2	22	66	0.30
17-21	CL	18.6	6	53.7			0	13.4	40.2	0.35
21-25	CL	18.6	17	114.3			0	28.6	85.8	0.35
25-31	SM	19.4	18		0	32	2	36	108	0.30
31-39	CL	18.9		195.0			0	48.6	145.8	0.35
39-44	CL	18.9		241.0			0	60.2	180.6	0.35
44-46	SM	19.7	30		0	32	2	60	180	0.30
46-60	GM	19.9	>100		0	40	5	250	750	0.35

2.4 Groundwater pressures

Piezometers were available in the Jingmei Formation and in the sandy sublayers in the Songshan Formation for monitoring the groundwater pressures. It was observed that prior to excavation, the piezometric levels in the Jingmei Formation, sublayer III and sublayer V were at EL. -9.0 m, EL. -5.0 m and EL. 0 m respectively. As depicted in Figure 5, the piezometric levels outside the diaphragm wall box in the Jingmei Formation, sublayer III and sublayer V dropped to EL. -15.0 m, EL. -9.5 m and EL. -1.5 m respectively at the end of excavation. Inside the pit, the groundwater levels lowered to 1 m below the excavation levels have been adopted in analyses.

3 TWO-DIMENSIONAL ANALYSES ON FREE-FIELD EXCAVATIONS

3.1 Effect of over-excavation and delay in strutting

To start with, 2D analyses are performed for calibrating the soil parameters adopted by comparing the wall deflections computed with those observed in Inclinometer SID-6. This inclinometer is located at 210 m west of the Gate and at 40 m east of the end wall of Xiaonanmen Station as depicted in Fig. 2. As these distances are more than 3 times the width of excavation of 12 m, the observed wall deflections would not likely be affected by the end walls or the cross-walls. The excavation to a depth of 17.8 m at the location of SID-6 was supported by 5 levels of struts S1 to S5, of which the properties are presented in Table 2.

Excavations mainly comprise 2 activities, namely, digging of soils and installation (including preloading) of struts. They are usually carried out by two different subcontractors and are carried out zone by zone. Once the desired depth is reached in each stage, the subcontractor for digging will move to the next zone to keep on digging. The subcontractor for struts installation will then move in to install the struts. This sequential construction essentially creates a three-dimensional (3D) effect on the performance of the bracing system.

Although the construction sequences are normally specified in the designs, in reality, the sequence of excavation is at the contractors' discretion with considerations given to the progress of the works and resource allocations. Due to the lack of the knowledge on how the excavation is to be carried out, this 3D effect is usually ignored by the designers and the excavation in each stage is assumed to be carried out in one shot; and all the struts at the same levels are assumed to be installed and preloaded at the same time. As a result, the wall deflections tend to be over-estimated. The same holds true in back-analyses. However, if the design is conducted by using the parameters calibrated by back-analyses

of previous case histories, the errors made in the back-analyses and the forward analyses would be mutually compensating to each other and the results computed would be suitable for design.

While it is common to specify that excavation shall be carried out to a depth of 1 m below the strut level, over-excavation by 1 m could also be specified to obtain sufficient space below the struts for moving excavators. The effect of over-excavation to wall deflections is taken into account in parameters calibration in this study.

Table 2: Strut properties

Strut level	Depth m	Strut type	Area A_s, cm^2	Stiffness E_sA_s/s, MN/m	Design preload, kN/m	Strut spacing s, m
S1	2.2	1H350x350x12x19	173.9	1,188	120	3.0
S2	5.2	1H400x400x13x21	218.7	1,494	250	
S3	8.2	2H350x350x12x19	347.8	2,377	500	
S4	11.0	2H350x350x12x19	347.8	2,377	500	
S5	14.2	2H400x400x13x21	437.5	2,989	553	
S6	17.0	2H400x400x13x21	437.5	2,989	500	

3.2 Effect of relaxation of preloads in struts

Another important factor, which is very influential to the results of analyses but is often overlooked, is the relaxation of the preloads in struts. In numerical analyses, the struts at the same level are usually assumed to be preloaded at the same time. However, in reality, the struts are preloaded one by one. As one strut is preloaded, the neighboring struts which had already been preloaded are somewhat relaxed and the loads in the struts would be dropped by a certain extent. Besides, the preloads in struts may be relaxed due to many other reasons, such as creeping of soils and/or changes in temperature. Therefore, the preloads shall be reduced in analyses to account for the loss to obtain more realistic results (Hwang and Wong 2018a; Hwang et al. 2018b).

To investigate the effects of over-excavation and loss of preloads to wall deflections, 5 cases are analyzed as summarized in Table 3. In Cases 1a to 1c, the excavation is assumed to stop at a depth of 1 m below the strut levels as normally specified in the design and in Cases 2a and 2b, an over-excavation of 1 m is assumed. The preloads applied on struts in different cases are as depicted in the table.

With 1 m over-excavation, i.e., excavating to a depth of 2 m below the strut levels, the wall deflections computed for the cases with the struts loaded to 100 % (Case 2a) and 50% (Case 2b) of the design preloads are presented in Figures 6b and 6c. The wall deflections computed for the 3 cases without over-excavation are depicted in Figure 7 for comparison. The computed maximum wall deflections and the movements at the toes of the diaphragm walls for the two series of cases are compared in Table 3. It is obvious that over-excavation increases the maximum wall deflections by 4 mm to 5 mm and a relaxation of preloads in struts of 50% would have a similar effect. Completely omission of the design preload would cause further 5 mm wall deflections. This trend of increasing in wall deflections due to the loss of preloads is in agreement with the findings presented in Hwang and Wong (2018a).

Table 3: Comparison of wall deflections with different strut preloads

Case number		Depth of excavation below strut levels, m	Strut preloading, %	Wall deflection in final stage, mm		
				Maximum	Increment due to loss in strut load	Toe
1	1a	1.0	100	33.0	–	5.4
	1b		50	37.7	4.7	5.4
	1c		0	43.0	10.0	5.3
2	2a	2.0	100	36.9	–	4.7
	2b		50	41.0	4.1	4.7

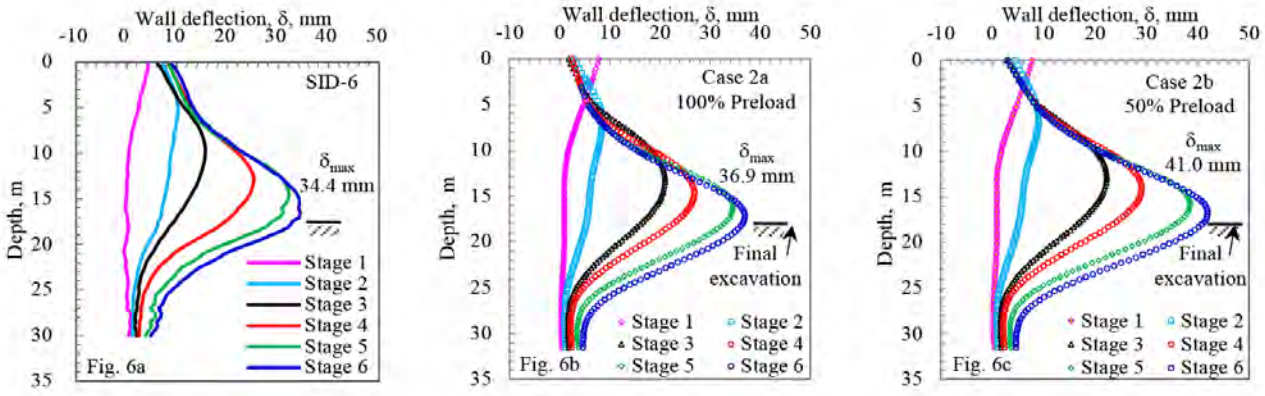

Figure 6: Observed and computed wall deflections with different preloads with over-excavation by 1 m

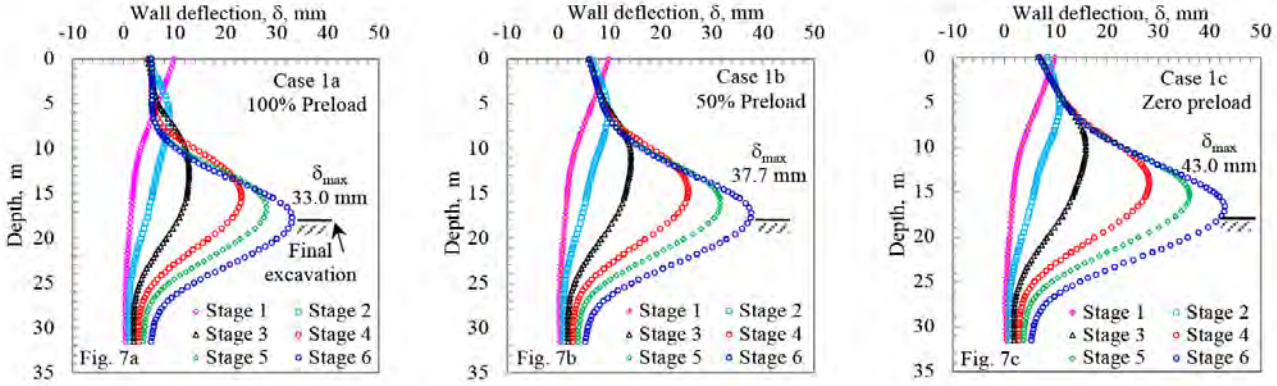

Figure 7: Computed wall deflections for struts with different preloads with normal excavation

3.3 Toe movements of the walls and correction of inclinometer readings

The tips of the inclinometers shall be embedded in competent stratum, for instance, the Jingmei Gravel, so that the tips can be taken as the reference points for interpreting the readings. The tips of inclinometers installed along the cross-over tunnel were however stopped at the toes of the diaphragm walls. The alternative of surveying the movements at the tops of the inclinometers and adopting the tops as the reference points was not conducted neither. In order to correctly interpret the inclinometer profiles, Hwang et al. (2007) proposed to correct the inclinometer readings by assuming the ends of the first-level struts to be unmoved once these struts are preloaded.

Figure 8 compares the deflection profiles at the end of the excavation for 0 %, 50 % and 100 % preloads, with and/or without over-excavation. The wall deflections above the final depth of excavation of 17.8 m are drastically affected by the magnitudes of the preloads. At the first struts level of 3 m depth,

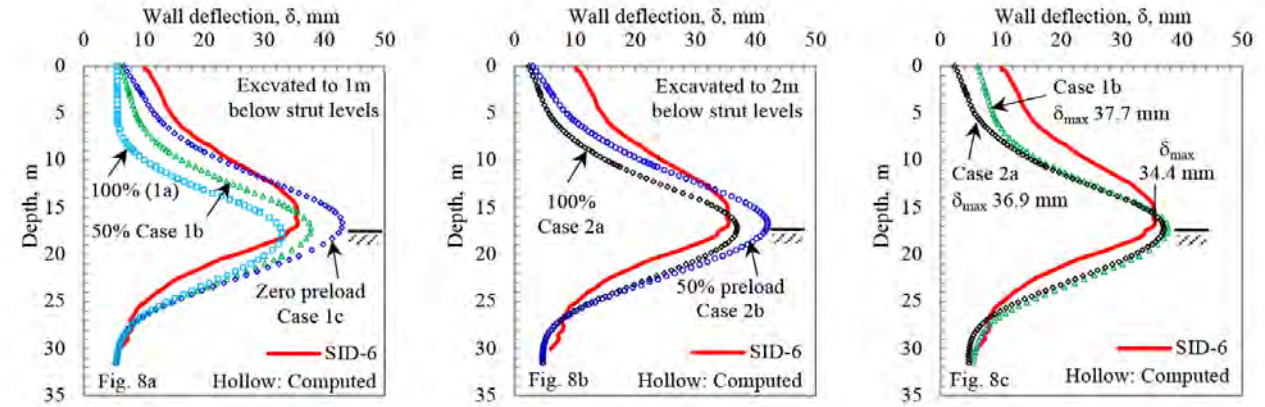

Figure 8. Computed wall deflections in the final stage of excavation with different preloads

Figure 8 show that the wall deflections range from 4 mm to 10 mm for the various preloading cases in the final stage. However, as summarized in Table 3, the toe movements in the final stage are rather unaffected and range from 4.7 mm to 5.4 mm, with the differences less than 1 mm among the various preloading cases. This finding is useful as the diaphragm wall toes can be taken as the reference points for adjusting the inclinometer readings instead of using the ends of the first-level struts. Accordingly, the inclinometer readings for SID-6, SID-2 and SID-3 are adjusted based on the toe movements obtained from the numerical analysis.

3.4 Calibration of the results against the readings obtained by Inclinometer SID-6

As shown in Figure 8c, the computed deflection profiles for Cases 1b and Case 2a fit better with that observed by SID-6 shown in Figure 6a. The performance of the case excavated to 1 m below the strut levels with 50% strut preloads would be quite similar to that excavated to 2 m below the strut levels with 100% preloads. The effect to wall deflections caused by over-excavation is compensated by applying 100% strut preloads. As a general rule, it is thus recommended in designs and in back-analysis to adopt 50% of the design preloads with no over-excavation unless there are data to prove otherwise.

The agreement between the computed deflections with the readings obtained from SID-6, duly corrected to account for toe movements, validates the use of the soil parameters shown in Table 1 in numerical analyses.

4 THREE-DIMENSIONAL ANALYSIS ON CROSS-WALLS

4.1 Modeling of the Gate

Figure 9 shows the 3D finite element model adopted in the analyses on the cross-walls. Although only the western half of the model along the longitudinal direction is shown, a full model is adopted in the analyses. The full model is 60 m in depth, 80 m in the transverse direction and 78 m in the longitudinal direction of the cross-over tunnel. As shown in Figure 1, the lower portion of the Gate is a castle built by using large blocks of rock of 400 mm x 400 mm x 800 mm. The foundation of the Gate is also made of blocks of rock of similar size.

The upper portion of the Gate was originally a masonry structure of a typical old Chinese style and was replaced by a pavilion in 1966. The castle is about 6 m in height and 12 m by 18 m in plan. It is conceivable that the foundation extends 2 m beyond the footprint of the castle, giving an area of 16 m by 22 m in plan dimensions. With due consideration given to the hallway and the empty spaces inside the castle, the surcharge load from the castle, including the weights of castle, the pavilion and

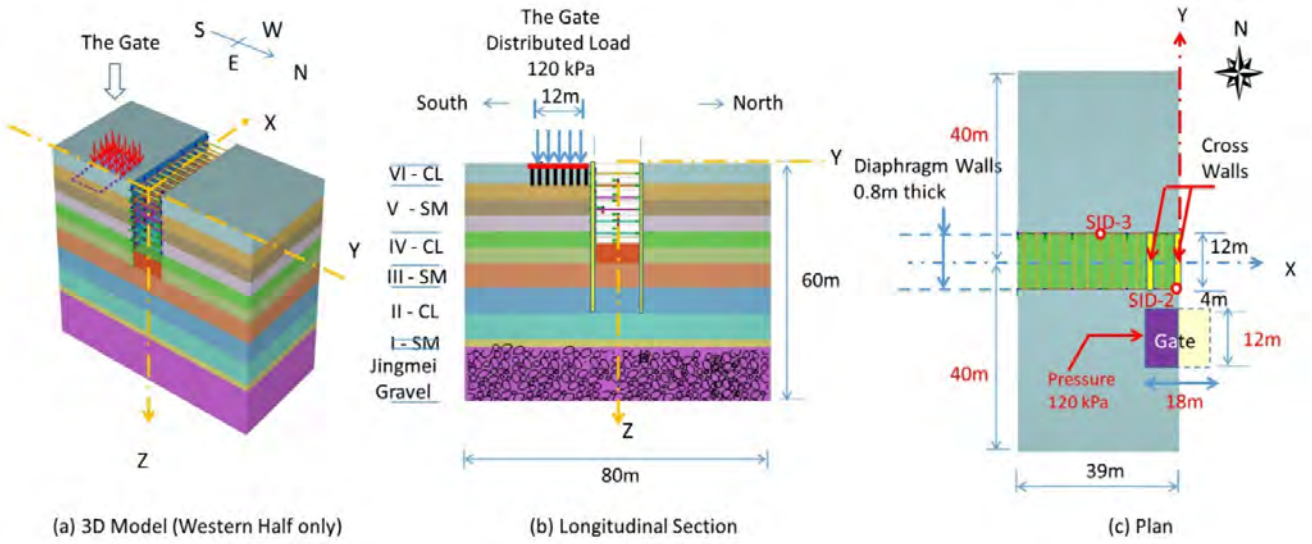

Figure 9: Western half of the 3D finite element model for numerical analyses using PLAXIS

the foundation, is estimated to be around 120 kPa. In consideration of the integrity of the castle and the rubbles foundation, the surcharge load 120 kPa is assumed to apply on a plate element of 0.8 m in thickness with an E value of 36 MPa. Analyses have shown that the rigidity of the plate has no influences on the wall deflections.

Because of the insufficient bearing capacity of the upper soil layers, timber piles were used to support the Gate. Li (2011) reported that timber piles of 3 m to 5 m in length were part of the foundation for a section of the masonry wall exposed at a nearby metro tunnel. For simplicity, these piles are considered as ground treatment in the finite element analyses. Timber piles of 200 mm in diameter are assumed to be installed at 0.6 m spacings to a depth of 6 m. The area ratio of the piles to soil mass is thus about 8.7 %. The E values of hardwoods range from 8 GPa to 15 GPa, and a value of 10 GPa is assumed to be representative. Accordingly, the equivalent E value of the treated soil mass would roughly be 1 GPA. The Poisson's ratio for the treatment zone is assumed to be 0.25.

4.2 Modeling of the supporting structures

The diaphragm walls are simulated by plate elements and an E_c value of 25,000 MPa is adopted for concrete with a characteristic compressive strength, i.e. f'_c value, of 28 MPa. The estimated flexural rigidity (denoted as E_cI_c where I_c is the moment of inertia) and the axial stiffness (denoted as E_cA_c where A_c is the sectional area) of the diaphragm wall are 750 MN-m and 14,056 MN/m respectively. These values are reduced by 30 % for accounting tensile cracks and creeping of concrete during excavation.

Struts are represented by node-to-node anchors. The steel is assumed to be an elastic material with Young's modulus of the steel strut (E_s) of 210 GPa. The structural properties of the struts are shown in Table 2. As mentioned in Section 3.4, the inputted preloads in the struts are reduced by half of those specified in Table 2 in the 3D analyses. The horizontal spacing of the struts (s) is 3.0 m.

4.3 Modeling of the cross-walls

The un-reinforced cross-walls were constructed by the diaphragm walling method. They were cast into the upper and the lower portions as depicted in Figure 3. The upper portions of these cross-walls, poured at the depths between 3 m and 20.1 m, were supposed to be demolished as the excavation proceeded. Therefore, concrete with a very low strength was used. The lower portions, located at the depths between 20.1 m and 25 m, were cast by using normal low-grade concrete.

The 3 cross-walls are modeled as plate elements with the thicknesses of 600 mm. Data are unavailable for estimating the properties of the lean concrete used to cast these cross-walls. In the lack of information, the E value for both the upper and the lower portions of 700 MPa is adopted in analyses. This E value would be validated by comparing the results of the analyses with the readings of Inclinometer SID-2.

5 RESULTS OF 3-DIMENSIONAL ANALYSES

5.1 Scenarios analyzed

The wall deflections obtained at the two ends of the cross-walls in front of the gate, i.e., Locations P2S and P2N (refer to Figure 3 for locations), are of primary interest for evaluating the effectiveness of the piles and the cross-walls in reducing wall deflections. As summarized in Table 4, four scenarios are analyzed to study the effects of the surcharge of the Gate to wall deflections with and without the cross-walls. The computed deflection profiles are presented in Figure 10 to Figure 12.

Firstly, analyses are performed for Scenario 1 in which the excavation is assumed to be conducted in the free-field, i.e., without the Gate nor the cross-walls. The computed wall deflection profiles at Location P2S are given in Figure 10a. A maximum deflection of 34.2 mm is computed as the excavation reached the final depth of 20.1 m. The toe movement at the depth of 31 m is 5.1 mm. Because of symmetry in geometry, the performance of the north wall is the same as that of the south.

The surcharge load of 120 kPa from the Gate increases the maximum deflection of the south wall from 34.2 mm to 41.9 mm as can be noted by comparing the results obtained in Scenario 1 with

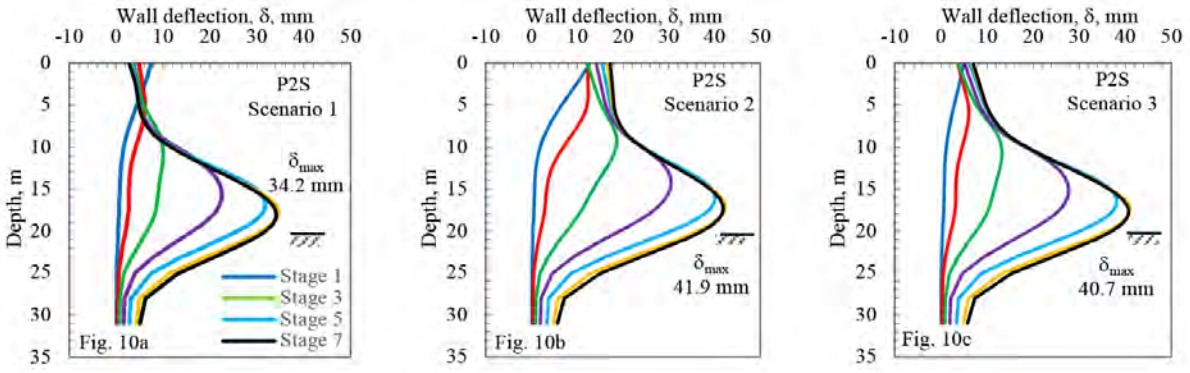

Figure 10: Wall Deflections at P2S obtained in the 3D analyses for Scenarios 1 to 3

Scenario 2 that depicted in Figures 10a and 10b. Figure 10c also shows that the piles under the Gate (Scenario 3) helped only a little as the maximum wall deflection would be reduced by only 1.2 mm, i.e., from 41.9 mm to 40.7 mm. The corresponding toe movements in the final stage in all the 3 scenarios vary from 5.1 mm to 5.8 mm and differ by less than 1 mm.

It can be noted by comparing Figure 10c with Figure 11b that the provision of the cross-walls reduces the maximum deflection of the south wall from 40.7 mm (Scenario 3) to 14.5 mm (Scenario 4). The maximum wall deflections have been reduced significantly by 2/3. The wall toe movements are also reduced from 5.8 mm to 4.2 mm. The cross-walls are thus proved to be indeed effective in reducing the wall deflections.

Table 4: Comparison of wall deflections in the final stage in different scenarios

	Scenario	Section	Maximum wall deflection, mm				Notes
			South	Toe	North	Toe	
1	Free-field excavation	2	34.2	5.1	-34.2	-5.2	Positive and negative values denote movements toward north and south respectively.
2	With gate	2	41.9	5.7	-30.3	-4.5	
3	With gate/piles	2	40.7	5.8	-30.9	-4.4	
4	With gate/piles/cross-walls	2	14.5	4.2	-9.8	-2.8	
	(the benchmark case)	3	33.3	5.3	-30.9	-4.2	

5.2 Calibration the results against the readings obtained by Inclinometers SID-2 and SID-3

Scenario 4 is considered as the benchmark case for further comparisons. The wall deflection profiles obtained by Inclinometer SID-2, duly corrected for the toe movements, are shown in Figure 11a; and the profile at the end of excavation is compared with the profiles obtained from the numerical analyses in Figure 11b. The maximum wall deflection computed in the final stage is 14.5 mm, which is only 0.9

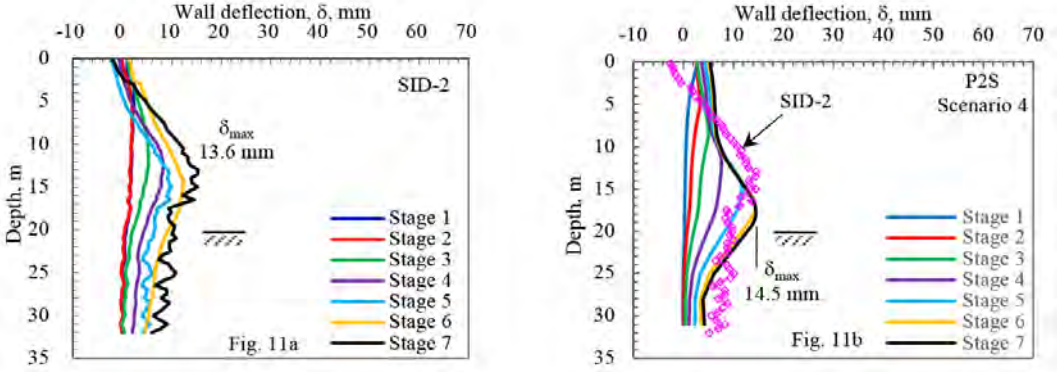

Figure 11: Observed and computed wall deflection profiles at Location P2S - Scenario 4

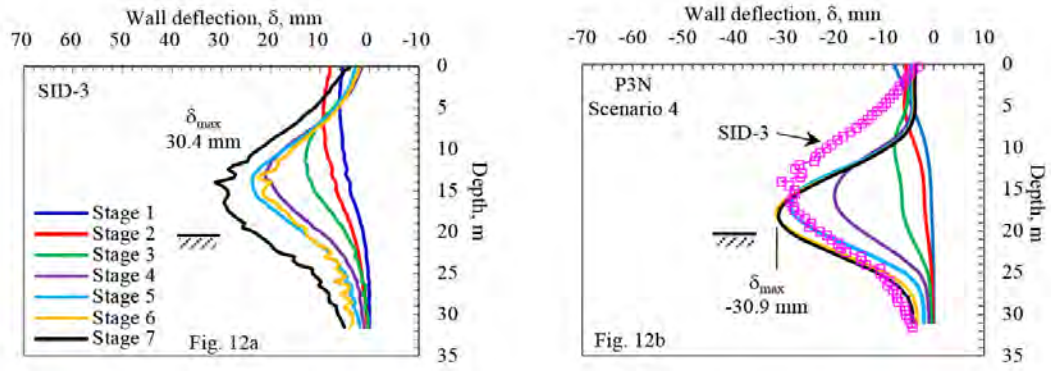

Figure 12: Observed and computed wall deflection profiles at Location P3N – Scenario 4

mm larger than 13.6 mm that observed in SID-2. As the calculated and the observed profiles are closely matched, it could be concluded that the soil parameters adopted, as depicted in Table 1, are appropriate.

Similarly, the wall deflection profiles obtained by SID-3, duly corrected for the toe movements, are shown in Figure 12a; and the measured profile at the end of excavation is compared with those obtained at Location P3N from the analyses in Figure 12b. The maximum deflection in the final stage is 30.9 mm, which is compatible with 30.4 mm that obtained by SID-3, with the readings duly corrected to account for the toe movements.

5.3 Effect of imbalance of earth-pressures and correction of inclinometer readings

The 3D numerical analyses show the occurrence of asymmetric wall deflections on the opposite sides of the excavation. Because of the imbalance of the earth-pressures on the two sides, the entire retaining system would have been pushed northward. As depicted in Figure 13, the longitudinal axis of the pit could move by as large as 22.4 mm at the first strut level in Section 2, where the gate is located, in Scenario 2 due to the surcharge load from the gate. Even with the support of the cross-wall in Scenario 4 (the full model), Figure 14 shows that the transverse movement of the axis of the retaining system would still be as large as 8.2 mm.

Even at a distance of about 12 m away from the edge of the Gate, Figure 15 still indicates a transverse movement of the axis of 3.0 mm in Section 3, refer to Figure 3 for location, in Scenario 4. These movements, caused by imbalance in earth-pressures, are quite significant in comparison with the maximum wall deflections computed in the analyses.

It is thus inappropriate to correct inclinometer readings, as proposed by Hwang et al. (2007), by assuming the ends of the first-level struts to be unmoved once these struts are preloaded. Instead, the tips of the inclinometers (the diaphragm wall toes in this study) shall be assumed as the reference points for the purpose of making corrections. The readings of Inclinometers SID-2 and SID-3 presented in Figure 11a and Figure 12a have been corrected accordingly by adopting the computed toe deflections summarized in Table 4.

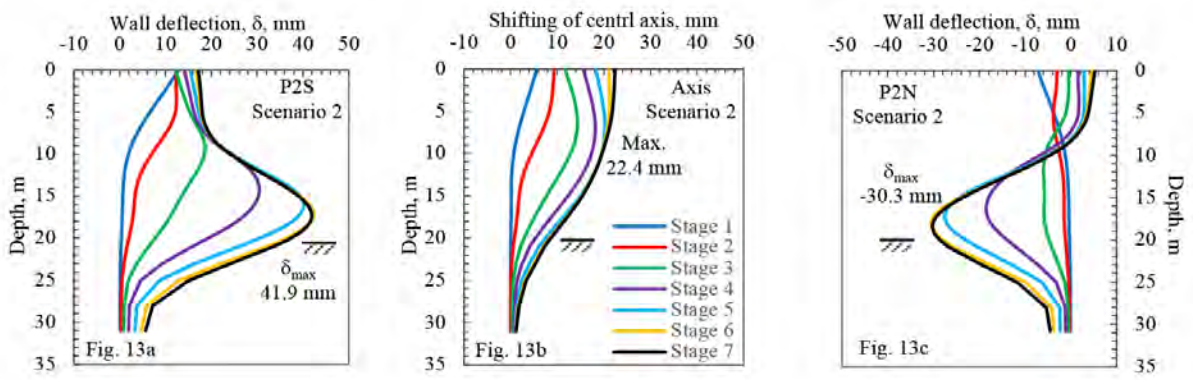

Figure 13: Effect of surcharge from the Gate to wall deflections at Section 2 without cross-wall - Scenario 2

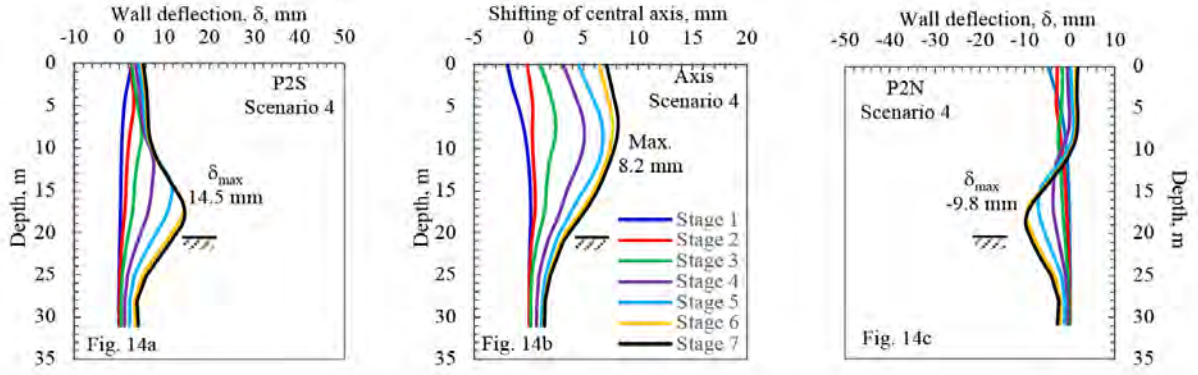

Figure 14: Effect of surcharge from the Gate to wall deflections at Section 2 with cross-wall - Scenario 4

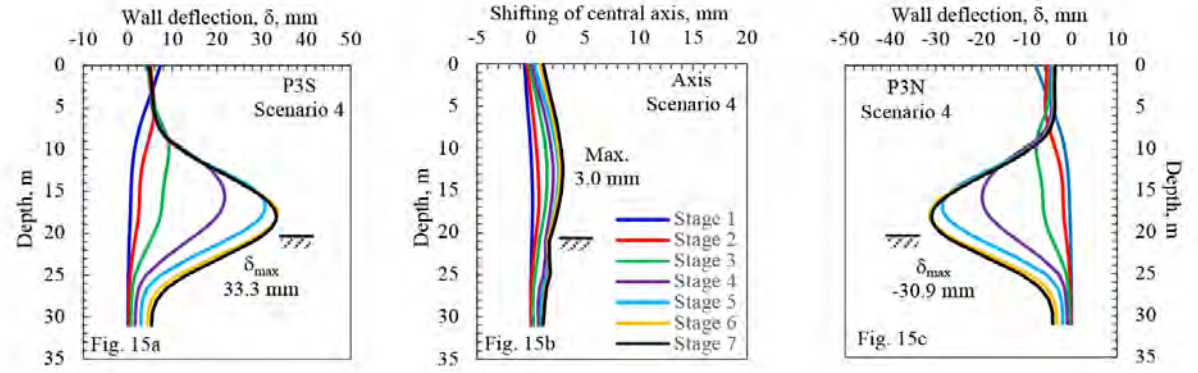

Figure 15. Effect of surcharge from the Gate to wall deflections at Section 3 with cross-wall - Scenario 4

5.4 The extent of the influence of the Gate and the cross-walls

As shown in Figure 10 and Figure 11, the maximum wall deflections occur at around 18 m depth. Figure 16 shows the computed wall deflection profiles at the depth of 18 m along the south and the north wall in the final stage of excavation for Scenarios 2 and 4. Figure 16a shows that at Section 3, which is located at 21 m to the central axis of the Gate, the deflections at the south and the north wall are 36.3 mm and 32.2 mm respectively, with the difference of 4.1 mm. The difference in wall deflections diminishes at around 30 m from the edge of the Gate, where the computed largest deflections at the south and the north wall are 34.3 mm and 33.0 mm respectively, with the difference of 1.3 mm.

With the support of the cross-walls, Figure 16b shows that the deflections at Section 3 at the south and the north wall are 33.3 mm and 30.9 mm respectively, with the difference of 2.4 mm. The difference in wall deflections between the south and the north wall is still significant at Section 3, which is 14 m to the nearest cross-wall. At 39 m from the central axis of the Gate, the computed largest deflections at the south and at the north walls are 33.4 mm and 33.3 mm respectively. It is noted that the wall deflections

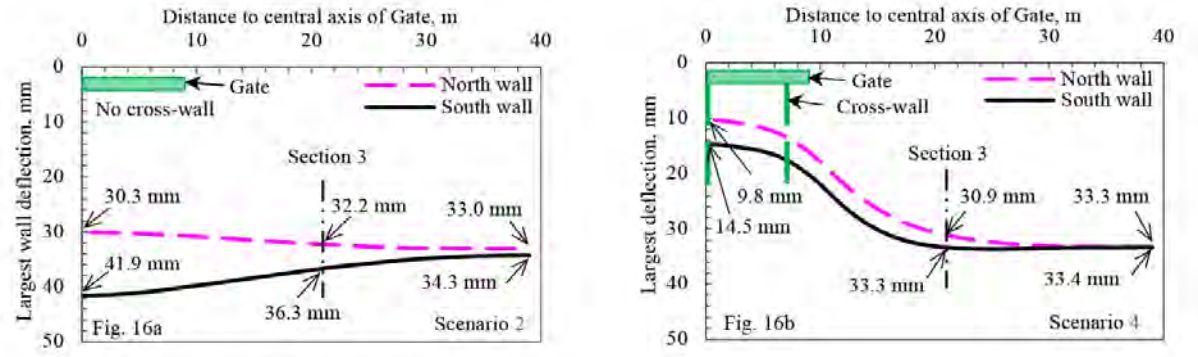

Figure 16: Largest wall deflection profiles along the south and the north wall in final stage - Scenarios 2 and 4

at the mid-point between 2 cross-walls, at 3.5 m to the axis of the Gate, have similar values with those at Locations P2S and P2N.

Adopting the 1 mm difference as the criteria, the influence of the cross-wall would diminish at the distance of 26 m from the Gate, where the computed deflections at the south and the north wall are 33.7 mm and 32.7 mm respectively. The distance from the nearest cross-wall to the end of influence is 19 m, which is approximately 1.5 times of the width of excavation of 12 m. Understanding the influence of the cross-wall would enable rational design on the cross-walls such as determining the spacing, the thicknesses and the depths of the cross-wall panels.

6 CONCLUSIONS

Based on results of two-dimensional and three-dimensional finite element analyses on an excavation braced with cross-walls using the non-linear Hardening-Soil constitutive model, the following conclusions could be drawn:

(1) Both the 2D and the 3D finite element models have been adopted in the analysis on the performance of the excavation for the cross-over tunnel. The matching between the computed wall deflection profiles with those observed in the inclinometers validates the soil parameters adopted for the Hardening-Soil model.

(2) Cross-walls are very effective in reducing wall deflections in deep excavations in soft deposits. The analyses show that the maximum wall deflections have been reduced approximately by 2/3, from 40.7 mm without cross-wall to 14.5 mm with cross-walls.

(3) The 3D analysis shows that the influence of the cross-walls extend to 19 m from the nearest cross-wall panel or approximately 1.5 times the width of excavation.

(4) Translation of the axis of the pit due to the imbalance of the earth-pressures on the two sides of the excavation shall be taken into account in making corrections to the inclinometer readings.

(5) The finite element analyses show that the toe movements of diaphragm walls are significant. In order to correctly interpret the inclinometer readings, the tips of the inclinometers shall be embedded in competent stratum such as the Jingmei Gravel or bedrock. Surveying the displacements at the tops of the inclinometers shall be carried out in case the toe anchorage in the competent stratum is not achieved.

(6) When the tops of inclinometer surveying results are not available, the inclinometer readings shall be corrected by taking the toes of the diaphragm walls at the reference points. The toe deflection values could be obtained from the numerical analysis.

(7) Struts preloading have significant influences on wall deflections and shall be adjusted in the analyses for the purpose of matching the inclinometer readings. In designs, it is proposed to adopt 50 % of the design preloads on struts so that the wall deflections computed could be close to the realistic conditions.

(8) Over-excavation by 1 m would increase the maximum wall deflections by 4 mm to 5 mm and a relaxation of preloads in struts by 50% would have a similar effect of increase in wall deflections. Completely omission of the design preload would cause further 5 mm wall deflections. Workmanship is therefore an important factor influencing the performance of walls. Wall deflections can be reduced by limiting the areas excavated, avoiding over-excavation and by preloading struts promptly.

The data presented above demonstrate how difficult it is to match the results of numerical analyses with the observations because wall deflections are affected by too many factors. Good agreement between the analyzed and the observed values cannot be ascertained either in designs and/or in back analyses. Good agreement can only be hoped but cannot be expected. On the other hand, as computer technology has been improved, user-friendly software packages are now available for, and the hardware is capable of, performing three-dimensional analyses of complicated soil-structural systems at affordable

costs and efforts. This enables studies on the influences of numerous parameters on the performance of the retaining systems in deep excavations to be evaluated more accurately and with ease.

REFERENCES

Chin, C. T., Crooks, A. J. H. and Moh, Z. C. (1994). Geotechnical properties of the cohesive Sungshan deposits. *Geotechnical Engineering, J. Southeast Asian Geotechnical Society,* 25(2), 77-103. (in Chinese)

Chin, C. T. and Liu, C-C. (1997). Volumetric and undrained behaviors of Taipei silty clay. *J. Chinese Institute of Civil and Hydraulic Engineering,* 9(4), 665-678. (in Chinese)

Eide, O., Aas, G, and Jϕsang, T. (1972). Special application of cast-in-place slurry trench walls for tunnel in soft clay in Oslo. *Proc. 5 ECSMFE,* Vol. 1, Madrid 1972, 485-489.

Hwang, R., Moh, Z. C. and Hu, I-C. (2013). Effects of Consolidation and specimen disturbance on strengths of Taipei Clays, *Geotechnical Engineering, J. of SEAGS & AGSSEA,* v44, no. 1, March, Bangkok, 9-18.

Hwang, R. N. and Wong, L. W. (2018a). Effects of preloading of struts on retaining structures in deep excavations. *Geotechnical Engineering, J. of SEAGS & AGSSEA,* June, 49(2), 104-114.

Hwang, R. N., Wang, C-H, and Wong, L. W. (2018b). Verification of back analyses of deep excavations and applications of wall deflection paths. *Sino-Geotech, J. Sino-Geotechnics Research and Development Foundation,* March, 155, 101-116. (in Chinese)

Karlsrud, K. and Andresen, L. (2008). Design and performance of deep excavations in soft clays. *6th International Conference on Case Histories in Geotechnical Engineering,* Arlington, VA. August 11-16.

Lee, S. H. (1996). Engineering geological zonation for the Taipei City. *Sino-Geotechnics, J. Sino-Geotechnics Research and Development Foundation,* March, 54, 25-34. (in Chinese)

Li, C. L. (2011). *The beauty of Taipei architecture.* https://mypaper.pchome.com.tw/tfjxb/post/1322383095/? Show_map=1 (in Chinese).

MAA (1987). *Engineering characteristics of Taipei Clay.* Taipei, Taiwan: MAA Group Consulting Engineers, Taipei.

Moh, Z. C. and Ou C. D. (1979). Engineering characteristics of Taipei Silt. *Proc., 6th Asian Regional Conference on Soil Mechanics and Foundation Engineering,* Singapore, 1, 155-158.

Ou, C.Y., Lin, Y.L. and Hsieh, P.G. (2006). Case record of an excavation with cross-walls and buttress walls. *Journal of GeoEngineering,* Vol. 1, No. 2, December.79-86.

PLAXIS, B. V. (2013). *PLAXIS reference manual.* Plaxis BV, Delft, the Netherlands.

Schanz, T. and Vermeer, P. A. (1998). On the Stiffness of Sands. *Pre-failure Deformation Behaviour of Geomaterials,* ICE, London, UK, 1998.

Schanz, T., Vermeer, P.A. and Bonnier, P.G. (1999). The hardening soil model: formulation and verification. *Beyond 2000 in Computational Geotechnics.* Rotterdam. 281-290.